

IN-22
NASA PT 1

20-273

NASA/CP-1999-209136/PT 1



CEAS/AIAA/ICASE/NASA Langley International Forum on Aeroelasticity and Structural Dynamics 1999

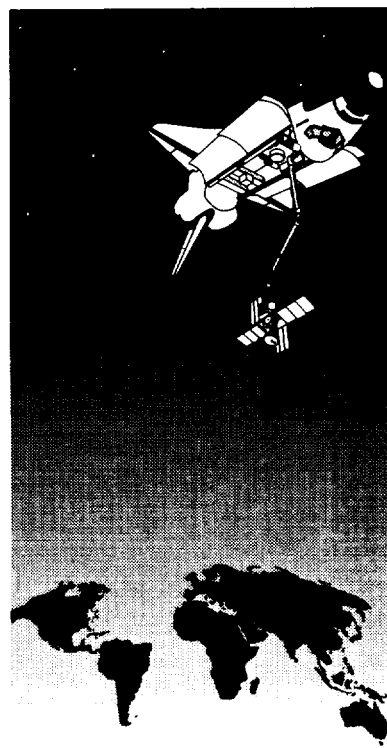
Edited by

Woodrow Whitlow, Jr.

*NASA John H. Glenn Research Center at Lewis Field
Cleveland, Ohio*

Emily N. Todd

*Institute for Computer Applications in
Science and Engineering (ICASE)
Hampton, Virginia*



The NASA STI Program Office . . . in Profile

Since its founding, NASA has been dedicated to the advancement of aeronautics and space science. The NASA Scientific and Technical Information (STI) Program Office plays a key part in helping NASA maintain this important role.

The NASA STI Program Office is operated by Langley Research Center, the lead center for NASA's scientific and technical information. The NASA STI Program Office provides access to the NASA STI Database, the largest collection of aeronautical and space science STI in the world. The Program Office is also NASA's institutional mechanism for disseminating the results of its research and development activities. These results are published by NASA in the NASA STI Report Series, which includes the following report types:

- **TECHNICAL PUBLICATION.** Reports of completed research or a major significant phase of research that present the results of NASA programs and include extensive data or theoretical analysis. Includes compilations of significant scientific and technical data and information deemed to be of continuing reference value. NASA counterpart or peer-reviewed formal professional papers, but having less stringent limitations on manuscript length and extent of graphic presentations.
- **TECHNICAL MEMORANDUM.** Scientific and technical findings that are preliminary or of specialized interest, e.g., quick release reports, working papers, and bibliographies that contain minimal annotation. Does not contain extensive analysis.
- **CONTRACTOR REPORT.** Scientific and technical findings by NASA-sponsored contractors and grantees.

- **CONFERENCE PUBLICATION.** Collected papers from scientific and technical conferences, symposia, seminars, or other meetings sponsored or co-sponsored by NASA.
- **SPECIAL PUBLICATION.** Scientific, technical, or historical information from NASA programs, projects, and missions, often concerned with subjects having substantial public interest.
- **TECHNICAL TRANSLATION.** English-language translations of foreign scientific and technical material pertinent to NASA's mission.

Specialized services that complement the STI Program Office's diverse offerings include creating custom thesauri, building customized databases, organizing and publishing research results . . . even providing videos.

For more information about the NASA STI Program Office, see the following:

- Access the NASA STI Program Home Page at <http://www.sti.nasa.gov>
- Email your question via the Internet to help@sti.nasa.gov
- Fax your question to the NASA STI Help Desk at (301) 621-0134
- Telephone the NASA STI Help Desk at (301) 621-0390
- Write to:
NASA STI Help Desk
NASA Center for AeroSpace Information
7121 Standard Drive
Hanover, MD 21076-1320

NASA/CP-1999-209136/PT 1



CEAS/AIAA/ICASE/NASA Langley International Forum on Aeroelasticity and Structural Dynamics 1999

Edited by

*Woodrow Whitlow, Jr.
NASA John H. Glenn Research Center at Lewis Field
Cleveland, Ohio*

*Emily N. Todd
Institute for Computer Applications in
Science and Engineering (ICASE)
Hampton, Virginia*

Proceedings of a workshop sponsored by the Confederation of European Aerospace Societies (CEAS), the American Institute of Aeronautics and Astronautics (AIAA), the National Aeronautics and Space Administration (NASA), Washington, D. C., and the Institute for Computer Applications in Science and Engineering (ICASE), Hampton, Virginia, and held in Williamsburg, Virginia
June 22-25, 1999

National Aeronautics and
Space Administration

Langley Research Center
Hampton, Virginia 23681-2199

June 1999

The use of trademarks or names of manufacturers in this report is for accurate reporting and does not constitute an official endorsement, either expressed or implied, of such products or manufacturers by the National Aeronautics and Space Administration.

Available from:

NASA Center for AeroSpace Information (CASI)
7121 Standard Drive
Hanover, MD 21076-1320
(301) 621-0390

National Technical Information Service (NTIS)
5285 Port Royal Road
Springfield, VA 22161-2171
(703) 605-6000

PREFACE

Aeroelasticity is a multidisciplinary technology area that integrates steady and unsteady aerodynamics and elastic structures. Its importance has been recognized and considered since the early days of flight. It is critical in that proper aeroelastic design reduces or eliminates the need for costly fixes later in the development process. As the performance of vehicles increased, the need for control systems to control the structural responses increased and, for very high-speed vehicles, the effects of structural heating on the structural dynamic response had to be modeled. The advent of the computer led to the development of computational unsteady aerodynamics methods that are used to predict aeroelastic response across the aircraft flight envelope. The effects of aerodynamics and elastic structures must be considered and modeled accurately to predict aeroelastic responses and to provide data for designing active control systems. In recent years, smart materials and adaptive structures have been introduced as a means to control the response of flexible structures.

Even as prediction methods advanced, the role of testing maintained its importance in the design and certification processes. Models have improved, allowing for more realistic representation of aircraft. Facility capabilities have increased, measurement techniques have improved, and the prediction methods have been used to guide tests. This resulted in more efficient and effective use of test facilities.

As we strive to improve the performance of aircraft during flight, we have made significant advances in understanding their behavior during ground operations. The dynamic response during taxi, takeoff, and landing have been shown to be critical to the performance of the flight crew, to the ride comfort of the passengers, and to the safe operations of aircraft. The design of landing gear, brakes, and tires is taking on more importance in the aircraft design process.

With the importance of aeroelasticity and structural dynamics increasing in the design and operation of aircraft and spacecraft, it was with great pleasure that I accepted the responsibility of serving as Technical Chair of the International Forum on Aeroelasticity and Structural Dynamics 1999. I would like to thank the CEAS Specialists Committee on Structures and Materials for allowing me to take on this important and honorable task. This is the premier gathering of aeroelasticians and structural dynamicists anywhere. We have an outstanding program that will spark rewarding discussion and lead to many advances in the future. Because of the success of this forum, I feel honored to recognize those who worked so diligently to make this great event happen.

I would like to acknowledge Irving Abel for his efforts in bringing this outstanding forum to the United States for the first time. The Program Committee members deserve special congratulations for their efforts in selecting an outstanding series of papers to be presented. I thank the Organizing Committee members, especially Dr. Robert Moses, for their help with the organization of the forum. Mr. Lee Pollard deserves recognition for his efforts in designing the artwork that is featured on the forum program and on the website. Finally, I wish to acknowledge the outstanding support of Ms. Emily N. Todd of the Institute of Computer Applications in Science and Engineering for all of her help in addressing the administrative details necessary to make the conference a success and in preparing this document.

Woodrow Whitlow, Jr.
NASA John H. Glenn Research Center at Lewis Field

Organizing Committee:

Howard M. Adelman, NASA Langley Research Center, Hampton, VA, USA
Peretz P. Friedmann, University of Michigan, Ann Arbor, USA
Robert W. Moses, NASA Langley Research Center, Hampton, VA, USA
Thomas E. Noll, NASA Langley Research Center, Hampton, VA, USA
Boyd Perry III, NASA Langley Research Center, Hampton, VA, USA
Emily Todd, Institute for Computer Applications in Science and
Engineering, Hampton, VA, USA (Administrative Chair)
Woodrow Whitlow, Jr., NASA John H. Glenn Research Center at Lewis Field,
Cleveland, OH, USA (Technical Chair)

Program Committee:

H. Climent, CASA, Madrid, Spain
L. Balis Crema, University of Rome "La Sapienza", Rome, Italy
P. P. Friedmann, University of Michigan, Ann Arbor, USA
H. G. Höninger, DLR-Institut für Aeroelastik, Göttingen, Germany
R. Labourdette, ONERA, Chatillon, France
A. J. Morris, Cranfield University, Cranfield, UK
M. Nash, Defence Research Agency, Farnborough, UK
M. Pecora, CIRA, Capua, Italy
C. Petiau, Dassault Aviation, Saint Cloud, France
R. Pyrah, B. Ae. Military Aircraft, Warton, UK
O. Sensburg, DASA, Daimler-Benz Aerospace AG
Munich-Ottobrunn, Germany
C. Stavrinidis, ESA/ESTEC, Noordwijk, The
Netherlands
G. R. Tomlinson, The University of Sheffield, Sheffield, UK
W. Whitlow, Jr., NASA John H. Glenn Research Center at Lewis Field,
Cleveland, OH, USA
B. Winzell, SAAB, Linkoping, Sweden
R. J. Zwaan, NLR, Amsterdam, The Netherlands

CONTENTS

PREFACE	iii
---------------	-----

PART 1

COMPUTATIONAL FLUID DYNAMICS

A New Compendium of Unsteady Aerodynamic Test Cases for CFD: Summary of AVT WG-003 Activities	1 - /
Luis P. Ruiz-Calavera, Robert Bennett, John H. Fox, Robert W. Galbraith, Evert Geurts, Michael J deC Henshaw, XingZhong Huang, Ian W. Kaynes, Thomas Löser, Pierre Naudin, and Masato Tamayama	

FLEXIBLE AIRCRAFT

A Combined Modal/Finite Element Analysis Technique for Nonlinear Beam Dynamic Response Under Harmonic Excitation	13 ✓
Matthew I. McEwan, Jan R. Wright, Jonathan E. Cooper, and Andrew Y. T. Leung	
An H_∞ Approach to Control Synthesis with Load Minimization for the F/A-18 Active Aeroelastic Wing	23 ~3
Rick Lind	

MULTIDISCIPLINARY DESIGN OPTIMIZATION

Aeroelastic Constraints in MDO	33 ~4
F. Mastroddi, E. Ciancaleoni, and L. Morino	
MDO of an Innovative Configuration – Aerodynamic Issues	43 ~5
G. Bernardini, A. Frediani, and L. Morino	

LIMIT CYCLE OSCILLATION

Simulation of Nonlinear Airfoil/Control-Surface Flutter at Subsonic Speeds using Classical Unsteady Aerodynamics and an Euler Method	53 ~6
Silvio Schulze	
Limit Cycle Oscillation Prediction Using Artificial Neural Networks	71 ~7
Charles M. Denegri, Jr. and Michael R. Johnson	

TEST METHODS

A Procedure to Improve Convergence and Accuracy of Iterative Model Updating Methods	81 ~8
Stefan Keye	
Computer-controlled Normal Mode Tuning	89 ~9
J. M. Sinapius and R. C. Lake	

Vibro-Acoustics Modal Testing at NASA Langley Research Center 101 - 10
Richard S. Pappa, Jocelyn I. Pritchard, and Ralph D. Buehrle

Wind Tunnel Tests and Analysis on Flutter of Spacecraft Including Pitching Effects in Its Launching Configuration 115 - 11
Atsushi Kanda and Tetsuhiko Ueda

TILTROTOR

Aeroelastic Tailoring for Stability Augmentation and Performance Enhancements of Tiltrotor Aircraft 121 - 12
Mark W. Nixon, David J. Piatak, Lawrence M. Corso and David A. Popelka

Analysis of Fuselage Vibrations Induced by the Proprotor in a Tiltrotor Aircraft 139 - 13
M. Gennaretti and U. Iemma

Multi-Body Analysis of an Active Control for a Tiltrotor 149 - 14
G.L. Ghiringhelli, P. Masarati, P. Mantegazza, and M. W. Nixon

Rotary Wing Test Stand Capability for the Republic of Korea 159 - 15
Jeffrey Breaks and Michael Cooper

PANEL FLUTTER

Review of Nonlinear Panel Flutter at Supersonic and Hypersonic Speeds 171 - 16
Chuh Mei, K. Abdel-Motagaly, and R. Chen

Nonlinear Response of Composite Panels under Combined Acoustic Excitation and Aerodynamic Pressure 189 - 17
K. Abdel-Motagaly, B. Duan, and C. Mei

Panel Flutter Analyses for the First Brazilian Satellite Launcher 201 - 18
J. G. Damilano, Jamil C. Said, and João L. F. Azevedo

LANDING DYNAMICS I

Self-Induced Brake Torque Oscillations of Landing Gear as an Interaction of Non-linear Tyre with Brake Control System 211 - 19
Wolfgang G. Luber

Nonlinear Transient Whirl Vibration Analysis of Aircraft Brake Systems 225 - 20
Craig F. Chang

CERTIFICATION

An Unsteady Aerodynamics Identification Procedure for Flutter Prediction 235 - 21
S. Prudhomme, C. Blondeau, M. Humbert, and A. Bucharles

Parameter Estimation in Flutter Analysis by Wavelet and Neural Network 245 - 22
Y. S. Wong, B. H. K. Lee, and T. K. S. Wong

Flutter Speed Prediction during Flight Flutter Testing Using Neural Networks 255 - 23
J. E. Cooper and W. J. Crowther

Overview of Recent Flutter Boundary Prediction Techniques Based on Testing	265	~24
Data Analysis		
Pei Chengming, Qiu Zihua, and Zhai Kun		

COMPUTATIONAL FLUID DYNAMICS II

Aeroelasticity Simulations in Turbulent Flows	275	~25
Jean-Pierre Grisval, Cédric Liauzun and Zdeňek Johan		

FLUTTER CONTROL

Active Control of Flutter in Compressible Flow and Its Aeroelastic Scaling	287	~26
E. Presente and P. P. Friedmann		

New Experimental Stall Flutter Active Control of a Bridge Section	311	~27
L. Lecce, E. Selvaggi, F. Nicolosi, M. Baruffo, and A. Abate		

STRUCTURAL OPTIMIZATION

A Reduced Basis Model for Aeroelastic Optimization	325	~28
S. Grihon and J. P. Esquerre		

A Survey of Shape Parameterization Techniques	333	~29
Jamshid A. Samareh		

Reduced Order Design-Oriented Stress Analysis using Combined Direct and Adjoint Solutions	345	~30
Eli Livne and Guillermo D. Blando		

REDUCED-ORDER MODELS

Reduced-Order Models Based on Linear and Nonlinear Aerodynamic Impulse Responses	369	~31
Walter A. Silva		

NONLINEARITY

Transonic Flutter Suppression Control Law Design, Analysis, and Wind Tunnel Results	381	~32
Vivek Mukhopadhyay		

TESTING

Wavelet Applications for Flight Flutter Testing	393	~33
Rick Lind, Marty Brenner and Lawrence C. Freudinger		

LINEAR METHODS

Aerodynamic and Aeroelastic Insights using Eigenanalysis	403	~34
Jennifer Heeg and Earl H. Dowell		

Influence of Nonplanar Supersonic Interference on Aeroelastic Characteristics	415	~35
V. Kouzmin, S. Kouzmina, V. Mosounov and F. Ishmuratov		

An Application of the P-Transform Method for Transient Maneuvering Analysis	425	-36
John R. Dykman and William P. Rodden		

A Damping Perturbation Method for Flutter Solution: The g-Method	433	-37
P. C. Chen		

PART 2*

AEROELASTIC APPLICATIONS I

Vortex-Lattice-Method to Analyze Aerodynamic Interference of Wing/Pylon/Store Configurations of an F-16 Wing	443	
J. Cattarius, S. Preidikman, D. T. Mook, and D. J. Inman		

Flutter Stability of Movable Control Surfaces for Aircraft Stores	457	
Claudio Ponzi and Johannes Schweiger		

STRUCTURE AND AERODYNAMICS INTEGRATION

Structural Optimization using Computational Aerodynamics	469	
Daniella E. Raveh, Yuval Levy and Moti Karpel		

Multidisciplinary Aero-Structural Modeling on Parallel Computers	483	
Ryoichi Onishi, Toshiya Kimura, Zhihong Guo, and Toshiyuki Iwaniya		

Astros: Seamless Integration of Astros with a Unified Aerodynamic Module: Applications Benchmarking and Testing	491	
A. G. Striz and S. Y. Jung		

NONLINEAR FLUTTER

Characterizing the Effects of Geometrical Nonlinearities on Aeroelastic Behavior of High-Aspect Ratio Wings	501	
Mayuresh J. Patil, Dewey H. Hodges, and Carlos E. S. Cesnik		

Simulation of Nonlinear Transonic Aeroelastic Behavior on the B-2	511	
D. R. Dreim, S. B. Jacobson, and R. T. Britt		

Singular Perturbation Technique for Nonlinear Aeroelastic Analysis	523	
D. Dessi and F. Mastroddi, and L. Morino		

Application of The Centre Manifold Theory in Nonlinear Aeroelasticity	533	
L. Liu, Y. S. Wong, and B. H. K. Lee		

DEVICES

Flutter Suppression and Vibration Control of Plate-Wing Structures Using Self-Sensing Active Constrained Layer Damping	543	
Jeng-Jong Ro and Ehab Elsaadawy		

An Examination of Applying Shunted Piezoelectrics to Reduce Aeroelastic Response	553	
Anna-Maria Rivas McGowan		

*Part 2 is presented under separate cover.

A Comparison Study of the Performance of a Saturation Absorber and Classical Vibration Control Methods	573
Hanafy M. Omar and Donald Kunz	
Creation of a Finite Element Model for F/A-18 Structural Dynamic Analyses Based on Ground Vibration Test Data	585
S. A. Dunn	
Effects of Transient Hypersonic Flow Conditions on Failure Prediction of Panels	595
Radu Udrescu and Giuseppe Surace	
Nonlinear Regular and Chaotic Flutter of an Airfoil with a Trailing Edge Flap in Supersonic Flow	605
Z. Dzygadlo, I. Nowotarski, and A. Olejnik	

BUFFET

Correlation of Fin Buffet Pressures on an F/A-18 with Scaled Wind-Tunnel Measurements	615
Robert W. Moses and Gautam H. Shah	
Twin-Tail Buffet Simulation using a Multi-Disciplinary Computing Environment (MDICE)	627
Essam F. Sheta, John M. Siegel, Jr., Freddy N. Golos and Vincent J. Harrand	
Adaptive Suction and Blowing for Twin-Tail Buffet Control	639
Osama A. Kandil and Zhi Yang	

LANDING DYNAMICS II

An Overview of Landing Gear Dynamics	649
Jocelyn Pritchard	
Actively Controlled Landing Gear for Aircraft Vibration Reduction	665
Lucas G. Horta, Robert H. Daugherty and Veloria J. Martinson	
Aircraft and Ground Vehicle Winter Runway Friction Assessment	679
Thomas J. Yager	

AEROELASTIC TAILORING

Application of Direct Search Method to Aeroelastic Tailoring of an Arrow Wing Configuration	691
Koji Isogai	
Ply Angle Optimization of Non-Uniform Composite Beams Subject to Aeroelastic Constraints	699
T. Evrard, R. Butler, S. W. Hughes, and J. R. Banerjee	
Influence of Aeroelastic Tailoring in the Multidisciplinary Design of a New Aircraft	709
Roland Kelm, Michael Dugas, Rudolf Voit-Nitschmann, and Michael Grabietz	

Synergistic Interaction of Aeroelastic Tailoring and Boundary Moment Control on Aircraft Wing Flutter	719
Frank H. Gern and Liviu Librescu	

FLUID-STRUCTURE INTERACTION

Non-Linear Fluid and Structures Interaction Simulation	735
Reid B. Melville and Raymond E. Gordnier	
Divergence and Flutter of Adaptive Laminated Composite Aircraft Wings Featuring Damaged Bonding Interfaces	747
L. Librescu, U. Icardi and M. Di Sciuva	

AEROELASTIC APPLICATIONS II

Improving the Convergence of the Doublet-Lattice Method Through Tip Corrections	763
Myles L. Baker and William P. Rodden	
Aeroelastic Analysis of a Trimmed Generic Hypersonic Vehicle	777
I. Nydick and P. P. Friedmann	
Stiffness and Damping Effects of Launch Vehicle Aeroelastic Coupling	811
K. W. Dotson, R. L. Baker, and B. H. Sako	

SYSTEM MODELING

Finite Element Model Updating using Experimental Vibration Data: Parameterisation and Regularisation	821
Michael I. Friswell, and John E. Mottershead	
Optimal System Realization in Frequency Domain	831
Jer-Nan Juang and Peiman G. Maghami	
Identification of a Non-Proportionally Damped Truss Structure	847
Steven Naylor, Jan R. Wright and Jonathan E. Cooper	
Nonlinear Aeroelastic System Identification via Wavelet Analysis in the Neighbourhood of a Limit Cycle	857
F. Mastroddi and A. Bettoli	

A New Compendium of Unsteady Aerodynamic Test Cases for CFD: Summary of AVT WG-003 Activities

51-02

Luis P. Ruiz-Calavera, INTA, Spain (ruizcl@inta.es)

Robert Bennett, NASA Langley Research Center, USA (r.m.bennett@larc.nasa.gov)

John H. Fox, Sverdrup Technology, Inc., USA (fox@hap.arnold.af.mil)

Robert W. Galbraith, Glasgow University, UK (r.a.m.galbraith@aero.gla.ac.uk)

Evert Geurts, NLR, The Netherlands (geurts@nlr.nl)

Michael J deC Henshaw, BAe, UK (Michael.Henshaw@bae.co.uk)

XingZhong Huang, IAR, Canada (xingzhong.huang@nrc.ca)

Ian W. Kaynes, DERA Farnborough, UK (iwkaynes@dra.hmg.gb)

Thomas Löser, DLR Braunschweig, Germany (Thomas.Loeser@dlr.de)

Pierre Naudin, ONERA, France (naudin@onera.fr)

Masato Tamayama, NAL, Japan (masato@nal.go.jp)

INTRODUCTION

With the continuous progress in hardware and numerical schemes, Computational Unsteady Aerodynamics (CUA), that is, the application of Computational Fluid Dynamics (CFD) to unsteady flowfields, is slowly finding its way as a useful and reliable tool (turbulence and transition modeling permitting) in the aircraft, helicopter, engine and missile design and development process. Before a specific code may be used with confidence it is essential to validate its capability to describe the physics of the flow correctly, or at least to the level of approximation required, for which purpose a comparison with accurate experimental data is needed. Unsteady wind tunnel testing is difficult and expensive; two factors which dramatically limit the number of organizations with the capability and/or resources to perform it. Thus, unsteady experimental data is scarce, often classified and scattered in diverse documents. Additionally, access to the reports does not necessarily assure access to the data itself. The collaborative effort described in this paper was conceived with the aim of collecting into a single easily accessible document as much quality data as possible.

The idea is not new. In the early 80's NATO's AGARD (Advisory Group for Aerospace Research & Development) Structures and Material Panel (SMP) produced AGARD Report No. 702 'Compendium of Unsteady Aerodynamic Measurements', which has found and continues to find extensive use within

the CUA community. In 1995 AGARD's Fluid Dynamics Panel (FDP) decided to update and expand the former database with new geometries and physical phenomena, and launched Working Group WG-22 on 'Validation Data for Computational Unsteady Aerodynamic Codes'. Shortly afterwards AGARD was reorganized as the RTO (Research and Technology Organization) and the WG was renamed as AVT (Applied Vehicle Technology) WG-003. Contributions were received from AEDC, BAe, DLR, DERA, Glasgow University, IAR, NAL, NASA, NLR, and ONERA. The final publication with the results of the exercise is expected in the second part of 1999.

The aim of the present paper is to announce and present the new database to the Aeroelasticity community. It is also intended to identify, together with one of the groups of end users it targets, deficiencies in the compendium that should be addressed by means of new wind tunnel tests or by obtaining access to additionally existing data.

REQUIREMENTS FOR EXPERIMENTS

The type of experiment included in the database falls under the general category of validation experiments, that is, those made on geometrically simple "generic shapes" designed to provide sufficiently detailed measured data for the verification of the physical representation provided by the CFD code. This requires that the data be taken and presented in a form and level of detail consistent with CFD requirements and that the accuracy of the experimental data be thoroughly documented and understood. The ideal test case should thus provide:

- a) Accurately measured model shape and surface finish.
- b) The actual position and motion of all points of the model, including both static and dynamic elastic deformations.
- c) Well defined state of the boundary layer on the model.
- d) Inflow and outflow conditions.
- e) Wall conditions and wall boundary layer.
- f) Specification of support interference
- g) Specification of the accuracy of the measured data.

After a thorough screening of the candidate test cases available for general distribution, it was found that ideal test cases are rare indeed, so the acceptance criteria had to be dramatically modified to the minimum requirements of knowing the geometry, and the motion, as accurately as possible. Nevertheless the authors believe the test cases included in the database to be generally of very high quality. Wherever possible experiments have been selected which include test points with different levels of physical difficulty, so that the CFD researcher can use a staircase approach to the problem of validating the code.

COMPUTATIONAL RESULTS

In addition to the experimental data, the database includes computational results. Before a code can be validated, the developer must verify that it solves accurately the mathematical model of the real world that it uses. Given the lack of analytical solutions to the 3-D versions of the various sets of equations of interest to CUA, verification is best achieved by means of comparison with another computational

solution of the same set of equations.

To this aim a benchmark exercise was performed on the F-5 wing. Computational results covering the whole spectrum from Transonic Small Perturbations to Navier-Stokes codes were generated and are provided in the database, thus facilitating the verification of the new code against the same level of physical modeling. Some results of this exercise are presented in another paper of this meeting.

Additionally, attempts have also been made to complement each experimental data set with an example of a numerical calculation of at least one of its test points. These results may also be useful in cases where the CFD developer finds intriguing differences with experimental data, which cannot be attributed in a straightforward way to deficiencies in the numerical model, or in the test. Comparison with another computational result may clarify whether code improvement is required. Unfortunately it has not been possible to obtain numerical results for all the test cases, but the door is left open for interested groups to submit their calculations to complete the picture. These 'late arrivals' could be compiled as an addendum to the database.

No claim is made that these, or any of the other CFD solutions included, are free of discretization or solution errors. They should be treated as examples of what people with experience in the field have produced using mature codes, but not as absolute truth.

ORGANIZATION OF THE DATA BASE

The compendium includes 20 self-contained test cases, which are summarized in Table 1. They address different phenomena, namely:

- Flutter
- Buffet
- Stability & Control
- Dynamic Stall
- Cavity Flows
- Store Separation

For each test case the following information is provided:

- A brief overview of the purpose and salient features of the experiment.
- A standard form (the same prepared in AGARD Report 702, which was considered to be still appropriate and difficult to improve) with the key information about the test conditions and equipment that a user may require.
- An example of the layout of the data files provided.
- Figures and pictures to illustrate the case.
- The data itself is provided in machine-readable form in a CD-ROM that accompanies the publication.

Whenever there are associated CFD results, they are contained in an accompanying chapter.

OVERVIEW OF THE CASES

Most of the test cases provided are well known ones, which have already been extensively reported in symposia and/or scientific journals. A brief description of those more relevant for aeroelastic applications is provided in the following.

F-5 Wing + Tip Store

The database starts with the well-known F-5 wing tested at the High Speed Wind Tunnel of NLR [1]. The original purpose of the experiment was to determine the unsteady airloads characteristics on a representative fighter type wing oscillating in pitch. It constitutes a very comprehensive data set, which progressively builds up in geometric complexity from the clean wing to a wing with a tip launcher and an A-A missile (Fig. 1). From a computational point of view, the clean wing case can be considered as rather benign, as it involves only small static angles of attack, small amplitudes of oscillation and limited viscous effects. This fact together with its simple geometry and wide range of Mach numbers tested (from subcritical to low supersonic) make it an ideal 'first case' in the validation process of a new code. This was the main reason why it was selected for the benchmark exercise mentioned before. On the other hand, the wing plus launcher plus missile cases provide excellent opportunities to check the ability of the code to tackle rather complex geometries.

Rectangular Supercritical Wing

The Rectangular Supercritical Wing model RSW [2] was tested at the NASA Langley Transonic Dynamic Tunnel with the specific aim of obtaining data for CFD comparison. It has a simple low aspect ratio unswept rectangular planform with no twist, a constant 12% thick supercritical airfoil and a tip of revolution. The model undergoes pitching oscillations. Data is provided corresponding to a wide range of flow conditions from low subsonic to strong transonic well beyond the design Mach number, as would be required for flutter verification beyond cruise conditions. A broad range of reduced frequencies is also covered. Special care has been taken to select data points, which illustrate the trends with Mach number, reduced frequency, amplitude of oscillation and static angle of attack. Some cases for high angle of attack (at low speed) and others for the effect of transition have been also included. Despite its simple geometry, the case has proved to be a difficult one to calculate. Typically for low-aspect ratio rectangular wings, transonic shock waves tend to sweep forward from root to tip such that there are strong three-dimensional effects. Additionally it has been found to be very sensitive to viscous and transition effects, specially on the undersurface.

Benchmark Model Program

NASA's Benchmark Model Program (BMP) tested a series of models in the Langley Transonic Dynamics Tunnel with the primary objective of assisting in the evaluation of aeroelastic CUA codes. The present database includes results from three of the models, all of which have an identical rectangular planform. The first model has a NACA0012 airfoil which develops strong shocks [3]; the second model has a supercritical SC(2)0414 airfoil which generates weaker hard to capture shocks [4]; and the last model, called the Benchmark Active Controls Technology BACT [5], has again a

NACA0012 airfoil but with a trailing edge control surface, and a pair of independently actuated upper and lower surface spoilers. All the models were mounted on the PAPA (Pitch and Plunge Apparatus) 2 Degrees of Freedom dynamic system, which allows rigid models to undergo flutter. Cases corresponding to classical pitch-plunge flutter, stall flutter and shock-induced plunge flutter are included. The actual wing motion together with the corresponding pressures are provided, thus allowing a staircase approach to validation, from forced oscillations (using the motion as input) to a 'simple' aeroelastic simulations (using the known elastic characteristics of PAPA). Finally the transfer functions of control surface inputs measured with the BACT can be used to validate aeroservoelastic codes.

Clipped Delta Wing

The Clipped Delta Wing CDW model was also tested in the NASA Langley Transonic Dynamics Tunnel [6]. The planform was derived by simplifying a proposed Boeing design for a supersonic transport, resulting in a trapezoid wing with an unswept trailing edge and without twist and camber (Fig. 2). The model undergoes pitching and trailing edge control surface oscillations. A rather thick (for a supersonic transport) 6% symmetrical circular arc section was used, which very much enhances transonic effects. Additionally the highly swept sharp leading edge separates the flow at relatively low angles of attack forming a leading edge vortex. Rapid changes in shock wave position over a small Mach range, sometimes in conjunction with the leading edge vortex makes this a challenging case for any numerical method.

Supersonic 2D Wing with Control Surface

This case was tested at ONERA S2 to obtain a database of the unsteady behavior of control surfaces in high supersonic conditions [7]. It consists of a 5.5 aspect ratio rectangular wing with a 7% symmetric bi-convex airfoil and an oscillating trailing edge flap (Fig. 3). The model had also a spoiler, but no data corresponding to it is provided in the present database. Pressures were measured at the mid semi-span section, which at the supersonic Mach numbers tested (1.65, 2.0 and 2.5) is effectively in 2D conditions. Test points are provided that illustrate the effect on the unsteady airloads of: Mach number, steady angle of attack, mean flap deflection, flap oscillation amplitude and oscillation frequency.

SST Arrow Wing with Oscillating Flap

This model of a double-swept-back arrow wing with a fuselage and an oscillating trailing edge flap (Fig.4) representing a SST was tested at NAL's 2mx2m transonic wind tunnel with the specific purpose to accumulate validation data for CUA and ACT (Active Control Technology) codes [8]. A NACA0003 airfoil was used, resulting in a very thin wing with non-negligible static and dynamic elastic deformations, which were carefully monitored tracing optical targets installed on the wing surface. Information on pressures and actual motion due to elastic deformation is provided, thus constituting a good test of the ability of the code to handle both rigid body and elastic motions. Results are included for different transonic Mach numbers, mean flap positions and frequencies of oscillation.

BGK Airfoil Buffet

This model of a BGK No. 1 supercritical airfoil was tested at the IAR 2D High Reynolds Test Facility to investigate its shock induced buffet characteristics [9]. Very rich pressure information at different Mach/AoA combinations outside, near, and well inside the buffet onset boundary is provided. Additionally, skin friction measurements are available; allowing the CFD developer to monitor the merging of the shock induced separation bubble with the trailing edge separated region.

M2391 Diamond Wing Buffet

The M2391 model (Fig. 5) tested at DERA Bedford 13ftx9ft low speed wind tunnel [10] is a low mass, high stiffness model designed to obtain data of the aerodynamic excitation arising from unsteady separated flow without the interferences due to model vibration and/or support natural frequencies. It is a 40° sweep diamond wing with a streamwise clipped tip. Two interchangeable fuselages were tested, respectively rectangular and chined, with the former providing a perpendicular wing-fuselage interface, and the later allowing the study of buffet due to mixed vortical flow. Very rich pressure information for angles of attack up to 30° is included, thus providing an excellent test case to validate the buffet part of any buffeting prediction code.

Straked Delta Wings

These two different straked delta wing models (Figs. 6) were tested respectively in NLR's LST [11] and HST [12] wind tunnels with the aim to improve understanding of unsteady loading on straked fighter like wings during pitch oscillations and maneuvers. They present a wide range of flow topologies, from attached to vortex breakdown over the whole model. Additionally the transonic test includes cases with shock induced trailing edge separation and LCO. The data points selected cover all the different flow types, including the influence of Mach number, static incidence and sideslip, amplitude and frequency of oscillation. The resulting database constitutes a real challenge of any fluid dynamics code.

CONCLUSIONS

The work of RTO WG-003 aims at collecting into a single document, computational and experimental data that can be used to verify and validate Computational Unsteady Aerodynamic codes. It is recognized that the present database still has many gaps, which are due either to the lack of a suitable experiment, or the authors not being aware of its existence, or its results being classified. Additional contributions of experimental and/or numerical data are very welcomed

ACKNOWLEDGMENTS

Funding for this work was provided by AGARD/RTO, the different AGARD/RTO national delegations, and the individual member's organization. Their contributions are gratefully acknowledged.

REFERENCES

- [1] Tijdeman, H.; van Nunen, J.W.G.; et al.; "Transonic Wind Tunnel Test of an Oscillating Wing with External Store". Parts I: to IV"; NLR-TR-78106 U; 1978
- [2] Ricketts, R. H.; Sandford, M. C.; Watson, J.; Seidel, D. A.; "Subsonic and Transonic Unsteady- and Steady-Pressure Measurements on a Rectangular Supercritical Wing Oscillated in Pitch"; NASA TM 85765.; 1984.
- [3] Rivera, J.A.; Dansberry, B.E.; Farmer, M.G.; Bennett, R.M.; Durham, M.H.; Silva, W.A.; "NACA0012 Benchmark Model Experimental Flutter Results with Unsteady Pressure Distributions"; NASA TM-107581; 1992
- [4] Dansberry, B.E.; Durham, M.H.; Bennett, R.M.; Rivera, J.A. Jr.; Silva, W.A.; Wieseman, C.D.; "Experimental Unsteady Pressures at Flutter on the Supercritical Wing Benchmark Model"; AIAA Paper 93-1592; 1993
- [5] Scott, R.C.; Hoadley, S.T.; Wieseman, C.D.; "The Benchmark Active Control Technology Model Aerodynamic Data"; AIAA 97-0829; 1997
- [6] Hess, R. W.; Cazier, F. W., Jr.; Wynne, E. C.; "Steady and Unsteady Transonic Pressure Measurements on a Clipped Delta Wing for Pitching and Control-Surface Oscillations"; NASA TP-2594; 1986
- [7] Naudin, P.; "Results d'essais d'une maquette bi-dimensionnelle munie d'un spoiler et d'un gouverne en supersonic"; ONERA Report 24/5115RN031R; 1996
- [8] Tamayama, H.; Miwa, H.; Nakamichi, J.; "Unsteady Aerodynamic Measurements on an Elastic Wing Model of SST"; AIAA 97-0836; 1997
- [9] Lee, B.H.K.; Ohman, L.H.; "Unsteady Pressure and Force Measurements Associated with Transonic Buffeting of a Two-Dimensional Supercritical Airfoil"; National research Council of Canada AN-14; 1983
- [10] Lynn, R.; Gibb, J; Shires, A; "Buffet tests on a 40 degree diamond wing – Model M2391"; DERA/MSS4/TR98309/1.0; 1998
- [11] Cunningham, A.M. Jr.; den Boer, R. G.; et al; "Unsteady Low Speed Wind Tunnel Test of a Straked Delta Wing oscillating in Pitch. Parts I to VI"; NLR TR 87146; 1987
- [12] Cunningham, A.M. Jr.; den Boer, R. G.; et al; "Unsteady Transonic Wind Tunnel Tests on a semi-span Straked Delta Wing Model, oscillating in Pitch. Parts I to III"; NLR-CR 93570; 1993

Table 1. Test cases

Test case	Configuration	Motion	Speed Regime	CFD?
NLR F-5 Wing & Wing+Store	Wing+Missile	Pitch	Subsonic to Supersonic	YES
NASA RSW	Wing	Pitch	Subsonic to Transonic	
NASA BMP Rectangular Wing	Wing	Pitch Plunge	Subsonic to Transonic	
NASA BMP BACT	Wing + Flap + Spoiler	Flap spoiler	Subsonic to Transonic	YES
NASA Clipped Delta Wing	Wing + Flap	Pitch Flap	Subsonic to Supersonic	YES
ONERA 2D Supersonic TE Control	Airfoil + Flap	Flap	Supersonic	
RAE Tailplane	Wing	Pitch	Supersonic	
NAL SST	Wing + Flap + Fuselage	Flap	Transonic	
IAR BGK Airfoil	Airfoil	Buffet	Transonic	
DERA Model 2391	Wing + Fuselage	Buffet	Subsonic	
IAR SDM Fin Buffet	Wing + Fuselage + Fin	Buffet	Subsonic	
IAR 65° Delta Wing	Wing + Centerbody	Roll	Subsonic	YES
DLR 65° Delta Wing	Wing + Centerbody	Pitch Yaw Roll	Subsonic	YES
NLR Low Speed Straked Delta Wing	Wing	Pitch	Subsonic	
NLR Transonic Simple Straked Delta Wing	Wing	Pitch	Subsonic to Transonic	YES
AEDC WICS	Cavity	-	Transonic	YES
BAe/DERA Cavity	Cavity	-	Subsonic to Supersonic	
DLR COM TWG1	Cavity	-	Transonic Supersonic	
Glasgow U. Dynamic Stall	Airfoil Wing	Pitch	Subsonic	
AEDC Wing/Pylon/Moving Store	Wing + Pylon + Store	Drop	Transonic Supersonic	

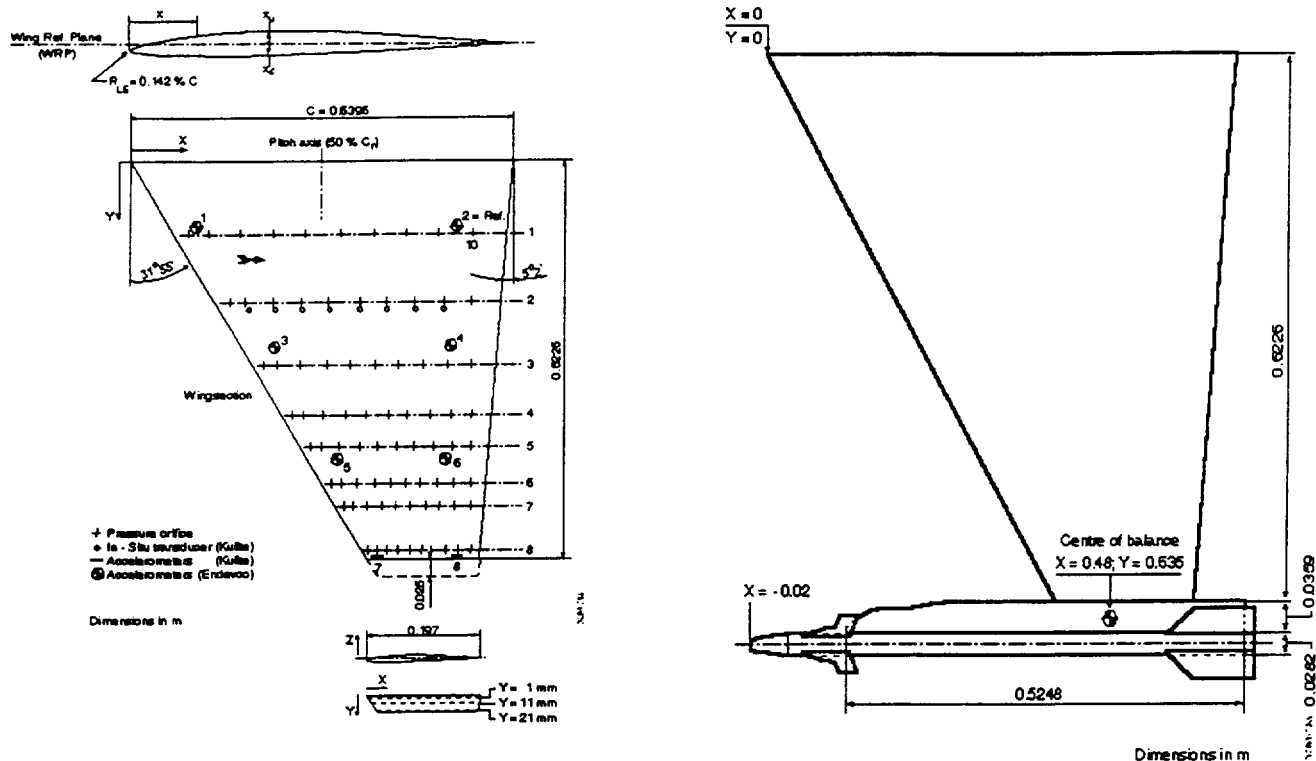


Fig. 1 F-5 Wing alone and Wing + Tip Missile

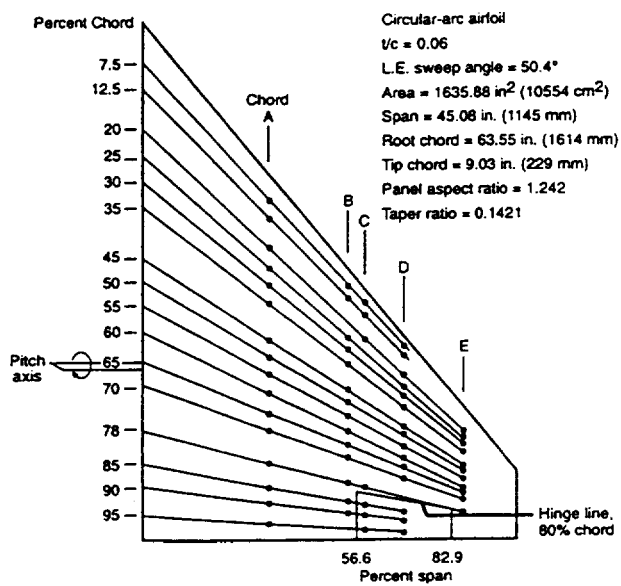


Fig. 2 Clipped Delta Wing

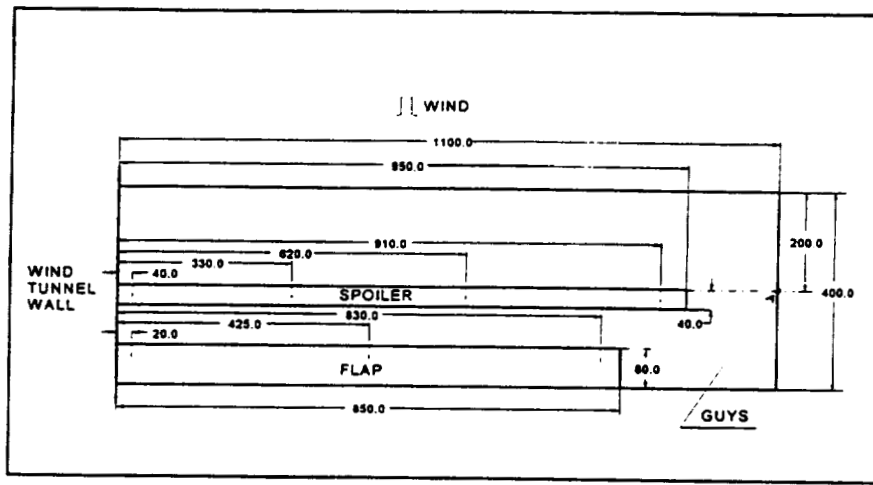


Fig. 3 Supersonic 2D Wing with Control Surface

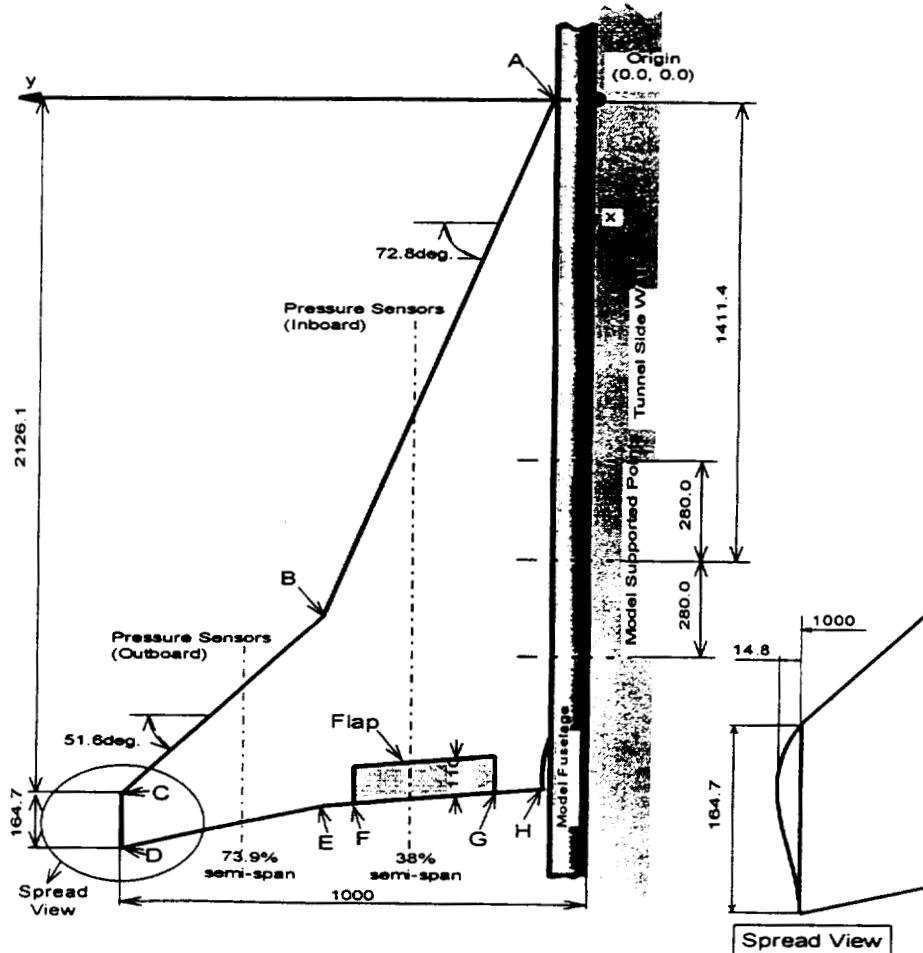


Fig. 4 SST Arrow Wing

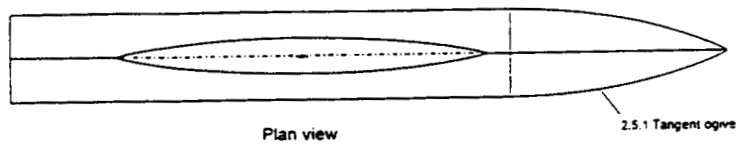
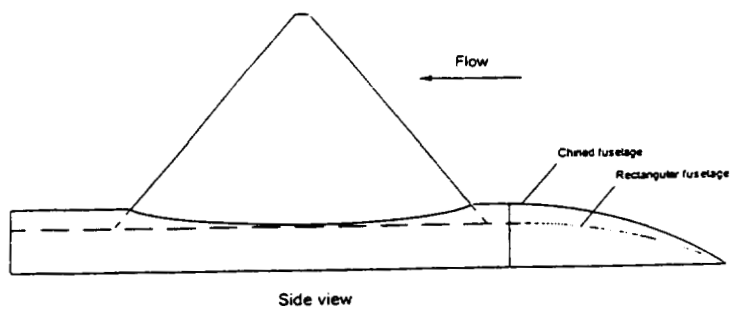


Fig. 5 M2391 Diamond Wing

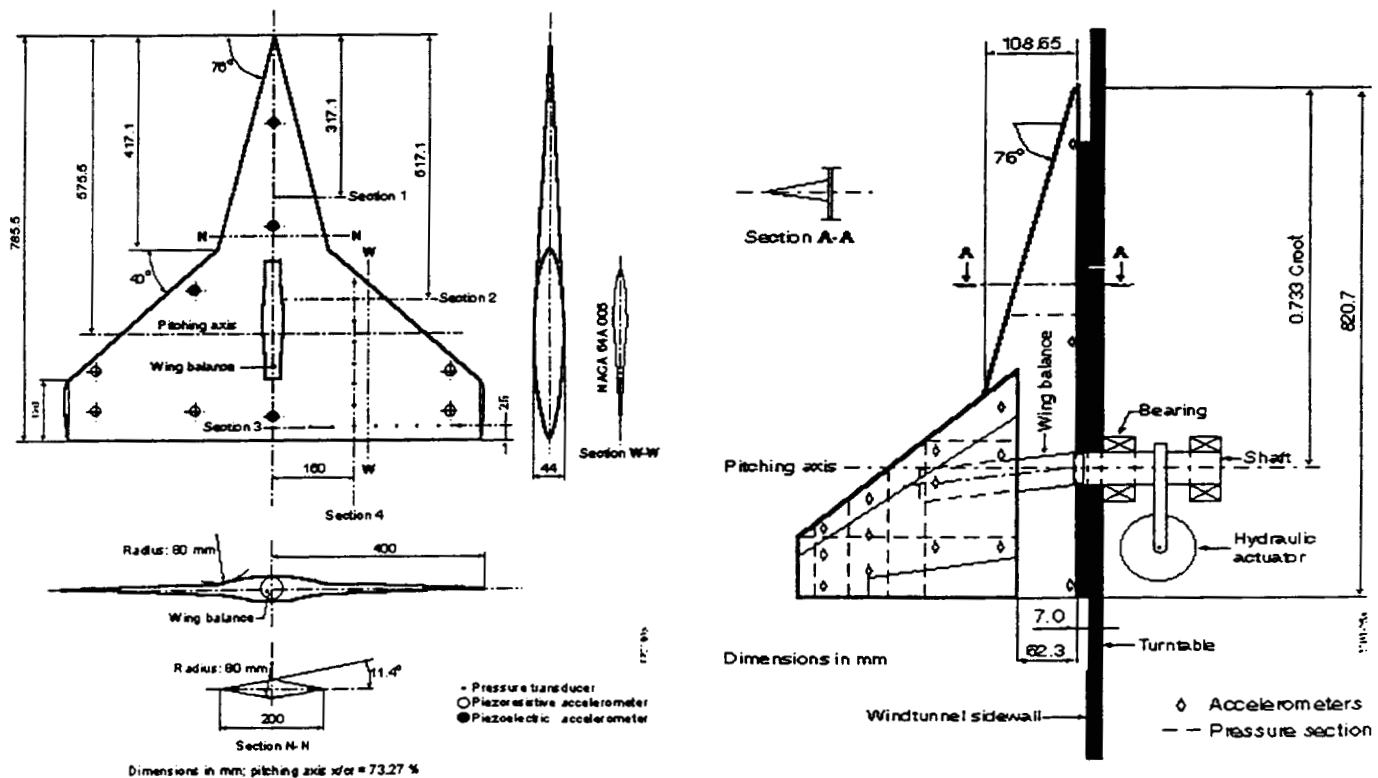


Fig. 6 Subsonic (Left) and Transonic (Right) Straked Delta Wings

A Combined Modal / Finite Element Analysis Technique for Nonlinear Beam Dynamic Response Under Harmonic Excitation

by

Matthew I. McEwan¹, Jan R. Wright², Jonathan E. Cooper³, and Andrew Y. T. Leung².

1 Abstract.

A method is proposed for modelling multi-mode large deflection beam response. Significant savings in computational time can be obtained compared with the direct integration nonlinear finite element method. The deflections from a number of static nonlinear finite element test cases are transformed into modal co-ordinates using the modes of the underlying linear system. Regression analysis is then used to find the unknown nonlinear modal stiffness coefficients. The governing nonlinear equations of motion are completed by including finite element derived modal mass, and an arbitrary damping model. The response of the beam to excitation of an arbitrary nature may then be found using time domain numerical integration. The work presented here extends upon the work of previous researchers to include non-coupled multi-modal response, and the effect of buckling due to axial loads.

The proposed method is applied to the case of a homogeneous isotropic beam, which is simply supported and axially constrained at both ends. For the case of steady state harmonic excitation, results are compared with the direct integration nonlinear finite element method.

2 Nomenclature

$[M]$	= Assembled finite element mass matrix.
$\{w\}$	= Vector of assembled finite element transverse displacements.
α	= Coefficient of linear mass proportional damping.
$[K_L]$	= Assembled linear finite element stiffness matrix.
$[K_{NL}]$	= Assembled nonlinear finite element stiffness matrix.
$\{F\}$	= Assembled finite element force vector.
n	= Mode number.
N	= Total number of modes considered.
$\{\phi\}_n$	= Displacement mode shape vector for mode n .
p_n	= Displacement modal amplitude coefficient for mode n .
$[\phi]$	= Displacement mode shape matrix.
$\{p\}$	= Vector of displacement modal amplitudes.
ω_{Ln}	= Linear natural frequency of mode n .
$[m]$	= Modal mass matrix.

¹ Postgraduate Research Student.

² Professor of Mechanical Engineering.

³ Senior Lecturer in Aerospace Engineering.

All of the Dynamics and Aeroelasticity Research Group, Manchester School of Engineering, University of Manchester, Oxford Road, Manchester M13 9PL, UK.

$[k]$	= Linear modal stiffness matrix.
$[k_{NL}]$	= Nonlinear modal stiffness matrix.
$\{f\}$	= Modal force vector.
A_n^r	= Quadratic modal nonlinearity coefficient, involving the coupling of arbitrary modes n and r
B_n^{rs}	= Cubic modal nonlinearity coefficient, involving the coupling of arbitrary modes n, r and s.

3 Introduction.

The surface panels of modern high-speed aircraft are subjected to high intensity acoustic loading from sources such as jet efflux and turbulent fluid flow. Frequently this high intensity noise environment is combined with elevated panel temperatures, caused by aerodynamic heating and jet exhaust impingement. Preliminary concept evaluations of aircraft such as the National Aerospace Space Plane (NASP) indicate that at some points on the structure, the sound pressure levels will be in the range 170-180 dB (relative to 20 μ Pa), with panel temperatures up to 1480°C [1]. The case of a beam that is simply supported at both ends can be regarded as a simplified case of the more complex structural models used in the design of high speed aircraft components. Because of this, considerable effort has been directed into developing models for the nonlinear beam "test bed", which may eventually be applied to more general structures.

There has been an enormous amount of work published in the study of nonlinear beam vibration. It should be noted that only a few of the many authors in this subject are mentioned here. The accepted benchmark for ideal nonlinear simply supported beam behaviour is the work of Woinowsky-Krieger [2], which uses the elliptic integral function to evaluate the equation of motion. Subsequent researchers have used a variety of methods. Raju et al [3], and later Lewandowski [4] have applied the Rayleigh-Ritz technique, the latter utilising an iterative approach to determine the natural frequencies and nonlinear modes. Sarma and Varadan [5] have used a Lagrangian finite element formulation. Singh et al [6] have also obtained excellent results by using an iterative process to exactly satisfy the axial and out of plane equations.

Much of the work of Mei and his associates has utilised the finite element method. Earlier work [7,8,9] assumed simple harmonic response behaviour and neglected transverse displacement and inertia in the finite element formulation. The work of Mei and Decha-Umphai [10] included the effect of transverse displacement and inertia, and simplified the strain displacement relationship by using a linearising function. The more up to date works of Shi and Mei [11], and Shi, Lee, and Mei [12] have considered the simply supported beam problem as part of the validation of a formulation developed for laminated composite plates. The finite element equations of motion are expanded in terms of linear modal co-ordinates, then numerically integrated in the time domain. The results show excellent agreement with [2] (see table 2). All of the finite element techniques mentioned here operate directly on the stiffness and mass matrices, rather than using an output only approach.

The work presented here extends upon the work of Maymon [13], to include multi-mode vibration in a situation where the form of the nonlinear modal couplings is known *a priori*. Maymon's original work described a fundamental mode expansion of an arbitrary nonlinear structure. A single unknown nonlinear stiffness coefficient was found by considering the nonlinear response to static loading. The stress response was found by treating the stress modes of the structure in a similar manner. The response to random temporal excitation was found using an equivalent linearisation scheme.

In this work an alternative approach to that of a 'first principles' derivation and solution of the system equations of motion is proposed. The output from a series of static finite element 'test

'cases' is transformed into modal co-ordinates using the mode shapes of the underlying linear system. Regression analysis is then performed in order to extract the nonlinear stiffness coefficients in the modal co-ordinate system. Time domain numerical integration is then applied to the nonlinear modal equations of motion, thus finding the response of the beam to any excitation time history. The method is an approximation, and is 'simplified' from the point of view that considerations of finite element formulation and solution are handled by the proprietary finite element code, and are not dealt with explicitly by the method.

The method differs from many existing 'first principles' formulations in the fact that proprietary finite element packages may be used without modification to the code or direct access to the stiffness and mass matrices. An autonomous program post-processes the output from these codes. Significant savings in computational time compared to standard direct integration routines can be obtained without sacrificing the flexibility of the large-scale packages. The derivation that follows is that for a simply supported beam, but it is envisaged that with refinement the method will be expandable to thermally postbuckled plates and built up structures such as stiffened panels.

4 Formulation.

Consider the case of an initially straight, geometrically nonlinear beam with mass proportional damping subject to forced vibration. The assembled finite element equation of motion in physical co-ordinates for forced vibration in the transverse direction is of the form:

$$[\mathbf{M}]\{\ddot{\mathbf{w}}(x, t)\} + \alpha[\mathbf{M}]\{\dot{\mathbf{w}}(x, t)\} + [\mathbf{K}_L]\{w(x, t)\} + [\mathbf{K}_{NL}(w(x, t))]\{w(x, t)\} = \{F(x, t)\} \quad (1)$$

The overdots imply differentiation with respect to time. The spatial and temporal components of the beam motion can be separated by expressing the equations of motion in terms of modal amplitudes and mode shape vectors as:

$$\{w(x, t)\} = \sum_{n=1}^N \{\phi(x)\}_n p(t)_n = [\phi]\{p(t)\} \quad (2)$$

Here $\{p\}$ is a time dependent vector of modal amplitudes, and $[\phi]$ is a time independent mode shape matrix of the N modes of the underlying linear system, which may be obtained by solving the standard eigenvalue problem for undamped free vibration:

$$[\mathbf{K}_L]\{\phi(x)\}_n = \omega_{L_n}^2 [\mathbf{M}]\{\phi(x)\}_n \quad n = 1, 2, \dots, N \quad (3)$$

The number of degrees of freedom required to model the beam with reasonable accuracy can be reduced by considering only those modes with natural frequencies in the frequency range of interest. Upon completion of the modal transformation the new system equations of motion in modal space are:

$$[\mathbf{m}]\{\ddot{\mathbf{p}}(t)\} + \alpha[\mathbf{m}]\{\dot{\mathbf{p}}(t)\} + ([k_L] + [k_{NL}])\{p(t)\} = \{f(t)\} \quad (4)$$

Here the lower case terms are associated with the modal co-ordinates. The normal modes of the system are orthogonal, and hence the linear mass and stiffness matrices are diagonal. Let us consider the nonlinear stiffness term k_{nl} as function of terms in $\{p\}$. Consider some arbitrary mode n :

$$\begin{aligned}
k_{NL}(p_i) &= A_i^1 p_i^2 + A_i^1 p_i p_i + A_i^2 p_i p_2 + \dots + B_i^{ii} p_i^3 + B_i^{i1} p_i^2 p_1 + B_i^{i2} p_i^2 p_2 + \dots \\
&= \left(\sum_i^N A_i^1 p_i \right) \{p_i\} + \left(\sum_{r=1}^N \sum_{s=1}^N B_i^{rs} p_r p_s \right) \{p_i\}
\end{aligned} \tag{5}$$

i.e. the nonlinear stiffness is a quadratic function of the modal co-ordinates $\{p(t)\}$.

4.1 Regression analysis using the static finite element method.

If the beam system is considered in a static sense only, then equations (4) and (5) may be simplified as:

$$(k_L)_n p_n + \left(\sum_{r=1}^N \sum_{s=1}^N B_i^{rs} p_r p_s \right) p_n = f_n \quad n = 1, 2, \dots, N \tag{6}$$

Due to the symmetry of the transverse deflections of the beam in tension and compression, the second-degree terms (terms in A_i^{ii}) disappear. At this stage the coefficients k and B are unknowns. The linear modal stiffness coefficients may be calculated by utilising the modal mass and linear natural frequency data [14].

$$(k_L)_n = m_n \omega_{Ln}^2, \quad n = 1, 2, \dots, N \tag{7}$$

In the case of a simply supported beam, the form of the modal cross couplings is known *a priori*. It may be shown that the governing modal equations are of the Duffing type, with no cross couplings between modes.

$$m_n \ddot{p}_n(t) + \alpha m_n \dot{p}_n(t) + k_n p_n(t) + B_n^{nn} p_n^3(t) = f_n(t), \quad n = 1, 2, \dots, N \tag{8}$$

The nonlinear coefficient B_n^{nn} in equation (8) can be determined by considering the results of a number of nonlinear static finite element test cases. Running static nonlinear finite element analyses of the beam in question allows the accumulation of a series of load / deflection data relationships for use in a regression analysis.

In the case of a beam that is postbuckled due to axial loading or uniformly distributed thermal effects, there is a region of the response where the resultant stiffness of the beam is negative and the beam becomes unstable. It is in this region that snap-through motion occurs. A load-deflection analysis using the modified Riks algorithm [14,15] was used to generate the load cases for the postbuckled beam, as the conventional static finite element method cannot be used to provide test cases in regions of instability. The modified Riks algorithm is a standard procedure available in many finite element software packages.

For each given nonlinear modal coefficient of interest, the spatial distribution of the test case load was chosen to be the same as the mode shape. Using this spatial distribution of the load ensured that the mode in question was 'excited' effectively. Tests for each coefficient with a number of different load magnitudes ensured that the beam was excited throughout the range of interest.

Following static finite element analysis, the set of nodal force and displacement vectors is transformed into modal co-ordinates using the mode shape vectors. The unknown cubic coefficients may be determined by regression analysis of the modal load / displacement data. Increasing the number of test cases increases the accuracy of the result. The inertial and

damping terms are now included to complete the governing modal equations of motion. The choice of damping model at this point is arbitrary and may be nonlinear, although linear mass proportional damping is used here for the purposes of verification. The nonlinear dynamic behaviour of the simply supported beam can now be found for any form of excitation.

5 Numerical Examples.

In order to illustrate the proposed method, a finite element model of a simply supported beam was created. The material and geometric properties of the beam were as follows:

Length, L	1 m
Thickness, a	0.01 m
Width, b	0.03 m
Mass Density, ρ	7800 kgm^{-3}
Tensile Elastic Modulus, E	$200 \times 10^9 \text{ Nm}^{-2}$
Poisson's Ratio, ν	0.3

The Finite Element code ABAQUS/Standard was used to model the beam. The beam was modelled using 16 quadratic interpolating shear deformable beam elements (B22). An important point to note in the proposed formulation is that the underlying assumptions in the analysis, such as the inclusion of axial deflection and inertia, are determined by the type of element used to model the beam rather than the method itself. In the elements used in the present study, the assumption is made that plane sections remain plane and that shear deformation, axial deflection and inertia are included in the formulation. The first three linear symmetric modes were used for the modal model. The linear natural frequencies of these modes were 22.9 Hz, 206.4 Hz and 572.8 Hz

5.1 Response to Harmonic Excitation.

As the proposed method is based on the results of a proprietary finite element code, a comparison was made between the response of the modal model and that of the direct integration routines of the proprietary finite element code. The fourth order Runge-Kutta algorithm was used for the time stepping integration of the modal model, while the implicit integration routine used in ABAQUS/Standard was a Hilber-Hughes-Taylor integration operator. In each case a steady state response was allowed to develop before a fast Fourier transform algorithm was applied to a whole number of cycles of response, in order to calculate the autopower spectral density without leakage effects. The fast Fourier transform was applied to 500 cycles of response.

5.2 Prebuckled Beam

The first case considered was that of the beam without any axial pre-load. A uniformly distributed normal load, which varies sinusoidally in time, was applied to the beam. The maximum amplitude of the loading was 1000 Nm^{-1} . Figure 1 shows the time history of the displacement response of the beam to excitation at 10 Hz. It may be seen that the response as calculated by the two methods is nearly identical. Figure 2 shows the autopower spectral density of the same two sets of results. At this excitation frequency the response is dominated by the fundamental and fifth harmonics.

For excitation at near to the fundamental natural frequency (23 Hz), the response is strongly asymmetric with respect to the unperturbed position (figure 3). This can be seen in the plot of

the frequency response (figure 4), where even harmonics and a spectral component at 0 Hz form a large proportion of the response.

5.3 Postbuckled Beam.

The second case considered was that of a beam in the postbuckled state. An axial load of 1.7 times the linear critical buckling load was applied to the beam. If the material properties of the beam are assumed to be constant with temperature, this is equivalent to a uniform thermal loading of 1.7 times the critical buckling temperature. In order to produce a deterministic response that can be compared in the time domain, a harmonic excitation with a large steady state component was applied. The maximum amplitude of the loading was 1500 Nm^{-1} while the minimum amplitude of the loading was 500 Nm^{-1} .

Figure 5 shows the time history of the displacement response of the postbuckled beam to excitation at 10 Hz. The beam is vibrating in a stable manner in the postbuckled region. Again the correlation between the proposed modal method and the direct integration finite element method is good. The plot of the frequency response (figure 6) shows that the even harmonic components form a considerable portion of the response.

In this investigation no attempt has been made to quantitatively compare the computer solution times of the proposed modal method and the direct integration finite element method. On a qualitative level however, the timesavings gained by using the modal approach were considerable. The proposed method does require the solution of a number of static finite element test cases prior to the modal transformation, however once the modal model has been constructed, it can be used with any form of excitation.

It should also be noted that the proposed method is an approximate method based upon the finite element method, which is itself an approximation of the 'true' nonlinear beam vibration. The overall quality of the results given by employing this method will be dependent upon the accuracy of the original static finite element model used to model the beam.

6 Conclusion.

In this work the Finite Element based modal approach of Maymon [13] is extended to consider multi-modal beam response and thermally induced buckling. A series of finite element load-deflection relationships is generated using the modified Riks algorithm. These 'test cases' are transformed into modal co-ordinates using the mode shapes of the underlying linear system. Regression analysis is then performed in order to extract the nonlinear stiffness coefficients in the modal co-ordinate system. The beam problem can then be solved for any excitation time-history in the reduced degree of freedom modal system. The proposed method is applied to the case of a homogeneous isotropic beam, which is simply supported and axially constrained at both ends. For the case of steady state harmonic excitation, the results compare well with the standard direct integration finite element routine, with a significant saving in computational expense.

7 References.

- [1] Blevins, R. D, Holehouse, I, Wentz, K. R., "Thermoacoustic Loads and Fatigue of Hypersonic Vehicle Skin Panels", *Journal of Aircraft*, Vol. 30, No. 6, 1993, pp. 971-978.
- [2] Woinowsky-Krieger, S., "The Effect Of Axial Force On The Vibration Of Hinged Bars", *Transactions of the American Society of Mechanical Engineers*, Vol. 72, 1950, pp. 35-36.

- [3] Raju, I. S., Rao, V. N., Raju, K. K., "Effect Of Longitudinal Or In-Plane Deformation And Inertia On The Large Amplitude Flexural Vibrations Of Beams And Thin Plates", *Journal Of Sound And Vibration*, Vol. 49, 1976, pp. 415-422.
- [4] Lewandowski, R., "Application Of The Ritz Method To The Analysis Of Nonlinear Free-Vibrations Of Beams", *Journal Of Sound And Vibration*, Vol. 114, No. 1, 1987, pp. 91-101.
- [5] Sarma, B. S., Varadan , T. K., "Certain Discussions In The Finite-Element Formulation Of Non-Linear Vibration Analysis", *Computers and Structures*, Vol. 15, No. 6 1982, pp. 643-646.
- [6] Singh, G., Rao, G. V., Iyengar, N. G. R., "Reinvestigation Of Large-Amplitude Free-Vibrations Of Beams Using Finite-Elements", *Journal Of Sound And Vibration*, Vol. 143, No. 2, 1990, pp. 351-355.
- [7] Mei, C., "Nonlinear Vibrations Of Beams By The Matrix Displacement Method", *AIAA Journal*, Vol. 10, No. , 1972, pp. 355-357.
- [8] Mei, C., "Finite Element Analysis Of Nonlinear Vibrations Of Beam Columns", *AIAA Journal*, Vol. 11, No. , 1973, pp. 115-117.
- [9] Mei, C., "Finite Element Displacement Method For Large Amplitude Free Flexural Vibrations", *Computers and Structures*, Vol. 3, 1973, pp. 163-174.
- [10] Mei, C., Decha-Umphai, K., "A Finite-Element Method For Non-Linear Forced Vibrations Of Beams", *Journal Of Sound And Vibration*, Vol. 102, No. 3, 1985, pp. 369-380.
- [11] Shi, Y., Mei, C., "A Finite-Element Time-Domain Modal Formulation For Large Amplitude Free-Vibrations Of Beams And Plates", *Journal Of Sound And Vibration*, Vol. 193, No. 2, 1996, pp. 453-464.
- [12] Shi, Y., Lee, R. Y. Y., Mei, C., "Finite Element Method For Nonlinear Free Vibrations Of Composite Plates" *AIAA Journal*, Vol. 35, No. 1, 1997, pp. 159-166.
- [13] Maymon, G., "Response Of Geometrically Nonlinear Elastic Structures To Acoustic Excitation - An Engineering Oriented Computational-Procedure", *Computers & Structures*, Vol. 18, No. 4, 1984, pp. 647-652.
- [14] ABAQUS/Standard Users Manual, Hibbet, Karlsson and Sorensen, Inc, Version 5.7, Copyright 1997.
- [15] Crisfield, M. A., "A Fast Incremental/Iteration Solution Procedure that Handles 'Snap-Through'", *Computers & Structures*, Vol. 13, 1981, pp. 56-62.

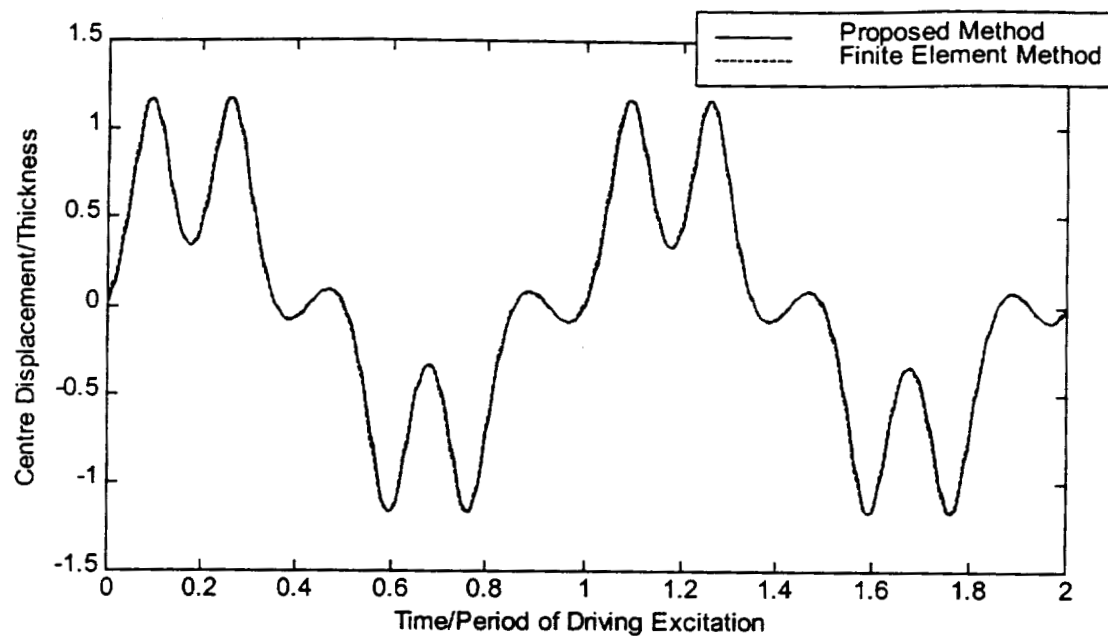


Figure 1. Prebuckled Beam Time History, Excitation Frequency=10 Hz

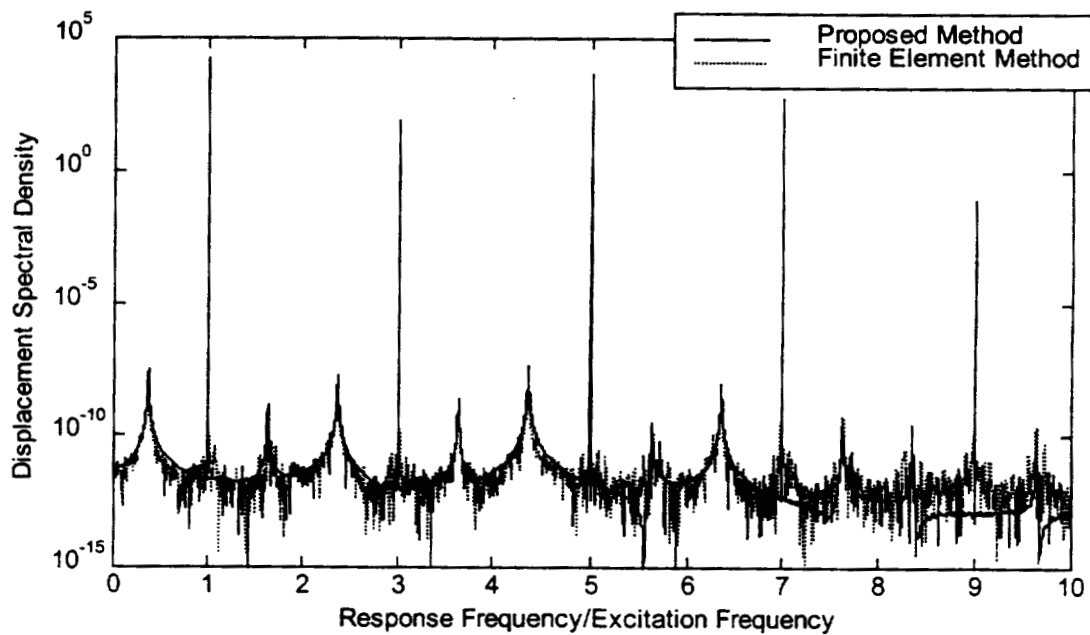


Figure 2. Prebuckled Beam Autopower Spectral Density, Excitation Frequency=10 Hz

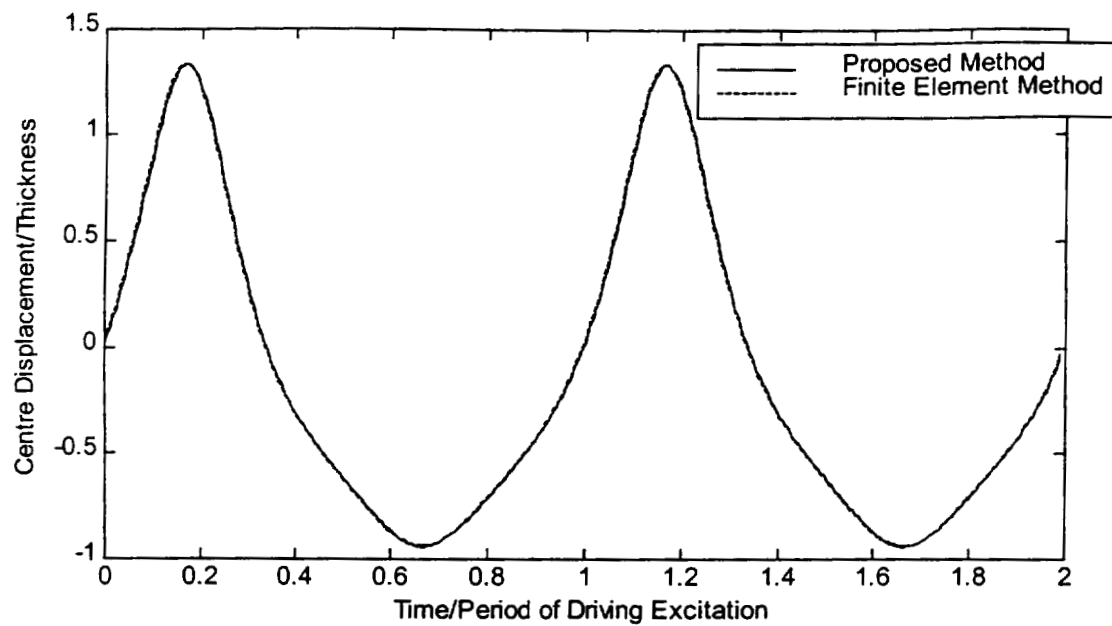


Figure 3. Prebuckled Beam Time History, Excitation Frequency=23 Hz

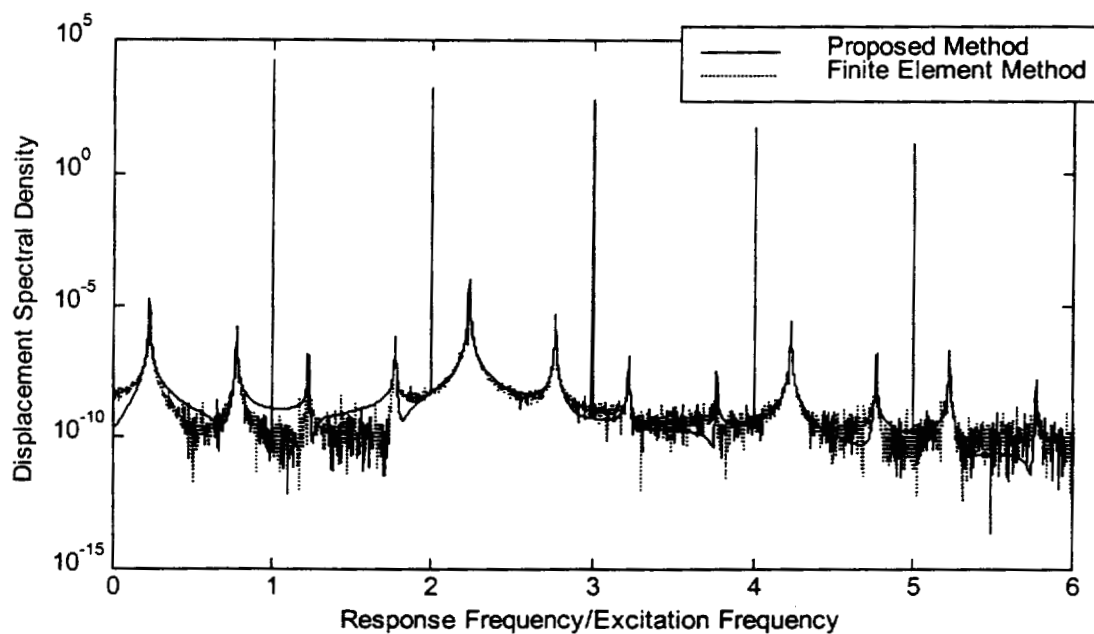


Figure 4. Prebuckled Beam Autopower Spectral Density, Excitation Frequency=23 Hz

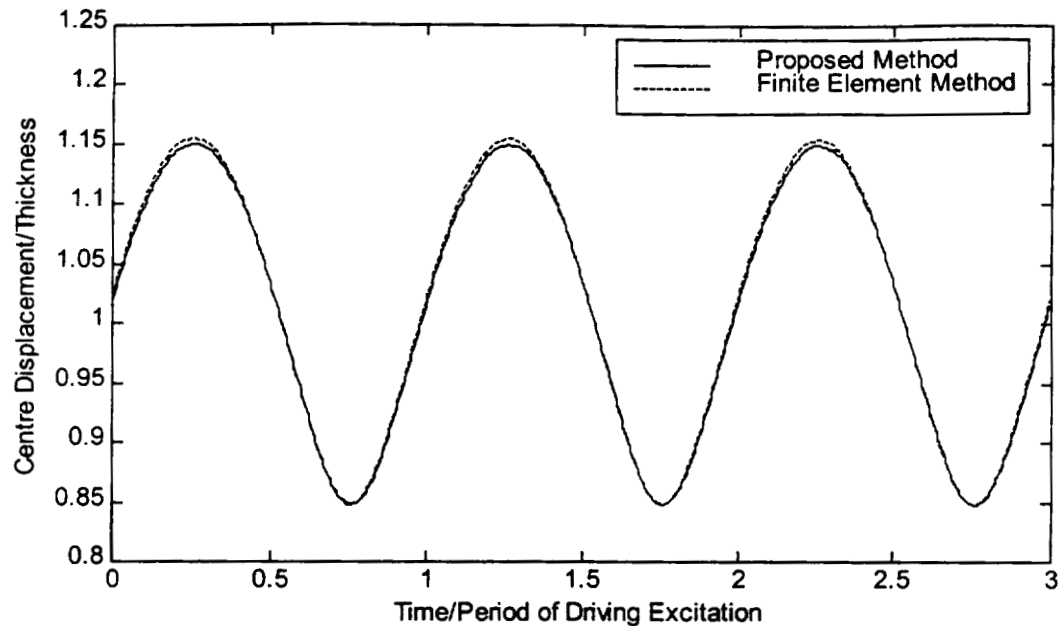


Figure 5. Postbuckled Beam Time History, Excitation Frequency = 10Hz. $T/T_c=1.7$

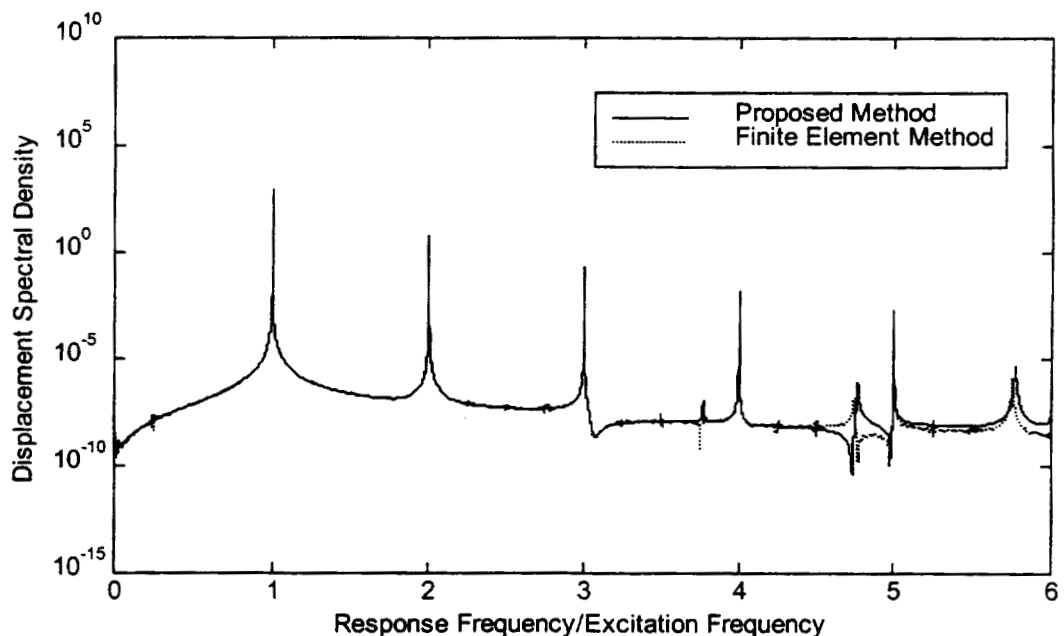


Figure 6. Postbuckled Beam Autopower Spectral Density. Excitation Frequency = 10 Hz. $T/T_c = 1.7$.

AN \mathcal{H}_∞ APPROACH TO CONTROL SYNTHESIS WITH LOAD MINIMIZATION FOR THE F/A-18 ACTIVE AEROELASTIC WING

Rick Lind¹

NASA Dryden Flight Research Center

Abstract

The F/A-18 Active Aeroelastic Wing research aircraft will demonstrate technologies related to aeroservoelastic effects such as wing twist and load minimization. This program presents several challenges for control design that are often not considered for traditional aircraft. This paper presents a control design based on \mathcal{H}_∞ synthesis that simultaneously considers the multiple objectives associated with handling qualities, actuator limitations, and loads. A point design is presented to demonstrate a controller and the resulting closed-loop properties.

Nomenclature

Acronyms

AAW	Active Aeroelastic Wing
SRA	Systems Research Aircraft

Symbols

A	actuator model for AAW
L	loads model for AAW
P	open-loop dynamics for AAW
T	closed-loop dynamics for SRA
K	controller
W	weighting function
δ	control surface position (deg)
$d\delta$	control surface rate (deg/s)
μ	structured singular value
\mathcal{H}_∞	induced norm on transfer functions
Δ	uncertainty operator

Subscripts

ail	aileron
lei	leading-edge inboard flap
leo	leading-edge outboard flap
rud	rudder
tef	trailing-edge flap
stb	stabilator
in	input
out	output
701E	production F/A-18 controller

1. Introduction

The F/A-18 Active Aeroelastic Wing (AAW) research testbed is being developed to demonstrate aeroservoelastic technology [7]. The main concept of this technology is the active use of aeroelasticity to maneuver the aircraft. Many aspects of the technology have been initially studied in wind tunnel tests; however, the AAW aircraft is a full-scale system from which information for future designs can be derived [8].

One important aspect of the AAW program will be the use of wing twist to produce rolling moments. Controllers designed using rigidity assumptions move the ailerons to generate roll but the wing flexibility acts to oppose this roll. Roll reversal is defined at a dynamic pressure at which the flexibility actually causes a roll in the opposite direction than is desired [3]. Controllers for the AAW will generate roll by moving the leading-edge surfaces to create a wing twist and thus be able to efficiently operate past the roll reversal of the ailerons.

The issue of load minimization is also an important aspect of AAW technology that will be addressed by the flight program. Essentially, the wing should experience reduced loads because the control surfaces are not inducing a large load to overcome wing twist; rather, the surfaces promote wing twist in an efficient manner. The reduction in loads may allow a reduction in structural weight and consequently reduce production and operating costs of future aircraft.

This paper presents an approach to design a flight controller for the F/A-18 AAW aircraft using an \mathcal{H}_∞ -synthesis framework. This framework is particularly useful because several objectives and constraints can be directly included in the synthesis. The resulting controllers can be efficiently computed and an approximation can be realized that conforms to a desired architecture.

A closed-loop model of the AAW airplane is presented as a design example to demonstrate the design methodology and resulting properties. This example shows the \mathcal{H}_∞ controller is able to constrain loads and achieve desired levels of handling qualities and roll performance without violating actuator limitations.

¹Structural Dynamics, MS 4840/D, Edwards CA 93523,
rick.lind@dfrc.nasa.gov

This paper provides a limited presentation of the actual \mathcal{H}_∞ controller to be flown on the aircraft. Firstly, only the lateral-directional dynamics will be discussed because the roll performance is of more interest than the pitch performance. Secondly, a gain-scheduled controller has been formulated but only a point design is presented for brevity. Thus, the purpose of this paper is to present the general design methodology whereas future papers will present the final design and flight test results.

2. Closed-Loop Objectives

The fundamental objective of the AAW program is to investigate technologies related to the utilization of aeroservoelasticity for modeling and control of flexible aircraft. These technologies include open-loop concepts such as commanding wing twists and controlling loads. The controller for the aircraft must be designed to allow flight tests that can achieve the program objectives; however, these objectives are only indirectly considered for control synthesis. There are several related closed-loop objectives that are actually used to design controllers.

Several of the closed-loop objectives are essentially applicable to any aircraft and are required for flight safety. The most basic of these objectives is to stabilize the aircraft within a flight envelope. Another objective is to provide handling qualities that are at or near Level 1 ratings for a variety of maneuvers. Finally, the controller must avoid saturating actuator positions and rates except for minor and brief saturation that may be allowed in response to full-stick commands from the pilot.

Some of the controller objectives are specific to AAW technology. One of these objectives is to maximize the roll performance of the aircraft. Previous wind tunnel experiments have indicated that wing twist may provide large amounts of control authority so the AAW program seeks to demonstrate this on a full-scale vehicle [9].

Another objective is to reduce the maneuvering loads throughout the structure. This objective requires more of a formal definition than the others because it may not be immediately obvious how to select a preferred set of loads. For example, some controllers may reduce bending but increase torsion whereas others may reduce torsion by sacrificing bending. Similarly, the relative amount of loads at the wing root and fold must be considered when defining the concept of reduced loads.

An additional objective that is being enforced is that the controller must be realized with an acceptable architecture. This objective is not necessarily an AAW technology; however, it is important to facilitate the flight test. \mathcal{H}_∞ synthesis generally generates high-order controllers

that are difficult to implement on a flight computer. Alternative controllers for the AAW have been proposed that use extensive scheduling over flight condition and also aircraft states such as roll rate and acceleration [11]. The \mathcal{H}_∞ controller will be required to utilize a low-order filter with gain tables that are scheduled over standard flight condition variables.

Furthermore, all these objectives must be achieved without using the stabilator to generate roll moments. This constraint is important because the production aircraft uses the stabilator to generate almost the entire roll moment when flying at high dynamic pressures. Thus, the controller will have to compensate for the loss of this powerful control surface by commanding wing twist through the aeroservoelastic dynamics of the wing.

The flight test program for the AAW will be limited to a flight envelope that allows the technology to be efficiently demonstrated. This envelope has a subsonic region that covers Mach number from .85 to .95 and altitudes from 5 kft to 15 kft. A supersonic region is also included that covers Mach number from 1.1 to 1.3 and altitudes from 10 kft to 25 kft. A remaining objective is for the controller to operate at any flight condition within these regions.

3. Controller Architecture

The controller architecture for the \mathcal{H}_∞ design is chosen to match that of the controller on the production F/A-18 aircraft. This standard controller is denoted as K_{701E} [5]. The architecture involves several first-order filters and a set of gains that are scheduled over Mach number and altitude. The filters are used for stick shaping, response determination, and notching of aeroelastic modes.

The formulation of the gains and filters may require an indirect computation because standard tools for \mathcal{H}_∞ synthesis do not compute a structured controller [2]. The realization will be accomplished by synthesizing a full-order controller that minimizes the \mathcal{H}_∞ norm of the closed-loop system and then employing an approximation to the dynamic compensator. Basically, the essential frequency-domain characteristics of the full-order controller will be captured and a first-order system that approximates these characteristics will be used for control.

The controller can be formulated in the \mathcal{H}_∞ framework using only information about the open-loop plant but the design of the AAW controller can be simplified by taking advantage of elements from the K_{701E} controller. Specifically, directional control provided by the commands to the rudder is anticipated to be adequate for both the standard F/A-18 and the AAW airplane. Thus, K_{AAW} will generate gains for the wing surfaces from an \mathcal{H}_∞ synthesis and use gains for the rudder from K_{701E} .

The measurements used to generate lateral control are stick command and roll rate. These measurements are chosen to match the signals that are used by K_{701E} to generate commands for the wing control surfaces so that K_{AAW} and K_{701E} have the same architecture and measurement paths. The outputs of the lateral controller are commands to the aileron, leading-edge inboard and outboard flaps, and trailing-edge flap.

The complete lateral-directional controller, K_{AAW} , is composed of the gain matrix, G , and first-order filter, $F(s)$, to generate commands for the wing control surfaces and also K_{701E} to generate commands for the rudder as shown in Figure 1. Note the stabilator command is generated by a 0-gain element to ensure the horizontal tails are not used for rolling maneuvers.

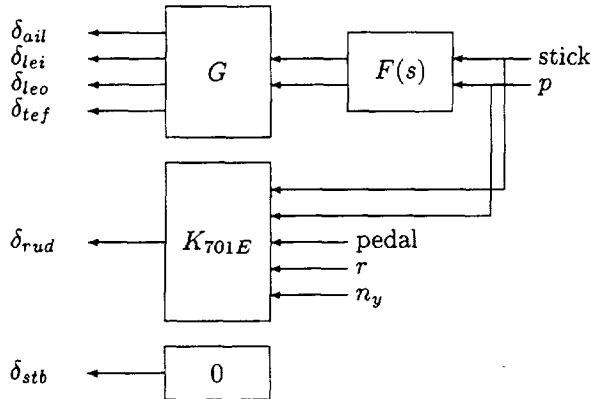


Figure 1: Architecture of K_{AAW}

4. Control Design Approach

The standard framework for \mathcal{H}_∞ synthesis is to formulate a design model such that the objective is to minimize the \mathcal{H}_∞ norm of the closed-loop system [4]. This objective is equivalent to minimizing the largest output that results from any bounded input signal. Thus, the design model must include a set of error signals that should be small if the closed-loop objectives are satisfied.

One of the error signals in the design model is used to ensure the AAW aircraft has acceptable handling qualities. This error signal can be generated by considering traditional metrics for linear models; however, the design for the AAW controller can be simplified by taking advantage of current F/A-18 controllers. Specifically, the Systems Research Aircraft (SRA) is an F/A-18 that operates with the K_{701E} controller and represents a model with acceptable handling qualities [10].

The error signal for handling qualities is defined by requiring the closed-loop response of the AAW airplane to be similar to the closed-loop response of the SRA airplane. This design approach is often called model fol-

lowing or model matching in reference to the objective of making the closed-loop characteristics of a model match the characteristics of another model [1]. The handling qualities of an aircraft are qualitative evaluations of response characteristics so matching the closed-loop AAW and SRA models should attempt to make their handling qualities similar also.

Define a linear system, T , to represent the closed-loop model of the SRA with K_{701E} . The inputs to this model are pilot commands through the lateral stick and rudder pedal and the outputs are the measured values of roll rate, yaw rate, and lateral acceleration. An error signal, e_P , is defined by weighting the subtracted output of T and the corresponding measurements of the AAW.

The weighting function associated with e_P is used to indicate the acceptable levels of difference between the AAW and SRA responses. Essentially, this weighting is the inverse of the acceptable differences such that if $\|e_P\|$ is less than 1 then the error is acceptable. The weighting is frequency-varying to reflect a desire for good tracking performance at low frequencies but allow larger errors at high frequencies.

Define W_P as the performance weighting associated with the model-following error of e_P . The diagonal elements of this weighting are the filters associated with errors in roll rate, yaw rate, and lateral acceleration. For example, the difference in roll rate for the low-frequency response of the AAW and SRA models is desired to be less than 1.15 deg/s so the weighting function has $\frac{1}{1.15} = .87$ as the low-frequency magnitude. Also, the bandwidth of the filter is chosen by placing a pole at $.1 \text{ rad/s}$ to denote the frequency range over which performance is desired. Similar elements of W_P are using a 3.5 weight for yaw rate error and .02 weight for lateral acceleration error.

$$W_P = \begin{bmatrix} \frac{.87}{1000} \frac{s+100}{s+1} & 0 & 0 \\ 0 & \frac{3.5}{1000} \frac{s+100}{s+1} & 0 \\ 0 & 0 & \frac{.02}{1000} \frac{s+100}{s+1} \end{bmatrix}$$

The desire to track only low-frequency responses is also reflected by filtering the stick command. This filter, W_u , is chosen with a maximum magnitude of 3 to reflect that the largest stick command is 3 in. Also, the bandwidth of the filter is chosen to reflect the types of stick motions that are often encountered during maneuvering.

$$W_u = .03 \frac{s + 5000}{s + 50}$$

Another error signal, e_K , is defined to penalize actuator commands such that a large error implies a large actuator command. Associated with this error is a penalty filter to indicate the acceptable magnitudes and rates of the actuator commands. The low-frequency magnitude of this penalty is chosen as the inverse of the position limit of the actuator and the high-frequency magnitude

is chosen to be large to penalize any high-frequency commands. Also, the bandwidth of this filter is chosen to match the actuator bandwidth and ensure the controller does not cause rate saturation.

Define W_K as the weighting associated with the actuator penalty. The filters along the diagonal note frequency-varying upper bounds on the allowable commands to the control surfaces. For example, the leading-edge outboard flaps are limited to positions with magnitudes less than 15 deg so the low-frequency magnitude of the penalty weighting on δ_{leo} and δ_{lei} is .066 as determined by the inverse of the allowable magnitude. The zero of the filter at 4 rad/s is chosen to shape the response near the actuator bandwidth of approximately 0.7 rad/s. Similar elements of W_K are chosen to penalize the other actuators with .02 low-frequency weight on ailerons and .038 low-frequency weight on trailing-edge flaps.

$$W_K = \begin{bmatrix} 2.0 \frac{s+40}{s+4000} & 0 & 0 & 0 \\ 0 & 6.6 \frac{s+4}{s+400} & 0 & 0 \\ 0 & 0 & 6.6 \frac{s+4}{s+400} & 0 \\ 0 & 0 & 0 & 3.8 \frac{s+40}{s+4000} \end{bmatrix}$$

The design model must also include an error signal that represents the objective of load reduction. The approach does not explicitly perform a load minimization; rather, desired loads are noted such that the synthesis computes a controller that restricts the induced loads to be less than these desired loads during a closed-loop maneuver.

The desired loads are chosen based on analysis of the approximate loads encountered by the SRA in response to pilot commands. The bending moments at the wing root and fold are chosen to be similar in magnitude to the SRA responses. The torsion moments at the wing root and fold are allowed to be 4-times greater for the AAW than for the SRA airplane to allow for wing twist. Various values of desired loads were considered but the chosen loads lead to a controller that is able to satisfy the load objective while also satisfying handling qualities and actuator objectives.

An error signal, e_L , is defined as the weighted loads of the AAW. The weighting, W_L , is used to indicate the acceptable levels of loads and penalize loads that are above the desired levels. This error and weighting affect the moments for root bending, root torsion, fold bending, and fold torsion of the wing. A similar error, e_M , is defined by considering the hinge moments on the AAW control surfaces. This error is defined as the weighted values of the hinge moments for the aileron, leading-edge inboard flap, leading-edge outboard flap, and trailing-edge flap of the wing. The rudder could also be included in this error but it does not encounter large moments so it was omitted to reduce complexity of the design model. A weighting, W_M , is used to indicate the maximum moments that can be encountered and ensure that if $\|e_M\|$

is less than 1 then the hinge moments do not violate any structural constraints

$$W_L = \frac{s + 1000}{s + .001} * \begin{bmatrix} 50.0 \frac{s+.03}{s+10} & 0 & 0 & 0 \\ 0 & 6.0 \frac{s+.03}{s+10} & 0 & 0 \\ 0 & 0 & 30.0 \frac{s+.01}{s+10} & 0 \\ 0 & 0 & 0 & 1.5 \frac{s+.01}{s+10} \end{bmatrix}$$

$$W_M = \begin{bmatrix} \frac{1}{48000} & 0 & 0 & 0 \\ 0 & \frac{1}{333000} & 0 & 0 \\ 0 & 0 & \frac{1}{80000} & 0 \\ 0 & 0 & 0 & \frac{1}{130000} \end{bmatrix}$$

The design model used for controller synthesis that includes the error signals is shown in Figure 2. This model denotes P as the open-loop dynamics model of the AAW and L as the loads model of the AAW vehicle.

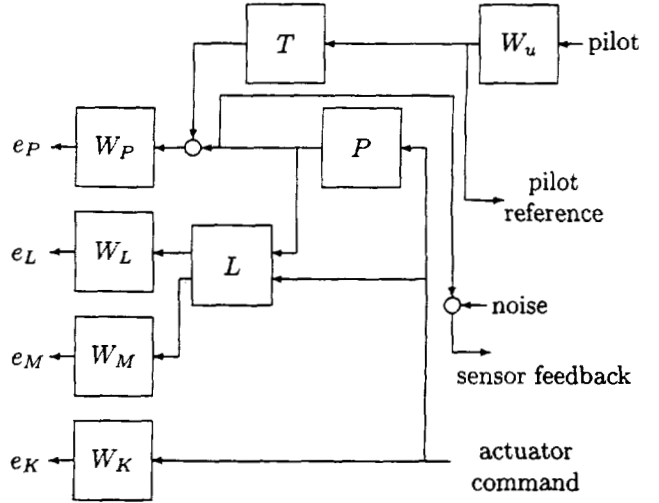


Figure 2: Synthesis Model for Control Design

The resulting controller, K_{AAW} , is actually a structured system that contains elements of K_{701E} as shown in Figure 1. Thus, the synthesis is actually intended to compute only the first-order filter and a set of gains; however, standard algorithms compute an unstructured state-space controller [2]. The procedure to be used for control design is to initially compute a state-space controller that relates the stick command and roll rate measurement to the commands for the wing control surfaces. This initial controller will then be approximated as a first-order filter and a set of gains by analyzing the Bode plot of the dynamical realization. The closed-loop properties are not guaranteed to be similar for the vehicle with the dynamic controller and the approximation; however, the design example demonstrates that such an approximation can be formulated for this aircraft without severely degrading the closed-loop responses.

5. Point Design

5.1. Controller Synthesis

A point design of a controller is computed for the model that represents the AAW in the center of the supersonic envelope at Mach number 1.2 and an altitude of 15 kft. This model was chosen because it is considered to be representative of the general dynamics of the models throughout the supersonic regime.

The controller is computed to minimize the \mathcal{H}_∞ norm of the closed-loop design model. The resulting norm is 1.12 and is slightly greater than the desired norm of 1; however, the objectives are violated by at most 12 percent so this controller achieves reasonable performance levels for the design model.

The objectives that are driving the control design are trying to achieve good handling qualities while avoiding actuator saturation. In particular, the closed-loop \mathcal{H}_∞ norm reflects properties of the transfer function from the stick to the performance objective for roll rate and from the stick to the actuator constraint on the leading-edge inboard flap. This implies the control synthesis is inherently limited by balancing the tradeoff between handling qualities and actuator constraints. Thus, attempting to minimize the loads, rather than simply reducing the loads, will cause a further tradeoff and result in larger violations of either the handling qualities or actuator objectives.

The initial realization of the controller is a state-space system with 60 states. Model reduction algorithms can reduce this dimension to 10 states without causing a noticeable degradation in performance; however, the desired architecture requires a first-order filter and gain implementation. An approximation of the controller that allows this implementation can be realized by considering the Bode plots of the transfer function from stick to the leading-edge surface commands as shown in Figure 3.

A notable feature of these frequency responses is their similarity to frequency responses of first-order filters. In particular, the magnitude and phase show little variation with frequency until 10 rad/s and then the magnitude shows a first-order rolloff. This behavior suggests a controller realization of a first-order filter that has a pole at 10 rad/s and a magnitude that matches the low-frequency magnitude of Figure 3.

A similar approximation must be performed to generate the gains that produce trailing-edge surface commands from controller inputs. The Bode plots of the corresponding transfer functions of the dynamic controller are shown in Figure 4. These plots show that a first-order approximation can not accurately capture the dynamics of the full-order controller; however, the approximation can still loosely represent the general features.

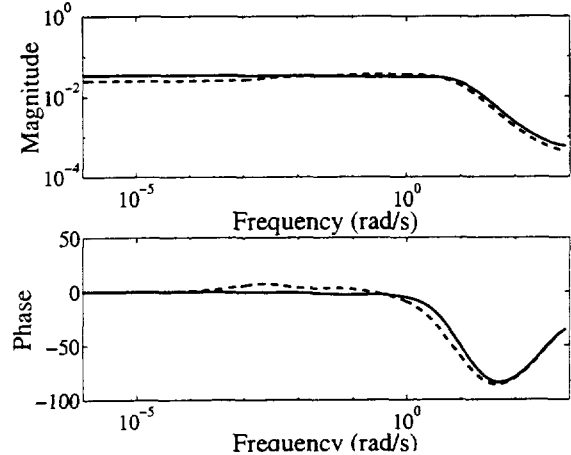


Figure 3: Bode Plot of the Dynamic Controller from Stick to Control Surface Command for Leading-Edge Inboard Flap (—) and Outboard Flap (---)

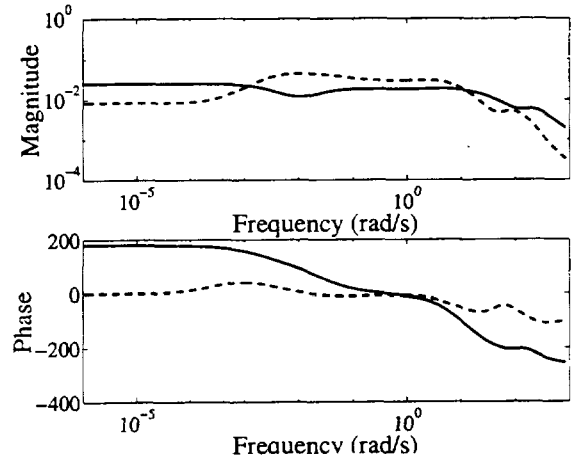


Figure 4: Bode Plot of the Dynamic Controller from Stick to Control Surface Command for Aileron (—) and Trailing-Edge Flap (---)

The approximation procedure is applied to the entire controller for both stick and roll rate inputs using the same first-order filter. The only parameters that are allowed to vary are the magnitude of the gains for each channel. This type of approximation is necessary because the implementation requires a single filter to be used. The resulting elements of K_{AAW} , labeled G and $F(s)$ in Figure 1, can be realized as a filter and matrix combination.

$$\begin{bmatrix} \delta_{ail} \\ \delta_{lei} \\ \delta_{leo} \\ \delta_{tef} \end{bmatrix} = .01 \frac{s + 1000}{s + 10} \begin{bmatrix} -0.025 & -7.0 \times 10^{-6} \\ 0.034 & -5.0 \times 10^{-7} \\ 0.025 & -1.1 \times 10^{-6} \\ 0.008 & -1.2 \times 10^{-5} \end{bmatrix} \begin{bmatrix} \text{stick} \\ p \end{bmatrix}$$

K_{AAW} has several features that can be related to K_{701E} . Firstly, the gains in different columns of the matrix have predominately different signs. This indicates the surface

commands are actually generated by a weighted difference between stick command and measured roll rate in a similar fashion as K_{701E} . The aileron command appears to differ from this structure but actually this flight condition is beyond roll reversal so the aileron has the opposite behavior of the leading-edge surfaces.

Another feature is the magnitude difference between the gains for the stick command and roll rate feedbacks. This difference matches the behavior of K_{701E} and weights the stick command larger than the roll rate. Essentially, the lateral-directional controller is like an open-loop gain that does not strongly depend on feedbacks.

The closed-loop model of the AAW with K_{AAW} is not guaranteed to have similar properties as the closed-loop model of the AAW with the full-order dynamic controller; however, the controller approximation is not anticipated to dramatically degrade closed-loop performance. Consider that the leading-edge surfaces are the main effectors for roll performance and handling qualities. The controller elements that generate commands for these surfaces are quite similar between the dynamic controller and K_{AAW} so the performance should be similar. Conversely, the commands for the trailing-edge surfaces are not generated by a high quality approximation but these commands do not strongly affect roll performance. Thus, the approximation used to formulate K_{AAW} should not drastically alter the closed-loop properties as compared to the full-order \mathcal{H}_∞ controller.

5.2. Linear Simulation

Time responses of the closed-loop system are simulated using a linear model of the lateral-directional dynamics and K_{AAW} . These simulations do not include all aspects of the aircraft and so are not intended to accurately predict the responses of the full-order nonlinear system. Despite this limitation, the simulated responses are valuable to consider because they demonstrate if the methodology is able to compute a controller that achieves the desired closed-loop objectives for a general model.

One of the main performance objectives of the control design is to match handling qualities for the AAW and SRA. There are several criteria used to evaluate handling qualities but a simple way to roughly compare handling qualities is to compare transient responses. Essentially, if the aircraft respond similarly then their handling qualities, which are based on response characteristics, are probably also similar. Responses from the AAW with K_{AAW} and the SRA with K_{701E} are simulated in response to a doublet command through the lateral stick as shown in Figure 5.

This stick command is chosen to demonstrate several closed-loop properties. The initial command of 1.5 in is a half-stick command so the AAW response and han-

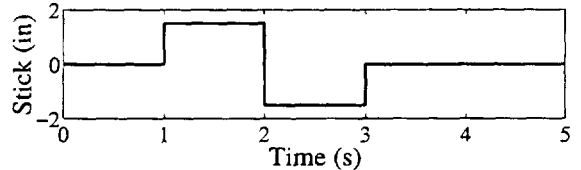


Figure 5: Stick Command

dling qualities should closely match the SRA performance without saturating the actuators. The response to this command should demonstrate half of the maximum roll rate that can be achieved with K_{AAW} . The second command of 3 in will demonstrate the full-stick response and indicate if excessive saturation is commanded.

The responses of the body-axis orientation angles to the lateral stick command are shown in Figure 6. The similarity of the AAW and SRA responses demonstrates the controller is able to achieve the desired model-following, and consequently handling qualities, characteristics.

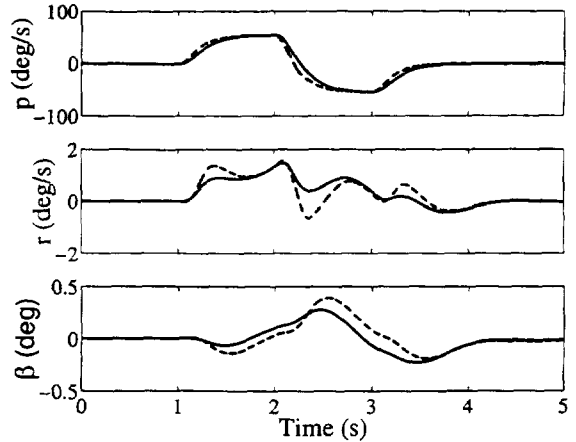


Figure 6: Sensor Measurements during Doublet Maneuver : AAW (—), SRA (---)

There are several features in the roll rate responses of Figure 6 that can be used to evaluate the performance of K_{AAW} . One feature is the similarity in roll rate that is achieved for the half-stick command. Both aircraft show roll rates near 55 deg/s so the maximum roll rate for the AAW is 110 deg/s in response to a full-stick command. This roll rate satisfies the performance objective of matching the maximum roll rate for the AAW and SRA. There is a slight lag in the AAW response as compared to the SRA; however, the small delay should not overly affect handling qualities and can perhaps be altered by simply tweaking the controller gains.

The remaining responses of Figure 6 also demonstrate interesting features. The angle of sideslip in the responses is similar in both magnitude and direction and this is an important factor in determining handling qualities.

Also, the yaw rate shows some difference between AAW and SRA responses so the elements of K_{701E} that are used in K_{AAW} may have to be slightly altered because K_{701E} does not account for the altered roll dynamics.

Figure 7 presents the control surface positions for each aircraft in response to the stick doublet. These positions demonstrate the actuator positions are not saturated during the transient maneuver despite the stick being moved to half of its maximum position. These linear results demonstrate that the leading-edge inboard flap would be slightly position saturated for a full 3 in stick command; however, the remaining surfaces would not be position saturated.

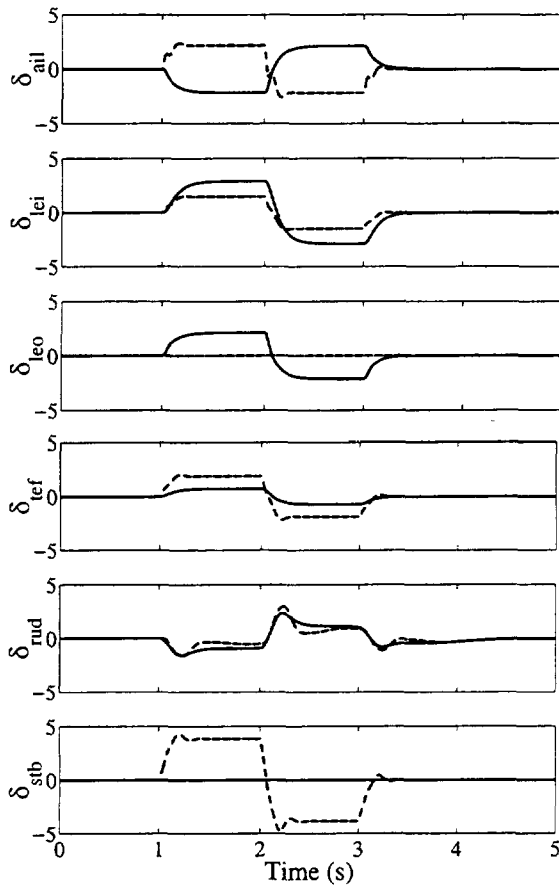


Figure 7: Surface Positions in *deg* during Doublet Maneuver : AAW (—), SRA (---)

Figure 7 clearly demonstrates the difference in control allocation for the AAW and SRA aircraft. The stabilator is the main effector for generating roll at this flight condition for the SRA airplane and this surface moves more than any other. Conversely, the stabilator does not move at all during the maneuver for the AAW. The AAW controller accounts for the loss of the powerful stabilator by commanding larger positions for the leading-edge inboard and outboard flaps to generate roll.

The aileron and trailing-edge flaps are noticeably different during the AAW and SRA responses. In particular, the aileron moves in the opposite direction. These differences result from the inclusion of loads minimization as a closed-loop objective. The design model restricted the bending moment to be similar for the AAW and SRA vehicles but allowed the torsion moment to increase for the AAW. The controller for the AAW is positioning these trailing-edge surfaces mainly to achieve the loads objectives because the leading-edge surfaces are already achieving the handling qualities objectives.

The issue of rate saturation for actuators is often more constraining than position saturation so the surface rates during the maneuver are shown in Figure 8. The surface rates are not saturated during the initial stick movement of 1.5 in; however, the leading-edge inboard and outboard surfaces are rate saturated for the stick movement of 3 in. This saturation is tentatively considered acceptable because it occurs for a very short time, and nonlinear simulations not presented in this paper indicate only a slight lag in the response due to rate limiting.

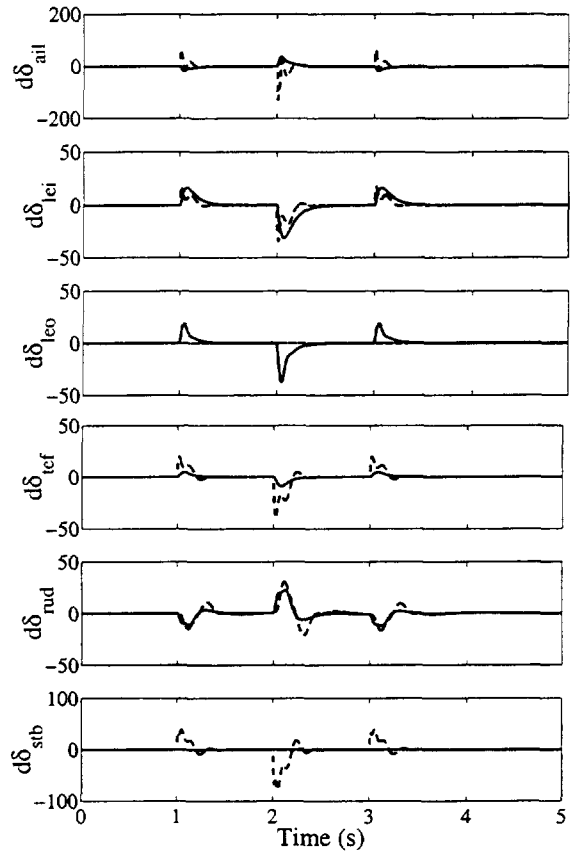


Figure 8: Surface Rates in *deg/s* during Doublet Maneuver : AAW (—), SRA (---)

The hinge moments on the control surfaces are also of importance for this maneuver because the aircraft is operating at high dynamic pressures. The main concern is for the wing surfaces so the corresponding moments are shown in Figure 9. The hinge moments encountered during the maneuver are generally greater for the AAW than for the SRA but remain within the allowable limits.

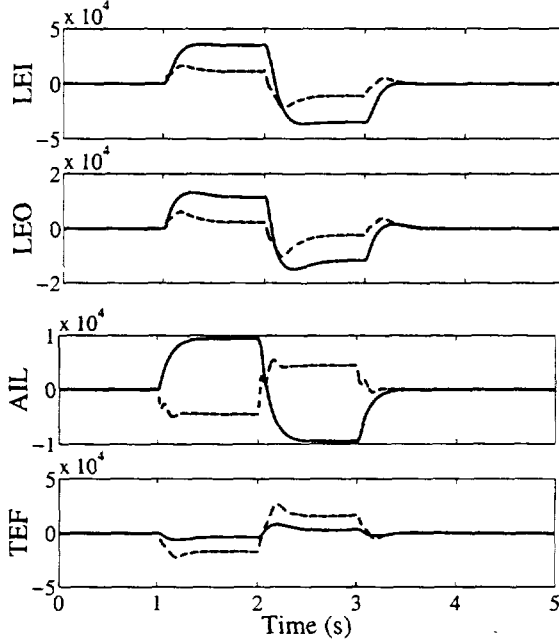


Figure 9: Left-Wing Hinge Moments during Doublet Maneuver : AAW (—), SRA (---)

The loads on the structure must be analyzed to demonstrate if the objective of load reduction is achieved and, more importantly, to ensure no loads on the structure exceed the physical limitations. Figure 10 shows that the bending and torsion moment at the wing root is within acceptable levels.

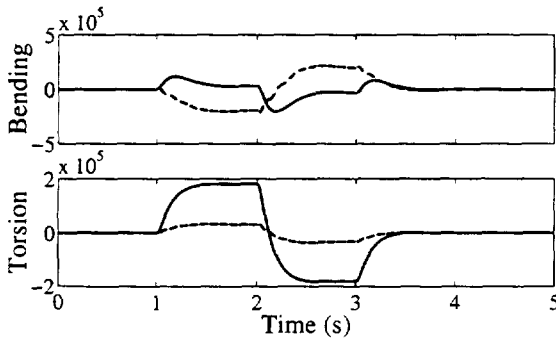


Figure 10: Left-Wing Root Moments during Doublet Maneuver : AAW (—), SRA (---)

The load magnitudes in Figure 10 agree with the loads objective that are in the design model. Specifically, the bending moment is similar between the AAW and SRA

but the torsion moment is greater for the AAW than for the SRA. This increase in torsion is expected because the SRA avoids wing twist by using the stabilator to generate roll at this flight condition whereas the AAW commands a wing twist, and consequently torsion, to generate roll. The loads at the wing fold are not shown here but they are similar in nature to the loads at the wing root; namely, the bending moment is smaller for the AAW and the torsion moment is greater but both are within acceptable limits.

5.3. Robustness Analysis

The issue of robustness with respect to modeling uncertainty is an important consideration for predicting the closed-loop properties of the AAW. Some indication of robustness can be obtained by performing extensive Monte Carlo simulations of the full-order nonlinear model; however, a more rigorous evaluation of robustness can be obtained for the linear model by analyzing the structured singular value. This value, μ , reflects whether a model is robust with respect to a set of uncertainty operators [6].

There are several areas of the open-loop model with which uncertainty should be associated. Consider that one of the fundamental flight test objectives of the AAW program is to investigate the technologies associated with modeling of aeroelastic deformation and structural loads at high dynamic pressures. Essentially, full-scale aircraft have not flown with these configurations before so the fidelity of the dynamic models is unclear.

Uncertainty should be associated with the open-loop model to account for potential errors and unmodeled dynamics in the effectiveness of the control surfaces. The model is formulated using static analysis that notes the amount of wing twist that results from placing the control surfaces at any position. This type of model may be overly simplistic because the wing may twist dynamically with nonlinear and time-varying effects.

Introduce a norm-bounded operator, Δ_{in} , to represent a multiplicative uncertainty on the plant input and account for errors in control surface effectiveness. This uncertainty is weighted to allow the error to increase from 5% error near $.1 \text{ rad/s}$ up to 500% error at high frequencies. This weighting is represented by a diagonal matrix, W_{in} , and associates the same levels of uncertainty with the effectiveness of each control surface.

$$W_{in} = 5 \frac{s + 5}{s + 500} \frac{s + .001}{s + .1} I$$

Uncertainty should also be associated with the output of the open-loop model to account for errors in the amount of roll that is predicted to be generated by wing twist. These predictions are partially based on roll rates that were measured during static testing of partial-scale models in wind tunnels; therefore, errors may occur from is-

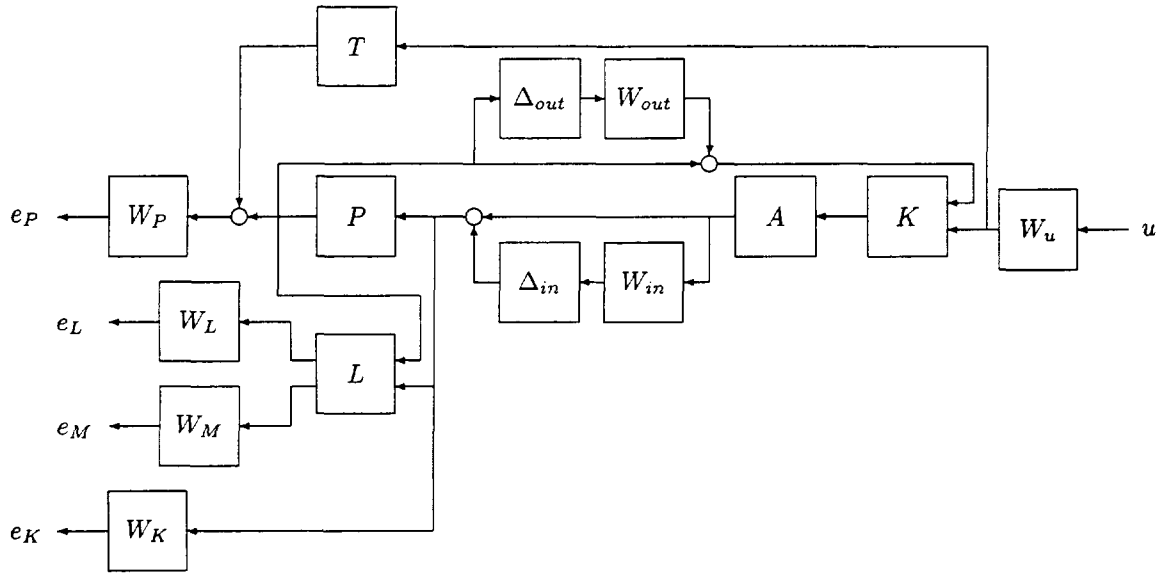


Figure 11: Model with Uncertainty Description

sues related to transients, scaling factors, and structural complexities associated with the wing fold.

Associate a norm-bounded operator, Δ_{out} , only with the sensor measurements of the open-loop model that represents errors in roll rate. A weighting function, W_{out} , scales this operator such that the robustness analysis considers errors in roll rate ranging from 10% near .1 rad/s to 1000% at high frequencies.

$$W_{out} = 10 \frac{s + 5}{s + 500} \frac{s + .001}{s + .1}$$

Figure 11 presents the closed-loop AAW model with uncertainty operators. Robustness is analyzed by computing μ with respect to Δ_{in} and Δ_{out} for the transfer function from pilot commands to errors.

Figure 12 presents the upper bound for μ that measures robust performance of the closed-loop system. The peak value shows $\mu \leq 1.5$ so the system does not quite meet the desired robustness goal of $\mu < 1$. The peak occurs near the natural frequency associated with the roll mode and agrees with the synthesis that noted the driving constraint for control design was achieving roll performance. Essentially, the controller is optimized to affect this roll mode and consequently is somewhat sensitive to modeling errors.

Also, the robustness of the AAW with the full-order dynamic controller and the approximation used as K_{AAW} is shown in Figure 12. This plot demonstrates that the robustness is quite similar for either closed-loop system. This indicates that the approximation was good and did not severely degrade performance or introduce any sensitivity to modeling errors. Actually, the robustness at lower frequencies is greater for K_{AAW} than for the dy-

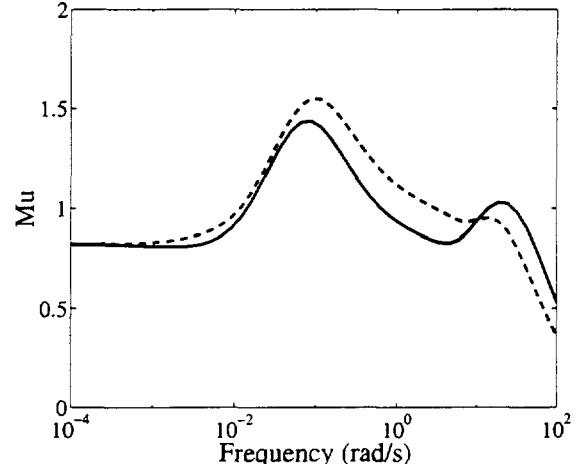


Figure 12: μ for Robust Performance of Error Signals : K_{AAW} (—), Full-Order \mathcal{H}_∞ Controller (---)

namic controller so the approximation was able to reduce sensitivity near the roll mode.

6. Control Design as an AAW Technology

The fundamental objective of the AAW program is to demonstrate several areas of technology including aeroservoelastic control; however, the methodology of designing the corresponding controller is generally not considered an AAW technology. This exclusion may be true for certain types of control design but an argument can be made that the \mathcal{H}_∞ approach can greatly facilitate the utilization of AAW technology. Thus, the method of control synthesis may be considered as an indirect, but related, area of AAW technology.

The synthesis objective is to minimize the \mathcal{H}_∞ norm of the closed-loop system or equivalently to minimize the maximum size of the errors that result from a pilot command. The nature of the \mathcal{H}_∞ norm directs the synthesis to reduce the size of the largest error and ensure the sizes of all the remaining errors are no greater than this largest error. For example, if the error related to handling qualities or actuator constraints is larger than the error related to loads then the controller does not minimize the loads error.

The \mathcal{H}_∞ approach for control design does not directly perform a loads minimization; rather, the compensator achieves a level of loads control. Essentially, the weighting on the error signal is chosen at a level for which a controller exists that makes the closed-loop \mathcal{H}_∞ norm to be unity. The AAW will achieve the handling qualities and actuator objectives while reducing the loads to less than the values associated with the error weighting if this norm condition is satisfied. In this way, the synthesis performs a simultaneous optimization for loads, handling qualities, actuator, and performance objectives.

This simultaneous optimization suggests that the \mathcal{H}_∞ methodology may be a valuable asset in realizing AAW technology on future aircraft. The ability to simultaneously consider several closed-loop objectives presents a method to easily determine the achievable properties of the aircraft. The designer simply iterates over values of the weighting functions to determine what levels of performance and loads reduction can be achieved for a particular set of actuator constraints. This approach allows a straightforward determination of the benefits that can be achieved by the remaining elements of AAW technology.

7. Concluding Remarks

The Active Aeroelastic Wing program has several objectives that present challenges for control design. This paper presents an \mathcal{H}_∞ approach that encompasses these objectives in the controller synthesis. The design model is formulated by generating errors that relate to handling qualities, performance, actuator, and loads objectives. The resulting controller is designed by simultaneously considering all these closed-loop objectives. A point design is used to demonstrate that the approach generates controllers that achieve these goals.

8. Acknowledgments

The author would like to acknowledge the valuable comments and suggestions from several members of the AAW project team at NASA Dryden. Marty Brenner was particularly instrumental in that he helped to develop the framework for including the objectives in the design model. John Carter and Joe Gera were especially helpful and their ideas were essential for formulating robust controllers that could be implemented on the aircraft. The author also appreciates the extensive tutorials on F/A-18 and the production controller that were provided by Joe Pahle, John Burken, and Mark Stephenson.

References

- [1] B.D.O. Anderson and J.B. Moore, *Optimal Control - Linear Quadratic Methods*, Prentice-Hall, Englewood Cliffs, NJ, 1990.
- [2] G. Balas, J. Doyle, K. Glover, A. Packard and R. Smith, μ -*Analysis and Synthesis Toolbox - Users Guide*, The Mathworks, Natick MA, 1991.
- [3] R.L. Bisplinghoff and H. Ashley, *Principles of Aeroelasticity*, Dover Publications, Inc., New York, 1962.
- [4] J. Doyle, K. Glover, P. Khargonekar, and B. Francis, "State-space solutions to standard \mathcal{H}_2 and \mathcal{H}_∞ control problems," *IEEE Transactions on Automatic Control*, Vol. 34, No. 8, August 1989, pp. 831-847.
- [5] S.K. Krone, L.D. Arnold, and R.K. Hess, *F/A-18 A/B/C/D Flight Control System Design Report Vol. 1 - System Description and Theory of Operation*, McDonnell Aircraft Company, MDC-A7813, December 1992.
- [6] A. Packard and J. Doyle, "The Complex Structured Singular Value," *Automatica*, Vol. 29, No. 1, 1993, pp. 71-109.
- [7] E. Pendleton, K.E. Griffin, M.W. Kehoe, and B. Perry, "A Flight Research Program for Active Aeroelastic Wing Technology," *AIAA Structures, Structural Dynamics, and Materials Conference*, AIAA-96-1574, April 1996.
- [8] E. Pendleton, D. Bessette, P. Field, G. Miller, and K. Griffin, "The Active Aeroelastic Wing Flight Research Program," *AIAA Structures, Structural Dynamics, and Materials Conference*, AIAA-98-1972, April 1998.
- [9] B. Perry, S.R. Cole, and G.D. Miller, "A Summary of an AFW Program," *Journal of Aircraft*, Vol. 32, No. 1, January 1995.
- [10] J.R. Sitz, *The F-18 Systems Research Aircraft Facility*, NASA-TM-4433, 1992.
- [11] S. Zillmer, *Integrated Structure/Maneuver Design Procedure for Active Aeroelastic Wings - User's Manual*, Wright Laboratory, Dayton OH, WL-97-3037, March 1997.

Aeroelastic Constraints in MDO

F. Mastroddi, E. Ciancaleoni

Dipartimento Aerospaziale – Università degli Studi di Roma “La Sapienza”
via Eudossiana, 16 – 00184 Rome – Italy – E-mail franco@mastroddi.ing.uniroma1.it

L. Morino

Dipartimento di Meccanica Industriale – Università di Roma Tre
via Della Vasca Navale, 79 – 00146 Rome – Italy – E-mail l.morino@uniroma3.it

Abstract

A Multidisciplinary Design Optimization (MDO) study for a transport configuration with emphasis on the integrated aerodynamic and structural design of the wing is presented. The novelty is in the use of aeroelastic constraints for flutter as well as gust response (both deterministic and stochastic).

1 Introductory remarks on MDO

Multidisciplinary Design Optimization (MDO) has recently recognized as a new and important field of study, dealing with analysis and optimal design of complex systems; these systems are typically assumed to be built by multi-disciplinary models. These disciplines may correspond either to fields of study (*e.g.*, for an aircraft, aerodynamics, structures, performance, propulsion), or may correspond to physical parts of the system (wing, fuselage, engines). Because of the relevance of the discipline modeling, probably a more appropriate definition of this kind of design could be Multi-disciplinary Modeling and Design Optimization (MMDO). The essential objective of MDO could be to enable the manufacturing companies to reduce the design time cycle and to produce reliable and efficient optimum designs in the preliminary design phase.

In the past decade a growing interest in multi/inter-disciplinary engineering optimization has been revealed and several approaches to problem formulation have emerged in the aerospace field (see Refs. [1, 2, 3] for recent references on the subject). Balling and Sobiesczanski-Sobieski have developed interdisciplinary optimization approach (Refs. [4, 5]), which is adopted in this paper. According to the standard MDO classification, the algorithm employed in this paper may be classified as a *single-NAND-NAND* approach. Finite-State Aerodynamics (FSA, [6]) is an essential tool used to describe the Generalized Aerodynamic Force (GAF) matrix in terms of state-space variables in framework of the MDO (see Ref. [7]). In this paper we have developed an aeroelastic model (stability and response) in the framework of an MDO: the obtained results for a transport wing have revealed that these constraints can significantly drive the aircraft preliminary design.

design variables		Aircraft reference configuration	
Root chord length	5.43 m	Fuel weight (W_{fuel})	24000 lbs
Tip chord length	1.105 m	Payload(W_{pl})	21917 lbs
Root thickness ratio	11.3%	Empty weight (W_e)	121000 lbs
Tip thickness ratio	9.42%	Take off weight (W_{to})	57190 lbs
Half span	14.23 m	Aerodynamic efficiency (E)	19.2
Swept angle at 1/4 c	24.5°	Range (R)	2480 mn
Root skin-panels thickness	1.5 mm	Cruise altitude	18000 ft
Tip skin-panels thickness	0.9 mm	Cruise Mach number	0.6
Root spar thickness	9 mm	Flutter speed	240 m/s
Tip spar thickness	4.5 mm	Bending stiffness distribution coefficient	0.3
Root stringer cross-area	0.0015 m ²	Torsional stiffness distribution coefficient	0.3
Tip stringer cross-area	0.00075 m ²		

Table 1: Design variables and aircraft reference configuration

2 Aircraft preliminary design as MDO problem

Aircraft design is typically a very complex problem as it involves several different fields. In the present work we have selected, as design disciplines, structural dynamics (modal description), stress analysis, aerodynamics (lift and drag evaluations), aeroelasticity (stability and gust response analysis), and flight performance (mission range estimate). The problem investigated is the integrated optimal design of a subsonic transport wing with focus on the influence of response and aeroelastic constraints (in addition to some performances and structural constraints). In the following, some aspects of the optimization problem for a fairly general objective function are briefly outlined.

The design variables and reference aircraft configuration are shown in Tab. 1 (to which the reader is referred for the symbols used for each variable): this airplane belongs to the same class as MD80, DC9-80, A320, or B737-300. The objective function to be minimized is given by:

$$F = \eta_1 \frac{W_e}{W_{er}} + \eta_2 \frac{R}{R_r} + \eta_3 \frac{W_{uf}}{W_{ufr}} + \eta_4 \frac{W_{pl}}{W_{plr}} \quad (1)$$

(where the subscript r denote “reference”, *i.e.*, the initial value of the optimization procedure, as obtained from the initial guess of the design variables). The factors assumed in the problem are: $\eta_1 = 0.7$, $\eta_2 = -0.1$, $\eta_3 = 0.1$, and $\eta_4 = -0.1$. The empty weight W_e is computed from the empty weight of the reference configuration, W_{er} , assuming that the reduction in the structural wing weight is reflected on the aircraft gross weight amplified by a factor $\beta > 1$, due to corresponding savings in the weight of tail and fuselage as well as non-structural weight: $W_e = W_{er} - \beta (W_{wr} - W_w)$, where W_{wr} and W_w denote the actual and the reference structural wing weight respectively. A value $\beta = 2$ is assumed in this study.

The constraints assumed in this design problem are structural, aeroelastic, response, and performance constraints. The constraints imposed are: (1) minimum range allowed, R_a ; (2) minimum wing volume available to contain fuel V_f required by the mission, V_{uf} ; (3) minimum aerodynamic efficiency allowed, E_a ; (4) maximum stress allowed in the spars, τ_a ; (5) maximum stress allowed in the stringers, σ_a ; (6) minimum flutter speed allowed U_{Fa} ; (7) maximum load factor allowed in presence of gust input (*e.g.*, as prescribed by the international aviation requirements); (8)

maximum covariance value of certain quantities of interest (such as load factor or wing root bending moment) in presence of gust random input (specifically, white noise input). Regarding the limit values associated to these constraints, a minimum range value of $R_a = 2000\text{nm}$ (3706km) has been imposed, whereas a value $E_a = 16$ has been assigned for the aerodynamic efficiency constraint. Maximum values assumed for stress in spars and stringers were respectively $\tau_a = 206\text{MPa}$ and $\sigma_a = 413\text{MPa}$. Moreover, a minimum flutter speed of $U_{Fa} = 250\text{m/s}$ is imposed. The upper value for the load factor constraint has been assigned equal to 3.5 according to widely used estimate for transport aircraft; on the other hand, the covariance limit value for the state-space variables has been estimated by using a white noise with intensity equal to the maximum value in the Dryden spectrum (Ref. [9]).

In order to solve the above problem the Sequential Unconstrained Minimization Technique (SUMT, see *e.g.*, Ref. [10]), with quadratic extended interior penalty function (see, *e.g.*, Ref. [11]), has been used. The sequence of unconstrained minimizations generated by this method have been resolved by the BFGS (*Broyden-Fletcher-Goldfarb-Shanno*, Ref. [12]) algorithm. The one-dimensional minimization associated to each search direction defined by the BFGS algorithm has been carried out by quadratic interpolation of the objective function. The optimization code used in the present paper was obtained from *FLOPS*, Refs. [14, 15], by replacing several modules; specifically, the unsteady aerodynamics module (generalized aerodynamic matrix), the static and dynamic aeroelastic module (finite-state aerodynamics and stability), and the structural dynamics module (FE model for a beam-like wing) have been introduced in Ref. [16], whereas the gust-response module introduced in this work.

3 Discipline modeling

MDO complexity makes important to assure the global efficiency of the discipline models. The models used to describe the disciplines (*e.g.*, aeroelasticity, structures and gust response) should combine accurate descriptions of the physical phenomena and reduced computational requirements. In the following the modeling for structure, aeroelastic, gust response, and performances modeling employed in the MDO process is presented.

3.1 Structural modeling for the wing

The structural analysis of the wing has been carried out by a bending/torsion beam model with geometrical and structural parameters varying in the spanwise direction (*i.e.*, spar and stringer cross section areas, skin panel thickness, bending and torsional moment of inertia etc.). Using standard Hermite function for FE beam description and linear function for FE torsion description, Galerkin method yields $\mathbf{M}\ddot{\mathbf{u}} + \mathbf{K}\mathbf{u} = \mathbf{f}$, where $\mathbf{u} = (w_1, w'_1, \theta_1, w_2, w'_2, \theta_2, \dots, w_N, w'_N, \theta_N)^T$, where w_i , w'_i , and θ_i are the FE nodal unknowns (bending displacement, bending angle, and torsion angle) and \mathbf{f} is the vector of the loads. The evaluation of the discrete natural angular frequency ω_n and eigenvector $\mathbf{z}^{(n)}$ is obtained from the associated eigenproblem $-\omega_n^2 \mathbf{M}\mathbf{z}^{(n)} + \mathbf{K}\mathbf{z}^{(n)} = 0$. The results of the structural dynamic analysis are presented in Tab. 2, which compares our results with those obtained with the MSC/NASTRAN code. In Reference [16], suitable design variables were also introduced in order to take into account the span-wise variations of the wing characteristic due to the taper ratio; in particular, we prescribed, for bending moment of inertia $I(y) = I_R + (I_T - I_R)(y/L)^{\gamma_1}$ and for the torsional moment of inertia $J(y) = J_R + (J_T - J_R)(y/L)^{\gamma_2}$ (γ_1 and γ_2 are the design variables defining the span-variation laws, the subscripts R and T

Mode	MSC/NASTRAN		MDO code	
	Hz	Hz	mode type	
-				
1°	0.79	0.79	Bending	
2°	3.10	3.23	Torsional	
3°	3.28	3.34	Bending	
4°	6.03	7.05	Torsional	
5°	7.71	8.1	Bending	
6°	8.21	11.16	Torsional	

Table 2: Half Wing Structural Dynamics

indicates the root and tip values respectively, and L is the half-span length): nevertheless, in the design process these variables did not change significantly from the values $\gamma_1 = \gamma_2 = 0.3$. This value has been adopted here.

3.2 Aerodynamics modeling: FSA for GAF matrix

The structure is represented in term of its natural modes of vibration, $\Phi_n(\xi^\alpha)$ (obtained from the analysis of Section 3.1), as $\mathbf{u}(\xi^\alpha, t) = \sum_n q_n(t) \Phi_n(\xi^\alpha)$, where the ξ^α are material curvilinear coordinates. In the absence of structural damping, the aeroelastic problem expressed in terms of Lagrangian variables $q_n(t)$ is governed by the equation:

$$\frac{d^2\mathbf{q}}{dt^2} + \Omega^2\mathbf{q} = \mathbf{e} + \mathbf{f}_g \quad (2)$$

where \mathbf{q} denotes the Lagrangian coordinate vector, Ω^2 the diagonal matrix of the eigenvalues of the structure, \mathbf{e} the vector of the generalized forces due to the elastic motion ($e_k := -q_D \oint_{S_B} c_p \mathbf{n} \cdot \Phi_k dS$), and \mathbf{f}_g the generalized gust input (see next Section). Next, consider the GAF matrix $E(s)$ which relates the Laplace transform of the generalized aerodynamic forces $\tilde{\mathbf{e}}$ to the Laplace transform of the Lagrangian variables $\tilde{\mathbf{q}}$: $\tilde{\mathbf{e}} = q_D E \tilde{\mathbf{q}}$, where q_D is the dynamic pressure. In order to perform the aeroelastic analysis in the framework of the optimization procedure, a finite-state approximation for the aerodynamic matrix has been considered: it consists of approximating the aerodynamic matrix as (Ref. [6])

$$E(p) \simeq A_2 p^2 + A_1 p + A_0 + (pI - P)^{-1} R \quad (3)$$

where $p = sl/U_\infty$ is the dimensionless Laplace variable and all the matrices on the right hand side may be evaluated by a least square procedure on a set of aerodynamic data. Substituting Eq. 3 into the Eq. 2, considering the definition for p , setting $\tilde{\mathbf{r}} := -q_D [(pI - P)^{-1} R] \tilde{\mathbf{q}}$, and introducing the matrices $M_e := I - q_D A_2 l^2 / U_\infty^2$, $C_e := -q_D A_1 l / U_\infty$, and $K_e := \Omega^2 - q_D A_0$ one obtains, in the time domain (for $l = 1$)

$$\begin{bmatrix} 1 & 0 & 0 \\ 0 & M_e & 0 \\ 0 & 0 & 1 \end{bmatrix} \begin{Bmatrix} \dot{x}_1 \\ \dot{x}_2 \\ \dot{x}_3 \end{Bmatrix} = \begin{bmatrix} 0 & 1 & 0 \\ -K_e & -C_e & -1 \\ -q_D U_\infty R & 0 & U_\infty P \end{bmatrix} \begin{Bmatrix} x_1 \\ x_2 \\ x_3 \end{Bmatrix} \quad (4)$$

with $x_1 \equiv \mathbf{q}$, $x_2 \equiv \dot{\mathbf{q}}$, and $x_3 \equiv r$. Then, the system has been reduced to the standard form $\dot{\mathbf{x}} = A_{U_\infty} \mathbf{x}$, where the parametric dependence of the matrices upon the air speed has been emphasized.

Note that this approach allows one to reduce the aeroelastic stability analysis to a root locus for the matrix A_{U_∞} , thereby avoiding classical methods (*e.g.*, V - g and p - k method), which would unnecessarily complicate the optimization procedure.

The Finite-State formulation for the forces due to gust is similar (see Ref. [17] for details).

3.3 Performance model

The mission profile considered in this study is described in the following: take-off, climbing, a cruise segment, descent and landing. The range is computed according to the Breguet equation $R = (v_c L/cD) \ln(W_i/W_f)$, where v_c is the cruise speed, c the specific fuel consumption, L/D the lift to drag ratio, and W_i and W_f the initial and final weights of the cruise mission segment, respectively; expressing the fuel consumptions in the mission segments before and during the cruise segment as fractions of the usable mission fuel weight W_{uf} (indicated as k_1 e k_2 respectively), W_i e W_f can be written as: $W_i = W - k_1 W_{uf}$ and $W_f = W - (k_1 + k_2) W_{uf}$.

4 Numerical results

Considering the reference aircraft configuration, given in Tab. 1, the preliminary design problem of the wing of a transport jet aircraft in cruise-flight conditions have been investigated. Specifically, special emphasis has been given to the role of aeroelastic and response constraints. The following mission requirements were assumed: *(i)* payload: 100-130 passengers; *(ii)* cruise altitude: 18,000ft; *(iii)* range: 2,000nm; *(iv)* cruise Mach number: $M_\infty = 0.6$. These characteristics are relative to medium-range aircrafts like *B737 – 300, DC9 – 80, A320*: in particular, the *DC9* configuration was assumed as the reference aircraft configuration in this optimization study (it has a relatively clean wing, without engine nacelles and kinks). Starting from the reference configuration, a preliminary analysis has been performed in order to obtain the reference parameters for the optimizer, see Eq. 1. Specifically, dynamic, aeroelastic, and performance analyses were carried out and the obtained results summarized in Tabs. 1 and 2. This preliminary analysis also required to define the constraint values as shown in the previous sections.

First, we have compared the results obtained without the flutter constraint with those obtained with this constraint: the constraint on the performances and on maximum stresses are always present in both analyses. Figure 1 and the Table presented in Fig. 2 show how the flutter constraint reduces the sweep and wing planform variations and limit the possibility to reduce the aircraft weight. When the flutter constraint is not present, the normal-stress constraint yields the design result as shown in Fig. 3. As apparent from Fig. 4 (corresponding to the same case), the removal of flutter constraint yields a considerable improvement of the payload. However, this yields also an unacceptable increasing of the flutter speed, thereby demonstrating the importance of including in the optimization design the flutter constraint.

Next, consider the results obtained in the presence of the gust-response constraints: using Liapunov equation (see, *e.g.*, Ref. [18]), the covariance matrix P_x for the state-space vector has been explicitly obtained analytically as a function of the white noise input level and the system matrix. Then, system response to the white-noise gust response has been considered as a constraint, as indicated in the following: the white-noise spectrum level (constant in the frequency domain) has been assigned equal to the maximum value of Dryden gust spectrum corresponding to $L = 2500$ and $\sigma = 1$ (Ref. [9]): see Fig. 5, and 6 for the payload and covariance matrix constraint *vs* iteration number.

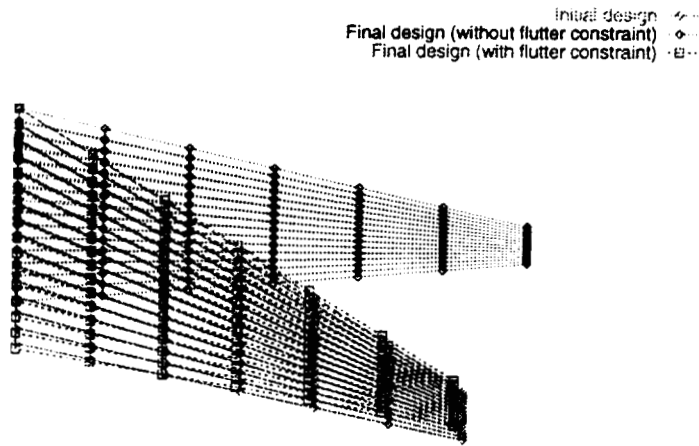


Figure 1: Wing planform: flutter constraint influence

	Initial design	Final design
$V_{flutter}$	240 m/s	280 m/s
Λ	24.5°	24.02°
b^2/S	8.71	8.48
λ	0.2	0.18
Range	2480 mn	2434 mn
W_{fuel}	24000 lbs	23870 lbs
W_{pl}	21917 lbs	22390 lbs

Figure 2: Influence of flutter-speed constraint in the MDO process

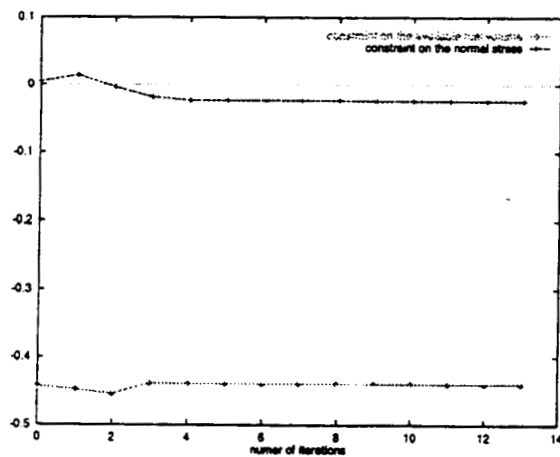


Figure 3: Normal stress and fuel volume constraints

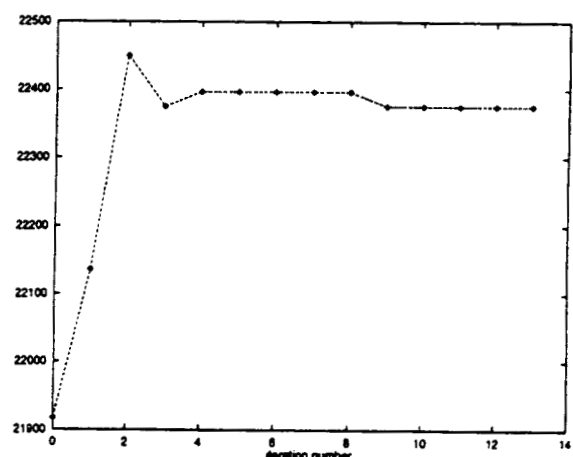


Figure 4: Payload (lb)

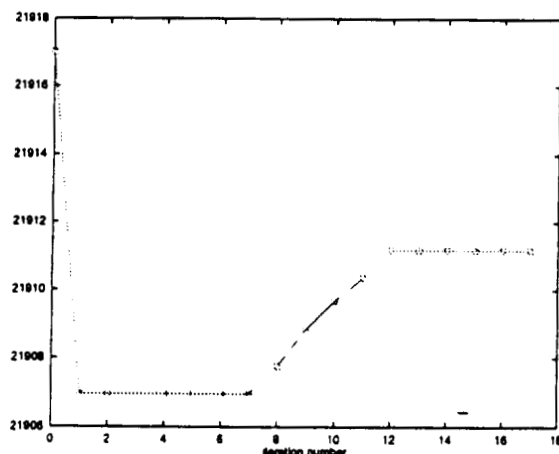


Figure 5: Payload

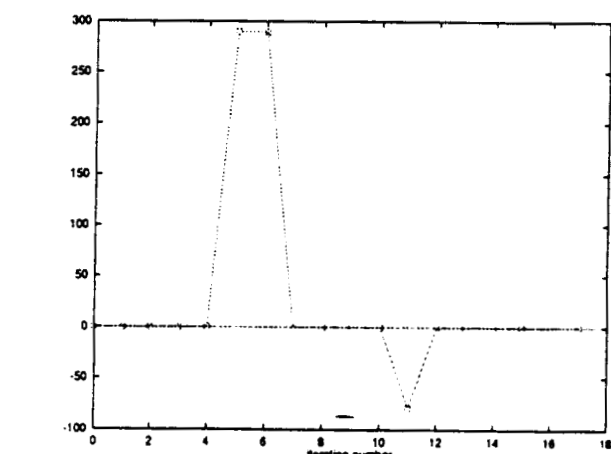


Figure 6: Covariance matrix constraint

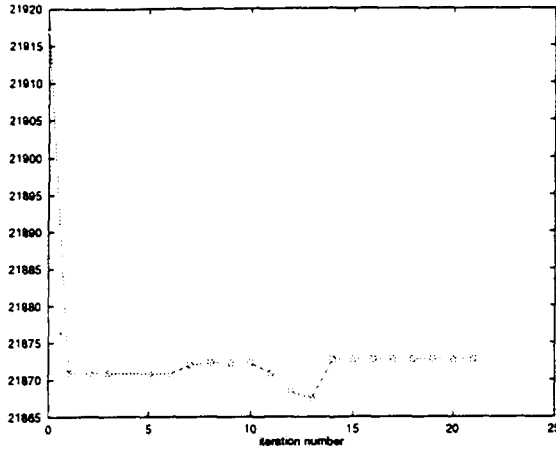


Figure 7: Payload

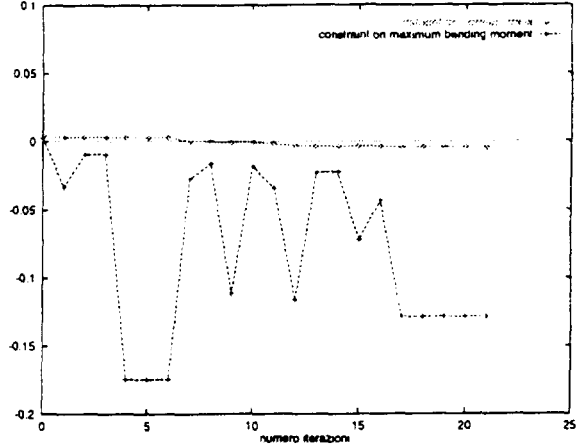


Figure 8: Dynamic bending moment and normal stress constraints

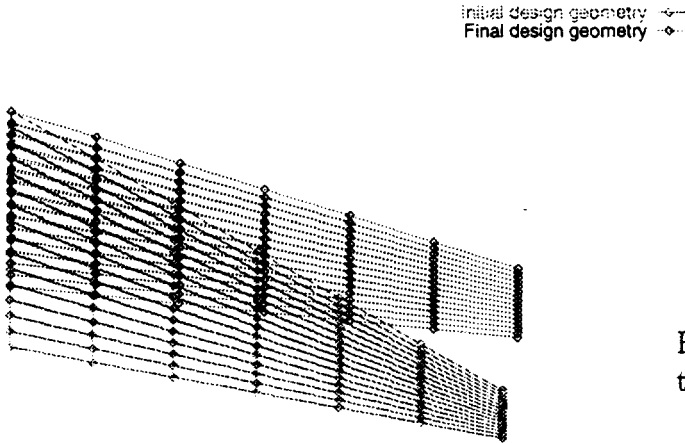


Figure 9: Wing planform: load factor constraint

	Initial Design	Final Design
Δ_n	2.07 m/s	2.07 m/s
Λ	24.5°	9.5°
b^2/S	8.71	15.7
Range	2480 mn	4200 mn
W_{fuel}	24000 lbs	34000 lbs
W_{pl}	21917 lbs	25000 lbs

Figure 10: Influence of load-factor constraint in the MDO process

Considering a random process with $\sigma = 1$ as input, system response has been evaluated using Matched Filter Theory (MFT, Ref. [19, 21]) results: so the response to the worst input has been obtained. Specifically the dynamic moment at the wing tip has been calculated. These constraints do not have a great influence on the optimal design as apparent from the very small variations of the design variables as shown in Figs. 7 and 8.

Next, consider the results obtained by taking into account of a constraint on the load factor: the load factor peak can be evaluated using Pratt formula based on airplane characteristic as recommended by the FAR 25. Results on final *vs* initial configuration are shown in Fig. 9 and in the Table shown in Fig. 10. Normal stress and fuel available volume in the wing constraints yields the final configuration as depicted in Fig. 11. Payload, fuel weight, and objective function are also shown in Figs. 12, 13, and 14.

Finally, the following results have been obtained for a wing-tail configuration: in this case we made a further step toward a more accurate aircraft model, which consists of including for the load factor evaluation the unsteady aerodynamics effects on flight mechanics of the horizontal tail. During the optimization process, we have frozen the tail geometrical characteristics; hence,

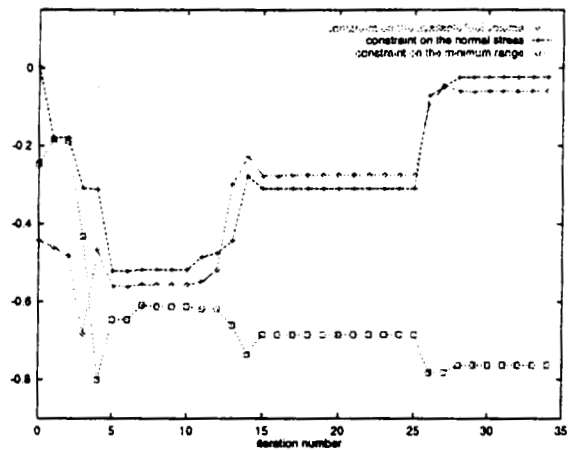


Figure 11: Range, Fuel volume, Normal stress constraints

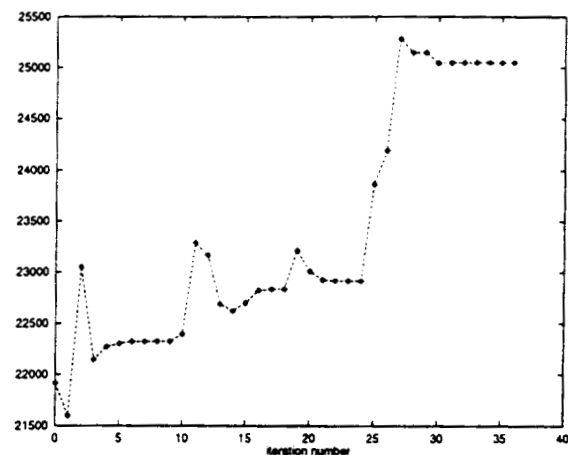


Figure 12: Payload (lb)

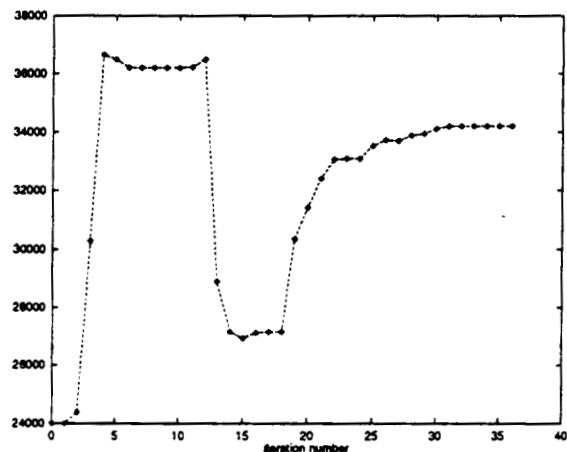


Figure 13: Fuel Weight (lb)

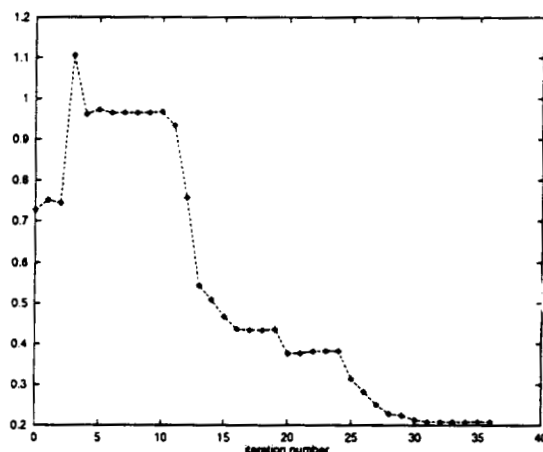


Figure 14: Objective function

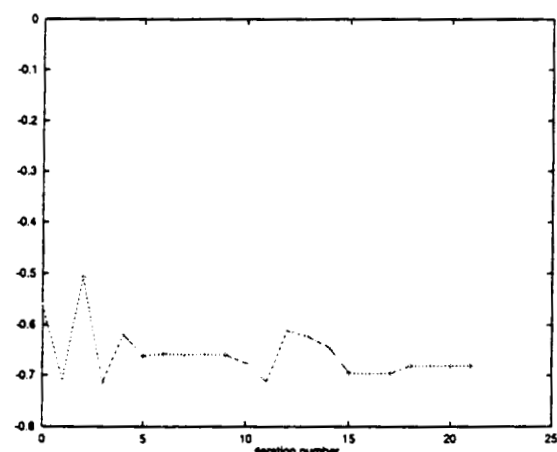


Figure 15: Load factor constraint

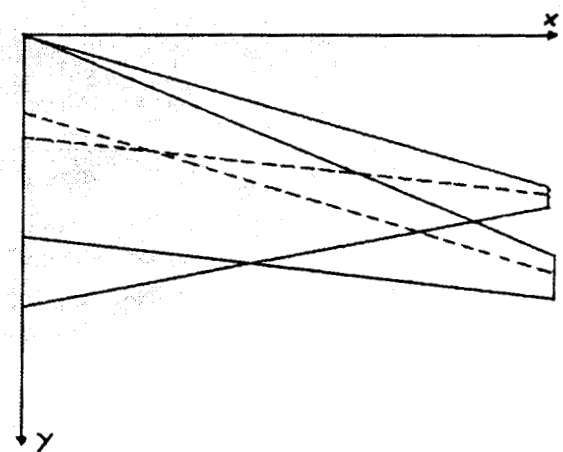


Figure 16: Wing planform: wing-tail configuration

-	Initial Aircraft design	Final Aircraft design
Δ_n	1.3	1.1
Λ	24.5°	6°
b^2/S	8.71	8
Range	2480 mn	4560 mn
W_{fuel}	24000 lbs	45000 lbs
W_{pl}	21917 lbs	22500 lbs
c_{root}	17.82 fts	24 fts
c_{tip}	3.73 fts	1.1 fts
W_{wing}	9116 lbs	8948 lbs

Table 3: Design considering a Wing-tail configuration

the corresponding design variables are the same as in Tab. 1. The maximum load factor has been obtained through numerical search in the time response. Table 3 and Figs. 15–16) show the results obtained.

Acknowledgements: this work has been supported by the Ministero dell'Università e della Ricerca Scientifica e Tecnologica, Grant 1996: “*Problematiche aeroelastiche per configurazioni innovative.*”

References

- [1] Rajadas, J.N., Jury IV, R.A., Chattopadhyay, A., “Enhanced Multiobjective Optimization Technique with Application to High Speed Aircraft Design,” *AIAA Jour.*, 1998, pp. 1044-1054.
- [2] Tappeta, R., Nagendra, S., Renaud, J.E., “A multidisciplinary Design Optimization Approach for High Temperature Aircraft Engine Components,” *AIAA Journal*, 1998, pp. 1055-1064.
- [3] Eldred, L.B., Byun, B., Guruswamy, G.P., “Integration of High Fidelity Structural Analysis into Parallel Multidisciplinary Aircraft Analysis,” *AIAA Journal*, 1998, pp. 3122-3128.
- [4] Balling, R.J., Sobiesczanski-Sobieski, J., “An Algorithm for Solving the System-Level Problem in Multilevel Optimization,” *Structural Optimization*, Vol. 9, 1995, pp. 168-177.
- [5] Balling, R.J., Sobiesczanski-Sobieski, J., “Optimization of Coupled System: A Critical Overview of Approaches,” *AIAA Journal*, Vol. 34, No. 1, January 1996, pp. 6-17.
- [6] Morino, L., Mastroddi, F., De Troia, R., Ghiringhelli, G.L., Mantegazza, P., “Matrix Fraction Approach for Finite-State Aerodynamic Modeling,” *AIAA Journal*, Vol. 33., No. 4, April 1995, pp. 703-711.
- [7] Karpel, M., “Multidisciplinary Optimization of Aeroelastic Systems Using Reduced-Size Models,” *Journal of Aircraft*, Vol. 29, No. 5, Sept.-Oct. 1992, pp. 939-946.
- [8] Balling, R.J., Wilkinson, C.A., “Execution of Multidisciplinary Design Optimization Approaches on Common Test Problems,” *AIAA Jour.*, Vol. 35, No. 1, Jan. 1997, pp. 178-186.

- [9] Hoblit, F.M., "Gust Response Equations of Motion: Formulation and Solution," in *Gust Loads on Aircraft: Concepts and Applications*, AIAA Education Series, 1988, Ed. Przemieniecki, J.S., pp. 115-122.
- [10] Fiacco, A.V., Mc Cormick, G.P., *Non Linear Programming: Sequential Unconstrained Minimization Techniques*, John Wiley & Sons, New York, 1968.
- [11] Hatfka, R.T., Gürdal, Z., *Element of Structural Optimization*, Kluwer, Dordrecht, 1992.
- [12] Gill, P.E., Murray, W., Wright, M.H., *Practical Optimization*, Academic Press, San Diego, 1981. N.Y., 1968.
- [13] Huang, X., Dudley, J., Haftka, R.T., Grossman, B., Mason, W.H., "Structural Weight Estimation for Multidisciplinary Optimization of a High-Speed Civil Transport," *Journal of Aircraft*, Vol. 33, No. 3, May-June 1996, pp. 608-616.
- [14] Mc Cullers, L.A., "Aircraft Configuration Optimization Including Optimized Flight Profiles," Proceedings of *Recent Experiences in Multidisciplinary Analysis and Optimization*, Hampton, Virginia, April 24-26, 1984.
- [15] Mc Cullers, L.A., "FLOPS - Flight Optimization System," Proceedings of *Recent Experiences in Multidisciplinary Analysis and Optimization*, Hampton, Virginia, April 24-26, 1984.
- [16] Mastroddi, F., Vitale, A., Arsuffi, G., Morino, L., "Integrated Aerodynamic-Structural Constrained Optimization of a Wing Structure," Proceedings of XIV Congresso Nazionale AIDAA, Napoli, 20-24 Ottobre, 1997, Vol. 3, pp. 1157-1168.
- [17] De Troia, R., Mastroddi, F., Gennaretti, M., Morino, "Finite-State Modeling for Flutter Suppression and Gust Alleviation," Proceedings of the 7-th International Conference on Adaptive Structures, Rome, Italy, Sept. 23-25, 1997, pp. 119-129.
- [18] Friedland, B, *Control System Design – An Introduction to State-Space Methods*, McGraw-Hill, New York, 1986.
- [19] Papoulis, A., "Maximum Response with Input Energy Constraints and the Matched Filter Principle," *IEEE Trans. Circuit Theory*, IEEE, New York, Vol. CT-17, No. 2, May 1970.
- [20] Pototsky, A.S., Zeiler, T.A., "Calculating Time-Correlated Gust Loads Using Matched Filter and Random Process Theories," *Journal of Aircraft*, Vol. 28, No. 5, pp. 346-352.
- [21] Balis Crema, L., Mastroddi, F., Coppotelli, G., "Aeroelastic Sensitivity Analyses for Flutter Speed and Gust Response," to appear in *Journal of Aircraft*.

MDO of an innovative configuration – aerodynamic issues.

G. Bernardini, A. Frediani
Dipartimento di Ingegneria Aerospaziale
Università degli Studi di Pisa
Via Diotisalvi 2, 56126 Pisa

55 - DL

L. Morino
Dipartimento di Ingegneria Meccanica e Industriale
Università degli Studi Roma Tre
Via della Vasca Navale 79, 00146 Roma

Abstract

A numerical methodology for the evaluation of aerodynamic loads acting on a complex lifting configuration is presented. The work is limited to the case of attached high-Reynolds number flows. A viscous/potential interaction technique is utilized to take into account the effects of the viscosity. For the potential-flow analysis, a boundary element formulation is used; for simplicity, only incompressible flows are examined; the wake geometry is either prescribed a priori or is determined as part of the solution (free-wake analysis). The theoretical basis of the present methodology is briefly described. Comparisons of present numerical results with analytical, numerical, and experimental results available in the literature are included.

Introduction

The aim of this paper is to present an MDO methodology for the analysis of innovative configurations (low-induced drag lifting configurations) with emphasis on the evaluation of aerodynamic load in viscous flows. This methodology is based on a boundary element formulation for the velocity potential introduced by Morino [9]; the effects of viscosity are taken into account by a classical viscous/inviscid coupling technique.

In recent years, the increased request for low-cost air transportation has generated considerable interest for non-conventional configurations characterized by a low induced drag. Specifically, some aeronautical research groups and airplane manufacturers are considering biplanes with wing tips connected to each other directly (joined wing configuration) or through a vertical surface (box-wing configuration).

Since the early work of Prandtl [15] on multiplanes, it is well known that such types of lifting configurations have certain aerodynamic advantages with respect to isolated wings. Specifically, by using an analytical model based on the lifting-line theory, Prandtl [15] has shown that the induced drag of a multiplane with elliptic distribution of circulation is lower than the induced drag of the equivalent monoplane (*i.e.*, of the monoplane having the same span and generating the same lift as the multiplane considered). In addition, in [15] it is also shown that the ratio, K , between the induced drag of a multiplane and that of the equivalent monoplane, decreases as the number of wings of the multiplane increases (with global height and lift kept constant). In the limit as the number of wings tends to infinity ("infinity-plane", according to Prandtl [15] definition), K has the minimum value. Also, Prandtl shows that there exists a box-wing type configuration that has the same distribution of circulation (and hence the same K) as the

“infinity-plane”; such configuration is therefore designated, still by Prandtl [15], at the ‘Best Wing System’ (BWS).

After the work of Prandtl [15], valid only for the limited case of multiplanes with elliptic distribution of circulation, several numerical and experimental studies have been published, in particular, the early work of Nenadovitch [14] on the efficiency of bidimensional biplanes; also, an experimental analysis of joined wing aircraft is presented by Wolkovitch [21], whereas experimental as well as numerical/empirical studies on biplanes and box-wing configurations are proposed by Gall and Smith [3].

In this paper, the attention is focused on an innovative configuration for a new large dimension aircraft (usually indicated as New Large Airplanes or NLA) proposed by Frediani *et al.* [1], [2]. This configuration is a biplane, with counter-swept wings (positive sweep for the front lower wing and negative sweep for the back upper wing, which acts as a horizontal tail as well) connected to each other by aerodynamic surfaces (see Figures 13 and 14). Following Frediani *et al.* [1], [2] we will refer to this configuration as the Prandtl-plane. Preliminary numerical and experimental studies (see Frediani *et al.* [1], [2]) have shown that the induced drag of this configuration is lower than the induced drag of an equivalent monoplane. This fact allows one to reduce the wingspan of this configuration without drag penalties and introduces the possibility of respecting the maximum span-wise dimensions (critical for the NLA with classical wing configuration), which would allow compatibility with the existing airports. Moreover, it allows one to have an optimal design for the control surfaces and hence, a better manoeuvrability and stability control. These considerations yield the conclusion that the Prandtl-plane should be an optimal wing configuration for applications to NLA.

Through an independent activity, the authors have been involved in the developement of an MDO code. The most recent developments in this effort are presented in Ref. [7] (in these Proceedings). The aerodynamic module in such a code is limited to potential flows around simply-connected domains. The configuration under consideration is multiply-connected; in addition, an item of much interest for this configurations is the drag, both induced and viscous. These issues are addressed in this paper, as a first step towards generating a suitable viscous aerodynamic module around multiply-connected configurations, to be incorporated in the above mentioned MDO code. Thus, here the emphasis is on the algorithm used in the recently developed aerodynamic module (indeed the present methodology yields accurate air-loads predictions, with relatively small computational efforts, and hence it is a good tool for the aerodynamic analysis in the optimizer code). Because of the complexity and the novelty of the configurations discussed above, it is necessary to develop an aerodynamic methodology for multiply-connected configurations capable of yielding accurate predictions with a relatively small computational effort, which takes into account the effects of viscosity and of the wake roll-up. The aerodynamic formulation is based on the classical viscous-potential interaction. For potential flows, we extend to multiply-connected regions the a direct boundary element formulation for incompressible inviscid flows around lifting objects of arbitrary shape in uniform translation, introduced in Ref. [9]. The geometry of the rolled-up wake is evaluated through the free-wake analysis of Ref. [18]. The viscous flow (in boundary layer and wake) is solved by using the strip-theory approach, with a two-dimensional boundary layer analysis of integral type. The viscous/inviscid coupling technique is based upon the Lighthill [6] equivalent-sources approach. Matching of the boundary-layer solution with the corrected potential-flow solution is obtained by direct iteration. The present numerical results are compared with the analyt-

ical results by Prandtl theory and with numerical and experimental results available in the literature.

Theoretical Formulation

The theoretical formulation used in the present work for the analysis of complex lifting configurations is briefly outlined in this section. First, the potential formulation for incompressible inviscid flows around lifting objects is outlined (for detailed discussion, see [12] and [10], where reviews are also presented). Next, the methodology used for the analysis of the viscous vortical layer and the viscous/inviscid coupling technique are discussed.

Potential-Flow Formulation: an inviscid, incompressible, initially-irrotational flow remains at all times quasi-potential (*i.e.*, potential everywhere except for the wake surface, *i.e.*, the locus of the points emanating from the trailing-edge). In this case, the velocity field, \mathbf{v} , may be expressed as $\mathbf{v} = \nabla\varphi$ (where φ is the velocity potential). Combining with the continuity equation for incompressible flows, $\nabla \cdot \mathbf{v} = 0$, yields

$$\nabla^2\varphi = 0. \quad (1)$$

The boundary conditions for this equation are as follows. The surface of the body, S_B , is assumed to be impermeable. This yields $(\mathbf{v} - \mathbf{v}_B) \cdot \mathbf{n} = 0$, *i.e.*, $\partial\varphi/\partial n = \mathbf{v}_B \cdot \mathbf{n}$ for $\mathbf{x} \in S_B$, where \mathbf{v}_B is the velocity of a point $\mathbf{x} \in S_B$, whereas \mathbf{n} is the outward unit normal to S_B . At infinity, in a frame of reference fixed with the unperturbed fluid, we have $\varphi = 0$. The boundary condition on the wake surface, S_w , are obtained by using the principles of conservation of mass and momentum across S_w , to yield: (*i*) the wake surface is impermeable, and (*ii*) the pressure, p , is continuous across it. In terms of φ , the first condition yields $\Delta(\partial\varphi/\partial n) = 0$ (where Δ denotes discontinuity across S_w), whereas the second one, using Bernoulli's theorem, yields

$$\left[\frac{\partial}{\partial t} + \mathbf{v}_w \cdot \nabla \right] \Delta\varphi = 0, \quad (2)$$

where \mathbf{v}_w denotes the velocity of a wake point (the average of the fluid velocity on the two sides of the wake). This equation implies that the value of $\Delta\varphi$ remains constant in time following a wake point \mathbf{x}_w and equals the value it had when \mathbf{x}_w left the trailing edge. This value is obtained by imposing (trailing-edge condition) that, at the trailing edge, $\Delta\varphi$ on the wake equals $\varphi_u - \varphi_l$ on the body (subscripts *u* and *l* denote, respectively, upper and lower sides of the body surface). For recent developments on the trailing-edge condition see Ref. [11].

In this paper, the above problem for the velocity potential is solved by a boundary integral formulation. Using the boundary integral representation for the Laplace equation, with a surface that surrounds and is infinitesimally close to body and wake, one obtains (using the above boundary conditions on body, wake, and at infinity)

$$\varphi(\mathbf{x}) = \int_{S_B} \left(G\chi - \varphi \frac{\partial G}{\partial n} \right) dS(\mathbf{y}) - \int_{S_w} \Delta\varphi \frac{\partial G}{\partial n} dS(\mathbf{y}), \quad (3)$$

with $\chi := \mathbf{v}_B \cdot \mathbf{n}$, whereas $G = -1/4\pi \|\mathbf{y} - \mathbf{x}\|$ denotes the fundamental solution for the Laplace equation in three-dimensional space. Note that, in the absence of the wake, Eq. 3, in the limit as \mathbf{x} tends to S_B , represents a boundary integral equation for φ on S_B , with χ on S_B known

from the boundary condition. Once φ on the body is known, φ (and hence \mathbf{v} and, by using Bernoulli's theorem, p) may be evaluated everywhere in the field. The situation is similar in the presence of the wake, since by applying the wake and trailing-edge conditions, $\Delta\varphi$ on the wake may be expressed in terms of φ over the body at preceding times.

In the present work, the boundary integral equation for φ based on Eq. 3 is solved numerically by boundary elements, *i.e.*, by discretizing the body and wake surfaces in quadrilateral elements, assuming φ , χ and $\Delta\varphi$ to be piecewise constant, and imposing that the equation be satisfied at the center of each body element (collocation method).

It should be noted that the geometry of the wake is not known *a priori*. For the case of bodies in uniform translation, a flat wake with vortical lines parallel to the unperturbed streamlines is typically used (prescribed-wake analysis). In the configuration of interest here, such *a priori* assumptions are not justified by past experience. Therefore a free-wake analysis is paramount: the boundary integral equation may be used to compute, at each time step t_n , the flow velocity at nodes \mathbf{x}_n of the discretized wake surface (free-wake analysis), and hence, the locations of wake nodes are modified by integrating the equation $\dot{\mathbf{x}}_n = \mathbf{v}_n(\mathbf{x}_n)$. An explicit Euler method is used here. Any change in the wake geometry determines a different contribution of the integral over \mathcal{S}_w in Eq. 3; hence, in the case of free-wake analysis the shape of the wake and the flowfield solution are obtained step-by-step, as part of the solution. For steady-state cases, the steady solution is obtained as the solution for $t \rightarrow \infty$ of a transient flow due to an impulsive start. This procedure resolves also the non-uniqueness issue connected with steady-state flows around multiply-connected region. Indeed, in the case of unsteady flow the non-uniqueness is not an issue because one may use Kelvin's theorem and obtain the circulation on the wing from the vorticity shed in the wake (see Ref. [11]).

Boundary Layer: the viscous flow analysis is limited to attached steady high-Reynolds number flows. Under these assumptions, a classical integral boundary-layer formulation may be used. Specifically, we use boundary-layer equations written in integral form (for attached flows, this approach yields results as accurate as those obtained by differential methods with considerably reduced computational effort). Also, we consider two-dimensional boundary-layer equations used as 'strip-theory': three-dimensional effects within the boundary layer are neglected with a minor loss of accuracy for applications to this specific configuration, because of the lack of tip effects. The laminar portion of the boundary layer is computed by using Thwaites' collocation method [19]. The transition from laminar to turbulent flow is detected by the classical Michel's method [8]. The turbulent portion of the boundary layer and the wake are studied by the 'lag-entrainment' method of Green *et al.* [5]: in this method, the flow is modelled by coupling three differential equations (the von Kármán equation, the 'entrainment' equation taking into account the flow entering the boundary-layer, and the 'lag' equation – a transport equation for the turbulent kinetic energy) with semi-empirical algebraic closure relationships.

Viscous/Inviscid Coupling: once the boundary-layer equations are solved, the viscosity correction to the potential flow is evaluated as a transpiration flow, across \mathcal{S}_B and \mathcal{S}_W (equivalent source method by Lighthill [6]); the transpiration velocity is given by

$$\chi_v = \frac{\partial}{\partial s} (u_e \delta^*) = \frac{\partial}{\partial s} \int_0^\delta (u_e - u) dz, \quad (4)$$

where s denotes the arclength in the 2D boundary-layer and wake, and δ^* is the displacement

thickness. In addition, u and u_e denote, respectively, the velocity within the vortical layer and at its outer edge (in a frame of reference fixed with the body). Hence, the boundary condition for φ over the body surface is modified as follows (for details, see Morino *et. al.* [13], where it is shown that the method has a much greater validity than usually believed): $\partial\varphi/\partial n = \mathbf{v}_B \cdot \mathbf{n} + \chi_v$, whereas, on the wake surface one has $\Delta(\partial\varphi/\partial n) = (\chi_v)_u + (\chi_v)_l$, (subscripts u and l denote, respectively, upper and lower sides of the wake surface). Thus, the solution of the potential-flow equations containing the viscous correction above gives a prediction for u_e , which is in turn the input for the boundary-layer solution and hence for the evaluation of χ_v . Matching of the boundary-layer solution with the corrected potential-flow solution is obtained through iteration (direct method, valid for attached flows).

Numerical Results

Consider first the potential flow case. For all the results, the airloads are determined by using the formulation of Ref. [4], which is an exact generalization of the Trefftz-plane theory [20] for the evaluation of aerodynamic loads around objects of arbitrary shapes. First, we present a comparison between our numerical results and the analytical results by Prandtl [15] for the evaluation of the efficiency of biplanes. As mentioned above, Prandtl [15] shows that, if the two wings have equal lift and elliptic distributions of the circulation, the ratio K between the induced drag of a biplane and that of the equivalent monoplane is optimal (for a biplane of prescribed ratio G/b , where G is the gap and b is the span). Even better values (better even than multiplanes) for K are obtained for a box-wing configuration, (*i.e.*, the Prandtl [15] Best Wing System) described in the introduction. Figures 1 and 2 show, respectively, results for the case of a biplane with elliptic wings and for the case of Prandtl's BWS. These figures depict the parameter K (hereafter referred to as the 'Prandtl factor') as a function of G/b , and show an excellent agreement between the results (note that in [15] the geometry of the BWS is not specified, whereas our results have been obtained by considering a box-wing configuration with rectangular wings and a rectangular vertical surface at zero angles of attack).

It should be observed that the above results have been obtained by using a prescribed-wake approach, in order to be consistent with the Prandtl model which is based on the lifting-line theory. However, the present methodology is able to capture the effects of the wake roll-up on the airloads by using a free-wake approach, as described above. Figures 3 and 4 depict the Prandtl factor K as a function of G/b , for free-wake and prescribed-wake analysis, (respectively, for a biplane with rectangular wings and for the corresponding box-wing body). The results obtained by a free-wake approach show that the wake roll-up effect is to reduce the value of K . For the range of G/b of practical interest in aeronautical applications (*i.e.*, $0.1 < G/b < 0.2$), we have that the reduction of K is about 3% for the case of a biplane, and 6% for the case of a box-wing. This demonstrates the importance of including a rolled-up wake in the analysis. For the sake of completeness, Fig. 5 depicts the geometry of the wake as a result of the free-wake analysis for a box-wing in which the two wings are identical and have the same angle of attack, $\alpha = 5^\circ$.

In order to analyze the mechanism of induced-drag reduction for biplanes and box-wing configurations, it is interesting to study the efficiency K of a rectangular biplane with facing tip winglets on the two wings. Our calculations have confirmed that the Prandtl factor K decreases, for a fixed G/b , as the length of the two winglets increases. In particular, if the gap d between the winglets tips goes to zero, K tends to the value of the corresponding box-wing

configuration: Figure 6 depicts a comparison of the curves $K = K(G/b)$ for a biplane without winglets, for the corresponding box-wing body, and for a biplane with winglets (winglet length $0.4c$, where c is the root chord). In addition, Fig. 7 shows the circulation as a function of the arclength along the trailing-edge line (oriented from the lower wing root to the upper wing root) of a box-wing configuration (with the gap d as a parameter). This Figure shows that in the limit, as the gap d tends to zero, the circulation of a biplane with winglets tends to the circulation of a box-wing configuration.

Next, for both biplanes and box-wing configurations, examine the dependence of the Prandtl factor upon the spanwise circulation distribution. To this end, we have considered three different configurations: (1) rectangular and untwisted wings (angle of attack $\alpha = 5^\circ$), (2) untwisted swept wings (sweep angle $\Lambda = 30^\circ$), and (3) unswept and linearly twisted wings ($+5^\circ$ at root and -5° at tip). For simplicity a non-rolled-up wake has been used. Figures 8 and 9 (for the biplane and the box-wing configuration, respectively) show K as a function of G/b for the three cases above. It may be noted that for straight and swept wings the parameter K is lower than that of a biplane with elliptic distribution of circulation (these results appear to contradict the fact that monoplanes with elliptic distribution of circulation produce an optimal efficiency; however, here the Prandtl factor K is evaluated by comparing a biplane with the monoplane having same sweep angle and twist).

Next, consider some preliminary results for attached high-Reynolds viscous flows. In the present work, the evaluation of the viscous component of drag is obtained by using the expression of Squire and Young [17]. As an example, in Fig. 10 it is shown that, for the case of the polar of a rectangular wing at $Re = 2.7 \cdot 10^6$, our numerical results are in good agreement with the experimental results in [16]. Next, consider the case of biplanes and box-wing bodies. As a comparison we have considered the work of Gall and Smith [3], who present both numerical and experimental results for the evaluation of lift and drag of those configurations (the numerical/empirical approach used in Ref. [3] is based on the evaluation of the inviscid loads by lifting-line theory, whereas the viscous drag is obtained from available experimental results for two-dimensional biplanes, given in Ref. [14]). Figure 11 depicts the polar at $Re = 5.1 \cdot 10^5$ of a biplane, whereas Fig. 12 depicts the polar at $Re = 5.1 \cdot 10^5$ of a box-wing configuration. Our numerical results are in good agreement with the experimental and numerical results by Gall and Smith [3].

Finally, we present the polar of the box-wing body shown in Fig. 13. As stated in the introduction, this particular case of box-wing configuration has been recently proposed as the basic geometry for an optimization process for low-induced drag complex configurations (see [1] and [2] for details). Figure 15 depicts the polar at $Re = 2.7 \cdot 10^6$. Figure 16 shows the geometry of the rolled-up wake (angle of attack $\alpha = 5^\circ$). No numerical or experimental results are available for the present configuration.

References

- [1] Frediani, A., Chiarelli, M., Longhi, A., D'Alessandro, C.M., Lombardi, G., "Structural Design and Optimization of the Lifting System of a Non-Conventional New Large Aircraft," proceedings of the CEAS International Forum on Aeroelasticity and Structural Dynamics, Rome 1997.

- [2] Frediani, A., Lombardi, G., Chiarelli, M., Longhi, A., D'Alessandro, C.M., Bernardini, G., "Proposal for a New Large Airliner with a Non-Conventional Configuration," Proceedings of the XIV AIDAA Congress, Naples, 1997.
- [3] Gall, P.D. and Smith, H.C., "Aerodynamic Characteristics of Biplanes with Winglets," *J. Aircraft*, Vol. 24, No. 8, pp. 518-522, 1987.
- [4] Gennaretti, M., Salvatore, F., Morino, L., "Forces and Moments in Incompressible Quasi-Potential Flows," *Journal of Fluids and Structures*, Vol. 10, pp. 281-303, 1996.
- [5] Green, J.E., Weeks, D.J., Broome, J.W.F., "Prediction of Turbulent Boundary Layers and Wakes in Compressible Flow by a Lag-Entrainment Method," RAE RM 3791, 1973.
- [6] Lighthill, M.J., "On Displacement Thickness," *J. Fluid Mech.*, Vol. 4, pp. 383-392, 1958.
- [7] Mastroddi, F., Ciancaleoni, E., and Morino, L., "Aeroelastic constraints in MDO," Proceedings of the International Forum on Aeroelasticity and Structural Dynamics, Williamsburg 1999.
- [8] Michel, R., "Etude de la Transition sur les Profils d'Aile-Etablissement d'un Point de Transition et Calcul de la Trainée de Profil en Incompressible," ONERA Rep. No. 1/1578A, 1952.
- [9] Morino, L., "A General Theory of Unsteady Compressible Potential Aerodynamics," NASA CR-2464, 1974.
- [10] Morino, L., "Boundary Integral Equation in Aerodynamics," *Appl. Mech. Rev.*, Vol. 46, August 1993.
- [11] Morino, L., and Bernardini, G., "Singularities in Discretized BIE's for Laplace's Equation; Trailing-Edge Conditions in Aerodynamics," Wendland, W.L., (ed.): *Mathematical Aspects of Boundary Element Methods*, CRC Press, London, UK, (in print).
- [12] Morino, L. and Gennaretti, M., "Boundary Integral Equation Methods," in Atluri, S.N. (ed.), *Computational Nonlinear Mechanics in Aerospace Engineering*. Progress in Aeronautics and Astronautics, 146, AIAA, Washington, DC, 1992.
- [13] Morino, L., Salvatore, F., Gennaretti, M., "A Velocity Decomposition for Viscous Flows: Lighthill Equivalent-Source Method Revisited," in: Morino, L., and Wendland, W.L., (eds.): *Boundary Integral Methods for Nonlinear Problems*, pp. 161-166. Kluwer Academic Publishers, Dordrecht, The Netherlands, 1997.
- [14] Nenadovitch, M., "Recherches sur les Cellules Biplanes Rigides d'Envergue Infinie," Publications Scientifiques et Techniques du Ministere de L'Air, Institute Aerotechnique de Saint-Cry, Paris, 1936.
- [15] Prandtl, L., "Induced Drag of Multiplanes," NACA TN 182, 1924.
- [16] Schlichting, H. and Truckenbrodt, E., "Aerodynamics of the Airplane," McGraw-Hill, New York, 1979.

- [17] Squire, H.B. and Young, A.D., "The Calculation of the Profile Drag of Airfoils," ARC RM No. 1838, 1938.
- [18] Suciu, E.O., and Morino, L., "Nonlinear Steady Incompressible Lifting-Surface Analysis with Wake Roll-Up," AIAA Journal, Vol. 15, No. 1, pp. 54-58, 1976.
- [19] Thwaites, B., "Approximate Calculation of the Laminar Boundary Layer," *Aeron. Quart.* Vol. 1, pp. 245-280, 1949.
- [20] Trefftz, E., "Prandtl'sche Tragflächen und Propeller Theorie," Zeitschrift für Angewandte Mathematik und Mechanik, 1, Berlin, 1921.
- [21] Wolkovitch, J., "The Joined Wing: An Overview," *J. Aircraft*, Vol. 23, pp. 161-178, 1986.

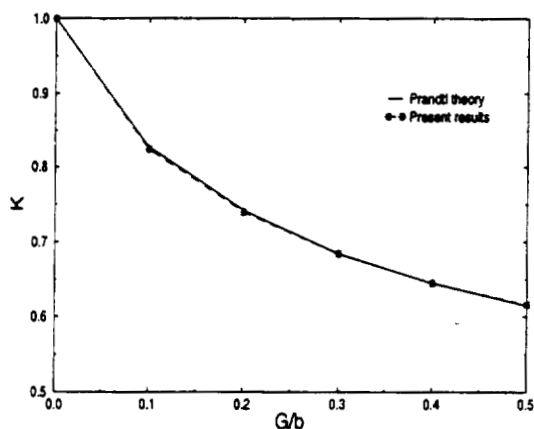


Fig. 1. Prandtl factor of elliptic biplane ($b/c = 10$, $\alpha = 5^\circ$, unstaggered).

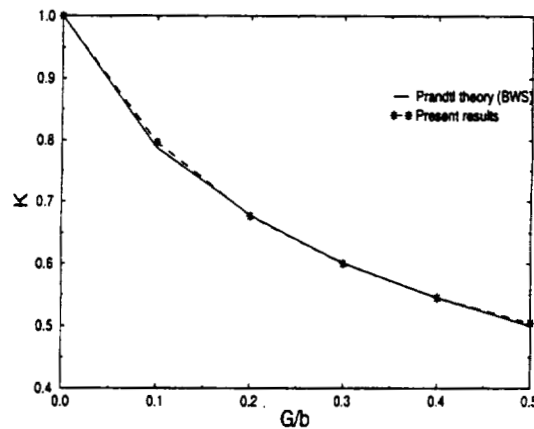


Fig. 2. Prandtl factor of box-wing body ($b/c = 10$, $\alpha = 5^\circ$, unstaggered).

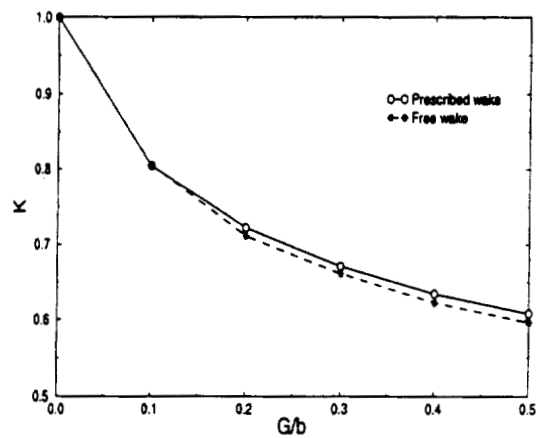


Fig. 3. Effect of wake roll-up on Prandtl factor: rectangular biplane ($b/c = 10$, $\alpha = 5^\circ$, unstaggered).

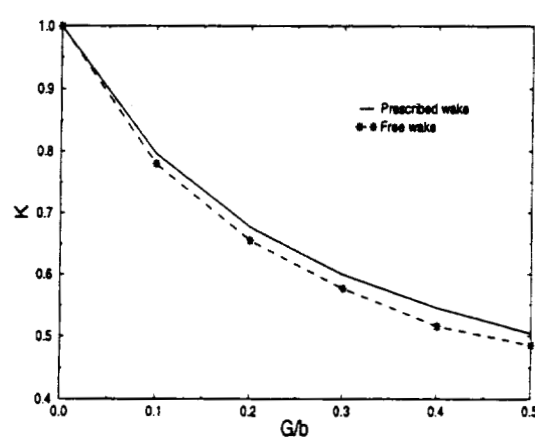


Fig. 4. Effect of wake roll-up on Prandtl factor: box-wing body ($b/c = 10$, $\alpha = 5^\circ$, unstaggered).

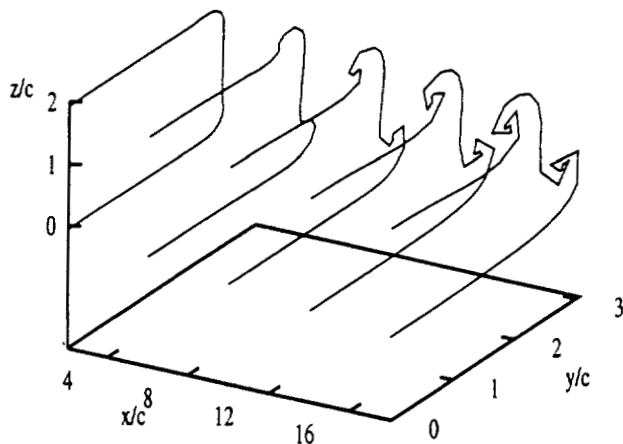


Fig. 5. Free-wake analysis of box-wing body (lifting): wake sections on planes normal to freestream.

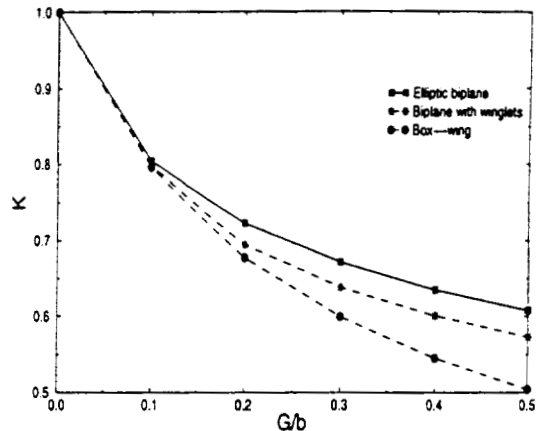


Fig. 6. Effect of winglets on Prandtl factor: rectangular biplane ($b/c = 10$, $\alpha = 5^\circ$, unstaggered).

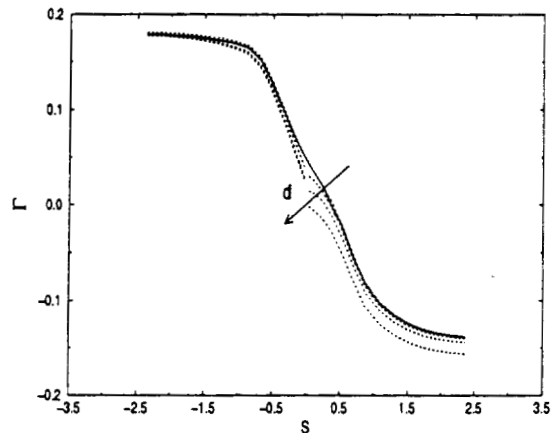


Fig. 7. Distribution of circulation on rectangular biplanes with winglets ($b/c = 10$, $\alpha = 5^\circ$, unstaggered).

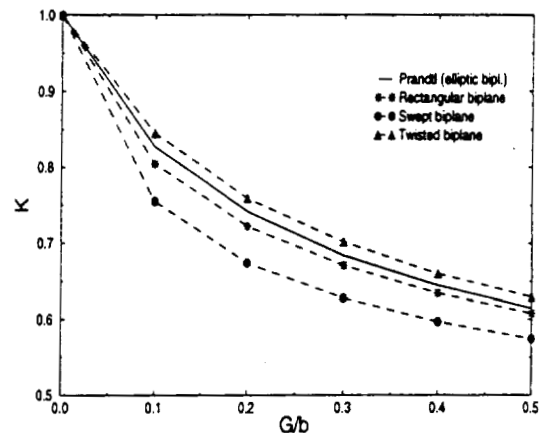


Fig. 8. Effect of spanwise distribution of circulation on the Prandtl factor of biplanes.

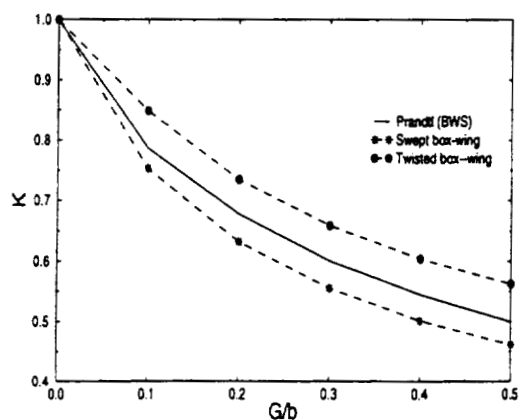


Fig. 9. Effect of spanwise distribution of circulation on the Prandtl factor of box-wing bodies.

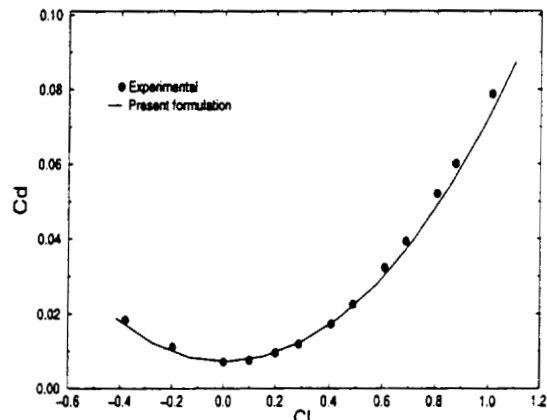


Fig. 10. Polar of isolated wing (aspect ratio 5, section: NACA 2412) at $Re = 2.7 \cdot 10^6$.

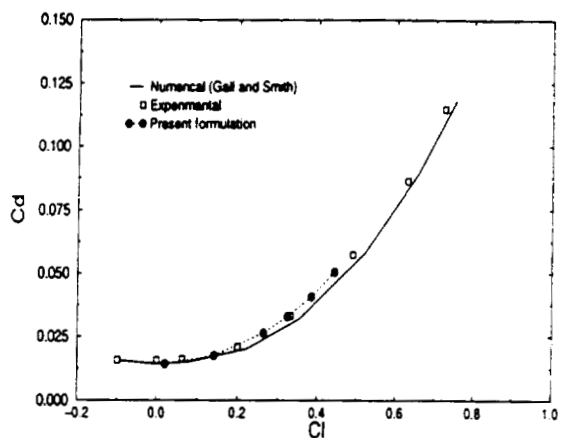


Fig. 11. Polar of rectangular biplane (aspect ratio 5, $G/c = 1$, stagger = c , section: NACA 0012) at $Re = 5.1 \cdot 10^5$.

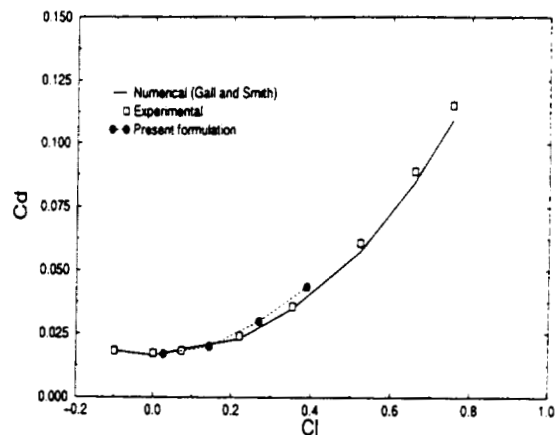


Fig. 12. Polar of box-wing body (aspect ratio 5, $G/c = 1$, stagger = c , section: NACA 0012) at $Re = 5.1 \cdot 10^5$.

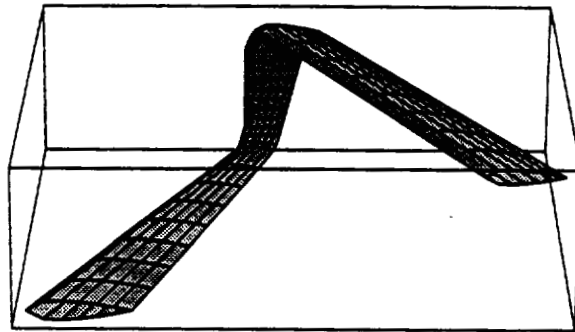


Fig. 13. Isometric view of Prandtl-plane.

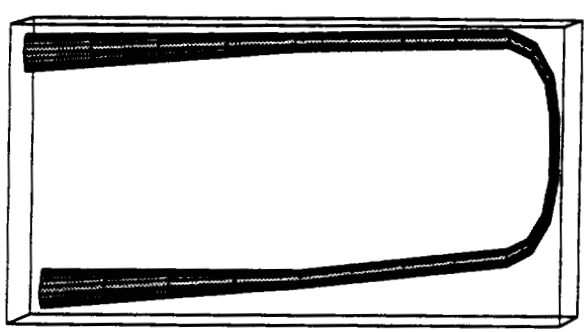


Fig. 14. Front view of Prandtl-plane.

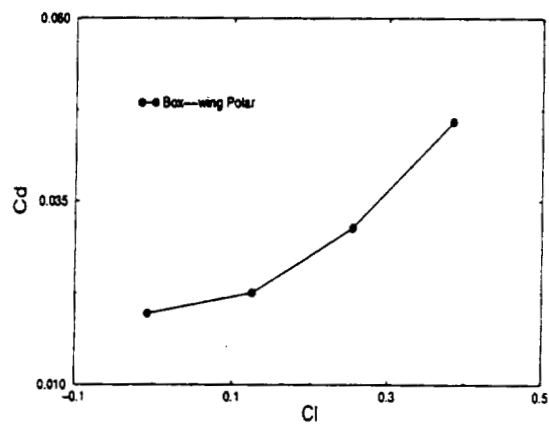


Fig. 15. Polar of Prandtl-plane of Fig. 13 at $Re = 2.7 \cdot 10^6$.

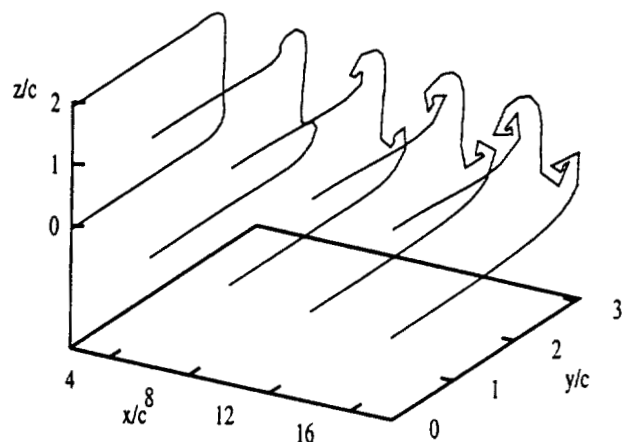


Fig. 16. Free-wake analysis of Prandtl-plane of Fig. 13: wake sections on planes normal to freestream.

SIMULATION OF NONLINEAR AIRFOIL/CONTROL-SURFACE FLUTTER AT SUBSONIC SPEEDS USING CLASSICAL UNSTEADY AERODYNAMICS AND AN EULER METHOD

Silvio Schulze

Se - 08

German Aerospace Center (DLR), Institute of Aeroelasticity

Bunsenstr. 10, 37073 Göttingen, Germany

email address: Silvio.Schulze@dlr.de

Abstract - A flutter simulation method for aeroelastic systems with discrete structural nonlinearities is presented and applied. The computational approach is based on the coupling of the discretized fluid and structural equations which are solved in the time domain. Embedded in an effective procedure to compute complete flutter boundaries (bifurcation diagrams), the method is employed to investigate the flutter stability of an airfoil/control-surface system for hardening and softening stiffness characteristics in the control mechanism. The aerodynamic forces are predicted under the assumption of subsonic inviscid flow by the classical linear airfoil theory as a basis of comparison and by an Euler method. The typical flutter behavior of the system is described and explained by comparing it with the flutter properties of a predefined linear reference model. The results presented here demonstrate the practicability of the method and provide a deeper insight into the nonlinear airfoil/control-surface flutter mechanisms.

1 INTRODUCTION

The limited applicability of classical analysis methods to predict the flutter stability of nonlinear aeroelastic systems hinders the development process of modern airplanes. The nonlinearities are structural or aerodynamic in nature and can significantly alter the stability properties of a system. In structural dynamics several methods are available to solve the respective nonlinear equations which are usually set up by means of the Finite Element Method (FEM) in a Lagrangian system. Fluid equations are preferably derived in an Eulerian system and finite difference methods have proven to be a powerful tool for their solution within the research field of Computational Fluid Dynamics (CFD). In order to take full advantage of developments in these single disciplines, the coupling of fluid and structural models is desirable to solve nonlinear aeroelastic problems, typically referred to as Computational Aeroelasticity [10, 12].

Advances in this field have been mostly in the application of CFD methods to predict aeroelastic phenomena related to nonlinear fluid flow, while the motion of the structure was assumed to be describable by linear mathematical models, primarily

based on the generalized modal approach. However, beginning with the pioneer efforts of Breitbach [5] and Woolston *et al.* [28], investigations into the effects of structural nonlinearities on the aeroelastic stability behavior of control surfaces, wings, and aircraft also have a long tradition. The applied computational approaches range from analog time simulation [5, 28] and digital time simulation [4, 9, 14, 16, 17, 18, 19, 23, 29, 30] to semi-analytical frequency domain, eigen analysis, and perturbation methods, i.e., approximation techniques based on a linearization approach [6, 15, 17, 20, 23, 25, 29]. Experimental investigations were also undertaken to confirm the numerical methods [9, 14, 28, 29].

With regard to the digital time simulation approach of this paper, it can be summarized that, with few exceptions, only a single discrete nonlinearity in a simple structural system was considered. Especially the typical airfoil section capable of plunging and pitching motions was extensively studied using generalized Theodorsen two-dimensional unsteady incompressible aerodynamics [26]. In order to obtain a continuous representation of the aerodynamic forces needed for transient analysis from discrete values of reduced frequency, Wagner's function and

approximate transfer functions were employed. The latter approach required the introduction of additional variables. Moreover, the flutter equations were frequently written in state-space form, whereby the number of equations was further increased. For the sake of simplicity, some investigators based their analysis on the quasi-steady representation of the aerodynamic forces which can produce unrealistic results [23], while others preferred a piecewise linear structural model, which did not always simplify the problem. Considering the advanced capabilities of modern computer hardware, today there is no obvious necessity for either approximation.

In this paper, a straightforward time-marching algorithm is presented which, based on the coupling of the governing equations for the fluid and the structure, enables the numerical simulation of the flutter behavior of nonlinear aeroelastic systems. The proposed method does not rely on a state-space modelling, but directly tackles the governing equations. The procedure is similar to that commonly in use in Computational Aeroelasticity [11, 21, 22] and accurately solves the coupled field problem by properly linking the fluid and the structural time-marching algorithms using a simple predictor-corrector method. It also has the advantage of being set up in single-step form, and therefore does not require a cumbersome starting procedure and is easily extendable to varying time step sizes.

Next, the flutter behavior of a nonlinear airfoil/control-surface system is investigated in detail using the proposed time-marching algorithm which is incorporated in the two-dimensional aeroelastic simulation code SNAP2d (Simulation of Nonlinear Aeroelastic Phenomena) [24]. The unsteady aerodynamic forces are predicted for inviscid flow by the classical linear airfoil theory of Theodorsen and an Euler method employing a uniform approach. In spite of the application of the Euler method, however, the flutter investigations are confined to subsonic flow with the use of the classical linear airfoil theory as a basis of comparison. Emphasis is placed on the study of the effects of discrete structural nonlinearities in the control surface attachment on the flutter stability of a predefined linear reference model.

Results of aeroelastic computations are presented and discussed for hardening and softening springs using both aerodynamic models.

2 AEROELASTIC MODEL

2.1 Structural Model

The two-dimensional representative wing section with control surface is used as structural model as shown in Fig. 1 together with the usual geometric parameters, cf. reference [26]. The coordinates h , α , and β denote the plunging, pitching, and flap motion of the rigid system, while the spring constants k_h and k_α represent the bending and torsional stiffness of the wing. The control-surface stiffness is allowed to be an arbitrary continuous function of β , consisting of a linear part with the stiffness coefficient k_β and a nonlinear part:

$$f_\beta(\beta) = \underbrace{k_\beta \beta}_{\text{linear}} + \underbrace{f_{NL\beta}(\beta)}_{\text{nonlinear}}. \quad (1)$$

The entire system of mass m is exposed to a subsonic air flow of density ρ_∞ and velocity U_∞ , where the subscript ∞ denotes the undisturbed quantities infinitely far upstream from the airfoil. The resulting generalized aerodynamic forces F_h , M_α , and M_β are obtained through integration of the pressure over the respective part of the airfoil surface and can be determined by either of the methods described below.

Introducing the radii of gyration of the airfoil and the control surface about the elastic axis and the hinge axis, $r_\alpha = \sqrt{I_\alpha / (b^2 m)}$ and $r_\beta = \sqrt{I_\beta / (b^2 m)}$, respectively, and the uncoupled natural frequencies $\omega_h = \sqrt{k_h / m}$, $\omega_\alpha = \sqrt{k_\alpha / I_\alpha}$, and $\omega_\beta = \sqrt{k_\beta / I_\beta}$, where I_α and I_β are the moments of inertia of the entire airfoil and the flap about the elastic axis and the hinge axis, the equations of motion for small amplitudes of oscillation can be expressed as:

$$M\ddot{\mathbf{u}}(t) + K\mathbf{u}(t) + f_{NL}(\mathbf{u}(t)) = \mathbf{f}(\mathbf{u}, \dot{\mathbf{u}}, \ddot{\mathbf{u}}; t), \quad (2)$$

$$M = \begin{bmatrix} 1 & x_\alpha & x_\beta \\ x_\alpha & r_\alpha^2 & (c_\beta - e)x_\beta + r_\beta^2 \\ x_\beta & (c_\beta - e)x_\beta + r_\beta^2 & r_\beta^2 \end{bmatrix},$$

$$K = \begin{bmatrix} \omega_h^2 & 0 & 0 \\ 0 & r_\alpha^2 \omega_\alpha^2 & 0 \\ 0 & 0 & r_\beta^2 \omega_\beta^2 \end{bmatrix}, \quad u = \begin{bmatrix} h \\ \bar{b} \\ \alpha \\ \beta \end{bmatrix}, \quad f_{NL} = \begin{bmatrix} 0 \\ 0 \\ \frac{f_{NL\beta}}{b^2 m} \end{bmatrix},$$

where M and K are the constant mass and stiffness matrices, u the vector of coordinates, f_{NL} the vector of nonlinear terms, and f the aerodynamic load vector as a function of the motion of the system.

2.2 Aerodynamic Models

2.2.1 Classical Linear Airfoil Theory

The theory of determining the aerodynamic forces on a thin airfoil with a control surface oscillating harmonically with small amplitudes in incompressible subsonic potential flow is documented in great detail and can be found in many classical texts on aeroelasticity. Here, the theory of Theodorsen [26] is employed and its generalization for arbitrary unsteady motions is achieved via Laplace transformation using Wagner's function and the principle of superposition through Duhamel's integral. The aerodynamic load vector in Eq. 2 can then be written as:

$$f = M_A \ddot{u}(t) + D_A \dot{u}(t) + K_A u(t) + f_C(t), \quad (3)$$

where M_A , D_A , and K_A are the constant aerodynamic mass, damping, and stiffness matrices, and f_C denotes the circulatory part of the aerodynamic forces using Wagner's function and Duhamel's integral.

2.2.2 Euler Equations

The two-dimensional conservation form of the unsteady Euler equations for boundary-fitted moving coordinates $\xi = \xi(x, z; t)$, $\zeta = \zeta(x, z; t)$, $\hat{t} = t$ are

$$\frac{\partial \hat{Q}}{\partial \hat{t}} + \frac{\partial \hat{F}}{\partial \xi} + \frac{\partial \hat{H}}{\partial \zeta} = 0, \quad (4)$$

with the transformed vectors \hat{Q} , \hat{F} , and \hat{H} as linear combinations of their Cartesian counterparts Q , F , and H , where Q is the vector of conservative variables, and F and H are the two flux vectors corresponding to the x and z direction, respectively. The system is completed with the equations of state for a thermally and calorically perfect gas.

In this study a C-mesh is used for the spatial discretization of the flow field. The mesh consists of 149

points in the ξ direction and 21 in the ζ direction with 105 points coinciding with the airfoil surface. The influence of the gap between the wing and the flap on the fluid flow is assumed to be negligible, thus not included in the discretization. The necessary mesh deformations are computed by an elliptic mesh generation method described in [7].

As far as the boundary conditions are concerned, non-reflecting boundary conditions are applied on the outer boundary, while tangent flow is enforced along the airfoil surface. The pressure on the surface is determined from the normal momentum equation and yields the required generalized aerodynamic forces F_h , M_α , and M_β through evaluation of the respective surface integrals.

3 NUMERICAL METHOD

For the description of the numerical method, the general coupled field problem can be considered:

$$M\ddot{u}(t) + D\dot{u}(t) + f_E(u(t)) = p(t) \quad (a)$$

$$p(t) = f(u, \dot{u}, \ddot{u}; t) \quad (b)$$

where Eq. (a) represents the structural equations of motion (2) with an added viscous damping term $D\dot{u}(t)$ and the elastic forces,

$$f_E(u(t)) = Ku(t) + f_{NL}(u(t)), \quad (6)$$

while Eq. (b) symbolically stands for the computation of the aerodynamic forces as functions of the motion of the structure u , \dot{u} , \ddot{u} , and time t by either of the aerodynamic models outlined above. For example, $p(t)$ is simply equal $f(u, \dot{u}, \ddot{u}; t)$ in Eq. (3), while when using the CFD method, the entire system of Euler equations (4) has to be solved first before the pressure on the surface of the airfoil/control-surface system and, thus, the generalized forces can be computed.

3.1 Structural Analysis Procedure

For the time integration of the structural equations of motion (5(a)), Newmark's method [2] is used, which is a single-step algorithm of second-order convergence in Δt and can be set up in explicit or implicit form by variation of two specific parameters. Since a simple three-degree-of-freedom structural system is considered in this study, the explicit

variant of Newmark's method is employed, which avoids the iterative minimization of error terms due to nonlinear elastic behavior in each time step [2]. It also possesses better accuracy properties than most implicit variants. The required finite difference expressions for the displacements and the velocities for the explicit algorithm using the notations

$$\begin{aligned} \boldsymbol{u}_i &:= \boldsymbol{u}(t_i), \\ \boldsymbol{u}_{i+1} &:= \boldsymbol{u}(t_i + \Delta t) = \boldsymbol{u}(t_{i+1}), \end{aligned} \quad (7)$$

are:

$$\boldsymbol{u}_{i+1} = \boldsymbol{u}_i + \Delta t \dot{\boldsymbol{u}}_i + \frac{\Delta t^2}{2} \ddot{\boldsymbol{u}}_i, \quad (8)$$

$$\dot{\boldsymbol{u}}_{i+1} = \dot{\boldsymbol{u}}_i + \frac{\Delta t}{2} (\ddot{\boldsymbol{u}}_i + \ddot{\boldsymbol{u}}_{i+1}). \quad (9)$$

These equations, together with the equilibrium equations (5(a)) at time $t_i + \Delta t$:

$$\boldsymbol{M}\ddot{\boldsymbol{u}}_{i+1} + \boldsymbol{D}\dot{\boldsymbol{u}}_{i+1} + \boldsymbol{f}_{E|i+1} = \boldsymbol{p}_{i+1}, \quad (10)$$

where

$$\boldsymbol{f}_{E|i+1} = \boldsymbol{K}\boldsymbol{u}_{i+1} + \boldsymbol{f}_{NL}(\boldsymbol{u}_{i+1}) \quad (11)$$

allow the three unknowns \boldsymbol{u}_{i+1} , $\dot{\boldsymbol{u}}_{i+1}$, $\ddot{\boldsymbol{u}}_{i+1}$ to be determined.

The critical time step required for stability is reciprocally proportional to the highest eigenfrequency ω_{\max} of the structural system. Note that this frequency is generally not constant as in linear systems, but varies with changes in stiffness. It can be estimated using the tangent stiffness matrix

$$\boldsymbol{K}_T(\boldsymbol{u}_i) = \left. \frac{\partial \boldsymbol{f}_E(\boldsymbol{u}(t))}{\partial \boldsymbol{u}} \right|_{\boldsymbol{u}_i} = \boldsymbol{K} + \left. \frac{\partial \boldsymbol{f}_{NL}(\boldsymbol{u}(t))}{\partial \boldsymbol{u}} \right|_{\boldsymbol{u}_i} \quad (12)$$

in an incremental formulation of the equilibrium equations if an upper bound for ω_{\max} is not known in advance [2].

3.2 Aerodynamic Analysis Procedures

3.2.1 Classical Linear Airfoil Theory

By use of Eq. (3) for the determination of the aerodynamic forces, we can distinguish between the non-circulatory part and the circulatory part of the forces. The non-circulatory forces, also called the apparent mass forces, depend only on the instantaneous values of \boldsymbol{u} , $\dot{\boldsymbol{u}}$, $\ddot{\boldsymbol{u}}$, so that the constant aerody-

namic matrices \boldsymbol{M}_A , \boldsymbol{D}_A , and \boldsymbol{K}_A can be added to the structural equations of motion. To account for the non-circulatory forces $\boldsymbol{f}_C(t)$, Duhamel's integral must be solved for every time t_i . This is accomplished by replacing it by its time-discrete counterpart. The required time-discrete values of Wagner's function are approximated using the representation of Garrick:

$$\Phi(U_\infty t_i/b) = 1 - \frac{2}{4 + (U_\infty t_i/b)}. \quad (13)$$

During the simulation, Duhamel's integral has to be evaluated concurrently with the structural equations of motion (5(a)), as described in section 3.3.

3.2.2 Euler Algorithm

The Euler code was written by the author of [8], where it is described in detail and applied to transonic cascade flow. The reliability of the code for flutter prediction of airfoils in transonic flow was demonstrated in Refs. [24, 27].

As in structural dynamics, an explicit or an implicit approach can be followed to obtain time-discrete solutions $\hat{\boldsymbol{Q}}$ of the flow equations (4) which, for this purpose, are rearranged in the convenient form:

$$\frac{\partial \hat{\boldsymbol{Q}}}{\partial t} = -\boldsymbol{R}(\boldsymbol{Q}) \quad (13)$$

with $\boldsymbol{R}(\boldsymbol{Q}) = \partial \hat{\boldsymbol{F}} / \partial \xi + \partial \hat{\boldsymbol{H}} / \partial \zeta$ representing the spatial flux balance as function of \boldsymbol{Q} . The code applies the flux vector splitting technique of Anderson *et al.* [1] using a cell-centered finite volume formulation with a MUSCL-type extrapolation for the spatial discretization, which is second-order accurate. The subsequent discretization in time is first-order accurate for the explicit and implicit scheme. More precisely, a simple explicit scheme solving the forward difference equation

$$\hat{\boldsymbol{Q}}_{n+1} = \hat{\boldsymbol{Q}}_n - \Delta t \boldsymbol{R}(\boldsymbol{Q}_n) \quad (14)$$

and the approximately factored Beam/Warming implicit scheme solving the backward difference

$$\hat{\boldsymbol{Q}}_{n+1} = \hat{\boldsymbol{Q}}_n - \Delta t \boldsymbol{R}(\boldsymbol{Q}_{n+1}) \quad (15)$$

are applied, both of which are non-iterative single-step algorithms.

The condition for the numerical stability of the fluid solver depends on the spatial and temporal discretization of Eq. (4) and can be expressed by means of a linear stability analysis through the CFL number.

3.3 Coupled Analysis Procedure

Irrespective of the chosen aerodynamic model, the general problem in solving the coupled equations (5) lies in the fact that the solution of the structural equations of motion (5(a)) at time t_{i+1} , i.e. Eq. (10), requires the aerodynamic forces in Eq. (5(b)) at the same time, i.e. p_{i+1} which, without the knowledge of the actual state of motion of the structure, characterized by $u_{i+1}, \dot{u}_{i+1}, \ddot{u}_{i+1}$, can not be computed, and vice versa. In this sense, an accordant algorithm needed to solve the coupled equations (5) can therefore be classified as implicit.

In the past, the above problem was frequently circumvented by using p_i instead of p_{i+1} in Eq. (10), which results in artificial phase errors. Avoiding such an approximation, the coupled equations have to be solved through the application of a predictor-corrector method, typically used to treat implicit systems. There are several ways to set up such a predictor-corrector algorithm. In the method presented here the structural state is predicted to compute the aerodynamic forces. For example, the structural variables at t_{i+1} can be calculated using a Taylor series for the displacements, i.e. Eq. (8), and the trapezoidal rule for the velocities and accelerations:

$$\dot{u}_{i+1} = \frac{2}{\Delta t} (u_{i+1} - u_i) - \ddot{u}_i, \quad (16)$$

$$\ddot{u}_{i+1} = \frac{2}{\Delta t} (\dot{u}_{i+1} - \dot{u}_i) - \ddot{u}_i. \quad (17)$$

It should be noted that these predictor equations have the same local truncation error as the Newmark method, and thus provide results within the full accuracy of the structural integration scheme. Accordingly, only a single correction step for the structural variables is needed, whereby the otherwise mandatory definition of an effective termination criterion for the iteration process is superfluous.

Assuming the same time step Δt for the fluid and the structural domain, the coupled time integration procedure can be described as follows:

(A) Initialization:

Obtain starting values from the actual state of the system, i.e., displacements u_i , velocities \dot{u}_i , accelerations \ddot{u}_i , and aerodynamic loads p_i at time t_i . The system can already be in motion, e.g., when its aeroelastic behavior after a prescribed motion or the continuation of a foregoing computation is desired.

(B) Each time step $t_{i+1} = t_i + \Delta t$:

1. Compute displacements u_{i+1} and nonlinear elastic forces $f_{E|i+1}$ via Eqs. (8) and (11),
2. Predict velocities \dot{u}_{i+1} and accelerations \ddot{u}_{i+1} via Eqs. (16) and (17),
3. Update solutions of Euler equations or Duhamel's integral, respectively, and calculate aerodynamic load vector p_{i+1} ,
4. Correct accelerations \ddot{u}_{i+1} via the equilibrium equations (10) and velocities \dot{u}_{i+1} via Eq. (9).

Subcycling of the fluid domain is allowed when the Euler method is employed as discussed in reference [24]. Confirmed by experience, this coupled algorithm is numerically stable as long as stability of the single domain solvers is assured. However, due to accuracy requirements the actual time step size for each solver has to be chosen smaller than the critical time step necessary for stability. The mutual time step for the coupled field integration procedure is determined from the condition:

$$\Delta t = \min \{ \Delta t_S(\omega_{\max}), \Delta t_F(\text{CFL}) \}, \quad (18)$$

where Δt_F and Δt_S denote the admissible time steps for the fluid and the structural solver, which are restricted by the following relations:

$$\Delta t_S \leq \frac{0.15}{\omega_{\max}}, \quad \text{CFL} \leq \begin{cases} 0.3 & (\text{explicit}) \\ 15.0 & (\text{implicit}) \end{cases}.$$

These conditions are also adequate if strong nonlinearities are present. In addition, note that by the use of the classical linear airfoil theory the CFL number has no meaning, instead the apparent mass terms mentioned above are included in the eigenvalue analysis of the structural equations of motion.

3.4 Analysis of Response Data and Finding of Flutter Boundary

To extract the frequency, damping, amplitude, and phase information from the simulation data, two approaches were applied. First, the method of Bennett and Desmarais [3], in which the time series are fitted in a least square sense with complex exponential functions, and second, Ibrahim's time domain technique in a modified version of Füllekrug [13].

The problem of finding the critical flutter solution, which - by definition - is an oscillation with steady amplitude, thus with zero damping, was iteratively solved by employing the Newton-Raphson method, which is quadratic in convergence. The iteration cycle: (1) prescribe (in- or decrease) flight speed, (2) compute aeroelastic time response, and (3) determine vibration parameters, was continued until a predefined tolerance for the damping coefficients δ_j was achieved. In this study, $|\delta_j| \leq 10^{-3}$ 1/s was required to stop the iteration.

This iterative cycle, of course, is only needed when amplitude-dependent solutions of the system are searched, e.g., a subcritical Hopf bifurcation. In this case, the iteration process can be applied to find the flutter solutions for an array of initial conditions. In case of a supercritical Hopf bifurcation, the above condition defines a convergence criteria for limit cycle oscillations.

4 RESULTS OF AEROELASTIC COMPUTATIONS

This section is divided into two main parts. The first deals with linear systems and the second with nonlinear systems. The aim of the preliminary investigations for linear systems is to gain insight into the general aeroelastic stability behavior of a pre-defined linear reference model, and to contrast the solutions for both of the aerodynamic models described above. In this context, the U, g -method in combination with Theodorsen unsteady aerodynamics is used to provide an "exact" basis of comparison for the time simulation results.

In the second part, the effects of hardening and softening stiffness characteristics in the control mechanism on the flutter stability of the reference model are addressed.

4.1 Linear Systems

The linear aeroelastic reference model is defined by the following non-dimensional parameters:

$$\begin{aligned} e &= -0.2, & c_\beta &= 0.5, & \mu &= 12.0, \\ x_\alpha &= 0.1, & x_\beta &= 0.005, & \omega_\alpha/\omega_h &= 3.0, \\ r_\alpha^2 &= 0.25, & r_\beta^2 &= 0.0204, & \omega_\beta/\omega_h &= 0.5. \end{aligned}$$

With the scales

$$b = 1.0 \text{ m}, \quad \omega_h = 18\pi \text{ 1/s},$$

the critical velocity of the system determined by the U, g -method using Theodorsen's unsteady aerodynamics is $U_F^{(1)} = 100$ m/s and the flutter frequency $\omega_F^{(1)} = 51.22$ 1/s. Note that the system parameters were properly coordinated to obtain this easily memorized value of 100 m/s for the lowest velocity at which flutter occurs for the reference model. The solution belongs to the h, β -branch, i.e., plunge/control-surface flutter. This branch again has stable solutions at higher velocities. As the velocity increases, a second flutter case at $U_F^{(2)} = 247$ m/s ($\omega_F^{(2)} = 137.5$ 1/s) occurs due to the coupling of the pitch and the control-surface degrees of freedom. This type of flutter is referred to as pitch/control-surface flutter, in short: α, β -flutter.

Since both flutter cases involve the control-surface motion, the flutter boundary for both branches, the h, β -branch and the α, β -branch, depends on the actual stiffness in the control-surface attachment. Thus, a first insight into the possible aeroelastic stability behavior of the system with nonlinear stiffness characteristic $f(\beta)$ (Fig. 2) can be obtained by investigating the effect of stiffness changes in the control-surface attachment on the flutter behavior of the linear system. The results of these investigations are summarized in Fig. 3 where the flutter velocity U_F is depicted as function of the frequency ratio ω_β/ω_h (ω_β varied). The frequency domain results of the U, g -method using Theodorsen's classical linear airfoil theory are compared to the solutions of the proposed time simulation method for both unsteady aerodynamic models: Theodorsen's theory and the Euler method. All Euler calculations were performed for the NACA64A006 airfoil,

the air density $\rho_\infty = 0.81913 \text{ kg/m}^3$ and the speed of sound $a_\infty = 324.58 \text{ m/s}$. This corresponds to flight conditions at an altitude of 4000 m in the standard atmosphere.

As can be seen from Fig. 3, the agreement between the solutions obtained by the different computational approaches and aerodynamic models is extraordinary good for the h, β -branch and still satisfactory for the α, β -branch. Most importantly, this validates the time simulation procedure for linear systems.

4.2 Nonlinear Systems

4.2.1 Nonlinear Stiffness Characteristics

Exemplary for the typical nonlinear dependence of the control-surface restoring moment from the deflection β , the symmetric stiffness characteristic defined in Fig. 2 is considered. It is essentially a bilinear characteristic with the stiffness constants k_{β_1} and k_{β_2} , but the discontinuities at $\pm\beta_g$ are locally smoothed out with cubic polynomials where the coefficients a_k are determined for $r \leq \beta_g$ to obtain a continuous function $f(\beta)$. Throughout this investigation, k_{β_1} is fixed and corresponds to the stiffness of the linear reference model represented by the frequency ratio $\omega_{\beta_1}/\omega_h = 0.5$. Only the stiffness coefficient k_{β_2} , also expressed by $\omega_{\beta_2}/\omega_h$, is varied, yielding hardening and softening stiffness behavior for $k_{\beta_2} < k_{\beta_1}$ and $k_{\beta_2} > k_{\beta_1}$, respectively. The linear reference case is obtained for $k_{\beta_2} = k_{\beta_1}$, i.e. $\omega_{\beta_2} = \omega_{\beta_1} = 0.5 \omega_h$. In addition, $\beta_g = 0.05^\circ$ and $r = \beta_g/2$ for all considered cases.

4.2.2 Results for Hardening Stiffness

Characteristics

A frequently encountered type of nonlinearity on aircraft is due to the freeplay in the linkage elements of the control system. This special case of a hardening stiffness characteristic is represented by the function $f(\beta)$ defined in Fig. 2 if $k_{\beta_2} = 0.0$, which is synonymous with $\omega_{\beta_2}/\omega_h = 0.0$ for small amplitudes $|\beta| < (\beta_g - r)$. With increasing amplitude level, the effective stiffness approaches that of the linear reference model, k_{β_1} , which corresponds to $\omega_{\beta_1}/\omega_h = 0.5$. According to the equivalent linearization approach, real values of the frequency ratio

ω_β/ω_h can therefore vary between 0.0 and 0.5. As can be seen in Fig. 3, the critical flutter boundary (h, β -branch) steadily drops for this range. More precisely, using Theodorsen aerodynamics, the flutter velocity is $U_F^{[2]} = 121.5 \text{ m/s}$ for $\omega_{\beta_2}/\omega_h = 0.0$ and $U_F^{[1]} = 100 \text{ m/s}$ for $\omega_{\beta_1}/\omega_h = 0.5$. The corresponding values obtained for Euler aerodynamics are $U_F^{[2]} = 129.0 \text{ m/s}$ and $U_F^{[1]} = 107.1 \text{ m/s}$, respectively. Consequently, the flutter boundary of the nonlinear system is expected to vary between the critical velocities $U_F^{[2]}$ and $U_F^{[1]}$, depending on the actual oscillatory amplitude level. The spectrum of possible initial conditions to investigate this amplitude dependence of the flutter velocity is very rich. Yet, to limit the effort, only a variation of the initial displacement of the control surface β_0 is considered in this study.

The critical flutter boundaries for the nonlinear system, as obtained by the described time simulation method using both aerodynamic models, are shown in Fig. 4. There, the flutter velocity U_F is depicted as a function of the ratio $|\beta_0|/\beta_g$ with β_g defining the freeplay region together with r as specified in Fig. 2. As can be seen, the upper and the lower bound of the respective flutter boundary, $U_F^{[2]}$ and $U_F^{[1]}$, directly correlate with the results obtained for the linear system for $\omega_{\beta_2}/\omega_h = 0.0$ and $\omega_{\beta_1}/\omega_h = 0.5$, respectively. This is because these frequency ratios become operative for low and high amplitude levels. More specifically, the system actually behaves linearly for oscillatory amplitudes $|\beta| < (\beta_g - r)$ with zero stiffness in the control mechanism, thus yielding the same result as in the linear case. With increasing amplitude, the effective stiffness increases likewise and approaches that of the linear reference model k_{β_1} as upper limit, which corresponds to $\omega_{\beta_1}/\omega_h = 0.5$. Accordingly, for sufficiently high amplitude levels, the system again can be considered as quasi-linear with the aeroelastic properties of the reference model.

As can be seen from the course of the flutter velocity for each aerodynamic model in Fig. 4, beyond the critical flutter speed of the reference model $U_F^{[1]}$, unstable behavior does only occur if a certain amplitude level is exceeded. The required disturbance am-

plitude is smaller, the closer the flight speed approaches the upper bound $U_F^{[2]}$, above which the system is unstable for all initial disturbances. Referring to the upper bound $U_F^{[2]}$, this subcritical unstable periodic bifurcation, i.e., the branching of the unstable equilibrium points above $U_F^{[2]}$ to unstable limit cycles below $U_F^{[2]}$ is known as subcritical Hopf bifurcation. This type of bifurcation is representative for the stability behavior of the considered system for hardening stiffness characteristics $f(\beta)$, as becomes evident in Fig. 5. There, the results of further four examples using Theodorsen's unsteady aerodynamic theory are presented in addition to the case just considered. Please note that all solutions for small initial amplitude ratios $|\beta_0|/\beta_g$ with oscillatory amplitudes $|\beta| < (\beta_g - r)$ directly correlate to the discrete solutions depicted in Fig. 3 for the respective ratios $0.0 \leq \omega_\beta/\omega_h \leq 0.5$ denoted by the symbol '□'. For the linear reference case, of course, the flutter boundary is independent of the amplitude and, consequently, represented by a straight line (dashed line).

4.2.3 Results for Softening Stiffness Characteristics
The aeroelastic stability properties of the examined system are richly varied for softening stiffness characteristics defined by $k_{\beta_2} > k_{\beta_1}$ (Fig. 2). This can already be inferred from the results obtained by linear analysis illustrated in Fig. 3. With regard to the subsequent nonlinear analysis for softening stiffness characteristics with $\omega_{\beta_2} > \omega_{\beta_1} = 0.5 \omega_h$, the first notable point in the graph of Fig. 3 is that in the frequency range $0.5 < \omega_\beta/\omega_h \leq 2.0$, the h, β -branch abruptly ends at $\omega_\beta/\omega_h = 1.0$. This is due to the stiffening effect of the aerodynamic forces on the control-surface degree of freedom, which eliminates plunge/control-surface flutter for frequency ratios $\omega_\beta/\omega_h > 1.0$. Instead, the α, β -branch represents the critical flutter boundary of the system from here on. The second point, which lets one expect a different and more versatile stability behavior of the system for softening stiffness characteristics, is that the slope of the flutter curve of the h, β -branch changes after passing a minimum at $\omega_\beta/\omega_h = 0.94$. With regard to this previous knowledge, the flutter investigations for softening stiffness characteristics

are grouped according to the value of $\omega_{\beta_2}/\omega_h$ into systems defined by:

- (1) $0.5 < \omega_{\beta_2}/\omega_h \leq 0.9$,
- (2) $\omega_{\beta_2}/\omega_h = 1.0$,
- (3) $1.0 < \omega_{\beta_2}/\omega_h \leq 2.0$.

(1) Systems with softening stiffness characteristics defined by $0.5 < \omega_{\beta_2}/\omega_h \leq 0.9$

To begin with, the nonlinear system given by $\omega_{\beta_2}/\omega_h = 0.7$ is considered. In this case, the frequency ratio ω_β/ω_h can take real values of about 0.5 up to 0.7 for large and small amplitudes β , respectively, depending on the actual amplitude level. As can be seen from Fig. 3, the critical flutter velocity continues to decrease along the h, β -branch for $0.5 < \omega_\beta/\omega_h \leq 0.7$ because plunge/control-surface flutter is promoted as ω_β approaches ω_h . In contrast to the cases with hardening stiffness characteristics addressed in the previous section where, for small amplitudes $|\beta| < (\beta_g - r)$, the flutter velocity for real values $\omega_\beta/\omega_h < 0.5$ is higher than that of the linear reference model ($\omega_\beta/\omega_h = 0.5$), the flutter velocity for $\omega_\beta/\omega_h = 0.7$ is now smaller than that of the reference model. This fact is important to note since it is the very reason why the flutter boundary of the system considered here is now amplitude independent. This is in sharp contrast to the aeroelastic stability behavior of the system for hardening stiffness characteristics which was shown to be highly amplitude dependent.

The flutter characteristics for the nonlinear system defined by $\omega_{\beta_2}/\omega_h = 0.7$ as obtained for Theodorsen and Euler unsteady aerodynamics are shown in Fig. 6. The lower and the upper bound of the critical flight speed, $U_F^{[2]}$ and $U_F^{[1]}$, again are determined by the stiffness coefficients k_{β_2} and k_{β_1} which define the nonlinear stiffness characteristic and directly correspond to the frequency ratios $\omega_{\beta_2}/\omega_h = 0.7$ and $\omega_{\beta_1}/\omega_h = 0.5$. This implies that flutter is possible beyond the critical flight speed of the linear reference model for small amplitude oscillations. Referring to the lower bound $U_F^{[2]}$, the run of the stability curve now agrees with a supercritical Hopf bifurcation, i.e., the branching of the stable equilib-

rium points below $U_F^{[2]}$ to stable limit cycles above $U_F^{[2]}$. Thus, the curves connecting $U_F^{[2]}$ and $U_F^{[1]}$ depict the limit cycle amplitude β of the control-surface oscillation (non-dimensionalized with β_g) as a function of flight speed U_∞ . This amplitude precisely marks the boundary between the region of aerodynamically damped and aerodynamically excited motions of the system.

A precise explanation for this aeroelastic behavior can be given with the aid of the preliminary results obtained for the linear system. These results summarized in Fig. 3 reveal that, with respect to the linear reference case defined by $\omega_\beta/\omega_h = 0.5$, any increase in the frequency ratio ω_β/ω_h has a destabilizing effect on the flutter boundary, or referring to the flutter point for $\omega_\beta/\omega_h = 0.7$, any decrease of the ratio ω_β/ω_h has a stabilizing effect. Consequently, in the nonlinear case for a certain flight speed $U_F^{[2]} < U_\infty < U_F^{[1]}$ leading to a limit cycle oscillation with a definite limit cycle amplitude β , all system motions with instantaneous control-surface amplitudes larger than this specific limit cycle amplitude are damped because these larger amplitude motions cause smaller effective values ω_β/ω_h due to the softening stiffness characteristic. But, as mentioned above, the flutter velocity increases for smaller values of ω_β/ω_h , thus larger amplitude motions are aerodynamically damped. Conversely, all system motions with instantaneous control-surface amplitudes smaller than this specific limit cycle amplitude are, of course, unstable and aerodynamically excited because they lead to larger values of ω_β/ω_h as a result of the softening stiffness characteristic. Thus, all oscillations meet this limit cycle, which therefore is termed a stable limit cycle. The observed limit cycle amplitude becomes larger, the closer the flight speed approaches the upper bound $U_F^{[1]}$, above which the system is unstable for all initial disturbances.

The tendency of how the stability behavior of the system changes when the stiffness characteristic is varied can be seen in Fig. 7 where, next to the case just discussed, the flutter boundaries for three additional cases defined by frequency ratios $0.5 < \omega_{\beta_2}/\omega_h \leq 0.9$ are depicted.

Comment:

The numerical results shown thus far for linear systems as well as for nonlinear systems demonstrate that the aeroelastic stability behavior of the considered systems as predicted by the proposed time simulation method is practically independent of the chosen aerodynamic model. The application of the Euler method for the determination of the aerodynamic forces only leads to systematic differences in the solutions, yet the general results of the aeroelastic stability analyses agree with each other in every essential detail. Therefore, all subsequently presented results are based on the linear airfoil theory of Theodorsen which requires less computational effort than the Euler method.

(2) System with softening stiffness characteristic defined by $\omega_{\beta_2}/\omega_h = 1.0$

The nonlinear system defined by $\omega_{\beta_2}/\omega_h = 1.0$ takes an exceptional position among the systems with softening stiffness characteristics. Its stability plot is shown in Fig. 8 using the same axis labelling as in Figs. 6 and 7. As can be seen, the stability curve below $U_F^{[2]}$ now consists of two branches, one of which represents unstable limit cycles and the other stable limit cycles. More precisely, the inner curve is related to unstable limit cycles while the outer curve represents stable limit cycles. Thus, the aeroelastic stability behavior of the system does not only depend on the flight speed but also on the actual amplitude level of the motion.

Again, the results for the linear system (Fig. 3) obtained for different values of ω_β/ω_h provide valuable information to explain this particular behavior. In these investigations for $\omega_{\beta_2}/\omega_h = 1.0$, the flutter velocity $U_F = 49.06$ m/s was determined along the h, β -branch. This result is identical with the critical velocity $U_F^{[2]}$ of the nonlinear system for small amplitude motions, $|\beta| < (\beta_g - r)$, where k_{β_2} takes effect which corresponds to the frequency ratio $\omega_{\beta_2}/\omega_h = 1.0$. As the frequency ratio decreases, the linear flutter boundary also declines, but rises after passing the minimum at $\omega_\beta/\omega_h = 0.94$ until it reaches the critical flight speed of the reference model at $\omega_\beta/\omega_h = 0.5$.

In the nonlinear case, real values of ω_β/ω_h become smaller as the control-surface amplitude β increases because of the softening stiffness characteristic. It is therefore easy to understand that, starting from the flutter speed $U_F^{[2]} = 49.06 \text{ m/s}$ for small amplitude levels, the flutter speed of the system decreases with increasing amplitude according to a subcritical Hopf bifurcation. This decrease in flutter speed is expected to continue to a minimum as observed in the preliminary studies for linear systems. However, as can be shown for the linear case using Theodorsen's unsteady airfoil theory, the influence of the aerodynamic forces near the minimum of the flutter curve at $\omega_\beta/\omega_h = 0.94$ is very weak. This implies that the system can be considered as quasi-conservative for real values of ω_β/ω_h of about 0.94, free from aerodynamic damping or excitation. As a result, any arbitrary initial disturbance of the system leads to periodic solutions using the time simulation approach, whereby the determination of the sought flutter solutions becomes very difficult and time consuming. Consequently, flight speeds $U_\infty < 25.0 \text{ m/s}$ were not considered in this study.

With a further increase in amplitude level, the aeroelastic stability behavior of the system changes in that all motions with sufficiently large control-surface amplitudes are aerodynamically excited, and, for a certain flight speed, enter a specific stable limit cycle represented by the outer curve. With that, the stability behavior of the system changes to the one previously described in detail for softening stiffness characteristics with $0.5 < \omega_{\beta 2}/\omega_h \leq 0.9$, cf. Fig. 7.

As becomes evident from this particular example, the nonlinear flutter behavior of the system does not only depend on the considered type of nonlinearity, but also on the general aeroelastic stability properties of the system. More precisely, the results presented here clearly show the strong relation between the slope of the flutter boundary obtained for the corresponding linear system as function of ω_β/ω_h (Fig. 3) and the flutter behavior of the nonlinear system, which is characterized accordingly by unstable and stable limit cycle oscillations (Fig. 8) for the same type of nonlinear stiffness function $f(\beta)$.

(3) Systems with softening stiffness characteristics defined by $1.0 < \omega_{\beta 2}/\omega_h \leq 2.0$

Finally, systems with softening stiffness characteristics defined by $1.0 < \omega_{\beta 2}/\omega_h \leq 2.0$ are considered. The computed stability curves are depicted in Figs. 9 and 10. Fig. 9 shows the results for the case $\omega_{\beta 2}/\omega_h = 2.0$ with the non-dimensionalized limit cycle amplitude of the control-surface oscillation $|\beta|/\beta_g$ as function of flight speed U_∞ . As can be seen in this plot, the system exhibits stable limit cycle oscillations both below and above the critical flight speed $U_F = 100.0 \text{ m/s}$ of the linear reference model. Moreover, the respective stability curves represent different types of limit cycle flutter, i.e., plunge/control-surface flutter (h, β -branch) and pitch/control-surface flutter (α, β -branch). Which type of flutter occurs depends on the actual amplitude level and the flight speed. While the amplitude level determines the effective value of the control-surface hinge stiffness, and with it the frequency ratio ω_β/ω_h , with increasing flight speed the aerodynamic forces gain more influence on the aeroelastic behavior of the system. Particularly the stiffening effect of the aerodynamic forces on the control-surface degree of freedom is the major reason that, for sufficiently high flight speeds, plunge/control-surface flutter no longer occurs even for large disturbance amplitudes. In this sense, the dashed line in Fig. 9 divides the stability plane into two regions, one of which represents the domain of attraction of the plunge/control-surface flutter branch and the other, the domain of attraction of the pitch/control-surface flutter branch. The type of flutter changes at this demarcation line.

Under the conditions which lead to h, β -flutter, the system then shows the same stability behavior like the previously discussed systems with softening stiffness characteristics. The most important of these prerequisites is, of course, that the frequency ratio takes real values $\omega_\beta/\omega_h \leq 1.0$ as the preliminary investigations have shown, cf. Fig. 3. For the nonlinear system with softening stiffness characteristic considered here, however, frequency ratios of this magnitude become active only at sufficiently high amplitudes β . Consequently, the aeroelastic re-

sponse of the system is dominated by pitch/control-surface oscillations for small initial amplitude motions with effective frequency ratios $\omega_\beta/\omega_h > 1.0$. These oscillations are stable and the system returns to its equilibrium position as long as the critical value of 127.7 m/s for the flight speed U_∞ is not exceeded. By achieving this critical velocity, which corresponds to the frequency ratio $\omega_{\beta_2}/\omega_h = 2.0$, cf. Fig. 3, the stability behavior of the system changes according to a supercritical Hopf bifurcation. Accordingly, all motions within the domain of attraction of the α, β -branch meet a specific stable limit cycle of amplitude β depending on the actual flight speed U_∞ . As U_∞ increases, the limit cycle amplitude also rises until the system becomes unstable for all disturbances beyond $U_f^{[1]} = 247.0$ m/s.

A plausible explanation for this behavior is again provided by the results of the preliminary investigations summarized in Fig. 3. There, the critical velocity determined for the α, β -branch continuously increases from 127.7 m/s to 247.0 m/s as the frequency ratio ω_β/ω_h decreases from 2.0 to 0.5. But these values for the frequency ratio directly correspond to the actual stiffness of the nonlinear system for small and large control-surface deflections, respectively. The lower and the upper bound of the α, β -branch in Fig. 9 therefore coincide with the solutions obtained for the linear system for the frequency ratios in question. Since the lowest effective control-surface hinge stiffness which can be reached within the limit for growing amplitudes β is that of the linear reference model k_{β_1} , by which the operative frequency ratio ω_β/ω_h approaches real values of 0.5, cf. Fig. 3, the system is unboundedly unstable beyond the critical flight speed $U_\infty = 247.0$ m/s. Below this upper bound within the domain of attraction of the α, β -branch, however, an unstable motion with growing amplitude β decreases the effective control-surface hinge stiffness and, with that, the effective value of the frequency ratio ω_β/ω_h due to the softening stiffness characteristic. But according to the results shown in Fig. 3 the critical flight speed is increased by this. Thus, the system stabilizes into a time-periodic equilibrium solution, i.e., a stable limit cycle oscillation. It

should be noted that this mechanism, which causes the system to settle in stable limit cycles along the α, β -branch, is precisely the same as was discussed above for the h, β -branch.

The effect of a variation of the nonlinear stiffness function $f(\beta)$ on the stability behavior of the system is shown in Fig. 10, where the stability characteristics for reduced stiffness coefficients k_{β_2} and thus reduced frequency ratios $\omega_{\beta_2}/\omega_h$ are plotted. Given the results of the preliminary investigations shown in Fig. 3, the bifurcation point of the α, β -branch predictably moves to higher velocities as the stiffness coefficient k_{β_2} and, hence, the frequency ratio $\omega_{\beta_2}/\omega_h$ decreases. In addition, the required amplitude level at which the type of flutter switches from pitch/control-surface flutter to plunge/control-surface flutter drops. This is because the stiffness coefficient k_{β_2} approaches k_{β_1} whereby the stiffness characteristic becomes continuously smoother until stiffness characteristics are obtained for yet smaller constants k_{β_2} which were already considered in the previous sections.

5 SUMMARY

A time simulation method for the accurate prediction of the flutter characteristics of aeroelastic systems with concentrated structural nonlinearities has been developed and demonstrated. Its algorithmic core consists of a simple predictor-corrector scheme in which the respective finite difference operators, as applied to the fluid and the structural equations, are linked with each other in a time-accurate manner. The applied finite difference operators are all single-step formulas commonly in use in fluid and structural dynamics, thus this method is also applicable to varying time step sizes and does not need an additional starting procedure. This also facilitates the uncomplicated and accurate continuation of a previously executed and aborted calculation.

A typical airfoil section with discrete control-surface nonlinearities was considered in order to demonstrate the practicability of the method, where the unsteady aerodynamic forces were predicted by the classical linear airfoil theory of Theodorsen and by an Euler method assuming inviscid subsonic flow.

Results for linear systems showed good agreement to solutions of classical linear frequency domain flutter calculations. These were provided for systematically varied spring constants in the torsional degree of freedom of the control surface and proved to be very helpful in verifying the results obtained for nonlinear systems. With this knowledge, an explanation could be given for the typical bifurcation of the flutter boundary of the airfoil/control-surface system for hardening and softening control-surface stiffness characteristics with respect to a predefined linear reference model. In particular, it was found that the branching of the flutter boundary according to a sub- or supercritical Hopf bifurcation does not only depend on the special type of nonlinearity but also on the general aeroelastic stability properties of the system. A strong relation between the slope of the flutter boundary obtained for the linear system as function of control-surface stiffness and the bifurcation of the flutter boundary of the nonlinear system was shown. This was revealed by an example in which the flutter behavior of the airfoil/control-surface system for a given nonlinear stiffness function was characterized by stable as well as unstable limit cycle oscillations according to the slope of the linear flutter boundary. This implies that the flutter behavior of such simple nonlinear systems can be qualitatively inferred from the knowledge of the aeroelastic stability properties of the corresponding linear system. As was shown, the latter also gives an indication on the type of flutter to be expected, which can alter with changes in amplitude level and/or flight speed in the nonlinear case.

Although in this study the method was applied to investigate nonlinear flutter at subsonic speeds, it was developed in view of its application to transonic flight conditions by the implementation of the Euler method, which can also be replaced by a Navier-Stokes code if necessary. According to the results obtained so far, it has been concluded that the method is equally valid for transonic flow. It is also applicable to other types of nonlinearities than those considered here and to more than one nonlinear degree of freedom. It is, however, clear that the latter will complicate the interpretation of the results.

REFERENCES

- [1] Anderson, W. K.; Thomas, J. L.; van Leer, B.: A Comparison of Finite Volume Flux Vector Splittings for the Euler Equations, AIAA Paper 85-0122, 1985
- [2] Bathe, K.-J.: Finite Element Procedures in Engineering Analyses, Prentice-Hall, Inc., 1996
- [3] Bennett, R. M.; Desmarais, R. M.: Curve Fitting of Aeroelastic Transient Response Data with Exponential Functions, Flutter Testing Techniques, NASA SP-415, 1975, pp. 43-58
- [4] Brase, L. O.; Eversman, W.: Application of Transient Aerodynamics to the Structural Nonlinear Flutter Problem, J. Aircraft, Vol. 25, No. 11, 1988, pp. 1060-1068
- [5] Breitbach, E.: Effects of Structural Nonlinearities on Aircraft Vibrations and Flutter, AGARD Report R-665, 1978
- [6] Breitbach, E. J.: Flutter Analysis of an Airplane with Multiple Structural Nonlinearities in the Control System, NASA TP-1620, 1980
- [7] Carstens, V.: Two-Dimensional Elliptic Grid Generation for Airfoils and Cascades, DFV-LR-FB 88-52, Göttingen 1988
- [8] Carstens, V.: Computation of the Unsteady Transonic 2D Cascade Flow by an Euler Algorithm with Interactive Grid Generation, AGARD CP 507, 1990
- [9] Conner, M. D.; Tang, D. M.; Dowell, E. H.; Virgin, L. N.: Nonlinear Behavior of a Typical Airfoil Section with Control Surface Freplay: A Numerical and Experimental Study, J. Fluids and Structures, Vol. 11, 1997, pp. 89-109
- [10] Edwards, J. W.: Computational Aeroelasticity, In: Noor, A. K.: Structural Dynamics and Aeroelasticity, Vol. 5, Flight-Vehicle Materials, Structures, and Dynamics - Assessment and Future Directions, ASME, 1993, pp. 393-436
- [11] Farhat, C.; Lesoinne, M.: Fast Staggered Algorithms for the Solution of Three-Dimensional Nonlinear Aeroelastic Problems, AGARD-R-822, 1998, pp. 7:1-7:11

- [12] Försching, H.W.: Challenges and Perspectives in Computational Aeroelasticity, Proc. of the Int. Forum on Aeroelast. and Struct. Dynamics, Vol. 1, Manchester (UK), 1995, pp. 1.1-1.9
- [13] Füllekrug, U.: Strukturdynamische Identifikation im Zeitbereich - Bestimmung modaler Parameter aus den Zeitverläufen freier Schwingungen, DLR - IB 232-96 C 07, 1996
- [14] Hauenstein, A. J.; Zara, J.; Eversman, W.; Qumei, I.: Chaotic and Nonlinear Dynamic Response of Aerossurfaces with Structural Nonlinearities, AIAA/ASME/ASCE/AHS/ASC 33rd Structures, Structural Dynamics, and Materials Conf., Dallas, TX., April 1992, pp. 2367-2375
- [15] Küssner, H. G.: On the Nonlinear Approach to the Aeroelastic Stability Problem, AGARD Report 246, 1959
- [16] Kousen, K. A.; Bendiksen, O. O.: Limit Cycle Phenomena in Computational Transonic Aeroelasticity, J. Aircraft, Vol. 31, No. 6, Nov.-Dec. 1994, pp. 1257-1263
- [17] Laurenson, R. M.; Hauenstein, A. J.; Gubser, J. L.; Briley, R. P.: Effects of Structural Nonlinearities on Limit Cycle Response of Aerodynamic Surfaces, AIAA Paper 86-0899, 1986
- [18] Lee, B. H. K.; Desroches, J.: Flutter Analysis of a Two-Dimensional Airfoil Containing Structural Nonlinearities, Aeronautical Report LR-618, NRC No. 27833, Ottawa, 1987
- [19] Lee, I.; Kim, S.: Aeroelastic Analysis of a Flexible Control Surface with Structural Nonlinearity, J. Aircraft, Vol. 32, No. 4, July-August 1995, pp. 868-874
- [20] Morton, S. A.; Beran, P. S.: Effects of Structural Nonlinearity in the Bifurcation Analysis of Transonic Airfoil Flutter, Proceedings of 27th AIAA Fluid Dynamics Conference, New Orleans, LA, June 17-20, 1996
- [21] Piperno, S.; Farhat, C.; Larrourou, B.: Partitioned Procedures for the Transient Solution of Coupled Aeroelastic Problems, Part I, Computer Methods in Appl. Mechanics and Engineering, No. 124, 1995, pp. 79-112
- [22] Prananta, B. B.; Hounjet, M. H. L.: Large Time Step Aero-Structural Coupling Procedures for Aeroelastic Simulation, CEAS Int. Forum on Aeroelasticity and Structural Dynamics, Rome, Italy, June 17-20, 1997, CP Vol. II, pp. 63-70
- [23] Price, S. J.; Alighanbari, H.; Lee, B. H. K.: The Aeroelastic Response of a Two-Dimensional Airfoil with a Bilinear and Cubic Structural Nonlinearity, J. Fluids and Structures, 9, 1995, pp. 175-193
- [24] Schulze, S.: Transonic Aeroelastic Simulation of a Flexible Wing Section, AGARD-R-822, 1998, pp. 10:1-10:20
- [25] Shen, S. F.: An Approximate Analysis of Nonlinear Flutter Problems, J. Aeron. Scien., Vol. 26, 1959, pp. 25-32 and 51-53
- [26] Theodorsen, T.: General Theory of Aerodynamic Instability and the Mechanism of Flutter, NACA Report 496, 1935
- [27] Voß, R.; Carstens, V.: Computation of Unsteady Transonic Flows around Oscillating Airfoils Using Full Potential and Euler Equations, Proceedings of the European Forum on Aeroelasticity and Structural Dynamics, Aachen, Germany, April 17-19, 1989
- [28] Woolston, D. S.; Runyan, H. W.; Andrews, R. E.: An Investigation of Effects of Certain Types of Structural Nonlinearities on Wing and Control Surface Flutter, J. Aeron. Scien., Vol. 24, Jan. 1957, pp. 57-63
- [29] Zhao, L.C.; Yang, Z. C.: Analysis of Limit Cycle Flutter of an Airfoil in Incompressible Flow, J. Sound and Vibration, Vol. 123, No. 1, 1988, pp. 1-13
- [30] Zhao, L.C.; Yang, Z. C.: Chaotic Motions of an Airfoil with Non-Linear Stiffness in Incompressible Flow, J. Sound and Vibration, Vol. 138, No. 2, 1990, pp. 245-254

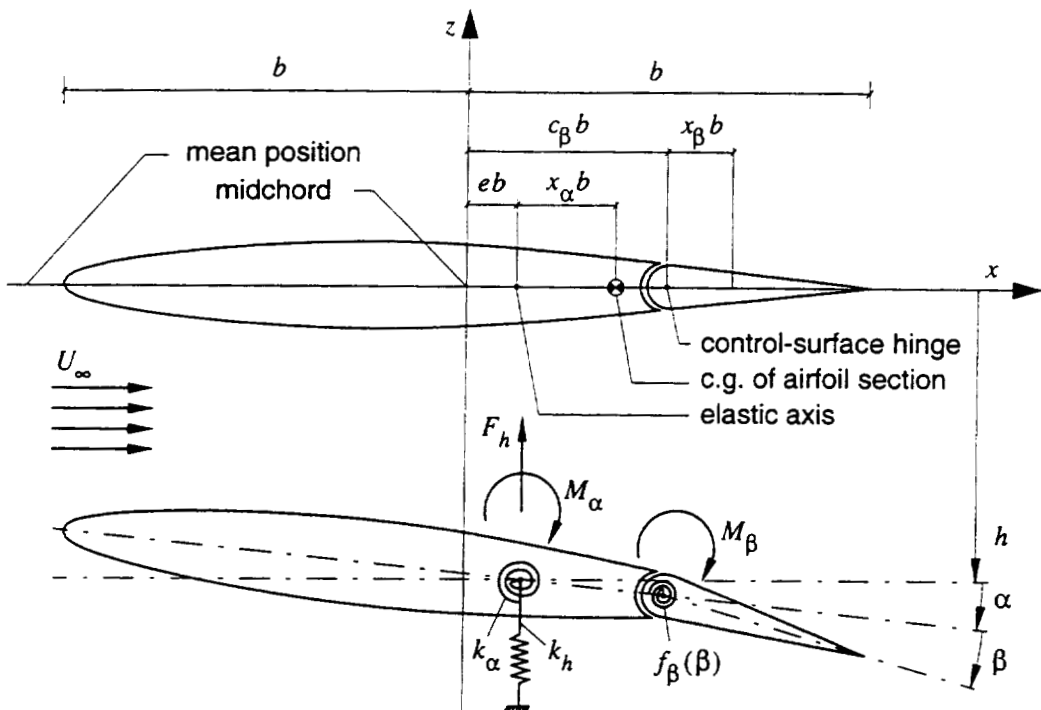


Fig. 1 Definition of parameters and coordinates for airfoil section with three degrees of freedom

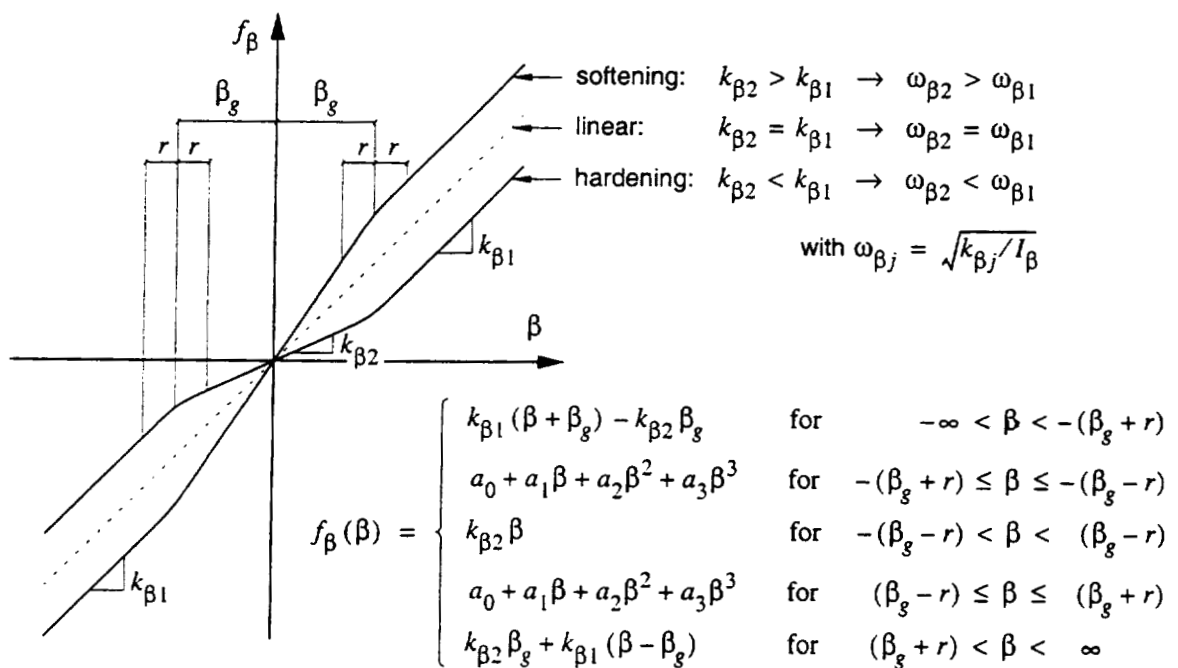


Fig. 2 Nonlinear stiffness characteristic in control-surface degree of freedom

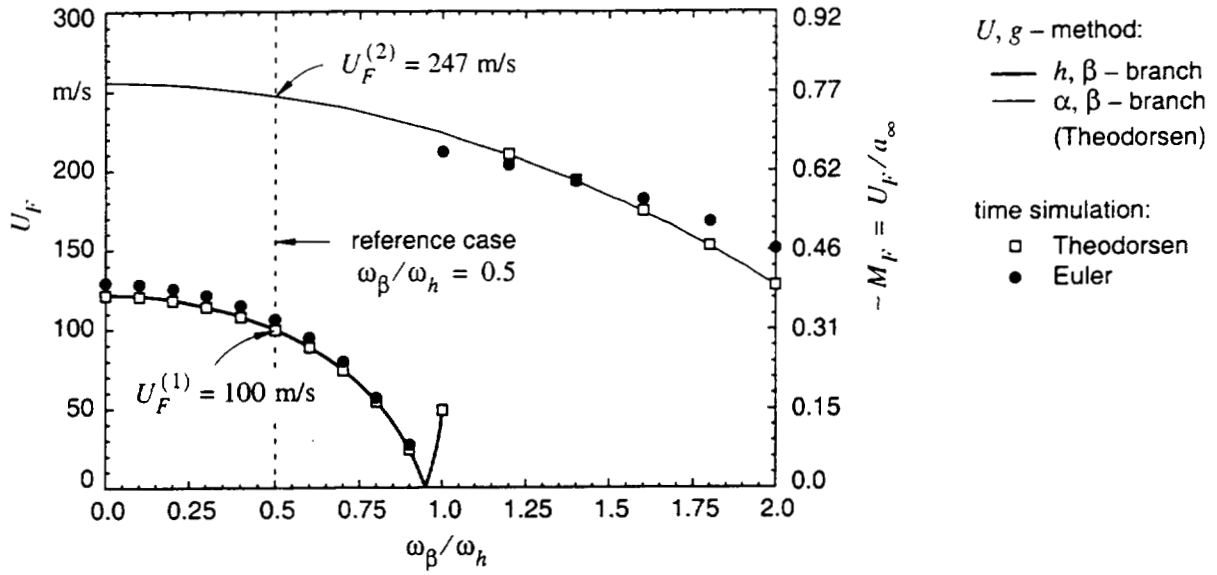


Fig. 3 Comparison of time domain solutions for flutter velocity U_F as function of frequency ratio ω_β/ω_h with frequency domain results using the U, g -method

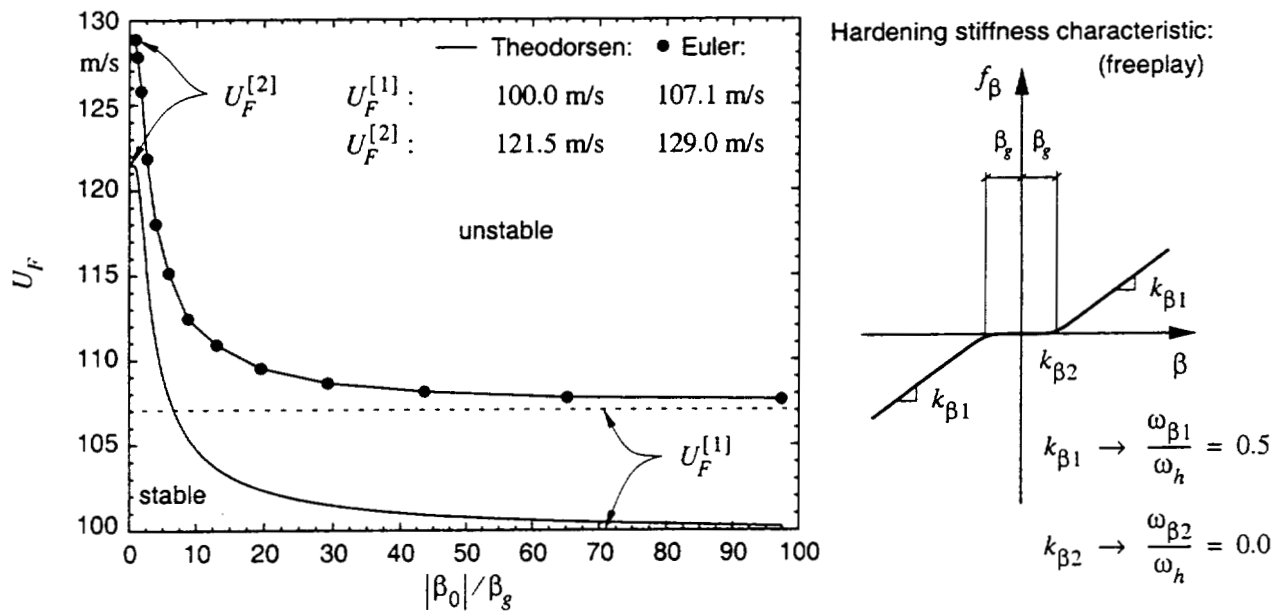


Fig. 4 Flutter velocity U_F as function of non-dimensionalized initial displacement $|\beta_0|/\beta_g$ for hardening stiffness characteristic - case defined by $\omega_{\beta 2}/\omega_h = 0.0$ (freeplay)

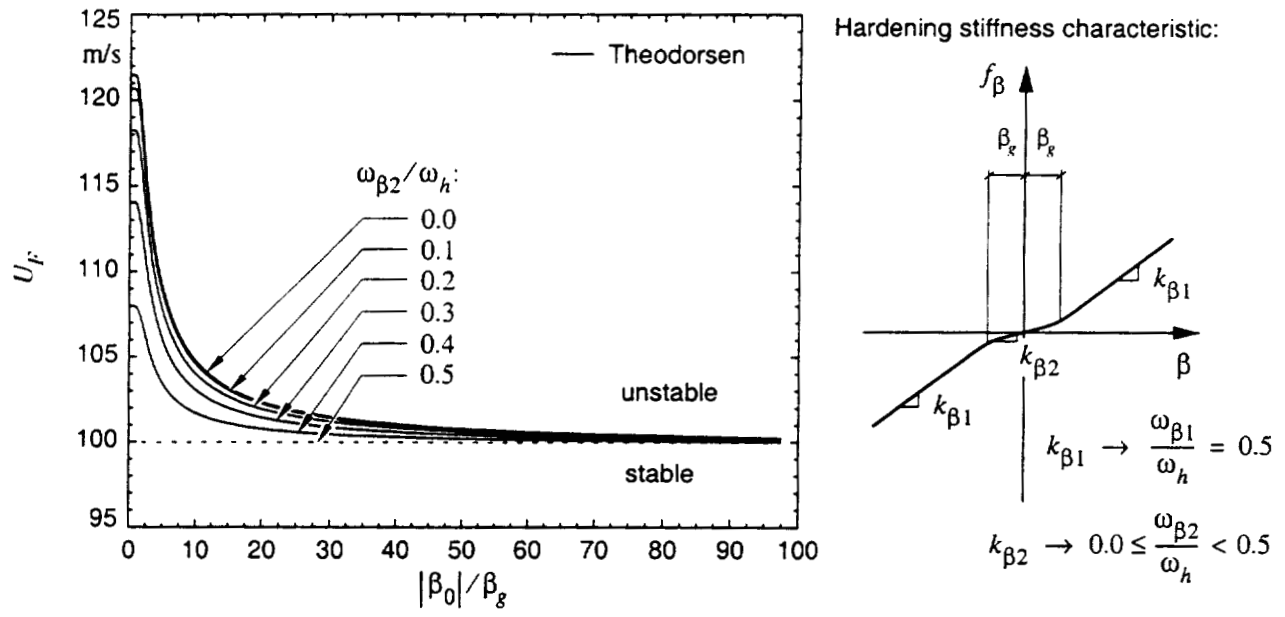


Fig. 5 Flutter velocity U_F as function of non-dimensionalized initial displacement $|\beta_0|/\beta_g$ for hardening stiffness characteristics - cases defined by $0.0 \leq \omega_{\beta_2}/\omega_h < 0.5$

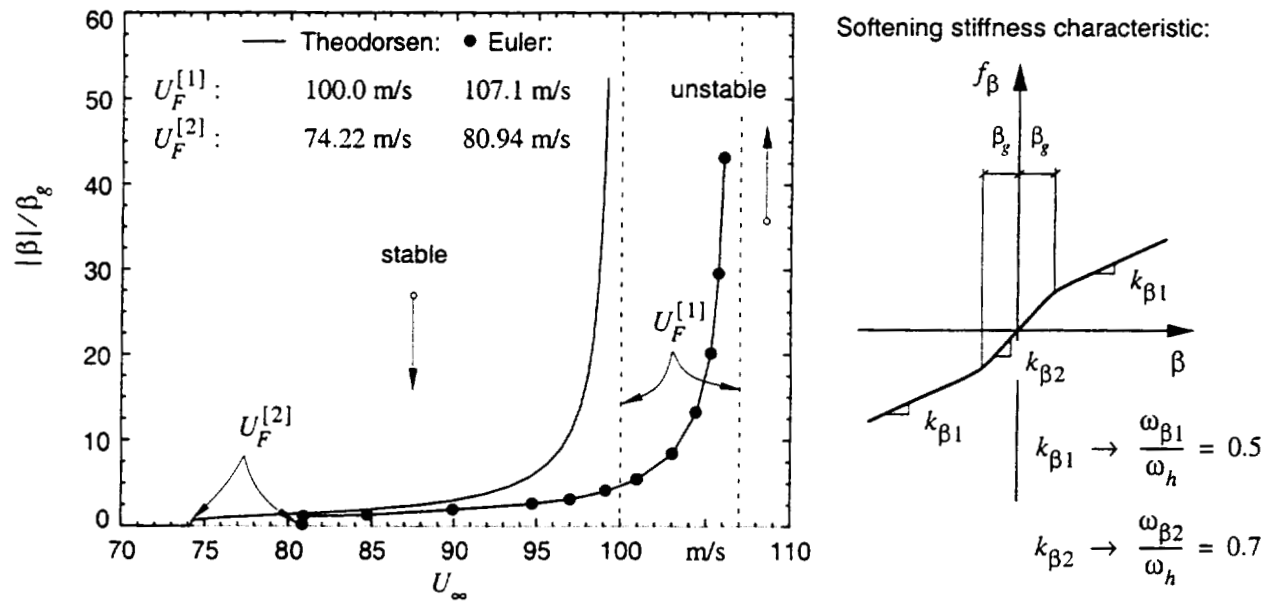


Fig. 6 Non-dimensionalized limit cycle amplitude of control-surface oscillation $|\beta|/\beta_g$ as function of flight speed U_∞ for softening stiffness characteristic - case defined by $\omega_{\beta_2}/\omega_h = 0.7$

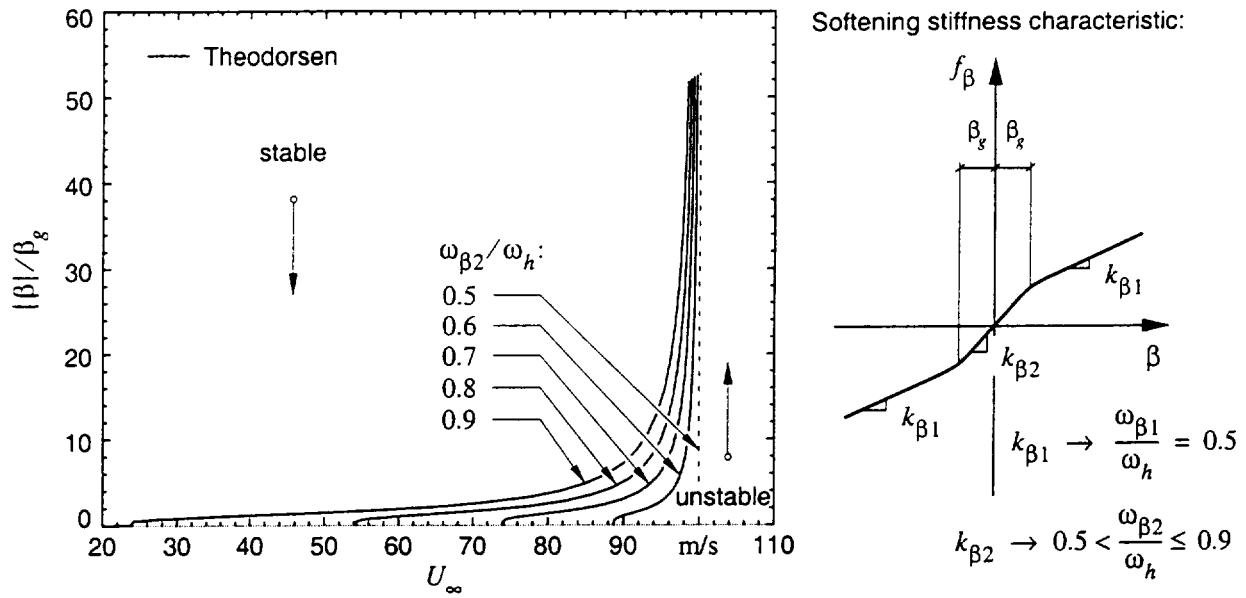


Fig. 7 Non-dimensionalized limit cycle amplitude of control-surface oscillation $|\beta|/\beta_g$ as function of flight speed U_∞ for softening stiffness characteristics - cases defined by $0.5 < \omega_{\beta_2}/\omega_h \leq 0.9$

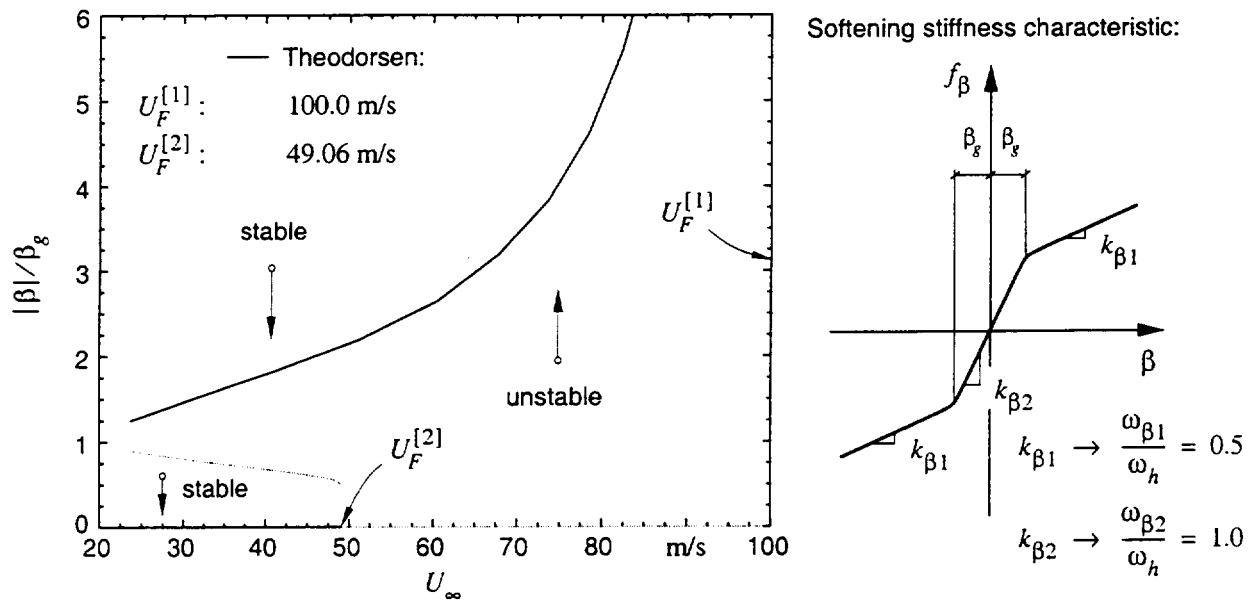


Fig. 8 Non-dimensionalized limit cycle amplitude of control-surface oscillation $|\beta|/\beta_g$ as function of flight speed U_∞ for softening stiffness characteristic - case defined by $\omega_{\beta_2}/\omega_h = 1.0$

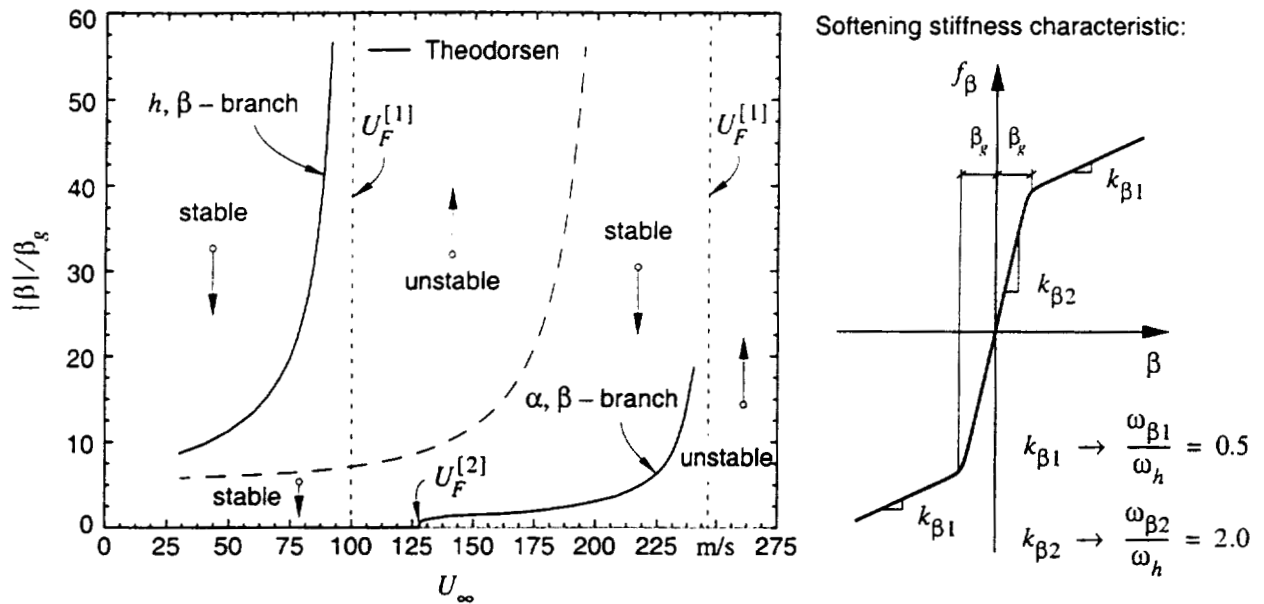


Fig. 9 Non-dimensionalized limit cycle amplitude of control-surface oscillation $|\beta|/\beta_g$ as function of flight speed U_∞ for softening stiffness characteristic - case defined by $\omega_{\beta 2}/\omega_h = 2.0$

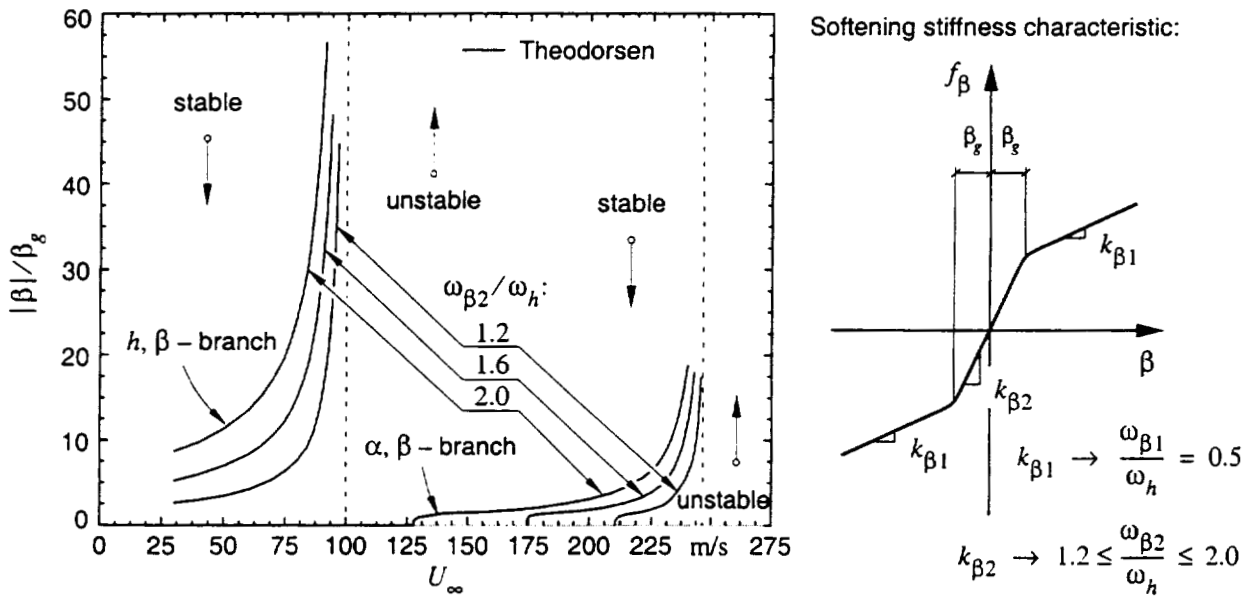


Fig. 10 Non-dimensionalized limit cycle amplitude of control-surface oscillation $|\beta|/\beta_g$ as function of flight speed U_∞ for softening stiffness characteristics - cases defined by $1.2 \leq \omega_{\beta 2}/\omega_h \leq 2.0$

LIMIT CYCLE OSCILLATION PREDICTION USING ARTIFICIAL NEURAL NETWORKS

57-63

Charles M. Denegri, Jr.* and Michael R. Johnson†
*Air Force SEEK EAGLE Office
Eglin Air Force Base, Florida*

Abstract

A static artificial neural network in the form of a multi-layer perceptron is investigated to determine its ability to predict linear and nonlinear flutter response characteristics. The network is developed and trained using linear flutter analysis and flight test results from a fighter test. Eleven external store carriage configurations are used as training data and three configurations are used as test cases. The network was successful in predicting the aeroelastic oscillation frequency and amplitude responses over a range of Mach numbers for two of the test cases. Predictions for the third test case were not as good. Several network sizes were investigated and it was found that small networks tended to over-generalize the training data and are not capable of accurate prediction beyond the sample space. Conversely, networks that were too large, or trained to error levels that were extreme, tended to memorize the training data, and are also unable to produce adequate predictions beyond the sample space. The results of this study indicate that relatively simple networks using small training sets can be used to predict both linear and nonlinear flutter response characteristics.

Introduction

Limit Cycle Oscillations (LCO) have been a persistent problem on several fighter aircraft and are generally encountered on external store configurations that are theoretically predicted to be flutter sensitive. These sensitivities are quite evident during flight and are often the subject of extensive examination during flutter flight tests of aircraft that exhibit this behavior. Ref. 1 provides a detailed description of the LCO phenomenon as well as a discussion of its evolution and its relationship to classical flutter. An excellent overview of LCO of fighter aircraft car-

rying external stores and its sensitivity to the store carriage configuration and mass properties is given in Ref. 2. These articles describe LCO as a phenomenon characterized by sustained periodic oscillations which neither increase nor decrease in amplitude over time for a given flight condition.

The particular variety of LCO of interest here is the nonlinear flutter response of major aircraft components such as the wing. The large number of store carriage configurations possible due to external store downloading increases the likelihood of encountering LCO in the flight envelope for a store carriage permutation. LCO arises

This paper is declared a work of the U.S. Government and is not subject to copyright protection in the United States.

* Lead Flutter Engineer, Senior Member AIAA.

† Electronics Engineer, Member AIAA.

from the nonlinear interaction of the structural and aerodynamic forces acting on the affected aircraft component. Linear flutter analyses adequately identify the oscillation frequency and modal composition of the LCO mechanism. However, because of the nonlinearities involved, the linear flutter analysis fails to predict the onset or severity of the LCO, which are of prime importance in the certification of external store configurations on fighter aircraft. Some success in theoretically predicting LCO has been achieved^{3,4,5} but these methods have not yet been shown practical for applications which require a large amount of analyses (such as weapon certification efforts on fighter aircraft).

The present work evaluates the feasibility of using an Artificial Neural Network (ANN) for predicting LCO of a fighter aircraft with external stores. No attempt is made to explain the physics of the LCO phenomenon. The method presented simply attempts to predict the occurrence of LCO based on historical flight test results. The ultimate goal is to develop a practical non-linear LCO prediction capability, which provides greater insight into expected test results, thus reducing the need for expensive flight-testing.

Analysis Approach

The concept of the Artificial Neural Network is an attempt to simulate one popular model of the memory structure of the human brain. The ANN is designed to reproduce the brain's behavior in terms of learning and adaptation. The desirable characteristics of the ANN lie in its ability to identify and model highly non-linear systems. ANNs have been shown to exhibit a potential for highly effective interpolation within a problem space, and can be used as a tool for the prediction of non-linear states beyond the problem space bounds. It is the ability to predict system behavior that makes ANNs attractive for the prediction of LCO.

A static neural network in the form of a Multi-Layer Perceptron (MLP) was chosen for this study because of its ease of design and evaluation, as well as its simplicity. A static network is

designed to simply feed forward input sets one at a time and provide a prediction. By its nature, there is no inherent knowledge of past inputs or outputs. The problem then is reduced to one of functional representation. It is from this perspective that the ANN is employed for LCO prediction. Since the prediction is not intended as a real-time system, training time and learning rate are not primary factors in the design and testing of the network.

The ANN is trained using both flight test data and linear flutter analysis data. The flight test data from a wide variety of external store configurations is used and are presented in Table 1. These configurations exhibit characteristics which are representative of the broad spectrum of flutter and LCO responses encountered by fighter aircraft with external stores. Ref. 6 categorizes these characteristics and shows a correlation between the modes comprising the predicted linear flutter mechanism and the flight response characteristics. Based on these results, the dynamic characteristics of the aircraft store configuration are represented as inputs to the ANN by the quantized free vibration mode shapes and frequencies that comprise the linear flutter analysis predicted mechanism. This is done in an effort to ensure the applicability of the method to store configurations that have not been flight-tested. Finally, the aerodynamic characteristics are represented to the ANN by the linear analysis flutter speed and frequency and by a quantized representation of the wingtip store configuration. Known LCO response level and response frequency are used for output training.

After the ANN has been trained, it is tested using selected LCO cases from Ref. 7. The ANN gives, as output, the LCO response level and frequency as a function of Mach number and pressure altitude. The analysis results are discussed and possible improvements to the approach methodology are presented. The correlation between the size of the training set and the convergence of the method is discussed.

Table 1 External store configurations

Configuration	Station 1 launcher	Station 2 launcher	Station 2 missile	Station 3 launcher	Station 3 missile	Station 4 fuel tank
1	A	A	1	C	3	1/4-full
2	A	A	none	C	3	none
3	A	none	none	C	3	empty
4	A	A	1	C	1	1/4-full
5	A	A	1	C	1	empty
6	A	A	1	C	none	1/2-full
7	A	A	none	C	3	empty
8 ^a	A	none	none	C	3	none
12	B	A	1	C	3	1/4-full
13 ^a	A	A	2	C	3	empty
15	A	A	2	C	1	empty
16	B	A	1	C	none	1/2-full
17 ^a	B	A	2	C	1	empty
18	B	A	2	C	3	empty

^a Network test configuration

LCO Characteristics

Ref. 7 describes three categories of response behavior seen on fighter aircraft. These categories are described as flutter, typical LCO, and non-typical LCO. Classical flutter behavior is characterized by the sudden onset of high amplitude wing oscillations. Typical LCO is characterized by the gradual onset of sustained limited amplitude wing oscillations where the oscillation amplitude progressively increases with increasing Mach number and dynamic pressure. Non-typical LCO is characterized by the gradual onset of sustained limited amplitude wing oscillations where the oscillation amplitude does not progressively increase with increasing Mach number and oscillations may be present only in a limited portion of the flight envelope.

The linear flutter analyses results for each configuration are presented in Table 2. It should be noted that these analyses are not matched analyses but merely worst case “screening” analyses. In this manner, all analyses are performed using sea-level density and 0.95 Mach Doublet-Lattice method⁸ aerodynamic influence coefficients. The free vibration analyses are performed for a half-airplane model using a matrix iteration method and the first 16 anti-symmetric

flexible modes are retained for the flutter solution. The flutter equations are solved using the Laguerre iteration method, which is a variation of the classical k-method of flutter determinant solution. Details on the structural and aerodynamic models used for these analyses are provided in Ref. 7.

For these flutter analysis results, a critical point is considered to be the velocity at which a modal stability curve crosses from stable (negative damping required to produce neutral stability) to unstable (positive) damping. The analytical flutter speed is the critical point associated with the known aeroelastically sensitive mode for the particular configuration. For comparison purposes, the analytical flutter speed is considered to be directly comparable to the lowest airspeed at which self-sustained oscillations are encountered in flight. These oscillations could be either LCO or flutter. The slope of the modal damping curve indicates the velocity sensitivity of a mode. The velocities at the 0% and 1% damping levels determine this slope. Steep slopes indicate rapid decreases in stabilizing damping with increased velocity.

The flight test results are presented in Table 3 where it is seen that each configuration exhibits

Table 2 Linear flutter analysis, 0.95 Mach, sea-level aerodynamics

Configuration	Flutter speed, KCAS		Flutter frequency, Hz	Flutter mode	Natural frequency, Hz	Coupled mode	Natural frequency, Hz
	Damping 0%	Damping 1%					
1	467	537	6.89	FWB ^b	7.03	AWB ^c	6.34
2	726	776	9.09	1WB ^d	8.88	1WT ^e	9.76
3	635	689	9.21	1WB	9.02	1WT	9.89
4	473	533	6.92	FWB	7.07	AWB	6.45
5	876	924	7.51	1WB	7.80	1WT	6.93
6	509	566	6.90	FWB	7.09	AWB	6.49
7	658	702	8.91	1WB	8.68	1WT	9.69
8 ^a	726	790	9.35	1WB	9.19	1WT	9.96
12	435	516	6.95	FWB	7.07	AWB	6.40
13 ^a	327	519	8.09	FWB	8.14	AWB	7.89
15	449	616	8.15	AWB	8.13	FWB	8.25
16	493	554	6.97	FWB	7.14	AWB	6.55
17 ^a	455	653	8.25	1WT	8.31	1WB	8.28
18	291	538	8.19	FWB	8.23	AWB	7.98

^a Network test configuration^b Forward wing bending^c Aft wing bending^d First wing bending^e First wing torsion

one of the three previously discussed categories of response behavior. From the flutter analysis results (Table 2) it is seen that for each of the three response categories a particular set of modes are present in the linear flutter mechanism. Ref. 6 showed a distinct correlation between flutter and LCO behavior and the free vibration wing modes composing the linear analysis flutter mechanism. Essentially, it was shown that different linear analysis flutter mechanisms correlated to different aeroelastic responses in flight. To this end, the mode shapes and the frequencies of the critical modes are used as primary inputs to the ANN. The flight test results presented in Table 3 are for level flight at 5,000-ft. pressure altitude. The tests were generally conducted in 0.05 Mach increments beginning at the lower Mach number. Smaller increments were used when large response amplitudes were encountered or expected. A test point maneuver was terminated when the response amplitude ei-

ther exceeded a pre-determined termination criteria, or the response amplitude increased at such a rate as to rapidly approach the predetermined termination criteria. Details on the flight test procedures can be found in Ref. 7.

Preliminary Network Design

For the present work, an ANN is designed in the form of a multi-layer perceptron as shown in Fig. 1. This consists of an input layer, two hidden layers, and an output layer. The multiple node layers are represented in the figure as a single summing node fed into a nonlinearity. It is understood that each layer consists of multiples of such nodes. The inputs are directed to summing nodes through the input weights, whose sum is fed into nonlinearities in the form of hyperbolic tangents (\tanh). The outputs of the \tanh nodes are then weighted again, summed and fed into another \tanh layer. The process is repeated again, this time through saturated linear (satlin)

Table 3 Flight test response^a characteristics

Configuration	Mach number									Frequency, Hz	Category	
	0.80	0.85	0.90	0.91	0.92	0.93	0.94	0.95	0.98			
1	0.0	0.5	1.5	-	-	-	-	-	2.5	6.60	typical LCO	
2	0.0	0.0	0.0	-	-	2.5	4.0	-	-	9.40	flutter	
3	0.0	0.0	0.0	-	-	-	-	4.5	-	9.40	flutter	
4	0.0	1.0	2.0	3.0	-	-	-	-	-	6.80	typical LCO	
5	0.0	0.0	1.5	-	-	-	-	-	0.0	7.00	non-typical LCO	
6	0.0	0.0	0.5	-	-	-	-	-	1.0	1.5	6.90	typical LCO
7	0.0	0.0	0.0	-	-	-	-	-	0.5	9.20	flutter	
8 ^b	0.0	0.0	1.0	-	2.0	-	-	-	-	9.50	flutter	
12	0.0	1.0	2.0	-	-	-	-	-	2.5	6.80	typical LCO	
13 ^b	0.0	1.0	3.0	4.0	-	-	-	-	-	7.80	typical LCO	
15	0.0	0.5	1.0	-	-	2.0	-	0.0	-	8.10	non-typical LCO	
16	0.0	0.0	0.0	-	-	-	-	0.5	-	7.00	typical LCO	
17 ^b	0.0	0.0	0.5	0.0	-	-	-	-	-	8.20	non-typical LCO	
18	0.0	1.0	2.5	3.0	-	-	-	-	-	8.10	typical LCO	

^a Amplitude in units of gravitational acceleration, g

^b Network test configuration

- No response data explicitly measured

Blanks indicate no test data acquired

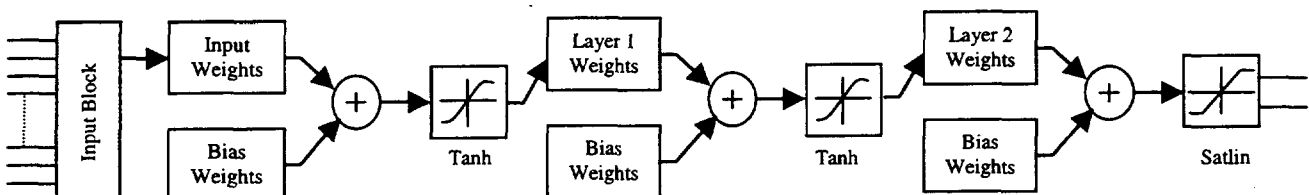


Fig. 1 Network diagram.

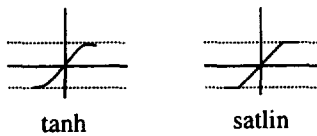


Fig. 2 Network nonlinear functions.

output nodes. Both the tanh and satlin functions have the property of limiting outputs to the range $\epsilon[-1,1]$. These functions are shown in Fig. 2.

The size of the weight matrices and the number of nodes necessary to successfully represent the underlying non-linear function are not easily determined. The network must be large enough

to fully absorb all training data and allow reasonable interpolation and extrapolation, yet be small enough to be manageable. On the other hand, networks that are too large or trained to very high levels tend to memorize the training data are of little use for generalizing a function. Lacking firm design rules, many network sizes were considered.

Supervised learning, i.e., presenting the desired output to the network in order to generate an error signal, which is then fed back through the network by back propagation, is used to train the network. The networks were batch trained using the Levenberg-Marquardt⁹ algorithm, which uses the Jacobian matrix, containing the

first derivatives of the network errors with respect to the weights and biases. The weights are updated using the equation

$$\mathbf{W}_{k+1} = \mathbf{W}_k - [\mathbf{J}^T \mathbf{J} + \mu I]^{-1} \mathbf{J}^T \mathbf{e}$$

where \mathbf{W} are the weights, \mathbf{J} is the Jacobian matrix, \mathbf{e} is the error vector, and μ is a weighting factor (less than 1) that is decreased proportionally to \mathbf{e} as the solution approaches a minimum. Training continues until the error vector falls below a preset value.

All networks considered used the data shown in Tables 1-3. Thirteen inputs were given for each output frequency and amplitude Mach combination. Inputs are quantized representations of the aircraft configuration, flight Mach number, and linear flutter analysis results for the configuration. All input data was normalized to span the range $\epsilon[-1,1]$, consequently the outputs fall within that range as well and have to be scaled back to workable values. Over all, there are 14 flight test/linear model combinations available for training and testing the network. Three of these combinations were held aside for testing and evaluating the effectiveness of each network. These were flight test configurations 8, 13, and 17 (Table 1) and represented a flutter case, a typical LCO case, and a non-typical LCO case.

The network is trained using the squared-error fed back as described earlier. Initially the minimum value used to indicate a successfully trained network was set at $\mathbf{e} = 10^{-6}$. A large network (30 nodes in the first hidden layer, 12 nodes in the second; i.e. 30×12) was initially trained. This network fit the training data very well but did not predict the test data set, indicating that the network was too large and over-trained. In effect, it had memorized the training data. Upon further consideration, the decision was made to set the minimum error-squared value at 10^{-2} . This more closely reflects the data characteristics, in that both the desired oscillation frequency and amplitude are accurate to one significant digit. Consequently, the squared-error is

on the order of 10^{-2} . Subsequent trial networks were trained to this value.

Several network sizes were investigated, the smallest having a single layer of five nodes. The largest was a 50 by 50 double hidden layer MLP. The small networks tended to over-generalize the data, while the large networks memorized the data and did not give reasonable extrapolation outside the solution space. Each network was trained several times in order to increase the probability of truly finding the global minimum in the error space.

Different output node-types were evaluated as well. Three were considered: the tanh function; the saturated linear node; and a linear node (output range $\epsilon[-\infty, \infty]$). The tanh function performed similarly to the satlin. Since the output data in this study is assumed linear, the design tended toward the satlin function. This function gives true linear characteristics, while bounding the solution to the defined solution space.

Final Network Design

The final design scheme selected for the static MLP contains 12 tanh nodes in the first hidden layer and five in the second, with two satlin nodes as outputs (12×5). This configuration gave good generalization over the solution space, while learning the training data well. The outputs are the combined oscillation frequency in Hertz, and oscillation amplitude measured in units of gravitational acceleration (g). All input data is normalized to $\epsilon[-1,1]$. The output is also contained in $\epsilon[-1,1]$ due to the saturated linear output nodes. All output data is then processed back to usable values.

Results

Network inputs for the test cases consisted of the Mach number of the desired flight condition, the store carriage configuration, and the linear flutter analysis results (flutter speed, frequency, modal composition of the flutter mechanism, and the free vibration frequencies of the mechanism modes). The output from the network was in the

form of an oscillation response amplitude and frequency. Several Mach numbers were examined for each set of input conditions and responses were noted. The classification of the predicted response is described as follows. The network indicated a flutter condition if the output oscillation amplitude increased dramatically as Mach number increased. The network indicated a typical LCO condition if the amplitude increased progressively with no sudden high-level responses. The network indicated a non-typical LCO condition if the amplitude rose to a level, then began to decrease.

Outputs from three of the evaluated networks are shown in Figs. 3-5. The small 6x3 network yielded inadequate results for all three test cases. For the flutter case (Fig. 3), the amplitude computed by this network remained zero for all input Mach numbers. The network shows good amplitude correlation between 0.80 and 0.85 Mach for the typical LCO case (Fig. 4) but fails to track the subsequent amplitude increase. As Mach number is increased, the network diverges from the measured response by showing the amplitude to decrease. Finally, the amplitudes computed for the non-typical LCO case (Fig. 5) were extremely high for all Mach numbers except 0.80 and clearly represent an unsuccessful extrapolation by the network. The small network showed good correlation to the measured oscillation frequency for the flutter case only.

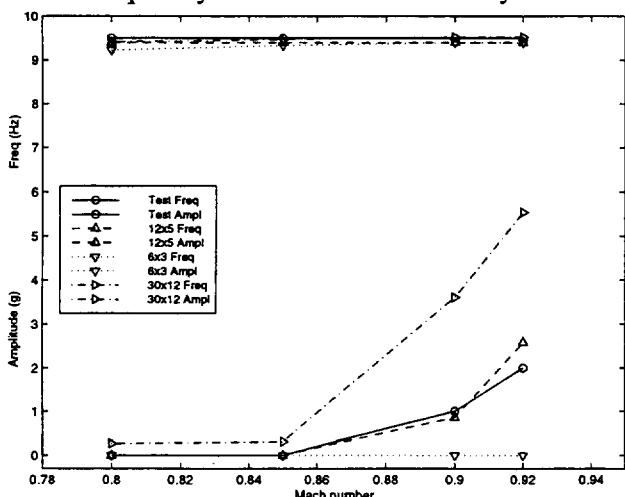


Fig. 3 Flutter test case.

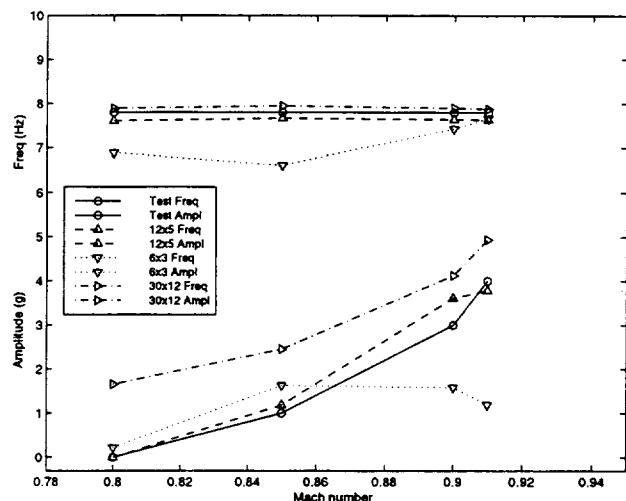


Fig. 4 Typical LCO test case.

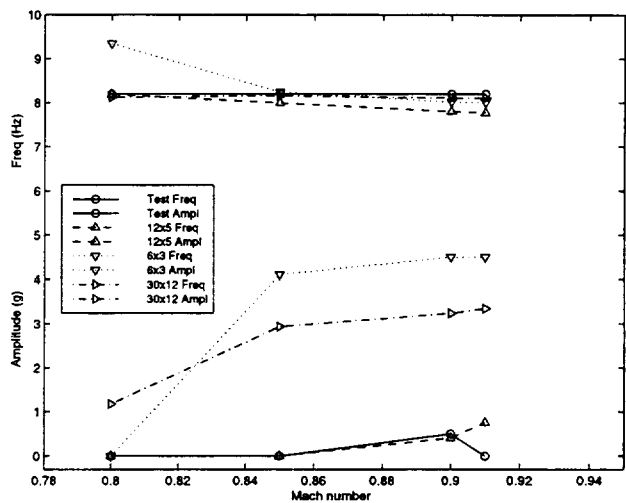


Fig. 5 Non-Typical LCO test case.

Logically, it was thought that a larger network would perform better than a smaller one in part because of its inherent ability to store more data and cover a larger portion of the solution space. Unfortunately, the observed results were contrary to this. In all three test cases the 30x12 network tracked the oscillation frequency well, but failed to adequately track the response amplitudes. For the flutter case (Fig. 3) it is seen that the computed amplitude has the desired characteristics, i.e., amplitude increases dramatically with Mach number. However, this network tended to yield significantly higher response amplitudes than were measured in flight. The ability of this network to track the shape and trend of the ampli-

tude response is also seen for the typical LCO case (Fig. 4). However, for this case the amplitude is again consistently higher than the measured response. The computed amplitude for the non-typical LCO case (Fig. 5) is excessively high for all Mach numbers.

The 12x5 network showed the best overall agreement with the test data for both oscillation frequency and amplitude. For the flutter test case (Fig. 3), the computed frequency and oscillation amplitude show very good correlation to the measured data. The network amplitude prediction showed a dramatic increase at 0.92 Mach consistent with the flight-measured response.

For the typical LCO test case (Fig. 4), the network amplitude tracks the measured response very well except for the last point at 0.91 Mach. There, the network output shows a trend of leveling off while the measured response amplitude continues to increase. As was observed in the flutter case, it is seen that the frequency of oscillation was predicted nearly exactly. The typical LCO data available for training was more diverse. This allowed the network's solution space to be larger, but increased the potential for errors in the interpolation between points.

The non-typical LCO case was the most revealing of the three test cases because it exposed several limitations of the static MLP. As shown in Fig. 5, frequency was not tracked as well as for the previous cases, indicating that there was not enough information about frequency available to the network for it to form a functional representation. The network amplitude tracked the flight response well up to 0.91 Mach. There, the network indicated a slight increase in amplitude while the flight data showed a decrease. This can be explained by the fact that in the non-typical LCO training cases the amplitude is zero, or near zero, and grows only slightly. Further, the non-typical LCO test case falls outside the sample space of the training data (This is almost a trivial observation. With only two training data sets a sample space of more than two dimensions cannot be defined). This forces the network to attempt to extrapolate beyond its 'experience'.

This is, of course, one of the benefits of using ANNs but in this case, the network was evidently pushed beyond its capability.

Conclusions

As a feasibility study, it is concluded that the static ANN was very successful considering the small data set used for training and the limitations of the static network itself. It was shown that both the flutter and typical LCO cases were reasonably predicted with this network. The limitation of the network is shown in the non-typical LCO case. The limited size of the data used for training was such that virtually any prediction outside those two cases constituted an extrapolation into unknown regions of the solution space. As such, the network had little 'experience' to draw from in forming reasonable outputs.

Evaluating the various networks that were considered for this work shows the strengths and weaknesses of their architectures. It was seen that small networks over-generalize the training data and cannot be used for accurate prediction beyond the sample space. This was demonstrated in the 6x3 network. Conversely, networks that are too large, or trained to error levels that are extreme, tended to memorize the training data, and therefore are also inadequate for prediction beyond the sample space as well. This was shown to be the case in the 30x12 network trained to $e=10^{-6}$. The most reasonable results were seen for the moderately sized 12x5 network trained to $e=10^{-2}$.

Giving consideration to the limited data set used for network training, especially in the non-typical LCO case, the results presented offer positive evidence of the feasibility of using an ANN for predicting LCO of flexible wings. It is shown that, based on the available training data, flutter behavior was adequately predicted, both in amplitude and in frequency. Typical LCO was also predicted adequately, again by observing amplitude levels. The network had difficulty predicting the (decreasing) change in oscillation amplitude that would indicate non-typical LCO.

The training data available for non-typical LCO was limited to two flight-test/linear modeling output data sets and the test set inputs were outside the training data space. Since prediction of that case constitutes an extrapolation outside the solution space, it is reasonable to expect the errors seen in this study. It should be possible to remedy this limitation to the methodology by using the network modifications proposed in the following section.

Elaborating on the strengths of ANNs vs. linear flutter analysis it is seen that the linear analyses adequately identify store configurations that are flutter and LCO sensitive. These analyses give a good indication of the instability frequency but do not accurately identify the instability onset speed. In addition, these analyses provide no indication of the response amplitude. By comparison, ANNs gives good response frequency and amplitude trends but rely on the linear analyses as well as flight test results to accomplish this.

Recommendations

The intent of this study was to evaluate the feasibility of using an ANN for predicting LCO. In doing so, a conscious effort was taken to keep the process as simple as possible. During the course of evaluation, several limitations to the approach were discovered, as well as several possible improvements that should be evaluated. Major areas that could provide improved results are briefly discussed below.

The first modification that could dramatically increase the likelihood of successfully predicting each of the three types of aeroelastic instabilities would be to increase the amount of data available for training. This is especially true for the non-typical LCO case. Since data from linear prediction can easily be obtained, and there exists a substantial flight test database, this is proposed as the first step in improving the predictive power of the network.

One characteristic of the satlin function is that it effectively limits the output of the network to values that are contained in the training data.

This is because the inputs and outputs are normalized with the training data. It would be interesting to evaluate the increase in interpolation capability if the satlin nodes were modified such that the output $\in [-1, \infty]$. This would prevent negative outputs, but would allow larger positive numbers than those used in training.

Based on careful observation of the input data, it is concluded that there exist some redundancies. The linear modeling data used as network input is in fact a function of the aircraft configuration. Using configuration data as empirical input to the network may be confusing the functional representation capability of the network. Too much emphasis may have inadvertently been given to configuration allowing it more influence on the outcome than it realistically deserves. A statistical evaluation of the inputs used may be in order.

Logically, an improvement to the network that should be evaluated is stepping up from a static network to a dynamic network. A form of the Tapped Delay Neural Network (TDNN) would give the network the capability to predict based on a series of past inputs, rather than only on the current. An extension of this may be to use a feedback from the output to the input, giving the network the capability to use current predictions for future use.

References

- ¹ Bunton, Robert W., and Denegri, Charles M., Jr., "Limit Cycle Oscillation Characteristics of Fighter Aircraft," submitted to *Journal of Aircraft*, January 1999.
- ² Norton, William J., "Limit Cycle Oscillation and Flight Flutter Testing," *Proceedings of the Society of Flight Test Engineers 21st Annual Symposium*, August 1990.
- ³ Cunningham, Atlee M., Jr., and Meijer, Jos J., "Semi-Empirical Unsteady Aerodynamics for Modeling Aircraft Limit Cycle Oscillations and Other Non-Linear Aeroelastic Problems," *Proceedings of the Royal Aeronautical Society In-*

ternational Symposium on Aeroelasticity, Paper no. 74, June 1995.

⁴ Meijer, Jos J., and Cunningham, Atlee M., Jr., "A Semi-Empirical Unsteady Nonlinear Aerodynamic Model to Predict Transonic LCO Characteristics of Fighter Aircraft," *36th Structures, Structural Dynamics, and Materials Conference*, AIAA-95-1340, April 1995.

⁵ Chen, P. C., Sarhaddi, D., and Liu, D. D., "Limit-cycle Oscillation Studies of a Fighter With External Stores," *39th Structures, Structural Dynamics, and Materials Conference*, AIAA-98-1727, April 1998.

⁶ Denegri, Charles M., Jr., and Cutchins, Malcolm A., "Evaluation of Classical Flutter Analyses for the Prediction of Limit Cycle Oscillations," *38th AIAA Structures, Structural Dynamics, and Materials Conference*, AIAA-97-1021, April 1997.

⁷ Denegri, Charles M., Jr., "Limit Cycle Oscillation Flight Test Results of a Fighter With External Stores," submitted to *AIAA Journal of Aircraft*, January 1999.

⁸ Albano, E., and Rodden, W. P., "A Doublet-Lattice Method for Calculating Lift Distributions on Oscillating Surfaces in Subsonic Flows," *AIAA Journal*, Vol. 7, No. 2, February 1969, pp. 279-285.

Press, William H., Teukolsky, Saul A., Vetterling, William T., and Flannery, Brian P., Numerical Recipes in FORTRAN, 2nd Edition, Cambridge University Press, 1992, pp. 678-683.

A PROCEDURE TO IMPROVE CONVERGENCE AND ACCURACY OF ITERATIVE MODEL UPDATING METHODS

38-64

Stefan Keye
Structural Dynamics Department
Institute for Aeroelasticity
Deutsches Zentrum für Luft- und Raumfahrt (DLR)
37073 Göttingen, Germany
E-mail: Stefan.Keye@dlr.de

ABSTRACT

An improvement to enhance both convergence and accuracy of iterative finite element model updating methods is proposed. The sensitivity of each individual correction parameter with respect to the eigenvectors and eigenvalues is modified in order to reduce the influence of mathematical constraints on the optimization process. This allows for a broader and more physically based selection of correction parameters and accordingly leads to more significant validation results. The performance of the method is demonstrated on a laboratory test structure using a simulated modal matrix and real experimental data from a ground vibration test.

1. INTRODUCTION

Iterative updating usually is associated with a major drawback. The correction parameter sensitivities affect convergence and parameters with lower sensitivities may cause iteration instabilities or lead to uncertain results. For successful updating, it is therefore most important that the analytical eigenvalues and eigenvectors are sensitive with respect to all chosen correction parameters. Therefore, the parameter selection is constrained by mathematical considerations, which sometimes do not allow for the correction of the physical parameters corresponding to the modelization errors embodied in the numerical model. To bypass this problem, it is proposed to balance the individual parameter sensitivities by appropriate weighting factors and hence to eliminate any undesired sensitivity influences that may affect the optimization.

2. UPDATING METHOD

The iterative updating approach (Link, 1993) applied here, eqs. (1), exploits a factorial correction of substructures superimposed to the initial analytical model:

$$[\mathbf{k}] = [\mathbf{k}_a] + \sum \alpha_i [\mathbf{k}_i] \quad i = 1, \dots, I . \quad (1)$$

and

$$[\mathbf{m}] = [\mathbf{m}_a] + \sum \beta_j [\mathbf{m}_j] \quad j = 1, \dots, J .$$

Symbols $[\mathbf{k}]$ and $[\mathbf{m}]$ represent the system matrices of the improved model, subscript a denotes initial analytical quantities, and α_i and β_j are the unknown correction factors for the submatrices $[\mathbf{k}_i]$ and $[\mathbf{m}_j]$, corresponding to areas with modeling uncertainties or errors.

The model corrections are controlled through the minimization of the differences between measured and analytical data. A weighted least squares approach leads to a linear system of equations for the unknown correction factors $\{\mathbf{p}\} = \{\alpha_i, \beta_j\}$:

$$\Delta \{\mathbf{p}\} = [[\mathbf{G}_0]^T [\mathbf{W}] [\mathbf{G}_0] + [\mathbf{W}_p]]^{-1} \cdot [\mathbf{G}_0]^T [\mathbf{W}] \{ \varepsilon_0 \} . \quad (2)$$

The solution usually is attained in an iterative process. In order to control the iteration, the weighting matrices $[\mathbf{W}]$ and $[\mathbf{W}_p]$ need to be chosen appropriately.

Updating based on modal data frequently requires a simultaneous correction of eigenfrequencies and mode shapes. This is achieved by using both the differences between measured natural frequencies and modes and analytical eigenfrequencies and eigenvectors to define a residual vector:

$$\{\varepsilon_0\} = \begin{Bmatrix} \{\varphi_{m,1}\} - \{\varphi_{a,1}\} \\ \vdots \\ \{\varphi_{m,N}\} - \{\varphi_{a,N}\} \\ \hline \lambda_{m,1} - \lambda_{a,1} \\ \vdots \\ \lambda_{m,N} - \lambda_{a,N} \end{Bmatrix}. \quad (3)$$

Consistent eigenvector scaling and mode assignment are essential to a correct comparison of experimental and analytical data.

The appropriate sensitivity or gradient matrix $[G_0]$ is assembled from the derivatives of the analytical modal data with respect to the correction parameters. For a correction with N natural frequencies and modes and K correction parameters (substructures) the gradient matrix reads

$$[G_0] = \begin{Bmatrix} \frac{\partial \{\varphi_{a,1}\}}{\partial p_1} & \frac{\partial \{\varphi_{a,1}\}}{\partial p_2} & \cdots & \frac{\partial \{\varphi_{a,1}\}}{\partial p_K} \\ \vdots & \vdots & & \vdots \\ \frac{\partial \{\varphi_{a,N}\}}{\partial p_1} & \frac{\partial \{\varphi_{a,N}\}}{\partial p_2} & \cdots & \frac{\partial \{\varphi_{a,N}\}}{\partial p_K} \\ \hline \frac{\partial \lambda_{a,1}}{\partial p_1} & \frac{\partial \lambda_{a,1}}{\partial p_2} & \cdots & \frac{\partial \lambda_{a,1}}{\partial p_K} \\ \vdots & \vdots & & \vdots \\ \frac{\partial \lambda_{a,N}}{\partial p_1} & \frac{\partial \lambda_{a,N}}{\partial p_2} & \cdots & \frac{\partial \lambda_{a,N}}{\partial p_K} \end{Bmatrix}. \quad (4)$$

The eigenvector derivatives for stiffness and mass corrections are

$$\frac{\partial \{\varphi_{a,r}\}}{\partial \alpha_i} = \sum_{s=1}^N \frac{-1}{(\lambda_{a,s} - \lambda_{a,r}) M_{a,s}} \cdot \{\varphi_{a,s}\}^T [k_i] \{\varphi_{a,r}\} \cdot \{\varphi_{a,s}\}$$

$$(5a)$$

$$\frac{\partial \{\varphi_{a,r}\}}{\partial \beta_j} = \sum_{s=1}^N \frac{\lambda_{a,r}}{(\lambda_{a,s} - \lambda_{a,r}) M_{a,s}} \cdot \{\varphi_{a,s}\}^T [m_j] \{\varphi_{a,r}\} \cdot \{\varphi_{a,s}\}$$

for $r \neq s$.

and

$$\frac{\partial \{\varphi_{a,r}\}}{\partial \alpha_i} = 0 \quad (5b)$$

$$\frac{\partial \{\varphi_{a,r}\}}{\partial \beta_j} = \sum_{s=1}^N -\frac{1}{2M_{a,s}} \cdot \{\varphi_{a,s}\}^T [\mathbf{m}_j] \{\varphi_{a,s}\} \cdot \{\varphi_{a,s}\}$$

for $r = s$ with analytical mode numbers $r, s \in N$ and $M_{a,r}$ the generalized mass of analytical mode r . The eigenvalues are computed from

$$\frac{\partial \lambda_{a,r}}{\partial \alpha_i} = \frac{1}{M_{a,r}} \cdot \{\varphi_{a,r}\}^T [\mathbf{k}_i] \{\varphi_{a,r}\} \quad (6)$$

and

$$\frac{\partial \lambda_{a,r}}{\partial \beta_j} = \frac{-\lambda_{a,r}}{M_{a,r}} \cdot \{\varphi_{a,r}\}^T [\mathbf{m}_j] \{\varphi_{a,r}\} .$$

Eqs. (5) and (6), establish linear relations between the eigenvector and eigenvalue sensitivities and the correction submatrices $[\mathbf{k}_i]$ and $[\mathbf{m}_j]$. These relations will be used in the following section to modify the parameter sensitivities.

3. WEIGHTED PARAMETER SENSITIVITIES

The iterative computation of updating parameters p_k in eq. (2) does not always converge to a stable solution and the exact correction factors. Conditioning of the optimization problem is only one aspect here. Problems also arise, when the sensitivities within the given set of updating parameters are widely scattered. This imposes an undesired side constraint on the selection of substructures, which, on the other hand, should be based entirely on physical considerations. In order to remove this mathematical restriction, the parameter sensitivities may be individually scaled by appropriate weighting factors to yield equally distributed values for the complete set of substructures. The weighting factors are computed from the inverse of the norm of each column vector (= correction parameter) k of $[\mathbf{G}_0]$

$$\{w_k\} = \|[\mathbf{G}_0]_k\|^{-1} \quad k = 1, \dots, K , \quad (7)$$

Likewise, the gradient submatrices containing only the eigenvector sensitivities or the eigenvalue sensitivities may be used to calculate the w_k . The weighting factors are used to directly alter the stiffness and mass matrix elements of the updating substructures defined in eq. (1):

$$[\tilde{\mathbf{k}}_i] = w_i \cdot [\mathbf{k}_i] \quad \text{and} \quad [\tilde{\mathbf{m}}_j] = w_j \cdot [\mathbf{m}_j] . \quad (8)$$

A weighting factor $w_k > 1$ leads to an increase of the stiffness/mass elements in the corresponding submatrix, for $w_k < 1$, the values of the submatrix elements are scaled down. Since the initial correction factors α_i and β_j in eq. (1) are equal to zero, the modal parameters of the initial model remain unchanged by these modifications. The new eigenvector and eigenvalue sensitivity components $\partial \{\varphi_{a,n}\} / \partial p_k$ and $\partial \lambda_{a,n} / \partial p_k$, eqs. (5) and (6), are now computed using the modified submatrices from eq. (8).

Since the eigenvector and eigenvalue gradients depend on the analytical modal parameters and therefore may slightly change as the correction proceeds, the weighting factors need to be recomputed in every iteration step.

4. TEST STRUCTURE

A three-dimensional laboratory test structure, fig. 1, representing a typical aircraft design with fuselage, wings and tail is used for the investigations. The total mass is 44 kg and the dimensions are 1.5 m (length) by 2.0 m (wing span). Realistic damping levels are obtained through the use of a viscoelastic tape, which is bonded to the upper wing surface and covered by a thin aluminium constraining layer.

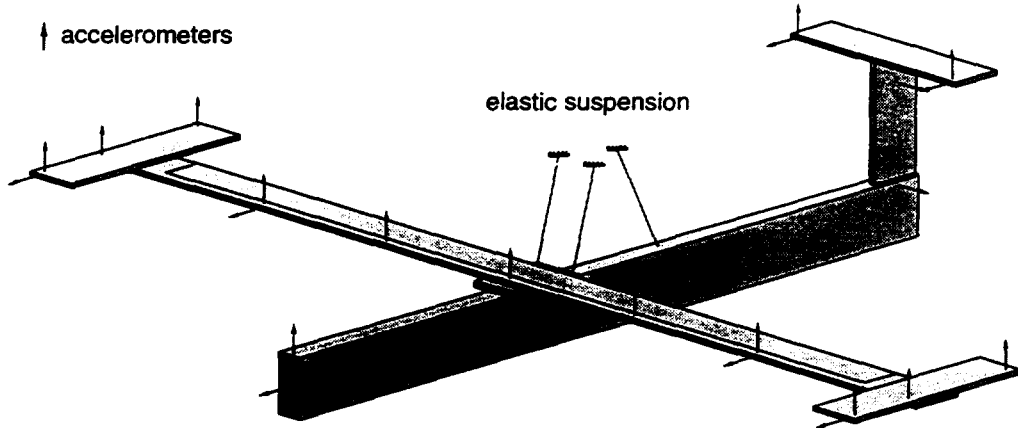


Figure 1: The GARTEUR SM-AG19 laboratory test structure

For ground vibration testing the structure was equipped with 24 acceleration pickups and a low frequency bungee cord suspension ensured correct free-free boundary conditions. The experimental data base available for updating consists of 14 normal modes covering a frequency range from 6.38 to 151.32 Hz (Degener & Hermes, 1996).

The finite element model, fig. 2, will be used for the initial simulation study in order to test the weighted sensitivities approach, and for a succeeding model validation using real test data. Special care was taken to accurately modelize the stiffening effects caused by the joints between fuselage & wing and wing & tailplane respectively. For the damping layer stiffness and mass distribution initial estimations are used. Due to the high deflection amplitudes and low mass in some structural regions, a detailed mass matrix taking into account all connecting bolts and the accelerometer masses has been set up. In order to correctly reflect the test boundary conditions, the measured rigid body modes are used to tune the model's elastic suspension. The actual accelerometer positions, e.g. at the wing leading and trailing edges, are realized through supplementary offset nodes.

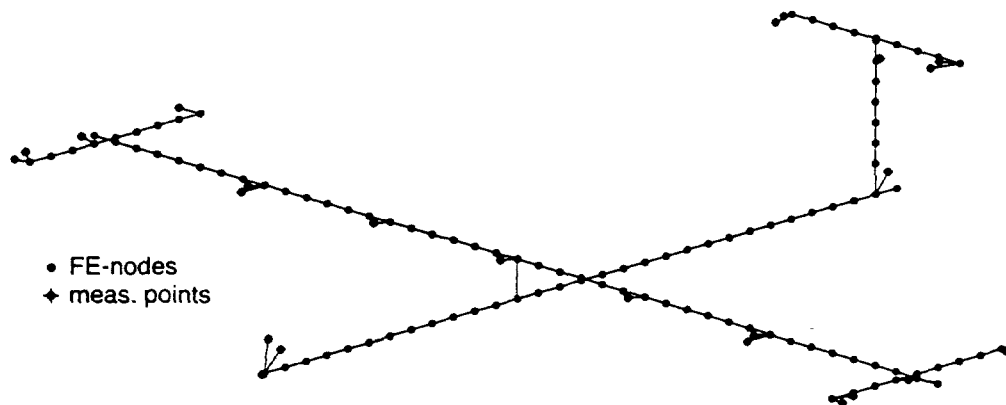


Figure 2: 636 degree-of-freedom finite element model

5. SIMULATION STUDY

This section describes the simulation study carried out to assess the performance of the weighted sensitivities approach. The application to experimental modal data is described in Section 6.

In the simulation study, a numerical model with known modelization errors is updated using analytical modal data. Eigenvectors and eigenvalues from the initial finite element model (without the modelization errors) are used as 'experimental' reference for the corrections. The inaccurate numerical model is obtained by means of introducing artificial modelization errors into the system matrices of the initial model. Then, the regions corresponding to the modelization errors are defined as updating substructures in eq. (1). With these initial conditions given, the updating procedure should, after some iterations, exactly counterbalance the modelization errors. This is usually the case for a well-conditioned updating problem with a sufficient amount of input data, but for largely scattered parameter sensitivities, deviations from the exact solution are observed. The parameter set defined for the simulation study precisely represents this situation.

After computing the 'experimental' mode shapes and natural frequencies from the initial model, three modelization errors are introduced into the finite element model. The wing horizontal and lateral bending stiffnesses and the drum bending stiffness are reduced by 1/1.05, i.e., the exact correction factors are 0.05 or +5.0 %. Table 1 lists the corresponding correction parameters and their eigenvector and eigenvalue sensitivities for modes no. 1 to 14. Note that the parameter sensitivities are normalized to unity and that the absolute values of the eigenvector gradients are much smaller than for the eigenvalue gradients.

Parameter no.	Location	Correction Parameter	Eigenvector Sensitivity	Eigenvalue Sensitivity
1	Wing	I_{max}	0.30	1.00
2	Wing	I_{min}	0.60	0.30
3	Drums	I_{min}	1.00	0.01

Table 1: Correction parameters and normalized parameter sensitivities

In this set of updating parameters, the eigenvalue sensitivity for the drum lateral bending stiffness is two orders of magnitude lower than for the wing inplane bending stiffnesses; in other words, the drum stiffness only has a minor influence on the model's overall dynamic characteristics in the frequency range considered. Nevertheless, a consistent and physically exact correction of this parameter may be crucial, when a prediction of modal or frequency response data beyond the frequency range used for updating is required.

The quality of the updated finite element model is assessed through the correlation between (simulated) measured mode shapes $\{\Phi_m\}_r$ and analytical eigenvectors $\{\Phi_a\}_s$

$$MAC_{rs} = \frac{|\{\Phi_m\}_r^T \cdot \{\Phi_a\}_s|^2}{(\{\Phi_a\}_s^T \cdot \{\Phi_a\}_s)(\{\Phi_m\}_r^T \cdot \{\Phi_m\}_r)} \quad (9)$$

(Allemand & Brown, 1982), and the frequency deviations between measured natural frequencies f_m and analytical eigenfrequencies f_a :

$$\Delta f = (f_a - f_m) / f_m \quad (10)$$

Fig. 3 comprises the results for the model corrections using unweighted (left) and weighted (right) parameter sensitivities. Here, the weighting is based on eigenvalue sensitivities alone.

For regular updating without weighted sensitivities, the eigenfrequencies and mode shapes correctly match the 'experimental' reference data after 4 to 5 iteration steps. The residual is sufficiently minimized, the correction factor for parameter no. 3 however, has not converged to the exact value. This is due to the fact, that the drum stiffness only causes marginal changes to the overall dynamics in the frequency range consid-

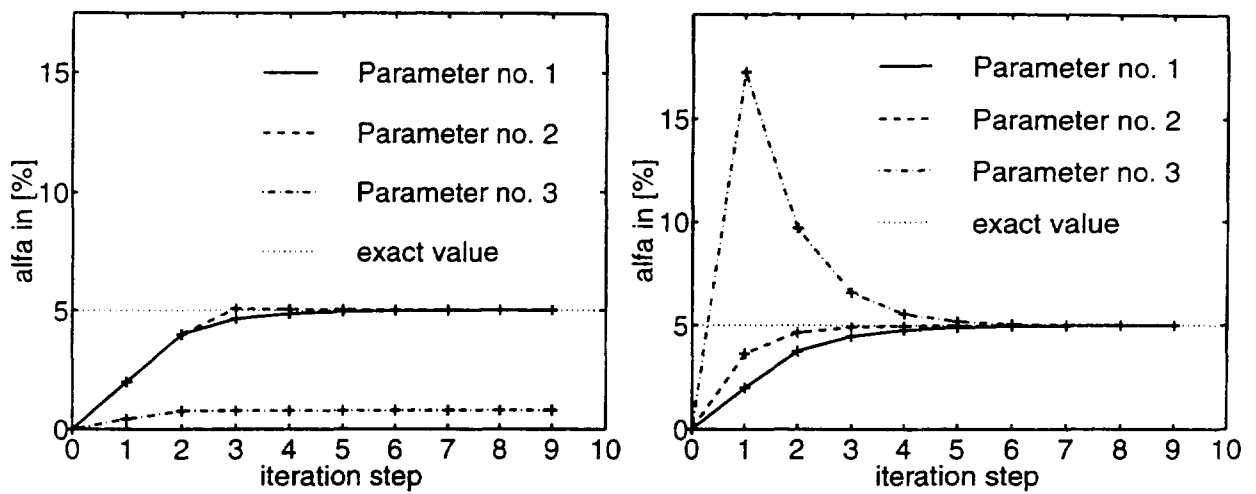


Figure 3a): Correction factors for simulated modal data (unweighted/weighted parameter sensitivities)

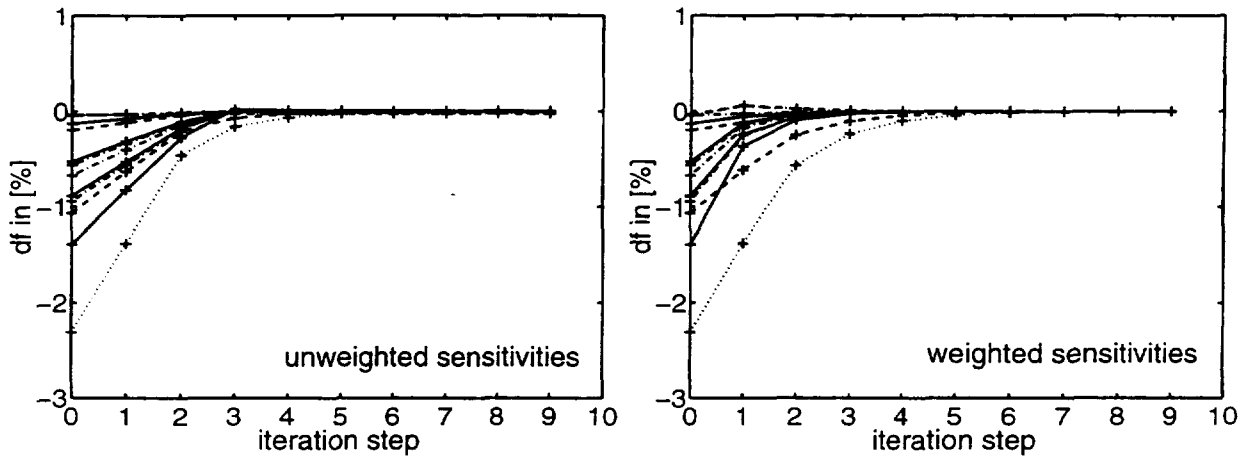


Figure 3b): Frequency deviations

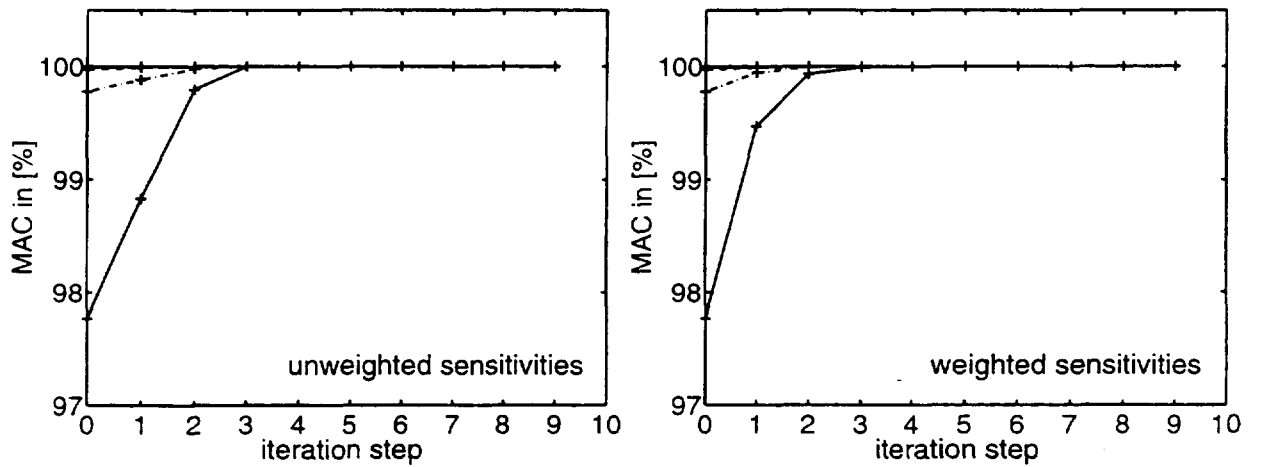


Figure 3c): MAC values

ered. Accordingly, the error of parameter no. 3 does not significantly disturb the frequency deviations and mode correlations, which are used to control the optimization process. Consequently, a further improvement of the model is not achieved.

Updating using weighted sensitivities leads to exact results for all correction factors. Convergence with respect to the eigenfrequencies is not significantly affected in this case, but the residual deviations in the last iteration step are one order of magnitude smaller. Faster convergence is observed for the mode shape correlation, the improvements observed in this test example however, are of no practical use.

6. APPLICATION TO EXPERIMENTAL TEST DATA

Finally, an application of the weighted sensitivities approach to updating using real ground vibration test data is demonstrated. Here, the definition of correction parameters has to be focussed on the actually existing finite element modelization errors.

The fundamental modelization uncertainties are assumed to be in the fuselage-wing joint, the tail-tail-plane joint and in the damping layer stiffness and mass distribution. Especially, the influence of the frequency dependent shear modulus of the viscoelastic tape on the upper wing surface and the asymmetrical deflection amplitudes observed during the test need to be considered in the model corrections.

Preliminary parameter studies proved that changes in the joint stiffnesses do not significantly affect the modal parameters. It is believed that the joint stiffnesses are high compared to the distributed stiffness of the wing and tail structure, and that therefore the representation through rigid body elements is sufficiently accurate. The selection of updating parameters is therefore focused on the model's main components.

Eight substructures have been selected for updating. The initial parameter sensitivities, before weighting was applied, are plotted in fig. 4a), figs. 4b) to 4d) show the correction factors, frequency deviations, and mode correlation as the iteration proceeds. Convergence is attained after 4 iteration steps. A reference solution obviously does not exist in case of real experimental data, but the various correction factors values appear quite reasonable, that is, they lie within the accuracy limits, which had been previously estimated for the analytical modelization. This emphasizes the assumption, that the substructures correctly match the regions where the finite element model differs from the test structure and that therefore the updating parameters yield consistent and physically meaningful results. Moreover, some measured natural frequencies beyond the frequency range used for updating have been predicted successfully.

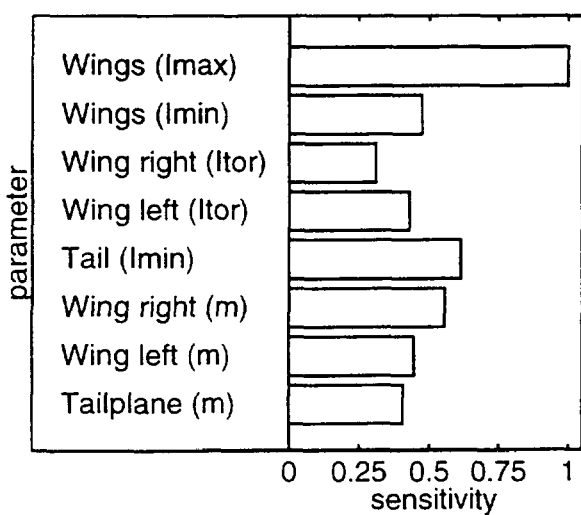


Figure 4a): Parameter sensitivities

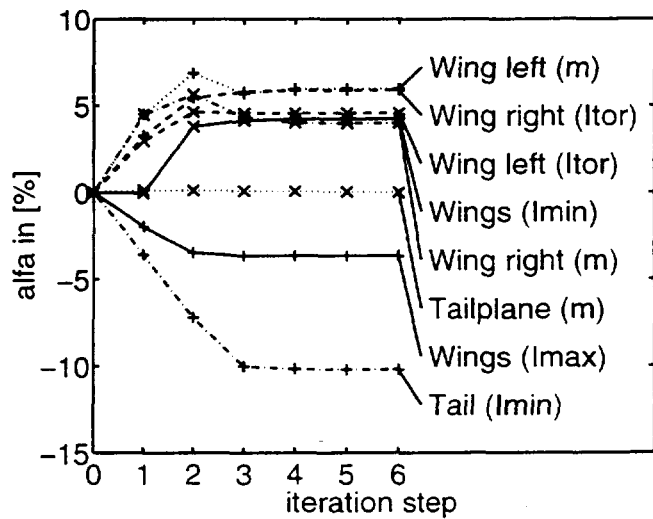


Figure 4b): Correction parameters

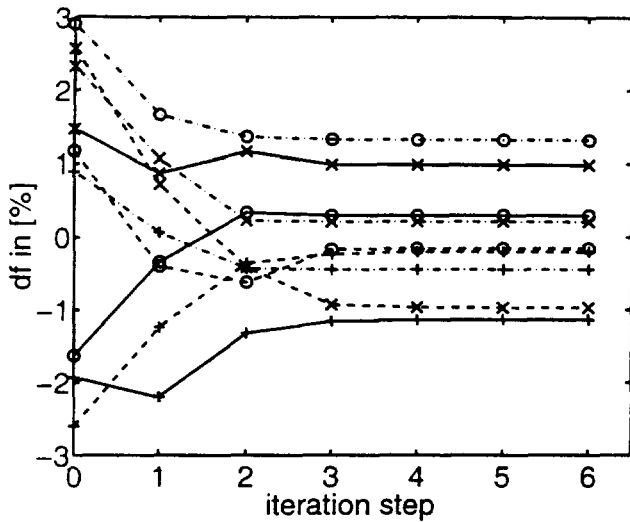


Figure 4c): Frequency deviations

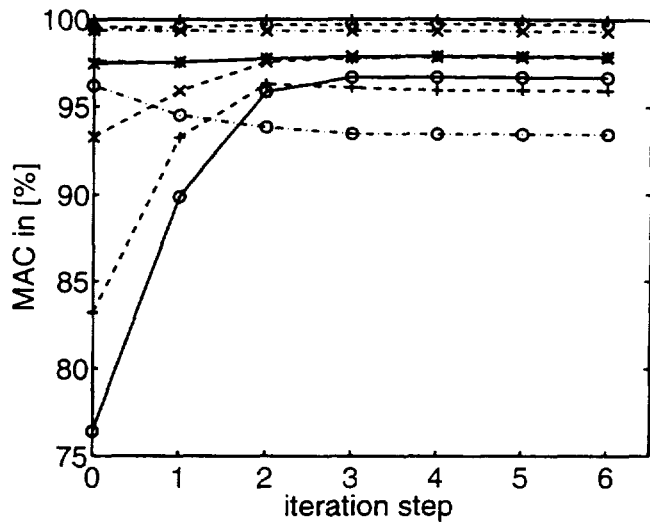


Figure 4d): MAC values

The application to the laboratory test structure has shown that updating using sensitivity-modified substructures is capable of handling real experimental modal data including measurement errors and random noise. After this first simple application, the new method appears to provide a helpful tool for updating the analytical models of today's complex aerospace structures.

7. CONCLUSIONS

A method to improve iterative finite element model updating approaches is introduced. Higher accuracy and faster convergence is achieved in case of large deviations between the individual parameter sensitivities. The technique is based on weighting the individual correction parameter sensitivities by means of a modification of the submatrices defined for updating. Performance is assessed in a simulation study and an application to real test data from a laboratory test structure is described. The new technique allows for a less confined selection of updating parameters and more consistent correction results.

REFERENCES

- Link, M., 1993, "Updating of Analytical Models - Procedures and Experience", *Proceedings of the Conference on Modern Practice in Stress and Vibration Analysis*, Sheffield Academic Press, GB.
- Degener, M., Hermes, M., 1996, "Ground Vibration Test and Finite Element Analysis of the GARTEUR SM-AG19 Testbed", *DLR IB 232 - 96 J 08*, Deutsches Zentrum für Luft- und Raumfahrt, Göttingen, D.
- Allemand, R.J., Brown, D.L., 1982, "A Correlation Coefficient for Modal Vector Analysis", *Proceedings of the 1st International Modal Analysis Conference*, Orlando, FL, pp. 110-116.

Computer-controlled Normal Mode Tuning

J.M. Sinapius
 Deutsches Zentrum
 für Luft- und Raumfahrt
 Bunsenstrasse 10
 37073 Göttingen, GERMANY

R.C. Lake
 US Army
 Vehicle Technology Center (ARL)
 NASA Langley Research Center
 Hampton, VA 23681, USA

Abstract

Normal mode testing is a long-standing test method of experimental modal analysis. Typically, the harmonic responses of a harmonically-excited structure are investigated during normal mode testing with regard to their phase relation to the excitation. While classical phase resonance methods are suitable for checking the linearity of the structural dynamic behaviour of aerospace structures, a significant amount of time is required to perform normal mode tuning, consequently resulting in considerable costs incurred during the prototype development period. However, improvements in computer technologies and measurement techniques enable improvements in the classical phase resonance procedure, especially with regard to minimizing the test schedule without loss of accuracy of the results. This paper focuses on new methods for automated tuning and on-line data evaluation procedures for normal mode testing by investigating band-limited frequency responses for analytical and experimental vibration systems during the on-line tuning process. Three different approaches for accelerating the tuning process are investigated with respect to their on-line capabilities. In general, these methods deliver estimations about eigenfrequency, modal damping, and generalized mass, but differ in the amount of modal information delivered and, consequently, in the computational effort required. The three different methods of computer-controlled normal mode testing were experimentally verified via ground testing using the Piezoelectric Aeroelastic Response Tailoring Investigation (PARTI) testbed at NASA Langley's Transonic Dynamic Tunnel, as well as the 20m spanwidth sailplane FS-33 located at DLR. Experimental results obtained from these applications are described and initial experiences are discussed.

Nomenclature

$[C]$, $[K]$, $[M]$	viscous damping matrix, stiffness matrix, mass matrix
$\{f\}$	force vector
$\{q\}$	vector of modal coordinates
$\{v\}$	deformation vector
$\{\psi\}_r$	mode shape vector
Q	complex quotient
a	modal constant

\hat{f}	force amplitude
k, l	summation indices
m_r	generalized mass
np	number of measured degrees of freedom
nf	number of spectral lines
p_r	generalized force
λ_r	eigenvalue
ζ_r	modal damping
η_r	dimensionless frequency
ω	excitation frequency
ω_r	eigenfrequency ($= 2\pi f_r$)
\Im	imaginary part of a complex amplitude
\Re	real part of a complex amplitude
MIF	modal indicator function
SMIF	signed modal indicator function

1 Introduction

Normal mode testing is a long-standing test method of experimental modal analysis. Although the application of phase separation techniques based on measured transfer functions increased during the past two decades, normal mode testing by means of multiple input tuned sine excitation still remained as a standard procedure for large aerospace structures, especially in Europe. The quality of the results obtained using the phase resonance method was demonstrated in a recent European round robin exercise [4]. Normal mode testing is a method of experimental modal analysis performed on a high vibration energy level. In addition, the method is suitable to check the linearity of the structural dynamic behavior of the test object. However, a disadvantage of normal mode tuning is the significant time requirement of the method, which subsequently results in considerable costs during the prototype development of aerospace structures. Thus, it is worthwhile to consider methods which accelerate the tuning process without loss of accuracy of the results and deliver as much on-line information as possible during the tuning process.

Usually, normal mode testing consists of four steps. Pre-tests provide test data for a mode indication as well as for computing optimized exciter force configurations for each indicated mode. Numerous methods have been proposed and investigated for exciter force pattern optimization [6, 7, 10, 12]. In the second step of normal mode tests each eigenmode of vibration is tuned. This means the exciter force pattern, as well as the excitation frequency, are varied around each resonance until the phase resonance criterion is fulfilled sufficiently. In the third step, the modal damping and generalized masses are evaluated from narrow-band frequency response measurements. Finally, the linearity of each mode can be checked by increasing the level of the excitation forces.

This paper focuses on methods for automated tuning and on-line data evaluation during the tuning process. Three different approaches are investigated with regard to their accuracy and their on-line capabilities. The methods differ in the amount of modal information delivered. While the global parameter estimation method delivers all modal parameters, the method of finite differences delivers an eigenfrequency and damping estimation, and the Signed Mode Indicator Function is useful for automated frequency tuning only. Experimental applications of the methods are described and initial experiences are reported.

2 Normal Mode Testing

The fundamental equations of the phase resonance method are based on the assumption of structural linearity and passive, time-invariant physical properties. The equation of motion of a discretized viscously-damped structure is given by

$$[M]\{\ddot{v}(t)\} + [C]\{\dot{v}(t)\} + [K]\{v(t)\} = \{f(t)\} \quad (1)$$

where $[M]$, $[C]$ and $[K]$ are the physical mass, damping and stiffness matrices, respectively. In the phase resonance test, a real force vector of harmonic excitation $\{\hat{f}\}e^{i\omega t}$ is applied which yields a stationary harmonic structural response $\{v(t)\}$. In this case eq.(1) can be separated into its real and imaginary part

$$(-\omega^2[M] + [K])\Re\{\hat{v}\} - \omega[C]\Im\{\hat{v}\} = \{\hat{f}\} \quad (2a)$$

$$(-\omega^2[M] + [K])\Im\{\hat{v}\} + \omega[C]\Re\{\hat{v}\} = \{0\} \quad (2b)$$

where $\Re\{\hat{v}\}$ and $\Im\{\hat{v}\}$ are the real and imaginary part, respectively, of the structural responses related to the real excitation vector. In eq.(2b) the real part of the structural responses only vanishes if the eigenproblem

$$(-\omega^2[M] + [K])\Im\{\hat{v}\} = \{0\} \quad (3)$$

is fulfilled. Then, the excitation frequency ω is the resonance frequency ω_r and the imaginary part of the structural responses becomes a multiple of the real normal mode $\{\psi\}_r$. If the phase resonance criterion $\Im\{\hat{v}\} = \{0\}$ is fulfilled, the external damping forces compensate for the internal damping forces. During the tuning process, the phase resonance criterion is observed by a weighted average of all measured structural responses given by the mode indicator function [2, 3]

$$MIF = 1 - \frac{\{\Re(\hat{v})\}^\top \{\hat{v}\}}{\{\hat{v}\}^\top \{\hat{v}\}} \quad (4)$$

The evaluation of the modal damping value and generalized mass during normal mode testing is based on the assumption of proportional damping which leads to the structural responses expressed by the modal parameters

$$\{v\} = \sum_{r=1}^n \{\psi\}_r \frac{p_r}{m_r(\omega_r^2 - \omega^2 + 2\zeta_r\omega_r\omega i)} \quad (5)$$

where p_r is the generalized excitation, ζ_r the modal damping value and m_r the generalized mass.

Due to the adaptation of the excitation vector only one mode dominates the structural responses. Thus eq.(5) can be rewritten as

$$\{v\} = \{\psi\}_r \left(\frac{a_r}{i\omega - \lambda_r} + \frac{a_r^*}{i\omega - \lambda_r^*} \right) \quad (6)$$

where λ is the complex eigenvalue

$$\lambda_r = -\zeta_r\omega_r + i\omega_r\sqrt{1 - \zeta_r^2} \quad (7)$$

and a_r is the r-th modal constant

$$a_r = \frac{p_r}{2i m_r \omega_r \sqrt{1 - \zeta_r^2}} \quad (8)$$

while a_r^* and λ_r^* are the complex conjugate values of a_r and λ_r . Eq.(6) can be simplified by an approximation considering the magnitude of both summands in the vicinity of a resonance. The relation of the summands in eq.(6) can be written by means of the dimensionless frequency parameter $\eta = \frac{\omega}{\omega_r}$ as

$$Q = \frac{\zeta_r + i(\eta - \sqrt{1 - \zeta_r^2})}{\zeta_r + i(\eta + \sqrt{1 - \zeta_r^2})} \quad (9)$$

which becomes for $\eta = 1$

$$|Q| \approx \frac{\zeta_r}{2} \quad (10)$$

Thus, the first summand of eq.(6) dominates the structural responses in the vicinity of resonances and eq.(6) can be approximated by

$$\{v(\omega)\} \approx \{\psi\}_r \frac{a_r}{i\omega - \lambda_r} \quad (11)$$

2.1 Global Parameter Estimation During Tuning Process

The global parameter estimation method starts with eq.(11) and is based on a similar formulation developed for the investigation of transfer functions [11]. Eq.(11) can be written in matrix notation as

$$\left[\{v(\omega)\} [1] \right] \begin{Bmatrix} \lambda_r \\ a_r \{\psi\}_r \end{Bmatrix} = i\omega \{v\} \quad (12)$$

which can be solved for nf frequencies ω in a global least square sense

$$\begin{Bmatrix} \lambda_r \\ a_r \{\psi\}_r \end{Bmatrix} = \left[\begin{array}{cc|c} \sum_{k=1}^{np} \sum_{l=1}^{nf} v_k^2(\omega_l) & \left\{ \sum_{l=1}^{nf} v(\omega_l) \right\}^\top & \\ \left\{ \sum_{l=1}^{nf} v(\omega_l) \right\} & \begin{array}{ccc|c} nf & nf & \dots & nf \end{array} & \end{array} \right]^{-1} \begin{Bmatrix} \sum_{k=1}^{np} \sum_{l=1}^{nf} i\omega_l v_k^2(\omega_l) \\ \left\{ \sum_{l=1}^{nf} i\omega_l v(\omega_l) \right\} \end{Bmatrix} \quad (13)$$

which delivers an approximation for the eigenfrequency ω_r , the modal damping ζ_r , and a multiple of the mode shape $\{\psi\}_r$. The generalized mass can be derived from

$$m_r = \frac{p_r}{2i a_r \omega_r} \quad (14)$$

if the maximum norm is used for the mode shape normalization.

The on-line capability of the global parameter estimation method is determined by the calculation effort solving the system of equations of the order $np + 1$, where np is the number of measured degrees of freedom. Since the structure of the matrix to be inverted in eq.(14) is simple, this calculation effort is modest. The eigenvalue λ_r can easily be calculated by

$$\lambda_r = \frac{nf \cdot \sum_{k=1}^{np} \sum_{l=1}^{nf} i\omega_l v_k^2(\omega_l) - \sum_{k=1}^{np} \left(\sum_{l=1}^{nf} v_k(\omega_l) \cdot \sum_{l=1}^{nf} i\omega_l v(\omega_l) \right)}{nf \cdot \sum_{k=1}^{np} \sum_{l=1}^{nf} v_k^2(\omega_l) - \sum_{k=1}^{np} \left(\sum_{l=1}^{nf} v_k(\omega_l) \right)^2} \quad (15)$$

A multiple of the mode shape can be derived from

$$n_f \cdot a_r \cdot \{\psi\}_r = \left\{ \sum_{l=1}^{n_f} i \omega_l v(\omega_l) \right\} - \lambda_r \left\{ \sum_{l=1}^{n_f} v(\omega_l) \right\} . \quad (16)$$

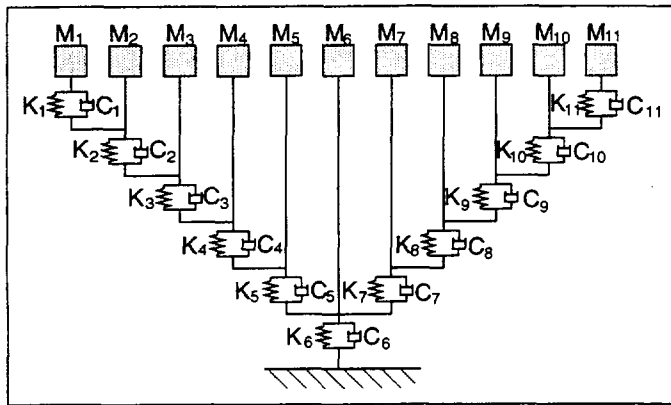


Figure 1: Analytical Vibration System

the fundamental mode is shown in Figure 2. The abscissa gives the number of frequency lines applied in the modal parameter estimation based on a frequency resolution of 0.01 Hz. The ordinate relates the estimations of the modal parameters to the exact values. Whereas the eigenfrequency differs in the given frequency range by a maximum of 2.8 % from the exact value, the damping value and generalized mass are more strongly effected for a larger bandwidth. The application of a small bandwidth yields accurate modal parameter estimations.

Next, the position of a small bandwidth related to the resonance is investigated in Figure 3. In this simulation the position of a 0.5 Hz bandwidth is varied. The abscissa relates the center frequency of the investigated frequency band to the exact eigenfrequency. Again, the ordinate relates the estimations of the modal parameters to the exact values. Additionally, the mode indicator function (eq.(4)) is plotted.

mode	frequency [Hz]	damping [%]	gen. mass [kg]	shape
1	2.737	0.761	4.709	symmetric
2	2.954	0.939	5.149	antisymmetric
3	7.244	2.602	5.763	symmetric
4	7.805	3.050	5.645	antisymmetric
5	11.467	4.388	7.249	symmetric
6	12.124	4.881	5.477	antisymmetric
7	14.983	5.665	5.138	symmetric
8	15.596	5.905	4.906	antisymmetric
9	18.453	5.583	3.948	symmetric
10	19.284	5.612	4.597	antisymmetric
11	28.543	4.287	1.146	symmetric

Table 1: Modal Parameters of the Analytical Vibration System

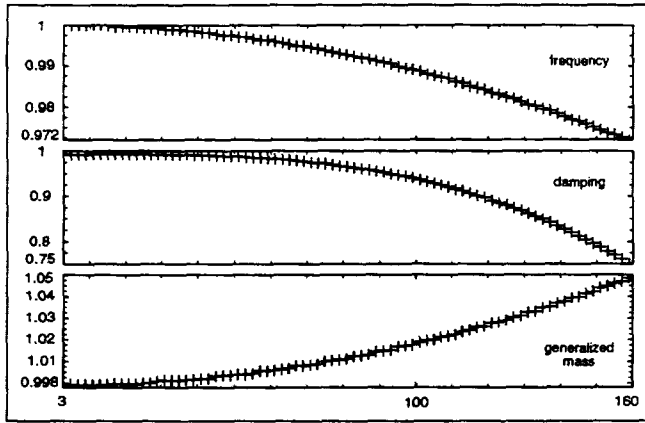


Figure 2: Effect of the bandwidth on the accuracy

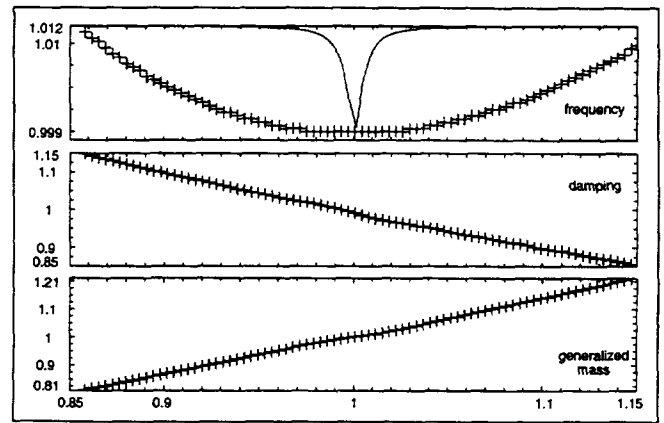


Figure 3: Effect of the position of the investigated frequency band

The figure reveals that accurate parameter estimations are possible far beyond the indication given by the mode indicator function. All estimations within the peak of the mode indicator function are nearly perfect.

2.2 Pole Estimation by Means of Finite Differences

The pole estimation by means of finite differences [1, 11] starts with the approximation of eq.(11). The method estimates the eigenfrequency from the differences of structural responses at two frequencies in the vicinity of a structural resonance

$$\Delta_1 = \{v(\omega_1)\} - \{v(\omega_2)\} \approx i a_r \{\psi_r\} \frac{\omega_2 - \omega_1}{(i\omega_1 - \lambda_r)(i\omega_2 - \lambda_r)} \quad (17)$$

Relating this difference to the difference of the derivative of the structural responses at these two frequencies

$$\Delta_2 = i\omega_1 \{v(\omega_1)\} - i\omega_2 \{v(\omega_2)\} \approx i a_r \{\psi_r\} \frac{\lambda_r (\omega_2 - \omega_1)}{(i\omega_1 - \lambda_r)(i\omega_2 - \lambda_r)} \quad (18)$$

yields for np measurements and nf frequencies, a pole estimation in a least squares sense

$$\lambda_r = \frac{\sum_{k=1}^{np} \sum_{l=1}^{nf} (i\omega_1 v_k(\omega_1) - i\omega_l v_k(\omega_l)) (v_k(\omega_1) - v_k(\omega_l))}{\sum_{k=1}^{np} \sum_{l=1}^{nf} (v_k(\omega_1) - v_k(\omega_l))^2} \quad (19)$$

Since the solution of eq.(19) requires only a summation of several products it is suitable as an on-line tool for pole estimation during the tuning process of the phase resonance methods. Additionally, the generalized mass can be estimated from the input energy p_r and the damping estimation delivered from eq.(19)

$$m_r = \frac{p_r}{2i\zeta_r\alpha_r\omega_r^2} \quad (20)$$

where α_r is introduced in this equation as a mode shape normalization factor, e.g., the vector maximum norm.

Again, the analytical vibration system is utilized to investigate two effects on the accuracy of the pole estimation by means of finite differences. First the influence of the position of the finite difference related

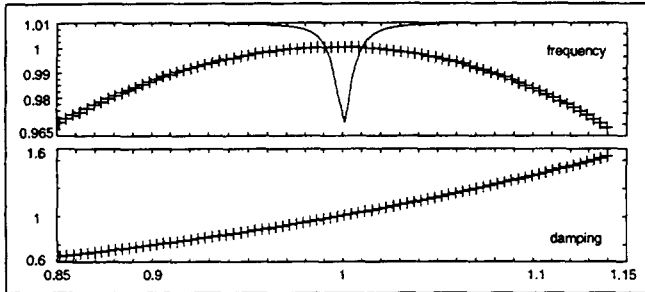


Figure 4: Effect of the position of the investigated finite difference

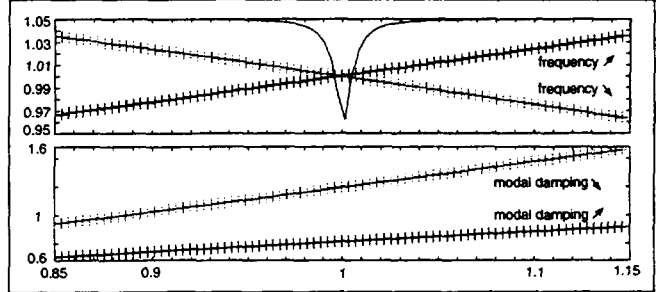


Figure 5: Effect of the bandwidth of the finite difference

to the resonance is investigated. Then the effect of the bandwidth of the finite difference on the pole estimation is shown. Figure 4 shows the effect of the position of a 0.06 Hz finite difference which is a typical frequency step in a final tuning process of the phase resonance method on the accuracy of the pole estimation. The abscissa relates the center frequency of the investigated finite difference to the exact eigenfrequency. Again, the ordinate relates the estimations of the modal parameters to the exact values. Additionally, the mode indicator function (eq.(4)) is plotted. The figure reveals that even at frequencies $\pm 15\%$ below or above the resonance the eigenfrequency is estimated with an error of only 3%. However, the damping estimation at these frequencies contains considerable error. In the vicinity of the resonance the pole estimation is nearly exact.

Figure 5 demonstrates the effect of the bandwidth of the finite difference investigated. For this investigation, one frequency (ω_2) remains constant while the other (ω_1) varies. Two curves are shown in Figure 5; one depicts the fixed frequency at 85 % of the resonance frequency while the roving frequency increases, and the dotted curve shows the fixed frequency at 115 % while the roving frequency decreases. The pole estimation is exact whenever ω_1 meets the exact resonance frequency. However, the damping estimation is faulty. The estimation can be improved by a narrower frequency difference as is indicated by Figure 4. Both figures confirm that an improved pole estimation is achieved while tuning the resonance frequency in the phase resonance method because the resonance frequency is approached in an iterative manner.

2.3 Automatic Tuning via Signed Mode Indicator Function

The automatic tuning of the resonance frequency by means of the mode indicator function eq.(4) requires differentiating an approximation of the function, which contributes to measurement errors. This may lead to a tuning of the structure on local minima or maxima of the mode indicator function. A way to avoid this is the use of a variation of the mode indicator function which allows a simple search for zeroes.

$$SMIF = \frac{\{\text{sign}(\Im(\hat{v}))\Re(\hat{v})\}^T\{|\hat{v}|\}}{\{|\hat{v}|\}^T\{|\hat{v}|\}} \quad (21)$$

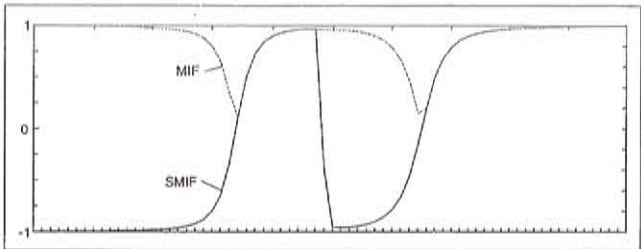


Figure 6: Signed Mode Indicator Function tuning can be accomplished by a damped-Newton algorithm

$$\omega_r \approx \omega_i - (1 - MIF(\omega_i)) \frac{SMIF(\omega_i)}{\frac{d}{d\omega}(SMIF)|_{\omega_i}} \quad (22)$$

where the Signed Mode Indicator Function of eq.(21) can be approximated by a straight line. This requires a low computational effort. In order to avoid large changes of the excitation frequency in the vicinity of the resonance, the mode indicator function is used as a damping parameter of the algorithm.

3 Experimental Investigation

3.1 GVT of the PARTI Wing

The initial experimental verification of the three methods of computer-controlled tuning in phase resonance testing was performed in the Smart Structures Lab of the Aeroelasticity Branch at NASA Langley Research Center. The methods were applied on the test structure of the *Piezoelectric Aeroelastic Response Tailoring Investigation (PARTI)* program [9]. The test structure is a 1.2 m long, high aspect-ratio wing model designed to flutter at low speeds in aeroelastic wind-tunnel tests. The model consists of an interior composite plate which serves as a primary load carrying structure and exterior fiberglass shells used to obtain aerodynamic lift. The interior plate is composed of an aluminum honeycomb core sandwiched by graphite epoxy face sheets of $[-20^\circ/0^\circ]$ laminate, and is swept aft 30° . The interior plate is additionally instrumented with a total of 72 piezoelectric actuators adhered to both sides of the plate (36 actuators per side). A more complete description of the wing construction and components may be found in ref.[9]. For the purpose of this investigation, the fiberglass shells were removed during modal testing to alleviate any potential dynamic influence on the interior plate.

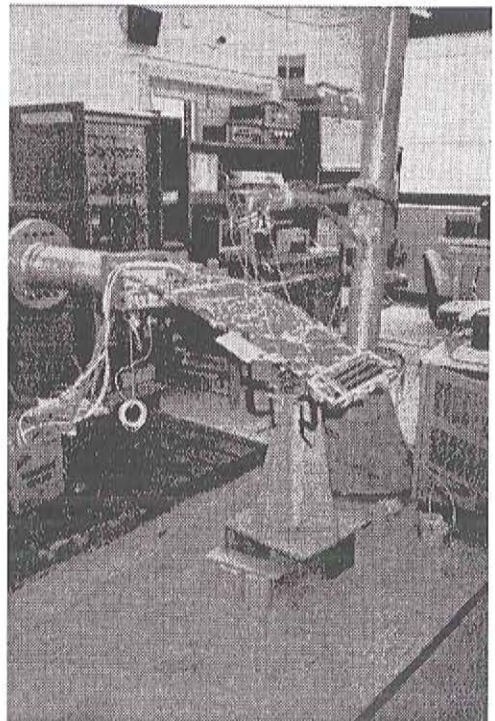


Figure 7: Test setup of GVT on the PARTI wing

Figure 7 depicts the test setup. In addition to the phase resonance test combined with computer-controlled tuning, frequency response functions were measured as well as free decays of the wing. The FRF's were modally analyzed by means of the phase separation technique FDPI [8] operating in the frequency domain, while the free decays were analyzed by a modified Ibrahim Time Domain method [ITD] [5]. Table 2 compares the modal parameters of the three different methods of experimental modal analysis. Additionally, the results of the global parameter estimation method [GLS] performed during the tuning process of the phase resonance test [PRM] are given.

	FDPI		ITD		GLS		PRM	
	f_r	ζ	f_r	ζ	f_r	ζ	f_r	ζ
1st bending	2.64	1.70	2.66	0.13	2.66	0.12	2.66	0.23
1st torsion	14.94	0.36	14.83	0.52	14.81	0.25	14.81	0.47
2nd bending	20.13	0.57	20.23	0.64	20.14	0.57	20.14	0.68

Table 2: Modal parameters of the PARTI wing

There are no major differences except for the damping value of the fundamental bending mode. This damping divergence for the FRF analysis may be traced back to the fact that FRF's from roving accelerometers are used in the analysis. The resulting mass loading effect may have caused the higher damping value.

3.2 GVT of the Sailplane FS-33

The methods of computer-controlled tuning during phase resonance testing were applied during the ground vibration test of the sailplane FS-33 (Gavilan). The sailplane was developed and entirely built by the AkaFlieg Stuttgart (Academic Flight Group of the University of Stuttgart, Germany). The sailplane with two seats is made of carbon fibre material and has wings with a plain flaps profile. The wings partly contain water ballast tanks. The plane has a spanwidth of 20 m, a fuselage length of 9 m, and an empty weight of 375 kg. The GVT was performed in October 1998. The test setup is depicted in Figure 8. Frequency Response Function (FRF) measurements by means of random excitation were performed as well as normal mode tuning. The FRF's were modally analyzed by means of the phase separation technique FDPI [8]. During the tuning process the response data were analysed on-line by means of the Finite Difference method.

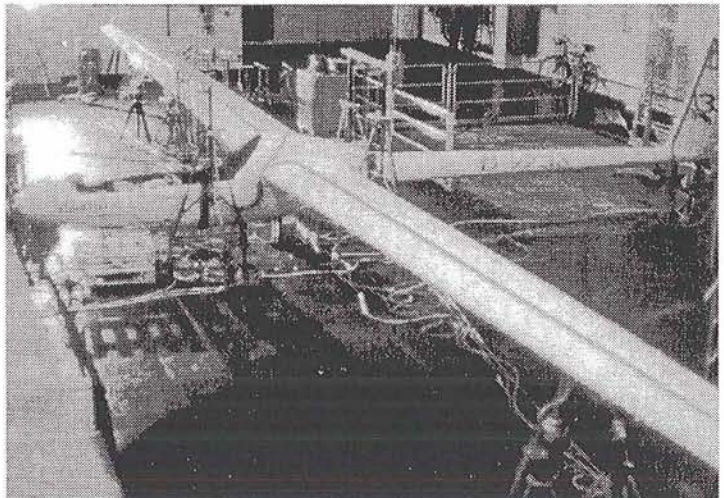


Figure 8: Test setup of GVT on FS-33

Table 3 summarizes the deviation of the phase separation results as well as the on-line data evaluation results obtained during the tuning process from the phase resonance testing (PRM) results.

In the table, the mean values of the relative deviation $\bar{\varepsilon}$ of the modal parameters taken from 17 modes and the standard deviation σ_n are given. The results obtained from the phase separation analyses FDPI differ from the PRM results because the excitation level was significantly lower during the FRF acquisition. The results obtained during the tuning process by means of the Finite Difference method correspond with the final tuning results, which indicates that the on-line investigation of the vibration responses during the tuning process is a valuable support of normal mode testing.

	FDPI		Fin Diff	
	$\bar{\varepsilon}[\%]$	$\sigma_n[\%]$	$\bar{\varepsilon}[\%]$	$\sigma_n[\%]$
frequency	1.9	1.8	0.3	0.3
damping	44.7	37.8	12.8	8.9
gen. mass	34.5	32.9	14.9	12.1

Table 3: Mean deviation of results

4 Conclusion

A lot of information about the structural dynamics of the aerospace structure undergoing test are measured during the tuning process of the normal mode testing procedure. This paper investigates different methods used to evaluate nearly on-line these vibration response data. The proposed methods differ in the amount of modal parameters delivered and, consequently, in the required computational effort. While the global parameter estimation method delivers all the modal parameters (eigenfrequency, damping, mode shape, and generalized mass), the finite differences delivers eigenfrequency and damping estimates, and the Signed Mode Indicator Function is useful for automated frequency tuning only. The effect of frequency bandwidth and positioning on the accuracy of the results is investigated using the different methods. Initial experimental applications on structures of different complexity are discussed. The next step in the development of the on-line data evaluation during normal mode tuning will be the inclusion of robust phase separation techniques in order to utilize the benefits of both the phase separation and the phase resonance tests.

References

- [1] R.J. Allemang and D.J. Brown. *Experimental Modal Analysis*; in: *Shock and Vibration Handbook*. McGraw-Hill, 4th edition, 1995.
- [2] E. Breitbach. A Semi-Automatic Modal Survey Test Technique for Complex Aircraft and Spacecraft Structures. In *Proc. of 3rd ESA Testing Symposium*, pages 519–528, Noordwijk, The Netherlands, 1973.
- [3] E.J. Breitbach. Recent Developments in Multiple Input Modal Analysis. *Journal of Vibration, Stress, and Reliability in Design*, 110:478–484, 1988.
- [4] M. Degener. Ground Vibration Tests on an Aircraft Model Performed as Part of a European Round Robin Exercise. In *Int'l Forum on Aeroelasticity and Structural Dynamics*, pages 269–274. Roma, Italy, 1997.

- [5] U. Füllekrug. Strukturdynamische Identifikation im Zeitbereich - Bestimmung modaler Parameter aus den Zeitverläufen freier Schwingungen. Int. Bericht IB 232-96 C 07, DLR-Inst. für Aeroelastik, 1996.
- [6] D.L. Hunt. Optimal Selection of Excitation Methods for Enhanced Modal Testing. In *Proc. of Structures, Structural Dynamics and Materials*, volume 2, pages 549–553, Palm Springs, CA, 1984.
- [7] S. Keye and U. Füllekrug. A New Method for Computing Optimized Exciter Forces in Phase Resonance Testing. In *Int'l Forum on Aeroelasticity and Structural Dynamics*, pages 269–274. Roma, Italy, 1997.
- [8] M. Lembregts. *Frequency Domain Identification Techniques for Experimental Multiple Input Modal Analysis*. PhD thesis, Kath. Uni. Leuven, Belgium, 1988.
- [9] A.R. McGowan, J. Heeg, and R.C. Lake. Results of Wind-Tunnel Testing From the Piezoelectric Aeroelastic Response Tailoring Investigation. In *Proc. of 37th Structures, Structural Dynamics, and Materials Conference*, paper 96-1511, pages 1722-1732. Salt Lake City, UT, 1996.
- [10] N. Niedbal and E. Klusowski. Optimal Exciter Placement and Force Vector Tuning Required in for Experimental Modal Analysis. In *Proc. of AIAA Dynamic Specialist Conference*, pages 130–141. Palm Springs, CA, 1990.
- [11] A.W. Phillips and R.J. Allemang. Single Degree-of-Freedom Modal Parameter Estimation . In *Proc. XIV Int'l Modal Analysis Conference*, pages 253–260. Orlando, FL, 1996.
- [12] C. Schedlinski and M. Link. An Approach to Optimal Exciter Placement. In *Proc. XIV Int'l Modal Analysis Conference*, pages 376–382. Dearborn, MI, 1996.

Vibro-Acoustics Modal Testing at NASA Langley Research Center

Richard S. Pappa and Jocelyn I. Pritchard
 Structural Dynamics Branch
 NASA Langley Research Center
 Hampton, VA 23681

Ralph D. Buehrle
 Structural Acoustics Branch
 NASA Langley Research Center
 Hampton, VA 23681

ABSTRACT

This paper summarizes on-going modal testing activities at the NASA Langley Research Center for two aircraft fuselage structures: a generic "aluminum testbed cylinder" (ATC) and a Beechcraft Starship fuselage (BSF). Subsequent acoustic tests will measure the interior noise field created by exterior mechanical and acoustic sources. These test results will provide validation databases for interior noise prediction codes on realistic aircraft fuselage structures. The ATC is a 12-ft-long, all-aluminum, scale model assembly. The BSF is a 40-ft-long, all-composite, complete aircraft fuselage. To date, two of seven test configurations of the ATC and all three test configurations of the BSF have been completed. The paper briefly describes the various test configurations, testing procedure, and typical results for frequencies up to 250 Hz.

INTRODUCTION

Aircraft interior noise reduction is a multidisciplinary problem involving both structural and acoustic aspects (Ref. 1). Current research focuses on developing validated analytical models of sound transmission through complex structures and within vehicle interiors, forming the basis of design tools for interior noise prediction and control. The work discussed in this paper is one aspect of a collaborative effort in this area between the Structural Dynamics Branch (Ref. 2) and the Structural Acoustics Branch (Ref. 3) at NASA Langley Research Center.

Two fuselage structures are being used for validation of various interior noise prediction codes (such as NASTRAN, COMET/Acoustics, and Boeing's Matrix Difference Equation technique). The first structure is an in-house-designed, generic "aluminum testbed cylinder" (ATC). The ATC is an all-aluminum, ring-and-stringer stiffened cylinder 12 ft in length and 4 ft in diameter that uses representative aircraft construction. It consists of a cylindrical shell, floor, and end cap components, allowing testing to occur at various stages of assembly. Final phases in the program will use a pressurized interior of up to 7 psi to simulate flight conditions.

The second structure is a complete Beechcraft Starship fuselage (BSF), manufactured about 10 years ago during the development phase of the commercial vehicle. The BSF is an all-composite, reinforced shell 40 ft in length and 6 ft in diameter (in the cabin section) constructed using honeycomb core and graphite-epoxy face sheets. Figure 1 shows the Beechcraft Starship in operation. The Starship is a 10-passenger business aircraft with aft-mounted pusher turboprops, variable-sweep canards, and large winglets that serve as vertical stabilizers. It was the first all-composite plane certified by the FAA. Approximately 50 Starships are currently in service.

This paper summarizes on-going modal tests of the ATC and BSF being conducted for validation of structural finite-element models. Subsequent acoustic tests will measure the interior noise field created by exterior mechanical and acoustic sources. The test objective is to identify the modal parameters (natural vibration frequencies, damping, and mode shapes) of each testbed configuration to as high a frequency as possible. References 4 and 5 contain supplemental information on the structural modeling and model updating aspects of the project. This paper covers only the modal testing activities.

TEST CONFIGURATIONS

Table 1 lists the seven test configurations of the ATC and the three test configurations of the BSF. To date, the first two tests in the ATC program and all three tests in the BSF program have been completed. Figure 2 shows both structures in their initial modal test configurations. The first ATC test article consisted of the bare ring-and-stringer frame. The first BSF test article consisted of the bare fuselage without side windows or door. Each structure was mounted on soft supports to simulate free-free boundary conditions. The ATC used bungee cord at each end, and the heavier Starship fuselage used four air bags. Figure 3 shows a close-up view of the two rear airbags supporting the BSF. Two additional units supported the front of the vehicle. Test configurations 4 through 7 of the ATC will switch over to a similar airbag support system because of the increased weight of these assemblies.

Figure 4 shows ATC configurations 2 and 3. Configuration 2 adds two 100-lb particleboard end plates to the framework. The end plates provide stiff, terminating reflective surfaces for the enclosed acoustic cavity. They contain several $\frac{1}{2}$ -in-diameter holes designed to allow the pressure on both sides of the end plates to equalize during pressurized tests. Configuration 3 adds a 0.040-in-thick aluminum skin. The skin is attached along each of the 11 equally spaced ring frames and the 24 equally spaced stringers with a double line of rivets and epoxy. This attachment assures airtight operation at internal pressures up to 7 psi. Figure 5(a) shows the end domes for the ATC. They are $\frac{1}{4}$ -inch-thick fiberglass composite structure weighing approximately 80 lb each. The end domes are designed to safely carry the interior pressure loads without applying a bending load to the cylinder. The ATC floor, shown in Fig. 5(b), uses dense-core aluminum honeycomb construction. It is supported by a row of stiff aluminum cross members spanning each ring frame. The floor lies 9 inches below the centerline of the cylinder. Fully assembled, the aluminum testbed cylinder weighs approximately 600 lb.

Figure 6 shows interior views of the Starship fuselage. The interior space is essentially empty except for the seat rails and a few miscellaneous items on or near the firewall and in the nose of the aircraft. All of the side window openings are identical in size except for the second-last one on the right side of the plane, visible in the upper-left corner of Fig. 6(b). This larger window is an emergency exit for passengers. Fully assembled (with side windows and door), the BSF weighs approximately 1600 lb.

TESTING PROCEDURE

The intent of this testing is to provide a validated structural acoustic model to as high a frequency as finite-element modeling technology permits. The important motion of the structure for interior noise prediction is the normal motion of the fuselage wall, which is the only structural component that couples to the interior acoustics.

Figure 7 shows the distribution of accelerometers used in the modal tests conducted to date. These measurement positions were selected based on pre-test predictions of the first 100 modes of each structure. The 207 locations in Fig. 7(a) apply to ATC test configurations 1 through 5. ATC test configurations 6 and 7 will use approximately 50 additional accelerometers on the floor and floor supports. The 245 locations in Fig. 7(b) apply to all 3 of the BSF test configurations. Both test articles used a similar sensor distribution. Several rings around each structure were heavily instrumented with radial accelerometers primarily to characterize the “breathing” shell modes (also known as “radial-axial” modes). Several longitudinal lines were heavily instrumented with radial and biaxial accelerometers primarily to characterize the bending and torsional modes. A few triaxial accelerometers captured the secondary axial motion. The ATC sensor distribution had 5 instrumented rings and 3 instrumented longitudinal lines, and the BSF sensor distribution had 8 instrumented rings and 4 instrumented longitudinal lines. The Starship fuselage required more measurements than the aluminum cylinder because of its larger size, and also because of the structural nonuniformity caused by the holes for the side windows and door, and by the tapering of the nose and tail sections.

Figure 8 shows the shaker locations used in the modal tests. These excitation positions were also selected based on pre-test predictions of the first 100 modes of each structure. Figure 8(a) shows the four ATC shaker locations. Shaker 1 applies a tangential side force at a 45-degree angle below the horizontal direction, which primarily excites the torsional and axial modes of the structure. Shakers 2 through 4 apply radial forces at various locations, which primarily excite the bending and breathing modes of the structure. Figure 8(b) shows the seven BSF shaker locations. Shakers 1-2 and 3-4 apply lateral forces at slightly different orientation angles to the passenger cabin on its left and right sides, respectively. Shaker 5 applies a radial force to the top of the fuselage near the door position. Shakers 6 and 7 apply forces at the front wingbox attachment bolts on the left and right sides of the vehicle, respectively. All seven BSF shakers excite both the bending and breathing modes of the structure to some degree. In most ATC and BSF tests, all shakers operated simultaneously using uncorrelated, burst random or pure random excitation forces. A mechanical impedance sensor measured the input force and corresponding drive-point acceleration at each shaker location.

Figures 9 and 10 are flowcharts of the principal data-acquisition and data-analysis steps, respectively. In each modal test, all of the excitation forces and corresponding response accelerations were recorded simultaneously on a large 432-channel data acquisition system. This system has matched anti-aliasing filters, 16-bit analog-to-digital converters (ADCs), and auto-ranging capability to assure high quality measurements. Prior to digitization, the measurement chain used computer-controlled signal conditioning to optimize voltage amplitudes and low-pass (LP) noise filters on every channel to reject out-of-band instrumentation noise. The force and acceleration time histories were recorded onto several ADC throughput disks located within the data acquisition system. After each test, the time histories were transcribed (i.e., sorted by channel number) onto the system disk of the host workstation. All time histories measured in every test were also written on CD-ROMs for permanent archival data storage, allowing future reanalysis if necessary.

Next (see Fig. 10), the system disk of the host workstation was cross-mounted to a faster computer containing a suite of Fortran data analysis software. Cross-mounting the disk simply means that this software could directly read the data files located on the host workstation. The first data analysis step created high-resolution frequency response functions (FRFs) and multiple coherence functions (MCFs) using traditional multiple-input calculation techniques (Ref. 6). MCFs are commonly computed

functions that measure the reliability of the corresponding FRFs at each frequency line. Because of the large number of modes excited in each test and the relatively low damping levels of the structures, particularly the ATC, Fourier transform blocksizes as high as 64K (65,536) were used. Mode indicator functions (MIFs) were then calculated from the FRF data (Ref. 7). MIFs provide excellent estimates of the natural vibration frequencies of the structure, particularly at lower frequencies. These natural frequency estimates should correlate closely with those obtained in the rigorous modal identification step, performed next using the Eigensystem Realization Algorithm (ERA).

ERA is a multiple-input, multiple-output, time-domain technique that uses all available frequency response functions simultaneously to identify structural modal parameters. The method was developed at NASA Langley in 1984, and an accompanying Fortran software package has been continuously improved since then in conjunction with many applications. A large bibliography of ERA-related technical publications is available on the Internet (Ref. 8). The reader should consult this on-line listing for additional information on the technique.

The final data analysis step is a mode-condensation procedure that sifts through large amounts of ERA results and extracts the best, unique set of modal parameters. This recently developed technique uses an autonomous supervisor to condense multiple estimates of modal parameters using the Consistent-Mode Indicator (CMI), the principal accuracy indicator of ERA, and correlation of mode shapes (Refs. 9,10).

TYPICAL RESULTS

Experimental results are presented for the initial test configuration of each structure. Figures 11 and 12 show FRFs and MIFs in the frequency range of 0 to 250 Hz. Other data (not shown) extend to a maximum frequency of 1000 Hz. These frequency-response and mode-indicator functions show the quality and complexity of the measurements and reveal an appreciable difference between the two test articles. Specifically, the ATC frame is a lightly damped structure with corresponding lightly coupled modes, whereas the BSF is a more heavily damped structure with corresponding higher modal coupling. Higher damping and modal coupling complicate experimental modal identification. Linearity test data (not shown) also disclose a higher nonlinearity for the BSF than for the ATC frame. Nonlinearity also complicates experimental modal identification, which assumes that the structural dynamic characteristics are approximately linear (i.e., the vibration response varies linearly with the excitation force level).

Figure 11 shows only one FRF from each test, while the MIF data in Fig. 12 incorporate all of the FRFs measured in each test. Multiplying the number of accelerometers by the number of shakers, a total of 828 FRFs were obtained in the ATC modal test and a total of 1715 FRFs were obtained in the BSF modal test. The MIFs are derived from the complete set of FRFs by solving an Nth-order eigenvalue problem at each frequency line, where N is the number of shakers. To a significant degree, the dips in the MIF plots (particularly the dips that extend down to approximately zero) indicate reliably and precisely the natural frequencies of the modes of vibration. However, they provide no corresponding damping or mode shape information. Also, there is a fair amount of uncertainty concerning the number of modes in those frequency intervals with overlapping and/or shallow dips. The estimated natural frequencies from the MIF plots are not used directly in the ERA modal identification process. They are only used to correlate with and corroborate the ERA results. ERA

calculates all modal parameters (natural frequencies, damping, and mode shapes) using all FRFs simultaneously.

Approximately 100 modes of the ATC and 40 modes of the BSF have been identified below 250 Hz for each initial test configuration. Figures 13 and 14 show four typical results for each structure, arranged in order of increasing frequency. For interior noise prediction, the radial-axial modes ("breathing" modes) tend to be the most important type of modes. However, the other modes also provide valuable additional information for validating and refining the physical properties of the finite-element models, resulting in improved prediction accuracy for the acoustically important modes as well.

The radial-axial modes (Figs. 13d, 14b, and 14d) are described by parameters i and j , where i is the number of circumferential waves in the mode shape and j is the number of axial (longitudinal) half-waves in the mode shape. These modes occur in pairs at approximately the same frequency because of the circular cross-sectional shape of the fuselages. The bending modes (Figs. 13a and 14c) also occur in pairs, whereas the torsional modes (Fig. 13c) occur individually. The 1st shear mode of the ATC (Fig. 13b) has longitudinal shearing of the top of the cylinder relative to its bottom, indicated by the two end rings moving in this manner. Recall from Fig. 7 that axial accelerometers are located only on the end rings of the cylinder, so that the measured shape of the shearing modes must be carefully interpreted considering the locations and directions of the sensors. The pitch mode of the BSF (Fig. 14a) is one of six rigid-body modes of each test article. Experimentally obtained rigid-body modes are useful for validating the proper placement and functioning of the instrumentation. For example, it is not uncommon in modal tests to accidentally switch the polarity of one or more accelerometers. This error is quickly disclosed in the rigid-body modes because of their familiar shapes.

CONCLUSIONS

This paper gave a brief overview of a series of modal tests underway at NASA Langley Research Center for validation of finite-element models of two structures: 1) a generic, scale-model fuselage section known as the "aluminum testbed cylinder" (ATC) and 2) a complete Beechcraft Starship fuselage (BSF). Both test articles will be used for evaluating interior noise prediction codes. The ATC has seven distinct test configurations and the BSF has three distinct test configurations. The modal test objective for each configuration is to identify the natural vibration frequencies, damping, and mode shapes to as high a frequency as possible. To date, approximately 100 modes of the ATC and 40 modes of the BSF have been obtained below 250 Hz using the Eigensystem Realization Algorithm. The modes of the BSF are generally more difficult to identify at higher frequencies than those of the ATC due to its higher damping and modal coupling. Most of the mode shapes of both fuselage structures have a complex, three-dimensional nature, requiring many accelerometers and shakers to characterize properly.

REFERENCES

1. Ohayon, R. and Soize, C., *Structural Acoustics and Vibration*, Academic Press, San Diego, 1998.
2. Adelman, H. M., "Structural Dynamics Branch," NASA Langley Research Center, Website: <http://sdb-www.larc.nasa.gov/SDBranch>, August 1997.

3. Shepherd, K. P., "Structural Acoustics Branch," NASA Langley Research Center, Website: <http://fmad-www.larc.nasa.gov/fmad/sab/SAB.html>, February 1999.
4. Grosveld, F. W., "Structural Normal Mode Analysis of the Aluminum Testbed Cylinder (ATC)," AIAA Paper 98-1949, *Proceedings of the 39th AIAA/ASME/ASCE Structures, Structural Dynamics, and Materials Conference*, Long Beach, CA, April 1998.
5. Hassiotis, S., "Update of the Starship Fuselage Finite Element Model Using Modal Data," *Proceedings of the 17th International Modal Analysis Conference*, Kissimmee, FL, February 1999, pp. 1563-1569.
6. Allemand, R. J. and Brown, D. L., "Experimental Modal Analysis," Chapter 16 in *Handbook on Experimental Mechanics*, Prentice-Hall, Inc., Englewood Cliffs, NJ, 1987.
7. Williams, R., Crowley, J., and Vold, H., "The Multivariate Mode Indicator Function in Modal Analysis," *Proceedings of the 3rd International Modal Analysis Conference*, Orlando, FL, January 1985, pp. 66-70.
8. Pappa, R. S., "ERA Bibliography," Website: http://sdb-www.larc.nasa.gov/SDB/Research/data/ERA_biblio.html, September 1998.
9. Pappa, R. S., Elliott, K. B., and Schenk, A., "Consistent-Mode Indicator for the Eigensystem Realization Algorithm," *Journal of Guidance, Control, and Dynamics*, Vol. 16, No. 5, September-October 1993, pp. 852-858.
10. Pappa, R. S., James, G. H. III, and Zimmerman, D. C., "Autonomous Modal Identification of the Space Shuttle Tail Rudder," *Journal of Spacecraft and Rockets*, Vol. 35, No. 2, March-April 1998, pp. 163-169.

Table 1 – Modal Test Configurations

(a) Aluminum Testbed Cylinder (ATC)			(b) Beechcraft Starship Fuselage (BSF)		
No.	Description	Status	No.	Description	Status
1	Bare Frame	Completed	1	Bare Fuselage Without Side Windows or Door	Completed
2	No. 1 + End Plates	Completed	2	No. 1 + Side Windows	Completed
3	No. 1 + Skin	In Progress	3	No. 2 + Door	Completed
4	No. 3 + End Plates	Future			
5	No. 4 + End Domes	Future			
6	No. 5 + Floor (Fully Assembled)	Future			
7	No. 6 + Internal Pressure	Future			



Fig. 1 – Starship in Flight

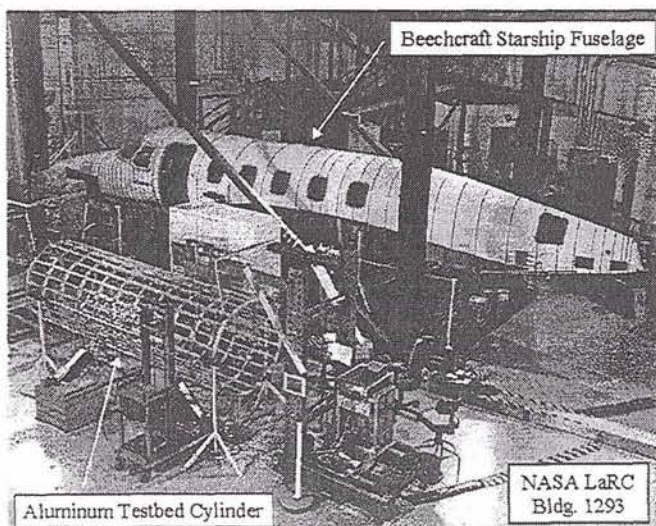


Fig. 2 – Initial Test Configurations
of the ATC and BSF

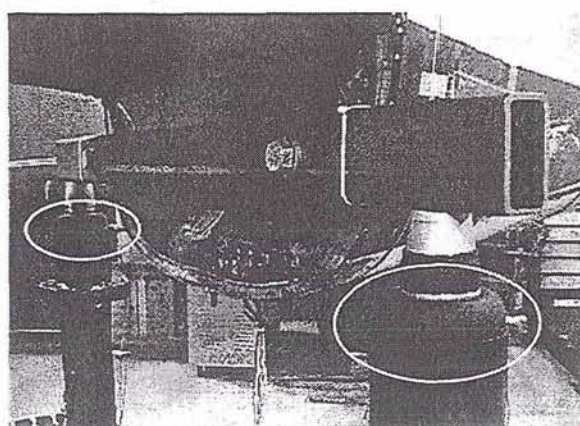
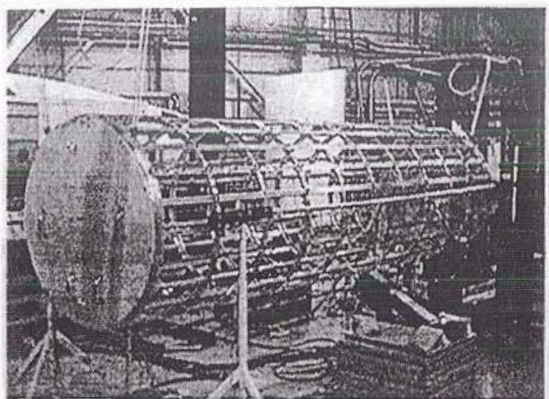
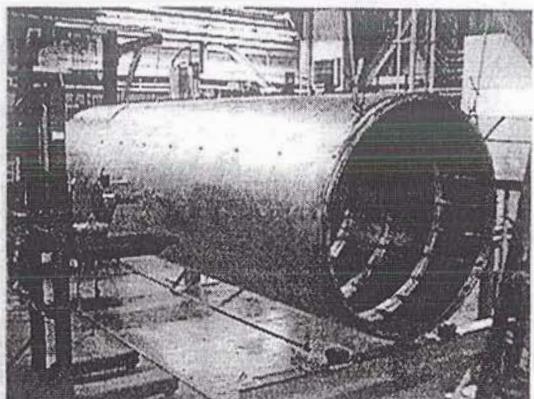


Fig. 3 – Rear BSF Airbags

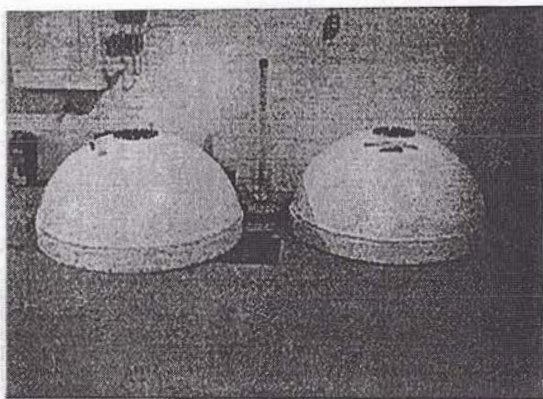


(a) Config. 2: Bare Frame + End Plates

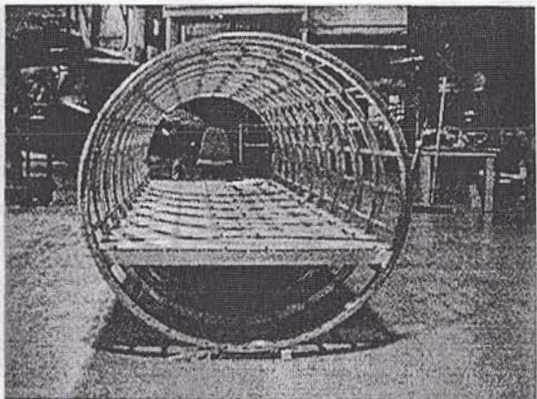


(b) Config. 3: Bare Frame + Skin

Fig. 4 – Second and Third Test Configurations of the ATC

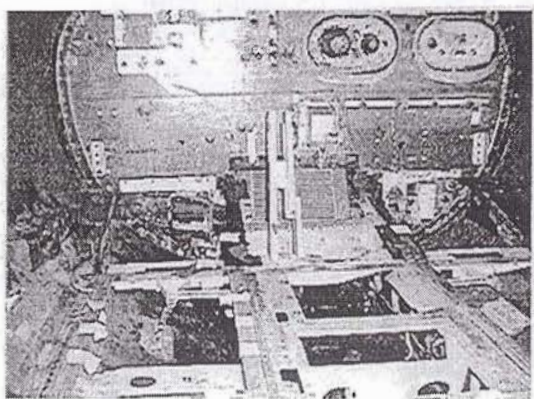


(a) End Domes

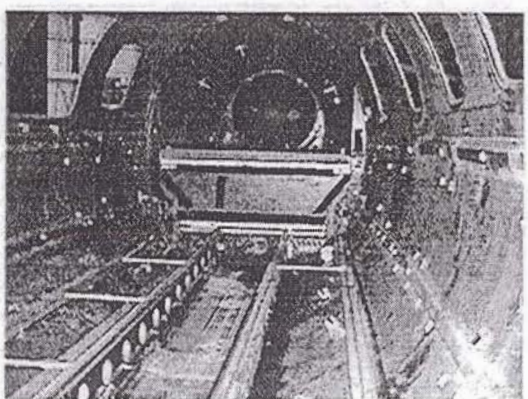


(b) Floor

Fig. 5 – Additional ATC Components

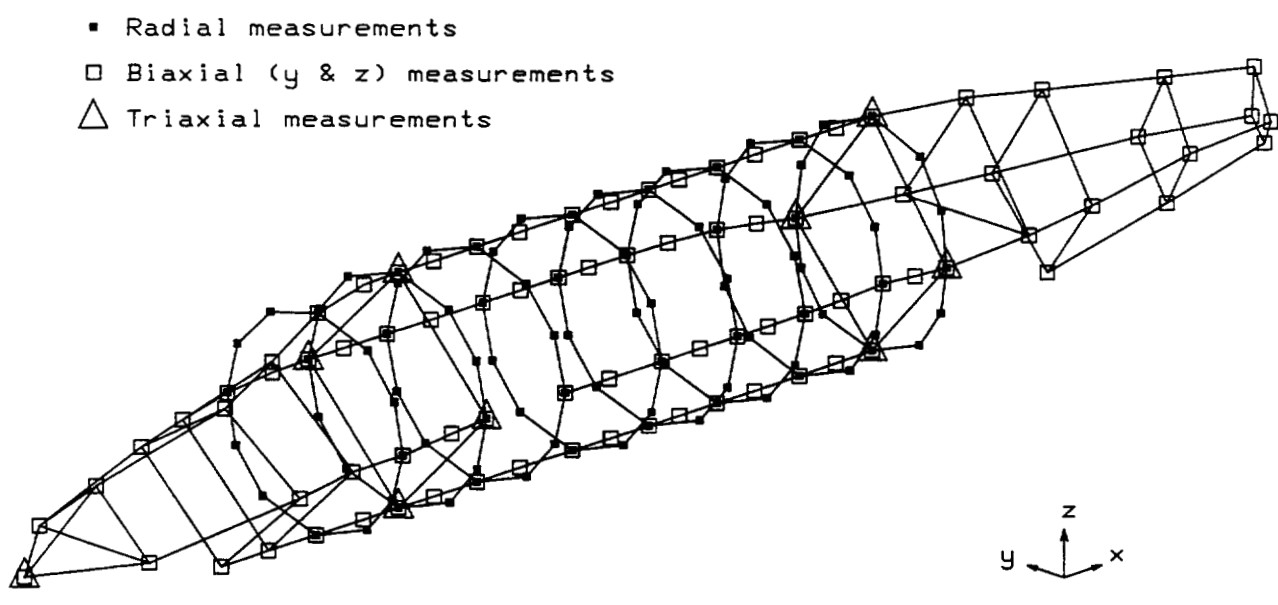
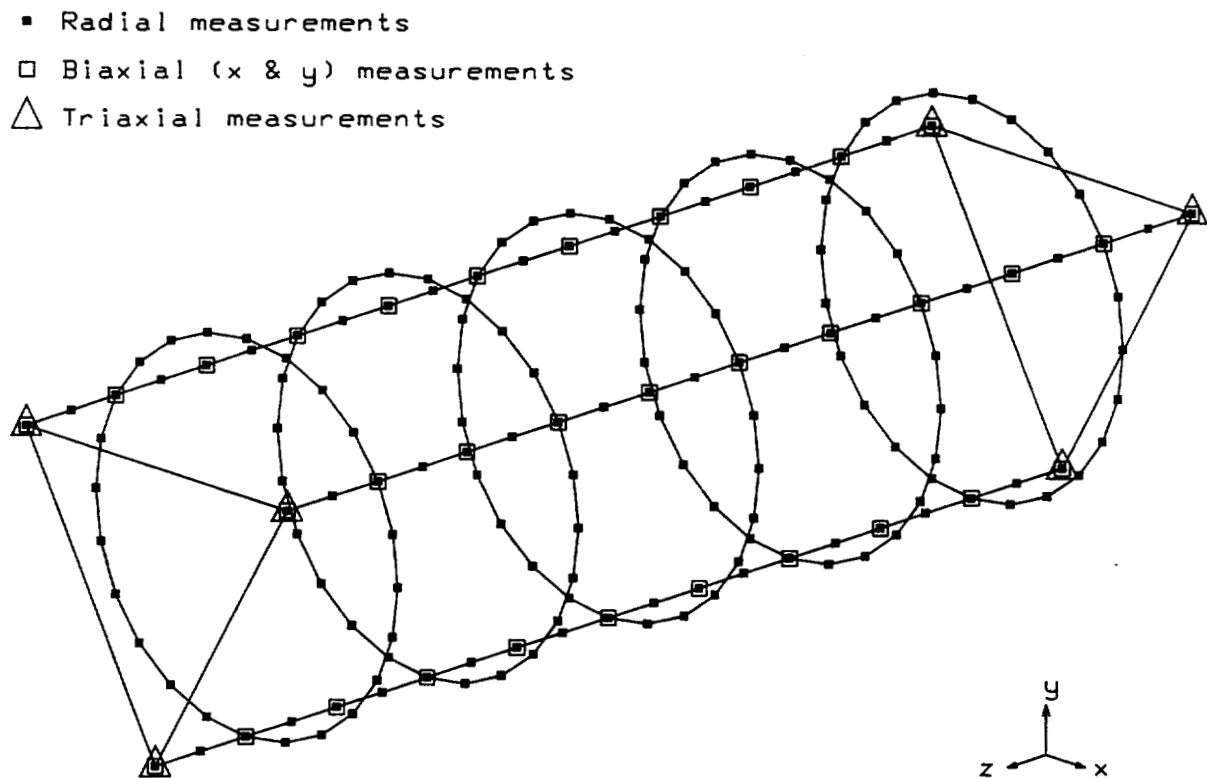


(a) Looking Forward



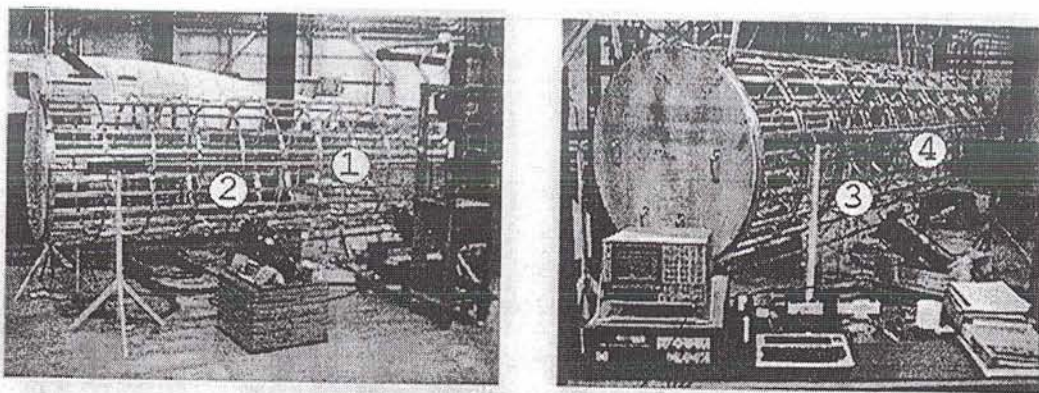
(b) Looking Aft

Fig. 6 – Interior of the BSF

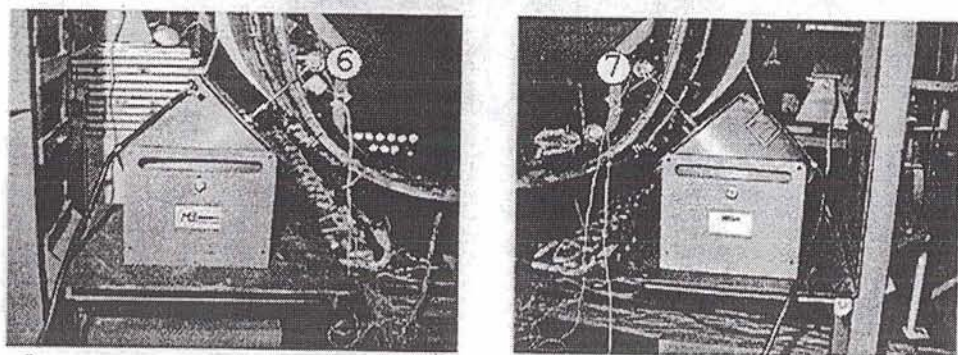
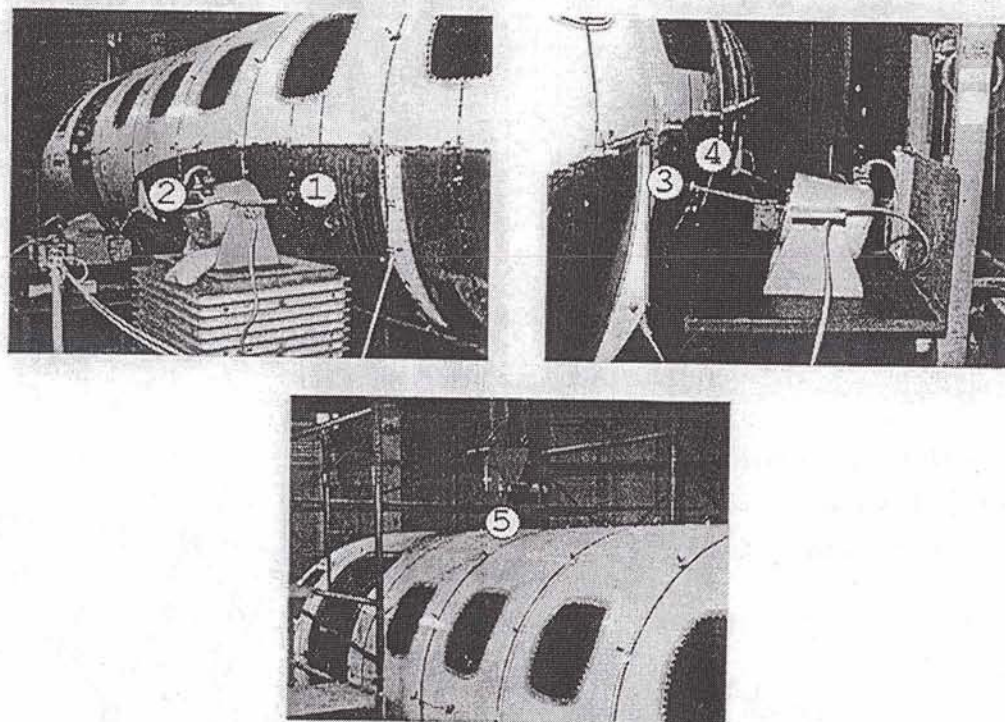


(b) 245 Accelerometers on BSF

Fig. 7 – Accelerometer Locations



(a) 4 Shakers on ATC



(b) 7 Shakers on BSF

Fig. 8 – Shaker Locations

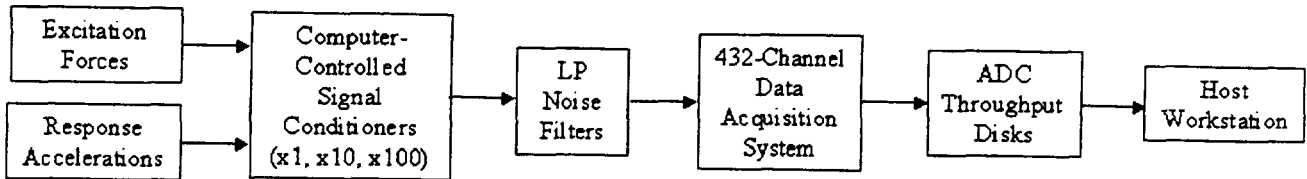


Fig. 9 – Data Acquisition Flowchart

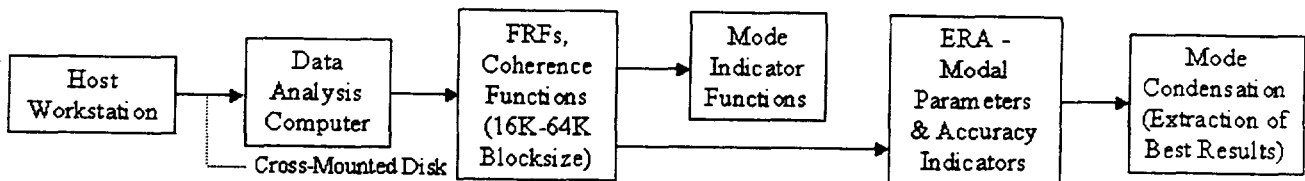
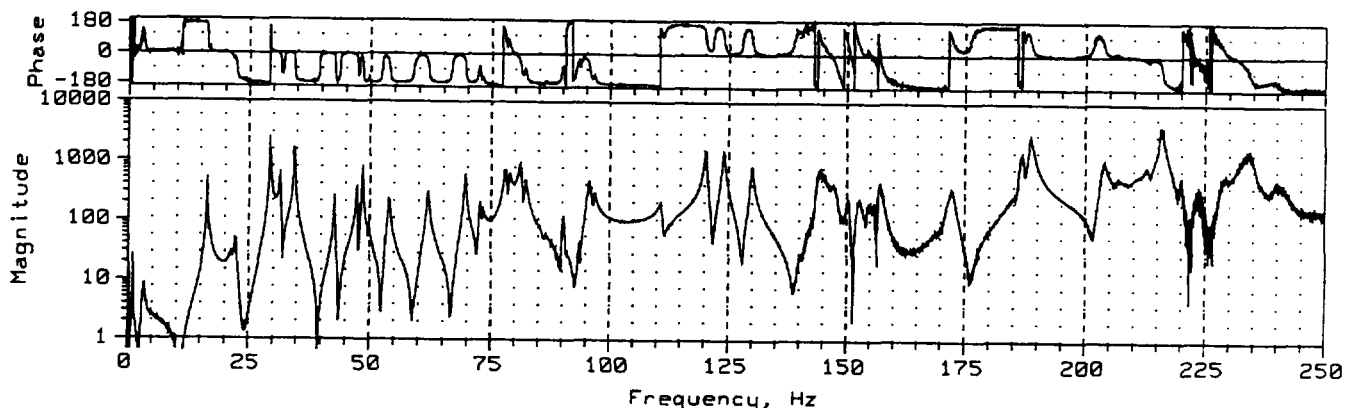
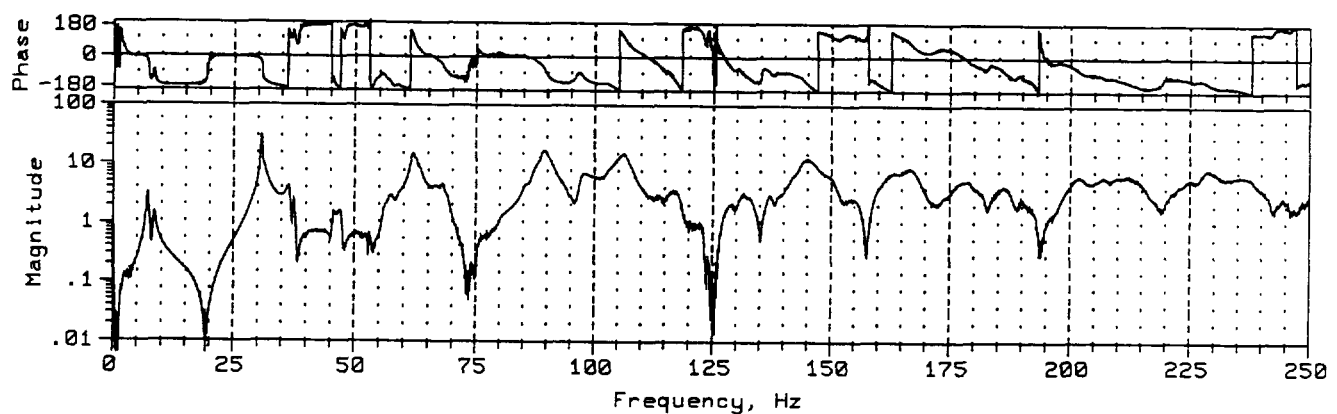


Fig. 10 – Data Analysis Flowchart

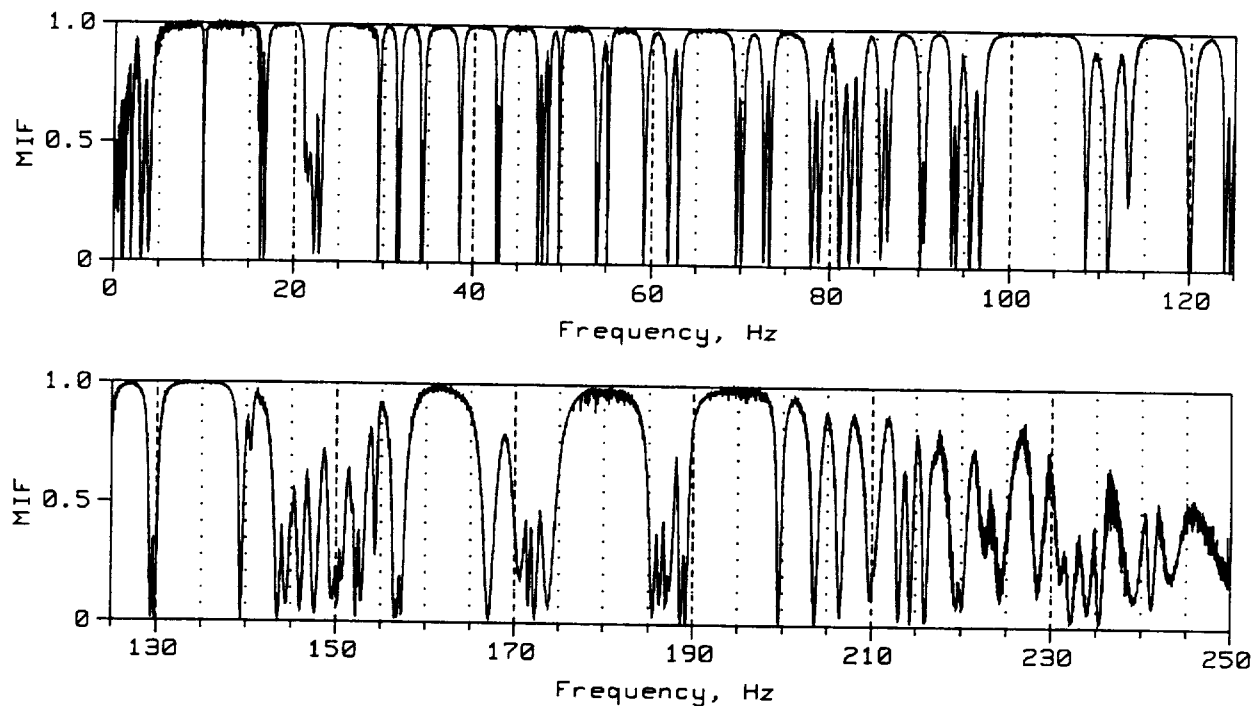


(a) ATC - Config. 1: Bare Frame

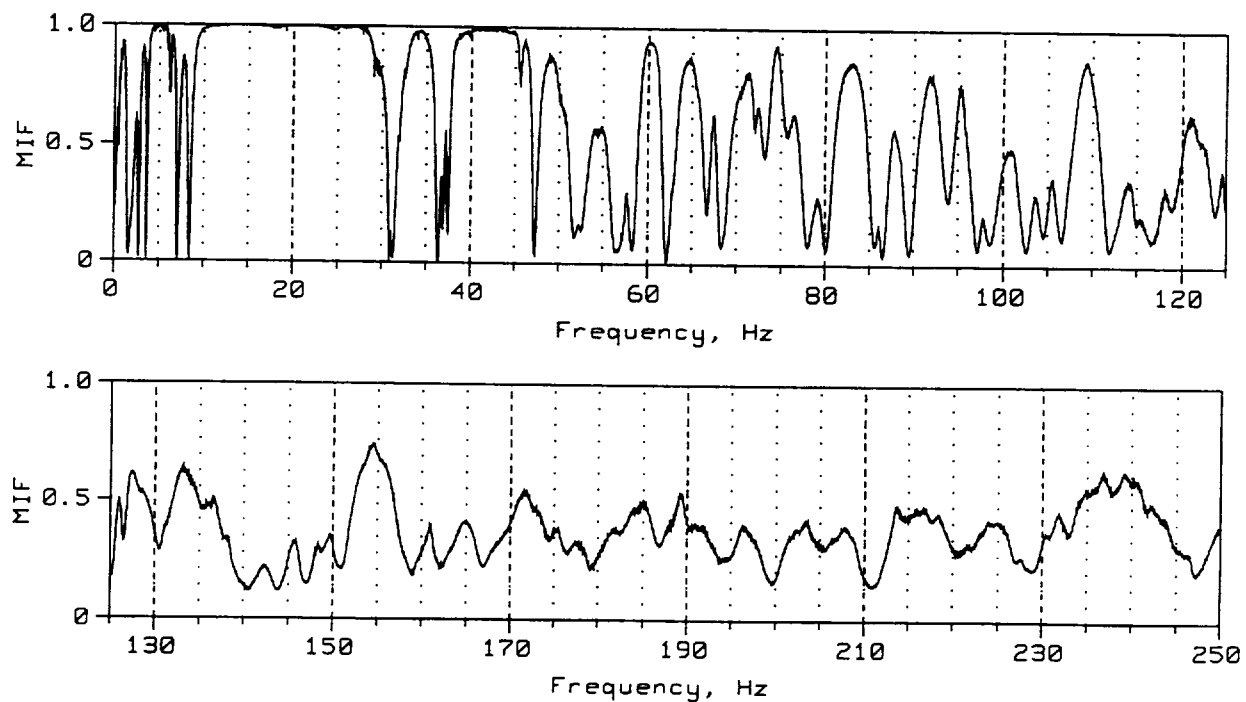


(b) BSF - Config. 1: Bare Fuselage Without Side Windows or Door

Fig. 11 – Typical Frequency Response Functions



(a) ATC - Config. 1: Bare Frame



(b) BSF - Config. 1: Bare Fuselage Without Side Windows or Door

Fig. 12 – Mode Indicator Functions (Dips Indicate Natural Frequencies)

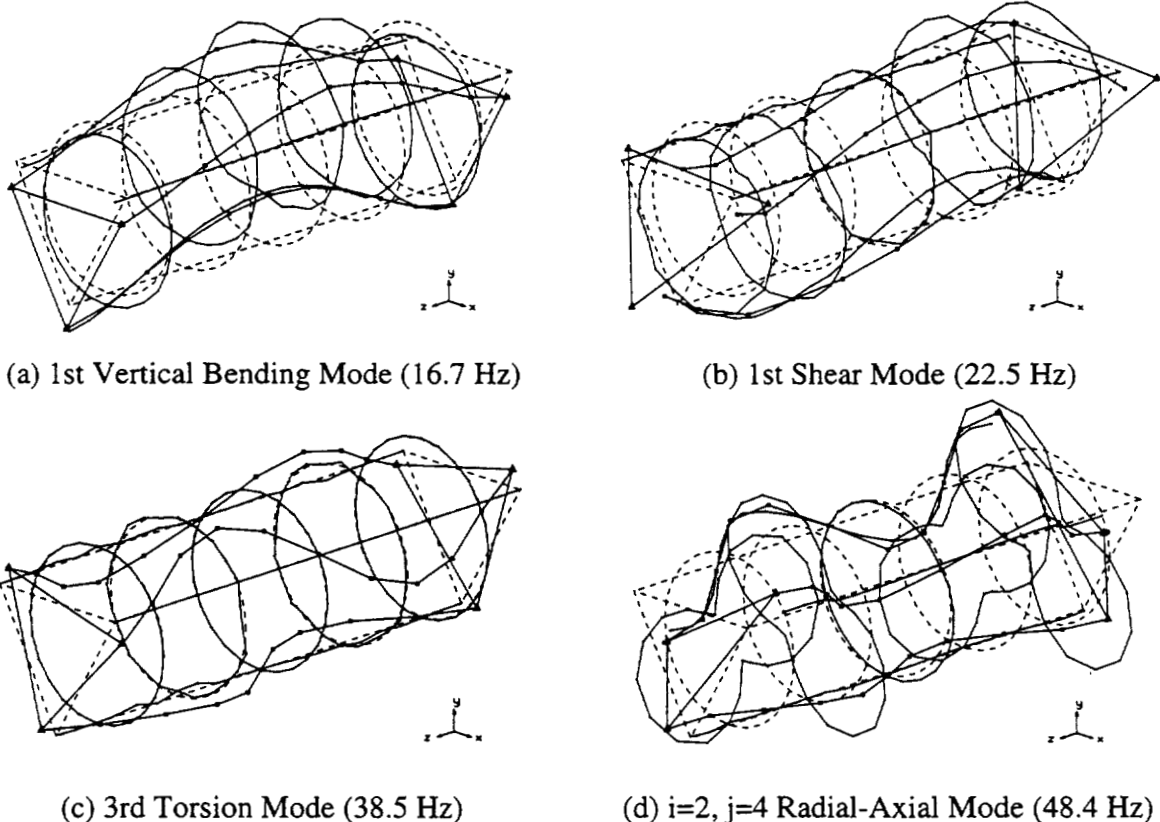


Fig. 13 – Typical ATC Mode Shapes (Config. 1: Bare Frame)

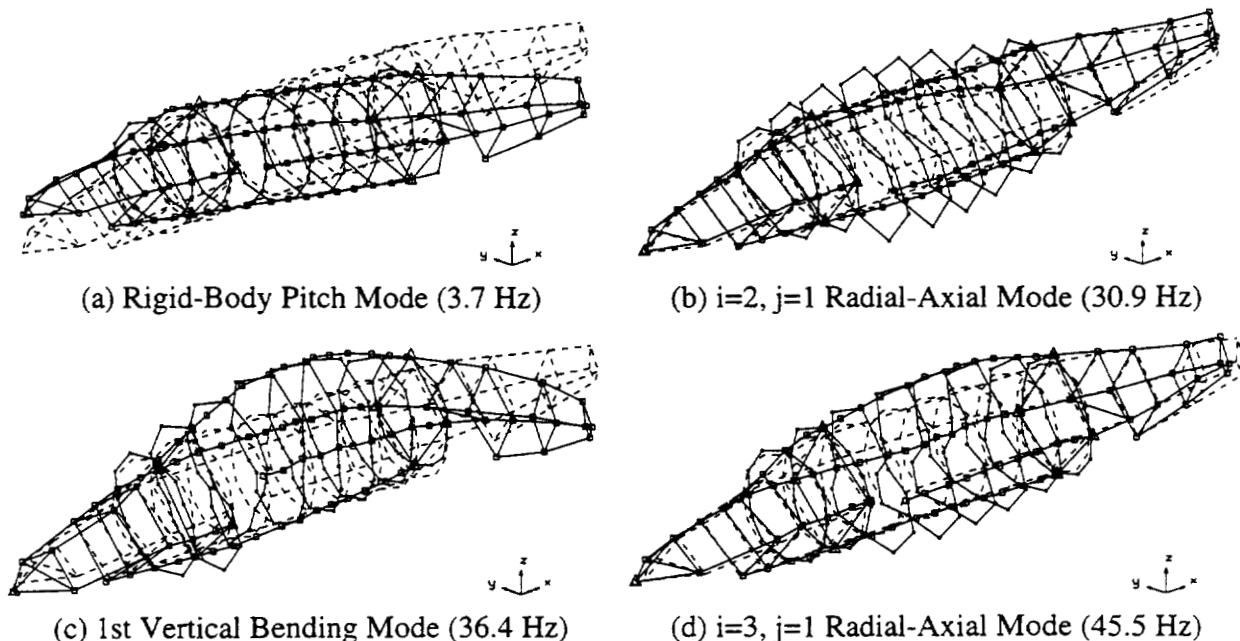


Fig. 14 – Typical BSF Mode Shapes (Config. 1: Bare Fuselage Without Side Windows or Door)

Wind Tunnel Tests and Analysis on Flutter of Spacecraft Including Pitching Effects in Its Launching Configuration

Atsushi Kanda and Tetsuhiko Ueda

Structures Division

National Aerospace Laboratory, Tokyo, Japan

Abstract

A project of experimental reentry winged space vehicle "HOPE-X" is proceeding in Japan. An elastically supported pitching mode may be involved in the dynamic characteristics of this vehicle since it is attached to the H-II rocket in the launching configuration. It is of importance to take this kind of modes into consideration for flutter analysis because the flutter affected with this mode can be critical at the launching phase. A sting support system with controllable pitching rigidity was innovated and tested in a transonic wind tunnel. As the results, the flutter related to the pitching mode was observed. This type of flutter was also confirmed in the analysis using DPM (Doublet Point Method). Further, it was found that a different type of flutter occurred in anti-symmetric mode at relatively low dynamic pressure.

1. Introduction

A project of experimental reentry winged space vehicle "HOPE-X" is proceeding in Japan. This vehicle will be mounted atop of H-II rocket in its launching configuration. It is anticipated to have pitching mode in this configuration since the vehicle follows the bending mode of the rocket and/or the deformation of an adapter between HOPE-X and the rocket. It should be considered that this pitching mode may affect flutter characteristics of the HOPE-X.

A sting support system containing a device to control the pitching rigidity was innovated. A vehicle model with the plate wing which is designed just for confirming the effectiveness of the support system was installed. The flutter experiments were carried out on this model in the transonic wind tunnel of NAL (National Aerospace Laboratory). The results showed that the symmetric flutter mode in which the pitting mode was involved could lower the flutter dynamic pressure below that for the typical bending-torsion flutter. An anti-symmetric mode flutter was also observed at much lower dynamic pressure. As the results, it was demonstrated that these flutter characteristics could become critical depending on the vibration characteristics of the actual launching configuration.

2. Supporting system and model

2.1. Supporting system

A schematic of the sting support system is shown in Figure 1. The sting is cylindrical with the length of 927mm (the mounting part is not included). The diameter of the tip is 120mm and the mass is 58kg. Inside the cylinder, this support system has a plate spring to provide pitching mode and its control mechanism. The supporting part of the plate spring can be shifted without changing its axis of pitching motion by the ball screw which is connected to the servomotor following the commands from the outside host computer. The spring rigidity K is changeable in the range from 20000 to 50000Nm/rad within 7.4 seconds. It can suppress flutter if you utilize the difference of flutter dynamic pressure that comes from the difference of pitching mode characteristics.

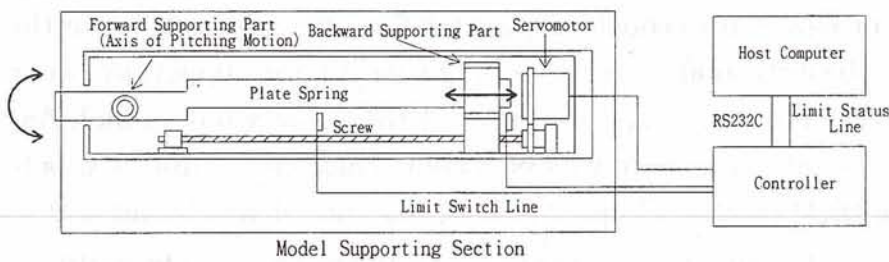


Figure 1 Supporting System

2.2. Vehicle model

The model is designed for confirming the function of the support system. It consists of fuselage made of GFRP and aluminum plate wing with 2mm thickness. Strain gauges for bending and torsion of the flutter vibration were embedded at both wing roots. The fuselage is 2.79kg and the limb is 0.54kg in mass. The wing has a 27.6° sweepback angle at the 1/4 wing chord with an aspect ratio of 2.75, and the taper ratio is 0.56. The contour and dimensions are shown in Figure 2. The model installed in the wind tunnel is shown in Figure 3.

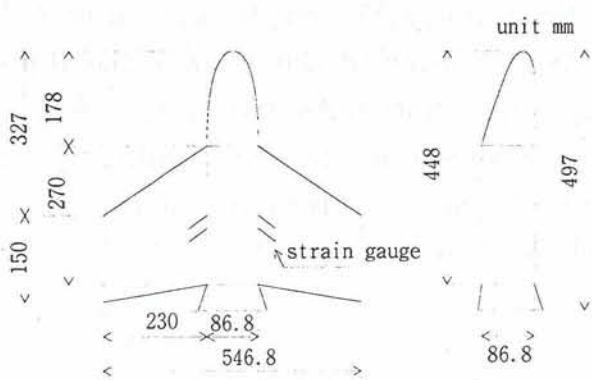


Figure 2 Vehicle Model

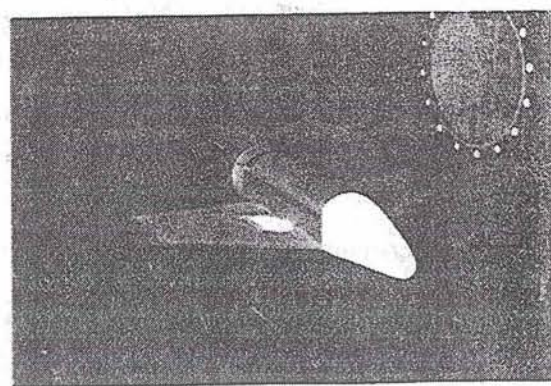


Figure 3 Model in TWT

3. Vibration characteristics

3.1. Vibration tests

The fuselage was excited from underneath by a magnetic shaker (B&K 4814), and the transfer functions were measured in an automatic way by using an output of a non-contacting laser velocity transducer (B&K 3544). The 84 measurement points (37 points on each wing and 10 points on the fuselage) were selected. Since the exciting point is almost on the axis of the model, only the symmetrical modes are excited. The result with the spring rigidity $K=20000\text{Nm/rad}$ is shown in Table 1. The dotted line shows the undeformed base line of the model, and the solid line depicts its mode shapes. The mode numbers are not continuous, corresponding to the analytical results shown later. The 4th mode was measured separately with the accelerometer by the hammer impact method because it could not be excited in the test setup described above.

Table 1 Analytical Mode Shape (at $K=20000$)

2nd mode	3rd mode	4th mode	6th mode	8th mode
32 [Hz]	47 [Hz]	64 [Hz]	97 [Hz]	179 [Hz]

3.2. Vibration analysis

The vibration analysis of the vehicle model at spring constants $K=20000, 35000, 50000$ was carried out by using PATRAN/FEA (PDA Engineering). The analytical model consists of wings, a plate spring and a fuselage. Wings are divided into plate elements. The plate spring has a beam and a spring element. The fuselage includes dummy elements to adjust mass properties to those of the wind tunnel model. First 8 modes were selected for the flutter analysis. The model constructed in the computer is shown in Figure 4. The results are shown in Table 2. It can be seen that the mode shape and the frequencies obtained with the FEM model agree well with the experimental results.

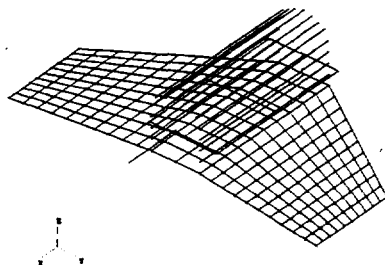


Figure 4 FEM Model

Table 2 Natural Frequencies

Mode	Mode shape	Frequency [Hz]	
		Experiment	Analysis
1	Anti-sym. 1st bending		32
2	Sym. 1st bending	32	32
3	Pitching	47	48
4	Anti-symmetry	64	
5	Anti-sym. 1st torsion		96
6	Sym. 1st torsion	97	98
7	Anti-symmetry	120	
8	Sym. 2nd bending	179	187

	Frequency [Hz]	
	Pitching mode	
Spring rigidity K	Experiment	Analysis
20000	47	48
25000	52	
30000	56	
35000	60	61
40000	62	
45000	66	
50000	69	70

4. Flutter characteristics

4.1. Flutter experiments

The flutter experiments were carried out in the transonic wind tunnel (test section is $2\text{m} \times 2\text{m}$) of NAL. The outline of experiments is shown in Figure 5. The test setup of the model is shown in Figure 6. In the experiments, the total pressure P_0 is increased while the Mach number M is kept constant.

As the results, the supporting system functioned quite well and many flutter points could be obtained. The representative results are listed in Table 3. The flutter points near 50Hz are of symmetric mode which involves the pitching mode and flutter points near 90Hz are of anti-symmetric mode. We call this symmetric mode flutter as “pitching mode flutter”. On the other hand, the anti-symmetric mode flutter appearing in the list had not been anticipated because of the symmetric support system. However, we may consider that this supporting system allows the anti-symmetric modes in the low frequency range if it has an imperfection on the plate spring.

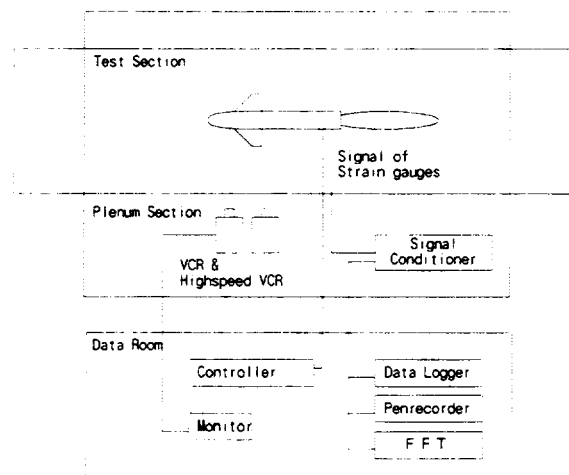


Figure 5 Outline of Experiment

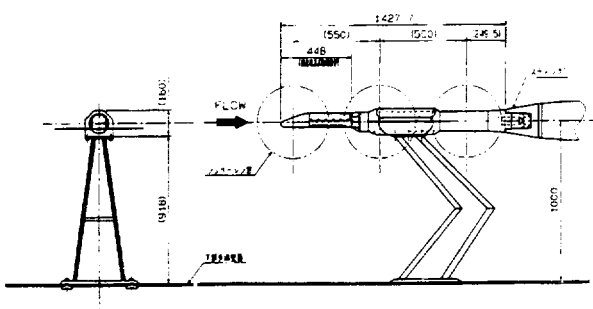


Figure 6 Model and Supporting System

4.2. Flutter analysis

The flutter points were calculated by DPM (Doublet-Point Method) and p-k Method. An analytical model has only a right half and consists of 200 elements with 286 nodes (See Figure 7). As the generalized forces, unsteady aerodynamic forces of the 31 cases were calculated by every 0.1 of non-dimensional frequency in $k=0.0 \sim 3.0$ for the 1st~8th modes by FEM. The flutter is analyzed for $M=0.4, 0.6, 0.8, 1.1, 1.3, 1.5$ with the spring constants, $K=20000, 35000, 50000\text{Nm/rad}$ in the range of total pressure $P_0, 0 \sim 170\text{kPa}$. The flow condition assumes ideal, inviscid and isentropic because they are thought to be acceptable assumptions for this test in the transonic wind tunnel of NAL. The results of the flutter analysis are shown in Table 4. The experimental and analytical results of the pitching mode flutter and the anti-symmetric flutter are compared in Figure 8 and Figure 9, respectively. The abscissa is Mach number M , and the ordinate is dynamic pressure Q in these figures. In addition, isobars for total pressure are also depicted in the figures with dotted lines.

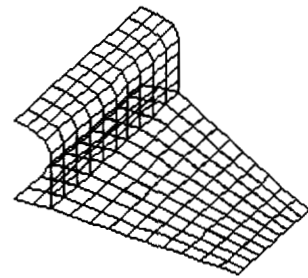


Figure 7 Aerodynamic Model

Table 3 Experimental Flutter Points

Mach Number M	Spring Rigidity K [Nm/rad]	Total Pressure P ₀ [kPa]	Dynamic Pressure Q [kPa]	Total Temperat ure T ₀ [K]	Flow Speed U [m/s]	Frequency F [Hz]	Flutter Mode
0.30	50000	70.1	4.1	296	102	91	Anti-sym.
0.47	50000	44.3	5.9	291	157	91	Anti-sym.
0.55	35000	122	21.1	308	188	57	Sym.
0.80	30000	65.0	19.0	312	266	51	Sym.
	35000	67.9	19.9	312	267	52	Sym.
	45000	70.1	20.6	312	266	53	Sym.
	1.03	51.2	19.4	313	332	45	Sym.
1.10	50000	52.7	20.9	313	350	45	Sym.
1.20	35000	59.7	24.8	313	375	48	Sym.
	40000	62.8	26.1	313	375	49	Sym.
	45000	65.0	27.0	312	374	49	Sym.
1.30	25000	63.1	26.9	313	398	47	Sym.
	30000	67.0	28.6	313	399	48	Sym.
	35000	72.0	30.8	313	399	50	Sym.

Table 4 Analytical Flutter Points

Mach Number M	Pitching mode flutter						
	K=20000			K=35000		K=50000	
	Total Pressure P ₀ [kPa]	Frequency F [Hz]		Total Pressure P ₀ [kPa]	Frequency F [Hz]	Total Pressure P ₀ [kPa]	Frequency F [Hz]
0.40	150	45	-----	-----	-----	-----	-----
0.60	74	44	96	54	107	58	
0.80	50	43	66	51	71	53	
1.10	44	40	54	44	57	45	
1.30	56	43	68	50	74	53	
1.50	78	44	83	53	91	57	

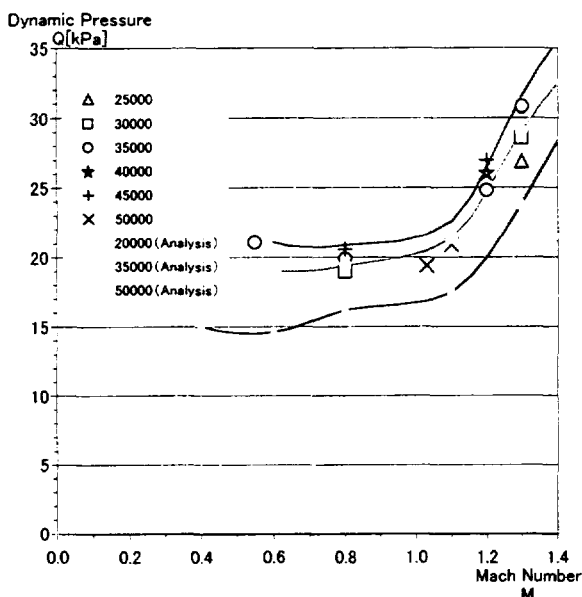


Figure 8 Pitching Mode Flutter

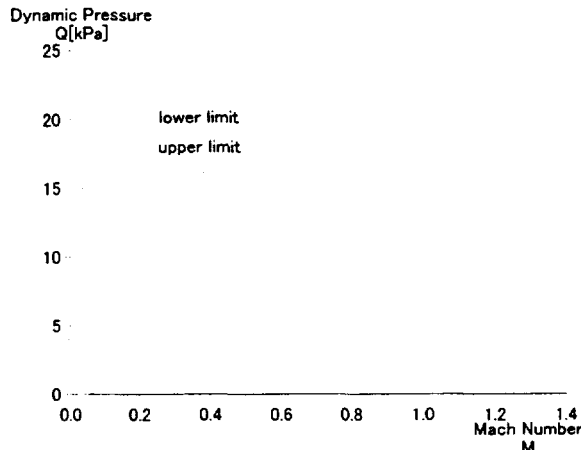


Figure 9 Anti-symmetric Mode Flutter

5. Conclusions

As the results of flutter analysis and experiments for the test model with controllable pitching rigidity, the followings were clarified.

- It was confirmed that the dynamic pressure of the flutter which involves a pitching mode coupling with a bending mode is lower than that of the bending-torsion flutter.
- The supporting system developed was effective also as a suppressing device for the pitching mode flutter.
- An anti-symmetric mode flutter occurred at relatively low dynamic pressure. We consider that it may be attributed to the imperfection of the plate springs. The mechanism of this flutter has not been clarified in the analysis yet.
- The experimental results agree well with the analysis using DPM in both subsonic and supersonic speeds.

5/2 - 09

Aeroelastic Tailoring for Stability Augmentation and Performance Enhancements of Tiltrotor Aircraft*

Mark W. Nixon
U.S. Army Vehicle Technology Directorate
Langley Research Center
Hampton, VA

David J. Piatak
NASA Aeroelasticity Branch

Lawrence M. Corso
Engineer, Rotor Dynamics
Bell Helicopter Textron, Inc.
Fort Worth, TX

David A. Popelka
Group Engineer, Rotor Dynamics

ABSTRACT

The requirements for increased speed and productivity for tiltrotors has spawned several investigations associated with proprotor aeroelastic stability augmentation and aerodynamic performance enhancements. Included among these investigations is a focus on passive aeroelastic tailoring concepts which exploit the anisotropic capabilities of fiber composite materials. Researchers at Langley Research Center and Bell Helicopter have devoted considerable effort to assess the potential for using these materials to obtain aeroelastic responses which are beneficial to the important stability and performance considerations of tiltrotors. Both experimental and analytical studies have been completed to examine aeroelastic tailoring concepts for the tiltrotor, applied either to the wing or to the rotor blades. This paper reviews some of the results obtained in these aeroelastic tailoring investigations and discusses the relative merits associated with these approaches.

INTRODUCTION

Tiltrotor aircraft have advantages over conventional helicopters with respect to speed and range. While a helicopter is limited at high speeds by compressibility effects on the rotor advancing side and stall on the rotor retreating side, a tiltrotor converts from a helicopter mode to an airplane mode for high speed flight which is less restrictive in terms of adverse aerodynamic effects. For these reasons a typical tiltrotor can travel nearly twice as fast as a typical helicopter. Furthermore, while significant increases in airspeeds are unlikely to be provided for

helicopters because of the limitations imposed by aeroelastic physics, there is hope that tiltrotor top-end and cruise speeds may increase further with improved engineering. Current limitations on speed for the V-22 tiltrotor are associated with control loads, control margins, and power, while the XV-15 tiltrotor is power limited. The aeroelastic stability of tiltrotor systems is also an important concern, as the stability margins associated with current tiltrotors are not far beyond the speed limitations set by loads and power today. It is anticipated that the upper velocity limit for future high-speed tiltrotors may be set by both loads and aeroelastic stability considerations. To achieve higher speeds for tiltrotors, structural tailoring of blades and wings using advanced composite materials has been considered in several past investigations.

Researchers at Langley Research Center and Bell Helicopter have devoted considerable effort to assess the potential for using composite materials to obtain aeroelastic responses which are beneficial to the important stability and performance considerations of tiltrotors. Both experimental and analytical studies have been completed which examine aeroelastic tailoring concepts for the tiltrotor, applied either to the wing or to the rotor blades. This paper reviews some of the results obtained in these aeroelastic tailoring investigations and discusses the relative merits associated with these approaches. While the material presented in this report focuses on activities at NASA Langley Research Center (LaRC) and Bell Helicopter, the research efforts of other organizations are included in the discussions when appropriate. The report is organized into four major sections: tiltrotor aeroelastic design considerations, wing aeroelastic tailoring studies, rotor blade aeroelastic tailoring studies, and a summary which includes a discussion on the relative merits of wing versus blade tailoring.

Presented at the CEAS / AIAA / ICASE / NASA LaRC International Forum on Aeroelasticity and Structural Dynamics, June 22-25, 1999. This paper is declared a work of the U.S. Government and is not subject to copyright protection in the United States.

TILTROTOR AEROELASTIC DESIGN CONSIDERATIONS

To help explain the aeroelastic tailoring investigations to be discussed in this paper and the reasons these studies have been conducted, this section of the paper addresses the aeroelastic challenges which have driven current designs associated with tiltrotor blades, hubs, and wings.

Rotor System Aeroelasticity Considerations

Rotor System Type. The significant changes in configuration, aerodynamics, and system frequencies associated with the tiltrotor flight envelope make rotor system design an even more challenging prospect for tiltrotors than for conventional helicopters. The most critical achievement for successful implementation of the tiltrotor to date has been the development of the gimballed rotor system, used in conjunction with the constant velocity joint. This combination of hub and joint solves three fundamental problems which are associated with tiltrotor design: 1) the gimbal joint can accommodate large flapping as is required to produce adequate control power for maneuvers in helicopter mode, 2) the constant velocity joint eliminates the 2P ($P = \text{rotor rotational frequency}$) drive system torsional loading due to the Hooke's-joint effect, and 3) for a gimballed hub the blade rotational velocity vector tilts when flapping occurs to remain approximately perpendicular to the blade tip path plane, greatly reducing the Coriolis forces normally encountered with blade flapping.

While the use of bearingless, hingeless, or articulated rotors may eventually prove fruitful for application to tiltrotors, there are several characteristics of these systems which have made them an undesirable option for tiltrotor application to date. The use of hingeless and bearingless rotor systems is not currently feasible because of the large flapping requirements associated with tiltrotor control in the helicopter mode. Adequate control power requires about 8° degrees of flapping on current systems while these types of hubs are limited to about 4° . A bearingless system would have the additional problems associated with addressing the large pitch changes required of the tiltrotor control system. The articulated rotor hubs tend to be larger and heavier than other types of hubs. Weight is an issue that is driving many modern hubs away from articulated design even for conventional rotorcraft, and the profile drag associated with these hubs is an even more significant problem for tiltrotors because of the high-speed airplane mode configuration. Bearingless, hingeless, and articulated rotor systems are also susceptible to several fundamental design problems associated with frequency placement, air resonance, and

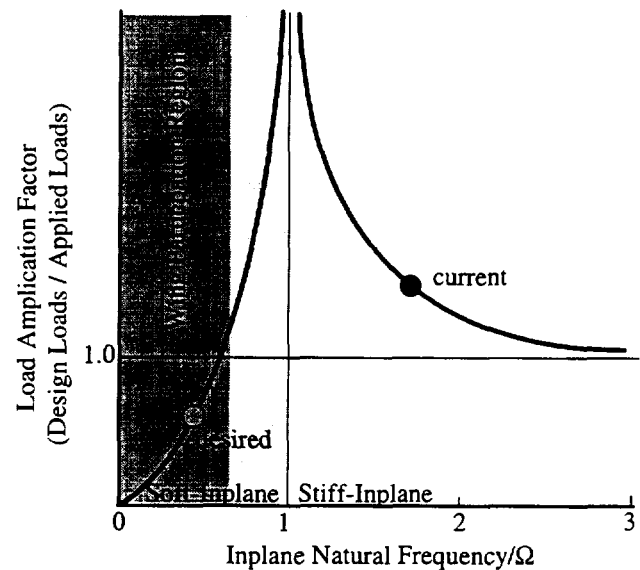


Figure 1: Load factor associated with inplane natural frequency of rotor systems.

Coriolis-based instabilities as is addressed in references 1 and 2. Lastly, and perhaps most significantly, these three rotor systems are generally soft-inplane (fundamental lag frequency below the design rotor speed Ω) where the issues of ground and air resonance can create significant problems with tiltrotors for which an acceptable solution has not yet been determined.

A soft-inplane rotor is desirable from a loads perspective, as is illustrated in the diagram of figure 1. This diagram indicates the approximate load amplification factor associated with current stiff-inplane tiltrotor systems and shows the loads advantage associated with developing a soft-inplane rotor, which becomes significant when the lag frequency is below about 0.7 per rev. These loads reductions can also lead to significant reductions in structural weight of the blades, hub, and pylon. The shaded region of the diagram shows the potential for ground resonance conditions which occur below 1P, and the darker shaded region indicates the approximate lag frequency range in which the elastic wing modes are likely to participate in the ground resonance. The potential involvement of elastic wing modes makes design of soft-inplane rotor systems a particularly difficult problem for tiltrotors.

Ground resonance is a mechanical instability in which the inertial coupling between the inplane blade lag mode and a fixed-system mode (which contains significant hub inplane participation) produce an increasing response as the frequencies of these coupled modes coalesce during rotor wind-up. This instability can only occur when the blade lag mode frequency is below 1P (soft-inplane)

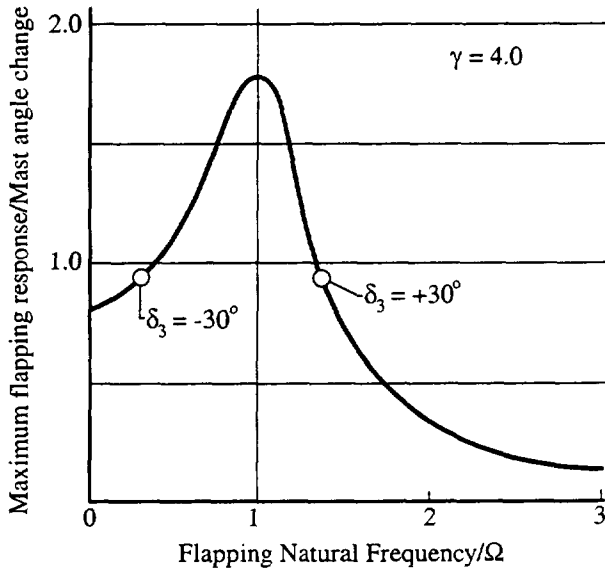


Figure 2: Effect of flapping natural frequency and δ_3 on transient flapping response.

and occurs when the coupled fixed-system frequency approaches the regressive low frequency lag mode ($\Omega - \omega_L$). The conventional solution to this instability is to provide damping to both the rotor lag mode and the associated fixed system modes that contain hub inplane motion. For example, helicopters with articulated rotor systems generally have dampers in the rotor hub attached across the lead-lag hinge and either dampers or highly-damped structural components in the ground support structure. For a tiltrotor, in addition to the rigid body modes, the wing elastic modes can couple with the rotor lag motion to cause ground resonance, and because these modes are elastic the addition of damping is a more difficult prospect. Because soft-inplane rotors are subject to ground and air resonance, and to a lesser extent because these systems tend to have lower whirlflutter stability margins, the stiff-inplane rotor system has been the preferred choice to date for tiltrotors.

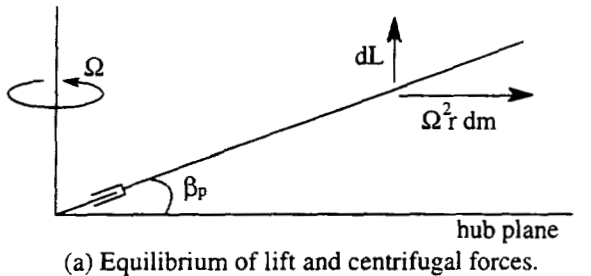
Pitch-Flap Coupling. The natural flapping mode of a gimbal rotor system in-vacuum is at the rotation frequency (1P), and the addition of gimbal hub springs does not significantly change this frequency. This resonant condition creates large flapping and high blade loads in flight, and therefore requires the use of pitch-flap coupling to create an aerodynamic spring force to move the rotor system flap frequency away from 1P, as may be approximated by the fundamental flapping equation as

$$\omega_\beta = \sqrt{1 + \frac{\gamma \tan \delta_3}{8 \cos \phi_{\frac{3}{4}}}} \quad (1)$$

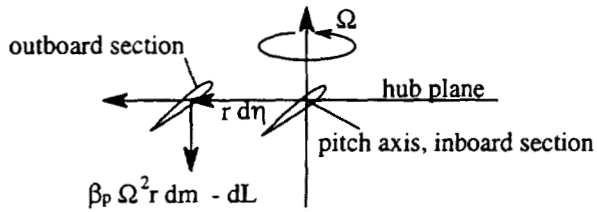
where γ is the Lock number, δ_3 is the pitch-flap skew angle, and $\phi_{\frac{3}{4}}$ is the inflow angle at the blade 75% station. The landmark paper of reference 3 discusses the advantages and disadvantages of using either positive or negative pitch-flap coupling to accomplish the task of moving the fundamental flap frequency away from 1P for a variety of rotor systems. This study also shows that use of the more conventional positive δ_3 (flap-up produces pitch-down blade motion) on a stiff-inplane proprotor results in a flap-lag blade instability for high inflow conditions (airplane mode). This instability occurs because positive δ_3 creates an aerodynamic-based increase in the flapping stiffness, leading to an eventual coalescence of the flapping and inplane blade frequencies as the collective is increased with airspeed. A negative δ_3 (flap-up produces pitch-up blade motion) eliminates the flap-lag instability by separating the flapping and inplane blade frequencies experienced during these conditions, and is just as effective as positive δ_3 in reducing the maximum transient flapping response associated with mast motion, as is illustrated in figure 2.

Rotor system design must also consider an important series of trade-offs between stability margin and blade loads (leading to higher structural weight) which are associated with the magnitude of pitch-flap coupling, rotor precone, and blade frequency placements. As indicated in the previous paragraph, there is a minimum magnitude of pitch-flap coupling which is acceptable to control flapping response and associated inplane blade loads. However, the addition of pitch-flap coupling is destabilizing for whirlflutter, and a compromise in the magnitude of δ_3 must be obtained. For gimballed rotor systems, the blade spacing places constraints on the range of δ_3 which can in practice be used. The δ_3 used on both the XV-15 and V-22 tiltrotors is -15°.

Pitch-Lag Coupling. Rotor precone serves to lessen the blade root bending moments during high disk loading operations such as helicopter hover. For airplane cruise the disk loading is an order of magnitude lower, and this serves to create a large centrifugal-force induced coupling between blade pitch and lag motions, as is illustrated in figure 3. In this figure β_p is the precone angle, dL is the local aerodynamic lift distribution, dm is the local distributed mass of the blade, r is the spanwise position along the blade, and η is the lag angle deformation. The pitch-lag coupling defined by these parameters is generally very destabilizing for whirlflutter as will be shown in later sections of this paper. The invention of the coning-hinge and flexured gimbal hubs by Bell Helicopter (initial tests of this hub type are discussed in reference 4) have



(a) Equilibrium of lift and centrifugal forces.



(b) Torsion about inboard sections due to lag motion.

Figure 3: Effect of precone on pitch-lag coupling.

lessened the effect of precone-related pitch-lag coupling by allowing the rotor system to flatten out (lower effective precone) in low disk loading conditions. This reduces the pitch-lag coupling effects on whirlflutter stability, leading to higher stability boundaries.

Blade Dynamics. Blade structural design for tiltrotors presents a very significant engineering challenge. The high number of constraints placed on the design and the importance of the frequency placement over a wide range of dynamic operating conditions creates a number of structural tailoring opportunities. The aerodynamic design, which is itself a complex compromise among design conditions, defines the shell into which the structural material must fit, creating upper and lower limits on aspirations for stiffness and mass tuning. The fundamental rotor flap, lag, and torsion frequencies must have adequate separations from harmonics of the two design rotor speeds to avoid high loads and vibration. Additionally, the movement of the blade frequencies between the two main design conditions must be considered so that significant resonances and destabilizing frequency crossings will not occur.

Blade Loads. An important driver for blade and hub design on stiff-inplane rotor systems is the oscillatory chord bending moments produced during maneuvers that are associated with large aircraft pitch rates, such as a symmetric dive and pull-up. These loads have been a concern for both the XV-15 and the V-22 tiltrotors as discussed in references 5 and 6, respectively. High rotor pitch rates can create blade stall which intensify the blade aerodynamic loads in both the flapwise and chordwise directions (chord loads are significant due to the high blade

twist and high pitch angles associated with proprotors). While these loads are alleviated in the out-of-plane direction due to presence of the gimbal, the in-plane loads are not alleviated and can significantly influence structural design for the rotor. As the blade and hub design is strengthened to account for these inplane loads, there is generally an associated increase in overall weight. Alternative approaches to solving the rotor loads issues are to 1) develop a soft-inplane rotor system whereby the in-plane loads are alleviated through lag motion about a virtual hinge, or 2) limit the inplane loads by controlling the pitching of the rotor system. The inplane loads associated with both the XV-15 and V-22 have been reduced using the latter. The study of reference 6 discusses the development of flight control systems for the V-22 which reduce the steady and oscillatory chord bending moments on the hub yoke which were found to exceed limit loads for the 5.7g maximum aerodynamic capability of the aircraft. Structural-load-limiting has been designed into the V-22 digital fly-by-wire control system to reduce the maximum load factor of the aircraft to 4g during pull-up maneuvers and reduce the rotor chordwise loads by limiting the rotor disk angle of attack through control of the longitudinal pitch motion of the aircraft.

Wing Aeroelasticity Considerations

There are several significant aeroelastic design considerations for a tiltrotor wing which make it more complicated than a conventional fixed-wing aircraft. One important influence on wing design is the stability margins imposed by whirlflutter. Whirlflutter is generated by the large oscillatory aerodynamic and dynamic forces of the rotor system which couple with the wing motion to modify classical wing flutter aeroelastic behavior. Whirlflutter considerations lead to much stiffer and thicker wing designs than those associated with conventional aircraft.

Wing Dynamics. Whirlflutter stability margins are greatly influenced by the dynamics of the wing and associated components which can affect hub motion such as stiffnesses of the transmission adapter, mast and pylon, downstop, conversion spindle, and wing root. The downstop has a particularly significant influence on aeroelastic stability because this mechanism effectively locks the pylon to the wing in airplane mode, resulting in a sharp change in wing frequencies. When the pylon is not engaged with the downstop then the stiffness of the pylon attachment to the wing is governed by stiffness of the conversion actuator. Typically, with the downstop engaged, the wing torsion and beam frequencies have much greater separation and the associated whirlflutter stability boundaries are significantly higher as is shown in figure 4.

As in classical fixed-wing design, and as suggested by

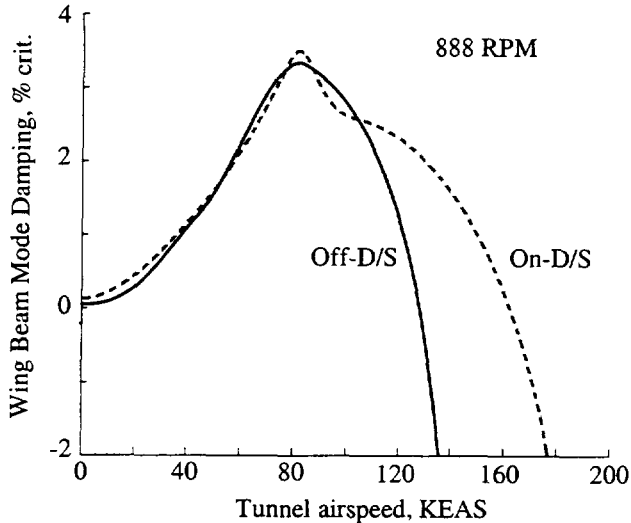


Figure 4: Comparison of predicted damping for the off-downstop and on-downstop configurations of the WRATS tiltrotor model.

the discussion in the previous paragraph, the separation of the fundamental beam and torsion frequencies plays an important role in the aeroelastic stability of a tiltrotor wing. This effect has been studied both analytically as in reference 7 and experimentally using reduced stiffness wings as discussed in reference 8. The plot of figure 5 shows how changes in wing beam stiffness influences stability boundaries associated with the fundamental wing modes. The dominant effect is a drastic lowering of the wing beam mode stability boundary with an increase in the wing beam stiffness, and this occurs because there is no corresponding increase in the wing torsion stiffness such that the beam and torsion wing frequencies move closer together. The plot of figure 6 shows that an increase in torsion stiffness is more beneficial than an increase in beam stiffness in terms of increased stability boundaries, but there are other flutter modes that can become dominant. In the example of figure 6, the stability boundary associated with the wing chord mode is only slightly higher than that associated with the wing beam mode, such that improvements to the beam-torsion aeroelasticity only raises the flutter boundaries to that associated with the wing chord mode. This is a typical problem in tiltrotor wing aeroelastic design. The chord mode instability is generally in the same vicinity as that associated with the beam mode, but it is common that improvements to one of the stability modes, either beam or chord, will have a negligible influence on the other, resulting in a smaller total improvement in stability margin than might otherwise be expected.

Wing Thickness. While there have been numerous

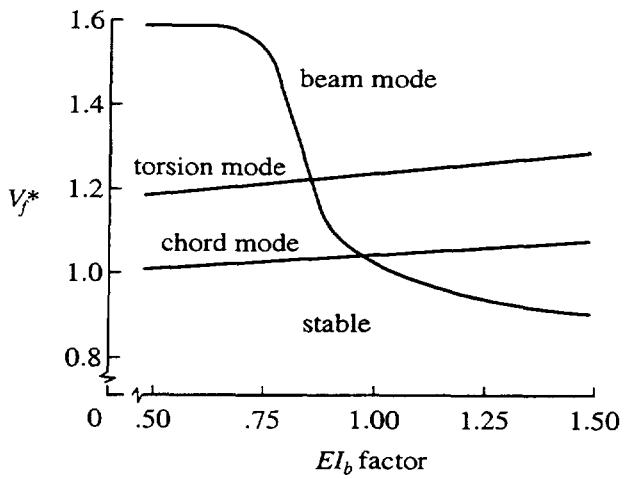


Figure 5: Effect of change in wing beam bending stiffness on tiltrotor stability.

analytical studies and model tests to expand aeroelastic stability boundaries, the current limits on tiltrotor top-end speeds are associated with control loads and power available. Many efforts to improve tiltrotor top-end speed have focused on reduction of profile drag so that higher speeds may be obtained using current power available. While a thin wing is desirable for high-speed performance, stiffness and fuel capacity considerations often require a thick wing design. Current wing thickness for tiltrotors is about 23% t/c while an 18% t/c ratio is desirable for high-speed and long-range designs as is discussed in reference 9.

Wing Sweep. Tiltrotor wings have a small forward sweep to increase flap clearance between the rotor blades and wing in airplane mode. While forward sweep creates divergence concerns for conventional aircraft, this concern is not influential in tiltrotor wing design due to high bending and torsion stiffness requirements for aeroelastic stability. Divergence speeds of current tiltrotor aircraft are predicted to be well above Mach 1. The wing sweep also creates separation between the blade and wing which helps reduce the NP harmonic loads created by the passage of the blades near the wing as is discussed in reference 10. The flow field near the wing is affected by lift produced by the wing, and blockage of the freestream flow by both the wing and fuselage. As each blade is subjected to this flow field for only a short period of azimuthal sweep there is a localized change in angle of attack resulting in significant 1P and higher harmonic loads on each blade. These blade loads sum to produce significant NP fixed-system loads which can be a concern for wing design as these loads are translated from the rotor into the pylon, along the wing, and into the airframe. Because of stiffness requirements for aeroelastic stability, much of the wing design is not influenced by these harmonic loads,

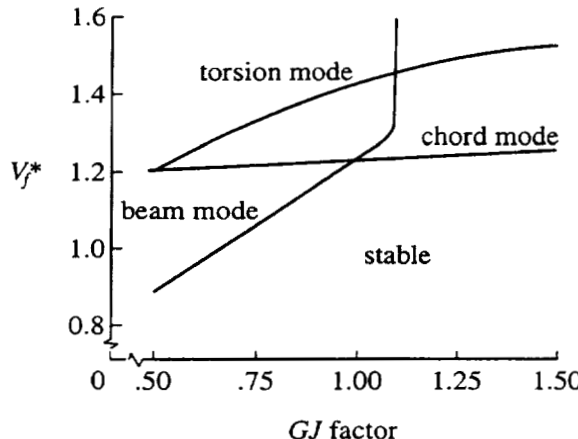


Figure 6: Effect of change in wing torsional stiffness on tiltrotor stability.

but some wing components are fatigue critical and are thus adversely affected by the NP loads. Specifically, the 3P loading on the three-bladed XV-15 and V-22 tiltrotors have created some design challenges with respect to engine loads and downstop loads.

AEROELASTIC TAILORING OF TILTROTOR WINGS

Tailored Wing Feasibility Study

When considering only airframe contributions, the two most important factors affecting proprotor stability are the frequencies and mode-shapes of the wing bending and torsion modes. The wing stiffnesses requirements associated with whirlflutter are typically as demanding as the wing strength requirements, as is discussed in a previous section of this paper. The whirlflutter stability is sensitive to the pitch/bending coupling (referring to the rotor hub pitch motion relative to its vertical translation) associated with the wing mode shapes, and this coupling can be controlled by several factors including: relative frequency placement of the wing modes, offset of the pylon center of gravity relative to the wing elastic axis, and structural bending/torsion coupling of the wing torque box.

To meet stability requirements, conventional tiltrotor wing designs use thick wings (23% t/c) that efficiently provide high torsional stiffness at minimum weight. To improve tiltrotor high-speed performance and productivity, it is desirable to reduce the wing thickness ratio (t/c) without increasing the weight. Performance analyses show that reducing the wing thickness to 18% t/c

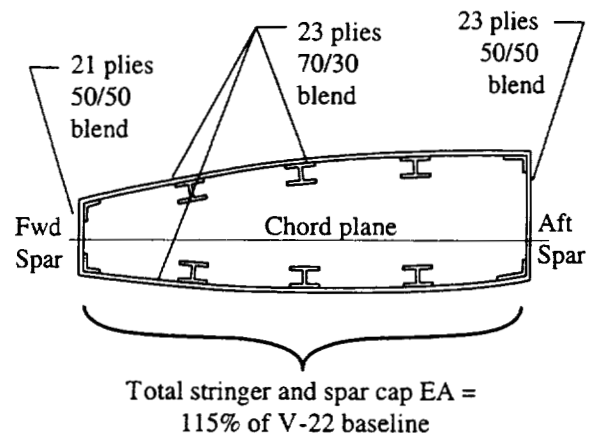


Figure 7: Final 18% t/c three-stringer design.

decreases the airframe drag by 10% and provides a substantial improvement in aircraft productivity. For a conventional tiltrotor wing design, reducing the wing thickness ratio also decreases the stability boundary due to the loss in stiffness. The stability boundary can be recovered by adding structure to increase the stiffness and restore the mode shapes and frequency placement; however, the additional weight reduces aircraft productivity. Composite tailoring provides an opportunity to increase the stability of tiltrotors with thin wings, without incurring a large weight penalty by favorably modifying the mode shapes and frequency placement of the fundamental wing modes.

The study of reference 11 considered the feasibility of a composite tailored wing for a 40-passenger civil tiltrotor. This study was conducted by Bell Helicopter under a 1993 NASA LaRC contract, and the objective was to apply composite tailoring to the design of a tiltrotor wing to achieve the aeroelastic stability requirements at reduced wing thickness for improved performance and aircraft productivity. The baseline configuration used in the study was the V-22 tiltrotor wing because the math models representative of an actual design in which the rotor, fuselage, wing, and pylon structural parameters are fully developed and accurately known provide the most realistic assessment of the benefits of composite tailoring. Design variables included wing skin and spar web laminate composition, stringer and spar cap area distribution, and wing thickness ratio. Parametric studies were conducted of each design variable to provide a basis for the design of a composite tailored 18% t/c wing which satisfied the proprotor stability goals with minimum weight.

Realistic constraints on the design were provided by using the codes used in the actual design process of the V-22. The structural model was developed using NASTRAN along with specialized pre and post processors for

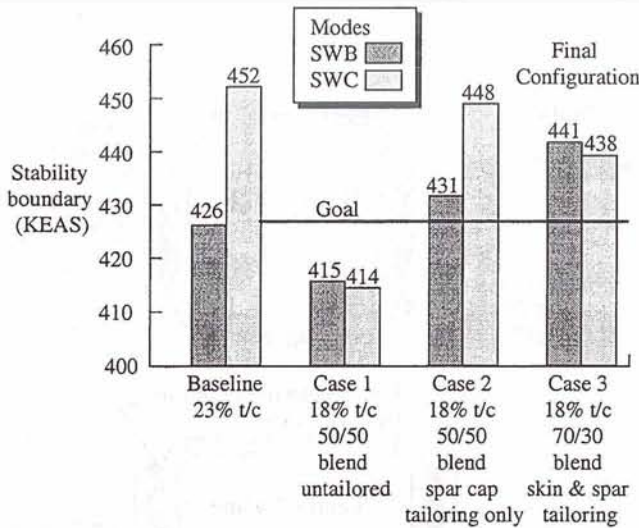


Figure 8: Tailored wing stability summary.

laminate analysis, structural loads analysis, stress analysis, and weight calculations. The natural frequencies and mode shapes associated with the NASTRAN model provided input into Bell's proprietary aeroelastic analysis code, ASAP (Aeroelastic Stability Analysis of Propellers), which also included input parameters defined by the rotor system, drive system, and flight control system.

Elastic couplings were developed in the parametric study by adjusting the ratio of +45° plies relative to the number of -45° plies while maintaining the existing number of 0° and 90° plies of the baseline laminates. A blend ratio was defined to indicate the amount of coupling in the laminate: a 50/50 blend of +45° and -45° would be balanced while a 100/0 blend would provide the maximum elastic coupling for the laminate construction considered. Results of adjusting blend ratios uniformly for all the wing components showed that stability boundaries of the wing beam bending mode (SWB) reached a peak between ratios of 70/30 and 80/20. However, stability boundaries of the wing chord mode were decreased as the blend ratio moved away from 50/50 because of a reduction in effective chord bending stiffness associated with the elastic coupling. To compensate for the loss in chordwise stiffness, the parametric studies considered moving up to 50% of the stringer cap cross-section area into the forward and rear spar caps where the blend ratios were held at 50/50 to maintain chordwise bending stiffness. The blend ratios of the upper and lower wing skins were held at 80/20 for this part of the study, and the results showed that adequate stability margins could be maintained using this approach. Strength analyses led to increasing the number of stringers in the wing from 2 to 3 so as to prevent buckling of the skin panels, and negative

margins of safety in the skin panels required addition of two additional skin plies.

The final design configuration developed based on the parametric study is defined in figure 7. It used a balanced laminate in the forward and aft spars to maintain chordwise stiffness while using a blend ratio of 70/30 in the upper and lower skins to achieve the optimum pitch/bending coupling to improve stability of the wing beam bending mode with respect to whirlflutter. Stress analysis determined that a three-stringer configuration with two additional skin plies were required to satisfy strength constraints. The resulting weight is nearly equivalent to that of the 23% t/c baseline, increasing by only 1.2%. The most significant results of the study are illustrated in figure 8 which show that the stability boundaries associated with the high-performance 18% t/c wings can actually be improved over that of the 23% t/c baseline.

Tailored Wing Wind-Tunnel Study

Encouraged by the results of the full-scale composite tailored wing study of reference 11 as discussed above, a model-scale test program was initiated to validate the composite tailored wing concept. The model test program was a joint effort between NASA Langley Research Center (LaRC) and Bell to evaluate the stability characteristics of a tiltrotor with a composite tailored wing. During the model program, two wind tunnel tests were conducted at the NASA LaRC Transonic Dynamics Tunnel (TDT) in Hampton, Virginia. For the wind tunnel tests, the Wing and Rotor Aeroelastic Test System (WRATS) was used as the test bed. This model originated from the 1/5-size Froude-scaled aeroelastic model of the V-22, which was designed by Bell during the full-scale development and used for flutter clearance tests of the aircraft. The first test of the WRATS model occurred during August 1995 and established baseline aeroelastic stability boundaries for a tiltrotor with a conventional untailored wing design. The wind-tunnel model represented a tiltrotor with a 23% thick conventional wing, pylon, and rotor system and was configured in airplane mode so that high speed stability could be evaluated. Figure 9 shows the aeroelastic model mounted to the tunnel support structure.

For the second TDT entry, a composite tailored wing was designed and fabricated by Bell to dynamically represent a full-scale composite tailored wing with a t/c ratio of 18%. The composite tailored wing and the baseline wing are interchangeable on the model, thus maintaining the same pylon, rotor, control system, and drive system characteristics in each test. The second TDT entry occurred in December 1995 and measured the aeroelastic stability of the composite tailored wing.

The 1/5-size baseline semi-span wing was designed around a central spar which provided the stiffness requirements necessary to dynamically represent the scaled

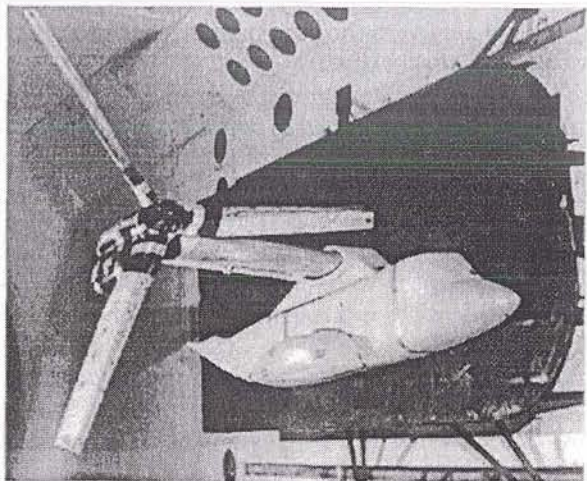


Figure 9: WRATS $\frac{1}{5}$ -size aeroelastic wind-tunnel model mounted in the NASA LaRC TDT.

stiffness properties of the full scale V-22 with a 23% t/c ratio. The full-scale design used a five-stringer carbon epoxy wing box with balanced laminates. For the model, carbon epoxy roving was wound at ± 45 deg to form a graphite torsion box with constant rectangular cross section. Additional beamwise and chordwise stiffness was obtained by bonding unidirectional carbon epoxy stiffeners to the sides of the torque box. Aluminum T-section flanges provided support for the nonstructural wing panels and increased the chordwise stiffness to the desired target values. The general construction of the wing torque box cross section is shown in comparison to the baseline design in figure 10. The model wing and full-scale wing provide no structural bending-torsion coupling attributable to the use of balanced laminates. Greater details of the construction process, tuning of the model, and NASTRAN finite element modeling of the structure are reported in reference 9.

Analytical Modeling and Stability Predictions.

The Bell Aeroelastic Stability Analysis of Proprotors (ASAP) code was used to predict the wing/pylon/rotor stability speed for tiltrotor aircraft in airplane mode flight. ASAP has shown good correlation with wind tunnel tests as described in reference 12 and full-scale V-22 flight test data as described in reference 13. ASAP performs a linear eigenvalue analysis based on the dynamic coupling of the rotor, airframe, drive system, and control system. The math model representation for each element used in the ASAP analysis is briefly described in the following paragraphs.

The rotor is modeled in ASAP by using a lumped parameter rigid-blade analysis, with hinges and springs for representing the flap, lag, and coning degrees of freedom. Rotor cyclic flapping motion is modeled as a hub

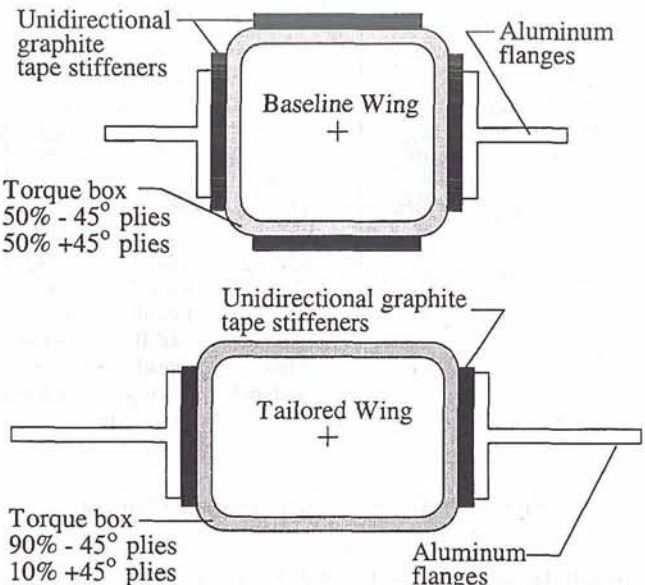


Figure 10: Comparison between baseline and tailored wing cross sections.

gimbal degree of freedom. Discrete coning and lead-lag hinges model the elastic bending of the blade to form the collective coning and cyclic inplane modes, respectively. Blade feathering motions are computed through kinematic relationships which include pitch/flap, pitch/cone, and pitch/lag coupling. These coupling parameters are calculated external to ASAP using fully coupled elastic rotor blade analyses to enhance the simple blade modeling approach used in ASAP. The rotor aerodynamics are calculated using quasi-steady strip theory aerodynamics, with constant chord and constant airfoil, and assumes uniform axial flow so that the equations have constant coefficients.

The airframe dynamics model consists of elastic modes derived from a NASTRAN finite-element-model (FEM) of the structure. For stability analysis, mode shapes at the rotor hub and control plane are required and input to ASAP. Structural and aerodynamic damping values of the airframe are measured from ground vibration tests and "rotors-off" wind tunnel tests. The drive system was disconnected during the wind tunnel tests which allowed the rotor to rotate freely in a windmill state. Previous tests as described in reference 4 have shown that an unpowered model can be used to accurately represent the powered flight condition when measuring stability boundaries in airplane mode.

The ASAP program generates plots of frequency and

damping versus airspeed which are used as pretest predictions for the wind tunnel tests. Stability speed predictions were calculated for the baseline and tailored wings at four critical design conditions, (1) pylon on the downstop at 84% RPM, (2) pylon on the downstop at 100% RPM, (3) pylon off the downstop at 84% RPM, and (4) pylon off the downstop at 100% RPM; where 84% RPM represents the airplane cruise rotor speed and 100% RPM represent the normal helicopter mode rotor speed.

Test Results and Correlation with Analysis. During the wind tunnel tests of the baseline and tailored wings, frequency and damping data were recorded for the fundamental wing bending modes. The frequency was determined using an on-line spectral analyzer. The wing beam, chord, or torsion mode was excited at the natural frequency using a heavy-gas pulse-jet excitation system mounted on the tip of the wing. The wing bending gage output was recorded on strip chart recorders and the TDT data system. The fixed system damping was determined from the time history decay of the bending gage output following the excitation. The damping was computed using two different methods: hand calculations were performed on the strip chart decay traces using a log decrement calculation, and analysis was performed on the digitized time history using an on-line Moving Block analysis (reference 14).

Typical correlation plots between measured and predicted frequencies and damping are shown in the plots of figure 11 for the TDT entry of the tailored wing. These plots represent the correlation for the tailored wing in the off-downstop configuration with a rotor speed of 84% RPM. Figure 11 shows the damping versus airspeed for the beam and chord modes, respectively. The damping predictions for the fundamental wing beam modes track well with increasing airspeed. An instability was recorded in the beam mode at 155 Knots Equivalent Airspeed (KEAS) which corresponds to about 347 KEAS full-scale. The ASAP analysis agrees well with the measured subcritical damping values and stability boundary.

To quantify the effects of composite tailoring on stability, the stability boundaries for the baseline and tailored wing were measured at several airspeed and rotor speed combinations. With the wind tunnel and model stabilized at a certain airspeed, the rotor speed was gradually increased in 5-10 RPM increments until a neutral damping condition was reached. This procedure was repeated until the stability boundaries were defined throughout the operating range of the rotor as shown in figure 12. A direct comparison between the baseline and tailored wing stability boundaries shows an increase of approximately 30 KEAS (58 KEAS full-scale). For a full-scale design, the 58-kt increase in stability boundary represents a significant stability improvement.

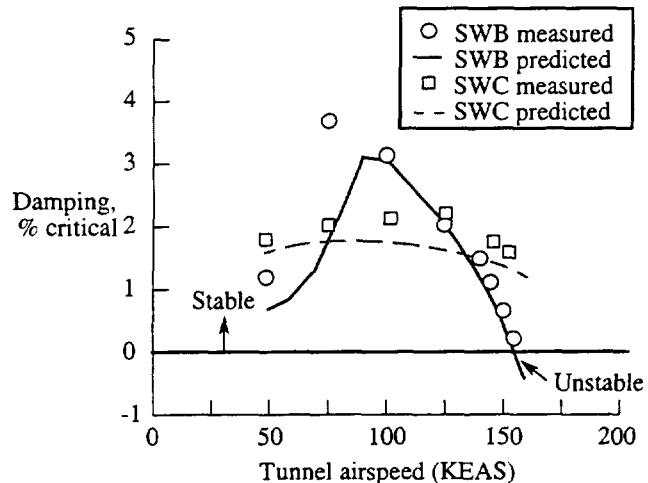


Figure 11: Comparison of analysis and test results for the off-downstop configuration.

Tailored Wing / Soft-Inplane Rotor Study

An analytical investigation of aeroelastic tailoring for stability augmentation of soft-inplane tiltrotors is being conducted at Penn State through a NASA LaRC Graduate Student Researcher Program (GSRP) grant. Some preliminary results of this study, as reported in reference 15, show that aeroelastic tailoring of the tiltrotor wing may be used to stabilize an air resonance instability associated with the Boeing Model 222 soft-inplane hingeless tiltrotor system. This particular system was free from any ground resonance instability, as discussed in reference 2, because the low frequency cyclic lag mode did not couple with the wing chord mode until a rotor speed of 1060 RPM was reached, which is well above the design rotor speed for this model. The wind-tunnel model could, however, experience an air resonance in low-speed airplane mode when subjected to a rotor speed sweep. The resonance would occur due to coupling of the wing beam bending mode (the wing mode of interest in airplane mode since it couples with the rotor inplane motion) with the low-frequency lag mode around 500 RPM. The Penn State investigation showed that the addition of beamwise-bending-twist coupling in the wing could be either stabilizing or destabilizing to the resonance, depending on the sign of the coupling used, as shown in figure 13. The positive bending-twist-coupling (bending up pitches hub up) in the amount considered shows that the air resonance may be completely stabilized. Positive beam-bending-twist coupling is, however, destabilizing to whirlflutter. Further analyses are to be performed under this grant to determine if a suitable compromise may be

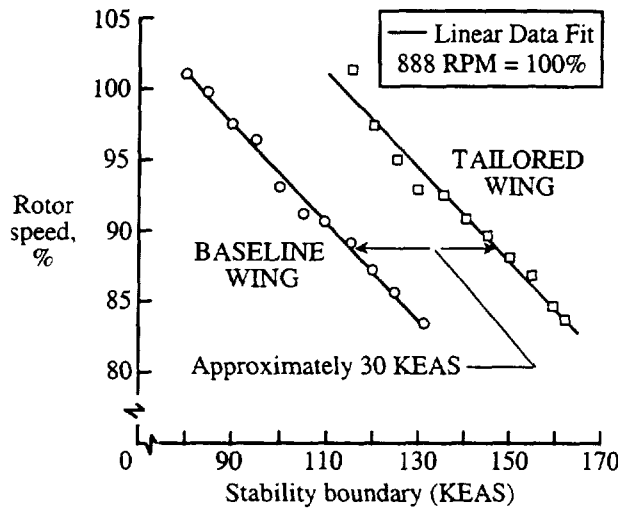


Figure 12: Comparison of measured stability boundaries for the baseline and tailored wings in the off-downstop configuration.

achieved between the stabilizing and destabilizing influences associated with wing aeroelastic tailoring.

AEROELASTIC TAILORING OF TILTROTOR BLADES

General Anisotropic Rotor Blade Modeling

There is a potential for improving the performance and aeroelastic stability of tiltrotor aircraft through the use of elastically-coupled composite rotor blades. An important aspect of achieving these potential improvements is the development of analyses which properly model the complex effects associated with elastic couplings. Currently, comprehensive aeroelastic rotocraft codes, because of their complexity and size, are limited to modeling the elastic rotor blade using a one-dimensional (beam) theory. Thus, there has been an emphasis on deriving one-dimensional generally anisotropic beam theories which can capture the important characteristics of anisotropic composite rotor blades, structures that are more readily defined using two and three-dimensional theories. With improved cross-section analyses and beam theories that include effects associated with warping, shear deformation, large pretwist, and anisotropy (such as those presented in references 16-18) there are few rotor blade structures, including the flexbeam, that cannot be accurately modeled using beam theory, at least in terms of predicting the global response, dynamic characteristics, and aeroelastic stability of rotor systems.

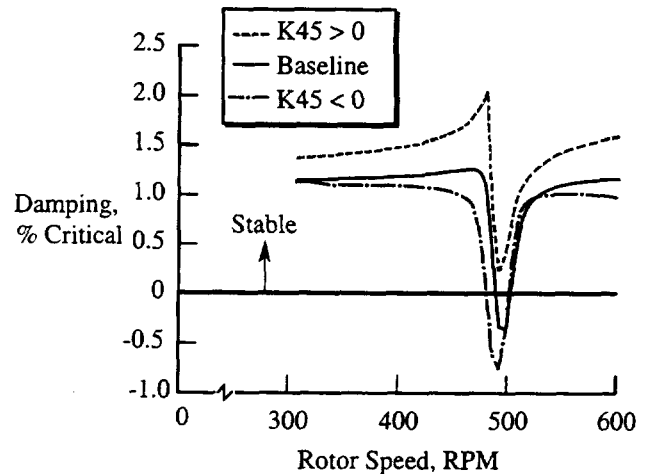


Figure 13: Influence of wing beamwise-bending-twist coupling on tiltrotor air resonance.

In developing a rotor blade design with elastic couplings it is desirable to maintain favorable elastic and dynamic characteristics of the blades, especially if a baseline system is used as a template for the elastically tailored design. The study of reference 19 provides a valuable resource for estimating the limits to which elastic couplings may be introduced into a baseline rotor blade, considering simultaneously the important constraints on changes to blade stiffness characteristics. A cross-section analysis such as that described in reference 18 can provide the coupled stiffness matrix of a general anisotropic beam as

$$\begin{bmatrix} k_{11} & k_{12} & k_{13} & k_{14} \\ k_{21} & k_{22} & k_{23} & k_{24} \\ k_{31} & k_{32} & k_{33} & k_{34} \\ k_{41} & k_{42} & k_{43} & k_{44} \end{bmatrix} \begin{Bmatrix} e \\ k_\eta \\ k_\zeta \\ \theta \end{Bmatrix} = \begin{Bmatrix} P \\ M_\eta \\ M_\zeta \\ M_z \end{Bmatrix} \quad (2)$$

where $[k]$ is the symmetric coupled stiffness matrix; e , k_η , k_ζ , and θ are the displacements in the extensional, chord-bending, flap-bending, and twist directions, respectively; and P , M_η , M_ζ , and M_z are the forces in the same respective directions. Many cross-section analyses will provide two additional degrees of freedom relating the shear strains and shear forces for the beam, but these may be statically condensed to the 4×4 representation above as is described in reference 20. For an isotropic, untwisted beam the elastic twist is independent of extension and bending ($k_{14} = k_{24} = k_{34} = 0$), and the diagonal terms represent the extension stiffness ($k_{11} = EA$), bending stiffnesses with shear deformation effects already included ($k_{22} = EI_f$, $k_{33} = EI_c$), and torsion stiffness ($k_{44} = GJ$). The remaining coupled stiffness terms, k_{12} , k_{13} , and k_{23} are used to define the centroid and principle axes of the cross section at which point they become zero.

By considering the appropriate subsets of equation 2, the study of reference 19 defines three nondimensional

coupling parameters that may be used to define the magnitude and type of coupling in a given structure as:

$$\Psi_{ET}^2 = \frac{k_{14}^2}{EAGJ} \quad (3)$$

$$\Psi_{FT}^2 = \frac{k_{24}^2}{EI_f GJ} \quad (4)$$

$$\Psi_{CT}^2 = \frac{k_{34}^2}{EI_c GJ} \quad (5)$$

where the subscripts *ET*, *FT*, and *CT* refer to extension-twist, flapwise-bending-twist, and chordwise-bending-twist, respectively; and because of the requirement that strain energy be positive the three coupling parameters are bounded between 0 and 1. These parameters are useful because they can be used to define realistic coupled stiffness terms for comprehensive aeroelastic analyses without performing a full anisotropic cross section analysis. While the coupling parameters are physically limited to values less than 1, the parametric studies of reference 19 show that in practice Ψ will be below 0.5, and the influence of the coupling on effective blade bending stiffnesses is generally small for values of Ψ below 0.2. The study also defined a set of nondimensional variables related to laminate thickness, ply angle, chord length, and spar width, and developed an associated set of plots which may be used to estimate realistic values of elastic coupling parameters for any rotor blade of typical construction based only on knowledge of the uncoupled classical stiffnesses. An example of the use of these plots is developed later in the bending-twist-coupled studies section of this paper.

Extension-Twist-Coupled Blade Studies

Passive Twist Control Studies. There have been a number of investigations which have focused on improving tiltrotor performance by using elastic tailoring to passively change rotor blade twist distribution between the helicopter and airplane flight modes. The concept of changing blade twist between flight modes can be realized with the use of composite rotor blades, designed to exhibit extension-twist coupling (ETC) through an arrangement of off-axis ply angles and stacking sequences. In forward flight, the rotor speed of a tiltrotor is typically 15% less than it is in hover. Thus, there is a net change in centrifugal forces which can be used to passively improve the twist distribution for each flight mode. The aerodynamic performance efficiency associated with a range of linear blade twist distributions for a tiltrotor in hover and forward flight modes is illustrated in figure 14. This plot is developed using momentum theory and a nonuniform inflow model, but does not consider wake recirculation and other three dimensional aerodynamic effects which

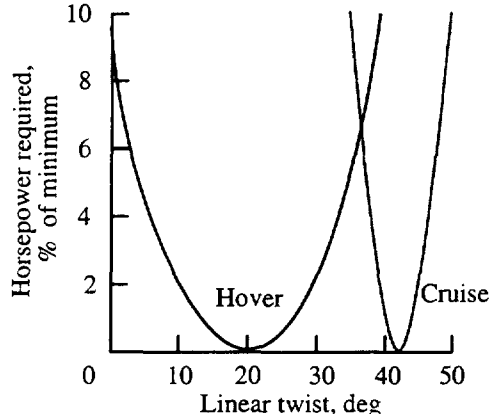


Figure 14: Power required in hover and forward flight as a function of blade linear twist.

may lessen the influence of twist on performance. While the plot suggests that about a 6% improvement to both the hover and cruise efficiencies is possible as compared to a compromised twist for both flight regimes, the extent of the improvement in aerodynamic performance depends on how closely the actual twist developed in hover and forward flight approaches the optimum twist in each of the two modes. This, in turn, depends on the magnitude of twist deformation which can be produced within the material strength limit of the blade structure. As the allowable twist deformation increases, so does the ability to obtain desirable twist distributions in both modes of flight. Although the desired twist change occurs between hover and cruise flight, it is the twist change caused by increasing rotation velocity from 0 to its maximum (hover) value which produces the maximum blade stresses. For structural substantiation of a design, the centrifugally generated stresses must be considered simultaneously with bending stresses resulting from air and inertia loads.

In reference 21, passive twist control concepts are applied to the extension-twist-coupled design of a rotor blade for the XV-15 tilt rotor assuming a 15% change in operation rotor speed between hover and cruise. This particular design was restricted to match the baseline XV-15 blade properties (mass distribution, bending and torsion stiffnesses, and c.g. locations), and with these requirements only about 0.5° of twist change was developed. A second study was performed which allowed deviations from the baseline XV-15 blade with respect to bending and torsion stiffnesses, but retained the baseline mass distribution and c.g. locations. This design resulted in a 2° twist change over the same 15% rotor speed range.

Experimental Studies of Extension-Twist-Coupled Structures. The experimental studies of reference 22 showed that composite tubes constructed to optimize twist deformation as a function of axial force

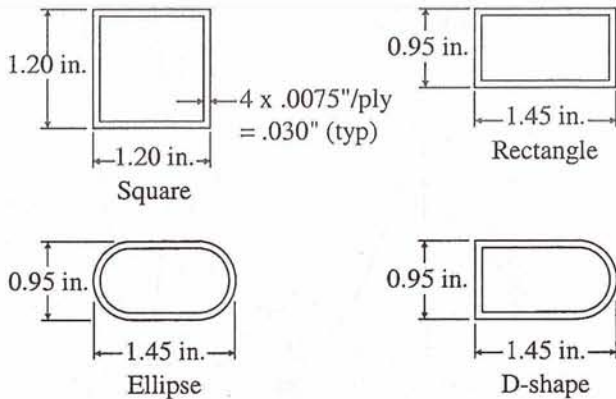


Figure 15: Four cross section shapes tested to determine effects of warping on ETC.

could produce extremely large twist rates within the material allowable stresses associated with the axial loads alone. Twist rates of nearly 0.5 deg/in were produced which translates to twist deformations on the order of 48° of twist over the tailorable span of an XV-15 rotor blade.

These experimental studies were extended in reference 23 to include cross sections of noncircular shape, as shown in figure 15, such that the effects associated with warping and shear deformation on the extension-twist behavior could be examined. This experiment, with setup illustrated in figure 16, demonstrated that the noncircular shapes were less effective at producing twist deformation for a given amount of axial load, but significant twist could still be produced within the material strength considerations. In particular, the important influence of warping restraint near a fixed boundary was shown to have an important effect on the prediction of the torsional stiffness and thus also the twist deformation produced under an axial load.

With the demonstration of large twist deformations produced by extension-twist-coupled test specimens, the analytical study of reference 24 was performed to determine the benefits of such structures to tiltrotor blade design. This study considered an extension-twist-coupled blade design subject to no restrictions on the structural blade properties other than to meet material allowable stress requirements for typical blade loadings. Unlike the study of reference 21, the study of reference 24 also considered the mass distribution as a design variable so that the centrifugal forces required to impart the elastic twist changes could be maximized. Three extension-twist-coupled rotor blade designs were developed with the most characterizing feature of each being the amount of tip weight used. Design-1 had 15 lbs. of tip weight which could be accommodated by conventional helicopter rotor

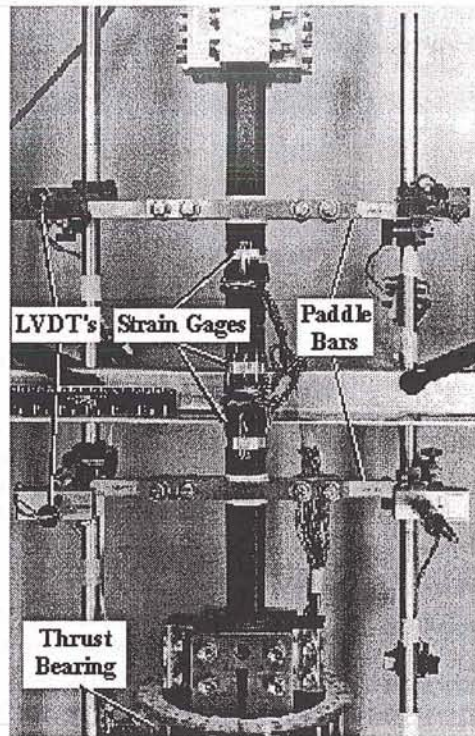


Figure 16: Experimental setup for ETC tube tests.

blades. Design 2 had 60 lbs. of tip weight which is much more than that used in conventional designs. Design-3 was not limited in tip weight which resulted in the maximum twist deformation possible under the design assumptions of the study, but the weight increase made the design impractical. All three designs were obtained by optimizing for maximum twist deformation subject to material strength constraints. The elastic twist change available for each design was used to determine its hover twist distribution based on using the optimum linear twist distribution for cruise. The plot of figure 17 shows the resulting twist distributions associated with the nonrotating, cruise, and hover conditions of Design-1. The performance in cruise mode was optimum for all the cases due to use of this twist distribution as a starting point for the designs. The hover performance associated with each design is illustrated in figure 18. This plot shows that if the optimum linear twist for cruise was used also for hover that about 8% more power would be required in the hover condition. The twist change associated with the extension-twist-coupled design is predicted to improve the power requirements in hover by 4% to 8%.

A hover study of passive extension-twist-coupled rotor blades was performed as described in reference 25 to determine if the twist deformations of ETC blades could be predicted accurately in a rotating environment, and to examine the influence on twist deformation that may

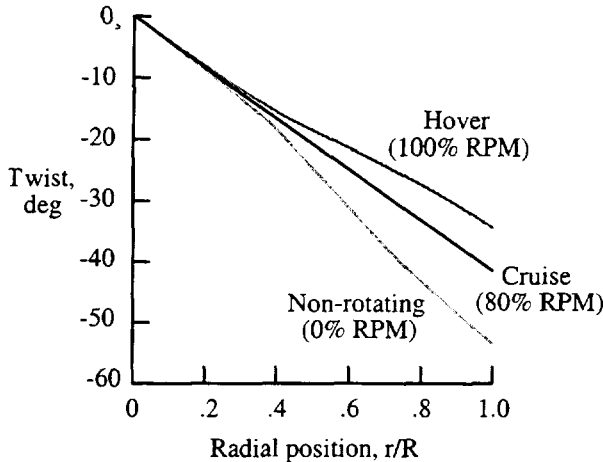


Figure 17: Twist distributions for the ETC blades in non-rotating undeformed state.

occur due to the propeller-moment and aerodynamic moment effects. For this test, a set of composite model rotor blades was manufactured from existing blade molds for a low-twist helicopter rotor blade, but the ETC design incorporated 20° off-axis plies in the Gr/E spar to obtain the desired coupling, the cross section of which is illustrated in figure 19. The figure shows that weight tubes were present, allowing additional mass to be added to the blade. Data were obtained for both a ballasted (increase in effective tip weight) and unballasted blade configuration in sea level atmospheric conditions over a large range in collective settings. The influence of collective on the twist deformation showed the influence of the propeller moment on the twist. The unique capabilities of the NASA LaRC TDT were used to repeat some of the tests in near-vacuum conditions as a means of determining the effect of aerodynamic contributions to the twist. Maximum twists of 2.54° and 5.24° were obtained at 800 RPM for the ballasted and unballasted cases, respectively. These results compared well with predictions from a NASTRAN finite element model as illustrated in figure 20. The influence of the propeller moment and aerodynamic moment were found to be minimal, with changes in twist less than 0.2° contributed from these effects.

Aeroelastic Stability of Extension-Twist-Coupled Rotor Blades. Despite the extensive analytical and experimental studies of ETC structures as described in the previous paragraphs, the capability to examine the dynamic effects of ETC rotor blades were limited during the time of these studies because the comprehensive aeroelastic analyses available did not provide modeling for such generally anisotropic elastically-coupled rotor blades. Most of these analyses

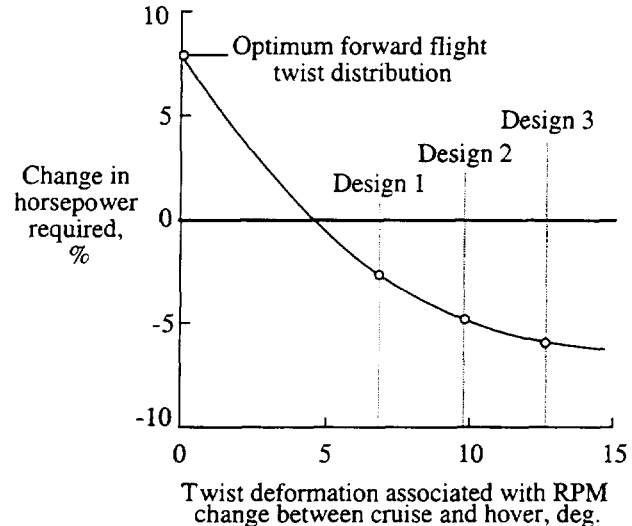


Figure 18: Power requirements in hover as a function of twist deformation produced.

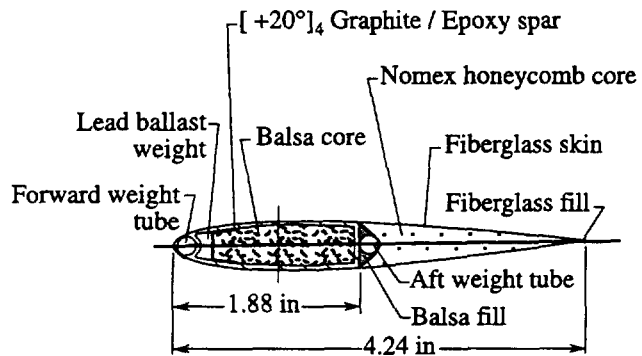


Figure 19: Cross section composition of the ETC blade hover tested in the TDT.

also did not contain an axial degree of freedom with which the analytical models could be modified for ETC coupling.

In the study of reference 26, the performance, response, and stability of a tiltrotor with elastically-coupled composite rotor blades was examined. This study included a development of the analytical tools required to perform these tasks by adding required capabilities associated with tiltrotor configuration modeling and general anisotropic beam modeling to the University of Maryland Advanced Rotor Code (UMARC). The modified analysis provided the capability to examine the influence of ETC on blade loads and aeroelastic stability in addition to the performance predictions as previously discussed. Using a similar procedure as that of reference 24, the performance of a tiltrotor in hover and cruise was predicted using ETC

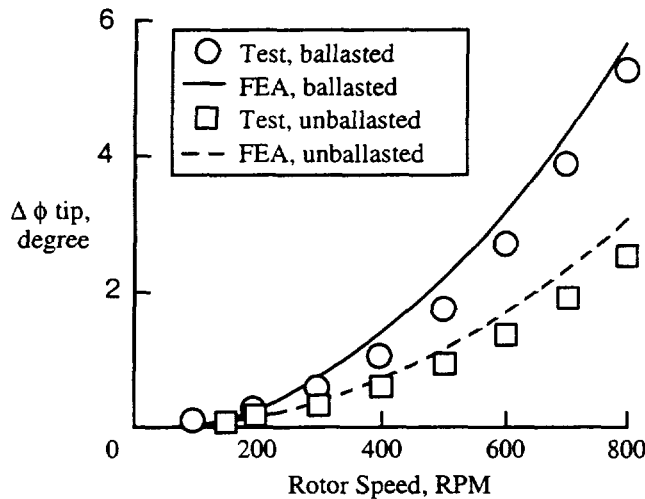


Figure 20: Twist deformations measured and predicted for the ballasted and unballasted ETC rotor blade set.

rotor blades with varying amounts of tip-weight added to develop twist distributions that were optimum for cruise and near-optimum for hover. The hover results as illustrated in figure 22 show that the ETC designs were predicted to improve the hover performance over the baseline twist distribution by as much as 7%. The performance for the cruise mode was predicted to improve by about 2% which is valid for all cases.

The study of reference 26 also examined the effect of the ETC rotor blades on aeroelastic stability. The addition of tip-weights as required to obtain the twist deformations desired to optimize performance were found to have a highly destabilizing influence on whirlflutter. The dominant effect is associated with the pitch-lag coupling in the rotor system that is created by the tip-weight in combination with precone and a reduction in the rotor thrust between hover and cruise. This effect, as is illustrated in figure 3, results in a large negative spring relating torsion moment about the pitch axis to blade lag deformation. The damping in airplane mode for a baseline XV-15 semispan wing and rotor blade model is compared with ETC blade version of the model in figure 23. These results show that the destabilizing influence of ETC blade designs can be quite significant, with flutter velocities predicted to drop by at least 50% for the designs considered.

Bending-Twist-Coupled Blade Studies

Whirlflutter Stability Augmentation. The study of reference 26 considered the use of bending-twist-coupling in rotor blades for augmenting tiltrotor whirlflutter stability. This coupling may be used to counteract the inherent negative pitch-lag coupling which is signifi-

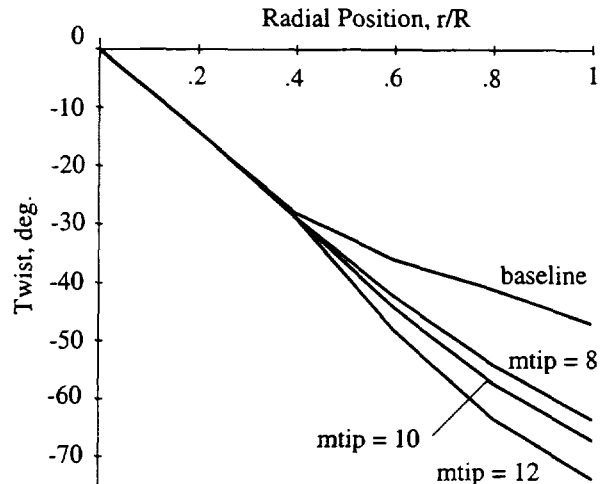


Figure 21: Undeformed (nonrotating) twist distributions of the ETC blade designs.

cant in the airplane mode of tiltrotors and is destabilizing to whirlflutter, as is discussed in previous sections of this paper. A more thorough explanation of the factors influencing rotor pitch-lag coupling is presented in references 26 and 27, and some of this discussion is offered in the following paragraph to help explain how the elastic coupling is beneficial.

Consider the rotor system in hover. Here the rotor disc loading is high, so to offset large blade bending moments, rotor precone is introduced. As shown in figure 6, the precone gives a component of centrifugal force which opposes the lift force. With ideal precone these forces balance, and there is no net bending moment imposed on the rotor blade (at least for some desired spanwise location on the blade). Now consider the rotor system in airplane cruise. The disc loading decreases by an order of magnitude compared to the hover value because lift is generated by the wing and the thrust now only is required to overcome drag. The centrifugal force component perpendicular to the blade also decreases because of the lowered rotor speed, but not nearly as much as the reduction in blade lift forces. Thus, in cruise there is a significant imbalance of centrifugal force tending to bend the rotor blade back (flap down). This imbalance creates a torsion moment about the blade inboard sections proportional to the lag bending deflection as illustrated in figure 6. Now consider a simplified static torsion balance of the rotor blade where only the lag deflection, torsion deflection and flapping moment are included. The net flap moment due to aerodynamic and centrifugal forces has a torsional component proportional to lag which must be balanced by the blade torsional stiffness:

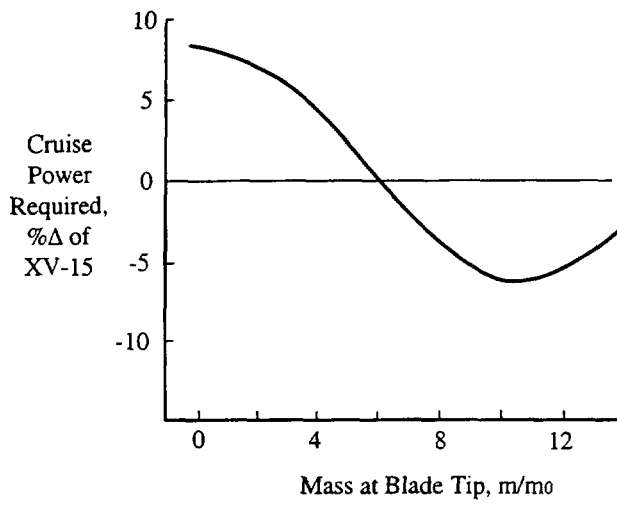


Figure 22: Hover performance for ETC blades as a function of tip-weight.

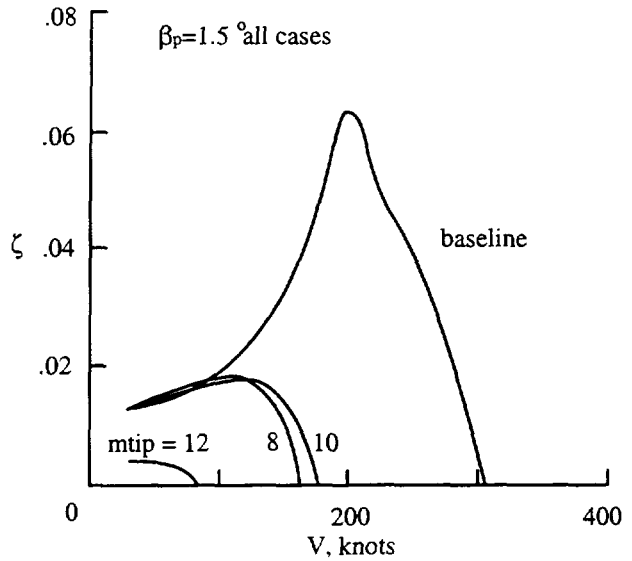


Figure 23: Destabilizing influence of extension-twist-coupling on tiltrotor stability.

$$M_\beta \eta + I_\theta \omega_\theta^2 \theta = 0 \quad (6)$$

where M_β is the net bending moment, η is the lag deflection, I_θ is the torsional inertia, ω_θ is the torsional frequency, and θ is the local torsional deflection. If the blade is considered to be semi-rigid such that the lag and torsional deflections occur at the root of the blade, then an effective kinematic pitch-lag coupling term can be defined as

$$K_{P\eta} = -\frac{\theta}{\eta} = \frac{M_\beta}{I_\theta \omega_\theta^2} \quad (7)$$

where $K_{P\eta} > 0$ gives lag-back/pitch-down coupling. The flap moment at the blade root is given by

$$M_\beta = \gamma \int \frac{L}{ac} r dr - \beta_p - \beta_{trim} \quad (8)$$

where L is the blade lift at a given spanwise position, β_p is the precone angle, and β_{trim} is the elastic coning angle. In hover, the precone is selected to balance the lift so M_β is small and $K_{P\eta}$ is small. In cruise, the precone term dominates so the kinematic pitch-lag coupling can be estimated by:

$$K_{P\eta} = \frac{\beta_p}{I_\theta \omega_\theta^2} \quad (9)$$

Therefore, the precone and torsional stiffness determine the pitch-lag coupling, and this coupling happens to have a significant effect on tiltrotor stability in high-speed

flight. The effective kinematic coupling of an XV-15 model is estimated in reference 27 to be -0.3 which is considered a high value.

From the discussion of the previous section, it appears that if positive pitch-lag coupling were introduced into the rotor system to offset the negative pitch-lag coupling introduced by rotor precone, then the stability characteristics should improve. There are two methods which may readily be used to introduce positive pitch-lag coupling (lag-back/pitch-down): kinematic coupling in the control system and elastic bending-twist coupling in the rotor blade. There are several reasons why the use of kinematic coupling to develop positive pitch-lag coupling may present difficulties, as are discussed in reference 26. The current paper focuses on explaining the potential for using elastic tailoring to produce the desired coupling effects.

A basic concept for a bending-twist-coupled rotor blade used in tiltrotor cruise mode is illustrated in figure 24. An untwisted blade is used in the diagram to clarify the deformation directions. The collective in tiltrotor cruise mode is on the order of 40° to 50° at the 75% spanwise station. As tiltrotor blades are also highly twisted, the inboard portion of the blade is at pitch angles on the order of 60° to 70°, which places the flapwise-bending direction of the local blade cross section more in line with the in-plane direction (defined by the plane of rotation) than the chordwise-bending direction. For a stiff-inplane system, where the virtual lag hinge is going to be outboard of the blade pitch axis, the rotor system pitch-lag coupling is influenced most effectively by flapwise-bending-twist cou-

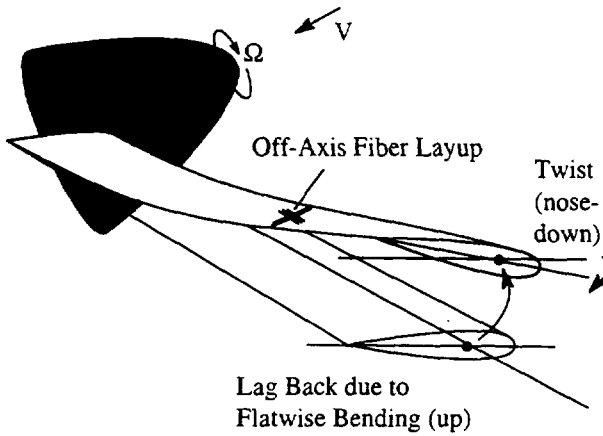


Figure 24: A Bending-Twist-Coupled Blade in Cruise Mode.

pling in the rotor blade.

Using the elastic coupling parameters definitions defined in reference 19, the aeroelastic analysis of reference 26 was used to determine the aeroelastic stability of a semi-span tiltrotor model with wing and rotor system characteristics similar to that of the XV-15, but with increasing amounts of flapwise-bending-twist coupling in the rotor blades. The influence on whirlflutter stability associated with the addition of elastic coupling is illustrated in figure 25 for three values of the flapwise-bending-twist elastic coupling parameter, Ψ_{FT} . The baseline case ($\Psi_{FT} = 0$) is predicted to become unstable at about 280 knots. The velocity at which the system becomes unstable is shown to increase with the magnitude of flapwise-bending-twist coupling, Ψ_{FT} , to near 400 knots with the maximum amount of Ψ_{FT} considered. Using the charts of reference 19, example of which are illustrated in figures 26 and 27, the elastic coupling used in this study may be achieved by rotating the principle axis of the laminate by less than 5°, and the corresponding reduction of the effective flapwise-bending stiffness is shown in figure 27 to be less than 2%. Similarly, the plots in reference 19 may be used to determine that the torsional stiffness would increase by about 2% and the chordwise stiffness would decrease by about 5% for $\Psi_{FT} = 0.1$. These results indicate that the use of flapwise-bending-twist-coupled blades may provide a very favorable influence on stability without creating adverse effects on performance, blade loads, or rotor system dynamics.

SUMMARY

The studies reported in this paper focus on four unique aeroelastic tailoring concepts: 1) bending-twist (pitch-bending) coupling in the wing to augment aeroelastic

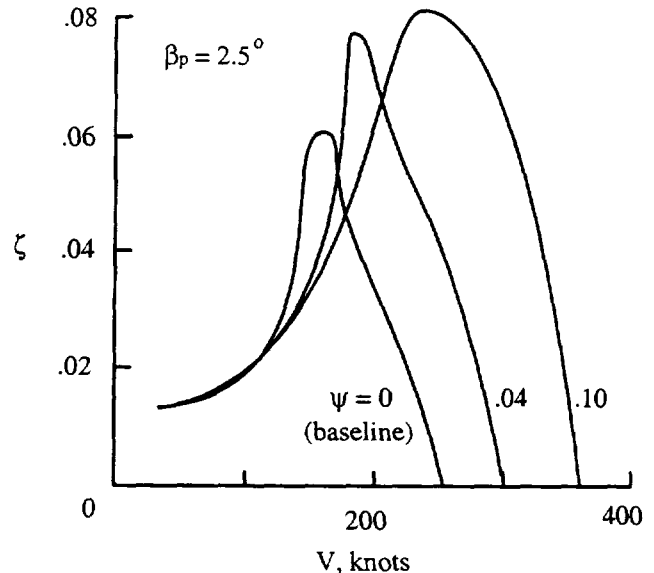


Figure 25: Effect of flapwise-bending-twist coupling on whirlflutter stability.

stability associated with whirlflutter in high-speed airplane mode, 2) bending-twist coupling in the wing to augment aeromechanical stability of soft-inplane rotor systems subject to ground and air resonance, 3) bending-twist coupling in the rotor blades to reduce rotor pitch-lag coupling and thereby augment aeroelastic stability associated with whirlflutter in high-speed airplane mode, and 4) extension-twist coupling in the rotor blades to optimize blade twist distribution between hover and cruise and thereby gain an aerodynamic performance improvement. The studies associated with augmenting whirlflutter stability show that both wing and blade tailoring are effective, with increases in stability boundaries of at least 50 knots predicted based on existing systems. The wing-tailoring study for soft-inplane rotor systems shows that bending-twist coupling in the wing can be used to avoid ground and air resonance, but these results are preliminary, and further analysis must be conducted to determine feasibility of the beneficial couplings on tiltrotor in other flight modes. Finally, the several studies devoted to extension-twist coupling indicate that, while there is a performance payoff for optimizing blade twist, the required stiffness and mass changes are shown to be extremely destabilizing to tiltrotors in whirlflutter, indicating that the passive twist control concept may not be feasible for the current tiltrotor systems.

Relative Merits of Blade and Wing Tailoring

The aeroelastic studies presented in this paper show that either wing or blade tailoring may be used to significantly increase the aeroelastic stability boundaries for

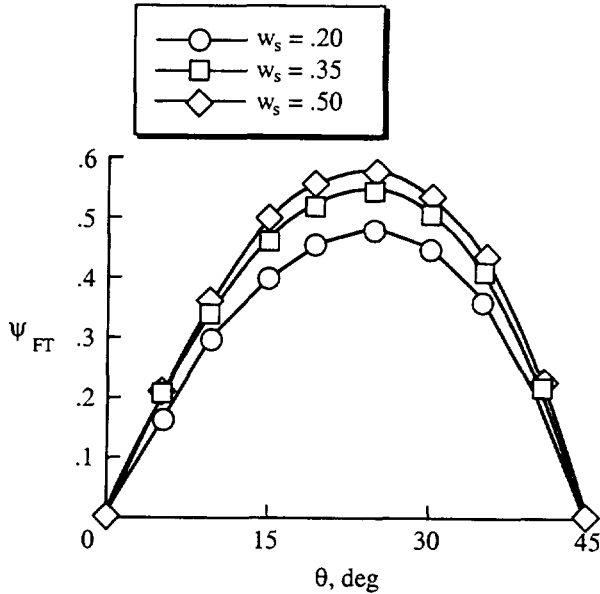


Figure 26: Flapwise-bending-twist coupling parameter as a function of ply angle.

tiltrotors in high-speed flight. Considering the complexities and greater risks associated with modifying structures designed for the rotating environment, it is generally accepted that fixed system modifications are preferred. This favors wing tailoring over blade tailoring and explains why the investigations associated with composite tailored wings have already been tested in the wind tunnel and considered in full-scale design studies. One drawback of wing tailoring, however, is that the stability augmentation of the wing may be limited by instabilities associated with the wing chord mode which is not necessarily improved by the elastic couplings used to augment aeroelastic stability of the wing beam mode. To obtain the stability margins necessary for even greater cruise speeds, such as the anticipated 400-knot class of tiltrotors predicted for future designs, the blade and wing tailoring concepts presented may need to be considered together.

REFERENCES

1. Alexander, H.R. and Leone, P.F., "VSTOL Dynamics and Aeroelastic Rotor-Airframe Technology," Volume I, AFFDL-TR-72-40, January 1973..
2. Alexander, H.R., Hengen, L.H., and Weiberg, J.A., "Aeroelastic-Stability Characteristics of a V/STOL Tilt-Rotor Aircraft with Hingeless Blades: Correlation of Analysis and Test," 30th Annual Forum of the American Helicopter Society, May 1974.
3. Gaffey, T. M., "The Effect of Positive Pitch-flap Coupling (Negative δ_3) on Rotor Blade Motion Stabil-
4. Settle, T.B. and Kidd, D.L., "Evolution and Test History of the V-22 0.2-Scale Aeroelastic Model," American Helicopter Society National Specialists' Meeting on Rotorcraft Dynamics, Arlington, TX, Nov 1989.
5. Schilings, J. J., Roberts, B. J., Wood, T. L. and Wernecke, K. G., "Maneuver Performance of Tiltrotor Aircraft," 43rd Annual Forum of the American Helicopter Society, St. Louis, MO, May 1987.
6. Agnihotri, A., Schuessler, W., and Marr, R., "V-22 Aerodynamic Loads Analysis and Development of Loads Alleviation Flight Control System," 45th Annual Forum of the American Helicopter Society, Boston, Massachusetts, May 1989.
7. Nixon, M. W., "Parametric Studies for Tiltrotor Aeroelastic Stability in Highspeed Flight", *J. American Helicopter Society*, October 1993
8. Johnson, W., "Dynamics of Tilting Proprotor Aircraft in Cruise Flight," NASA TN D-7677, May 1974.
9. Corso, L. M. and Nixon, M. W., "Design, Analysis, and Test of a Composite Tailored Wing," American Helicopter society 53rd Annual forum, Virginia Beach, VA, April 1997.
10. Schillings, J. J. and Reinesch, R., "The Effect of Airframe Aerodynamics on V-22 Rotor Loads," American Helicopter Society National Specialists' Meeting

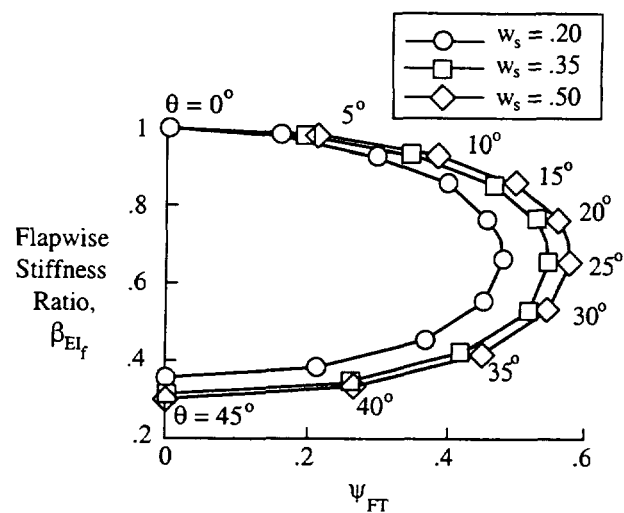


Figure 27: Flapwise-bending stiffness ratio as a function of the flapwise-bending-twist coupling parameter.

ity and Flapping,", *J. American Helicopter Society*, April 1969..

- ity and Flapping,", *J. American Helicopter Society*, April 1969..
4. Settle, T.B. and Kidd, D.L., "Evolution and Test History of the V-22 0.2-Scale Aeroelastic Model," American Helicopter Society National Specialists' Meeting on Rotorcraft Dynamics, Arlington, TX, Nov 1989.
 5. Schilings, J. J., Roberts, B. J., Wood, T. L. and Wernecke, K. G., "Maneuver Performance of Tiltrotor Aircraft," 43rd Annual Forum of the American Helicopter Society, St. Louis, MO, May 1987.
 6. Agnihotri, A., Schuessler, W., and Marr, R., "V-22 Aerodynamic Loads Analysis and Development of Loads Alleviation Flight Control System," 45th Annual Forum of the American Helicopter Society, Boston, Massachusetts, May 1989.
 7. Nixon, M. W., "Parametric Studies for Tiltrotor Aeroelastic Stability in Highspeed Flight", *J. American Helicopter Society*, October 1993
 8. Johnson, W., "Dynamics of Tilting Proprotor Aircraft in Cruise Flight," NASA TN D-7677, May 1974.
 9. Corso, L. M. and Nixon, M. W., "Design, Analysis, and Test of a Composite Tailored Wing," American Helicopter society 53rd Annual forum, Virginia Beach, VA, April 1997.
 10. Schillings, J. J. and Reinesch, R., "The Effect of Airframe Aerodynamics on V-22 Rotor Loads," American Helicopter Society National Specialists' Meeting

- on Aerodynamics and Aeroacoustics, Arlington, Tx, February 1987.
11. Popelka, D., Lindsay, D., Parham, T., Berry, V., and Baker, D., "Results of an Aeroelastic Tailoring Study for a Composite Tiltrotor Wing," American Helicopter Society 51st Annual forum, Fort Worth, Texas, May 1995.
 12. Popelka, D., Sheffler, M., and Bilger, J., "Correlation of Test and Analysis for the 1/5th Scale V-22 Aeroelastic Model, *J. American Helicopter Society*, Vol. 32, (2), April 1987.
 13. Idol, R., and Parham, T., "V-22 Aeroelastic Stability Analysis and Correlation with Test Data," American Helicopter Society 51st Annual forum, Fort Worth, Texas, May 1995.
 14. Hammond, C.E. and Doggett, R.V., "Determination of Subcritical Damping by Moving Block/Randomdec Applications," NASA Symposium on Flutter Testing Techniques, NASA SP-415, October 1975, pp. 59-76.
 15. Howard, A. K.T., "Aeroelastic Tailoring in Soft-Inplane Hingeless Tiltrotors," Presented at the AHS Lichten Competition Northeast Region, Philadelphia, PA, Jan 1999.
 16. Bauchau, O.A., "A Beam Theory for Anisotropic Materials," *J. Applied Mechanics*, Vol. 52, June 1985, pp. 416-422.
 17. Hodges, D.H., Atilgan, A.R., Cesnik, C.E.S., and Fulton, M.V., "On a Simplified Strain Energy Function for Geometrically Nonlinear Behaviour of Anisotropic Beams," *Composite Engineering*, Vol. 2, Nos 5-7, pp. 513-526, 1992.
 18. Kosmatka, J. B., "On the Behavior of Prewisted Beams With Irregular Cross-Sections," *J. Applied Mechanics*, vol. 114, March 1992, pp. 146-152.
 19. Piatak, D. J., Nixon, M. W., and Kosmatka, J. B., "Stiffness Characteristics of Composite Rotor Blades With Elastic Couplings," NASA TP 3641, ARL TR 1279, April 1997.
 20. Nixon, M. W., and Hinnant, H.E.: Dynamic Analysis of Prewisted Elastically-Coupled Rotor Blades. Presented at the 1992 ASME Winter Annual Meeting, Anaheim, CA, November 8-13, 1992 (Also available as NASA TM 109070 Jan 1994).
 21. Bauchau, O.A., Loewy, R.G., and Bryan, P.S.: An Approach to Ideal Twist Distribution in Tilt Rotor VSTOL Blade Designs. AHS 39th Annual Forum, May 1983.
 22. Nixon, M.W., "Extension-Twist Coupling of Circular Tubes with Application to Tilt rotor Blade Design," AIAA Paper 87-0772, 28th Structures, Structural Dynamics and Materials Conference, Monterey, CA, April 1987.
 23. Nixon, M.W., "Analytical and Experimental Investigations of Extension-Twist-Coupled Structures," Master's Thesis, The George Washington University, NASA Langley Research Center, Hampton, VA, May 1989.
 24. Nixon, M.W., "Improvements to Tilt Rotor Performance Through Passive Blade Twist Control," NASA TM 100583, AVSCOM 88-B-010, April 1988.
 25. Lake, R.C., Nixon, M.W., Wilbur, M.L., Singleton, J.D., Mirick, P.H., "Demonstration of an Elastically Coupled Twist Control Concept for Tilt Rotor Blade Application," *AIAA Journal*, Vol. 32, No. 7, pp. 1549-1551, July 1994.
 26. Nixon, M. W., "Aeroelastic Response and Stability of Tiltrotors With Elastically-Coupled Composite Rotor Blades," Ph.D. Diss., University of Maryland, 1993.
 27. Johnson, W., "Dynamics of Tilting Proprotor Aircraft in Cruise Flight," NASA TN D-7677, May 1974.

Analysis of Fuselage Vibrations Induced by the Proprotor in a Tiltrotor Aircraft

5/3-05

M. Gennaretti and U. Iemma

Assistant Professors

Department of Ingegneria Meccanica e Industriale
University Roma TRE
via Vasca Navale 79 - 00146 Rome, Italy
e-mail m.gennaretti@uniroma3.it

ABSTRACT

The aim of the present paper is the analysis of the aerodynamically induced fuselage vibrations for proprotor-fuselage configurations which are of interest in tiltrotor aircraft. As widely known, the development of technology concerning tiltrotor aircraft is of primary interest in modern aeronautical research. This type of vehicle combines advantageous takeoff and landing procedures (similar to those needed by helicopters), with cruise performances that are analogous to those of currently used propeller-driven airplanes. Noting such flexibility in flight operations, it may be anticipated a large impact of this kind of aircraft on the aeronautical transport field in the next future. Here, we consider different proprotor-fuselage configurations which include those related to vertical takeoff and landing (horizontal proprotor disk), and cruise conditions (vertical proprotor disk). In the fuselage vibration analysis, the elastic displacements are expressed in terms of series expansions on a complete set of orthogonal functions. The forcing terms in the structural dynamics equations, which depend on the exterior pressure field, are obtained from the analysis of the interactional aerodynamics of the fuselage-proprotor system. This will be accomplished by a boundary element method for compressible potential flows, based on a boundary integral equation for the velocity potential. The application of the Bernoulli theorem yields the pressure distribution and hence the aerodynamic loads acting on the fuselage. The formulation presented has been applied to a simple, but realistic, fuselage configuration. Numerical results are presented for external pressure fields generated by a proprotor in three different flight conditions, corresponding to the takeoff and landing phase (horizontal rotor disk), cruise (vertical rotor disk), and the conversion phase (45 degrees angle between the rotor axis and the fuselage axis). In order to validate the methodology on a simple test case, the results obtained for an external pulsating point source are also included.

INTRODUCTION

In the present paper we present an integrated modal-integral formulation for the aeroelastic analysis of the fuselage vibrations induced by the proprotor in a tiltrotor aircraft. This type of vehicle combines advantageous takeoff and landing procedures, similar to those needed by helicopters, with cruise performances aligned to those of the modern propeller-driven general aviation airplanes. Noting these characteristics, a large impact of this kind of aircraft in the short-midrange aeronautical transportation is to be expected in the next future. Consequently, the development of tools devoted to the analysis and design of tiltrotor aircraft is of primary interest in the modern aeronautical research. Here, we address the problem of the aerodynamically-driven fuselage vibrations induced by the proprotor during three typical flight conditions, corresponding to the vertical takeoff and landing configuration, the cruise, and the intermediate conversion phase. The fuselage is modeled as a thin cylindrical elastic shell closed at the upwind and downwind extremes by two rigid hemispherical domes. These enclosures are introduced in order to ensure the smoothness of

the streamlines around the fuselage-like body (eliminating the sharp edges introduced by a simple cylindrical geometry), without affecting the structural dynamics (note that the domes are assumed to remain in the position they have in the undeformed fuselage configuration has it would be obtainable in a wind tunnel test keeping them fixed by proper supports). The displacements of the elastic shell are expressed in terms of series expansions on a complete set of orthogonal functions. The application of the Galérkin method yields a set of ordinary differential equations for the modal amplitudes of the elastic deflections. To evaluate the generalized aerodynamic forces acting on the fuselage we use a boundary integral equation formulation for the velocity potential, based on that presented in Morino.⁴ This is solved by means of a boundary element method; the pressure is evaluated from the potential through the Bernoulli's theorem, and the generalized forces are determined by projection over the modes of the shell. The formulation above is closely related to that first presented in Iemma, Trainelli, and Morino¹ and Iemma *et al.*,² where preliminary applications to a spherical shell at rest were included, and extended in Iemma and Gennaretti⁸ to the analysis of a cylindrical shell in uniform translation. In those papers, the aeroelastic formulation used here is coupled to the acoustics of the cavity enclosed within the elastic shell, in order to predict the cabin noise induced by external sound sources. Here, the emphasis is on the analysis of the elastic behaviour of the fuselage; thus, the influence of the internal acoustics is not taken into account (this is justified by the fact that the feedback due to the interior acoustics on the elastic displacement is negligible for this kind of problems), and the external field is obtained by the solution of the complete interactional aerodynamics of the fuselage-propotor system.

In order to validate the methodology on a simple test case first, we present the results obtained for a translating fuselage-like shaped structure, forced by an external pressure field generated by a pulsating point source, rigidly connected to the shell. Then, we present applications of this formulation to the analysis of more realistic fuselage-propotor configurations, corresponding to different flight conditions. In particular, we consider the takeoff and landing phase, where the propotor disk is in a horizontal plane, the cruise condition, where the rotor disk is on a vertical plane, and the conversion phase, for which we assume an angle of 45 degrees between the rotor axis and the fuselage axis.

In the next section, the approach used for the structural dynamics of the fuselage is described. Then, the boundary element approach used for the solution of the exterior aerodynamic field and the aeroelastic operator are examined. Finally, preliminary numerical results for the configurations described above will be presented.

FUSELAGE STRUCTURAL DYNAMICS

As mentioned above, except for the nose and the tail-end that are assumed to be rigid, the fuselage is modeled as an elastic thin cylindrical shell with circular section. Here, we present the equations governing the dynamics of the fuselage, forced by the exterior unsteady pressure that is induced by the aerodynamic field generated by both the propotor rotation and the structural vibrations.

Following the linear theory developed in Ref. [5], the dynamics of this shell is described in terms of the elastic displacements $u(x, \theta, t)$, $v(x, \theta, t)$ and $w(x, \theta, t)$ that represent, respectively, the axial deformation, the azimuthal deformation and the radial deformation of its middle surface (with (x, θ) representing a system of cylindrical coordinates defined over the shell surface). Specifically, the shell dynamics is governed by a set of three coupled differential equations of the following type (see Ref. [5]),

$$\varrho_s \ddot{u} + \mathcal{L}_{uu}[u] + \mathcal{L}_{uv}[v] + \mathcal{L}_{uw}[w] = 0 \quad (1)$$

$$\varrho_s \ddot{v} + \mathcal{L}_{vu}[u] + \mathcal{L}_{vv}[v] + \mathcal{L}_{vw}[w] = 0 \quad (2)$$

$$\varrho_s \ddot{w} + \mathcal{L}_{wu}[u] + \mathcal{L}_{wv}[v] + \mathcal{L}_{ww}[w] = p, \quad (3)$$

where the \mathcal{L} 's are linear differential operators describing the effects of elastic displacements on the equilibrium equations (e.g., \mathcal{L}_{uv} is the linear operator describing the effects of the azimuthal displacement, v , on the axial equilibrium equation), and ϱ_s denotes the mass per unit area of the shell. Furthermore, p denotes the exterior normal pressure acting on the shell surface, given by the aerodynamic field generated by the fuselage and proprotor motions. In this work, we assume hinged edge conditions for the shell model of equations (1) – (3). These conditions (and the condition of periodic solution along the azimuthal coordinate) are satisfied if one expresses the elastic displacement in terms of the following series

$$u(x, \theta, t) \approx \sum_{m=1}^M \sum_{n=0}^N [a_{mn}^c(t) \Phi_{mn}^c(x, \theta) + a_{mn}^s(t) \Phi_{mn}^s(x, \theta)], \quad (4)$$

$$v(x, \theta, t) \approx \sum_{m=1}^M \sum_{n=0}^N [b_{mn}^c(t) \Phi_{mn}^c(x, \theta) + b_{mn}^s(t) \Phi_{mn}^s(x, \theta)], \quad (5)$$

$$w(x, \theta, t) \approx \sum_{m=1}^M \sum_{n=0}^N [q_{mn}^c(t) \Phi_{mn}^c(x, \theta) + q_{mn}^s(t) \Phi_{mn}^s(x, \theta)], \quad (6)$$

where

$$\Phi_{mn}^c(x, \theta) = \sin\left(\frac{m\pi x}{L}\right) \cos(n\theta), \quad \Phi_{mn}^s(x, \theta) = \sin\left(\frac{m\pi x}{L}\right) \sin(n\theta), \quad (7)$$

are a complete set of orthogonal functions (with L denoting the length of the shell under consideration), whereas the time dependent coefficients of the combinations, $a_{mn}^c(t)$, $a_{mn}^s(t)$, $b_{mn}^c(t)$, $b_{mn}^s(t)$, $q_{mn}^c(t)$ and $q_{mn}^s(t)$, represent the structural Lagrangean coordinates of the aeroelastic system under examination.

Then, combining equations (1) – (3) with equations (4) – (6), and applying the Galérkin approach, the shell dynamics is described by a set of $P = 3 \times M \times (2N + 1)$ ordinary differential equations for the unknown Lagrangean coordinates of the shell, which in matrix form is expressed as

$$\mathbf{M}\ddot{\mathbf{x}} + \mathbf{K}\mathbf{x} = \mathbf{f}, \quad (8)$$

where \mathbf{x} is the column matrix containing the Lagrangean coordinates, \mathbf{M} is the $P \times P$ diagonal mass matrix, \mathbf{K} is the $P \times P$ stiffness matrix, whereas \mathbf{f} is a P -element column matrix having the first $(2/3)P$ elements equal to zero, with the rest containing the following generalized aerodynamic forces

$$f_{mn}^c(t) = \int_0^L \int_0^{2\pi} p(x, \theta, t) \Phi_{mn}^c(x, \theta) dx d\theta, \quad f_{mn}^s(t) = \int_0^L \int_0^{2\pi} p(x, \theta, t) \Phi_{mn}^s(x, \theta) dx d\theta, \quad (9)$$

i.e., projections of the aerodynamic pressure in the direction of the functions in equation (7).

AERODYNAMIC OPERATOR

Observing equations (4) – (6), we note that the fuselage vibrations are induced by unsteadiness of aerodynamic pressure acting on its surface. Specifically, the pressure term forcing the shell dynamics appears in the equilibrium equation along the radial direction (equation (3)) and the coupling terms are responsible for extension of its effects in the axial and azimuthal equilibrium equations. From the application of the Galérkin approach, this forcing term yields the generalized aerodynamic forces mentioned above (see equation (9)). In our problem, the fuselage unsteady pressure distribution is influenced by the perturbation induced by the proprotor rotation and shell vibrations. Hence, the aerodynamic pressure field is decomposed as

$$p = p_{sc} + p_{inc}, \quad (10)$$

where p_{inc} is the incident pressure due to the external source of perturbation (the proprotor), whereas p_{sc} is the pressure scattered by the fuselage surface. Assuming that the external flow is potential (*i.e.*, such that $\vec{v} = \vec{\nabla}\phi$, with \vec{v} denoting the flow velocity and ϕ the potential function), and that p_{inc} (and the incident potential, ϕ_{inc}) is a known field, the scattered pressure field is here analysed by first using a boundary element approach for the solution of the scattered potential field, ϕ_{sc} , and then applying the Bernoulli theorem. Specifically, starting from the following wave equation for the scattered potential field in compressible subsonic flows, expressed in a frame of reference connected with the undeformed fuselage, and having velocity $\vec{v}_R = -u_0 \vec{i}$,

$$\nabla^2 \phi_{sc} - \frac{1}{c^2} \left(\frac{\partial}{\partial t} + u_0 \frac{\partial}{\partial x} \right)^2 \phi_{sc} = 0, \quad (11)$$

and applying a boundary integral equation approach, one obtains (see Ref. [6])

$$\phi_{sc}(\vec{x}, t) = \int_{S_F} \left[G \frac{\partial \phi_{sc}}{\partial \vec{n}} - \phi_{sc} \frac{\partial G}{\partial \vec{n}} + G \dot{\phi}_{sc} \frac{\partial \hat{\theta}}{\partial \vec{n}} \right]^\theta dS(\vec{y}). \quad (12)$$

In the integral equation (12), $G(\vec{x}, \vec{y}) = -1/(4\pi r_\beta)$ is the unit source solution of equation (11) with $r_\beta = ([\vec{m}_R \cdot (\vec{y} - \vec{x})]^2 + \beta^2 \|\vec{y} - \vec{x}\|^2)^{1/2}$, where $\vec{m}_R = (-u_0/c) \vec{i}$ is the Mach vector of the reference frame velocity and $\beta = (1 - m_R^2)^{1/2}$, whereas S_F denotes the fuselage surface having \vec{n} as a unit normal, and

$$\frac{\partial(\cdot)}{\partial \vec{n}} = \frac{\partial(\cdot)}{\partial n} - \vec{m}_R \cdot \vec{n} \vec{m}_R \cdot \vec{\nabla}(\cdot).$$

In addition, $[...]^{\theta}$ denotes evaluation at the retarded time $\hat{t} = t - \theta$, where the delay has the expression $\theta = [r_\beta - \vec{m}_R \cdot (\vec{y} - \vec{x})]/c\beta^2$ with $\hat{\theta} = [r_\beta + \vec{m}_R \cdot (\vec{y} - \vec{x})]/c\beta^2$. Furthermore, from the impermeability conditions on the fuselage surface, $\vec{v} \cdot \vec{n} = \vec{v}_F \cdot \vec{n}$, we have

$$\frac{\partial \phi_{sc}}{\partial n} = \vec{v}_F \cdot \vec{n} - \frac{\partial \phi_{inc}}{\partial n}, \quad (13)$$

from which it is apparent that the scattered potential depends upon both the fuselage motion (\vec{v}_F denotes the velocity of the fuselage surface) and the incident potential field.

Next, observing that $\vec{v}_F = \vec{v}_R + \vec{v}_{el}$, with \vec{v}_{el} denoting the fuselage surface velocity induced by the elastic deformation and such that $\vec{v}_{el} \cdot \vec{n} = f(q_{mn}^c, q_{mn}^s)$, taking the Laplace transformation of equation (12), writing its approximate discretized version by dividing the fuselage surface into panels (boundary element method - BEM), and applying the Bernoulli theorem, for the generalized forces acting on the fuselage structure, we finally have

$$\tilde{\mathbf{f}}_q = \mathbf{E}(s) \tilde{\mathbf{q}} + \mathbf{D}(s) \tilde{\phi}_{inc} \quad (14)$$

(see Ref. [7] for details on the determination of the matrices appearing in the equation above). In equation (14) \mathbf{f}_q is a $[M \times (2N + 1)]$ -element column matrix containing the generalized forces acting on the elastic portion of S_F , $\tilde{\mathbf{q}}$ is a $[M \times (2N + 1)]$ -element column matrix containing the structural Lagrangean variables q_{mn}^c, q_{mn}^s , and $\tilde{\phi}_{inc}$ is a column matrix containing the values of the incident potential at the center of the fuselage panels, whereas $\mathbf{E}(s)$ is the aerodynamic transfer function matrix describing the aeroelastic effects in the present analysis, and $\mathbf{D}(s)$ is the matrix that describes the influence of the incident potential (*i.e.*, the one generated by the proprotor). Note that, the matrix $\mathbf{D}(s)$ takes into account both the direct influence of the incident potential (*i.e.*, the forces due to the incident pressure), and the indirect one (*i.e.*, the influence of the incident potential on the boundary conditions of the scattered potential, and hence on the forces due to the scattered pressure).

AEROELASTIC OPERATOR

From the models described in the preceding sections for the fuselage structural dynamics and exterior aerodynamics, it is possible to determine the aeroelastic operator, *i.e.*, the transfer function matrix connecting the external disturbance (the incident potential due to the propotor in our analysis) to the Lagrangean variables describing the fuselage elastic deformation. Observing that

$$\mathbf{f} = \begin{Bmatrix} \mathbf{0} \\ \mathbf{0} \\ \mathbf{f}_q \end{Bmatrix}, \quad \text{and that} \quad \mathbf{x} = \begin{Bmatrix} \mathbf{a} \\ \mathbf{b} \\ \mathbf{q} \end{Bmatrix},$$

with \mathbf{a} and \mathbf{b} denoting the $[M \times (2N + 1)]$ -element column matrices containing, respectively, the structural Lagrangean variables a_{mn}^c, a_{mn}^s and b_{mn}^c, b_{mn}^s , Laplace-transforming equation (8), and combining it with equation (14), we have

$$[s^2 \mathbf{M} + \mathbf{K} - \hat{\mathbf{E}}(s)] \tilde{\mathbf{x}} = \hat{\mathbf{D}}(s) \tilde{\phi}_{inc}, \quad (15)$$

where

$$\hat{\mathbf{E}}(s) = \left[\begin{array}{c|c|c} \mathbf{0} & \mathbf{0} & \mathbf{0} \\ \hline \mathbf{0} & \mathbf{0} & \mathbf{0} \\ \hline \mathbf{0} & \mathbf{0} & \mathbf{E}(s) \end{array} \right], \quad \text{and} \quad \hat{\mathbf{D}}(s) = \left[\begin{array}{c} \mathbf{0} \\ \hline \mathbf{0} \\ \hline \mathbf{D}(s) \end{array} \right].$$

Finally, from equation (15) one obtains the following aeroelastic response model

$$\tilde{\mathbf{x}} = \mathbf{H}(s) \tilde{\phi}_{inc},$$

where the $[3 \times M \times (2N + 1)] \times [3 \times M \times (2N + 1)]$ transfer function matrix (aeroelastic operator), \mathbf{H} , is given by

$$\mathbf{H}(s) = [s^2 \mathbf{M} + \mathbf{K} - \hat{\mathbf{E}}(s)]^{-1} \hat{\mathbf{D}}(s).$$

NUMERICAL RESULTS

In this section we present some preliminary numerical results. The formulation outlined above has been applied to the aeroelastic response analysis of a fuselage-like shaped shell. The fuselage length, including the rigid emispherical enclosures, is $L_f = 14m$. The length of the elastic portion of the fuselage is $L = 10m$, and the radius of its section is $R = 2m$. All the results presented in the following, are given in terms of the elastic energy distribution on the shell surface computed using $M = N = 6$ in equations (4) – (6) (qualitatively similar results have been obtained for greater numbers of azimuthal and axial decomposition modes). Specifically, the harmonic content of the energy intensity is represented in the form of isolines plots on the developed shell surface, as a function of the axial abscissa x , and the azimuthal angle θ .

In order to validate the methodology on a relatively simple test case, first we present the results obtained considering the perturbation pressure field induced by a pulsating point source located in the horizontal plane of symmetry of the fuselage (corresponding to $\theta = 0^\circ$) at 5.3 meters from the fuselage axis. Figure 1 depicts the isoenergy lines on the surface of the shell, corresponding to the elastic response for an excitation frequency of $30Hz$, with no advancing velocity. As to be expected, the solution is symmetrical with respect to the azimuthal location of the external source, and the energy distribution is concentrated on the upwind and downwind region of the shell, due to the presence of the constraints. The effects of the motion of the fuselage-source system is presented in

Figure 2 where the same geometrical configuration is moving with a velocity $v_F = 140m/s$ in the negative x direction. The intensity of the elastic energy (not indicated in the figures, for the sake of illustration clarity) has been found to be much higher than in the preceding case (due to the higher dynamic pressure), and appears to be more distributed along the fuselage length. Furthermore, in Figure 3 the response to a perturbation having the same intensity and a frequency of $60Hz$, is depicted. In this case, the response energy levels are higher than in Figure 2, and this is due to a combination of both aerodynamic and structural effects.

Now, we move our attention to a more realistic tiltrotor configuration. The same fuselage-like shaped shell used in the preceding cases is coupled to a three-bladed proprotor, with radius $R_p = 3m$, and chord $c = 0.15m$. The blade is twisted in order to give an effective angle of attack variable from 0 degrees at the rotor hub, to 4 degrees at the blade tip. In all the following cases, the angular velocity is set to $600 RPM$, for a fundamental blade passing frequency of $f_0 = 30Hz$. The velocity potential induced on the surface of the fuselage by the proprotor has been evaluated using a boundary element method based on a boundary integral equation formulation for propellers, closely related to the one used here for the aerodynamics of the fuselage (see e.g., Gennaretti *et al.* 9). In Figures 4 to 6 we present the solution obtained for a fuselage–proprotor configuration corresponding to cruise conditions with velocity $v_F = 140m/s$. In this flight phase, the proprotor acts as a propeller, with the revolution axis parallel to the fuselage axis. The results presented in the three figures correspond, respectively, to the structural response at frequencies f_0 , $2f_0$, and $3f_0$. The rotor hub is located at the same position of the point source in the first test case. Figure 4 (corresponding to f_0) shows how the solution due to the input pressure signal generated by the proprotor is not symmetrical with respect to the hub azimuthal position. On the other hand, the comparison with Figures 5 and 6 reveals that this lack of symmetry gradually reduces for frequency corresponding to the second and third revolution harmonics. Note that, in this case the response energy levels slightly decrease as the frequency increases: the increase of the transfer function harmonic content is balanced by the fact that the harmonic content of the perturbation signal generated by the proprotor is much higher at $f = f_0$ than at $f = 2f_0$ and $f = 3f_0$.

Next, we have examined the aircraft in the conversion phase configuration and in the takeoff/landing condition. Specifically, for the solutions depicted in Figures 7 to 9 we assumed an angle between the fuselage axis and the rotor revolution axis of 45 degrees, whereas in Figures 10 to 12, dealing with the vertical flight phase, the proprotor disk is horizontal. Note that, in order to perform a comparison between the solution corresponding to different flight conditions, the advancing velocity is set at $v_F = 140m/s$ (although this implies unrealistic flight conditions). Again, the energy distributions appear to be concentrated at the fuselage extremes, but their values are much higher than those observed in the cruising case, mainly due to the difference in the relative orientation between the fuselage axis and the flight directions. Furthermore, in the takeoff/landing case, the energy levels decreases as the frequency increases, whereas, in the conversion phase, the energy levels computed for the frequency $2f_0$ are higher than those observed for the frequencies f_0 and $3f_0$.

A more realistic value for the translational velocity is used for the conversion and takeoff/landing test cases presented in Figures 13 to 18. It should be noted that, for both the conversion and takeoff/landing phases, the overall distribution of the elastic energy at the frequency of interest is similar to that obtained for the corresponding configuration at higher advancing velocity, whereas the energy levels have been computed to be much lower.

CONCLUDING REMARKS

An aeroelastic formulation for the prediction of the fuselage vibrations induced by the proprotor in a tiltrotor aircraft has been presented. The dynamics of the structure is described in terms of a linear combination of orthogonal functions, and is forced by the aerodynamic generalized forces due to the pressure acting on the exterior of the fuselage. The aerodynamic loads are obtained by

a boundary element method based on a boundary integral equation formulation valid for bodies in arbitrary motion. The methodology has been applied to the prediction of the aeroelastic response of a simple fuselage-like structure, when forced both by an external pulsating point source and by the pressure field induced by a close propulsor. The influence on the fuselage aeroelastic response of the aircraft velocity, and of the relative positions between fuselage and propulsor, has been examined.

REFERENCES

1. U. Iemma, L. Trainelli, and L. Morino, "A Finite State BEM Method for Acousto-aeroelasticity of Shells," Second AIAA/CEAS Aeroacoustics Conference, State College, PA, 1996.
2. U. Iemma, M. Gennaretti, L. Trainelli, L. Morino and A. Giordani, "A Unified Boundary Integral Formulation for Acousto-aeroelastic Analysis of Shells," 20th ICAS Conference Proceedings", Sorrento, Italy, 1996.
3. U. Iemma, L. Morino, and L. Trainelli, "Internal Noise Generated by Sources External to an Elastic Shell," First AIAA/CEAS Aeroacoustics Conference, Münich, Germany, 1995.
4. L. Morino, "Boundary Integral Equations in Aerodynamics," *Applied Mechanics Review*, Vol. 46, No. 8, pp. 445-466, 1993.
5. Timoshenko, S.P., and Woinowsky-Krieger, S., *Theory of Plates and Shells*, McGraw-Hill Intl. Editions, Singapore, 1959.
6. Morino, L., and Gennaretti, M., "Boundary Integral Equation Methods for Aerodynamics," in Computational Nonlinear Mechanics in Aerospace Engineering (Ed.: S.N. Atluri), AIAA Progress in Aeronautics and Astronautics, Vol. 146, AIAA, Washington, DC, 279-321, 1992.
7. Gennaretti, M., and Ponzi, C., "Finite-State Aerodynamic Modeling for Gust Load Alleviation of Wing-Tail Configurations," to appear in *The Aeronautical Journal*.
8. Iemma, U., and Gennaretti, M., "Integrated aeroacoustoelastic modeling for the analysis of the propeller-driven cabin noise", Fifth joint CEAS/AIAA Aeroacoustics Conference, Seattle, USA, 1999.
9. Gennaretti, M., Luceri, L., and Morino, L., "A Unified Boundary Integral Methodology for Aerodynamics and Aeroacoustics of Rotors", *Journal of Sound and Vibrations*, vol. 200, pp. 467-489, 1997.

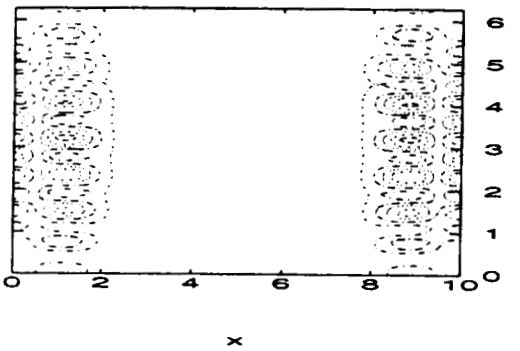


Figure 1: Isoenergy lines at 30 Hz for an external point source at rest.

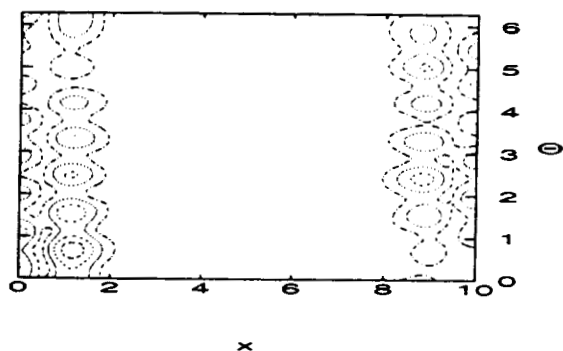


Figure 4: Isoenergy lines at 30 Hz for cruising tiltrotor. $v_F = 140\text{m/s}$.

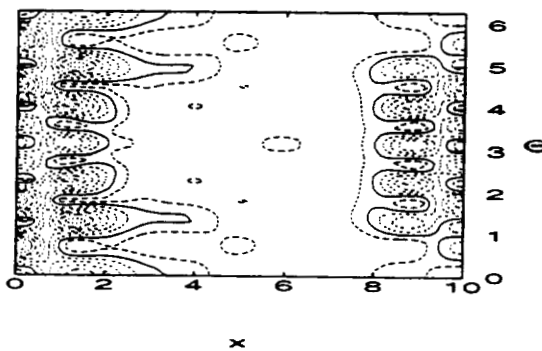


Figure 2: Isoenergy lines at 30 Hz for an external point source. $v_F = 140\text{m/s}$.

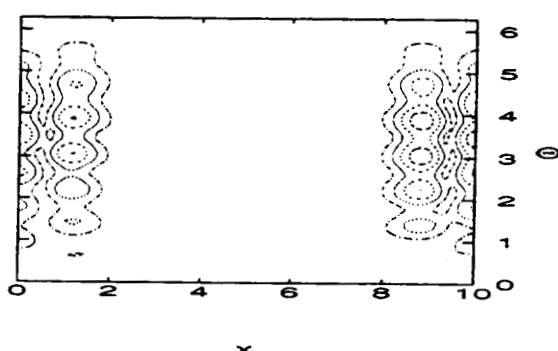


Figure 5: Isoenergy lines at 60 Hz for cruising tiltrotor. $v_F = 140\text{m/s}$.

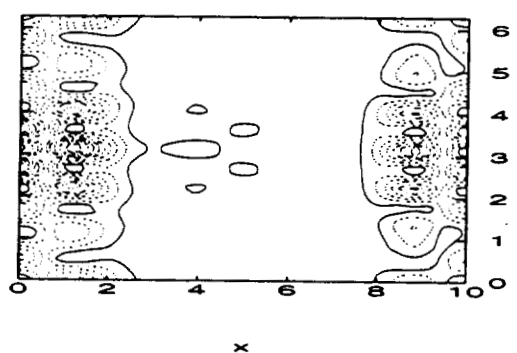


Figure 3: Isoenergy lines at 60 Hz for an external point source. $v_F = 140\text{m/s}$.

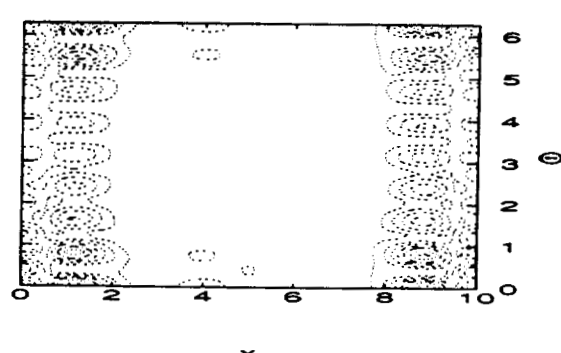


Figure 6: Isoenergy lines at 90 Hz for cruising tiltrotor. $v_F = 140\text{m/s}$.

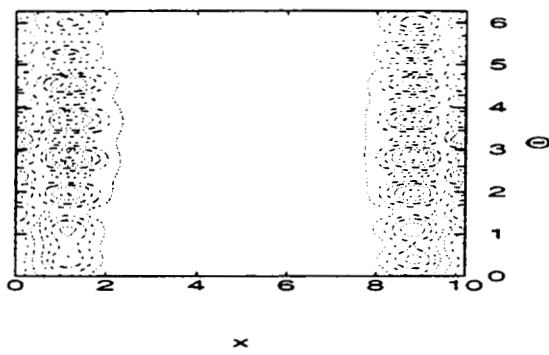


Figure 7: Isoenergy lines at 30 Hz during the conversion phase. $v_F = 140m/s$.

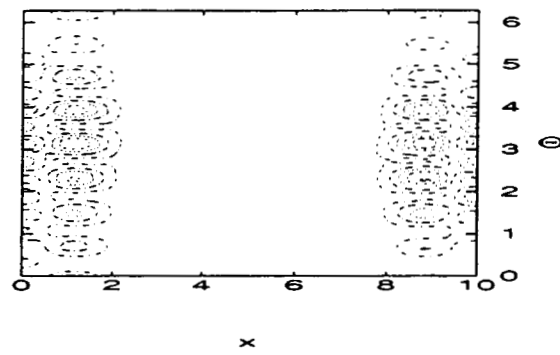


Figure 10: Isoenergy lines at 30 Hz in take-off/landing conditions. $v_F = 140m/s$.

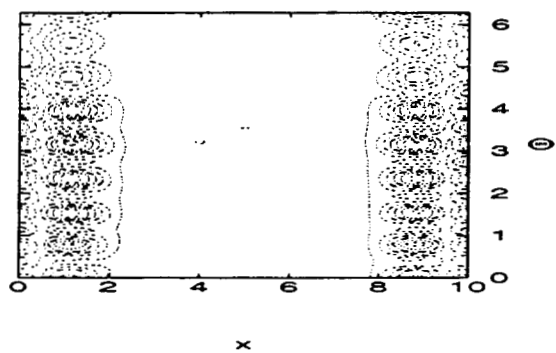


Figure 8: Isoenergy lines at 60 Hz during the conversion phase. $v_F = 140m/s$.

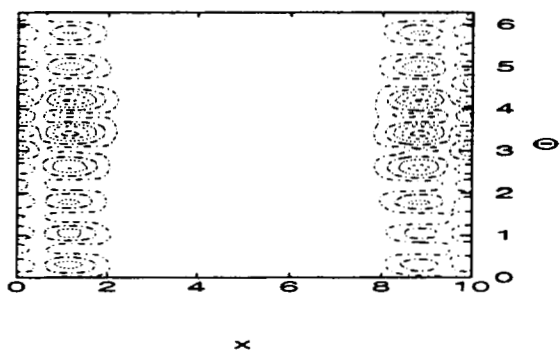


Figure 11: Isoenergy lines at 60 Hz in take-off/landing conditions. $v_F = 140m/s$.

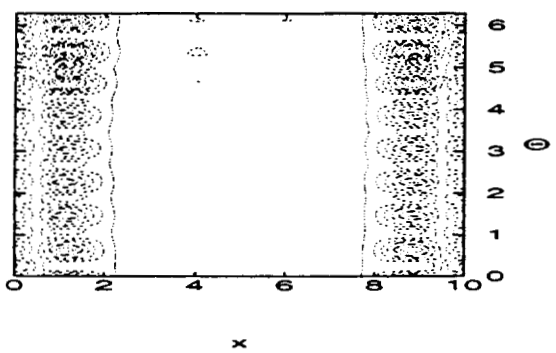


Figure 9: Isoenergy lines at 90 Hz during the conversion phase. $v_F = 140m/s$.

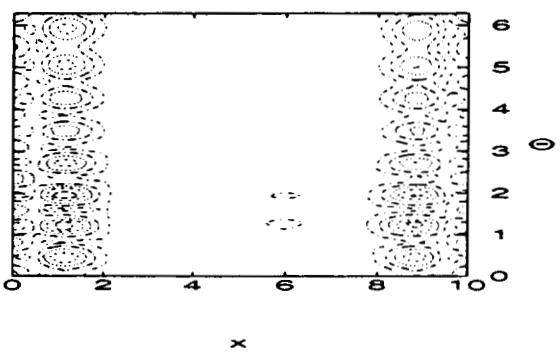


Figure 12: Isoenergy lines at 90 Hz in take-off/landing conditions. $v_F = 140m/s$.

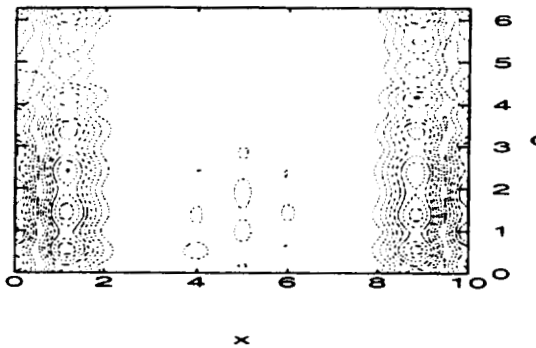


Figure 13: Isoenergy lines at 30 Hz during the conversion phase. $v_F = 14m/s$.

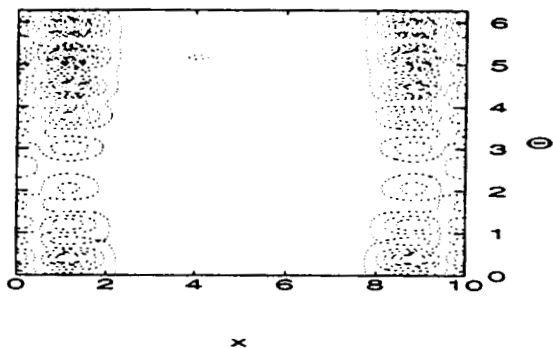


Figure 16: Isoenergy lines at 30 Hz in take-off/landing conditions. $v_F = 14m/s$.

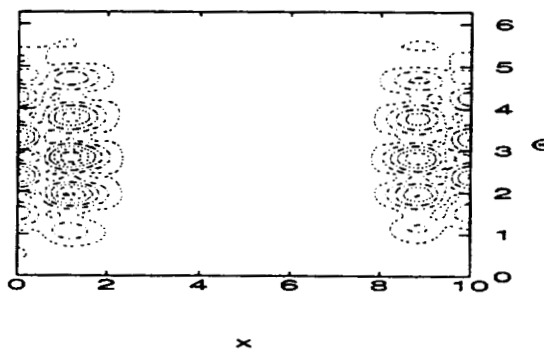


Figure 14: Isoenergy lines at 60 Hz during the conversion phase. $v_F = 14m/s$.

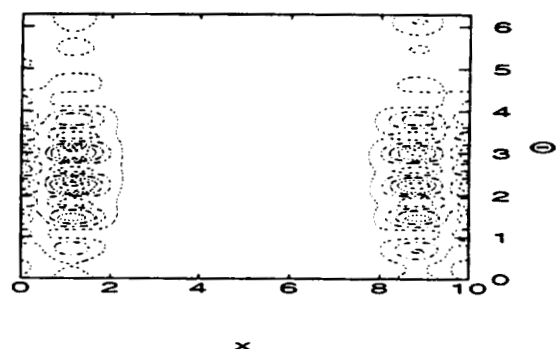


Figure 17: Isoenergy lines at 60 Hz in take-off/landing conditions. $v_F = 14m/s$.

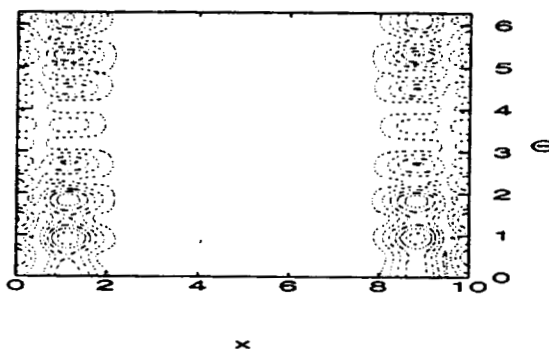


Figure 15: Isoenergy lines at 90 Hz during the conversion phase. $v_F = 14m/s$.

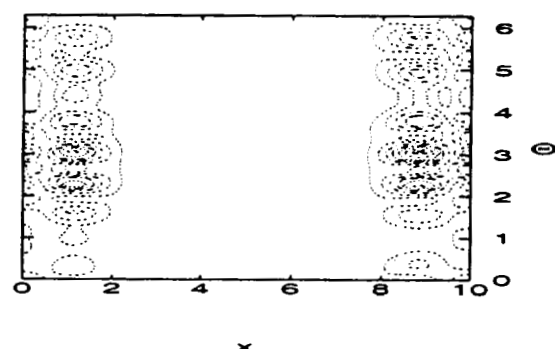


Figure 18: Isoenergy lines at 90 Hz in take-off/landing conditions. $v_F = 14m/s$.

Multi-Body Analysis of an Active Control for a Tiltrotor

G. L. Ghiringhelli

P. Maserati¹

P. Mantegazza

Politecnico di Milano

*Dipartimento di Ingegneria Aerospaziale
Milano, 20158 Italy*

M. W. Nixon

*Army Research Laboratories
NASA Langley Research Center
Hampton, VA 23681*

Abstract

The design of advanced rotorcrafts requires the ability to analyse sophisticated, interdisciplinar systems to a degree of refinement that only recently has become achievable at a low price, thanks to the improvements in computer power. Multi-body analysis allows the detailed modeling of the kinematics as well as of the structural properties of rather sophisticated mechanical systems, such as helicopter rotors. When integrated with aeroservoelastic analysis, it represents a powerful tool for both the analysis and the design of aircrafts, with particular regard to rotorcrafts. An original multi-body formulation is presented, based on the direct writing of a system of differential-algebraic equations (DAE) that describe the equilibrium and the kinematic constraints of a structural system. The finite rotations, during the time-step integration of the initial value problem, are handled in an efficient manner by means of a technique called "Updated-Updated Rotations", an *Updated Lagrangian* approach that uses as reference the predicted configuration of the system. This allows to neglect the rotation perturbations in the computation of the Jacobian matrix, with considerable computational savings, while preserving the accuracy by consistently computing the residual. Control equations and the related unknowns are added, to model the control system to the desired level of refinement, from idealised control input/output signals, to each servosystem component. The numerical analysis of a tiltrotor configuration is proposed, based on an analytical model of the WRATS wind tunnel model. This is a 1/5 scale model of the V-22 tiltrotor

aircraft, currently tested in the Transonic Dynamic Tunnel (TDT) at NASA Langley. The control strategy is based on the Generalized Predictive Control (GPC) technique, with a Recursive Least Mean Squares (RLMS) on-line identification of an equivalent discrete linear system, that is used to design the adaptive controller. The rotor pitch controls are used as actuators. Different combinations of strain gages and accelerometers are used as sensor devices.

Keywords: MULTI-BODY ANALYSIS, PREDICTIVE CONTROL, TILTROTOR

Introduction

Aerospace vehicles must satisfy many requirements on performances, but also on handling qualities, comfort, environmental impact. Aircraft and rotorcraft designers are required a great effort to allow operations close to, or even inside, highly populated areas, and to provide the crew and the passengers a confortable cockpit or seat, subject to as little vibrations and noise as possible. A viable answer to the latter requirements is represented by active control. The active control of rotorcraft has been investigated for a long time. Interest began early in the seventies, and grew continuously until today [16], [14]. Different techniques have been proposed to achieve the main goal of vibration and/or noise reduction. An exaustive *résumé* of

¹Corresponding Author,
via La Masa 34, 20158, Milano
Tel.: ++39(02)3933-2393
Fax: ++39(02)3933-2334
E-mail: masarati@aero.polimi.it

the state of the art and of the most promising developments can be found in Ref. [5]. Vibrations in the airframe can be reduced both by cancelling their effects or by eliminating their source, namely periodical blade airloads. In this paper the second approach is investigated. Basically, rotorcraft vibrations originate from the discrete nature of the rotor, that is made of a finite number of blades. This results in time-dependent aerodynamic loads in forward flight, related to the different airstream speed experienced by the blade when it is advancing and retreating, that results in dynamic stall and in reverse flow at the inner part, even for comparatively low advancing ratios. Noise and vibrations are also originated by the vortex sheet shed by a blade, when impacting on the following one (Blade-Vortex Interaction, or BVI). The loads generated by a rotor blade can be modified by acting on the blade pitch, both directly (i.e. by changing the pitch of the whole blade by means of the swashplate or other pitch control device) or indirectly (i.e. by actuating a trailing edge flap, that induces a blade twisting moment). Rotorcraft active control has been traditionally and naturally oriented towards Higher Harmonic Control-like (HHC) approaches ([10], [3], [13] among the others) because the blade pitch actuation mechanism represents an easy and cheap way to apply the required control power directly to the blade and requires limited additional power. Moreover, the periodic nature of the blade vibratory loads allow an easy design of harmonic control laws. Both open- and close-loop control have been investigated, the latter often being used in conjunction with the adaptive, in-line identification of a linearised, frequency domain transfer function of the rotorcraft. It suffers from some disadvantages, mainly related to the periodic nature of the control input and to the comparatively low maximum actuation frequency, resulting in limited flexibility. The Independent Blade Control (IBC) is complementary to the HHC. Each blade is considered as an independent system, and is controlled by an independent controller [9]. This technology is not as mature as HHC; the main problem that has to be faced is a viable and efficient means to deliver the control power into the rotating system [5], [8]. A different approach is used in the present work, based on the Generalised Predictive Control technique [2], [4], [11]. There is no exploitation of the periodic nature of the rotor dynamics as a means to generate

periodic control forces. On the contrary, the rotor, and the whole rotorcraft, are considered as a black-box that is identified on-line as a discrete-time, locally constant-coefficient linear system. The slow, long term variation of the system coefficients is accounted for by the recursive implementation of the identification. Based on the identified system, the response is predicted, and the control signal is designed by enforcing the desired behaviour of the controlled system. The paper first presents the predictive control theory that is used in the design of the control. A brief description of the multi-body formulation that is used for the analytical model of the tiltrotor is given, followed by a comparison with numerical and experimental results of the WRATS tiltrotor wind tunnel model [7]. This model, controlled by a proprietary implementation of the HHC called MAVVS, has been tested by Bell Helicopter at NASA Langley Research Center (LARC) [15]. Finally the numerical results of the proposed control technique are illustrated and discussed.

Discrete Control

Discrete Time Equation. A discrete time, Auto-Regressive, Moving Average, with exogenous input (ARMAX) equation has the form:

$$\begin{aligned} y(k) = & a_1 y(k-1) + \dots + a_p y(k-p) \\ & + b_0 u(k) + \dots + b_p u(k-p) \\ & + e(k) + c_1 e(k-1) + \dots + c_p e(k-p) \end{aligned}$$

where $y(t)$, $u(t)$ are the output and input arrays at time t , $e(t)$ is the error array at time t , a_j , $j = 1, p$, b_j , $j = 0, p$ and c_j , $j = 1, p$ are the matrices of a p -order, time-independent, linear discrete system. The number of equations is represented by the number of outputs m ; matrices a_i are $m \times m$, as matrices c_i are. Matrices b_i are $m \times n$, being n the number of inputs. Usually the matrices of the system are unknown, only measures of inputs and outputs being available; the error can be measurable or not, depending on its nature. An unmeasurable, biased error is assumed unless otherwise stated.

System Identification. The yet unknown system matrices can be stacked in a matrix Θ , while the observations can be stacked in an array $\varphi(k)$, as follows:

$$\Theta = [a_1, \dots, a_p, b_0, \dots, b_p, c_1, \dots, c_p]$$

$$\varphi = [y(k-1)^T, \dots, y(k-p)^T, u(k)^T, \dots, u(k-p)^T, e(k-1)^T, \dots, e(k-p)]^T$$

The predicted output is:

$$\hat{y}(k) = \Theta\varphi(k) \quad (1)$$

and the difference between the current and the predicted output represents the error at the current time step, which is unknown by definition. Matrix Θ depends on k as far as it is estimated from a finite set of measures; it approaches the exact value provided the true system has the form of the assumed model. Equation 1 gives a means to estimate the error at every time step in a recursive manner. The error may be due to unmeasured disturbances, errors in measures, and errors in the parameters of the model (type, order, and so on):

$$e(k) = y(k) - \hat{y}(k)$$

The observations at time steps ranging from i to j can be stacked by columns: $y = y(i:j)$, $\varphi = \varphi(i:j)$, $e = e(i:j)$, giving:

$$e = y - \Theta\varphi \quad (2)$$

where the expected output that results from the yet to be identified system, $y_e = \Theta\varphi$, is used. If the error is unbiased, Equation 2 does not depend on the error itself (the error does not participate in array φ) and thus Θ can be solved for a finite set of measures to determine the optimal value of the unknown parameters. In case of biased error, instead, it can be determined by recursively adding columns to Equation 2, and using each parameter estimate to compute the current estimate of the error. A global measure of the error is:

$$J = ee^T$$

The minimisation of J with respect to Θ gives a least squares fit of the system:

$$\Theta = y\varphi^T (\varphi\varphi^T)^+$$

where the \dagger denotes the pseudo-inversion, that is required in case the system is only semi-definite. In this case, the excitation is not persistent, or the system is not completely controllable.

Recursive Implementation. The recursive expressions of matrices $\varphi\varphi^T$ and $y\varphi^T$ are:

$$(\varphi\varphi^T)_{j+1} = (\varphi\varphi^T)_j + \varphi(k+j)\varphi(k+j)^T$$

and:

$$(y\varphi^T)_{j+1} = (y\varphi^T)_j + y(k+j)\varphi(k+j)^T$$

The inverse of matrix $\varphi\varphi^T$ can be directly updated instead of factorising the updated matrix, by using the LDL^T factorisation, since the matrix is symmetric and positive definite or semidefinite in the worst case; the positive definiteness can be artificially enforced. In this way, the numerical loss of accuracy can be reduced while improving the efficiency of the computation. The recursive algorithm is:

$$\begin{aligned} \Phi(k)^\dagger &= \mu\Phi(k-1)^\dagger + \varphi(k)\varphi(k)^T \\ \psi(k) &= \mu\psi(k-1) + y(k)\varphi(k)^T \\ \Theta(k) &= \psi(k)\Phi(k) \\ e(k) &= y(k) - \Theta(k)\varphi(k) \end{aligned}$$

The first two above equations update the matrices $\Phi(k) = (\sum_{j=1,k} \varphi(j)\varphi(j)^T)^\dagger$ and $\psi(k) = \sum_{j=1,k} y(j)\varphi(j)^T$, where a forgetting factor μ has been used to identify a comparatively slowly time-varying system. The third equation updates the estimate of the system parameters; the last equation estimates the error at the current step. Artificial stabilisation of the moving average part of the system is required, since unstable error dynamics, that can occur during the identification especially in the initial phase, have no physical meaning [1].

Output Prediction. As soon as an estimate of the system to be controlled is available, either by parametric modelling or by black box identification, the horizon of the prediction can be easily extended. The predicted value at time $t = k+1$ is:

$$\begin{aligned} y(k+1) &= a_1y(k) + \dots + a_py(k-p+1) \\ &\quad + b_0u(k+1) + \dots + b_pu(k-p+1) \\ &\quad + c_1e(k) + \dots + c_pe(k-p+1) \end{aligned}$$

the difference between the predicted and the actual values being the error. By substituting the predicted value of the output at time $t = k$, it becomes:

$$\begin{aligned} y(k+1) &= a_1^1y(k-1) + \dots + a_p^1y(k-p) \\ &\quad + b_0^1u(k+1) + b_0^1u(k) + \dots + b_p^1u(k-p) \\ &\quad + c_1^1e(k-1) + \dots + c_p^1e(k-p) \end{aligned}$$

where the new system matrices are recursively defined as:

$$x_i^0 = x_i, \quad x_i^j = a_1^{j-1}x_i^0 + x_{i+1}^{j-1}, \quad x_{p+1} = 0$$

where x stands for a , b , and c , respectively. The predicted error at step k and beyond is assumed to be null since the error is assumed to be uncorrelated with the outputs, the inputs and the

past errors, while the estimates of the output are supposed to be exact. The predicted value at time $t = k + j$ becomes:

$$\begin{aligned} y(k+j) &= a_1^j y(k-1) + \dots + a_p^j y(k-p) \\ &\quad + b_1^j u(k-1) + \dots + b_p^j u(k-p) \\ &\quad + c_1^j e(k-1) + \dots + c_p^j e(k-p) \\ &\quad + b_0^0 u(k+j) + \dots + b_0^j u(k) \end{aligned}$$

Let s be the number of steps ahead of the prediction. The predicted outputs from time $t = k$ to time $t = k + s - 1$ become:

$$Y_s = AY_p + BU_p + CE_p + PU_s \quad (3)$$

The arrays and the matrices in Equation 3 are obtained by stacking the equations of the output at the above mentioned time steps, i.e. Y_s contains the predicted output at s future time steps from the current one; Y_p , U_p and E_p contain the (measured) outputs, inputs and errors at the previous p time steps, being p the order of the system, and thus are known; U_s contains the control inputs that must be determined to obtain the desired behaviour. The predicted output should be equal to a desired sequence of values, namely $Y_d = Y_d$, resulting in:

$$Y_d = AY_p + BU_p + CE_p + PU_s \quad (4)$$

Generalised Predictive Control. The so called *Minimum Variance Control* [2] descends from Equation 4 by directly imposing the desired output and solving with respect to the required control input. Under the assumption that the system has a direct transmission term (namely, matrix b_0 is invertible) and provided that it is minimum phase, one prediction step is sufficient. Moreover, the response follows the desired behaviour regardless of the required control effort, except for the (unpredictable, because uncorrelated by assumption) error $e(k)$. As a consequence, the variance of the error is minimal. The *Generalised Predictive Control*, on the other hand, represents an extension and a generalisation of this behaviour. The control still tries to force the system to follow the desired output starting from the current step, but the desired behaviour is imposed over a higher number of steps ahead. A prediction horizon higher than the control one can be used; in this case the desired response is imposed in a least square sense. Moreover, the control effort is accounted for by weighting the control output against the prediction error, to avoid saturation of the actuators and/or a rough behaviour. Another form of predictive control is called *Deadbeat Control* [12]. It has not been considered in this work since it can be obtained as a special case of a more general

formulation of the GPC (the same applies to the Minimum Variance), and because it resulted less efficient than the GPC itself, at least in the investigated case. The control output results from the minimisation of the functional

$$J = (Y_d - Y_s)^T (Y_d - Y_s) + \lambda U_s^T U_s$$

with respect to the control input U_s , yielding:

$$U_s = (P^T P + \lambda I)^{\dagger} P^T (Y_d - AY_p - BU_p - CE_p)$$

where λ is the control weight coefficient. The control input at time $t = k$ is given by:

$$u(k) = \alpha_c Y_p + \beta_c U_p + \gamma_c E_p + \delta_c Y_d$$

where δ_c is the last block-row of matrix $Q = (P^T P + \lambda I)^{\dagger} P^T$, and the feedback matrices are $\alpha_c = -\delta_c A$, $\beta_c = -\delta_c B$ and $\gamma_c = -\delta_c C$.

Physical Interpretation of the Predictive Control. The minimum variance control clearly represents a form of zero-pole cancellation. The control cancels the system poles and zeroes by inverting the system $A^{-1}B$. This operation is permitted only if the system is stable and minimum phase, and the resulting close-loop system statically responds to the current, unpredictable input only. The GPC attenuates this effect by simply shifting the poles and zeroes of the system towards higher frequencies. By properly choosing the coefficient λ , both non-minimum phase and unstable systems can be controlled, with limited loss in performances. The choice of the model order and of the prediction and control horizons are key to the effectiveness of the control. The order p must be high enough to account for all the meaningful poles of the system (a rule of thumb says that $p \times m$ should be equal to or slightly higher than the number of poles). But too high an order could result in a poor, and time consuming, identification. The prediction horizon s must be as high as p to ensure that the complete dynamics of the system is accounted for; higher prediction horizons do not add further information to the prediction, but, together with a smaller control horizon, result in an overcollocated enforcement of the desired behaviour, thus overconstraining, and implicitly reducing, the control effort.

Multi-Body Model

A multi-body formulation has been used to describe the dynamics of the tiltrotor. The

equilibrium equations of each node are written; lumped inertia is associated to each node. The bodies are connected by kinematic and dynamic joints. The former are written as algebraic equations that add reaction forces and couples as unknowns, while the latter directly participate in the equilibrium equations by adding configuration-dependent forces. An important example of dynamic constraint is represented by the beam element. Initial value problems are considered, by time integrating the resulting Differential-Algebraic Equation (DAE) system from an initial compatible and *a la d'Alembert* balanced configuration. A Predictor-Corrector integration scheme is used, based on an original formulation that ensures second order accuracy and linear $A - L$ stability, with tunable algorithmic damping [7].

Kinematics. The basic unknowns are represented by the positions and the reference frames of the nodes. The total positions x are used as nodal translational unknowns. Finite rotations are intrinsically nonlinear and require a special treatment in multi-body formulation kinematics. The rotations are described by means of the Gibbs-Rodrigues rotation parameters in a modified *Updated Lagrangian* scheme, called *Updated-Updated* [7], that assumes the predicted configuration as reference. The unknown rotation parameters account for the correction only, and can be considered truly “small”, provided the prediction is accurate. The rotation matrix R , as function of the rotation parameters g , is:

$$R = I + \frac{4}{4 + g^T g} \left(g \times + \frac{1}{2} g \times g \times \right)$$

where the \times represents the cross product between vectors, such that $a \times$ is the matrix that multiplied by b gives $a \times b$. In case of an updated scheme, the total rotation at time $k + 1$ is $R_{k+1} = R(g) R_k$ and in the updated-updated approach it reads $R_{k+1} = R(g) R_{k+1}^0$, where the superscript 0 refers to the predicted value of R at time $k + 1$. The differentiation of a vector that is constant in the local frame gives the expression of the rate of change of the rotation: $v' = R' R^T v = (Gg') \times v$, where

$$G = \frac{4}{4 + g^T g} \left(I + \frac{1}{2} g \times \right)$$

The angular velocity is $\omega = G(g) \dot{g}$; in updated-updated form it is $\omega = G(g) \dot{g} + R(g) \omega^0$. Both matrices R and G , as well as other entities

that depend on the rotation parameters such as the angular velocity and those that are used in the linearisation of the kinematic quantities, assume a particularly simple expression when g is zero: both R and G become the identity matrix, the angular velocity becomes $\omega \cong \dot{g} + \omega^0$, while ΔG is zero. Since the unknown updated-updated rotation parameters are small, the simplified expressions are used to speed up the computation of the Jacobian matrix used in the correction iterations, while the residual is consistently computed by using the complete expressions to ensure the accuracy.

Dynamics. The equilibrium equations are written in terms of the derivatives of the momenta β, γ :

$$\begin{cases} \dot{\beta} = F \\ \dot{\gamma} - (\omega \times S) \times \dot{x} = M \end{cases}$$

where S is the first order inertia moment and F, M are generic forces and moments. The definitions of the momenta must be added:

$$\begin{cases} m\dot{x} + S \times \omega = \beta \\ -S \times \dot{x} + J\omega = \gamma \end{cases}$$

m, J being the mass and the second order inertia moment.

Constraint Equations. A kinematic constraint is a relationship between kinematic unknowns. Examples of basic constraints are the coincidence and orthogonality constraints, that can be used to build more complex cases. They result in algebraic or differential equations, depending on whether the constraint is or is not holonomic. A reaction force or couple is required to enforce the constraint. A *Lagrangian Multipliers*-like approach is used. The reactions are directly used as unknowns instead of the multipliers, to avoid the need of postprocessing to determine their value.

Finite Volume Beam. The finite volume beam results from the direct writing of the equilibrium of a finite piece of beam in terms of the internal forces at the boundaries and of the external loads. The internal forces and moments are expressed as functions of the spatial gradient of the configuration by means of arbitrary 6×6 constitutive laws, resulting in a C^0 formulation. The generalised deformations of the beam at the boundary sections result from the differentiation of a linear interpolation of the nodal positions and rotation parameters.

From a mathematical standpoint, the finite volume beam descends from a weighted residuals weak form of the differential equilibrium equation of the beam, with piecewise constant weighting functions. Advantages of the finite volume approach are the ease in the determination of the contribution to the equilibrium equations (only collocated evaluation of the forces is required), the absence of shear locking without the need of any numerical adjustment, and a more intuitive, physical meaning of the contribution to the equilibrium equations. A three-node beam element has been implemented [6].

Tiltrotor Model. The system under analysis is represented by a multi-body analytical model of the Wing and Rotor Aeroelastic Testing System (WRATS) tiltrotor aeroelastic wind-tunnel model. It is a semispan model of the V-22 currently used at LaRC to investigate the tiltrotor technology; it was originally built for the preliminary and full-scale design of the V-22. The analytical model, Figure 1, is made of a three blade, hingeless rotor mounted on a pylon, that is elastically attached to the clamped half-wing. The rotor blades are modelled by 4 beam elements each, plus one beam element for each flexbeam. The complete control chain has been modelled, from the swashplate to the blades through the flexible control links and the pitch horns. The hub is linked to the mast by means of a gimbal joint, that allows the flapped hub to maintain a constant rotation speed both in terms of amplitude and direction. The correct modelling of the gimbal required seven basic joints and one extra body. The analytical model has been validated in terms of kinematic, structural and aerodynamic properties [7]. The kinematic analyses have been used to assess the correct kinematic couplings between blade pitch, flap and lag. Some of these couplings involve the flexibility of the flexbeam and of the control chain, and required to be calibrated directly from the physical model. Structural properties have been compared to analytical results from Bell Helicopter, from previous analyses by means of University of Maryland Advanced Rotorcraft Code (UMARC) and NASTRAN, and to experimental results from Ground Vibration Tests (GVT) performed at LaRC. Basic aerodynamic and aeroelastic validation has been performed by comparing to data from previous wind-tunnel tests and numerical simulations.

Table 1: 888 rpm, $\theta_{75\%} = -3$ deg, Hz

Mode	Myklestad	UMARC	MBDyn
Gimbal	-	14.8	14.8
Cone	17.2	17.3	17.5
1 Lag	22.4	20.8	24.0
Coll Lag	42.	44.0	36.0
2 Flap	37.33	49.6	41.0
2 Flap asym.	-	70.2	65.0
3 Flap	75.33	90.3	73.0
Flap/Torsion	89.33	92.7	90.0
Lag/Torsion	-	113.4	104.0
Torsion	-	116.0	110.0

Numerical Results

Model Validation. Each component of the model has been validated separately. Both non-rotating and rotating analyses have been performed. Good agreement with numerical and experimental data has been found. The relatively rough discretisation used for the rotor blade has been able to capture all the desired modes. The full rotor vibration analysis highlighted the limits of conventional modal analysis of a single blade, since the gimbal joint and the three blade configuration break the symmetry the single blade analyses usually rely on. The UMARC code has been modified to model the three blades in the modal analysis phase, and it confirmed the results of the multi-body analysis. A comparison of modal analysis results is presented in Tables 1 and 2, referring to the rotating frequencies at 888 and 742 rpm, that correspond to the hover and cruise rotating speeds. More exhaustive results of the analysis may be found in Ref. [7].

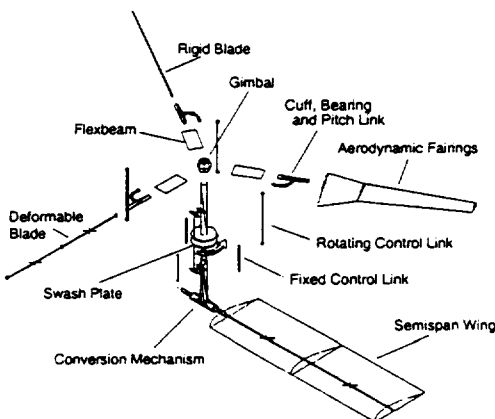


Figure 1: Analytical Model

Table 2: 742 rpm, $\theta_{75\%} = 55$ deg, Hz

Mode	Myklestad	UMARC	MBDyn
Gimbal	-	12.4	12.6
Cone	14.7	14.9	15.1
1 Lag	15.3	15.8	16.5
2 Flap asym.	-	42.3	44.2
Coll Lag	32.7	45.9	46.9
2 Flap	45.3	45.6	49.1
3 Flap asym.	-	46.9	60.3
3 Flap	66.0	60.1	65.2
Flap/Torsion	89.3	90.6	97.8
Lag/Torsion	90.0	90.8	89.7
3 Lag	-	92.0	92.9
Torsion	-	116.0	108.5

the required control force.

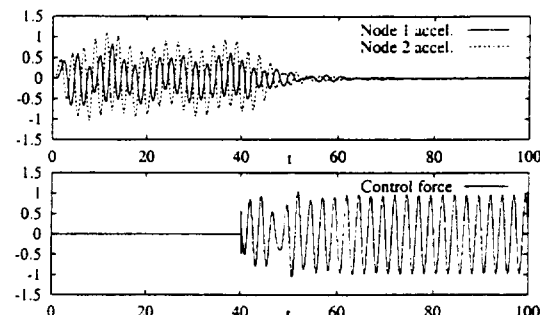


Figure 2: 3 Masses — Control Signals

Control Validation. A very simple system from Ref. [11] is studied. It is made of three masses in series with three springs and dampers; an excitation force is applied at the free end, and the control measures are the accelerations at the other two points, thus implementing a system with no direct transmission term. The properties are: $m_1 = m_2 = m_3 = 1$, $k_1 = 1$, $k_2 = 2$, $k_3 = 3$; the damping is assumed proportional to the square root of the stiffness, i.e. $c_i = 0.05\sqrt{k_i}$. The system has 6 poles. Different values for the order of the identified system p as well as for the control weight λ have been tested. The prediction and control advancing horizons have been chosen equal to p . The integration time step is 0.01 s; the sampling for the discrete controller is taken every 10 time steps. The system is excited by a unit amplitude harmonic force at 0.4 Hz; a white noise with 0.001 amplitude is applied and measured to identify the system. The control is activated after 40 s of simulation. An order $p = 6$ has been used, with $\lambda = 10^{-3}$. The control weight is gradually lowered to the nominal value in about ten seconds to avoid an abrupt intervention of the control. Figures 2, 3 show the two measured accelerations and the control force, and the displacements at the three nodes, respectively. When the first damping coefficient is set to a negative value $c_1 = -0.15\sqrt{k_1}$, the response, Figure 4, shows the effectiveness of this form of adaptive control for unstable systems. It is interesting to note that the control is not collocated and the unstable section of the system is close to one of the measures, but not directly controllable. The control weight λ can be reduced even more, with performance improvements especially in the unstable case, but with excessive penalty in

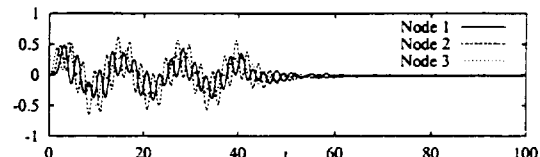


Figure 3: 3 Masses — Displacements

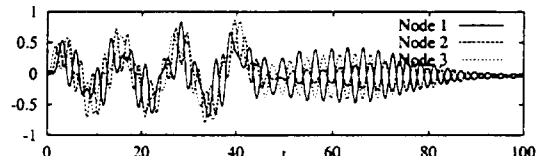


Figure 4: 3 Masses — Unstable Displacements

Hover Simulations. The effectiveness of the GPC applied to a more complex and realistic system has been assessed by performing simple SISO control analyses of the WRATS model in hover. The rotor is rotating at 888 rpm, and it is externally excited by a shaker with a harmonic load at 5 Hz, close to the first wing out-of-plane bending frequency, about 5.5 Hz. The time step is 0.001 s, and the control samples are taken every 8 steps, resulting in a frequency of 125 Hz, which is higher than the first torsional frequency of the blade, to prevent the blade resonance. The bending strain at the root of the wing is measured, filtered by a washout (band-pass) analog filter to cut out of the measured signal the static signal as well as the higher frequencies, and the rotor thrust is used as actuator by controlling the collective pitch. A pass-band filtered measure of the vertical acceleration at the pylon is alternatively used. A good compromise for the system order has been found in $p = 60$. The

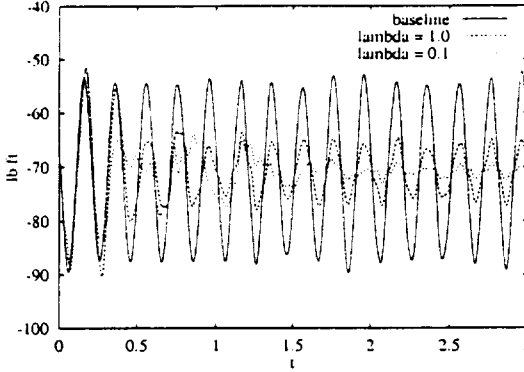


Figure 5: *Hover bending moment, str. meas.*

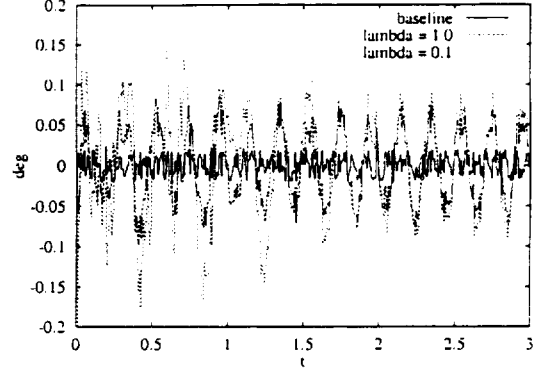


Figure 7: *Hover collective, str. meas.*

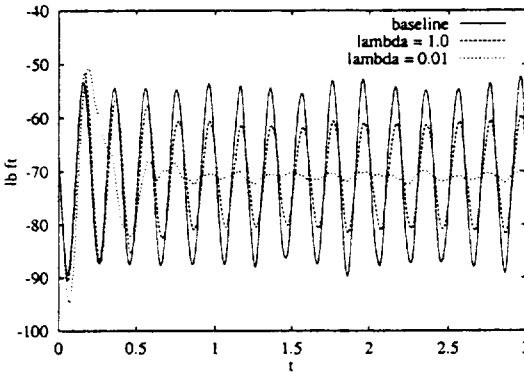


Figure 6: *Hover bending moment, acc. meas.*

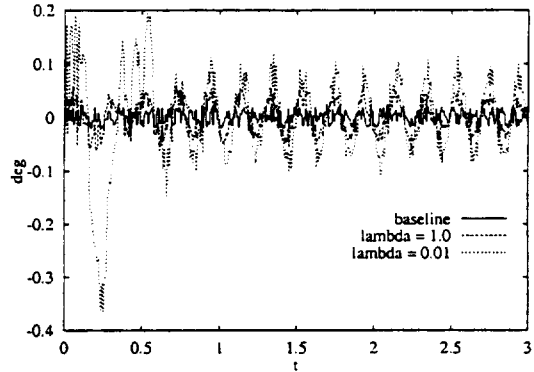


Figure 8: *Hover collective, acc. meas.*

results of the two cases, compared to a baseline analysis with harmonic excitation but without control, are presented in Figures 5, 6, for two different values of λ . They show the bending out-of-plane moment at the wing root. The control signals are shown in Figures 7, 8, while the vertical acceleration of the pylon in the latter case is shown in Figure 9; the high frequency noise is the persistent excitation that is used to continuously identify the system, while the control of the harmonic motion determines the main, low frequency oscillation.

Forward Flight Simulations. Forward flight analyses have been performed by controlling the collective and the cyclic pitch of the blades based on different measures of strains at the wing root. The model is in airplane configuration, at an air-speed of 100 ft/s, and the rotor is rotating at 742 rpm. In this case the order is $p = 20$, since the number of measures is higher (3 vs. 1). First the wing out-of-plane excitation force is offset aft of the wing to obtain also a twisting excitation. The rotor has little control authority in its plane in terms of force, the flapping of the

disk being required to tilt the thrust. Since the flapping response has a delay of about 90° , the accuracy of the prediction is key to the effectiveness of the control. In this case the actuation force, transverse to the wing, lies in the plane of the rotor, thus being not directly controllable by a simple change in thrust. Moreover, since the motion of the gimballed rotor is characterised by a wide spectrum dynamics, from the high frequency vibrations induced by the advancing blade modes, to the wing elastic modes, down to the very low frequency precession motion, a high number of physical and numerical poles are required for an adequate identification. The results of the simulations are reported in Figure 10, that shows the wing root bending moment. Figure 11 shows the control signals. The initial low frequency oscillations in the control signals are due to the precession of the rotor during the transient following the application of the harmonic excitation. The uncertain initial behaviour of the controller is related to a poor initial identification of the low frequency poles of the system. In fact, with $\lambda = 1.0$ the control authority is low, but with $\lambda = 0.1$, after a

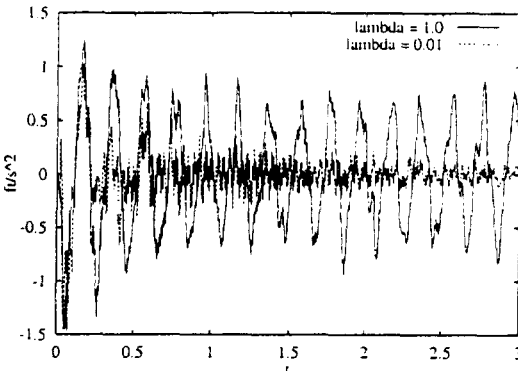


Figure 9: Hover accelerometer signal

few cycles the system goes slightly unstable (after about 1.5 s), returning under control as soon as the identification is improved. The following behavior is definitely better than the previous case, as can be appreciated in the last part of the plot. A more realistic case is considered, by using the control parameters tuned with the former case. A sinusoidal vertical gust, with an amplitude of 4 ft/s and a wavelength of 20 ft, is encountered by the model while the control is working. The effect of the control on the wing bending is shown in Figure 12: the free oscillations resulting from the wind-up of the rotor are damped as the control starts; when the model encounters the gust, the peak of the moment is attenuated first, then the control overshoots due to the need to re-identify the system. The newly identified system brings the bending moment, as well as the other measured internal moments, to a negligible value in a few cycles. The control signals, i.e. the pitch controls determined by the controller, are particularly meaningful. The col-

lective is negligible, since it mainly controls the in-plane bending of the wing, that is not directly excited by the vertical gust. The cyclic controls instead are heavily used by the controller to generate the rotor aerodynamic moment required to tilt the rotor disk. Since the disk tilts about an horizontal axis due to the wing bending and torsion excited by the gust, the rotor is mainly required to generate a pitch moment (in airplane sense) that counteracts this motion. In fact the higher cyclic control signal is the lateral pitch, about twice as large as the fore/aft pitch, which causes a fore/aft flapping of the rotor. Figure 13 shows a detail of the control signals across the gust input.

Concluding Remarks

The Generalized Predictive Control has been used in the multi-body numerical simulation of the active vibration control of a tiltrotor aeroelastic model currently investigated at NASA Langley Research Center. The control has been applied by means of the control mechanism that is used on the actual model, a conventional, hydraulically actuated swashplate. A combination of strain and acceleration measures have been used to identify the system, and different operating conditions and external disturbances have been considered. The predictive control resulted highly effective in most of the investigated conditions, giving substantial reduction of the load level. In detail, both the strain and the acceleration measurements allowed the correct identification of the system, and the intrinsic adaptivity of the proposed implementation of the generalised predictive control allowed the correction of inaccurate initial system identification even

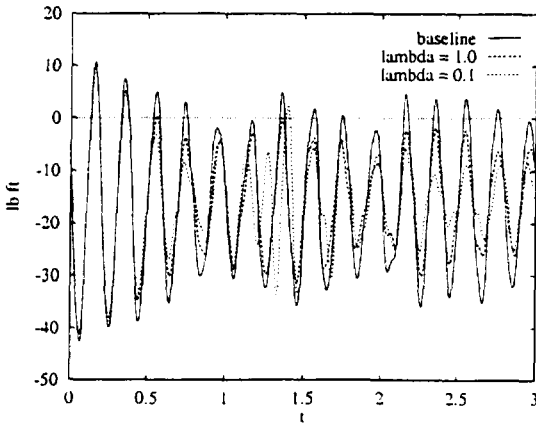


Figure 10: Forward flight bending

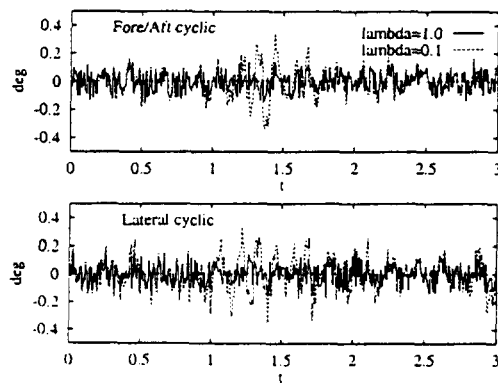


Figure 11: Forward flight control signals

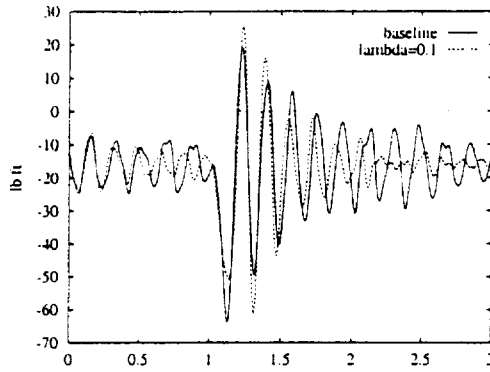


Figure 12: *Gust bending*

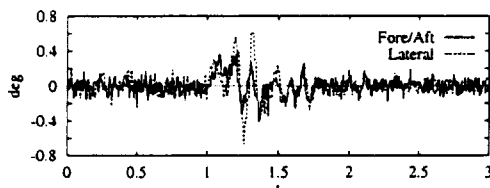


Figure 13: *Gust control signals*

in variable test conditions. The multi-body approach represented a viable solution for the analysis of complex systems requiring a high level of detail in the modelling of mechanisms. Future developments of the control will involve the introduction of the adaptivity of the weight coefficient, to reduce the need of an *ad hoc* tuning of the various control parameters, and a variable order model in the identification of the system.

References

- [1] Andriquettoni, M., and P. Mantegazza, 1998, "Multi-Input/Multi-Output Adaptive Active Flutter Suppression for a Wing Model", *Journal of Aircraft*, Vol. 35, No. 35, pp. 462-469
- [2] Åstrom, K. J., and B. Wittenmark, 1989, *Adaptive Control*, Addison-Wesley
- [3] Chopra, I., and J. L. McCloud, 1981, "A Numerical Simulation Study of Open-Loop, Closed-Loop and Adaptive Multicyclic Control Systems", Presented at the *American Helicopter Society Northeast Region National Specialists' Meeting on Helicopter Vibration, Technology for the Jet Smooth Ride*, Hartford, Conn.
- [4] Eure, K. W., and J. Juang, 1997, "Broadband Noise Control Using Predictive Techniques", *NASA TM 110320*
- [5] Friedmann, P. P., and T. A. Millot, 1995, "Vibration Reduction in Rotorcraft Using Active Control: a Comparison of Various Approaches", *J. of Guidance, Control, & Dynamics*, Vol. 18, No. 4, July-August
- [6] Ghiringhelli, G. L., P. Masarati, and P. Mantegazza, 1997, "Multi-Body Aeroelastic Analysis of Smart Rotor Blades, Actuated by Means of Piezo-Electric Devices", *CEAS Int. Forum on Aeroelasticity and Structural Dynamics*, June 17-20, Rome, Italy
- [7] Ghiringhelli, G. L., P. Masarati, P. Mantegazza, and M. W. Nixon, 1998, "Multi-Body Analysis of a Tiltrotor Configuration", Presented at the *7th Conference On Nonlinear Vibrations, Stability, and Dynamics of Structures*, July 26-30, Blacksburg, VA; to be published on the *J. of Nonlinear Vibrations*
- [8] Giurgiutiu, V., Z. Chaudry, and C. A. Rogers, 1995, "Engineering Feasibility of Induced Strain Actuators for Rotor Blade Active Vibration Control", *JoIAMS&S*, Vol. 6, September
- [9] Ham, N. D., 1987, "Helicopter Individual-Blade-Control Research at MIT 1977-1985", *Vertica*, Vol. 11, No. 1/2, pp. 109-122
- [10] Johnson, W., 1982, "Self-Tuning Regulators of Multicyclic Control of Helicopter Vibrations", *NASA TP 1996*
- [11] Juang, J., 1997, "State-Space System Realization With Input- and Output-Data Correlation", *NASA TP 3622*
- [12] Juang, J., and M. Q. Phan, 1997, "Deadbeat Predictive Control", *Journal of the Chinese Society of Mechanical Engineers*, Vol. 19, No. 1, pp. 25-37
- [13] Lehmann, G., 1985, "The Effect of Higher Harmonic Control (HHC) On a Four-Bladed Hingeless Model Rotor", *Vertica*, Vol. 9, No. 3, pp. 273-284
- [14] Loewy, R. G., 1984, "Helicopter Vibrations: A Technological Perspective", *Journal of the American Helicopter Society*, October, pp. 4-30
- [15] Nixon, M. W., R. G. Kwaternik, and T. B. Settle, "Higher Harmonic Control Tiltrotor Vibration Reduction", *CEAS Int. Forum on Aeroelasticity and Structural Dynamics*, June 17-20 1997, Rome, Italy
- [16] Reichert, G., 1981, "Helicopter Vibration Control - A Survey", *Vertica*, Vol. 5, N0. 1, pp. 1-20

1999066484

5/5-09

Rotary Wing Test Stand Capability for the
Republic of Korea

381317

By Jeffrey Breaks, Engineering Manager, Micro Craft-Hampton Division,
and Michael Cooper, Senior Analyst, Micro Craft-Hampton Division

p. 12

Abstract:

Two agencies in the Republic of Korea have commissioned the design and fabrication of rotor test stands to provide performance and dynamic testing capability for helicopter rotor systems in newly constructed wind tunnel facilities near Taejon, Korea. These test stands, based on the proven design of the 2 Meter Rotor Test Stand (2MRTS) that has been operating in the NASA Langley Research Center, 14 X 22-Foot Low Speed Tunnel for some time, incorporate significant improvements in the drive power and in the control and instrumentation subsystems. Both rotor test systems are robust and utilize many off-the-shelf components for durability and ease of maintenance.

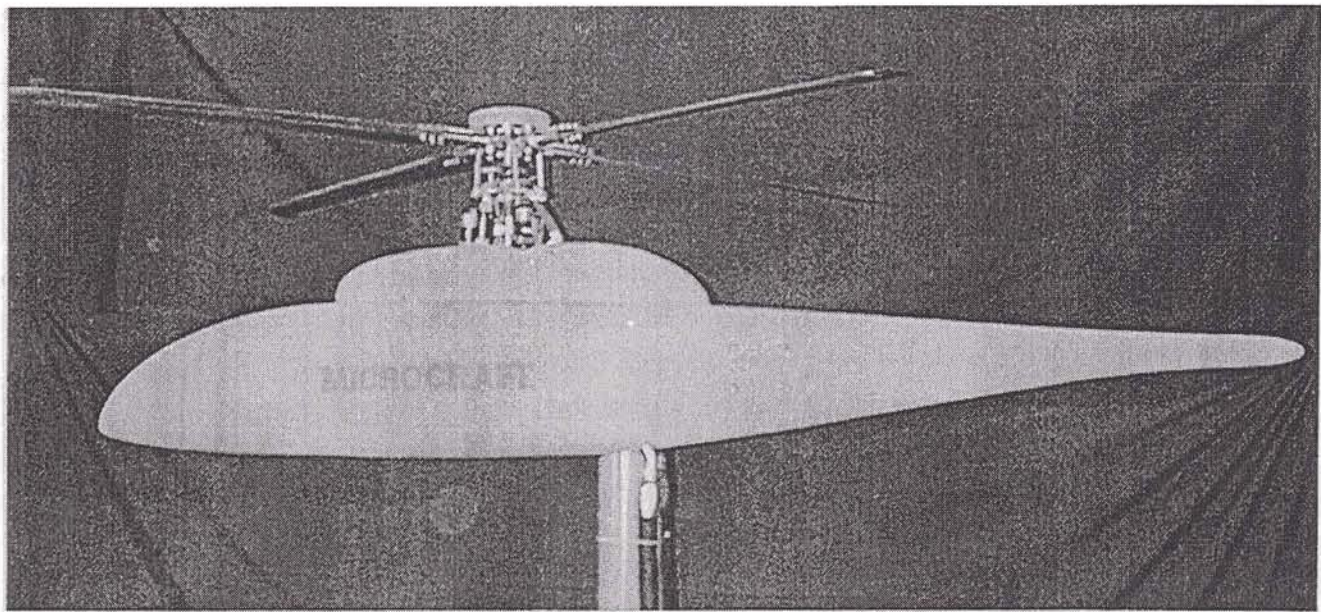


Figure 1 - MRTS General Arrangement

General Description:

The Main Rotor Test Stand (MRTS) is a specialized, Mach scaled system which provides the capability for conducting high-quality wind tunnel research on dynamically scaled models of rotors, rotor systems, and complete helicopter configurations. Power for the system is provided by a 75 –horsepower hydraulic motor driven by an hydraulic power source located outside of the wind tunnel test section. A comprehensive suite of instrumentation provides data for a wide variety of force and position measurements in both the rotating and fixed systems. The MRTS may be sting or strut mounted and is capable of operating away from the wind tunnel as a static test stand.

The second rotor test system is the General Small-Scaled Rotor Test System (GSRTS), designed for Froude-scaled and limited Mach-scaled testing. As a Froude-scaled system, keeping components light is a primary consideration. To accomplish this the hub is made of titanium, and aluminum is used extensively for other components such as the gearbox housing. Power for this system is provided by high power density, water-cooled electric motors driven by a solid state power supply located nearby. The transmission is capable of accepting one or two 20-horsepower motors. For Froude-scaled testing, one motor provides sufficient power. A second motor is added to bring the available horsepower up to 40 for limited Mach-scaled testing.

Reduction of data from a rotating system is especially dependent on knowing the position of the rotor with respect to other model components and the phasing of the measured loads. To provide the needed data, both test stands are provided with state-of-the art sensors and an advanced data acquisition system. Rotating and fixed-frame balances can be installed to measure loads on the total system, the rotating system, and the fuselage shell separately. Hall effect sensors mounted on the hub measure blade lead-lag, flapping, and feathering motions. Another Hall effect sensor and a rotary shaft encoder determine rotor azimuthal position that is corrected for drive shaft windup due to load. Encoders and linear variable displacement transducers (LVDT) on the swashplate actuators provide data on control inputs. The data system digitizes selected parameters, processes data in real time, and outputs results to the Control Consoles and/or the wind tunnel data system. The system can stand alone or interact with other systems through an Ethernet connection.

Control of the test stand and operation in conjunction with a wind tunnel, mandate displays and controls that present needed parameters clearly and conveniently and permit easy coordination of test stand operation with wind tunnel operation. Consoles are provided for a Pilot and a Safety Officer. The Pilot can input control commands through a joystick, a mouse, or the keyboard. Data displays are selected from a menu of all measured parameters and can include multiple windows and audible limit alarms. The Safety Officer's console is used to monitor system parameters such as bearing and gearbox temperatures and other operational and model data, as appropriate.

As rotating systems, both test stands present challenges that require specialized design features to control dynamics and analyses to identify system response characteristics. A complete Finite Element Model (FEM) of each test stand, including backup flexibilities, was developed. NISA finite element modeling software, from Engineering Mechanics Research Corporation, was used in this effort. Initial calculations were used in the design process to identify modal trends and avoid undesirable coalescence of operating frequencies. As fabrication proceeded, the FEM was revised and updated to reflect actual measured component weights and stiffness. During system operational checkout, data were taken and results were compared with FEM predictions. Adjustments were then made to the FEM so that the final FEM accurately calculated the hardware modes and frequencies.

Instrumentation:

Basic blade position instrumentation is included on the test stands and provision is made for future expansion. The heart of the blade position instrumentation is the suite of Hall Effect sensors located on the hub to measure the blade position directly. Two blades are instrumented for flapping position, lead-lag position and feathering position. The data from only one blade are processed during test, so the system provides redundancy of all three parameters. Hall Effects sensors detect changes in the lines of magnetic flux, so the sensor is mounted on the fixed portion of the hub and a small magnet is mounted on the moving component. Circuits located in the rotating system power the sensors, and data signals are passed through slippings to the data acquisition system.

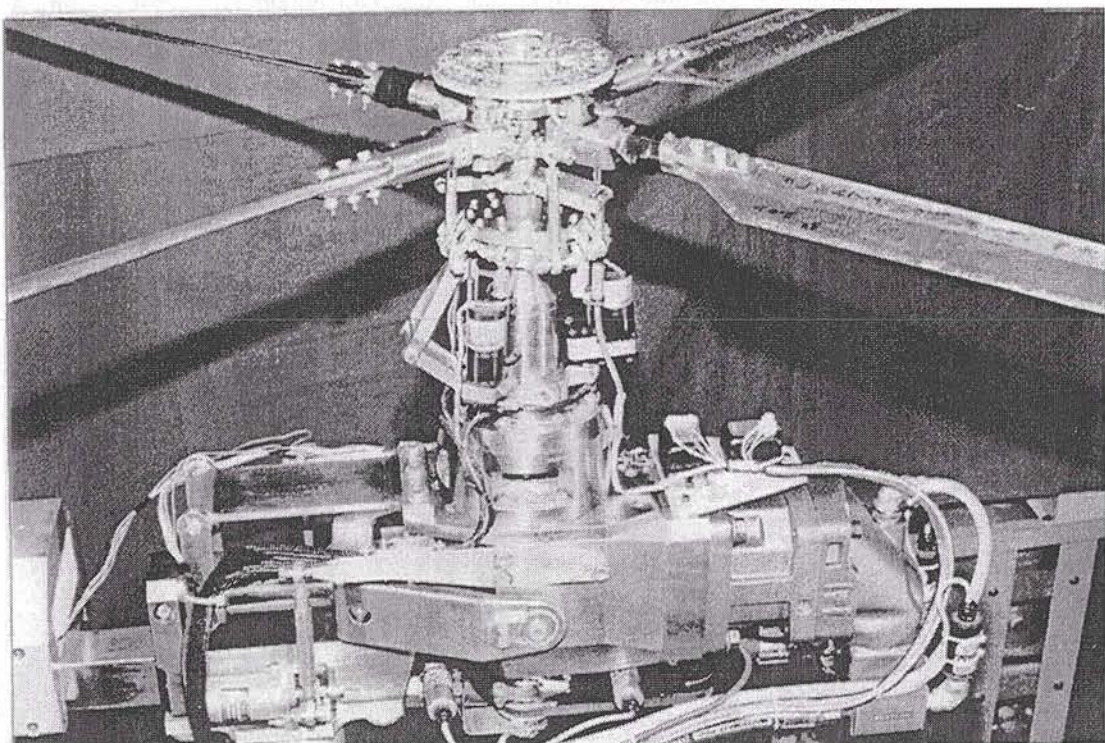


Figure 2 - Instrumentation

Azimuthal position of the blades must be known in order to correlate the blade aeromechanic data with the fixed system and control parameters. An encoder mounted on the transmission output shaft and a Hall Effects sensor mounted near the hub provide this information. The encoder provides 1-per-rev and 2048-per-rev position information. The sensor mounted near the hub provides a reference signal that allows correction for the torsional windup of the drive shaft under load.

Other instrumentation in the rotating system is provided to gather real time data from numerous sources. Twelve channels are available to obtain straingage load data or pressure transducer data at specific locations on individual blades. Pitch links are instrumented to provide information on input force levels. The MRTS is equipped

with a 5-component force and moment balance in the fixed system, and a torque gage on the driveshaft provides data on the rotor drive power. A rotary balance can be installed on the GSRTS to provide full 6-component force and moment data on the rotating assembly. Signal conditioning circuitry on the rotor hub is used to reduce the number of slipring channels required so that a maximum amount of data can be sent through a 60 or 80 channel slipring. This circuitry can provide supply power and amplification of the signals for the instrumentation in the rotating system.

Data Acquisition and the Control Console:

The data acquisition system gathers information from the model, processes it and displays it as needed by the Pilot, Safety Officer, and other users. The data system is built around a Pentium computer system. A graphical user interface (GUI) based on National Instruments LabView software running under Microsoft Windows NT 4.0 operating system provides data display that can be customized by the various users. With this approach, identical or custom displays can be monitored at remote stations to perform such features as model health monitoring or test data monitoring.

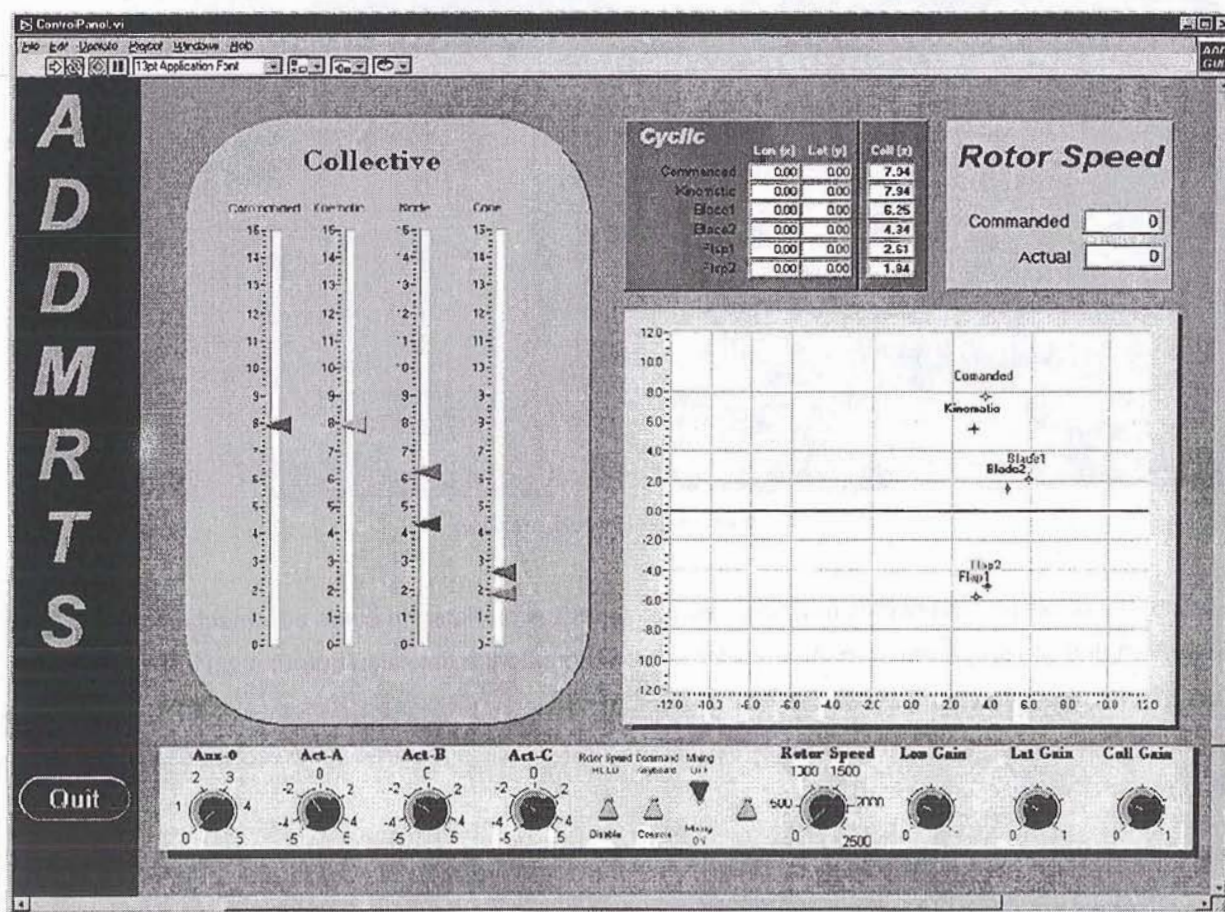


Figure 3 - Control Console Display

Rotary Wing Test Stand Capability for the Republic of Korea

Data acquisition is accomplished by ISA circuit boards mounted inside the computer. A Keithly Metrabyte DAS1702St analog-to-digital converter board processes low speed time-independent data. A Keithly Metrabyte DAS1802STDA analog-to-digital converter with four digital-to-analog outputs processes the high-speed time-dependent signals, such as blade position, and generates actuator reference commands.

Mechanical test stand controls are provided through a mechanical user interface containing ten-turn potentiometers, enabling switches, and two joystick controllers. The potentiometers can be used to provide direct control of model functions such as drive motor speed or swashplate actuators in an emergency or, if desired, for other reasons. The enabling switches are used to select the desired control mode. Joysticks are provided for collective and cyclic control in the mixer mode.

Installation of the test stand in a wind tunnel facility may require long cable runs. A custom line-driver circuit board is provided to allow communication between the model and the Control Console at longer separation distances than the native TTL level signals allow. In these applications the design distance is 125 feet, but this could be increased, if necessary.

The Pilot's Console is the only station allowed to control the actuators and motors of the test stand. All other consoles and data displays are for data monitoring only. Data received by the test stand computer system is passed through to the Wind Tunnel Data Acquisition System for recording, processing, or display. The individual user of each console or data display can tailor data displays to specific needs. A typical Pilot's Console display is shown in Figure 3. This display shows the commanded value and also the actual reading of the parameter. The rotor speed system has a time lag programmed into it so that a soft startup occurs and rotor acceleration or deceleration is limited during speed changes. The pilot is interested in real-time displays of rotor speed and actuator positions. He coordinates his control movements with wind tunnel operating conditions through an intercom connection with the wind tunnel operator and the test director.

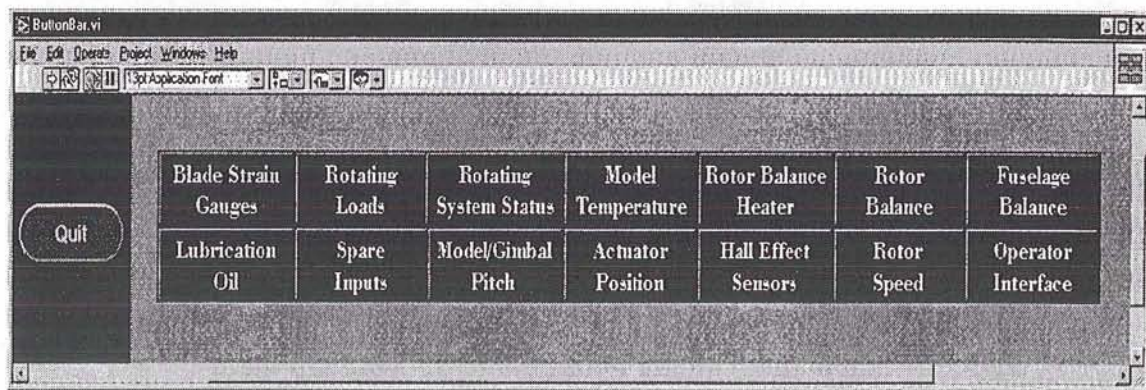


Figure 4 - Data Set Selection

Various system operating parameters such as bearing and transmission temperatures are of secondary interest to the Pilot and are not normally displayed on his console. Selected parameters can be monitored without distracting the operator from more important tasks. The LabView system is used to set limits on the parameter and if these limits are exceeded, an icon on the pilot's display flashes. The color of the flashing icon denotes the direction in which the limit is exceeded, blue for negative and red for positive. The Safety Officer's display is configured to show test stand health parameters. Selection of data is shown in Figure 4. Clicking on any of the buttons displays the data in that group and shows the current reading and limit settings. Like the Pilot's Console, the Safety Officer can program limits into the system. When a limit is exceeded or approached the icon will flash to alert the operator, even if that particular data set is not being monitored on the display. Figure 5 shows the window displayed when setting the limits on the swashplate actuators. As can be seen from the figure, the command value can be limited separately from the actuator limit. In this way the actuator limit is like a mechanical stop and the command limit can be used to place a limit on test conditions. The LabView system is flexible enough to be reconfigured to suit various operators and different test crews.

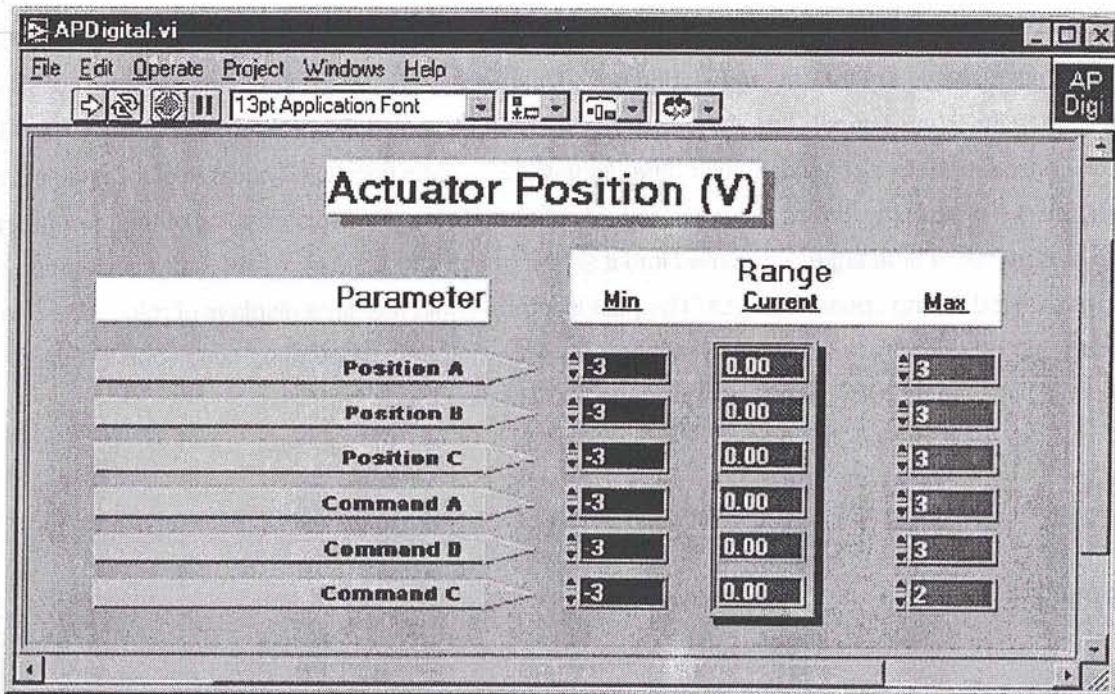


Figure 5 - Double Click to Set Limits

The control system passes data through to the Wind Tunnel Data Acquisition System and is linked to other systems in the Wind Tunnel Complex through an Ethernet connection. A separate display can be set up at a remote site so that the Test Director or a Data System Monitor can view the data as it comes from the model.

These data can be processed through any of the virtual instruments in the LabView System or can be connected to completely separate instruments such as a spectrum analyzer.

The GSRTS was specifically designed for research in rotor dynamics through Froude-scaled testing. One of the swashplate actuators is equipped with a small hydraulically actuated shaker for enhanced aeroelastic test capabilities. This shaker has only +/- .05 inch of travel, but this is sufficient to change the pitch of a blade by +/- 1 degree. A small electrically driven, hydraulic pump provides power. The shaker motion is actuated and controlled by an hydraulic servo valve capable of response at over 100Hz. Output of the shaker is generally in the form of a sine wave with the frequency controlled from any convenient location near the Control Console. A linear variable displacement transducer (LVDT) mounted on the actuator provides position data to the shaker control system. With these test stands, the Froude scaled testing design point is approximately 1000 RPM, so a shaker frequency of 16Hz would produce a 1 per rev excitation in the rotating system.

Analysis and the Finite Element Model:

These test stands are complicated structures with oscillating loads and, like any type of rotating machinery, are sensitive to unbalance, alignment, system flexibilities and mass. The blades are long, slender flexible beams beset with numerous natural frequencies that change with rotational speed. Encountering a resonant condition with the blades or the test stand could be catastrophic. Validating the design through analysis assures that these test stands will provide the desired data with a minimum of concern for dynamic instabilities.

Modal analyses of the MRTS and the GSRTS were performed to determine the natural modes and frequencies of each system. Separate modal analyses of each blade were also performed to determine the natural frequencies of the rotating rotor blades. Analyses were conducted to determine stand response over a frequency range from zero to about 35Hz, which corresponds to a 1/Rev frequency at a rotor speed of about 2100 RPM. These test stands are designed with pitch and roll springs and variable damping in the support system to decouple the rotor from ground resonances. The springs are designed to be replaceable and/or tunable so that the dynamic properties of various rotor systems can be accommodated. Proper "homework" must be done to be aware of potential instabilities, but the robust design and the combination of tuneable springs and adjustable damping in the support system allow the test rigs to be adapted to a wide variety of rotor systems.

Approach to modal analysis:

The test stands are designed to accept a wide range of rotor blade sizes, weights, and rotor configurations. For stress purposes, the heaviest possible blade was used to determine maximum centrifugal force and failure loads (from a single blade-out condition). Included in the analyses are Mach scaled blades on the MRTS and Froude-scaled blades on the GSRTS.

The blade modal analysis was conducted for a single articulated, blade rotating in a vacuum. This condition assumes that the hub and shaft are rigid, and that a preceding blade has no effect on the dynamics of the following blade. This is a relatively simple set of calculations to make because the structural model consists of a

single blade. The blade frequencies are known to vary dramatically with rotation speed, while the test stand dynamics are reasonably stable under rotation. However, the apparent hub mass and inertia does vary with rotation speed. Variation in hub mass and inertia is accounted for in the test stand dynamics by using an effective hub mass and inertia based on the method described in "Rotary Wing Structural Dynamics and Aeroelasticity" by Richard Bielawa. In his method, the effective mass and inertia is computed from a rotating beam that accounts for gyroscopic effects due to rotation. Using this approach allows the rotor blade dynamics to be computed separately from the test stand dynamics while still accounting for the apparent mass and inertia of the hub.

Description of the FEM's:

A detailed finite element model of a rotor blade was generated using shell and solid elements to verify the structural integrity of the as-built blade for the MRTS system. However, the rotor blade FEM for the dynamic analysis was comprised of 3D beam elements that accounted for the stiffness and mass distribution. There were 436 grid points and 404 elements, each with its own cross section properties. The mass distribution was applied using point masses and inertias. The proper locations were constrained to act as pinned hinges for flapwise and chordwise motion, and fixed in torsion (blade pitch). The centrifugal force was computed and the geometric stiffness matrix was recovered. This matrix was added to the elastic stiffness matrix and with the mass matrix, the natural modes and frequencies were computed for various rotation speeds.

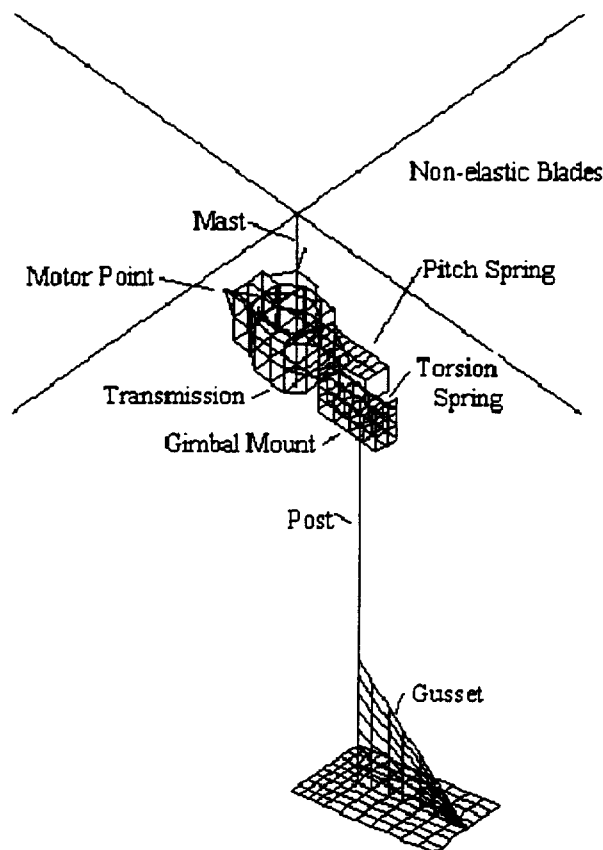


Figure 6 – Finite Element Model for MRTS

Finite element models of each rotor test stand were generated to estimate the natural modes and frequencies of the system. Care was taken to adequately represent the mass and stiffness of each structure. Component assemblies were weighed and the FEM was updated with the as-built information.

The major components included in the MRTS finite element model are shown in Figure 6.

- Support Post and Gusset
- Gimbal mount with yoke, pitch spring, and roll spring
- Transmission frame
- Drive system including drive shaft, output shaft, torque tube on flex couplings, and mast
- Four-post balance and bearing tower.

The major components included in the GSRTS finite element model are:

- Post
- Gimbal mount with yoke, pitch spring, and roll spring (arrangement differs from MRTS)
- Transmission frame
- Drive shaft system including motor shaft, output shaft, and mast
- Rotating Balance on mast.

Structural components missing from both FEMs are the fuselage shell, the motor(s), and the control linkage including actuators, control arms, and swashplates. These components do not contribute to the stiffness of the test stand, however their mass was accounted for. The natural modes and frequencies were computed using the NISA finite element code.

The following table lists the weight of various assemblies for the MRTS:

Assembly	Measured Weight, lb	Computed Weight, lb
Drive system	26.5	26.5
Rotating Controls	7.5	7.5
Hub (w/o blades)	10.5	10.5
Gear Box	70.0	74.7
Gimbal	68.25	68.20
Motor	not measured	50.0
Post Support	not measured	108.2
Total Weight		345.6

Results:

The overall mass properties of each test stand were computed to be:

Test Stand	Weight, lb	CG w/ respect to gimbal axes			Mass moments of inertia		
		X,in	Y, in	Z, in	J _{xx} , lb-in ²	J _{yy} , lb-in ²	J _{zz} , lb-in ²
MRTS	345.6	3.58	0.00	-12.97	1.780x10 ⁵	2.021x10 ⁵	2.614x10 ⁴
GSRTS	206.4	-0.1	0.00	-1.65	1.471x10 ⁴	2.268x10 ⁴	9.864x10 ³

Note: Hub effective mass and inertia computed for maximum rotation speed of 2100 RPM.

Seven flexible modes below 2100 RPM (35 Hz) were computed for the MRTS system, not counting the rigid body mode representing the rotation of the drive system shafts. The modes are listed in the table below. A subjective description of the modes is provided. The description indicates the major components that participate in the mode.

Mode #	ω , Hz	ω , CPM	MRTS System Modes Description
1	3.67	220.2	System roll spring mode
2	6.11	366.6	1 st side bending (coupled yaw and roll)
3	9.11	546.6	Pitch spring mode
4	15.69	941.4	1 st fore-aft bending mode
5	16.47	988.2	Torque tube vibrating on flex couplings
6	16.87	1012.2	2 nd side bending
7	23.58	1414.8	2 nd pitch spring mode

For the GSRTS, six modes under 2100 RPM were computed for the system, not counting the rigid body mode of the drive system shaft rotation. This system is relatively symmetric with respect to the fore-aft bending plane. Fore-aft modes are straightforward. However, the center of gravity lies off the post axis. Therefore, side-to-side motion necessarily couples post side bending with torsion.

Mode #	ω , Hz	ω , CPM	GSRTS System Modes Description
1	6.570	394.2	Motor/transmission rolling on the roll spring
2	7.775	466.5	1 st side-to-side motion of the drive system, twist of the post
3	9.022	541.3	1 st fore-aft bending mode of the post
4	14.573	874.4	2 nd fore-aft bending mode of the post
5	24.323	1459.4	Up-down motion of the motor/transmission
6	26.700	1602.0	2 nd side-to-side motion of the post, twist of the drive system

Summary:

Goals of the program were to produce test hardware capable of gathering the parameter and position data necessary for performance and aeroelastic research on rotor systems. System operational and control characteristics were to be well defined and operation of the systems should allow Pilot attention to be directed towards the test itself rather than system peculiarities. These goals were met in all areas.

The Mach scaled test stand is not horsepower limited and can achieve advance ratios, tip Mach number, and disk loadings of advanced rotor systems still on the drawing board. Hardware is designed to allow easy installation and test of hingeless and bearingless designs. For Froude scaled testing, the GSRTS provides a light weight responsive system able to gather large quantities of aeroelastic data.

Instrumentation provided gathers the high quality time-dependant data needed to test advanced systems and verify analyses.

Test Stand structure is documented with a FEM to assist in future analytical studies. Dynamic characteristics of the hardware are well separated from the operational envelope.

The Control System is user friendly, easy to operate, and provides real-time review of data and model operating conditions.

Special thanks to Dr. Seung-Ki Ahn and Dr. Gene Joo.

REVIEW OF NONLINEAR PANEL FLUTTER AT SUPersonic AND HYPERSONIC SPEEDS

Chuh Mei, K. Abdel-Motagaly and R. Chen

5/6 - 08

Department of Aerospace Engineering

Old Dominion University, Norfolk, Virginia 23529-0247

ABSTRACT

A review of various analytical methods and experimental results of supersonic and hypersonic panel flutter is presented. The analytical methods are categorized into two main methods. The first category is the classical methods, which include Galerkin in conjunction with numerical integration, harmonic balance and perturbation methods. The second category is the finite element methods in either the frequency domain (eigen solution) or the time domain (numerical integration). A review of the experimental literature is given. The effects of different parameters on the flutter behavior are described. The parameters considered include inplane forces, thermal loading, flow direction, and initial curvature. Active control of composite panels at supersonic speeds and elevated temperatures is also presented.

1. INTRODUCTION

This review is an attempt to assess the recent developments and advances in nonlinear panel flutter at supersonic and hypersonic speeds. With the resurgent interest in flight vehicles such as the High-Speed Civil Transport (HSCT), the X-33 Advanced Technology Demonstrator, the Reusable Launch Vehicle (RLV), the Joint Strike Fighter (JSF), and the X-38 Spacecraft using a lifting-body concept that will operate at supersonic/hypersonic Mach numbers, this brings an urgent need for panel flutter analysis. When a flight vehicle travels at high speeds, the aerodynamic pressure is not the only form of excitation. The skin-panel temperatures could potentially reach several hundred degrees (e.g. 350 F° for the HSCT cruising at Mach 2.4) due to aerodynamic heating. The presence of thermal loads results in a flutter motion at lower dynamic pressure or a larger limit-cycle amplitude at the same dynamic pressure. In addition, a high temperature rise may cause large thermal deflections of the skin panels, which could affect flutter response and motion. Thus the thermal effects on panel flutter response require special emphasis. The additional requirements for energy-efficient, high-strength and minimum-weight vehicles have become apparent. These requirements have generated an interest in advanced composite materials to meet the high-strength and minimum-weight requirements. There has been recent development in smart or adaptive materials such as piezoelectric materials and shape memory alloys that can be embedded into the laminated composite panels to control or suppress limit-cycle or chaotic random panel motions.

Dowell (1970) has grouped the vast amount of theoretical literature on panel flutter into four categories in a review on linear and nonlinear panel flutter. Gary and Mei (1993) added a fifth category for hypersonic flow. The five different categories of linear and nonlinear panel flutter are shown in Table 1. The weakness and remedies for the first four types of analysis were discussed in detail in (Dowell, 1970). An approach using the quasi-static Ackeret aerodynamic theory for the design of flutter-free surface panels was documented by Laurenson and McPherson (1977). The flutter-free design procedure considered the interaction of parameters such as support flexibility, inplane loads, pressure differential, and flow angularity; however, the thermal effects were not considered. A review of the finite element method of type 1 panel flutter analysis was recently given by Bismarck-Nasr (1992). A survey on various analytical methods including the finite element approach for nonlinear supersonic panel flutter type 3 analysis was given by Zhou et al. (1994). For fundamental theories and physical understanding of panel flutter the readers are referred to the published books (Dowell, 1975; Librescu, 1975).

This survey is an attempt to cover nonlinear panel flutter at supersonic and hypersonic speeds of type 3-5 analyses with the emphasis on thermal effects. Various analytical methods including the finite

element for nonlinear flutter response are discussed. The influence of other parameters of practical interest on nonlinear panel flutter is considered. The particular parameters considered in this survey include inplane loads, thermal, flow yaw angle, and active control effects.

Table 1. Panel Flutter Theories

Type	Structure Theory	Aerodynamic Theory	Range of Mach No.
1	Linear	Linear Piston	$\sqrt{2} < M_\infty < 5$
2	Linear	Linearized Potential Flow	$1 < M_\infty < 5$
3	Nonlinear	Linear Piston	$\sqrt{2} < M_\infty < 5$
4	Nonlinear	Linearized Potential Flow	$1 < M_\infty < 5$
5	Nonlinear	Nonlinear Piston	$M_\infty > 5$

2. AERODYNAMIC THEORIES

As disclosed by these survey papers, a vast quantity of literature exists on panel flutter using different aerodynamic theories. The aerodynamic theory employed for the most part of panel flutter at high supersonic Mach numbers ($M_\infty > 1.6$) is the quasi-steady first order piston theory aerodynamics by Ashley and Zartarian (1956). The aerodynamic pressure loading as given by this theory is

$$p - p_\infty = \frac{2q_a}{\beta} \left(\frac{M_\infty^2 - 2}{M_\infty^2 - 1} \frac{1}{V} \frac{\partial w}{\partial \alpha} + \frac{\partial w}{\partial x} \right) \quad (2.1)$$

where $q_a = \rho_a V^2 / 2$ is the free stream dynamic pressure, V the velocity, ρ_a the air density and $\beta = \sqrt{M_\infty^2 - 1}$. If the aerodynamic damping is neglected in Eq. (2.1), the quasi-static Ackeret aerodynamic theory, also known as the static strip theory, is simplified to

$$p - p_\infty = \frac{2q_a}{\beta} \frac{\partial w}{\partial x} \quad (2.2)$$

For air flow with Mach number close to one, the full linearized inviscid potential theory aerodynamics is usually employed (Dowell, 1967). The aerodynamic pressure loading is given by

$$p - p_\infty = -\rho_a \left(\frac{\partial \phi}{\partial \alpha} + V \frac{\partial \phi}{\partial x} \right) \quad (2.3)$$

where the velocity potential function ϕ must satisfy

$$\nabla^2 \phi - \frac{1}{c^2} \left(\frac{\partial}{\partial \alpha} + V \frac{\partial}{\partial x} \right)^2 \phi = 0 \quad (2.4)$$

subject to the boundary conditions

$$\left. \frac{\partial \phi}{\partial z} \right|_{z=0} = \begin{cases} \frac{\partial w}{\partial \alpha} + V \frac{\partial w}{\partial x} & \text{on plate} \\ 0 & \text{off plate} \end{cases} \quad (2.5)$$

Because of the recent renewed interest in flight vehicles that will operate not only at high-supersonic Mach numbers but well into hypersonic regime, there is an interest in approaches that can employ unsteady nonlinear aerodynamic theories. The piston aerodynamic theories, although several decades old, have generally been employed to approximate the aerodynamic loads on the panel from local pressures generated by the body's motion as related to the local normal component of the fluid velocity and the local pressure. For supersonic Mach numbers, the quasi-steady aerodynamic theory reasonably estimated the aerodynamic pressures and it gave fair agreement between theory and experiment for plates exposed to static pressure loads and buckled by uniform thermal expansion (Ventres and Dowell, 1970). In the hypersonic regime, the

unsteady full third-order piston theory aerodynamics (Ashly and Zartarian, 1956) is used to develop the aerodynamic pressure given by

$$p - p_\infty = \frac{2q}{M_\infty} \left(\frac{1}{V} \frac{\partial w}{\partial t} + \frac{\partial w}{\partial x} + \frac{(\gamma+1)M_\infty}{4} \left(\frac{1}{V} \frac{\partial w}{\partial t} + \frac{\partial w}{\partial x} \right)^2 + \frac{(\gamma+1)M_\infty^2}{12} \left(\frac{1}{V} \frac{\partial w}{\partial t} + \frac{\partial w}{\partial x} \right)^3 \right) \quad (2.6)$$

where γ is the ratio of specific heat.

By using piston theories and the potential flow theory for aerodynamic loading, it is assumed that continuum theory applies. For hypersonic vehicles at high altitudes the continuum hypothesis may not hold true. A free molecule flow with quasi-steady approximation was presented by Resende (1991) to obtain the aerodynamic loading for a two-dimensional simply supported panel. The proposed rarefied formulation was highly dependent on two parameters: the fraction of the molecules and the temperature ratio (panel temperature to the temperature of the undisturbed flow).

3. ANALYSIS METHODS

The partial nonlinear behavior of a fluttering panel was first considered by several investigators: Bolotin (1963), Fung (1958), Houbolt (1958) and Eisely (1956). They were primarily concerned with determining stability boundaries of two-dimensional plates. Using a two-mode Galerkin approach, Fralich (1965) studied the three-dimensional plate buckling effects on flutter boundaries using the von-Karmen plate theory and the Ackeret aerodynamic theory. In the following, the classical analytical and the finite element methods for nonlinear panel flutter at supersonic speeds are discussed first, followed by nonlinear flutter in hypersonic flows.

3.1 Classical Analytical Methods

For the full structural nonlinear limit-cycle approach, a variety of analysis methods have been employed to assess the panel flutter problem. The Galerkin's method was used to reduce the governing partial differential equations to a set of coupled ordinary differential equations in time, which were numerically integrated for arbitrary initial conditions. The integration was continued until a limit-cycle oscillation of constant amplitude, independent of the initial conditions, was reached. The nonlinear oscillations of simply supported (Dowell, 1966; Dowell, 1967) and clamped, inplane elastically restrained, (Ventres, 1970) fluttering plates were studied using this method. Dowell (1966) determined that the direct numerical integration approaches require a minimum of 6 linear modes, as the Galerkin approximate functions, to achieve a converged solution for displacements and possibly more if stresses are required (McIntosh, 1970). Recently, the limit-cycle oscillation of a cantilever plate was studied by Weiliang and Dowell (1991). They employed a Rayleigh-Ritz approach in conjunction with the direct numerical integration and showed that the length-to-width ratio of the cantilever plate was a significant factor on the flutter vibration.

A number of other classical analytical methods exist for the investigation of limit-cycle oscillations of panels in supersonic flow. In general, the Galerkin's method is used in the spatial domain, and the panel deflection is expressed in terms of two to six linear normal modes. Various techniques in the temporal domain such as harmonic balance and perturbation techniques have been successfully employed to study the subject of nonlinear panel flutter. The harmonic balance method requires less computational time than the method of direct integration and is mathematically comprehensible and systematic, but it is extremely tedious to implement. The method was used with a two-mode Galerkin solution to obtain the limit-cycle motions (Bolotin, 1963; Kobayashi, 1962). Rectangular plates were treated by Kuo et al. (1972), Eastep and McIntosh (1970), Eslami (1986; 1987) and Yuen and Lau (1991). The Rayleigh-Ritz approximation to Hamilton's variational principle was employed by Eastep and McIntosh to obtain the equations of motion in the spatial domain. Specific orthotropic panels were studied by Eslami. A hinged two-dimensional fluttering plate with moderately high postbuckling loads using a four-mode expansion and an incremental harmonic balance method was reported by Yuen and Lau.

The perturbation method was adopted to nonlinear panel flutter by Morino (1969) and Kuo et al. (1972). Detailed extensions (Morino and Kuo, 1971) and the stability (Smith and Morino, 1976) of the application of this technique to nonlinear panel flutter were studied. Correlation between perturbation techniques and the harmonic balance method has been shown to be in good agreement (Kuo et al., 1972; Morino and Kuo, 1971).

3.2 Finite Element Method

All of the early studies in nonlinear panel flutter using classical methods have been limited to isotropic or orthotropic of two or three dimensional rectangular plates with all four edges simply supported or clamped. Extension of the finite element method to study the linear panel flutter problem was due to Olson (1967; 1970) using a frequency domain eigen solution. Because of its versatile applicability, effects of aerodynamic damping, complex panel configurations and support conditions, laminated composite anisotropic panel properties, flow angularities, inplane stresses and thermal loads can be easily and conveniently included in the finite element formulation. A survey on the finite element methods to linear panel flutter was given by Yang and Sung (1977) and Bismarck-Nasr (1992), and to nonlinear panel flutter by Zhou et al. (1994).

Application of the finite element method to study the supersonic limit-cycle oscillations of two dimensional panels was given by Mei (1977) using an iterative frequency domain eigen solution. Mei and Rogers (1976) implemented the two-dimensional panel flutter analysis into the NASTRAN. Rao and Rao (1980) investigated the supersonic flutter of two-dimensional panels with ends restrained elastically against rotation. Sarma and Varadan (1988) studied the nonlinear behavior of two-dimensional panels using two solution procedures, both in the frequency domain.

Further extension of the finite element method to treat supersonic limit-cycle oscillations of three-dimensional rectangular plates was given by Mei and Weidman (1977). The effects of damping, aspect ratio, inplane forces and boundary conditions were considered. Mei and Wang (1982) employed an 18-degrees of freedom (DOF) triangular plate bending element to study supersonic limit-cycle behavior of three dimensional triangular plates. Han and Yang (1983) used the 54-DOF high order triangular plate element to study nonlinear panel flutter of three-dimensional rectangular plates with inplane forces.

All the investigations cited so far dealt with flutter of isotropic panels. Few papers in the literature investigated the supersonic limit-cycle oscillations of composite panels. Dixon and Mei (1993) studied the nonlinear flutter of rectangular composite panels. The limit-cycle response was obtained using a 24-DOF rectangular plate element and a linearized updated mode with nonlinear time function (LUM/NTF) approximate solution procedure. The LUM/NTF solution procedure in the frequency domain was developed by Gray (1991). Liaw and Yang (1993) used a 48-DOF rectangular element and investigated the effects of structural uncertainties occurring during the fabrication process on nonlinear supersonic flutter of laminated composite plates.

3.3. Analysis Methods for Hypersonic Panel Flutter

The aerodynamic nonlinearities were first considered in conjunction with structural nonlinearities by McIntosh (1970) and Eastep and McIntosh (1970) to a two-dimensional plate with simply supported ends. In their study a modified form of the second-order piston theory, in which the term $(\frac{1}{V} \frac{\partial w}{\partial t})^2$ was neglected, was used. They integrated the nonlinear modal equations of motion for given initial conditions and observed the resultant panel motion versus time until a limit-cycle of constant amplitude was reached. Flutter stability boundaries from linear and partial second-order piston theories were obtained for a nondimensional axial force varying between -3 and +1. The aerodynamic nonlinearities decrease the critical flutter dynamic pressure.

Because of the renewed interest in panel flutter at high-supersonic/hypersonic speeds for the National Aerospace Plane (NASP) (Reed et al., 1987), Gray et al. (1991) extended the finite element method to investigate the hypersonic limit-cycle oscillations of two-dimensional panels using the full third-

order piston aerodynamic theory. Gray (1991) and Gray and Mei (1993) extended further the finite element method to nonlinear flutter of three-dimensional thin laminated composite panels. The LUM/NTF solution procedure was presented to solve the nonlinear panel flutter finite element equations in structure node DOF. Nonlinear flutter analyses were performed for different boundary conditions and for various influence parameters: plate thickness to length ratio, plate aspect ratio, material orthotropic ratio, and number of layers. It was found that the $(\frac{\partial w}{\partial x})^2$ term of the full third-order piston aerodynamic theory is the most significant among the nonlinear aerodynamic terms for the large amplitude limit-cycle panel flutter.

Bein et al. (1993) investigated hypersonic flutter of simply supported curved shallow orthotropic panels with uniform temperature distribution. Coupled nonlinear panel flutter equations were obtained using Galerkin's method with eight linear modes (4 in the airflow or x-direction and 2 in the y-direction). Then numerical integration in time was used to compute limit-cycle amplitudes. They showed that the unsteady aerodynamic loading based on the third-order piston theory gives virtually identical pressure distributions to that obtained from the direct solution of the Euler equations. Hypersonic flutter on curved panel was further studied by Nydick et al. (1995). Aerodynamic heating, the presence of shock in the flow, and non-zero initial curvature were shown to significantly affect the aeroelastic behavior. It was found that the aerodynamic load obtained from the third-order piston theory differs substantially from that computed using Navier-Stokes equations. The limit-cycle results obtained by Nydick et al. compared well for the supersonic isotropic panel (Dowell, 1966) and for the hypersonic orthotropic case (Gray and Mei, 1993).

Chandiramani et al. (1995) investigated the non-periodic flutter behavior of simply supported buckled composite panels subjected to uniform edge compression. The higher-order shear deformation theory and the third-order piston theory aerodynamic were used and Galerkin's method with a 2×2 linear normal modes (2 each in the x- and y-directions). A predictor and Newton-Raphson type corrector technique was employed for the periodic solution, and the numerical integration was used for quasi-periodic or chaotic flutter solutions. Results showed that edges restrained parallel to the airflow do not significantly affect the immediate post-critical response, and that a higher-order shear deformation theory is required for a moderately thick composite panel.

Sri Namachchivaya and Lee (1997) recently studied the bifurcation behavior near critical points of a simply supported isotropic panel using Galerkin's method and two linear natural modes in the airflow x-direction. The third-order unsteady piston theory aerodynamics was employed in the formulation.

4. INFLUENCE SYSTEM PARAMETERS

The various influence parameters that affect supersonic/hypersonic nonlinear panel flutter characteristics are described in this section. Those system parameters considered include the effects of thermal loads, inplane forces, flow direction, and curved plates or cylindrical panels. The two types of system equations, in structural node DOF and in modal coordinates, for large amplitude panel flutter using the first-order piston theory aerodynamics based on finite element methods are briefly presented. Flutter of laminated composite panels at elevated temperatures are considered. Two solution procedures, the LUM/NTF approximation and the numerical integration, can be employed. Flutter behavior of composite panels at elevated temperatures: flat, buckled, limit-cycle, periodic and chaotic motions are shown.

4.1 Thermal Effects

Few investigations on panel flutter have dealt directly with thermal effects. Houbolt (1958) was the first to study the buckling stability and flutter boundaries for two-dimensional panels with uniform temperature distribution. Two linear modes were used for the thermal postbuckling deflection. Yang and Han (1976) used the finite element method to study linear flutter of thermally buckled two-dimensional panels. Abbas et al. (1993) studied the nonlinear flutter of simply supported orthotropic composite panels under aerodynamic heating. The governing equations were derived by the Reissner functional and Hamilton's principle. Galerkin's method with six mode was employed and the time history was obtained by numerical

integration. Hopkins and Dowell (1994) investigated a square cantilevered isotropic panel under temperature differential. The Rayleigh-Ritz assumed modes method was employed. Uniform and biquadratic temperature differentials were considered. Convergence of flutter response with number of transverse and inplane modes was investigated in detail. Stability regions for the two temperature differentials are quite different.

For non uniform temperature distribution, Xue et al. (1990) investigated flutter boundaries of thermally buckled two-dimensional panels. Xue (1991) and Xue and Mei (1991; 1993) extended to nonlinear panel flutter with non uniform temperature effects for two-dimensional and three-dimensional isotropic panels of arbitrary shape using the discrete Kirchhoff theory (DKT) triangular plate element. Dixon (1991) and Dixon and Mei (1992) investigated the limit-cycle oscillations of rectangular composite panels subjected to uniform temperature. Lee et al. (1997) have recently performed nonlinear flutter for stiffened composite laminated plates considering uniform temperature thermal effect. They employed the first-order shear deformable plate theory and the Timoshenko beam theory for the finite element modeling of a skin panel and stiffeners, respectively, and the influence of temperature dependent material properties on panel behavior was also considered. Liaw (1997) has used a 48-DOF rectangular thin-plate finite element to study the nonlinear panel flutter under uniform and sinusoidal temperature distributions. Effects of fiber orientation on supersonic flutter behavior of a rectangular symmetric angle-ply panel were investigated in detail. Recently, Udrrescu (1998) developed a 33-DOF triangular finite element to study a simply supported three-dimensional isotropic panel under uniform temperature distribution. The higher order finite element was based on Argyris' natural approach, then extended to large deflection theory. All four dynamic responses: damped solution, limit-cycle, buckled panel and chaotic solution were presented.

The system equations of motion for nonlinear flutter of composite panels at supersonic speeds and arbitrary temperature distributions based on the finite element methods (Xue, 1991; Xue and Mei, 1993; Dixon, 1991; Dixon and Mei, 1992; Lee et al., 1997; Liaw, 1997) can be expressed in the matrix form as

$$\frac{1}{\omega_o^2} [M] \{\ddot{W}\} + \frac{g_a}{\omega_o} [G] \{\dot{W}\} + (\lambda [A_a] + [K] - [K_{\Delta T}] + [K1(W)] + [K2(W^2)]) \{W\} = \{P_{\Delta T}\} \quad (4.1)$$

where $[M]$, $[G]$, $[A_a]$ and $[K]$ are the system mass, aerodynamic damping, aerodynamic influence and linear stiffness matrices, respectively; $[K1]$ and $[K2]$ are the first and second order nonlinear stiffness matrices which depend linearly and quadratically upon system structure DOF $\{W\}$, respectively; and $\{P\}$ is the load vector. The subscripts a and ΔT denote aerodynamic and thermal, respectively. The nondimensional dynamic pressure and aerodynamic damping are defined as

$$\lambda = \frac{2q_a a^3}{\beta D_{110}}, \quad g_a = \frac{\rho_a V (M_\infty^2 - 2)}{\rho h \omega_o \beta^3} \quad (4.2)$$

where $\omega_o = (D_{110}/\rho h a^4)^{1/2}$ is a reference frequency, and ρ , h and a are the panel density, thickness and length, respectively. The value D_{110} is the first entry of the laminate flexural stiffness $[D]$ calculated when all of the fibers of the composite layers are aligned in the airflow x -direction.

The system finite element equations in structural node DOF presented in equation (4.1) are mathematically separated into two sets of equations and then solved sequentially. The first set of equations yields the thermal-aerodynamic equilibrium position using the Newton-Raphson iteration method, and the second set of equations of motion leads to the flutter limit-cycle motions using the LUM/NTF approximate method. The use of iterative linearized eigen solution (for example LUM/NTF approximation) in the frequency domain has been successful to study nonlinear panel flutter. However, the application of the LUM/NTF method to the system equations in the form presented in equation (4.1) has three disadvantages: (1) the number of structure node DOF of $\{W\}$ is usually very large, (2) at each iteration, the element nonlinear stiffness matrices have to be evaluated and the system nonlinear matrices have to be assembled and updated, and (3) the periodic and chaotic panel motions can not be determined.

The remedy is to transform equation (4.1) into a set of modal coordinates of rather small DOF (e.g. 6 modes by Dowell, 1966). For a rectangular panel with airflow along its length, the chosen modes, eigen

solution of $\omega_r^2 [M]\{\phi_r\} = [K]\{\phi_r\}$, are the lowest few in the airflow free-stream direction and the first one in the cross-stream direction as

$$\{W\} = \sum_{r=1}^n q_r(t)\{\phi_r\} = [\Phi]\{q\} \quad (4.3)$$

The system equations, Eq. (4.1), are thus transformed to the general Duffing-type reduced modal equations of the form

$$[\bar{M}]\{q_{\tau\tau}\} + [C]\{q_{\tau}\} + ([\bar{K}] + [K_q] + [K_{qq}])\{q\} = \{p_{\Delta T}\} \quad (4.4)$$

where $\tau = \omega_0 t$ is the nondimensional time, and the modal mass, aerodynamic damping and linear stiffness matrices are

$$([\bar{M}], [C], [\bar{K}]) = [\Phi]^T ([M], g_a[G], \lambda[A_a] + [K] - [K_{\Delta T}]) [\Phi] \quad (4.5)$$

and the quadratic and cubic terms, and the modal thermal load vector are

$$\begin{aligned} [K_q]\{q\} &= [\Phi]^T \left(\sum_{r=1}^n q_r [K1]^{(r)} \right) [\Phi]\{q\} \\ [K_{qq}]\{q\} &= [\Phi]^T \left(\sum_{r=1}^n \sum_{s=1}^n q_r q_s [K2]^{(rs)} \right) [\Phi]\{q\} \\ \{p_{\Delta T}\} &= [\Phi]^T \{P_{\Delta T}\} \end{aligned} \quad (4.6)$$

The nonlinear modal stiffness matrices $[K1]^{(r)}$ and $[K2]^{(rs)}$ are assembled from the corresponding element nonlinear stiffness matrices which are evaluated with the corresponding element components obtained from the known system mode $\{\phi_r\}$. Therefore, the nonlinear modal stiffness matrices are constant matrices. For detailed description of the modal formulation, the readers are referred to Zhou et al. (1994). For various combinations of dynamic pressure λ , temperature change ΔT and aerodynamic damping $g_a \approx \sqrt{\lambda \mu / M_\infty}$ ($\mu = \rho_a a / \rho h$), all five types of panel behavior (flat, buckled, limit-cycle, periodic and chaotic motions) can be determined from the nonlinear modal equations, Eq. (4.4), using a numerical integration scheme.

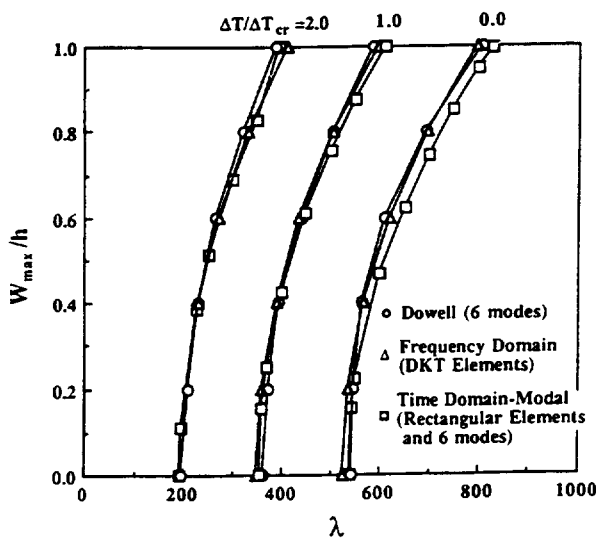


Fig. 1 Comparison of limit-cycle amplitudes for a simply supported square isotropic panel ($\mu/M_\infty = 0.1$).

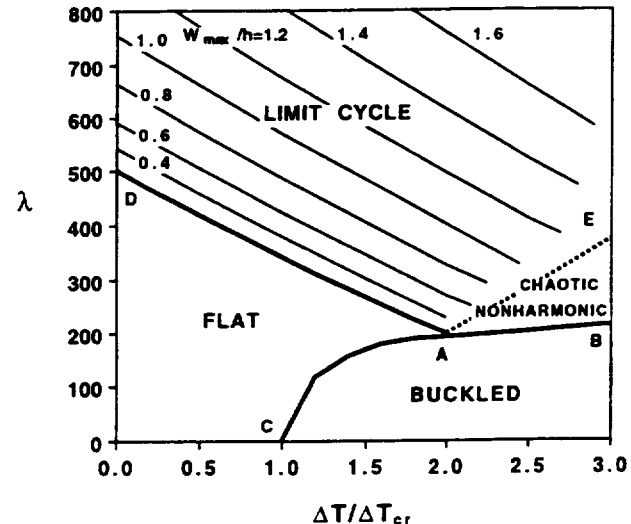


Fig. 2 Stability boundaries and limit-cycle amplitudes of a simply supported square panel with uniform temperature.

The limit-cycle results for a simply supported isotropic square plate at $\Delta T/\Delta T_{cr} = 0$, 1.0 and 2.0 using the time domain modal method are shown in Fig. 1. Results by Dowell (1966) using a six-mode model and by Xue and Mei (1993) using the LUM/NTF method in frequency domain are also shown for comparison. It demonstrates excellent agreement of these three approaches. Figure 2 shows the buckling and stability boundaries and limit-cycle oscillations for a simply-supported square isotropic panel subjected to uniform temperature distributions.

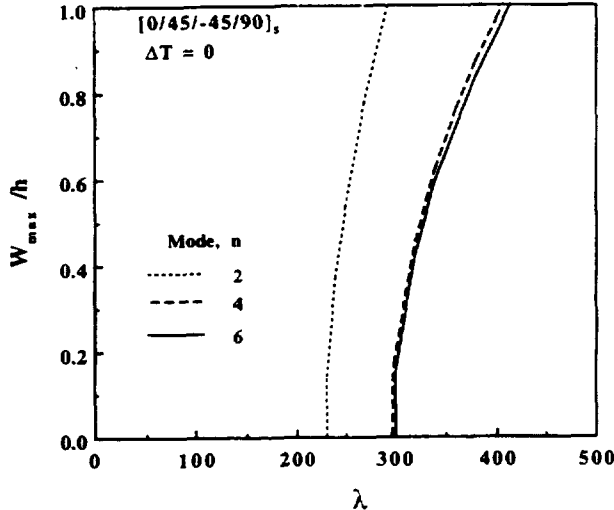


Fig. 3 Convergence of limit-cycle amplitudes for a simply supported $[0/45/-45/90]_s$ square panel ($\mu/M_\infty = 0.01$).

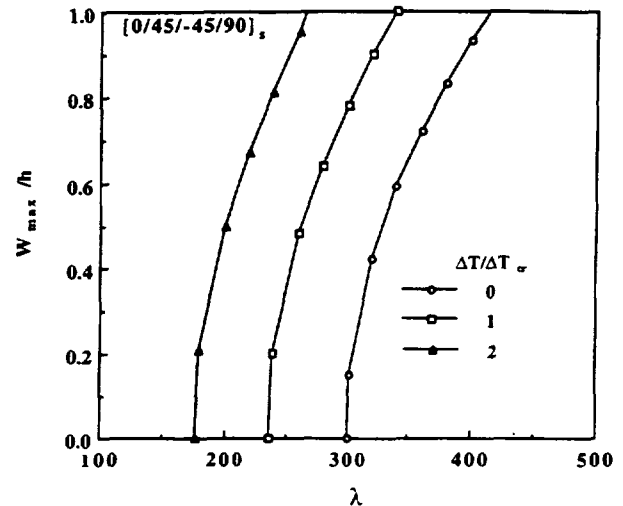


Fig. 4 Effect of temperature on limit-cycle amplitudes of a simply supported square $[0/45/-45/90]_s$ panel ($\mu/M_\infty = 0.01$).

Application of the finite element modal formulation presented in Eq. (4.4) to composite panels is demonstrated with a simply supported square graphite-epoxy eight-layer $[0/45/-45/90]_s$ laminate. The convergence of limit-cycle amplitudes by retaining different numbers of modes is shown in Fig. 3. It can be seen that a six-mode model will give accurate limit-cycle response. Figure 4 shows the limit-cycle oscillations at various temperatures $\Delta T/\Delta T_{cr} = 0, 1.0$ and 2.0 . The higher the thermal load, the lower the flutter dynamic pressure λ . Figure 5 illustrates the limit-cycle motions of the composite panel at $\lambda = 450$ and $\Delta T/\Delta T_{cr} = 1.0$. The harmonic behavior is clearly shown. In Fig. 6 the periodic motions are shown for the same composite panel at $\lambda = 140$ and $\Delta T/\Delta T_{cr} = 3.0$. The power spectral density (PSD) shows that there are four dominating frequencies and the phase plan plot indicates that there exist two weak wells. At higher temperature $\Delta T/\Delta T_{cr} = 6.0$ and moderate dynamic pressure $\lambda = 230$, the panel exhibits chaotic behavior as shown in Fig. 7.

Limited investigations on hypersonic panel flutter with aerodynamic heating exist in the literature. Bein et al. (1993) studied square isotropic and orthotropic panels with simply supported edges subjected to uniform temperature distribution. A 4×2 mode model (4 in the x or airflow and 2 in the y or cross-stream directions) was used with Galerkin's method. The numerical integration results showed that the aerodynamic heating reduces λ_{cr} and increases the limit-cycle amplitudes. Research is needed in this area including chaotic dynamic instabilities.

4.2 Inplane Force Effects

Numerous studies on nonlinear panel flutter have considered the inplane force effects. A buckled two-dimensional panel was investigated in detail and a physical interpretation of the merge of flutter and

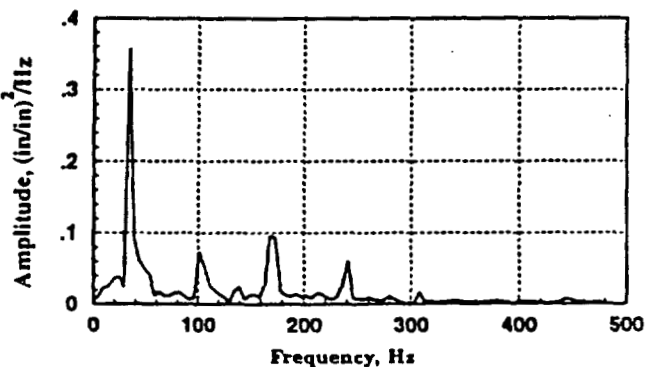
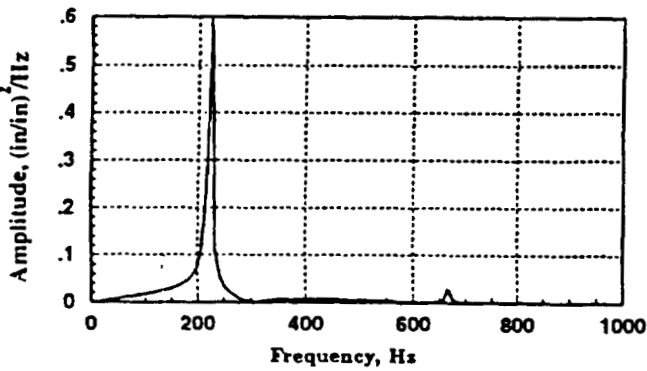
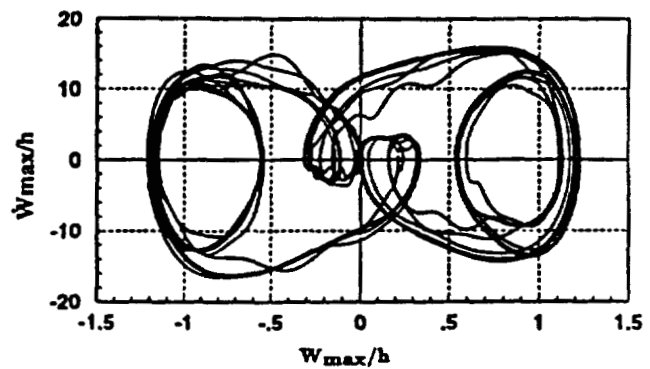
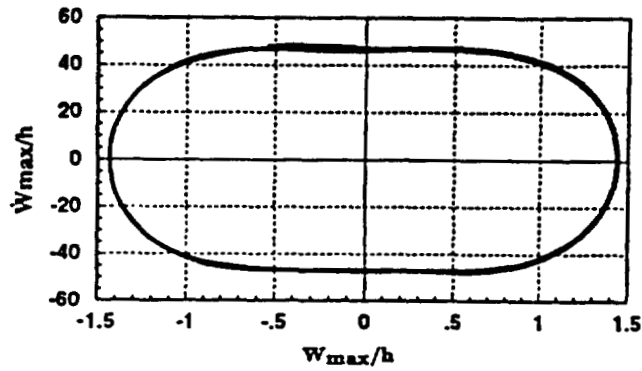
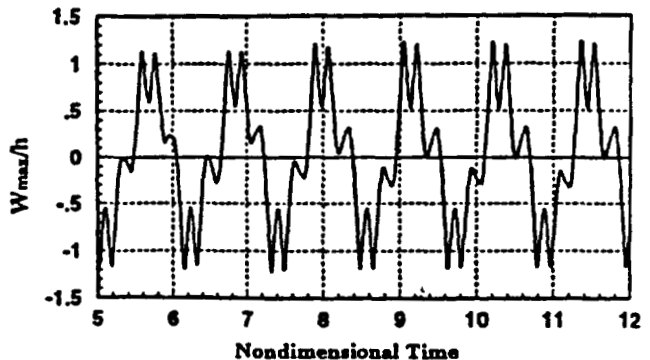
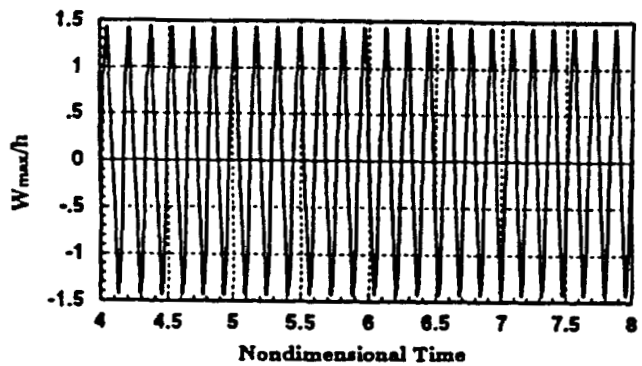


Fig. 5 Limit-cycle motions for a simply supported square [0/45/-45/90], panel ($\mu/M_\infty = 0.01$) at $\lambda = 450$, $\Delta T/\Delta T_{cr} = 1.0$.

Fig. 6 Periodic motions for a simply supported square [0/45/-45/90], panel ($\mu/M_\infty = 0.01$) at $\lambda = 140$, $\Delta T/\Delta T_{cr} = 3.0$.

buckling stability boundaries was given for chaotic motions by Dowell (1982). The influence of inplane forces on three-dimensional panels that have been discussed earlier include Dowell (1966; 1975), Morino and Kuo (1971), Kuo et al. (1972), Mei and Weidman (1977), Han and Yang (1983) and Liaw and Yang (1993). In general the influence on flutter behavior with the inplane force is similar to the behavior with the thermal loads. That is reduced critical dynamic pressure and increased limit-cycle amplitudes with the increase of compressive inplane forces.

Ibrahim et al. (1990) and Ibrahim and Orono (1991) have investigated the effect of random inplane forces acting on two-dimensional panels in supersonic flow. The response moment equations were generated by using the Fokker-Planck equations approach with two-mode and three-mode interactions. They found that the steady-state revealed in the response process is strictly stationary and that the inclusion

of more modes results in a reduction of the response levels and expands the stability region. Chin et al. (1995), however, considered that the inplane forces were harmonic. Galerkin's method and the multiple scales were used to obtain the five first-order nonlinear ordinary differential modal equations. A combination of a shooting technique and Floquent theory was employed to obtain limit-cycles and stability. They showed that the existence of a sequence of periodic-doubling bifurcations culminates in chaos.

4.3 Flow Direction Effect

A large number of studies which considered the influence of air flow direction on linear panel flutter or critical dynamic pressure λ_{cr} exist in the literature. The readers are referred to Laurenson and McPherson (1977) and Bismarck-Nasr (1992) for more review on this issue.

Friedmann and Hanin (1968) were the first to study supersonic nonlinear flutter of rectangular isotropic or orthotropic panels with arbitrary flow direction. They used the first-order quasi-steady aerodynamic theory and the Galerkin's method with a 4×2 mode model for panels with simply supported edges. Numerical integration was performed for limit-cycle motions. Chandiramani et al. (1995) used the third-order piston theory aerodynamics and the higher-order shear deformation theory to investigate nonperiodic flutter of a buckled composite panel. The flow yawing was considered, and Galerkin's method with a 2×2 mode model was employed for simply supported rectangular laminated panel.

Abdel-Motagaly et al. (1998) have recently extended the finite element method to study nonlinear flutter of composite panels with yawed supersonic flows. An efficient solution procedure was introduced by the application of LUM/NTF approximation to the reduced nonlinear modal equations. They employed a modal participation value to obtain accurate and converged limit-cycle response with a minimum number of linear natural modes. For laminated composite panels, the flow direction can affect the limit-cycle behavior greatly.

4.4 Effect of Streamwise Curved Plates

Dowell has shown theoretically the necessity for considering preflutter deformation under static aerodynamic pressure for nonlinear panel flutter at supersonic speeds. He investigated the effect of constant curvature on two-dimensional (Dowell, 1969) and three-dimensional (Dowell, 1970) rectangular

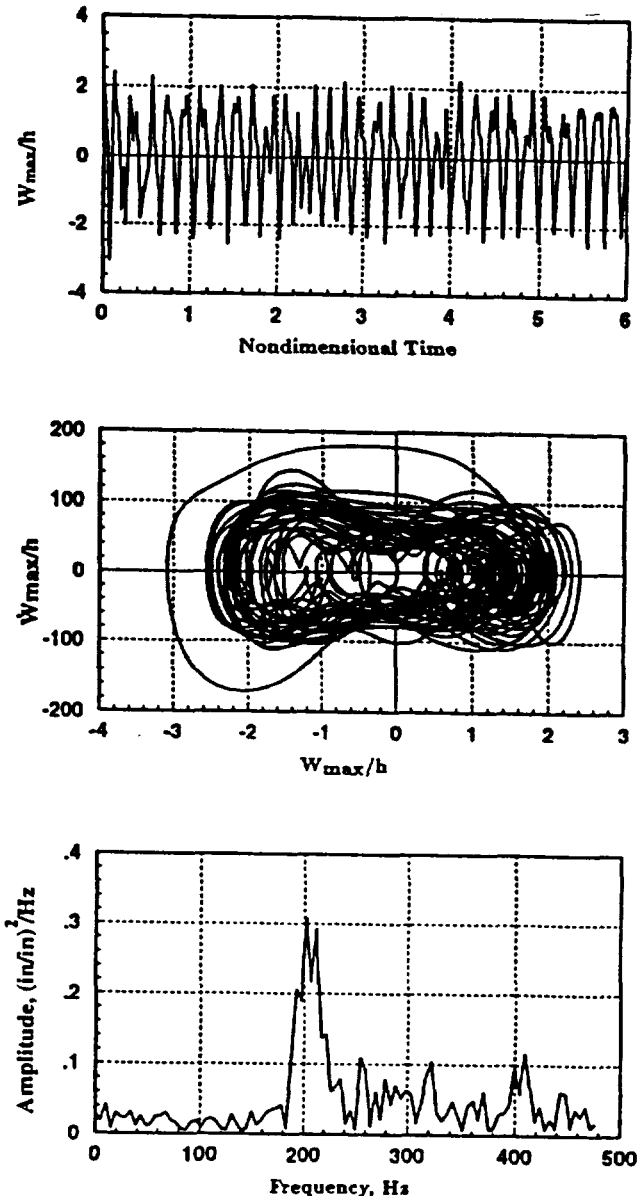


Fig. 7 Chaotic motions for a simply supported square $[0/45/-45/90]_s$ panel ($\mu/M_\infty = 0.01$) at $\lambda = 230$, $\Delta T/\Delta T_{cr} = 6.0$.

isotropic panels. It was shown that the streamwise curvature is detrimental both in lowering the dynamic pressure at which flutter starts and in increasing the flutter amplitude once flutter begins.

Nydrick et al. (1995) studied the hypersonic nonlinear flutter of curved panels. Two types of initial curvatures were considered. Krause and Dinkler (1998) investigated the influence of curvature on flutter behavior of simply supported two and three dimensional isotropic panels using finite element method. The first and third order piston theories were used and the curvature of the panels was described by imperfections. The effect of panel curvature on the hypersonic panel flutter case was found to be similar for that of the supersonic case.

4.5 Active Control of Panel Flutter

Many researchers have investigated the effectiveness of using smart or intelligent materials for passive or active control of flexible structures. Only a few studies have been reported in supersonic panel flutter suppression using smart materials. Scott and Weisshaar (1994) were the first to study controlling the linear panel flutter suppression using piezoelectric materials. The piezoelectric materials covered the full surface of the panel. Four modes were retained using the Ritz method, and the panel was modeled as a simply supported isotropic plate. Linear optimal control theory was employed in the simulation. Hajela and Glowasky (1991) applied piezoelectric elements in linear panel flutter suppression. Finite element models for panels with surface bonded and embedded piezoelectric materials were generated to determine the response. Using a multi-criterion optimization scheme, the optimal panel configuration with minimum weight and optimal sizing and layout of the piezoelectric elements for maximum flutter dynamic pressure were determined. In both studies by Scott and Weisshaar, and Hajela and Glowasky, the bending moment induced by the piezoelectric actuators is not effective in controlling panel flutter since there is no bending behavior in the linear case. Frampton et al. (1996) employed a collocated direct rate feedback control scheme for the active control of linear panel flutter. The linearized potential flow aerodynamics was used for the full transonic and supersonic Mach number range. An aeroelastic panel model was developed. They demonstrated that a significant increase of the flutter boundary was achievable for a simply supported square steel panel. Using a finite element approach, Suleman and Goncalves (1997) recently investigated a passive control methodology for linear panel flutter suppression. The methodology is to induce tensile inplane loads from a bonded or embedded piezoelectric patches, and it thus leads to an increased critical dynamic pressure for a stiffer panel. Since the main concern was reviewing nonlinear panel flutter, the search on the suppression of linear flutter was not exhaustive.

Lai et al. (1993) studied the control of nonlinear flutter of a simply supported isotropic plate using piezoelectric actuators. The Galerkin's method was adopted in obtaining the nonlinear modal equations. The optimal control theory and numerical integration were used in the simulation. They concluded that the bending moment induced by piezoelectric actuators was effective in flutter suppression.

Dongi et al. (1995) have presented a finite element method for investigations on adaptive panels with self-sensing piezoelectric actuators. The LUM/NTF algorithm was extended to include the linear and nonlinear active stiffness matrices due to output feedback. A control approach based on output feedback for active compensation of aerodynamic stiffness (ACAS) terms has been developed. They showed that the ACAS control is able to increase the linear flutter boundary to $M_\infty = 6.67$ from $(M_\infty)_\text{cr} = 3.22$ for a simply supported isotropic panel.

Zhou et al. (1995) recently have extended the finite element method to control isotropic panels with surface bonded piezoelectric patches. An optimal controller was developed based on the linearized modal equations, and the norms of the feedback control gain (NFCG) were used to provide the optimal shape and location of the piezoelectric actuators. Numerical simulations showed that the critical flutter dynamic pressure can be increased about four times and two times for simply supported case and clamped case, respectively. Zhou et al. (1996) further improved the finite element formulation to consider coupling between structural and electrical fields for laminated composite panels. A simply supported square [0/45/-45/90]_s graphite/epoxy composite panel was investigated. The panel becomes less stiff when piezoelectric

actuators are embedded, and the critical flutter dynamic pressure (λ_{cr}) is 298 and 227 for [0/45/-45/90]_s and [Piezo/45/-45/90]_s panels, respectively. Because of the limitation of the maximum operating electric field of the piezoelectric actuators (set to one-half of depolarization in the study), there is a maximum dynamic pressure beyond which the flutter motion can no longer be suppressed. This particular dynamic pressure is referred to as the maximum flutter-free dynamic pressure λ_{max} .

Table 2 Comparison of maximum flutter-free dynamic pressure λ_{max}
for one-set actuator placed at the leading edge

x_s/a	$\lambda_{max} (R = 500 \times I)$	$\lambda_{max} (R = 1000 \times I)$
0.0	298 (= λ_{cr})	298 (= λ_{cr})
0.1	600	616
0.2	819	878
0.3	877	975
0.4	1157	1262
0.5	1100	1171
0.6	1037	1150
1.0	597 ($\lambda_{cr} = 227$)	596 ($\lambda_{cr} = 227$)

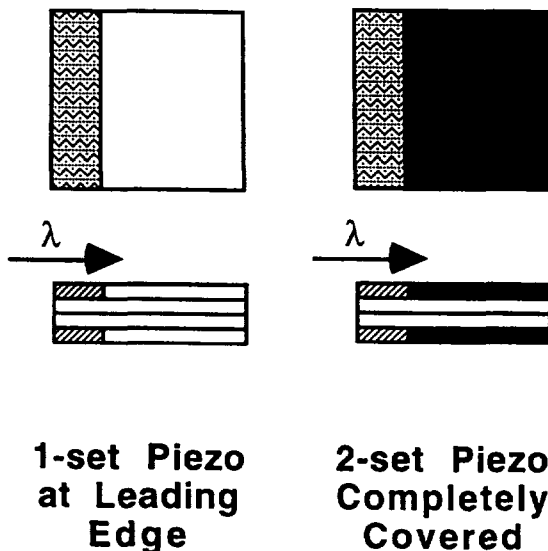


Fig. 8 Configurations of a composite panel with embedded piezoelectric actuators.

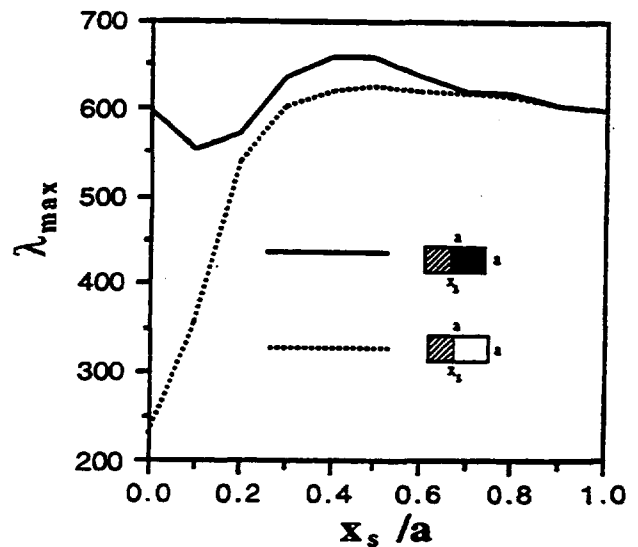


Fig. 9 Maximum flutter-free dynamic pressure vs. normalized separating position for a simply supported square [0/45/-45/90], panel.

Table 2 shows the maximum flutter-free dynamic pressure λ_{max} for the different sizes of one-set actuator design placed at the leading edge (Fig. 8) and two constants for the control penalty matrix R . λ_{max} is low for the small-size actuator design ($x_s/a < 0.3$) due to limited moments induced by piezoelectric actuation. When piezoelectric layers replace completely the top and bottom layers of the composite panel ($x_s/a = 1.0$), λ_{max} drops to 597 since the [Piezo/45/-45/90]_s has a small critical dynamic pressure $\lambda_{cr} = 227$. It can be concluded that more piezoelectric materials do not guarantee having a better performance for flutter suppression.

For the [Piezo/45/-45/90]_s panel, activating two independent sets of the piezoactuator (two-set actuator design) would yield a better performance than only activating a portion of the piezoactuator at the leading edge because of the flexibility of using two control variables. The variation of λ_{\max} with the normalized separating position for using one control variable (dotted line) and two control variable (solid line) designs is shown in Fig. 9. The two-set actuator design will increase the critical dynamic pressure three times ($\lambda_{\max}/\lambda_{cr} = 3.0$) for the case studied.

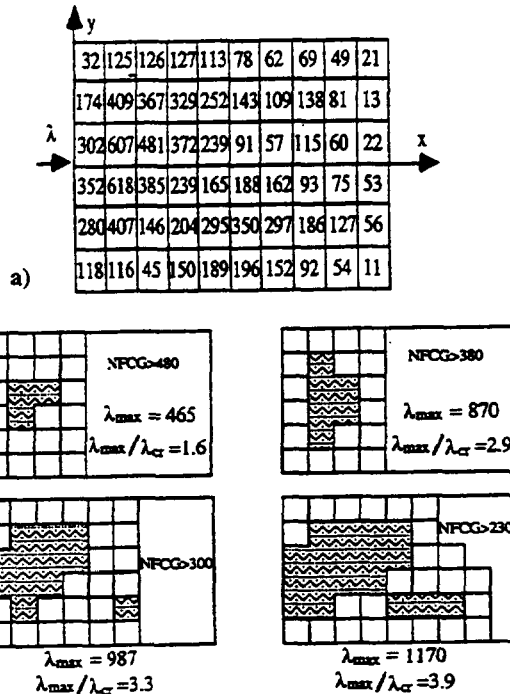


Fig. 10 For a simply supported square [0/45/-45/90], panel: a) NFCG and b) optimal location for one-set partially covered piezoelectric actuators.

Table 3 Comparison of λ_{\max} for two different designs

Actuator at the leading edge			Actuator based on NFCG		
x_s/a	λ_{\max}	$\lambda_{\max}/\lambda_{cr}$	Size	λ_{\max}	$\lambda_{\max}/\lambda_{cr}$
0.1	616	2.1	6	870	2.9
0.2	878	2.9	12	987	3.3
0.3	975	3.3	18	1170	3.9

The norms of feedback control gain (NFCG) developed earlier (Zhou et al., 1995) were employed to determine the optimal shape and location of piezoelectric actuators. The [Piezo/45/-45/90]_s is divided into a number of small patches which equal the number of finite elements used. The NFCG values are then calculated for each set at $\lambda = 1000$ and $R = 1000 \times I$ and the result is shown in Fig. 10a. The higher the value, the more control influence of the corresponding patch is for flutter control. By connecting these small patches, the optimal shape and location of the actuator can be determined. Four actuator designs are shown in Fig. 10b based on the NFCG. Table 3 gives the maximum flutter-free dynamic pressure λ_{\max} and the

ratio of $\lambda_{\max}/\lambda_{cr}$ for three different sizes of actuator (6, 12 and 18 element sizes) based on the two design methods. The advantage of using the NFCG rather than placing the actuator at the leading edge is evident.

Wind-Tunnel testing performed by Ho et al. (1997) has shown that panel limit-cycle motions observed in the wind tunnel can be successfully reduced for composite panels with one-sided surface mounted piezoelectric actuators, strain sensors and a simple iterative gain tuning algorithm were used.

5. EXPERIMENTS

A large number of experimental investigations on linear panel flutter exist in the literature. Those experiments were performed in the sixties and early seventies and most of the test results were published as AF Technical Reports, NASA Contractors Reports or Technical Notes.

However, experimental investigations on post or nonlinear flutter behavior of panels have been essentially non-existent. Kappus et al. (1971) conducted the panel flutter tests in the 1.1 to 1.4 Mach number range for flat rectangular $30 \times 6.7 \times 0.032$ in. aluminum panels clamped on four edges. The panel flutter boundary was defined as a function of primary variables: Mach number, in-plane compression load and pressure differential across the panel. Secondary variables consisting of cavity volume, boundary layer thickness, and panel cross stiffening were also investigated. Panel stresses and motion were measured at flutter onset and during penetration beyond the flutter onset boundary. Tests showed that minimum flutter onset dynamic pressures occurred between Mach 1.3 and 1.4. Panel buckling lowered the flutter onset dynamic pressure by about a factor of four over the no-load condition. A pressure differential as little as 0.1 psi raised the flutter onset dynamic pressure by 50 %. Maximum panel surface stresses of about 11,000 psi were measured at the panel trailing edge during a deep flutter penetration run (dynamic pressure set at 1000 psf which is 3.33 times the onset value). The maximum stress conditions were maintained for over 300,000 panel oscillations cycles without panel failure.

SUMMARY AND REMARKS

A review of large amplitude panel flutter at supersonic and hypersonic speeds has been presented. The review has been limited to nonlinear structure models due to space limitation. The classical analytical methods include the Galerkin's method with numerical integration, harmonic balance, and perturbation solutions. The finite element methods include the structure node DOF formulation with frequency domain eigen solution and the reduced modal coordinates formulation with time domain numerical integration or frequency domain solutions. Emphasis has been placed on the finite element methods. Interaction parameters or effects considered include temperature or aerodynamic heating, flow direction, inplane loads, curved panels and active control. Composite panel behavior at supersonic Mach numbers and elevated temperatures as well as active control using piezoelectric actuators were treated in detail.

For the aerodynamic pressure loading, the piston theory aerodynamics needs experimental validation, or better theories predicting the pressure loading need to be developed and verified as suggested by Nydick et al. (1993).

Material degradation at high temperature includes mechanical properties and cycles to fatigue failure, etc. The temperature dependent properties for the panel material have to be considered for high supersonic and hypersonic flutter analyses. Investigations on hypersonic flutter of composite panels using the third-order piston theory aerodynamics with temperature effects are almost non-existent. Curved or cylindrical panels at supersonic and hypersonic speeds need further research efforts.

Suppression of panel flutter motions including nonperiodic and chaotic motions using smart materials and adaptive nonlinear control algorithms requires investigation.

Finite amplitude panel flutter experiments performed at supersonic and hypersonic Mach numbers, high temperatures and flow yaw effects are urgently needed. The test data are needed for the validation of various analysis models. It is also to be hoped that those nonlinear panel flutter analysis capabilities will be incorporated into one of the general purpose finite element packages and the nonlinear structural panel flutter will be used for designing panels for fatigue rather than catastrophic failure.

ACKNOWLEDGMENTS

The authors acknowledge the furnishing of panel flutter articles by Dr. L. Huttell of AFRL, Dr. J. W. Sawyer of NASA LaRC, Professor P. Friedmann of UCLA and Professor M. Ferman of St. Louis University.

REFERENCES

1. Dowell, E. H., "Panel flutter: a review of the aeroelastic stability of plates and shells," AIAA Journal, Vol. 8, No. 3, 1970, pp. 385-399.
2. Gray, C. E. Jr. and Mei, C., "Large amplitude finite element flutter analysis of composite panels in hypersonic flow," AIAA Journal, Vol. 31, No. 6, 1993, pp. 1090-1099.
3. Laurenson, R. M. and McPherson, J. I., "Design procedures for flutter-free surface panels," NASA CR-2801, McDonnell Douglas, Co., St. Louis, MO, 1977.
4. Bismarck-Nasr, M. N. , "Finite element analysis of aeroelasticity of plates and shells," Applied Mechanics Review, Vol. 45, No 12, 1992, pp. 461-482.
5. Zhou, R. C., Xue, D. Y. and Mei, C., "On analysis of nonlinear panel flutter at supersonic speeds," First Industry/Academy Symposium on Research for Future Supersonic and Hypersonic Vehicles, NC A&T State University, Greensboro, NC, 1994, pp. 343-348.
6. Dowell, E. H., "Aeroelasticity of plates and shells," Noordhoff Int. Pub., Leyden, The Netherlands, 1975.
7. Librescu, L., "Elastostatics and kinetics of anisotropic and heterogeneous shell-type structures," Noordhoff Int. Pub., Leyden, The Netherlands, 1975.
8. Ashley, H. and Zartarian, G., "Piston theory- a new aerodynamic tool for aeroelastician," Journal of Aeronautical Science, Vol. 23, No. 12, 1956, pp. 1109-1118.
9. Dowell, E. H., "Nonlinear oscillations of a fluttering plate II," AIAA Journal, Vol. 5, No. 10, 1967, pp. 1856-1862.
10. Ventres, C. S. and Dowell, E. H., "Comparison of theory and experiment for nonlinear flutter of loaded plates," AIAA Journal, Vol. 8, No. 11, 1970, pp. 2022-2030.
11. Resende, H. B., "Nonlinear panel flutter in a rarefied atmosphere: aerodynamic shear stress effects," 32th Structure, Structural Dynamics and Materials Conf., Baltimore, MD, 1991, pp.1992-2001.
12. Bolotin, V. V., "Nonconservative problems of the theory of elastic stability," McMillan Co., New York, 1963, pp. 199-312.
13. Fung, Y. C., "On two-dimensional panel flutter," Journal of Aeronautical Science, Vol. 25, No. 3, 1958, pp. 145-160.
14. Houbolt, J. C., "A study of several aerothermoelastic problems of aircraft in high speed flight," Ph.D. Thesis, Mitteilnng aus dem Institute fur Hugzeugstatikund Leuchbau, Nr.5, ETH, Zurich, 1958.
15. Eisely, J. G., "The flutter of two-dimensional buckled plate with clamped edges in supersonic flow," AFOSR-TN-56-296, 1956.
16. Fralich, R. W., "Postbuckling effects on the flutter of simply supported rectangular panels at supersonic speed," NASA-TN D1615, 1965.
17. Dowell, E. H., "Nonlinear oscillations of a fluttering plate I," AIAA Journal, Vol. 4, No. 7, 1966, pp. 1267-1275.
18. Ventres, C. S., "Nonlinear flutter of clamped plates," Ph.D. Thesis, Princeton University, Princeton, NJ, 1970.
19. McIntosh, S. C. Jr., "Theoretical considerations of some nonlinear aspects of hypersonic panel flutter," Final Report , Sept. 1, 1965 to Aug. 31, 1970, NASA Grant NGR 05-020-102, Dept. of Aeron. and Astr., Stanford University, Stanford, CA, 1970. Also "Effect of hypersonic nonlinear aerodynamic loading on panel flutter," AIAA Journal, Vol. 11, No. 1, 1973, pp. 29-32.
20. Weiliang, Y. and Dowell, E. H., "Limit-cycle oscillations of a fluttering cantilever plate," AIAA Journal, Vol. 29, No. 11, 1991, pp. 1929-1936.

21. Kobayashi, S., "Flutter of a simply supported rectangular panels in a supersonic flow - two dimensional panel flutter, I simply supported, II clamped panels," Trans. Japan Soc. of Aeron. and Space Sci., Vol. 5, 1962, pp. 79-118.
22. Kuo, C. C., Morino, L. and Dungundji, L., "Perturbation and harmonic balance for treating nonlinear panel flutter," AIAA Journal, Vol. 10, No. 11, 1972, pp. 1479-1484.
23. Eastep, F. E. and McIntosh, S. C., "The analysis of nonlinear panel flutter and response under random excitation or nonlinear aerodynamic loading," 11th Structure, Structural Dynamics and Materials Conf., Denver, CO, 1970, pp. 36-47. Also AIAA Journal, Vol. 9, No. 3, 1971, pp. 411-418.
24. Eslami, H. and Ibrahim, S. R., "Nonlinear flutter of specially orthotropic laminated panels," 27th Structure, Structural Dynamics and Materials Conf., San Antonio, TX, 1986, pp. 393-302.
25. Eslami, H., "Nonlinear flutter and forced oscillations of rectangular symmetric cross-ply and orthotropic panels using harmonic balance and perturbation methods," Ph.D. Thesis, Old Dominion University, Norfolk, VA, 1987.
26. Yuen, S. W. and Lau, S. L., "Effects of inplane load on nonlinear panel flutter by incremental harmonic balance method," AIAA Journal, Vol. 29, No. 9, 1991, pp. 1472-1479.
27. Morino, L., "A perturbation method for treating nonlinear panel flutter problems," AIAA Journal, Vol. 7, No. 3, 1969, pp. 405-410.
28. Morino, L. and Kuo, C. C., Detailed extensions of perturbation methods for nonlinear panel flutter," ASRL TR-164-2, MIT, Cambridge, MA, 1971.
29. Smith, L. and Morino, L., "Stability analysis of nonlinear differential autonomous systems with applications to flutter," AIAA Journal, Vol. 14, No. 3, 1976, pp. 333-341.
30. Olson, M. D., "Finite element approach to panel flutter," AIAA Journal, Vol. 5, No. 12, 1967, pp. 226-227.
31. Olson, M. D., "Some flutters solutions using finite element," AIAA Journal, Vol. 8, No. 4, 1970, pp. 747-752.
32. Yang, T. Y. and Sung, S. H., "Finite element in three-dimensional supersonic unsteady potential flow," AIAA Journal, Vol. 15, No. 12, 1977, pp. 1677-1683.
33. Mei, C., "A finite element approach for nonlinear panel flutter," AIAA Journal, Vol. 15, No. 8, 1977, pp. 1107-1110.
34. Mei, C. and Rogers, J. L. Jr., "Application of NASTRAN to large deflection supersonic flutter of panels," NASA TM-X-3429, 1976, pp. 67-97.
35. Rao, K. S. and Rao, G. V., "Large amplitude supersonic flutter of panels with ends elastically restrained against rotation," Int. Journal of Computers and Structures, Vol. 11, No. 3, 1980, pp. 197-201.
36. Sarma, B. S. and Varadan, T. K., "Nonlinear panel flutter by finite element method," AIAA Journal, Vol. 26, No. 5, 1988, pp. 566-574.
37. Mei, C. and Weidman, D. J., "Nonlinear panel flutter- a finite element approach," Computational Methods for Fluid-Structure Interaction Problems, AMP-Vol. 26, ASME, New York, 1977, pp. 139-165.
38. Mei, C. and Wang, H. C., "Finite element analysis of large amplitude supersonic flutter of panels," Int. Conf. on Finite Element Methods, Shanghai, PRC, Gordon and Breach Sci. Pub., Inc., 1982, pp. 944-951.
39. Han, A. D. and Yang, T. Y., "Nonlinear panel flutter using high order triangular finite elements," AIAA Journal, Vol. 21, No. 10, 1983, pp. 1453-1461.
40. Dixon, I. R. and Mei, C., "Finite element analysis of large amplitude panel flutter of thin laminates," AIAA Journal, Vol. 31, No. 4, 1993, pp. 701-707.
41. Gray, C. E. Jr., "Large amplitude finite element flutter analysis of composite panels in hypersonic flow," Ph.D. Thesis, Old Dominion University, Norfolk, VA, 1991.

42. Liaw, D. G. and Yang, T. Y., "Reliability and nonlinear supersonic flutter of uncertain laminated plates," AIAA Journal, Vol. 31, No. 12, 1993, pp. 2304-2311.
43. Reed, W. H., Hanson, P. W. and Alford, W. J., "Assessment of flutter model testing relating to the National Aerospace Plane," NASP CR 1002, 1987.
44. Gray, C. E. Jr., Mei, C. and Shore, C. P., "A finite-element method for large-amplitude two-dimensional panel flutter at hypersonic speeds," AIAA Journal, Vol. 29, No. 2, 1991, pp. 290-298.
45. Bein, T., Friedmann, P., Zhong, X. and Nydick, I., "Hypersonic flutter of a curved shallow panel with aerodynamic heating," AIAA 93-1318, 34th Structure, Structural Dynamics and Materials Conf., La Jolla, CA, 1993.
46. Nydick, I., Friedmann, P., Zhong, X., "Hypersonic panel flutter studies on curved panels," 36th Structure, Structural Dynamics and Materials Conf., New Orleans, LA, 1995, pp. 2995-3011.
47. Chandiramani, N. K., Plaut, R. H. and Librescu, L., "Nonperiodic flutter of a buckled composite panel," Sadhana Journal, Vol. 20(2-4), 1995, pp. 671-689. Also "Nonlinear flutter of buckled shear-deformable composite panel in a high-supersonic flow," J. Nonlinear Mechanics, Vol. 30, No. 2, 1995, pp. 149-167.
48. Sir Namachchivaya, N. and Lee, A., "Dynamics of nonlinear aeroelastic systems," Symposium Fluid-Structure Interaction, Aeroelasticity, Flow-Induced Vibration and Noise, Vol. III, Dallas, TX, ASME, 1997, pp. 165-174.
49. Yang, T. Y. and Han, A. D., "Flutter of thermally buckled finite element panels," AIAA Journal, Vol. 14, No. 7, 1976, pp. 975-977.
50. Abbas, J. F., Ibrahim, R. A. and Gibson, R. F., "Nonlinear flutter of orthotropic composite panel under aerodynamic heating," AIAA Journal, Vol. 31, No. 8, 1993, pp. 1478-1488.
51. Hopkins, M. A. and Dowell, E. H., "Limited amplitude panel flutter with a temperature differential," 35th Structure, Structural Dynamics and Materials Conf., Hilton Head, SC, 1994, pp. 1343-1355.
52. Xue, D. Y., Mei, C. and Shore, C. P., "Finite element two-dimensional panel flutter at high supersonic speeds and elevated temperatures," 31st Structure, Structural Dynamics and Materials conf., Long Beach, CA, 1990, pp. 1464-1475.
53. Xue, D. Y., "A finite element frequency domain solution of nonlinear panel flutter with temperature effects and fatigue life analysis," Ph.D. Thesis, Old Dominion University, Norfolk, VA, 1991.
54. Xue, D. Y. and Mei, C., "Finite element nonlinear flutter and fatigue life of two-dimensional panels with temperature effects," 32nd Structure, Structural Dynamics and Materials Conf., Baltimore, MD, 1991, pp. 1981-1991. Also Journal of Aircraft, Vol. 30, No. 6, 1993, pp. 993-1000.
55. Xue, D. Y. and Mei, C., "Finite element nonlinear panel flutter with arbitrary temperatures in supersonic flow," AIAA Journal, Vol. 31, No. 1, 1993, pp. 154-162.
56. Dixon, I. R., "Finite element analysis of nonlinear panel flutter of rectangular composite plates under a uniform thermal load," MS Thesis, Old Dominion University, Norfolk, VA, 1991.
57. Dixon, I. R. and Mei, C., "Nonlinear flutter of rectangular composite panels under uniform temperature using finite elements," Nonlinear Vibrations, DE-Vol. 50/AMD-Vol.144, ASME Winter Annual Meeting, Anaheim, CA, 1992, pp. 123-132.
58. Lee, I., Oh, I. K. and Lee, D. M., "Vibration and flutter analysis of stiffened composite plate considering thermal effect," AD-Vol. 55, Int. Mech. Engr. Congress & Exp., Dallas, TX, 1997, pp. 133-141.
59. Liaw, D. G., "Nonlinear supersonic flutter of laminated composite plates under thermal load," Computers and Structure, Vol. 65, No. 5, 1997, pp. 733-740.
60. Udrescu, R., "A higher finite element model in nonlinear panel flutter analysis," 39th Structure, Structural Dynamics and Materials Conf., Long Beach CA, 1998, pp. 1252-1262.
61. Zhou, R. C., Xue, D. Y. and Mei, C., "Finite element time domain modal formulation for nonlinear flutter of composite panels," AIAA Journal, Vol. 32, No. 10, 1994, pp. 2044-2052.

62. Dowell, E. H., "Flutter of a buckled plate as an example of chaotic motion of deterministic autonomous system," *Journal of Sound and Vibration*, Vol. 85, No. 3, 1982, pp.333-344.
63. Ibrahim, R. A., Orono, P. O. and Madaboosi, S. R., "Stochastic flutter of a panel subjected to random inplane forces Part I: two mode interaction , " *AIAA Journal*, Vol. 28, No. 4, 1990, pp. 694-702.
64. Ibrahim, R. A. and Orono, P. O., "Stochastic nonlinear flutter of a panel subjected to random in-plane forces," *Int. J. Non-Linear Mechanics*, Vol. 26, No. 6, 1991, pp.867-883.
65. Chin, C., Nayfeh, A. H. and Mook, D. T., "The response of nonlinear system with nonsemisimple one-to-one response to a combination parametric resonance," *Int. Journal of Bifurcation and Chaos*, Vol. 5, No. 4, 1995, pp. 971-982.
66. Friedmann, P. and Hanin, M., "Supersonic nonlinear flutter of orthotropic or isotropic panels with arbitrary flow direction," *Israel Journal of Technology*, Vol. 6(1-2), 1968, pp. 46-57.
67. Abdel-Motagaly, K., Chen, R. and Mei, C., "Effects of flow direction on nonlinear supersonic panel flutter using finite element method," *AIAA Paper 99-1433*, 40th Structure, Structural Dynamics and Materials Conference, St. Louis, MO, 1999.
68. Dowell, E. H., "Nonlinear flutter of curved plates," *AIAA Journal*, Vol. 7, No. 3, 1969, pp. 424-431.
69. Dowell, E. H., "Nonlinear flutter of curved plates II," *AIAA Journal*, Vol. 8, No. 2, 1970, pp. 259-261.
70. Krause, H. and Dinkler, D., "The influence of curvature on supersonic panel flutter," 39th Structure, Structural Dynamics and Materials Conf., Long Beach CA, 1998, pp. 1234-1240.
71. Scott, R. C. and Weisshaar, T. A., "Controlling panel flutter using adaptive materials," 32nd Structure, Structural Dynamics and Materials Conf., Baltimore, MD, 1991, pp. 2218-2229. Also *Journal of Aircraft*, Vol. 31, No. 1, 1994, pp. 213-222.
72. Hajela, P. and Glowasky, R., " Application of piezoelectric elements in supersonic panel flutter suppression," *AIAA paper 91-3191*, Sept. 1991.
73. Frampton, K. D., Clark, R. L. and Dowell, E. H., "Active control of panel flutter with piezoelectric transducers," *Journal of Aircraft*, Vol. 33, No. 4, 1996, pp.768-774.
74. Suleman, A. and Goncalves, M. A., "Optimization issues in applications of piezoelectric actuators in panel flutter control," *Proceedings of the SPIE - The International Society for Optical Engineering*, Vol. 3039, 1997, pp. 335-347.
75. Lai, Z., Xue, D. Y., Huang, J. K. and Mei, C., "Nonlinear panel flutter suppression with piezoelectric actuation," 2nd Conf. on Recent Advances in Active Control of Sound and Vibration, Blacksburg, VA, 1993, pp. 863-874. Also, *Journal of Intelligent Material Systems and Structures*, Vol. 6, No. 2, 1995, pp. 274-282.
76. Dongi, F., Dinkler, D. and Kroplin, B., "Active panel flutter suppression using self-sensing piezoactuators," 36th Structure, Structural Dynamics and Materials Conf., New Orleans, LA, 1995, pp. 2264-2272.
77. Zhou, R. C., Lai, Z., Xue, D. Y., Haung, J. K. and Mei, C., "Suppression of nonlinear panel flutter with piezoelectric actuators using finite element methods," *AIAA Journal*, Vol. 33, No. 6, 1995, pp. 1098-1105.
78. Zhou, R. C., Mei, C. and Haung, J. K., " Suppression of nonlinear panel flutter at supersonic speeds and elevated temperatures," *AIAA Journal*, Vol. 34, No. 2, 1996, pp. 347-354.
79. Ho, M. T., Chen, R. and Chu, L. C., "Wind-tunnel testing of panel flutter control using piezoelectric actuation and iterative gain tuning," *SPIE Conf. Smart Struct and Matls*, 1997, pp. 564-577.
80. Kappus, H. P., Lemley, C. E. and Zimmerman, N. H., "An experimental investigation of high amplitude panel flutter," *NASA CR-1837*, 1971.

NONLINEAR RESPONSE OF COMPOSITE PANELS UNDER COMBINED ACOUSTIC EXCITATION AND AERODYNAMIC PRESSURE

K. Abdel-Motagaly, B. Duan, and C. Mei

5/7-39

*Department of Aerospace Engineering,
Old Dominion University, Norfolk, VA 23529-0247*

ABSTRACT

A finite element formulation is presented for the analysis of large deflection response of composite panels subjected to aerodynamic pressure at supersonic flow and high acoustic excitation. The first-order shear deformation theory is considered for laminated composite plates, and the von Karman nonlinear strain-displacement relations are employed for the analysis of large deflection panel response. The first-order piston theory aerodynamics and the simulated Gaussian white noise are employed for the aerodynamic and acoustic loads, respectively. The nonlinear equations of motion for an arbitrarily laminated composite panel subjected to a combined aerodynamic and acoustic pressures are formulated first in structure node degrees-of-freedom. The system equations are then transformed and reduced to a set of coupled nonlinear equations in modal coordinates. Modal participation is defined and the in-vacuo modes to be retained in the analysis are based on the modal participation values. Numerical results include root mean square values of maximum deflections, deflection and strain response time histories, probability distributions, and power spectrum densities. Results showed that combined acoustic and aerodynamic loads have to be considered for panel analysis and design at high dynamic pressure values.

1. INTRODUCTION

Aircraft and spacecraft skin-panels are subjected simultaneously to high levels acoustic (sonic fatigue) and aerodynamic (panel flutter) pressures.^{1,2} Sonic fatigue and panel flutter have been the major design considerations for aircraft, spacecraft and missiles since the late nineteen sixties. An excellent review of sonic fatigue technology up to 1989 was given by Clarkson.³ Various types of pressure loads, developments of theoretical methods, and comparisons of experimental results with theories and nomographs were given. Recently, Wolfe et al.⁴ gave reviews in-depth of sonic fatigue design guides, classical and finite element approaches, and identification technology. Experimental investigation of nonlinear beams and plates, and multimodal fatigue model were also reported. Sonic fatigue design guides have been developed by Rudder and Plumlee⁵ for isotropic metallic and by Holehouse⁶ for graphite-epoxy composite aircraft structures. The design guides, however, were based on the semi-empirical test data or the simplified single-mode approach. Vaicaitis et al. have developed a Galerkin-like procedure (PDE and modal method) and a time domain Monte Carlo approach for the nonlinear response of isotropic^{1,2} and composite^{7,8} panels to acoustic and thermal loads.

An excellent survey of nonlinear panel flutter through 1970 was given by Dowell.⁹ The vast amount of theoretical literature on panel flutter were grouped into four categories based on the linear or nonlinear structure theories, and the two aerodynamic theories (quasi-steady first-order piston or full linearized inviscid potential flow). The partial differential equations (PDE), the Galerkin's method and the numerical simulation results showed that a minimum of six modes are needed for a converged limit cycle amplitude response. Bismarck-Nasr¹⁰ gave a review of the linear panel flutter using the finite element methods. Recently, a review of various analytical methods and experimental results of nonlinear panel flutter at supersonic and hypersonic speeds was given by Mei et al.¹¹ An approach for the design of flutter-free surface panels using the quasi-static Ackeret aerodynamic theory was documented by Laurenson and McPherson.¹² A exhaustive search of the literature reveals that there is no study of nonlinear panel response to combined acoustic and aerodynamic loads.

When a flight vehicle travels at supersonic speeds, panel flutter caused by aerodynamic pressure is not the only form of dynamic instability. The surface panels also experience high frequency random pressure fluctuations (sonic fatigue).^{1,2} This paper presents a finite element formulation for the analysis of nonlinear large deflection response of composite panels subjected to high acoustic excitation and aerodynamic pressure at supersonic speeds. The first-order shear deformation theory is considered for the laminated composite plates. The von Karman nonlinear strain-

displacement relations are employed for the large deflection response of the panel. Simulated Gaussian white noise and the first order piston theory aerodynamics are employed for the acoustic and aerodynamic loads. The nonlinear equations of motion for an arbitrarily laminated composite panel subjected to a combined high acoustic and aerodynamic loads are formulated first in the structure node degrees-of-freedom (DOF). The system equations are then transformed and reduced to a set of coupled nonlinear equations in modal coordinates. Numerical integration is employed to obtain the panel response. Examples are given for an isotropic and a composite panel at various combinations of sound pressure level and dynamic pressure.

2. FORMULATION

2.1 Equations of Motion in Structure Node DOF

The inplane strain, curvature and shear strain vectors based on the von Karman large deflection and the first order shear deformation theories are given by

$$\begin{aligned}\{\varepsilon^o\} &= \{\varepsilon_m^o\} + \{\varepsilon_b^o\} = \begin{Bmatrix} u_x \\ v_y \\ u_{,y} + v_{,x} \end{Bmatrix} + \begin{Bmatrix} w_x^2/2 \\ w_y^2/2 \\ w_{,x}w_{,y} \end{Bmatrix} \\ \{\kappa\} &= \begin{Bmatrix} \Psi_{x,x} \\ \Psi_{y,y} \\ \Psi_{x,y} + \Psi_{y,x} \end{Bmatrix}, \quad \{\gamma\} = \begin{Bmatrix} w_{,y} + \Psi_y \\ w_{,x} + \Psi_x \end{Bmatrix}\end{aligned}\quad (1)$$

where u , v and w are the inplane and transverse displacements, respectively. Ψ_x and Ψ_y are the rotations of the normal to the midsurface about the y - and x -axes, respectively. The subscripts m and b denote membrane (inplane) and bending components, respectively. The constitutive equations for a laminated composite plate are

$$\begin{Bmatrix} N \\ M \end{Bmatrix} = \begin{bmatrix} A & B \\ B & D \end{bmatrix} \begin{Bmatrix} \varepsilon^o \\ \kappa \end{Bmatrix}, \quad \{Q\} = [A_s] \{\gamma\} \quad (2)$$

where $[A]$, $[B]$, $[D]$ and $[A_s]$ are the stretching, bending-stretching coupling, bending, and shear stiffnesses, respectively. The quasi-steady first-order piston aerodynamic theory is employed for the aerodynamic pressure at high supersonic Mach number ($M_\infty > 1.6$). The aerodynamic pressure is given by⁹

$$\Delta p = -\frac{2q_a}{\beta} \left(w_{,x} + \frac{M_\infty^2 - 2}{M_\infty^2 - 1} \frac{1}{V_\infty} w_{,t} \right) \quad (3)$$

where $q_a = \rho_a V_\infty^2/2$ is the free stream dynamic pressure, ρ_a the air density, V_∞ the velocity and $\beta = \sqrt{M_\infty^2 - 1}$.

Using the Hamilton's principle and the finite element expressions, the system equations of motion for a composite plate subjected to aerodynamic pressure and high acoustic excitation can be expressed as^{13,14}

$$\frac{1}{\omega_o^2} [M]_b \{\ddot{W}_b\} + \frac{g_a}{\omega_o} [G] \{\dot{W}_b\} + ([K_L] + [K_{NL}]) \{W_b\} = \{P_b(t)\} \quad (4)$$

where $\omega_o = (D_{110}/\rho h a^4)^{1/2}$ is a reference frequency and ρ , h and a are the panel density, thickness and length, respectively. The value D_{110} is the first entry in laminate bending rigidity $[D]$ calculated when all of the fibers of the composite layers are aligned in the airflow x -direction. The $[M]_b$, $[G]$ and $\{P_b\}$ are the system mass matrix, aerodynamic damping matrix and load vector due to random acoustic pressure, respectively. The linear and nonlinear system stiffness matrices are given by

$$\begin{aligned}[K_L] &= \lambda [A_a] + [K]_b + [K_S] - [K_B] [K]_m^{-1} [K_B]^T \\ [K_{NL}] &= -[K_B] [K]_m^{-1} [K]_{mb} + [K]_B + [K]_{Nm} + [K]_{Nb} + [K]_2 - [K]_{bm} [K]_m^{-1} ([K_B]^T + [K]_{mb})\end{aligned}\quad (5)$$

where the nondimensional dynamic pressure and nondimensional aerodynamic damping are given by

$$\lambda = \frac{2q_a a^3}{\beta D_{110}}, g_a = \sqrt{\lambda C_a} \quad (6)$$

where $C_a = \mu(M_\infty^2 - 2)^2 / \beta(M_\infty^2 - 1)^2$ is the aerodynamic coefficient and $\mu = \rho_a a / \rho h$ is the mass ratio. For high supersonic speeds $M_\infty >> 1$, Dowell⁹ approximated $C_a \approx \mu / M_\infty$. $[A_a]$ is the system aerodynamic influence matrix, and $[K1]$ and $[K2]$ are the first-order and second-order nonlinear stiffness matrices which depend linearly and quadratically upon the unknown system displacement vector $\{W\} = \{\{W_b\}, \{W_m\}\}^T$. The subscripts B , N_m and N_b denote that the corresponding stiffness matrix is due to the laminate extension-bending stiffness $[B]$, membrane force components $\{N_m\} = [A]\{\varepsilon_m^0\}$ and $\{N_b\} = [B]\{\kappa\}$, respectively, and the subscripts a and s denote aerodynamic and shear deformation, respectively. The derivation of Eq. (4) can be referred to references 13 and 14. In the absence of acoustic loading, $\{P_b(t)\} = 0$, Eq. (4) reduces to nonlinear panel flutter at supersonic speeds; On the other hand, by setting $\lambda = g_a = 0$, Eq. (4) describes nonlinear random response of a composite panel subjected to high acoustic excitations. According to the authors' knowledge, this is the first attempt in investigating of nonlinear response of panels subjected to a combined acoustic and aerodynamic pressures.

For a given set of λ and C_a (or μ/M_∞), Eq. (4) can be solved by numerical integration in the structure node DOF for combined load case. This approach has been carried out for sonic fatigue analysis with simulated random loads.^{15,16} It turned out to be computationally costly due to: (i) at each time step, the element nonlinear stiffness matrices are evaluated and the system nonlinear stiffness matrix $[K_{NL}]$ is assembled and updated, (ii) the number of structure node DOF of $\{W_b\}$ is usually very large, and (iii) the time step of integration should be extremely small.

An efficient solution procedure is to transform Eq. (4) into the modal coordinates with a modal reduction. This approach is presented as follows.

2.2 Equations of Motion in Modal Coordinates

Express the panel deflection as a linear combination of some known base functions as

$$\{W_b\} = \sum_{r=1}^n q_r(t) \{\phi_r\} = [\Phi] \{q\} \quad (7)$$

where the number of retained linear in-vacuo modes, n , is much smaller than the number of structure node DOF in bending, $\{W_b\}$. The normal mode $\{\phi_r\}$, which is normalized with the maximum component to unity, and the linear natural frequency ω_r are obtained from the linear vibration of the system

$$\frac{\omega_r^2}{\omega_o^2} [M]_b \{\phi_r\} = \left([K]_b + [K_s] - [K_B] [K]_m^{-1} [K_B]^T \right) \{\phi_r\} \quad (8)$$

A small number of most contributing modes to be retained in the analysis can be determined from the modal participation value which is defined as

$$\text{Participation of the } r^{\text{th}} \text{ mode} = \text{RMS}(q_r) / \sum_{s=1}^n \text{RMS}(q_s) \quad (9)$$

Since matrices $[K1]_{mb}$, $[K1_B]$, $[K1_{Nb}]$ and $[K2]$ are all functions of the unknown bending DOF $\{W_b\}$, they can now be expressed as the sum of products of modal coordinates and nonlinear modal stiffness matrices as

$$([K1]_{mb}, [K1_B], [K1_{Nb}], [K2]) = \sum_{r=1}^n q_r \left([K1]_{mb}^{(r)}, [K1_B]^{(r)}, [K1_{Nb}]^{(r)}, \sum_{s=1}^n q_s [K2]^{(rs)} \right) \quad (10)$$

where the super-indices of those nonlinear modal stiffness matrices denote that they are assembled from the corresponding element nonlinear stiffness matrices. Those element nonlinear stiffness matrices are evaluated with the corresponding element components $\{w_b\}^{(r)}$ obtained from the known system linear mode $\{\phi_r\}$. Therefore, the nonlinear modal stiffness matrices are constant matrices. The matrix $[K1_{Nm}]$, however, is a linear function of the inplane DOF $\{W_m\}$ which consists of two terms as

$$\begin{aligned}
\{W_m\} &= -[K]_m^{-1} \left([K_B]^T + [K1]_{mb} \right) \{W_b\} \\
&= -[K]_m^{-1} \left([K_B]^T + \sum_{s=1}^n q_s [K1]_{mb}^{(s)} \right) \sum_{r=1}^n q_r \{\phi_r\} \\
&= -\sum_{r=1}^n q_r \{\phi_r\}_m - \sum_{r=1}^n \sum_{s=1}^n q_r q_s \{\phi_{rs}\}_m
\end{aligned} \tag{11}$$

where the two inplane modes corresponding to the r^{th} bending mode $\{\phi_r\}$ are given by

$$\{\phi_r\}_m = [K]_m^{-1} [K_B]^T \{\phi_r\}, \quad \{\phi_{rs}\}_m = [K]_m^{-1} [K1]_{mb}^{(r)} \{\phi_s\} \tag{12}$$

The nonlinear stiffness matrix $[K1_{Nm}]$ can be expressed as the sum of two nonlinear modal stiffness matrices as

$$[K1_{Nm}] = -\sum_{r=1}^n q_r [K1_{Nm}]^{(r)} - \sum_{r=1}^n \sum_{s=1}^n q_r q_s [K2_{Nm}]^{(rs)} \tag{13}$$

The nonlinear modal stiffness matrices $[K1_{Nm}]^{(r)}$ and $[K2_{Nm}]^{(rs)}$ are constant matrices and they are assembled and evaluated with the known inplane modes $\{\phi_r\}_m$ and $\{\phi_{rs}\}_m$, respectively. Equation (4) is thus transformed to the reduced modal coordinates as

$$\frac{1}{\omega_o^2} [\bar{M}] \ddot{\{q\}} + \frac{g_a}{\omega_o} [\bar{G}] \dot{\{q\}} + 2\xi_r \omega_r \frac{\bar{M}_r}{\omega_o^2} [I] \{q\} + ([\bar{K}_L] + [K_q] + [K_{qq}]) \{q\} = \{\bar{P}(t)\} \tag{14}$$

where the modal matrices are given by

$$([\bar{M}]_b, [\bar{G}], [\bar{K}_L]) = [\Phi]^T ([M]_b, [G], [K_L]) [\Phi] \tag{15}$$

and the quadratic and cubic terms are

$$[K_q]\{q\} = [\Phi]^T \sum_{r=1}^n q_r \left(-[K_B] [K]_m^{-1} [K1]_{mb}^{(r)} + [K1_B]^{(r)} - [K1_{Nm}]^{(r)} + [K1_{Nb}]^{(r)} - [K1]_{bm}^{(r)} [K]_m^{-1} [K_B]^T \right) [\Phi] \{q\}$$

$$[K_{qq}]\{q\} = [\Phi]^T \sum_{r=1}^n \sum_{s=1}^n q_r q_s \left([K2]^{(rs)} - [K2_{Nm}]^{(rs)} - [K1]_{bm}^{(r)} [K]_m^{-1} [K1]_{mb}^{(s)} \right) [\Phi] \{q\} \tag{16}$$

and the modal force is

$$\{\bar{P}(t)\} = [\Phi]^T \{P_b(t)\} \tag{17}$$

A structural modal damping $2\xi_r \omega_r \frac{\bar{M}_r}{\omega_o^2} [I]$ has been added to Eq. (14), and ξ_r is the modal damping ratio which can

be determined experimentally or from the data base of structures of similar construction. The nonlinear response for a given panel at certain dynamic pressure λ and damping parameters C_a and ξ_r can be determined from Eq. (14) by any numerical integration scheme. The advantages in using Eq. (14) are: (i) there is no need to assemble and update the quadratic and cubic nonlinear terms since all the nonlinear modal matrices are constant matrices, and (ii) the number of modal equations, n , is small.

2.3 Random Surface Pressure

The input acoustic excitation is assumed to be band-limited Gaussian random noise and uniformly distributed over the structural surface. The power spectrum density (PSD) has the form

$$\begin{aligned}
S(f) &= p_0^2 10^{SPL/10} \quad 0 \leq f \leq f_c \\
&= 0 \quad \text{otherwise}
\end{aligned} \tag{18}$$

where p_0 is the reference pressure, $p_0 = 2.9 \times 10^{-9}$ psi (0.00002 N/m^2), SPL is the sound pressure level in decibels and f_c is the selected band width. The formulation presented in Eq. (14), however, is not limited to stationary Gaussian excitation. It can also handle nonstationary, non-Gaussian random loading which the high speed flight vehicles would probably experience. With recorded flight high frequency pressure

fluctuations, random panel response can be determined much realistically by numerical integration of Eq. (14).

3. EXAMPLES AND DISCUSSION

The nonlinear system equations presented in Eq. (4) are general in the sense that they are applicable for rectangular^{13,15} or triangular¹⁴ finite elements. The finite element employed in the examples is the three-node triangular Mindlin (MIN3) plate element with improved transverse shear.¹⁷ The shear correction factor is defined as $\alpha_s = 1/(1 + 0.5 \sum_{i=1}^3 k_{sii} / \sum_{i=1}^3 k_{bu,i})$. The MIN3 element has a total of 15 DOF, 5 at each apex node. The bending node DOF

{ w_b } comprise of transverse displacements and normal rotations (w , Ψ_x and Ψ_y) and the inplane node DOF { w_m } comprise of inplane displacements (u and v). Nonlinear response are obtained for a square isotropic plate and a rectangular composite plate. An aerodynamic coefficient $C_a = 0.01$ and a modal damping ratio $\xi = 0.01$, $r=1$ to n are used in the examples.

3.1 Square Isotropic Plate

A simply supported square aluminum panel under the combined acoustic and aerodynamic pressures is studied in detail. The plate is of $12 \times 12 \times 0.040$ in. ($30.5 \times 30.5 \times 0.1$ cm) with immovable inplane edge conditions $u(0,y) = u(a,y) = v(x,0) = v(x,a) = 0$. The material properties are $E = 10$ Msi (68.89 GPa) and $\nu = 0.3$. The plate is modeled with a 12×12 mesh or 288 MIN3 elements. The number of structural node DOF { W_b } is 407 for the system equations given in Eq. (4). It is well known that 6 modes in the airflow direction are needed for a converged limit cycle response for panel flutter and the lowest few symmetrical modes are needed for the uniform input random pressure distribution for sonic fatigue. Therefore the modes considered for the combined aerodynamic and acoustic loads are (1,1) to (6,1) for the panel flutter and (1,1), (1,3), (3,1) and (3,3) for the sonic fatigue analysis. No modal participation calculations are needed for this well studied problem in panel flutter and sonic fatigue. The root mean square (RMS) maximum deflections to plate thickness versus the nondimensional dynamic pressure λ at SPL of 0, 100, 110 and 120 dB are shown in Fig. 1.

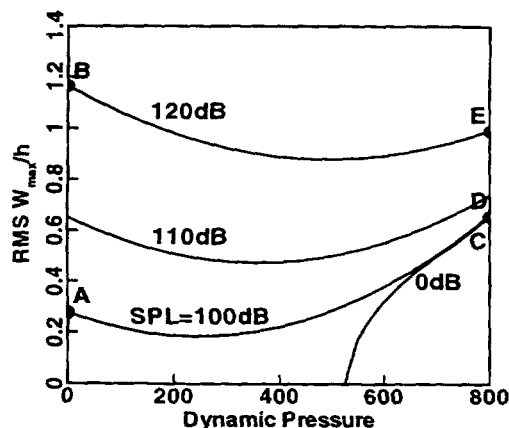


Fig. 1 RMS maximum deflection of a simply supported square isotropic plate

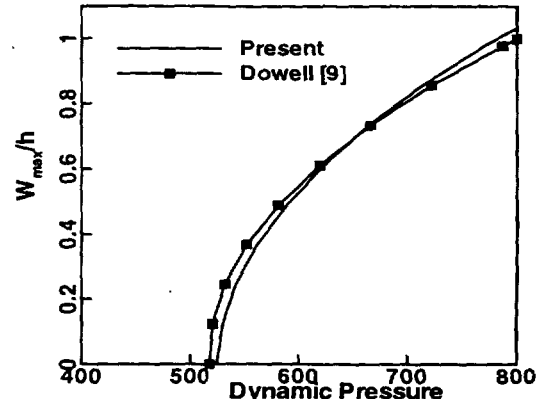


Fig. 2 Comparison of limit cycle amplitude for a simply supported square isotropic plate

The curve with the null acoustic pressure (0 dB SPL) is the conventional panel flutter limit cycle oscillations, and the RMS deflections at null dynamic pressure ($\lambda=0$) are the conventional nonlinear panel response to acoustic excitations. The accuracy of the present formulation for panel flutter and sonic fatigue is verified and shown in Fig. 2 and Table 1 for panel flutter and sonic fatigue, respectively. The Fokker-Planck-Kolmogorov (FPK) Equation [18] method is an exact solution to the single degree-of-freedom forced Duffing equation. The finite element/equivalent linearization (FE/EL) approach assumes that the equivalent linearized system obtained after the application of equivalent linearization technique is also stationary Gaussian, while the present time domain

numerical integration method does not assume that the displacement response is Gaussian, therefore, the present method should be more accurate and realistic.

Table 1. Comparison of RMS of (W_{max}/h) for a simply supported rectangular (15×12×0.040 in.) isotropic plate using different methods and number of modes

SPL (dB)	FPK [18] 1 mode	FE/EL [19]		Present 4 modes
		1 mode	4 modes	
90	0.249	0.238	0.238	0.266
100	0.592	0.532	0.533	0.489
110	1.187	1.030	1.031	1.092
120	2.200	1.902	1.905	2.113

The maximum deflection is located at the three-quarter length from the leading edge. ($3a/4, a/2$) for the panel flutter, however, it is at the plate center ($a/2, a/2$) for sonic fatigue. For a fixed SPL, the location of the maximum deflection thus moves from the plate center towards the three-quarter length as the dynamic pressure increases. On the other hand, for a fixed dynamic pressure, the location of the maximum deflection moves towards the center from the three-quarter length by increasing the SPL. The maximum deflection for the combined acoustic and aerodynamic loading case, therefore, is not at one fixed location, it can be anywhere between the plate center and three-quarter from the leading edge.

The deflection results shown in Fig. 1 indicate that: (i) the superposition method does not applicable to nonlinear system, (ii) for a given SPL, the RMS deflection at $\lambda=0$ is higher than the deflection at $0 < \lambda < \lambda_{cr}$, this is due to the increase of panel frequency with increasing of λ , thus increase the stiffness of the panel, and (iii) the RMS deflection at large dynamic pressure ($\lambda > \lambda_{cr}$) are always higher than those at $\lambda=0$. Thus important conclusions can be drawn for design and analysis of surface panels at supersonic speeds: (i) for $\lambda < \lambda_{cr}$, only acoustic loading or sonic fatigue has to be considered, and (ii) for $\lambda > \lambda_{cr}$, both acoustic and aerodynamic loads have to be considered.

Representative panel behavior at five loading combinations are presented in Figs. 3-7. Those five loading combinations correspond to A to E shown in Fig. 1. The maximum deflection and maximum strain response time histories, probability distribution and PSD for each loading case are presented. Figures 3 and 4 show the random response at SPL=100 and 120 dB and $\lambda=0$ (sonic fatigue; points A and B in Fig. 1), respectively. At the low 100 dB SPL, the panel basically experiences a small deflection linear random vibration dominated by the fundamental (1,1) mode. The panel motion at the high 120 dB SPL, however, is clearly a large deflection nonlinear random vibration. This is demonstrated by the peaks in PSD plots that are broadening and shifting to the higher frequency and by the presence of nonzero-mean inplane strain shown in strain plots.

At $\lambda=800$ and 0 SPL (panel flutter; point C in Fig. 1), the panel response shown in Fig. 5 is a large amplitude limit cycle motion. The displacement probability density and the PSD of (W_{max}/h) both describe a periodic motion. The maximum strain time history shows clearly the effect of large inplane strain component due to large amplitude periodic motions.

The panel responses at the combined loads of $\lambda=800$ and SPL=100 and 120 dB (points D and E in Fig. 1) are shown in Figs. 6 and 7, respectively. The maximum deflection and strain time histories show the nonlinear large deflection vibrations dominated by the fundamental mode and the presence of inplane strain components.

3.2 Rectangular Composite Plate

Nonlinear response of composite panels under aerodynamic and acoustic pressures can be determined using the present formulation and solution procedure. As an example, a clamped rectangular graphite-epoxy plate of eight layers [0/45/-45/90]s is analyzed. The dimensions and material properties of the panel are:

a=15 in. (38.1 cm)	E ₁ =22.5 Ms (155 GPa)
b=12 in. (30.5 cm)	E ₂ =1.17 Ms (8.07 GPa)
h=0.048 in. (0.122 cm)	G ₁₂ =0.66 Ms (4.55 GPa)
$\rho=0.1458 \times 10^{-3}$ lb-s ² /in. ⁴ (1550 Kg/m ³)	G ₂₃ =0.44 Ms (3.03 Gpa)
v ₁₂ =0.22	

The inplane edges are immovable and the plate is modeled with a 12×12 mesh. The number of system equations in structure node DOF $\{W_b\}$ is of 363. The system equations are reduced to the modal coordinates using the lowest n modes in increasing frequency order. The RMS W_{max}/h at 120 dB SPL and $\lambda=800$ using different number of modes are shown in Table 2. The results show that a 20- or 25-mode model would yield a converged RMS maximum deflection.

To demonstrate the advantage of using modal participation defined in Eq. (9), the participation values for the 25-mode model are shown in Table 3. By retaining those 13 modes with participation value $> 1\%$ in the analysis, the RMS W_{max}/h is 0.8124 at 120 dB SPL and $\lambda=800$. Using the 13 most contributing modes, the RMS (W_{max}/h) versus nondimensional dynamic pressure λ at SPL of 0, 100, 110 and 120 dB are shown in Fig. 8. Similar conclusion from the isotropic panel can be drawn for the composite panel, that is, at low dynamic pressure ($\lambda \ll \lambda_{cr}$) only acoustic loading needs to be considered, and at high dynamic pressure ($\lambda > \lambda_{cr}$) both aerodynamic and acoustic loads have to be considered for the design and analysis of surface panels at supersonic flow. Response time history, probability distribution and PSD are not repeated for the composite panel.

Table 2. RMS (W_{max}/h) for a clamped rectangular graphite-epoxy panel at 120 dB SPL and $\lambda=800$ using different number of modes

Number of modes, n	RMS (W_{max}/h)
1	0.5557
2	0.5845
6	0.7814
9	0.7798
16	0.8279
20	0.8110
25	0.8183
Selected 13 modes	0.8124

Table 3. Modal participation values for a clamped rectangular graphite-epoxy panel at 120 dB SPL and $\lambda=800$ using the lowest 25 modes

Mode number	1	2	3	4	5	6	7	8	9	10	11	12
Participation, %	36.72	5.24	19.30	4.25	4.01	7.67	1.71	0.76	0.33	1.54	4.77	0.35
13	14	15	16	17	18	19	20	21	22	23	24	25
0.28	4.19	0.38	0.99	1.38	2.55	0.21	0.27	0.53	0.33	0.54	0.14	1.54

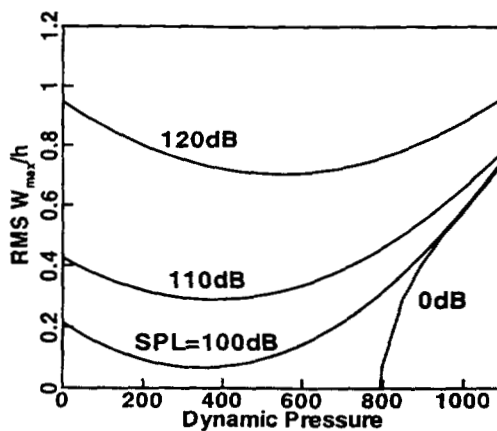


Fig. 8 RMS maximum deflection of a clamped rectangular graphite-epoxy plate

4. CONCLUDING REMARKS

A finite element time domain modal formulation is presented for the analysis of nonlinear response of composite panels subjected to combined acoustic and aerodynamic pressures. The advantage of using modal participation for retaining the most contributing modes was demonstrated. For panels at supersonic flow, only acoustic excitations (sonic fatigue) are to be considered for $\lambda < \lambda_{cr}$, and both acoustic and aerodynamic pressures have to be considered for $\lambda > \lambda_{cr}$. Future extension of the present work includes the combined acoustic, aerodynamic and thermal loads. Arbitrary flow directions and curved panels will also be considered.

ACKNOWLEDGMENTS

The first and the second authors would like to acknowledge the partial support by grant F33615-91-C-3205, AFRL. The third author would like to acknowledge the support by grant NAG1-2150, NASA Langley Research Center and by grant F33615-91-C-3205, AFRL.

REFERENCES

1. Vaicaitis, R., "Recent Advances of Time Domain Approach for Nonlinear Response and Sonic Fatigue," Proceedings of 4th International Conference on Structural Dynamics: Recent Advances, Institute of Sound and Vibration Research, University of Southampton, UK, July 1991, pp. 84-103
2. Vaicaitis, R., "Time Domain Approach for Nonlinear Response and Sonic Fatigue of NASP Thermal Protection Systems," Proceedings of 32nd Structures, Structural Dynamics and Materials Conference, Baltimore, MD, April 1991, pp. 2685-2708.
3. Clarkson, B. L., "Review of Sonic Fatigue Technology," NASA CR-4587, 1994.
4. Wolfe, H. F., Shroyer, C. A., Brown, D. L. and Simmons, L. W., "An Experimental Investigation of Nonlinear Behavior of Beams and Plates Excited to High Levels of Dynamic Response," WL-TR-96-3057, Wright-Patterson AFB, OH, 1995.
5. Rudder, F. F. and Plumbree, H. E., "Sonic Fatigue Design Guide for Military Aircraft," AFFDL-TR-74-112, Wright-Patterson AFB, OH, 1975.
6. Holehouse, I., "Sonic Fatigue Design Guide Techniques for Advanced Composite Airplane Structures," AFWAL-TR-80-3019, Wright-Patterson AFB, OH, 1980.
7. Arnold, R. R. and Vaicaitis, R., "Nonlinear Response and Fatigue of Surface Panels by the Time Domain Monte Carlo Approach," WRDC-TR-90-3081, Wright-Patterson AFB, OH, 1992.
8. Vaicaitis, R. and Kavallieratos, P. A., "Nonlinear Response of Composite Panels to Random Excitation," Proceedings of 34th Structures, Structural Dynamics and Materials Conference, La Jolla, CA, April 1993, pp. 1041-1049.
9. Dowell, E. H., "Panel Flutter: A Review of the Aeroelastic Stability of Plates and Shells," AIAA Journal, Vol. 8, No. 3, 1970, pp. 385-399.
10. Bismarck-Nasr, M. N., "Finite Element Analysis of Aeroelasticity of Plates and Shells," Applied Mechanics Review, Vol. 45, No. 12, 1992, pp. 461-482.
11. Mei, C., Abdel-Motagaly, K. and Chen, R., "A Review of Nonlinear Panel Flutter at Supersonic and Hypersonic Speeds," Proceeding of CEAS/AIAA/ICASE/NASA Langley International Forum on Aeroelasticity and Structural Dynamics, Williamsburg, VA, June 1999.
12. Laurenson, R. M. and McPherson, J. I., "Design Procedures for Flutter-Free Surface Panels," NASA CR-2801, 1977.
13. Zhou, R. C., Xue, D. Y. and Mei, C., "Finite Element Time Domain Modal Formulation for Nonlinear Flutter of Composite Panels," AIAA Journal, Vol. 32, No. 10, 1994, pp. 2044-2052.
14. Mei, C. and Chen, R. R., "Finite Element Nonlinear Random Response of Composite Panels of Arbitrary Shape to Acoustic and Thermal Loads Applied Simultaneously," WL-TR-97-3085, Wright-Patterson AFB, OH, 1997.
15. Robinson, J. H., "Finite Element Formulation and Numerical Simulation of the Large Deflection Random Vibration of Laminated Composite plates," MS Thesis, Old Dominion University, Norfolk, VA, 1990.

16. Green, P. D., and Killey, A., "Time Domain Dynamic Finite Element Modeling in Acoustic Fatigue Design," Proceedings of 6th International Conference on Structural Dynamics: Recent Advances, Institute of Sound and Vibration Research, University of Southampton, UK, 1997, pp.1007-1026.
17. Tessler, A. and Hughes, T. J. R., "A Three-node Mindlin Plate Element with Improved Transverse Shear," Computer Methods in Applied Mechanics and Engineering, Vol. 50, 1985, pp. 71-91.
18. Bolotin, V. V., "Random Vibration of Elastic Systems," Martinus Nijhoff Publishers, 1984, pp. 290-292, 314-316.
19. Chiang, C. K., "A Finite Element large Deflection Multiple-Mode Random Response Analysis of Complex panel with Initial Stresses Subjected to Acoustic Loading," Ph. D. Dissertation, Old Dominion University, Norfolk, VA, May 1983.

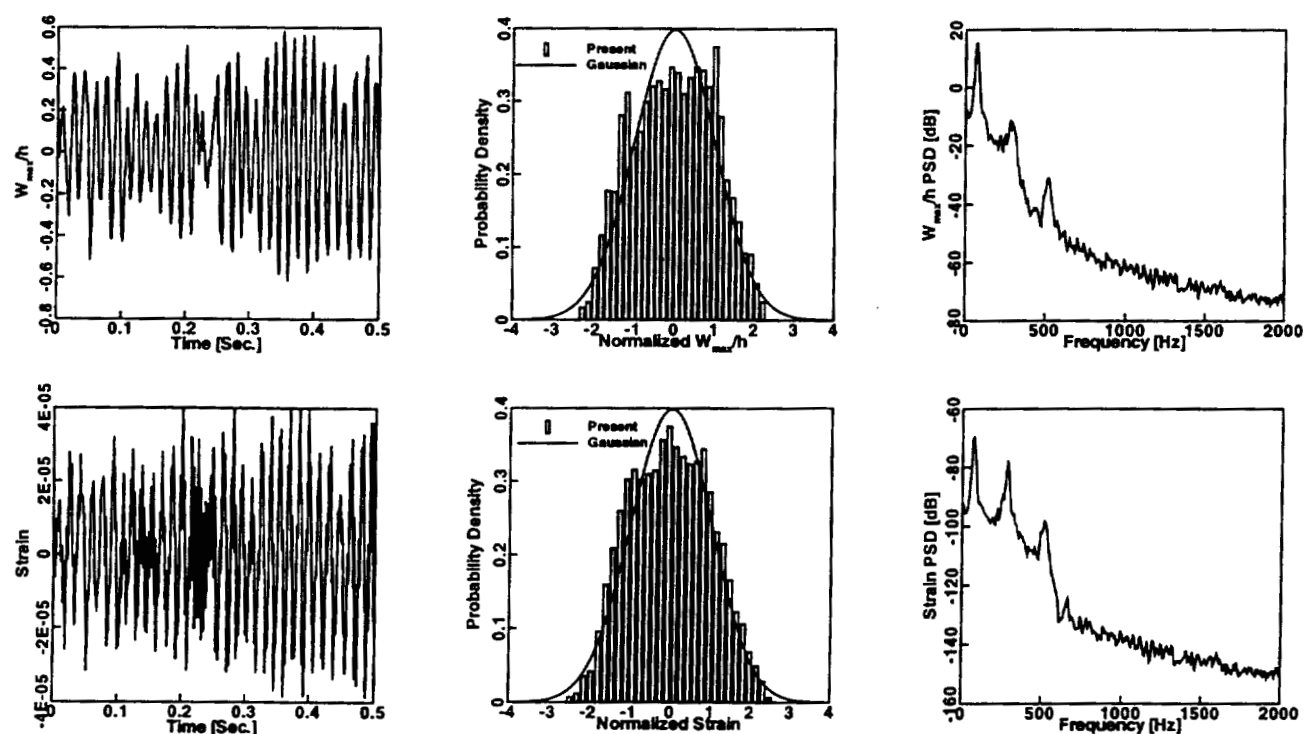


Fig. 3 Random Response of a simply supported square isotropic plate at 100 dB SPL and $\lambda=0$

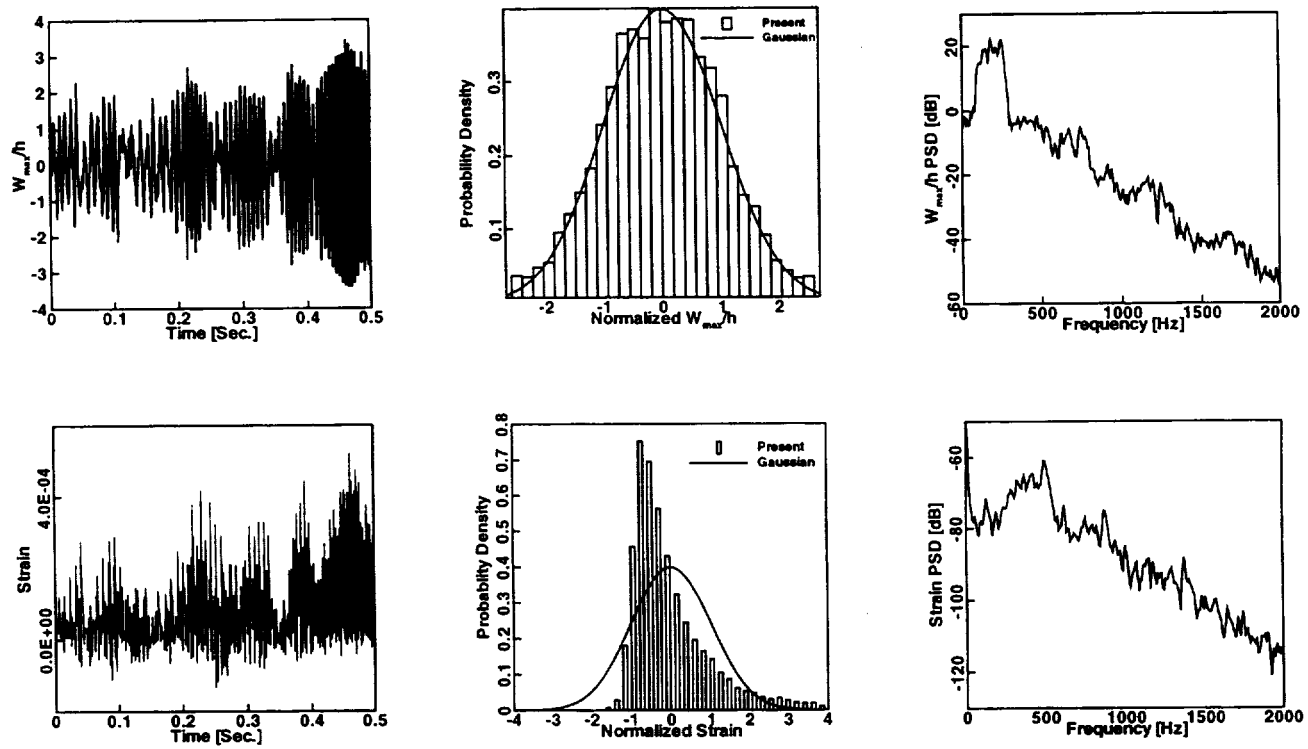


Fig. 4 Random Response of a simply supported square isotropic plate at 120 dB SPL and $\lambda=0$

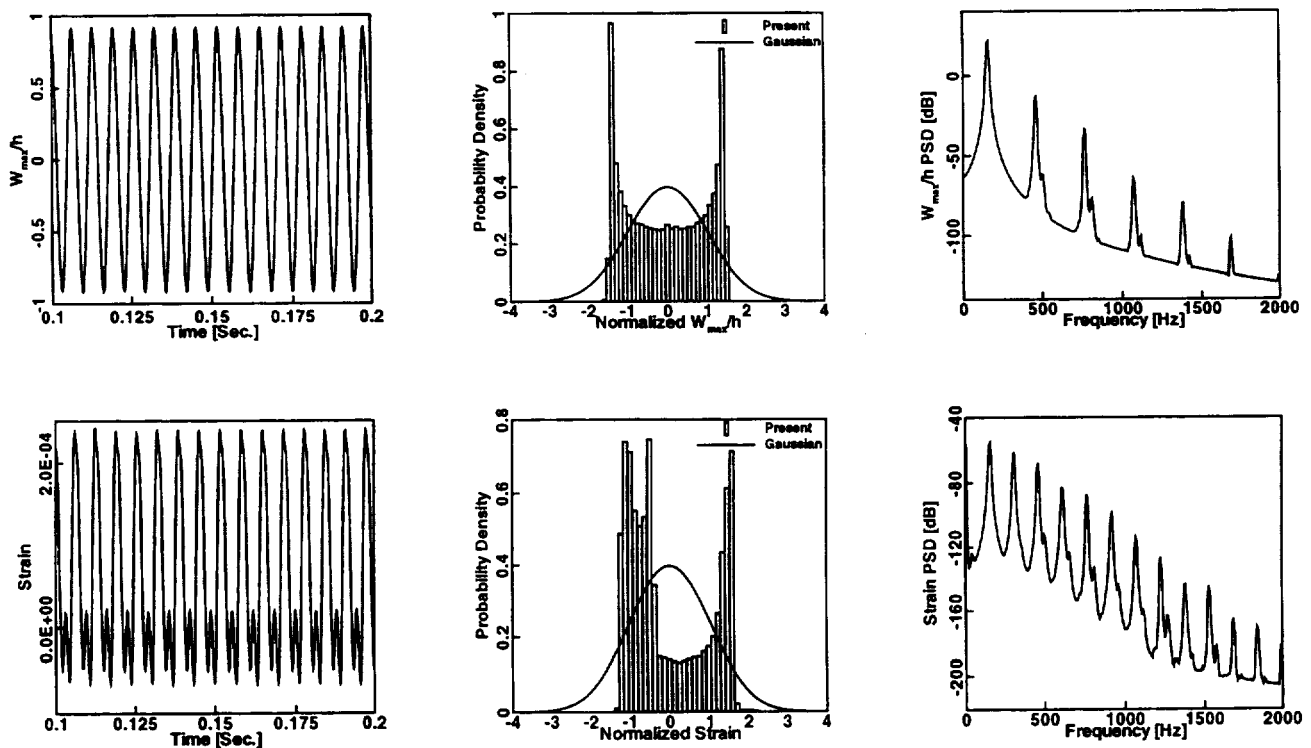


Fig. 5 Response of a simply supported square isotropic plate at 0 dB SPL and $\lambda=800$

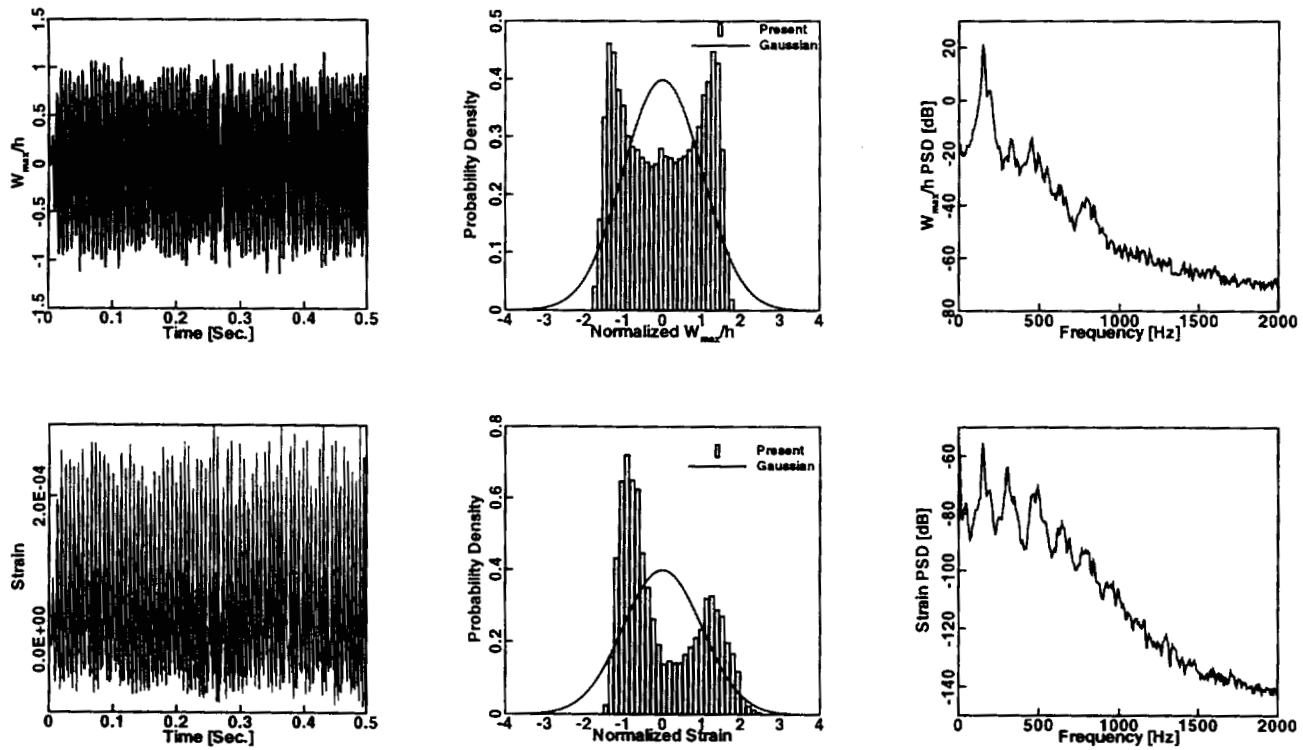


Fig. 6 Random Response of a simply supported square isotropic plate at 100 dB SPL and $\lambda=800$

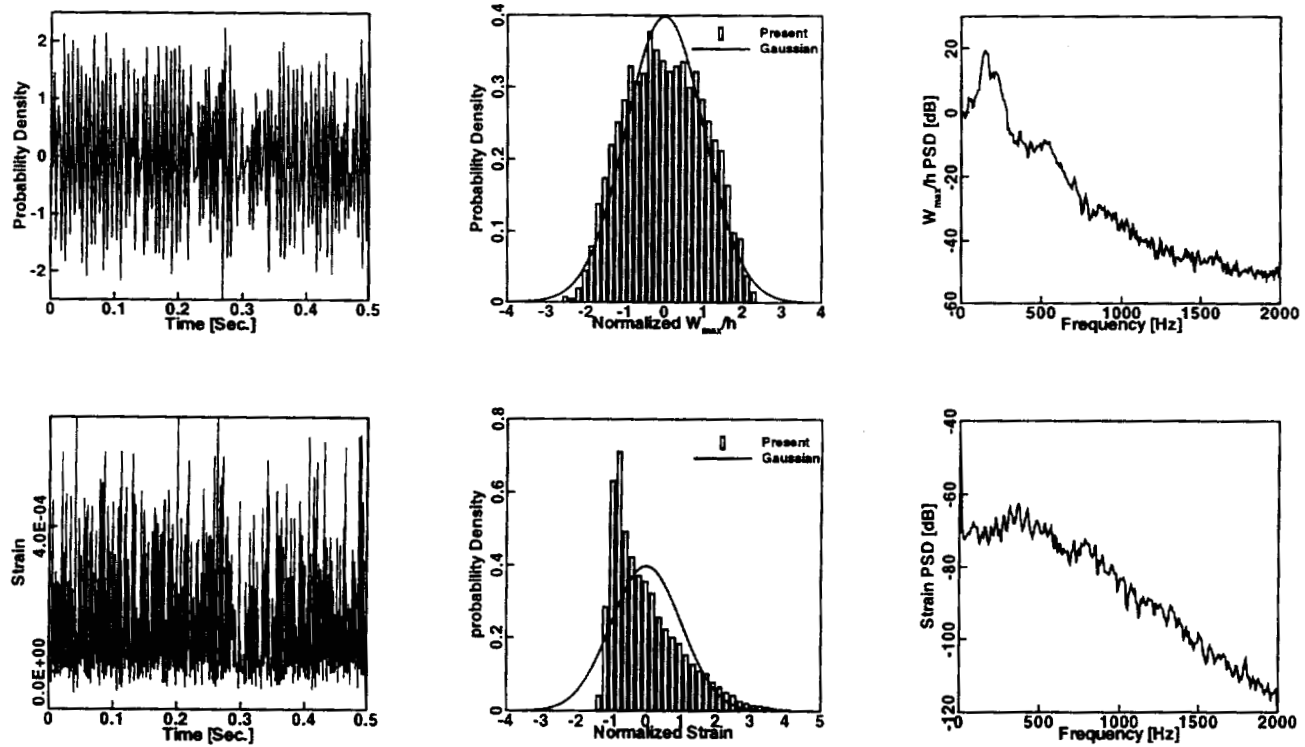


Fig. 7 Random Response of a simply supported square isotropic plate at 120 dB SPL and $\lambda=800$

PANEL FLUTTER ANALYSES FOR THE FIRST BRAZILIAN SATELLITE LAUNCHER

5/5-15

J. G. Damilano, Jamil C. Said and João L. F. Azevedo
Instituto de Aeronáutica e Espaço
Centro Técnico Aeroespacial
12228-904 - São José dos Campos - SP - BRAZIL

Abstract

The paper describes panel flutter analyses performed in the context of the development of the first Brazilian satellite launcher (VLS). The development of the structural-dynamic and aerodynamic formulations are presented, together with their coupling to obtain the aeroelastic equations. Two different approaches were used to describe the aerodynamic loading, namely formulations based on the quasi-steady, linearized, small perturbation potential equation and on 1st-order piston theory. Results are presented for the VLS main aerodynamic fairing panels, both at zero incidence and at angle of attack. The effect of the inclusion of the unsteady aerodynamic terms in the aeroelastic results was also investigated. The overall conclusion of the study indicates that the VLS payload shroud would be free from panel flutter even with a considerable reduction in the fairing panel thickness.

1 Introduction

The present work is concerned with panel flutter analyses performed in the context of the development of the first Brazilian satellite launcher, the VLS system. The VLS is a four-stage vehicle in which the first stage is composed of four strap-on boosters around a central core. The vehicle has a hammerhead-type payload shroud which is a configuration known to be prone to flow separation during the transonic or supersonic flight regimes. This observation, therefore, also indicates that considerably higher structural loads could be present over the payload fairing for these flight conditions. A schematic representation of the VLS system is presented in Fig. 1. The vehicle is being designed for the mission of launching small satellites, of the order of 150 to 200 kg, into low Earth orbit (LEO). Moreover, this vehicle is an integral part of the so-called Complete Brazilian Space Mission which has the goal of launching a Brazilian satellite, using a Brazilian-built rocket, from a Brazilian launching site. The satellite development is the responsibility of Instituto Nacional de Pesquisas Espaciais (INPE) whereas the launching site is the Alcântara Launching Complex (CLA). The responsibility of designing and building the launcher itself falls with Instituto de Aeronáutica e Espaço (IAE) which, together with its industrial partners, should deliver the VLS ready for launch.

The vehicle has been under development for a few years now and, recently, there was an intensive effort to try to finalize its aeroelastic clearance studies. In particular, as in the development of any satellite launcher, panel flutter analyses are an important issue to be considered. Moreover, it is correct to state that aeroelastic considerations were not taken into account in the original design studies and structural sizing of the vehicle. These considerations were treated as afterwards verifications, which is also a fairly common procedure in many organizations. The aspects which were mainly emphasized in the VLS aeroelastic clearance studies were transonic buffeting for the central body payload shroud, classical flutter and divergence of the vehicle fins, panel flutter and vortex shedding at takeoff conditions. It should be emphasized that the final VLS configuration, as shown in Fig. 1, does not have fins in the first stage boosters. However, until recently, the primary configuration under study was supposed to have those fins and there is no guarantee that future vehicle upgrades will not require the fins.

The present paper describes one of these studies, namely the verification of panel flutter stability for the vehicle main aerodynamic fairing, i.e., the payload shroud. The initial studies for the VLS design indicated that the payload shroud would be made with composite materials. For several reasons, which are beyond the

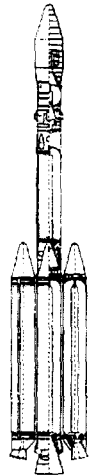


Figure 1: Sketch of the VLS system.

scope of the present paper, there was a decision to use standard aeronautical construction for the fairing. Hence, it currently has several longerons and stiffeners which are riveted to the aluminum skin. Stiffeners and longerons are also made of aluminum. The overall fairing construction allows its modeling as composed of several rectangular patches supported at the longerons and stiffeners. The flat patches are uniform, isotropic, thin and simply supported on the four edges. The aerodynamic loading is based on the two-dimensional “static approximation” in the first instance including the effect of yaw of the panel. Then, unsteady terms are included in the aerodynamic formulation. The approximate solution is obtained by using Lagrange’s equations and oblique coordinates. Numerical results indicate that, even at the maximum dynamic pressure flight condition and if the plate thickness were reduced in half, the flutter dynamic pressure would still be considerably higher than the actual flight dynamic pressure.

2 Structural Formulation

The parallelogrammic flat panel simply supported all around is assumed to be uniform, thin, and isotropic. Damping is neglected and the classical, small-deflection, thin-plate theory is used in the structural formulation. The effect of yaw of the parallelogramic panel is taken into account. Lagrange’s equations are used to derive the equations of motion of the approximate solution. The potential energy of the system is written based on the strain energy of deformation of the plate and the work of the mid-plane forces. The panel is exposed to supersonic flow on one side and to still air on the other. Figure 2 shows the geometry of the panel, the system of oblique coordinates and the aerodynamic flow. The use of the classical small-deflection theory allows the governing equation for the problem to be written as

$$D\nabla^4 W + N_x W_{,xx} + 2N_{xy} W_{,xy} + N_y W_{,yy} + \rho h W_{,tt} = \ell(x, y, t), \quad (1)$$

where $D = Eh^3/12(1 - \nu^2)$ is the stiffness of the plate, ∇^4 is the biharmonic operator in oblique coordinates, ρ is the mass density of the material, h and W are the thickness and transverse displacement of the panel, respectively, and $\ell(x, y, t)$ is the aerodynamic loading normal to the middle plane of the panel. Moreover, N_x , N_{xy} and N_y represent the structural loading at the mid-plane of the plate. Subscripts after a comma denote differentiation. The boundaries of the panel, in oblique coordinates, are $x_1 = 0$, $x_1 = a$, $y_1 = 0$ and $y_1 = b$. The rectangular coordinates and the oblique coordinates are related by the expressions $x_1 = x - y \tan \Psi$ and $y_1 = y \sec \Psi$, where Ψ is the angle of skew of the panel.

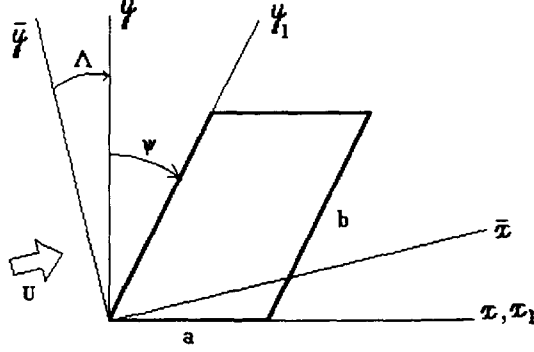


Figure 2: Parallelogramic panel and oblique coordinate system for the panel in yaw.

3 Aeroelastic Formulation

The aeroelastic equations for the problem are derived using two aerodynamic theories. The first one considers a quasi-steady aerodynamic formulation based on the linearized small perturbation potential equation. The second one uses a 1st-order piston theory which includes unsteady aerodynamic effects.

3.1 Quasi-steady Aerodynamic Formulation

The equations of motion of the system are obtained by the use of Lagrange's equations

$$\frac{d}{dt}\left(\frac{\partial T}{\partial \dot{q}_i}\right) - \frac{\partial T}{\partial q_i} + \frac{\partial U}{\partial q_i} = Q_i(t), \quad i = 1, 2, \dots, k. \quad (2)$$

The kinetic energy is given by

$$T = \frac{1}{2} \cos \Psi \int_0^b \int_0^a \rho h \dot{W}^2 dx_1 dy_1. \quad (3)$$

From thin-plate theory, the potential energy of the system U consisting of the strain energy of deformation of the plate expressed in oblique coordinates and the work of the mid-plane forces is given by

$$\begin{aligned} U = & \frac{D}{2} \cos \Psi \int_0^b \int_0^a [(\nabla^2 W)^2 - 2(1-\nu) \sec^2 \Psi (W_{,x_1 x_1} W_{,y_1 y_1} - W_{x_1 y_1}^2)] dx_1 dy_1 \\ & - \frac{1}{2} \cos \Psi \int_0^b \int_0^a [N_x W_{,x_1}^2 + N_y \sec^2 \Psi (W_{,y_1} - \sin \Psi W_{,x_1})^2 \\ & + 2N_{xy} \sec \Psi W_{,x_1} (W_{,y_1} - \sin \Psi W_{,x_1})] dx_1 dy_1, \end{aligned} \quad (4)$$

where $\nabla^2 W = \sec^2 \Psi (W_{,x_1 x_1} - 2 \sin \Psi W_{,x_1 y_1} + W_{,y_1 y_1})$ is the laplacian in oblique coordinates applied to W . The quasi-steady aerodynamic loading, based on the linearized small perturbation potential equation is given by

$$\ell(x, y, t) = -\frac{2q}{\beta} \left(\frac{\partial W}{\partial x} \right) \quad (5)$$

where $q = \frac{1}{2} \rho_a U^2$ is the dynamic pressure, ρ_a and U are, respectively, the air density and the mean flow velocity, and $\beta = \sqrt{(M^2 - 1)}$, with M denoting the freestream Mach number.

The deflection of the panel can be written as

$$W(\xi, \eta, t) = \sum_{i=1}^k q_i(t) \phi_i(\xi, \eta), \quad (6)$$

where $\xi = x_1/a$ and $\eta = y_1/b$ are nondimensional oblique coordinates. Thus, the kinetic and strain energies expressions can be rewritten, respectively, as

$$T = \frac{1}{2} \sum_{i=1}^k \sum_{j=1}^k m_{ij} \dot{q}_i \dot{q}_j \quad \text{and} \quad U = \frac{1}{2} \sum_{i=1}^k \sum_{j=1}^k k_{ij} q_i q_j, \quad (7)$$

where m_{ij} and k_{ij} are presented in Durvasula^[4].

Taking into account the effect of yaw of the parallelogramic panel, as shown in Fig. 2, the aerodynamic loading, considering a quasi-steady formulation based on the linearized small perturbation potential equation, is written, in normalized oblique coordinates, as

$$\ell(\xi, \eta, t) = \frac{-2q}{a\beta} [(\cos \Lambda - \sin \Lambda \tan \Psi) W_{,\xi} + \frac{a}{b} \sin \Lambda \sec \Psi W_{,\eta}] \quad (8)$$

where Λ is the angle between the flow direction and the axis x (yaw angle). The generalized forces $Q_i(t)$ can be calculated considering the virtual work of the aerodynamic loading as:

$$\begin{aligned} \delta \bar{W} = Q_i(t) \delta q_i = & - \frac{2qb \cos \Psi}{\beta} \int_0^1 \int_0^1 [(\cos \Lambda - \sin \Lambda \tan \Psi) W_{,\xi} \\ & + \frac{a}{b} \sin \Lambda \sec \Psi W_{,\eta}] \delta W d\xi d\eta \end{aligned} \quad (9)$$

from which one can write:

$$Q_i = - \frac{2qb \cos \Psi}{\beta} \sum_{j=1}^k L_{ij} q_j, \quad (10)$$

where

$$L_{ij} = \int_0^1 \int_0^1 [(\cos \Lambda - \sin \Lambda \tan \Psi) \phi_{j,\xi} + \phi_{j,\eta} \frac{a}{b} \sin \Lambda \sec \Psi] \phi_i d\xi d\eta.$$

Substituting the expressions for the kinetic energy T , strain energy U and generalized forces Q_i into the Lagrange's equations (2), one can write

$$[\tilde{M}]\{\ddot{q}\} + [\tilde{K}]\{q\} = [\tilde{L}]\{q\}. \quad (11)$$

At the critical flutter condition, as the motion is simple harmonic, the modal deformations can be written

$$\{q\} = Re\{C_i\} e^{i\omega t}, \quad (12)$$

where $\{C_i\}$ is the vector of constants to be determinated and ω is the frequency of oscillation. Substituting this equation into Eq. (11) the resulting system of algebraic homogeneous equations is

$$[[\tilde{K}] - \omega^2 [\tilde{M}] - [\tilde{L}]]\{C\} = \{0\}. \quad (13)$$

For the simply supported panel, the boundary conditions are $W = 0$ and $M_n = 0$ all along the boundary. For the polygonal boundary, the foregoing boundary conditions reduce to $W = 0$ and $\nabla^2 W = 0$ on the boundary. For the assumed displacement mode function ϕ_i one can take

$$\phi_i(\xi, \eta) \sim \phi_{mn}(\xi, \eta) = \sin m\pi\xi \sin n\pi\eta, \quad \text{with} \quad \begin{cases} m = 1, 2, \dots, M \\ n = 1, 2, \dots, N \end{cases} \quad (14)$$

and also, accordingly, $k_{ij} \sim k_{mnrs}$, $m_{ij} \sim m_{mnrs}$, $Q_i \sim Q_{mn}$ and $L_{ij} \sim L_{mnrs}$. Thus, Eq. (13) can be rewritten as

$$[E_{mnrs}]\{C_{rs}\} = \bar{k}^{*2}\{C_{rs}\} \quad (15)$$

where $\bar{k}^{*2} = \frac{\rho ha^4 \cos^4 \Psi}{D\pi^4} \omega^2$ and $[E_{mnrs}]$ is defined in Ref. [7]. Also, the dynamic pressure parameter, present in $[E_{mnrs}]$, is given by $Q^* = \frac{2qa^3 \cos^4 \Psi}{\beta D \pi^4}$.

The matrix equation (15) corresponds to the general flutter problem of a parallelogrammic panel simply supported all around acted upon by uniform in-plane loads N_x , N_y , and N_{xy} . This work, however, is concerned with the panel flutter of unstressed panels, i.e., with N_x , N_y , and N_{xy} all equal to zero. The eigenvalues \bar{k}^{*2} of the matrix $[E_{mnrs}]$ represent the frequencies of vibration of the panel. For the static aerodynamic theory used, all eigenvalues of $[E_{mnrs}]$ are real for sufficiently small values of Q^* . Actually, for $Q^* = 0$, Eq. (15) refers to a free vibration problem and the resulting eigenvalues correspond to the in vacuo frequencies of the panel. Gradually increasing Q^* , some eigenvalues approach each other and, for a certain value of Q^* , two roots coalesce forming an eigenvalue loop. Further increasing the value of Q^* , these two roots become complex. When the roots \bar{k}^{*2} become complex, the corresponding motion clearly is a divergent oscillation. Thus, the value of Q^* at which two eigenvalues coalesce defines the critical value Q_{cr}^* for flutter.

3.2 Aerodynamic Formulation with Piston Theory

The aerodynamic loading, considering first order piston theory^[3], can be written as

$$\ell(x, y, t) = -\left(\frac{2q}{M}\right)\left(\frac{1}{U}\frac{\partial W}{\partial t} + \frac{\partial W}{\partial x}\right). \quad (16)$$

The structural-dynamic formulation is still given by Eq. (1). Hence, the aerodynamic loading, rewritten in terms of the dimensionless coordinates and considering the coordinate system indicated in Fig. 2, can be expressed as

$$\ell(\xi, \eta, t) = -\frac{2q}{aM}\left[(\cos \Lambda - \sin \Lambda \tan \Psi)W_{,\xi} + \frac{a}{b}\sin \Lambda \sec \Psi W_{,\eta} + \frac{a}{U}W_{,t}\right]. \quad (17)$$

The $Q_i(t)$ generalized forces, obtained from the virtual work performed by the aerodynamic forces, can be written in this case as

$$Q_i(t) = -\frac{2qb \cos \Psi}{M}\left(\sum_{j=1}^k L_{1,ij}q_j + \sum_{j=1}^k L_{2,ij}\dot{q}_j\right), \quad (18)$$

where

$$\begin{aligned} L_{1,ij} &= \int_0^1 \int_0^1 \left[(\cos \Lambda - \sin \Lambda \tan \Psi)\Phi_{j,\xi} + \frac{a}{b}\sin \Lambda \sec \Psi \Phi_{j,\eta}\right] \Phi_i d\xi d\eta, \\ L_{2,ij} &= \int_0^1 \int_0^1 \frac{a}{b}\Phi_j \Phi_i d\xi d\eta. \end{aligned} \quad (19)$$

The equations describing the motion of the panel in terms of the modal coordinates can be obtained, using Lagrange's equations of motion, as

$$[\tilde{M}]\{\ddot{q}\} + [\tilde{K}]\{q\} = [\tilde{L}_1]\{q\} + [\tilde{L}_2]\{\dot{q}\}. \quad (20)$$

The present formulation does not allow a direct eigenvalue analysis, as performed in the previous case, due to the presence of the modal velocities in Eq. (20). If one considers the transformation of variables defined by $q_1 = q$ and $q_2 = \dot{q}$, it is possible to rewrite the equations of motion in a standard first-order form as

$$\begin{Bmatrix} \dot{q}_1 \\ \dot{q}_2 \end{Bmatrix} = \begin{bmatrix} [0] & [I] \\ [\tilde{L}'_1] - [\tilde{K}'] & [\tilde{L}'_2] \end{bmatrix} \begin{Bmatrix} q_1 \\ q_2 \end{Bmatrix}. \quad (21)$$

The various matrix terms in Eq. (21) were obtained from the matrices in Eq. (20) after appropriate normalizations. The interested reader is referred to Ref. [6] for further details of this derivation. It is also possible to show^[6] that these terms can be written as

$$\begin{aligned} [\tilde{L}'_2] &= -\frac{a_\infty \rho_a}{h \rho} [I], \\ [\tilde{L}'_1] - [\tilde{K}'] &= -\frac{D}{a^4 \rho h \cos^4 \Psi} [E_{mnrs}], \end{aligned} \quad (22)$$

where $[E_{mnrs}]$ appeared originally in Eq. (15). If one considers that, at the critical flutter condition, the motion is of the form

$$\{q\} = \text{Re}\{C_i\} e^{\omega t}, \quad (23)$$

it is again possible to perform an eigenvalue-based stability analysis for the system. In this case, the instability condition will be reached when the real part of any of the eigenvalues becomes positive, since this will yield an exponentially growing amplitude of motion.

4 Some Validation Results

The formulation described in Section 3.1 was validated based on numerical examples present in Ref. [4], whereas the formulation presented in Section 3.2 was partially validated, based on the same examples, however taking the terms of matrix $[\tilde{L}_2]$ equal to zero.

An evaluation of the effect of the unsteady aerodynamic terms present in the 1st-order piston theory formulation was also performed. Results in graphical form are not presented here for the sake of brevity. However, the calculations indicated that, all other parameters held fixed, the lowest values of Q_{cr}^* correspond to the results obtained without including the unsteady terms, i.e., using quasi-steady aerodynamics. Moreover, computations with 1st-order piston theory used two different values of freestream air density, namely $\rho_a = 0.600 \text{ kg/m}^3$ and 1.228 kg/m^3 . The results indicated that higher values of air density yield larger values of Q_{cr}^* . Therefore, the conclusion of these analyses is that, for the present cases, the inclusion of unsteady effects increases the flutter dynamic pressure because the unsteady aerodynamic terms add damping to the system. Moreover, higher air densities yield larger damping effects which, in turn, further increase the flutter dynamic pressure.

The results for a flutter analysis using 1st-order piston theory and considering a panel with $a/b = 1$, with air density $\rho_a = 1.228 \text{ kg/m}^3$ and $\Lambda = 0 \text{ deg.}$, are presented in Fig. 3 in terms of the root locus of the first eigenvalue that becomes unstable. One can observe that, as Q^* is increased, initially the real part of the eigenvalue is essentially constant. Further increase in Q^* makes the real part of the eigenvalue move towards the unstable right-hand semi-plane and, at $Q_{cr}^* = 5.9$, there is the onset of flutter for this case.

5 Flutter Analyses for the VLS Main Fairing

A typical panel was chosen from the cylindrical region of the VLS main fairing for the analyses. The rectangular panel is simply supported all around the boundary. The elastic deformations of the support, i.e., the elastic deformations of the longerons and stiffeners, were neglected. The panel to be analyzed is rectangular with $a = 115 \text{ mm}$ and $b = 120 \text{ mm}$. For the work herein described, firstly a yaw angle of 0 deg. was used. Since the chosen typical panel has sides parallel to the axes of the coordinate system, thus $\Psi = 0 \text{ deg.}$. The calculations were performed using 16 term series by taking $M = 4$ and $N = 4$, and with the mid-plane loads $N_x = N_y = N_{xy} = 0$. The results, pictured in Fig. 4, showed coalescence between the 1st and 2nd frequencies for $Q_{cr}^* = 5.11$. If the vehicle flies with angles of attack different from zero, it would be equivalent to having the side panels with angle of yaw, Λ , with respect to the flow, also different from zero. In the VLS case, all

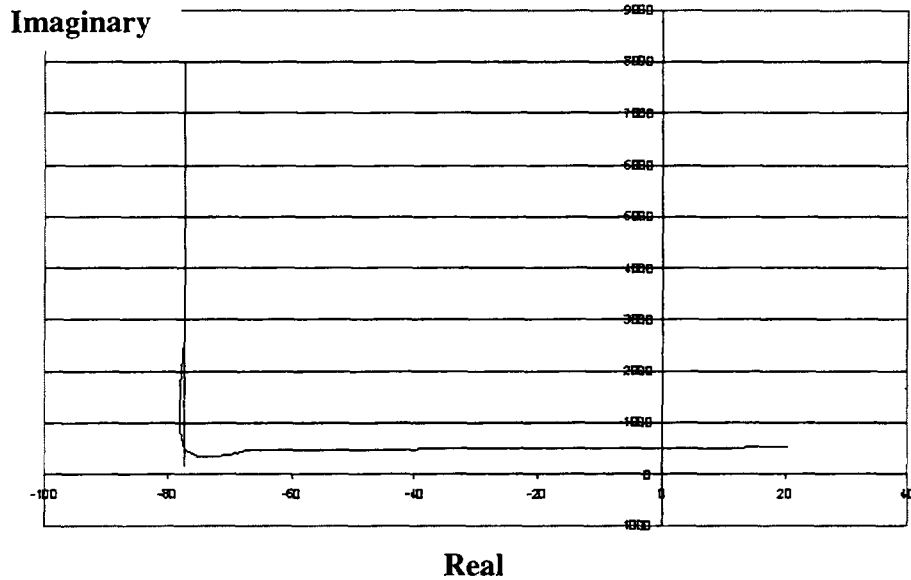


Figure 3: Root locus for the first eigenvalue that becomes unstable with $N_x = N_y = N_{xy} = 0$ and $\Psi = \Lambda = 0$.

along its trajectory, the angle of attack varies from 0 to 6 deg. As shown in the literature^[4], and confirmed by the results obtained, the existence of yawing angles, in the range of 0 to 10 deg., when $\Psi = 0$ deg. and $a/b = 1$, typically leads to higher critical flutter dynamic pressures. Thus, the results obtained for $\Lambda = 0$ were considered in the study described as follows. The panel's material is aluminum with $E = 70$ GPa, $\nu = 0.3$, and thickness $h = 1.0$ mm. It is possible to write q/β as function of Q^* by using the expression

$$\frac{q}{\beta} = \frac{\pi^4 E}{24a^3(1-\nu^2)\cos^4\Psi} Q^* h^3. \quad (24)$$

Then, substituting the value obtained for Q_{cr}^* into Eq. (24) results $q/\beta = 1.05 \times 10^6 \text{N/m}^2$. From the vehicle's flight data^[5] at time $t = 42$ s, the maximum dynamic pressure is $q_{max} = 9.28 \times 10^4 \text{N/m}^2$ corresponding to a Mach number $M = 2.383$, which results in $q/\beta = 4.29 \times 10^4 \text{N/m}^2$. The results clearly indicate a very safe vehicle operation, as far as panel flutter is concerned, since q/β , for the critical dynamic pressure parameter of the vehicle, is almost 2 orders of magnitude larger than the actual value obtained with the vehicle flight data. Moreover, if the panel thickness is reduced to 0.5 mm, the previous numerical procedures will produce $q/\beta = 1.31 \times 10^5 \text{N/m}^2$, which still represents a very stable condition, since the result is about 3 times larger than the one that actually occurs during the flight of the vehicle.

Another approach to present the previously discussed results would be to plot the stability region for the VLS main fairing for a fixed flight dynamic pressure, and as a function of the flight Mach number and panel thickness. This is indicated in Fig. 5 for the case in which the aerodynamic forces are calculated using the quasi-steady, small disturbances potential theory. All the geometric and material data used in this case are the same as in the previous discussion. For the present calculations, however, the point along the vehicle trajectory corresponding to 35 s after liftoff was considered, which yields a freestream dynamic pressure of $78.3 \times 10^3 \text{N/m}^2$. The points above the curve in Fig. 5 correspond to stable operation as far as panel flutter is concerned, whereas those below the curve are unstable points.

The actual point corresponding to the VLS payload shroud panels in the above conditions is also indicated in Fig. 5. One can see that this point is well within the stable region. Moreover, one can also observe that, all

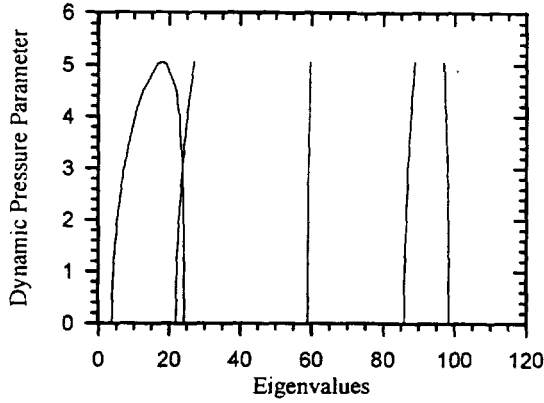


Figure 4: Eigenvalues as function of the aerodynamic loading Q^* .

other parameters remaining constant, the panel thickness could be reduced to approximately 0.4 mm without the occurrence of panel flutter for this flight condition.

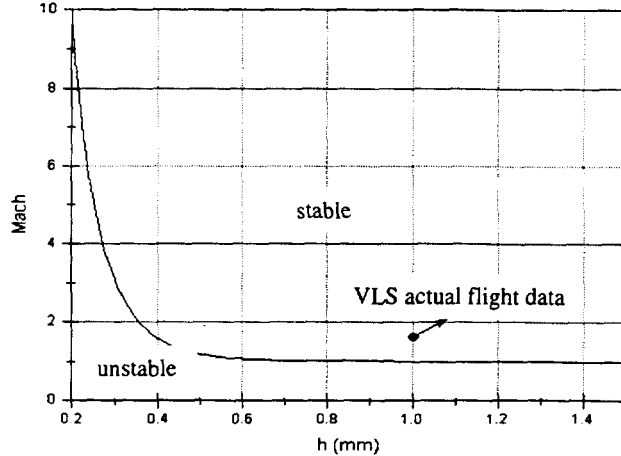


Figure 5: Stability region for the VLS payload shroud panels calculated using quasi-steady aerodynamics ($q = 78.3 \times 10^3 \text{ N/m}^2$).

Similar results are presented in Fig. 6, but for the aerodynamic loads computed using 1st-order piston theory. As before, all other parameters and the flight dynamic pressure are held fixed, whereas the Mach number and panel thickness are varied in order to determine the flutter stability limit. The dynamic pressure was fixed at $87.0 \times 10^3 \text{ N/m}^2$ in this case, which corresponds to flight at 40 s after liftoff for the VLS nominal trajectory. Again, the actual point corresponding to the VLS flight at this condition is also shown in Fig. 6, and one can observe that the vehicle is clearly stable for panel flutter under such conditions. The dimensionless critical flutter dynamic pressure at this condition, calculated using piston theory, is $Q_{cr}^* = 5.16$. For the same conditions, if the flutter limit were computed using quasi-steady aerodynamics, the calculation would yield

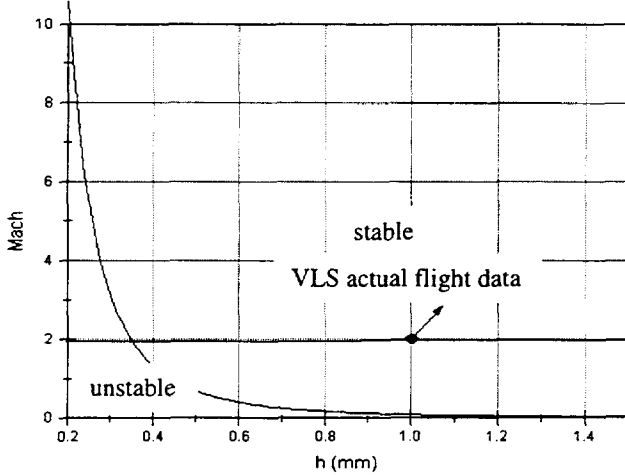


Figure 6: Stability region for the VLS payload shroud panels calculated using 1st-order piston theory ($q = 87.0 \times 10^3 \text{ N/m}^2$, $\rho_a = 0.447 \text{ kg/m}^3$ and altitude = 9375 m).

$Q_{cr}^* = 5.11$. This behavior is in agreement with the results previously discussed, since the addition of the unsteady terms adds damping to the system and, hence, increases the flutter speed.

A still different form of trying to summarize the results of the present investigation is shown in Fig. 7. In

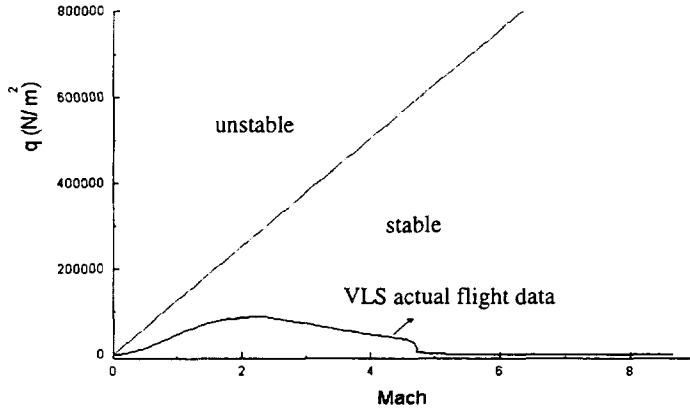


Figure 7: Comparison of flutter dynamic pressure and actual flight dynamic pressure along the VLS nominal trajectory for payload shroud panel thickness assumed as 0.5 mm.

this case, the panel thickness was held fixed at $h = 0.5 \text{ mm}$, and the dynamic pressure for the flutter stability limit was calculated as a function of the flight Mach number. All geometric and material parameters are equal to the values used in the previous analyses for the VLS, and the atmospheric data is taken, as a function of the flight Mach number, from the vehicle nominal flight trajectory. The panel thickness was considered at half of its actual value for the VLS panels because the authors wanted to emphasize that, even with such a drastic reduction on the fairing plate thickness, the vehicle was still safe with regard to panel flutter. The actual flight dynamic pressure for the VLS, as a function of Mach number, is also shown in Fig. 7 for comparison purposes. It is clear from this figure that the panel flutter margin for the payload shroud panels is very large throughout the relevant portion of the flight trajectory, even with half the actual plate thickness. The quasi-steady aerodynamic formulation was used for the calculations presented in Fig. 7.

6 Conclusions

Panel flutter analyses were performed in the context of the development of the first Brazilian satellite launcher (VLS). Lagrange's equations were used to derived the aeroelastic equations for the problem. The aerodynamic loading was obtained based on two different aerodynamic formulations, namely the quasi-steady linearized small perturbation equation and the 1st-order piston theory. The panels are considered flat, rectangular, isotropic, and simply supported all along the boundary. The numerical results obtained indicate that the VLS payload shroud should fly free from panel flutter even with a considerable reduction in the fairing panel thickness. Moreover, the results also indicated that the inclusion of unsteady aerodynamic terms in the formulation consistently increases the flutter dynamic pressure for the present cases. Future work will concentrate on the evaluation of the effect of the support flexibility in the overall panel flutter stability.

7 Acknowledgments

The present work was partially supported by Conselho Nacional de Desenvolvimento Científico e Tecnológico, CNPq, under the Integrated Project Research Grant No. 522413/96-0.

8 References

- [1] Bisplinghoff, R. L., Ashley, H., and Halfman, R. L., *Aeroelasticity*, Addison-Wesley, Cambridge, 1955.
- [2] Liepmann, H. W., and Roshko, A., *Elements of Gasdynamics*, John Wiley, New York, 1957.
- [3] Ashley, H., and Zartarian, G., "Piston Theory – A New Aerodynamic Tool for the Aeroelastician," *Journal of the Aeronautical Sciences*, Vol. 23, No. 12, 1956, pp. 1109-1118.
- [4] Durvasula, S., "Flutter of Simply Supported, Parallelogrammic, Flat Panels in Supersonic Flow," *AIAA Journal*, Vol. 5, No. 9, 1966, pp. 1668-1673.
- [5] Many authors, "VLS Database," Report No. 590-000000/B0004, Instituto de Aeronáutica e Espaço, São José dos Campos, SP, Brazil, Sep. 1991 (in Portuguese, original title is "Banco de Dados do VLS").
- [6] Said, J.C., Azevedo, J.L.F., and Damilano, J.G., "Panel Flutter Studies for the VLS," Report NT-158/ASE-N/98, Space Systems Division, Instituto de Aeronáutica e Espaço, São José dos Campos, SP, Brazil, Dec. 1998 (in Portuguese, original title is "Estudos de Flutter de Painéis para o VLS").
- [7] Damilano, J.G., and Azevedo, J.L.F., "Aeroelastic Analysis Applied to the Main Fairing of the Satellite Launcher Vehicle – VLS," Report RT-005/ASE-E/98, Space Systems Division, Instituto de Aeronáutica e Espaço, São José dos Campos, SP, Brazil, Dec. 1998 (in Portuguese, original title is "Análise Aeroelástica Aplicada à Coifa Principal do Veículo Lançador de Satélites – VLS").

Self-Induced Brake Torque Oscillations of Landing Gear as an Interaction of Non-linear Tyre with Brake Control System

Wolfgang G. Luber

DaimlerChrysler Aerospace AG
Military Aircraft MT24
81663 Munich, Germany
Phone : +49-89-607-26996
Fax: +49-89-607-28707
Email: wolfgang.luber@m.dasa.de

5/9-37

Abstract

The paper describes a Brake Torque Oscillations at Brake Initiation as a quasi self-induced oscillations due to the interaction of non-linear tyre circumferential force characteristics with the brake control system. Usual means to suppress oscillation (dampers or modification of landing gear geometry) are ineffective in this case. This case demonstrates that not only unsuitable combinations of structural stiffness, damping, and pneumatic tyre characteristics may lead to unexpected vibration problems on landing gears. Rather, an unlucky combination of brake system design with the peculiarities of circumferential force development by a tyre can also produce a serious vibration problem.

In a series of development rig tests for a fighter aircraft brake system, some test, were scheduled to demonstrate fastest possible brake force rise at high speed. A fast brake force rise was considered to yield, at least in theory, shortest possible landing ground run distance.

1. INTRODUCTION

An aircraft landing gear system has to be designed to meet various requirements covering all ground-based operations. It is a complex non-linear system which incorporates many sub-components often procured of sources which can produce structural dynamics and loading effects on the gear as well on the aircraft.

The landing gear must be capable to carry heavy weight for take off operations, hard impact of the landing as well as the kinetic energy of forward motion on landing to bring the aircraft safely to rest. Due to the long terms of developing an aircraft reducing the risk of redesign and the cost of testing it is desirable to be able to predict the dynamic behaviour of landing gear systems.

In the past methods were used to calculate via mathematical criteria, the stability of the nose landing gear against oscillation. Since landing gear are very non-linear systems a time domain simulation code must be applied to show the behaviour of the landing gear itself and also the involved subsystems. An integrated approach to the modelling of the subsystems of the landing gear and the interaction of the elastic aircraft is required to accomplish the task. To get reliable results, which can also be validated by tests various components must be considered and introduced in the calculations like tyre, wheel, bogie, leg, oleo, braking system, anti skid control, steering and flexible aircraft.

This report presents the straight forward trial to integrate the elastic aircraft into the shimmy investigation for nose landing gear of a fighter type aircraft development phase.

2. BRAKE TORQUE OSCILLATIONS AT BRAKE INITIATION

The case following demonstrates that not only unsuitable combinations of structural stiffness, damping, and pneumatic tyre characteristics may lead to unexpected vibration problems on landing gears. Rather, an unlucky combination of brake system design with the peculiarities of circumferential force development by a tyre can also produce a serious vibration problem.

2.1 THE SITUATION

In a series of development rig tests for a fighter aircraft brake system, some test, were scheduled to demonstrate fastest possible brake force rise at high speed. A fast brake force rise was considered to yield, at least in theory, shortest possible landing ground run distance.

The test set-up "dynamometer" consisted of one main wheel with brake running within a heavy drum, where the rotational inertia of the drum was to represent respective mass per braked wheel of the aircraft. This arrangement not only gives a representative picture of aircraft deceleration by the brake but also provides correct kinetic energy to be dissipated by the brake. The brake was actuated by representative hydraulic components. Brake control was performed by one lane of the brake control computer, pilot's pedal input being replaced by a synthetic signal. Anti-skid functions of the brake control computer were implemented and active.

2.2 DESCRIPTION OF THE PHENOMENON

At brake initiation ("pilot" quasi "jumping" onto brake pedal) there was not the expected crisp yet steady rise of brake force with eventual subsequent anti-skid system activity. Rather there was a sequence of rapid on/off switching of the brake which lasted for about 1.5 seconds at a frequency of about 6 Hz. Thereafter the system stabilised to a normal behaviour.

Fig. 1 shows a principal sketch of those three test measurement traces which are considered essential for description and explanation of the phenomenon. From top to bottom, these are Wheel Speed, Brake Pressure (i.e. pressure on brake piston face), and Brake Torque.

The very first increase of brake pressure is needed to overcome the piston lifting spring. To arrive at the net pressure acting on the brake pad, that "spring pressure" is to be subtracted from the value measured; thus, at the first three troughs in Brake Pressure trace, brake pads are practically unloaded. This becomes apparent in Brake Torque trace, where for all practical purposes torque reduces to zero at the corresponding non-zero troughs of Brake Pressure.

The initial phase of Brake Pressure deserves a further comment: While brake servo valve output pressure (not shown) follows solenoid current with negligible delay, this is not true for the brake pressure proper as long as brake pistons are moving to close the gaps between rotor and stator disks of the brake package. The flow of hydraulic fluid from servo valve to brake is restricted by a quite narrow Restrictor orifice which limits loss of hydraulic fluid in case of e.g. rupture of a flexible hose. The Restrictor leads to a pressure drop

between servo valve output and brake piston as long as the piston is moving. This pressure drop is the larger the faster the pilot tries to actuate the brake. However, when fluid flow stops, pressure drop across the Restrictor vanishes and full servo valve brake pressure gets through to brake pistons within fractions of a second. Thus indirectly the safety feature "Restrictor" is responsible for the extremely steep brake pressure rise following on the brake filling phase.

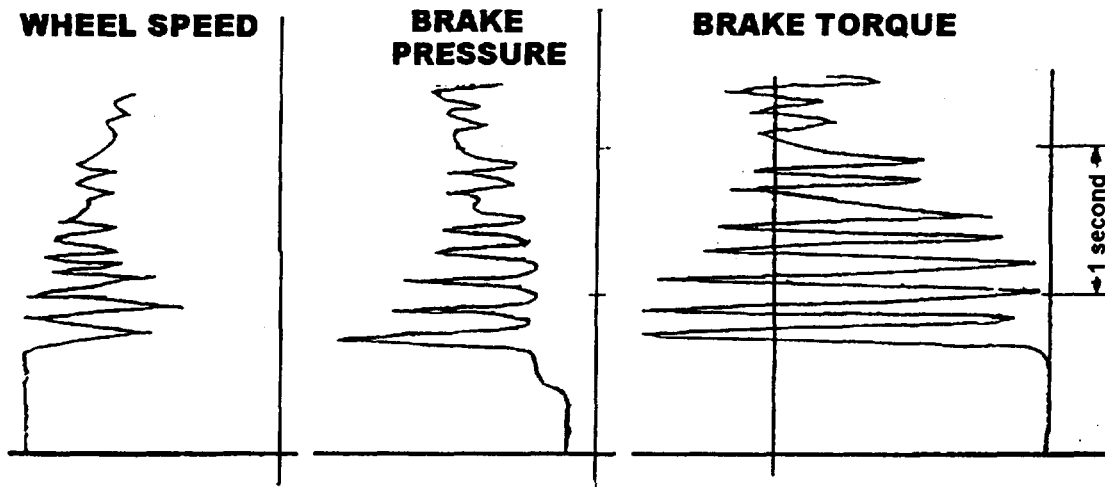


Fig. 1 Measurement Traces from Brake Dynamometer Test

2.3 EXPLANATIONS

From measurement traces not shown here it became apparent that oscillations observed were produced by anti-skid system action. However, given the software and the parameters for skid identification installed in the control algorithm, the anti-skid system worked correctly. The real reason for that disagreeable and inappropriate series of anti-skid actions at brake initiation is a mismatch of brake system control and tyre physics.

2.3.1 Physics of Tyre Braking Force

Explanations following aim for a basic understanding of tyre mechanics with regard to developing circumferential force.

When a tread element of a straight-rolling tyre enters the ground contact patch it will stick to that ground element. On a tyre rolling exactly at the forward speed of the wheel axle, the position in space of tyre tread element and ground element will be practically identical at entry to and exit from ground contact patch. Nevertheless within the patch there will be slight distortion due to the tyre tread being forced from originally circular shape to straight (ground) shape. Contact patch distortion changing sign at half patch length leads to approximately zero net circumferential force on the wheel.

Non zero net circumferential force develops when wheel circumferential speed differs from axle ground speed. Due to speed difference the tread point and the ground point which coincided at entry to the contact

patch depart from each other on their travel through the contact patch. As long as the relative distance of the two points is not too large, tread rubber will adhere to the original entry ground point; elastic deformation of the tread element increases on its travel through the contact patch, thereby increasing the local circumferential load on the tyre. If wheel circumferential speed is sufficiently less than ground speed, at some point along the contact patch shear force on the tread element will exceed adhesive friction capacity of the element. As a consequence, the tread element will start to slide on the ground. Sliding friction of rubber in quite complex manner depends, amongst other parameters, on sliding distance covered and sliding speed. In general it may gradually fall well below adhesive friction with increasing sliding distance and speed. This admittedly coarse view of rubber tyre mechanics leads to the following conjectures about circumferential force on a braked wheel:

- a) At low speed differences, circumferential force on the tyre should be approximately proportional to the distance between corresponding tread and ground points at exit from the ground contact patch. This "exit" distance d_e is, under stationary speed conditions, calculated to be

$$d_e = (v_g - v_c) \cdot \frac{l_p}{v_c}$$

where v_g ground speed

v_c wheel circumferential speed

l_p length of ground contact patch

Please note that circumferential force in this regime is dependent on a speed ratio rather than on actual speed.

- b) At increasing speed difference, adhesive friction capability will be exceeded in small portions of the footprint mainly at the exit end of the ground contact patch. Within the footprint spots affected, rubber will start to slip relative to ground albeit at a very low slip speed and for very short distance. This means that circumferential force will still increase with increasing speed difference. However, rise rate will decrease with friction limited areas covering increasing portions of the tyre footprint.

- c) At speed difference approaching ground speed practically all of the rubber in the footprint will be skidding at nearly ground speed and for extended distance. Since skidding friction depends on skidding speed and distance covered, circumferential force of a non-rotating tyre (full skid) will be less at high ground speed than at low ground speed. Furthermore, at fixed ground speed circumferential force of a skidding tyre will also be less than the maximum achievable at a lower differential speed, where almost all of the footprint area may also be skidding yet at a higher coefficient of friction.

Circumferential coefficient of friction (μ_c) of a tyre usually is presented as a function of "Slip Ratio" (SR), where

$$SR = \frac{v_g - v_c}{v_g}$$

This presentation compresses all tyre angular rates from rolling at ground speed (SR = 0) to full skid (SR = 1) into an abscissa from 0 to 1. However, as shown above μ_c with an increase of slip ratio becomes increasingly dependent on ground speed. Hence there will be different μ_c vs. SR curves for different values

of ground speed. Fig. 2 presents a qualitative picture of this speed effect on circumferential coefficient of friction.

Figures concerning tyre circumferential force are in essence modifications of figures presented at Ref. 2, which treats this subject in much more detail than it is done in present paper.

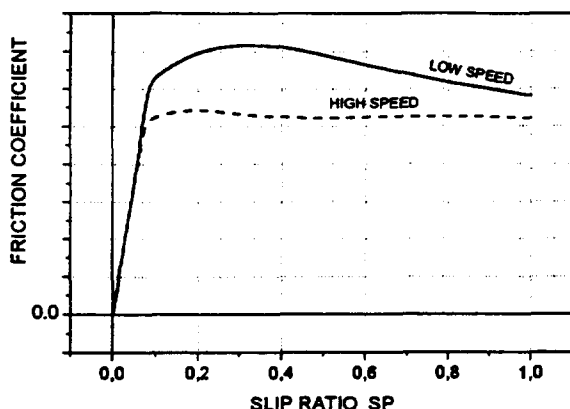


Fig.: 2 Friction Coefficient versus Slip Ratio

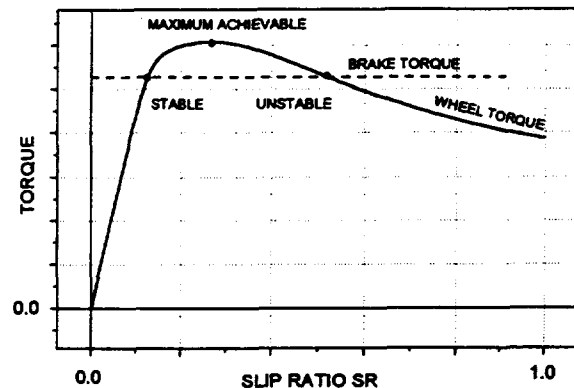


Fig.: 3 Torque Coefficient versus Slip Ratio

2.3.2 Conclusions with Regard to Sensible Brake Control

2.3.2.1 Brake Control during Braking

Fig. 3 is an somewhat exaggerated variation of Fig. 2. However, the ordinate has been renamed "Wheel Torque" after, in ideas, having multiplied circumferential friction coefficient with wheel load and ground-to-axle distance.

Best possible deceleration of the aircraft by wheel braking could certainly be achieved if retarding moment produced by the brake ("brake torque") was just equal to the maximum driving moment achievable by the tyre ("wheel torque"). However, this maximum point will move around very quickly due to wheel load fluctuation on uneven ground, due to fluctuation of ground to tyre friction on varying ground roughness, due to variation of ground-to-axle distance, and due to other effects (e.g. side load on a braked wheel).

Although brake torque is measurable directly, wheel torque is not. Hence it is virtually impossible to exploit 100 percent of achievable wheel torque throughout the braked ground run. Therefore, brake control systems in general are aiming for a working point below the maximum wheel torque on the left (stable) branch of the wheel torque vs. slip ratio curve. However, if by chance maximum wheel torque falls below brake torque or if brake torque is increased beyond maximum achievable wheel torque, this statically unbalanced torque difference will decelerate the wheel and thereby increase slip ratio. Provided torque difference is large enough and is acting for sufficiently long time, slip ratio will be increased to the unstable part of the wheel torque curve.

In order to avoid this critical situation it is necessary in the first place to timely recognise an incipient skid and to reduce brake torque fast enough such that slip ratio is kept on the stable side.

However, a backup procedure is needed in case that slip ratio has eventually reached the unstable side of the wheel torque vs. slip ratio curve. If this happened the wheel would continue to decelerate to an eventual standstill as long as brake torque is larger than actual wheel torque, even if maximum achievable wheel torque had meanwhile recovered beyond actual brake torque. To recover from this "deep skid" the safest way is to lift brake completely until wheel speed has returned to the stable part of the wheel torque vs. slip ratio curve.

For better understanding of the case presented it is necessary to explain the principal method applied here to recognise an incipient skid: Wheel angular deceleration is the most important parameter used for skid detection.

During perfectly steady braking wheel angular deceleration is proportional to aircraft linear deceleration. Hence, on first view one could assume that any wheel deceleration beyond this value could be interpreted as an incipient skid. In theory this assumption holds only if the brake is operating at the maximum wheel torque transmittable to ground, because any loss of transmittable wheel torque will drive the working point to the right (unstable) side of the curve (Fig.3 and 4).

If the brake operates on the stable side somewhere below maximum transmittable wheel torque a reduction of transmitted wheel torque will be followed by a "useful" increment of wheel deceleration which brings transmitted wheel torque back to brake torque. Therefore, anti-skid action should only be triggered on exceedance of this "useful" wheel deceleration increment. As stated above, admittable trigger level is zero if brake torque equals transmittable wheel torque; trigger level rises (progressively) with the ratio of transmittable wheel torque to brake torque.

Assumed that a brake control system in its anti-skid branch contains a fixed wheel deceleration trigger criterion, the control system should also provide for the appropriate torque reserve between brake torque and maximum transmittable wheel torque. Since maximum transmittable wheel torque is not measurable directly, anti-skid systems of the type considered here contain algorithms which reduce brake pressure output from the servo valve according to frequency and intensity of previous anti-skid actions. Brake pressure will be cautiously re-increased (eventually to the level corresponding to pilot's command) if no more anti-skid action was triggered in a sufficiently long time interval.

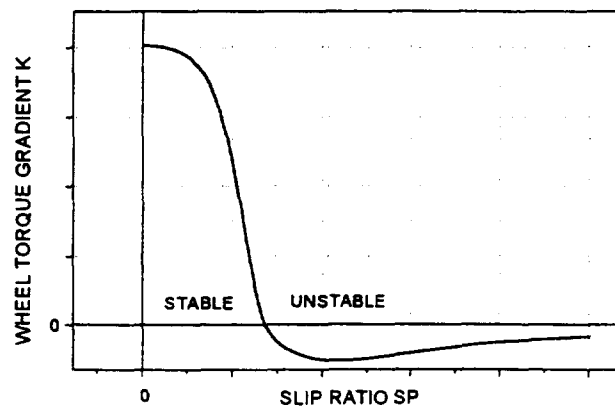


Fig.: 4 Wheel Torque Gradient versus Slip Ratio

2.3.2.2 Brake Initiation

Up to the point of brake initiation, the wheel rolls freely at negligible wheel torque just balancing rolling drag. Therefore at brake initiation, rise of brake torque cannot immediately be counteracted by wheel torque. Rather, momentary difference between wheel torque and brake torque leads to angular deceleration of the wheel. This effects an increase of slip ratio and wheel torque. If brake torque is limited to a value below maximum transmittable wheel torque, slip ratio will eventually tune in to stationary balance of brake torque by wheel torque.

Wheel deceleration occurs during brake initiation as well as during a skid. Hence, if during brake initiation wheel deceleration exceeds the threshold set for skid detection, anti-skid control will unnecessarily lift the brake. The wheel will recuperate to or nearly to freely rolling conditions. When brake pressure is re-applied by anti-skid control another undue skid prevention cycle may occur.

For sake of a vibration-free brake onset it appears useful to gain insight into the factors influencing wheel angular deceleration during brake initiation. To this end quite basic considerations may be helpful:

- a) Step increase of brake torque: If brake torque is assumed to follow a step function then extremum wheel deceleration will occur at $t = 0$ and will equal brake torque divided by wheel moment of inertia.
- b) Creeping increase of brake torque: If brake torque is applied very slowly, this will lead to low wheel deceleration values as well, because the wheel is being given ample time to adapt to the slowly increasing demand on slip ratio.
- c) Influence of "brakes on" aircraft speed: In a diagram showing wheel torque versus slip ratio (see e.g. Fig. 3) the initial linear part is virtually independent of ground speed. However, analysis of the equation defining slip ratio, viz.

$$SR = \frac{v_g - v_c}{v_g}$$

indicates that wheel torque rise rate over time will reduce with an increase of ground speed.

Assumed wheel torque is linearly dependent on slip ratio, i.e.

$$WT = K \cdot SR = K \cdot \frac{v_g - v_c}{v_g}$$

or

$$WT = K \cdot \left(1 - \frac{\omega_w \cdot r_w}{v_g}\right)$$

then wheel torque rise rate becomes

$$\frac{dWT}{dt} = -\frac{K \cdot r_w \cdot \omega_w}{v_g}$$

From this equation it is easily concluded that wheel deceleration will increase proportionally to "brakes on" ground speed (brake torque rise rate assumed independent of speed).

It is also concluded that wheel deceleration may vary with tyre type, e.g. if different tyre construction and/or tread material changes the slope K of the wheel torque vs. slip ratio, K may also change with operating conditions, e. g. dry or wet ground (Ref. 2)

Further on, wheel deceleration increases on transition from the quasi linear part of the wheel torque slope into the degressive part while approaching maximum transmittable wheel torque.

Fig. 5 shows simulation results of a braked wheel during brake initiation. The model used is quite simple. It contains just one degree of freedom representing rotation of a wheel moving at constant ground speed. Brake torque is assumed to form a ramp type function of time while K is assumed constant, i.e. brake torque is assumed to not exceed the linear part of wheel torque vs. slip ratio function. Eventual dynamic deviations of wheel torque vs. slip ratio from quasi-stationary behaviour were not taken into account.

Numerical results from simulation confirmed principal considerations presented above. Hence a systematic evaluation of simulations was performed and summarised in Fig. 6. This figure presents kind of a design chart. With maximum design "brake on" speed given it shows which brake torque rise rate is at best admissible if skid detection threshold shall not be exceeded during brake initiation. This type of diagram can easily be set up for a specific aircraft using its tyre and wheel characteristics (mainly moment of inertia and wheel torque curve) in combination with brake and anti-skid control characteristics (primarily skid detection threshold).

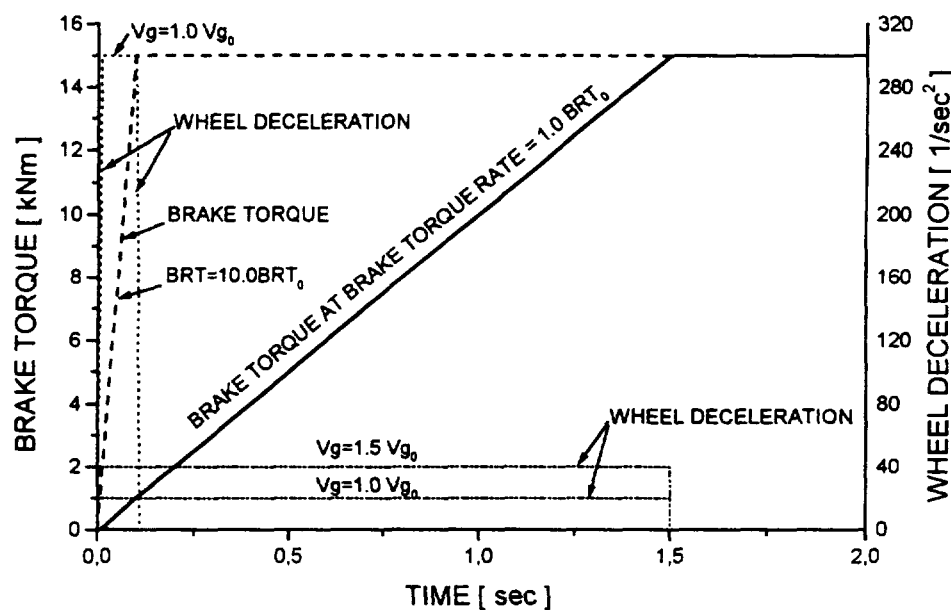


Fig. 5 Histograms of Wheel Deceleration

In developing Fig. 6 it was tacitly assumed that brake torque shall not exceed the straight part of the wheel torque vs. slip ratio curve. However, in reality this is rather improbable, because maximum brake torque achievable is mostly close to or even beyond maximum wheel torque achievable on dry runways. If brake torque ceiling is below maximum wheel torque achievable, wheel angular deceleration will increase on the

degressive slope and fall sharply off to the value corresponding to aircraft deceleration when brake torque ceiling is reached. If brake torque ceiling is beyond maximum wheel torque achievable, then wheel deceleration will not fall off at brake torque reaching its ceiling; rather it will progressively increase on the negative slope of the wheel torque vs. slip ratio curve. Unless skid detection level had been exceeded already on the degressively positive slope of the curve, it will be exceeded here, provided it is small enough. In addition, since brake torque rise rate is not at all perfectly controllable (e.g. due to brake temperature influence on brake torque vs. brake pressure characteristics), variations of rise rate will also lead to variations of wheel deceleration.

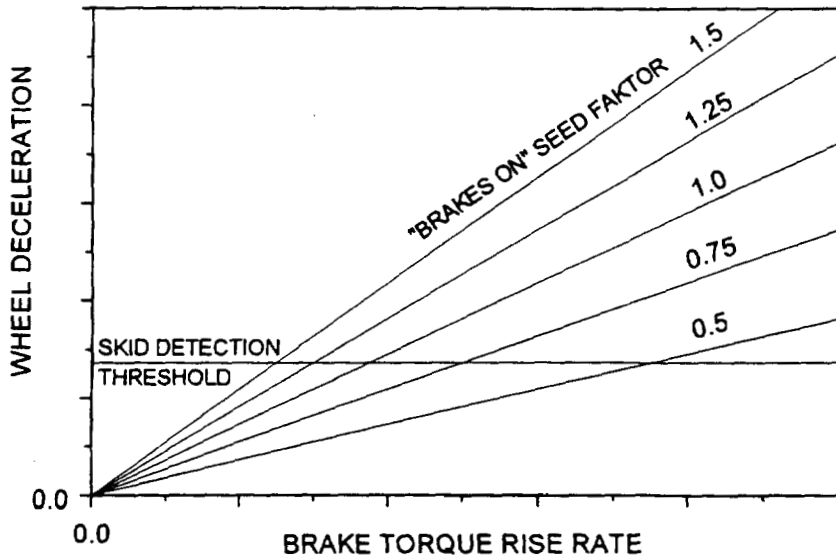


Fig. 6 Design Chart for Brake Torque Rise Rate

Assumptions taken for Fig. 6 are therefore on the optimistic side. It is advisable to apply more realistic assumptions (especially on wheel torque vs. slip ratio) in developing brake and anti-skid control system algorithms and parameters.

Nevertheless, the simplified approach which was taken here yields sufficient insight into the oscillation problem observed during dynamometer tests of rapid brake application at high aircraft speed.

2.4 RECOMMENDATIONS AND CONCLUSIONS

In the case treated here, both brake pressure and brake torque rise at enormous rates. Brake torque rise rate alone would have been sufficient to trigger anti-skid action. In addition, presumably due to slight time delays in the system, brake torque is allowed to overshoot maximum wheel torque achievable. Although in the next cycle the brake torque ceiling is lowered it is still too high due to the excessive overshoot in the previous cycle. In cycles following it is hard to decide whether sharp rises of brake torque or brake torque over stressing wheel torque capacity lead to further anti-skid actions.

In any case, a substantial reduction of brake pressure and brake torque rise rates during initial brake application would be beneficial in two ways: First, undue anti-skid action could be reliably avoided thereby. Second, eventual brake torque overshoot could be drastically reduced with the effect that brake pressure ceiling could adapt to wheel torque capacity within a single step and with significantly less pressure amplitude. In summary, reduced brake torque rise rate is suited to overcome the brake torque / brake force oscillation treated here.

From all insight gained into the problem there is no solution to be expected from any kind of bolt-on structural damping device.

2.5 POINTS OF IMPROVEMENT IN THE BRAKE SYSTEM

The brake torque oscillations observed in dynamometer tests at extreme "brakes on" speed and at extreme step input to the system can be avoided through improvement by design as well as through improvement by operation.

Improvement by operation means that pilots are instructed to initiate brakes such that brake torque rise rate is kept below critical values. Improvement by operation is viable as long as an average pilot is not overcharged by the operation required. At best, oscillations should not occur if the pilot just avoids "jumping" onto brake pedals.

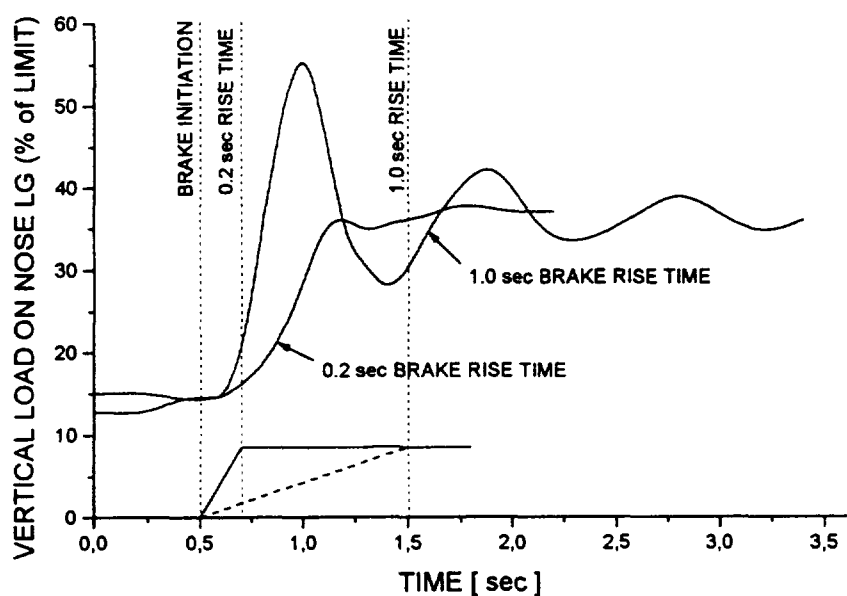


Fig. 7 Nose Landing Gear Histograms from Dynamic Braking Analyses

Nevertheless there are aspects of the problem rendering improvement by design a desirable alternative.

- Experience shows that aircraft get heavier in course of time. As a consequence maximum "brakes on" speed shows tendencies to increase, too. If safety margins against oscillations shall be kept constant then brake torque rise rate and/or skid detection threshold must be changed. If brake torque rise rate is a hardware constant then the necessary lifting of skid detection threshold will lead to reduction of skid detection quality. In turn, reduced skid detection quality reduces anti-skid system efficiency throughout all braked ground roll. Ground roll distance lost at soft yet non-oscillatory brake initiation is only a fraction of that which can be gained by improvement of brake efficiency by correspondingly lower skid detection threshold.
- Quickest possible brake reaction at braking onset appears desirable with regard to flight performance. However, nose diving provoked by abrupt braking will eventually produce critical loads and/or reduce aircraft capability to cope with rough ground (e.g. aircraft operation on bomb damaged and provisionally repaired runways) [Ref.1]. If brake torque rise rate is reliably controlled by brake system control then this can be advantageously used in structural design (Fig. 7).

Adjustable control of brake torque rise rate is considered a sensible means not only to avoid oscillatory anti-skid action at brake initiation but also to improve aircraft ground handling and performance.

4. REFERENCES

- [1] Krauss, A. J.
Considerations on Optimality of Landing Gear Arrangement and Design.
Paper #8 from AGARD Conference Proceedings 484: Landing Gear Design Loads
- [2] Brewer, H. K.
Parameters Affecting Aircraft Tire Control Forces.
AIAA Paper No. 74-966
- [3] Luber W., Kempf G., Krauss A.
Self-Induced Oscillations of Landing Gear as an Integral Landing Gear Aircraft System Problem
AGARD SMP Conference Banff, Canada, 1995

APPENDIX

Consider a wheel equipped with a pneumatic tyre. The wheel axle shall be connected to a straight guiderail by a linear spring/damper element. This guiderail shall be moved across the ground at constant speed; further on the guiderail shall be inclined against the ground.

Motion of the wheel axle relative to the guiderail is influenced by radial tyre force (also represented by a linear spring/damper element) and by circumferential tyre force. Modelling of circumferential force depends on assumptions made.

A1. "Cog-Wheel" Assumption

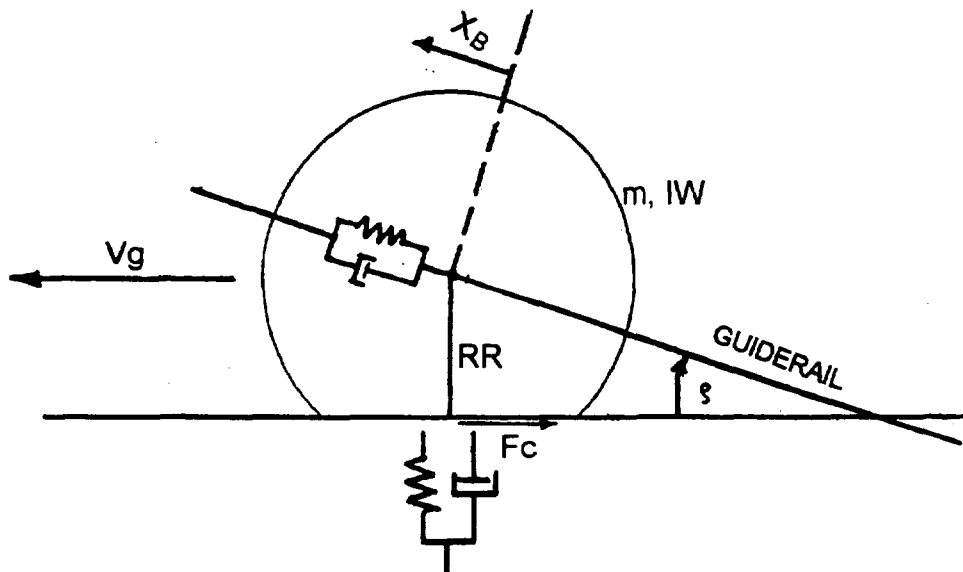
The wheel is assumed to rotate at that angular velocity which is defined by the ratio of ground speed to deflected tyre radius. Circumferential force is then defined by rotational acceleration of the wheel enforced by tyre radius variations. Since this radius depends only on the co-ordinate of the wheel axle relative to the guiderail, the equation of motion reflecting the "Cog-Wheel" assumption has one degree of freedom, viz the linear displacement of the wheel axle on the guiderail.

With regard to potential self-induced oscillations of this system it is interesting to study the various damping terms in that equation of motion.

With

DC Damping coefficient of the guiderail spring
 DT Damping coefficient of tyre radial spring
 IW Wheel moment of inertia
 VG Ground speed

XB Axe displacement relative to guiderail
 RR Distance axle to ground
 ρ Inclination of guiderail (positive front end up)



the complete damping term reads

$$D = DC + DT \cdot \sin^2 \rho - \frac{IW \cdot \sin \rho \cdot \cos \rho \cdot (VG + XB \cdot \cos \rho)}{(RR + XB \cdot \sin \rho)^3}$$

The damping term resulting from the "Cog-Wheel" assumption is negative (destabilizing). Since it increases approximately proportional to ground speed, the equation indicates that there might exist a critical ground speed at which overall damping becomes negative.

This critical speed can be increased by a "hardware" modification to the model by reducing inclination of the guiderail. In reality this would mean a reduction of landing gear leg forward rake.

Improvement can also be achieved by a quasi "software" modification, i.e. by pumping up the tyre to increase RR.

A2. The "Slip Ratio" Assumption

As already discussed in present paper, circumferential force on an almost freely rolling tyre is approximately proportional to slip ratio SR.

If this assumption is introduced to the model then linear displacement of the wheel axle and rotation of the wheel are two separate degrees of freedom which are coupled by the circumferential force.

This system is not as readily analyzed as the "Cog-Wheel" system. However, from the main part of this paper it is concluded, that one and the same axle linear velocity relative to the guiderail will effect different slip ratio rates, slip ratio rates becoming smaller with increasing ground speed. That means that the ratio of circumferential force oscillation amplitude to axle displacement amplitude reduces with increasing ground speed.

Apart from any phase shift effects it is therefore expected that an eventual destabilizing effect of tyre circumferential force on axle fore/aft motion will cease with speed.

A3 Conclusion

Comparison of the "Cog-Wheel" model and the "Slip Ratio" model perception lead to the conclusion that sustained fore/aft bending oscillations may well occur under unfavourable landing gear design parameters. However, this type of self-induced oscillation should be limited to the low to medium aircraft speed range.

In a realistic analysis of the phenomenon, care should be taken that all important effects are included in the model. For instance, effective "guiderail" inclination can be influenced by fuselage bending and / or by stroking motion of the oleo strut.

Nonlinear Transient Whirl Vibration Analysis of Aircraft Brake Systems

Craig F. Chang

520-37

Aircraft Landing Systems, AlliedSignal

South Bend, IN

Abstract

The objective of this paper is to present a nonlinear transient analysis method for understanding and solving aircraft brake whirl vibration problems. Mathematical modeling and derivations of the brake mechanism, which include the hydraulic interaction between the brake and the fluid, will be discussed. The factors that influence whirl will be presented. Potential methods for resolving whirl vibration will also be discussed.

1.0 Introduction

When designing an aircraft brake, such as the one shown in Figure 1, whirl vibration is one of the many design criteria that is to be minimized by brake dynamists. Whirl vibration of aircraft brakes can be characterized as the brake stack (rotors and stators) having a whirl axis around the aircraft axle, whirling with respect to the piston housing. This vibration phenomenon can be detected by measuring piston pressure oscillations, which will have phase angles proportional to the circumferential spacing of the respective pistons. Whirl vibration, if not controlled, is undesirable and may be destructive.

Previous studies investigating brake induced vibration, such as whirl, were either linear in nature [1], or the hydraulic system was not included [2,3]. However, laboratory tests have shown that changes in the hydraulic system, such as the addition of orifices between brake pistons, significantly reduce vibration. If the mathematical models excluded the fluid

phenomena, it was not possible to obtain accurate, meaningful conclusions. On the other hand, it would be very costly and time consuming to optimize brake vibration stability simply by repeated laboratory experiments. Thus, it is desirable to develop an analytical model to simulate the basic phenomenon of whirl for both whirl problem resolution and for proactively optimizing brakes for whirl prevention. This paper will focus on the interaction between the brake frame and the hydraulic fluid in the development of a whirl model. Factors that influence whirl vibration will be investigated.

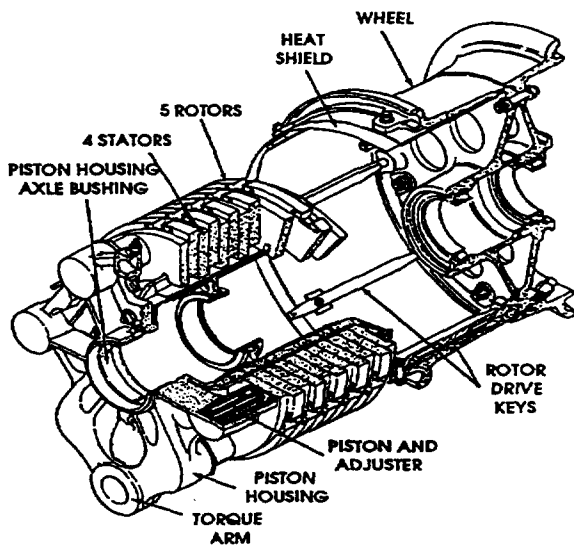


Figure 1: A typical aircraft brake assembly

2.0 Finite Element Model

Aircraft landing and braking systems of recent design have become more geometrically

complex. In order to understand braking system vibration and to provide optimized braking system designs, AlliedSignal Aircraft Landing Systems (ALS) has developed the ability to mathematically model all components and interfaces of the complete wheel and brake system. This includes the backup structure (such as the landing gear or the dynamometer). A 3-D finite element approach is used. Two typical models are shown in Figure 2a and 2b.

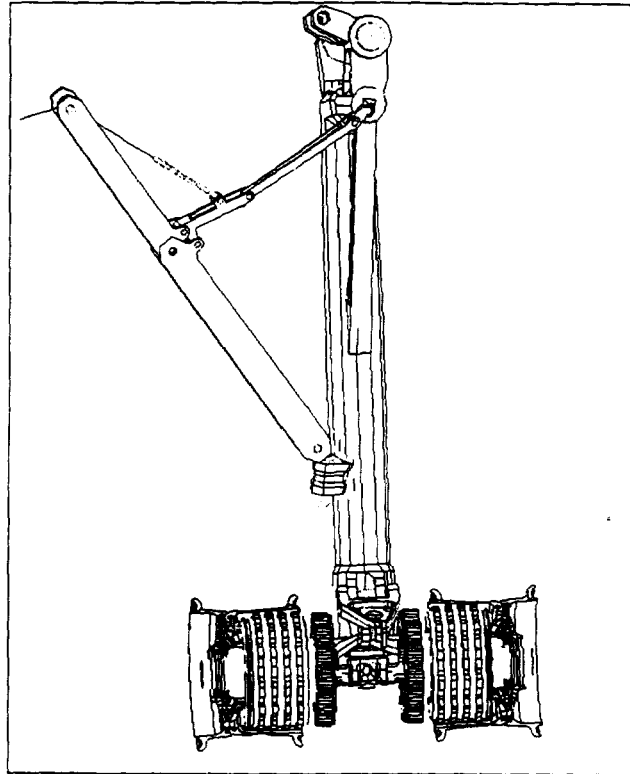


Figure 2a: A typical FE model of brakes and wheels on an aircraft.

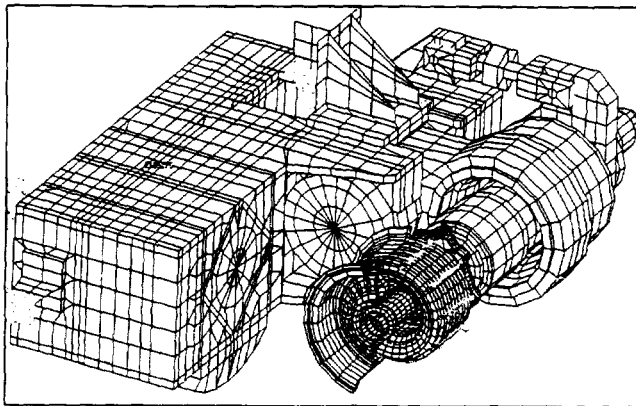


Figure 2b: A typical FE model of a brake and wheel mounted on a dynamometer.

The backup structures must be included in the model because they are dynamically coupled with the brakes and wheels.

The differential equation that governs a system as shown in Figure 2, excluding the non-linear fluid portion, can be written as:

$$[m]\ddot{x} + [c(x, \dot{x})]\dot{x} + [k]x = \{f\} \quad (1)$$

where $[m]$, $[c(x, \dot{x})]$, and $[k]$ are the system mass, damping, and stiffness matrices, respectively, and $\{x\}$, $\{\dot{x}\}$, and $\{\ddot{x}\}$ are the system displacement, velocity, and acceleration response vectors, respectively. Note that the damping matrix is non-linear to account for the presence of joint dry friction.

Due to the friction force, the formulation of the stiffness matrix $[k]$ is slightly different from the conventional method and will be discussed in the next section. The non-linear representations of the hydraulic fluid inside the pistons, which are not part of Equation (1), will be discussed in the section pertaining to orifices.

3.0 Stiffness Matrix Formulation

The root cause of whirl vibration is the non-conservative friction force. To illustrate, consider two contacting points, one on the rotor and one on the stator. The respective friction forces due to axially applied braking load are

$$\begin{aligned} f_{st} &= \mu k(x_n - x_{st}) \\ f_r &= -\mu k(x_n - x_{st}) \end{aligned} \quad (2)$$

where f_{st} and f_r are the friction forces acting at the stator and the rotor, respectively, due to axial applied braking load $k(x_n - x_{st})$. k is the contact stiffness between the friction surfaces, and μ is the friction coefficient, or brake

effectiveness. The matrix form of Equation (2) is

$$\{f_\mu\} = [k_\mu]\{x_\mu\} \quad (3)$$

where

$$\begin{aligned}\{f_\mu\} &= \begin{Bmatrix} f_{st} \\ f_n \end{Bmatrix}; \{x_\mu\} = \begin{Bmatrix} x_{st} \\ x_n \end{Bmatrix}; \\ [k_\mu] &= \begin{bmatrix} -\mu k & \mu k \\ \mu k & -\mu k \end{bmatrix}.\end{aligned}$$

Note that $[k_\mu]$ matrix will become unsymmetrical when it is placed into global stiffness matrix since vector $\{x\}$ is in normal DOF and vector $\{f_\mu\}$ is in tangential DOF.

To account for the braking friction effect, the above derived friction forces must be added to the linear global stiffness matrix. To do this, we define the linear global stiffness matrix $[k_g]$ as

$$\{f_g\} = [k_g]\{x\} \quad (4)$$

where $\{f_g\}$ and $\{x\}$ are global load and response vectors, respectively. Merging of Equations (3) and (4) yields

$$\{f\} = [k]\{x\}$$

where $\{f\} = \{f_g + f_\mu\}$ and $[k] = [k_g + k_\mu]$. Note that the stiffness matrix $[k]$ is the combined stiffness matrix from the linear portion, $[k_g]$, and the friction portion, $[k_\mu]$. Also note that $[k]$ is not symmetric due to the presence of $[k_\mu]$. The above stiffness matrix represents the stiffness term in Equation (1).

Due to the un-symmetrical nature of the stiffness matrix, the system governed by Equation (1) could become unstable. The dynamic instability caused by the presence of braking friction is called ***whirl vibration*** in brake dynamics

terminology. As can be seen, whirl instability is a function of (a) the friction coefficient (or brake effectiveness) μ ; (b) the contact stiffness $[k_\mu]$; (c) the brake frame stiffness, which influences $[k_g]$, $\{x_n\}$, $\{x_{st}\}$; and (d) the mass of the heat sink which influences the mass matrix and inertia.

4.0 Degree-of-Freedom Reduction

The governing differential equation, Equation (1), is usually large. Therefore, it is very time consuming to solve this equation when it is combined with the governing fluid equations. As previously noted from laboratory test data, the system governed by Equation (1) possesses unique modes of vibration. Thus, it is justifiable to reduce the size of Equation (1) by transforming it into generalized coordinates using normal modes. Thus, let $[\phi]$ be denoted as the generalized coordinates that uncouple the linear portion of the mass and stiffness matrix and that also satisfy

$$\phi^T m \phi = I, \quad \phi^T k_g \phi = \lambda, \quad x = \phi q,$$

where $[\lambda]$ is the system eigenvalue matrix, and $\{q\}$ is the participation vector. Equation (1) can then be transformed into

$$\{\ddot{q}\} + [c_q]\{\dot{q}\} + [k_q(\mu)]\{q\} = \{F_q\} \quad (5)$$

$$\text{where } c_q = \phi^T c(x, \dot{x}) \phi, \quad k_q(\mu) = \phi^T (k_g + k_\mu) \phi, \\ F_q = \phi^T f.$$

Note that c_q and k_q are not diagonal in general.

5.0 Fluid - Brake Frame Interaction

Whirl vibration is the rotors and stators whirling with respect to the piston housing with an axis of whirl motion about the axle. As a consequence of this motion, the piston hydraulic fluid is “pumped” by the phased axial motion of the pistons. This pumping will generate pressure

fluctuations, which, in turn, will force the brake frame. This is illustrated by the schematic pictures in Figures 3 and 4. Figure 3 shows the piston stroke. Figure 4 shows the piston fluid flow between adjacent pistons.

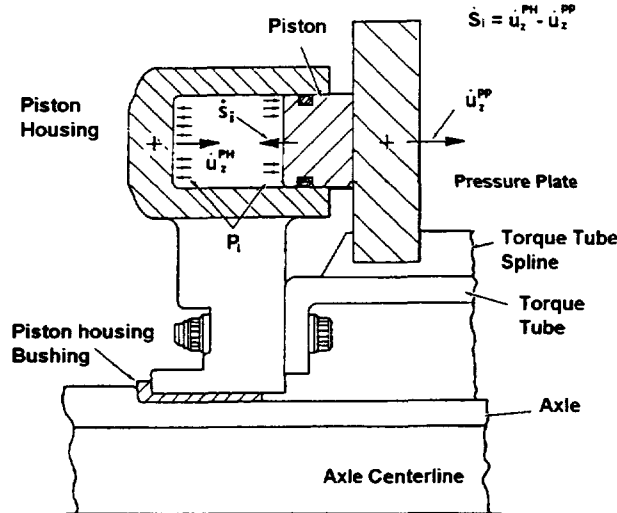


Figure 3: Piston stroke caused by whirl motion

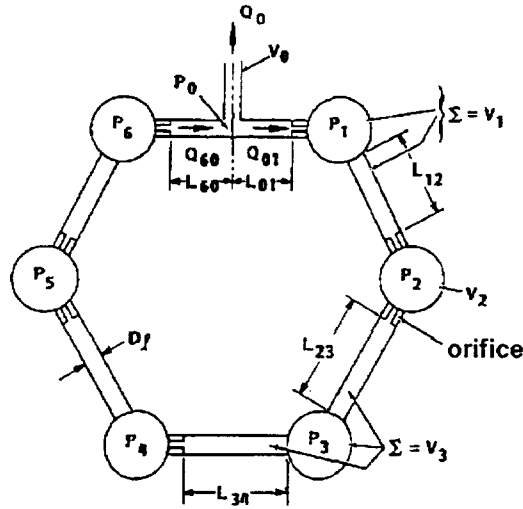


Figure 4: Piston housing fluid diagram.

The stroke of the piston, defined as the relative velocity of the pressure plate with respect to the piston housing, as shown in Figure 3, will cause “pumping” of the fluid because of the brake whirl vibration. The fluid will move from piston to piston. For this reason, orifices can be

introduced to damp the fluid motion and, in turn, damp the whirl vibration. This makes orifices an effective and efficient means of stabilizing whirl vibration.

The goal of the subject analysis is optimization of orifice sizes and locations. Two orifice related equations are introduced. One is the pressure drop between adjacent pistons. The other is the continuity constraint equation.

5.1 Pressure Drop

The pressure drop, $\Delta\dot{P}_{ij}$, between adjacent pistons due to an orifice is [4]

$$\Delta\dot{P}_{ij} = \dot{P}_i - \dot{P}_j = M_{ij}\ddot{Q}_{ij} + B_{ij}\dot{Q}_{ij} \quad (6)$$

where

$$M_{ij} = \rho \frac{L_{ij}}{A}$$

$$B_{ij} = \frac{\rho}{(C_D A_{ij})^2} |Q_{ij}| + 1.75 C_v \frac{\rho}{2} \left(\frac{v}{D} \right)^{0.25} \frac{L_{ij}}{A^{1.75}} |Q_{ij}|^{0.75}$$

L_{ij} = line length between piston i and piston j ;

A = cross-section area of passageways;

ρ = fluid density;

C_D = orifice discharge coefficient;

A_{ij} = orifice size between piston i and piston j ;

C_v = line loss coefficient;

D = diameter of passageway;

v = fluid kinematics viscosity (in²/sec);

Q_{ij} = fluid flow rate from piston i to piston j .

Note that

$$Q_{ij} = -Q_{ji} .$$

Equation (6) introduces a $2N$ -set of unknowns, however, there are only N equations. Thus, additional constraints must be sought. They are discussed in the next section.

5.2 Continuity Constraint

Continuity constraint requires the net fluid change due to (a) piston stroke, (b) fluid

compressibility, and (c) fluid discharge between adjacent pistons be zero:

$$\frac{\dot{P}_i \cdot V_i}{B} - A_p \dot{S}_i + Q_{ij} - Q_{ki} = 0 \quad (7)$$

where

\dot{S}_i = stroke velocity at piston i .

A_p = area of piston;

V_i = fluid volume, i -th piston;

\dot{P}_i = pressure oscillation, i -th piston;

B = fluid bulk modulus.

Solving for \dot{P}_i :

$$\dot{P}_i = \frac{B}{V_i} (A_p \dot{S}_i - Q_{ij} + Q_{ki}) \quad (8)$$

5.3 Fluid Differential Equations

The fluid differential equations may be obtained by substituting Equation (8) into Equation (6):

$$\begin{aligned} M_{ij} \ddot{Q}_{ij} + B_{ij} \dot{Q}_{ij} + \left(\frac{B}{V_i} + \frac{B}{V_j} \right) Q_{ij} \\ - \frac{B}{V_i} Q_{ki} - \frac{B}{V_j} Q_{ji} = \frac{B}{V_i} A_p \dot{S}_i - \frac{B}{V_j} A_p \dot{S}_j \end{aligned} \quad (9)$$

The matrix form is

$$[M_Q] \{ \ddot{Q} \} + [B_Q] (Q, \dot{Q}) \{ \dot{Q} \} + [K_Q] \{ Q \} = \{ \dot{S} \} \quad (10)$$

where

$$\{ Q \} = \begin{bmatrix} Q_{0,1} \\ \vdots \\ Q_{n,0} \end{bmatrix}, \quad [M_Q] = \begin{bmatrix} M_{0,1} & & & & 0 \\ & \ddots & & & \\ 0 & & M_{n,0} & & \end{bmatrix}$$

$$\{ \dot{S} \} = \begin{bmatrix} \frac{B}{V_0} A_p \dot{S}_0 - \frac{B}{V_1} A_p \dot{S}_1 \\ \vdots \\ \frac{B}{V_n} A_p \dot{S}_n - \frac{B}{V_0} A_p \dot{S}_0 \end{bmatrix},$$

$$[B_Q] = \begin{bmatrix} B_{0,1} & & & & 0 \\ & \ddots & & & \\ 0 & & B_{n,0} & & \end{bmatrix}$$

Equation (9) is the second order non-linear differential equation that governs the fluid responses.

6.0 Structural and Fluid Combination

Since the fluid interacts with the brake frame, the differential equations that govern the fluid and the brake frame must be combined and solved simultaneously. We thus introduce the state space vectors $\{Y\}$ as

$$\{Y\} = [Y_1, Y_2, Y_3, Y_4, Y_5]^T$$

where

$$Y_1 = q, \quad Y_2 = \dot{q}, \quad Y_3 = \dot{Q}, \quad Y_4 = Q, \quad Y_5 = P.$$

The total equation of motion, when combining fluid and structure, then becomes

$$\begin{bmatrix} \dot{Y}_1 \\ \dot{Y}_2 \\ \dot{Y}_3 \\ \dot{Y}_4 \\ \dot{Y}_5 \end{bmatrix} = \begin{bmatrix} Y_2 \\ (F_q - k_q Y_1 - c_q Y_2) \\ (\dot{S} - B_Q Y_3 - K_Q Y_4) \frac{1}{M_Q} \\ Y_3 \\ \frac{B}{V} (A_p \dot{S} - Q_i + Q_j) \end{bmatrix} \quad (11)$$

which is a first order nonlinear differential equation. Note, in Equation (11) $\{q\}$ is governed

by the brake frame structure, $\{Q\}$ is governed by the fluid, and they are coupled by $\{\dot{S}\}$.

The optimized orifices should minimize the work done by the fluid flow. The work done by the fluid flow between piston i and piston j is calculated using

$$E_{fu} = \frac{\Delta P}{\rho} (\rho V)$$

$$= \frac{\rho}{2(C_D A_{ij})^2} |Q_{ij}|^2 V.$$

When considering all pistons, it becomes:

$$E_{fu} = \sum \frac{\rho}{2(C_D A_{ij})^2} |Q_{ij}|^2 V \quad (12)$$

which has lb-in units.

7.0 Correlation with Test Data

In this section, the analytical model for a specific brake frame having six pistons and mounted on a dynamometer was solved numerically using Equation (11). Different orifice sizes were evaluated. The results are compared with the test data to verify and correlate the analytical model.

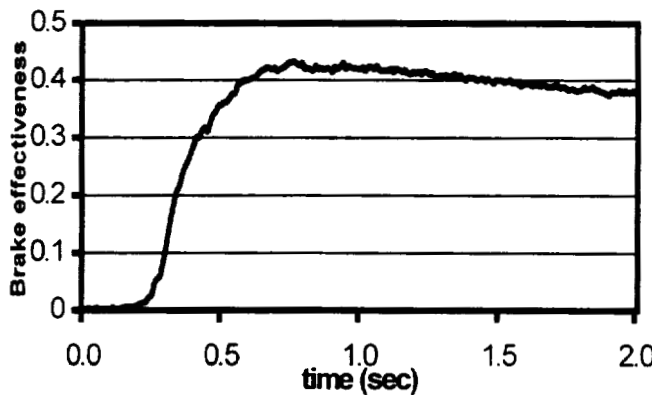


Figure 5: Brake effectiveness

The brake effectiveness shown in Figure 5 was chosen as the model input because the analytical model does not predict brake effectiveness, so it must be provided for the numerical solution.

For the first investigation, each orifice had a 0.110 inch diameter. The piston housing (PH) acceleration in the brake frame axial direction and the piston pressure were calculated using Equation (11). They are shown in Figure 6. The model whirl frequency was 238 Hz. compared to the test frequency of 225-235 Hz. The model acceleration level was about 120 g's (axial) with a pressure oscillation of about 250 psi. The test acceleration level was 100 g's. The Fourier Transform (FT) uses sample time of 0.25 seconds with 50% overlapping.

A second set of orifices having diameters of 0.070 inches was analyzed. The resulting accelerations and pressure oscillations are shown in Figure 7.

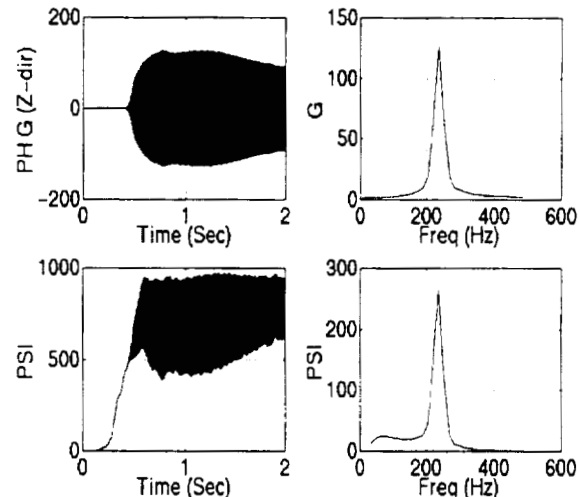


Figure 6: Acceleration and pressure responses
Orifices: 0.110 inches

A third set of orifices that had 0.070 inch diameters, except for one that was blocked, was analyzed. The resulting accelerations and pressure oscillations are shown in Figure 8.

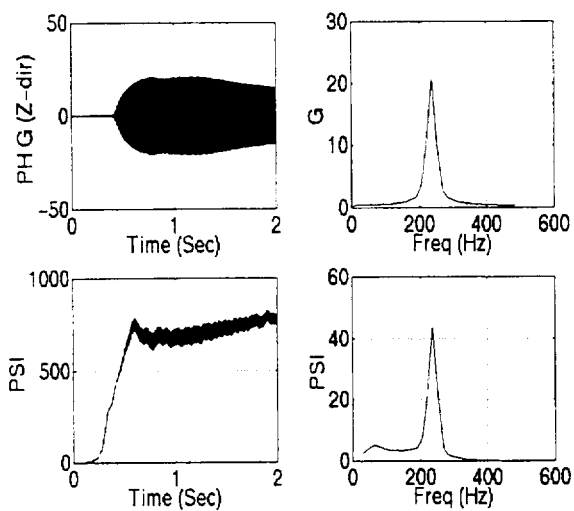


Figure 7: Acceleration and pressure responses
Orifices: 0.070 inches

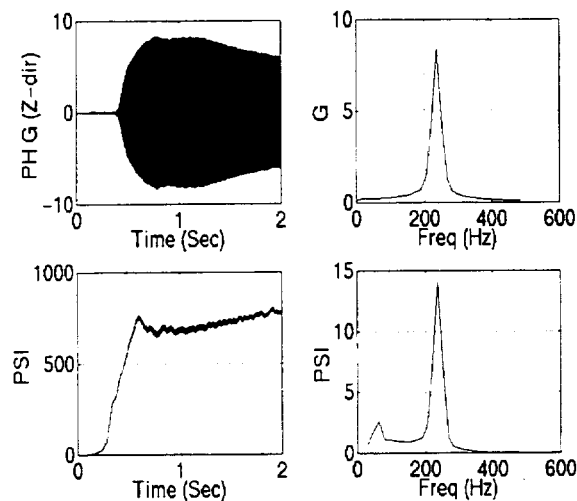


Figure 8: Acceleration and pressure responses
Orifices: 0.070 inches with one block

Comparison of Figures 6 and 7 shows that reducing the orifice size reduced the vibration level.

Comparison of Figures 7 and 8 shows that blocking one orifice reduced the vibration level.

A fourth set of orifices having 0.0375 inch diameters and a fifth set of variable diameter orifices were analyzed to complete a performance trend versus orifice size and

configuration comparison. First, the work by fluid were calculated for each of the cases using Equation (12). The results are shown in Figure 9. The piston housing calculated acceleration levels are shown in Figure 10 along with the correlation test data.

The trend shown in Figure 9 is that the work by fluid decreases as the size of the orifice size decreases. This implies the pressure oscillation will decrease as the orifice size decreases. Also, a blocked orifice performs better than a series of uniform orifices.

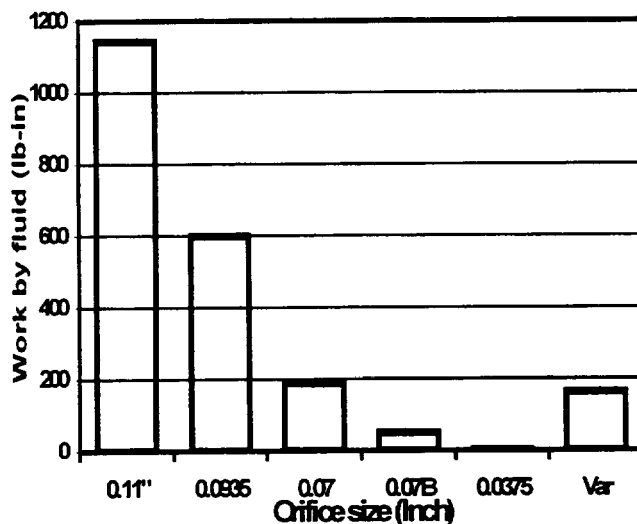


Figure 9: Work done by fluid

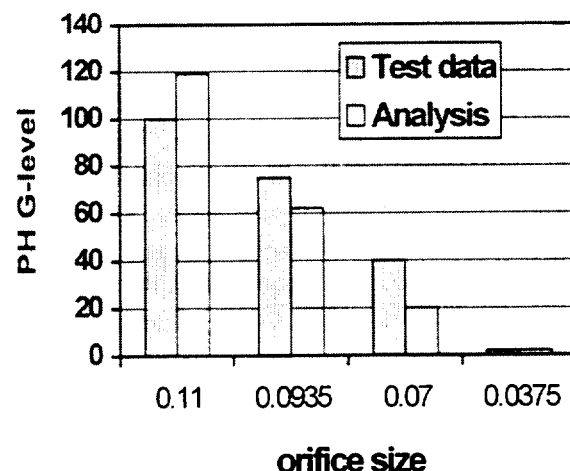


Figure 10: Piston housing acceleration levels – Correlation of analysis with test.

Comparing Figures 9 and 10, the work done by pressure drop has the same trend as that of the piston housing acceleration.

Figure 10 exhibits good correlation between the calculated and the test data accelerations for orifice size variation. The calculated acceleration amplitudes vary by 20% from the measured acceleration levels, which is of the same order of magnitude of variation expected within test data. Therefore, the analytical methods and models developed in this paper may be used to optimize orifices with good confidence.

8.0 Conclusions

The following conclusions were drawn from these studies.

8.1 Blocked Orifice

The fluid equations exhibit an incompressible mode, i.e., any fluid disturbance will cause a constant flow (which will eventually decay). The blocked orifice removes this mode by setting the fluid degree of freedom to zero ($Q=0$) at the blocked orifice. The physical system also becomes more stable when a blocked orifice is introduced.

Secondly, the blocked orifice effectively stiffens the fluid, which, in turn, reduces piston axial compliance and heat sink motion. Numerical analyses using just the linear portion of the model show that as the piston axial stiffness increases, the whirl stability also increases. Other evidence is entrained air in the fluid will lower the piston axial stiffness resulting in a less stable brake.

Lastly, the blocked orifice will reduce the total degrees of freedoms in Equation (12) since the summation index is reduced by one. Therefore, it will certainly make E_{fu} lesser.

In conclusion, a blocked orifice in the brake hydraulic system will increase brake whirl dynamic stability. The location of the blocked orifice should not inhibit brake bleeding.

8.2 Orifice Size

Orifice size can be selected using the developed analytical model, which will significantly reduce orifice optimization testing. Because each brake frame has its unique set of global stiffnesses, each brake frame may have a unique set of optimized orifices.

Variable size orifices provide another option when optimizing the brake frame for whirl vibration minimization. Using the techniques developed in this paper also makes this task easier.

8.3 Hydraulic Resonance

As with any structure, the fluid system also has its own resonance. If the fluid system resonant frequency coincides with the brake whirl frequency, orifice damping will be less effective. Key factors that affect hydraulic resonance are: (a) fluid bulk modulus, (b) fluid density, (c) fluid volume, and (d) number of pistons.

8.4 Number of Pistons

The number of brake pistons is usually based on the required performance of the brake, rather than a consideration for whirl vibration. However, the total number of pistons does have an influence on whirl vibration.

8.5 Brake Frame Geometry

The brake frame design will impact the whirl stability in many aspects. For instance, the torque tube backing plate affects whirl stability. The stiffer the backing plate in the axial direction, the better the whirl stability. Thus, a

stiffer torque tube backing plate design is usually viewed as positive when dealing with whirl vibration.

8.6 Stator Inserts

Stator inserts provide more Coulomb damping than direct carbon contact with the torque tube splines during whirl motion. An additional benefit of stator inserts is that they reduce stator slot wear.

Coulomb damping is very amplitude dependent. Its effectiveness is inversely proportional to the vibration amplitude. On the other hand, orifice damping is proportional to the vibration amplitude. Thus, Coulomb damping and orifice damping complement each other during whirl vibration.

References

- Chang, C. F., "The Dynamic Finite Element Modeling of Aircraft Landing System," 1995 Design Engineering Technical Conferences, DE-Vol. 84-1, Vol. 3, Part A, pp. 1217-1227, ASME 1995.
- Travis, M. H., "Nonlinear Transient Analysis of Aircraft Landing Gear Brake Whirl and Squeal," 1995 Design Engineering Technical Conferences, DE-Vol. 84-1, Vol. 3, Part A, pp. 1209-1216, ASME 1995.
- Feld, D. J., "Complex Eigenvalue Analysis Applied to an Aircraft Brake Vibration Problem," 1995 Design Engineering Technical Conferences, DE-Vol. 84-1, Vol. 3, Part A, pp. 1135-1142, ASME 1995.
- Streeter, V. L., Fluid Mechanics. McGraw-Hill, NY, NY, 1974.

Nomenclature

A	passageway cross-section area
A_p	piston area
B	fluid bulk modulus
$[B_Q]$	damping matrix of fluid equations
$[c]$	damping matrix
$[c_q]$	damping matrix, generalized coordinates
C_v	line loss coefficient
C_D	orifice discharge coefficient
E_{fu}	work done by fluid (lb inch)
$\{f\}$	force vector
f_{st}	force acting on stator
f_r	force acting on rotor
$\{F_q\}$	force vector, generalized coordinates
$[k]$	stiffness matrix
$[k_q]$	stiffness matrix, generalized coordinates
$[K_Q]$	stiffness matrix of fluid
$[k_g]$	linear portion of the global stiffness
$[k_\mu]$	stiffness matrix incurred by braking
L_{ij}	line length between piston i and j .
$[m]$	mass matrix of the brake frame
$[M_Q]$	mass matrix of the fluid
P	pressure
q	modal displacement of brake frame
Q	fluid flow rate
\dot{S}	piston stroke
V_i	fluid volume of i -th piston
$\{x\}, \{\dot{x}\}, \{\ddot{x}\}$	displacement, velocity, and acceleration response vectors.
$\{Y\}$	state space vector
ρ	fluid mass density
ν	fluid kinematic viscosity
$[\phi]$	generalized coordinates
μ	brake effectiveness
$[\lambda]$	system eigenvalue matrix

An unsteady aerodynamics identification procedure for flutter prediction.

521-08

S. Prudhomme¹, C. Blondeau², M. Humbert³, A. Bucharles¹

¹ ONERA-CERT, Flight Dynamics and Systems Control Dept, 2 av. E. Belin, 31055 Toulouse, France

² ONERA, Structural Dynamics and Coupled Systems Dept, 29 av. de la Div. Leclerc, 92322 Chatillon, France

³ AEROSPATIALE, 316 route de Bayonne, 31060 Toulouse, France

Abstract

This article introduces an identification procedure from flight-data, in the perspective of quasi real time flutter prediction models upgrading. Parameters are introduced to model uncertainties on the unsteady aerodynamics. While tests are performed for increasing velocity, identification algorithms use flight data to update the parameters and make flutter prediction more accurate for investigation towards higher velocity. Performance of identification is evaluated in terms of accuracy for unsteady aerodynamics estimation, and of flutter prediction capability, with and without turbulence.

1 Introduction

Motivation

Flight flutter tests must be conducted with much caution, in order to avoid entering unpredicted flutter for some flight conditions. The suggested strategy is to monitor flight flutter investigation, using both flutter prediction models and a convenient identification procedure.

Such an identification procedure may be difficult. It needs a suitable parameterization of the prediction models and fast algorithms. Turbulence may also significantly disturb flight tests measurements and corrupt flutter evaluation.

Overview

It is assumed that the structural dynamics is well known (i.e. previously identified during ground tests), and that most remaining uncertainties on the prediction model are due to the unsteady aerodynamics. Identification consists in updating some parameters which are introduced in the unsteady aerodynamics tensor. The procedure is developed in the article, including :

- a brief description of the prediction model with introduction of design parameters;
- the derivation of conditions for parameters *identifiability*;
- a presentation of algorithms for the search of an *optimal set* of parameters to fit flight data;
- practical considerations for the selection of flight test conditions;
- a preliminary validation of the identification procedure using simulated data;
- an interpretation of the results in term of unsteady aerodynamics and accuracy for flutter prediction.

2 Flutter prediction model

Basic model

The flutter prediction equation is obtained for the longitudinal motion of a conceptual transport aircraft, using both computations of the structural

dynamics model in the generalized coordinates basis and the generalized unsteady aerodynamics tensor. This yields:

$$\begin{aligned} \mu\ddot{q} + \beta\dot{q} + \gamma q &= F_a + F_\delta + F_w \\ y &= \Phi_s \ddot{q} \end{aligned} \quad (1)$$

where

- $F_a(q, V, k, \theta)$ are the generalized (potentially non-linear) unsteady aerodynamics forces, with θ a suitable low dimensional vector of design parameters;
- $F_\delta(V, k)$ are the forces due to the actuators δ , assumed to be constant versus k as a first order approximation $F_\delta(V, k) = \bar{q}A_{0\delta}(V)\delta$;
- $F_w(V, k)$ are the forces due to turbulence w , assumed to be constant versus k as a first order approximation $F_w(V, k) = \bar{q}A_{0w}(V)w$;
- y is a vector of measured accelerations on the structure, and Φ_s , the modal projection on the measured outputs;
- $k = \omega/V$ the normalized frequency and \bar{q} the dynamical pressure.

Unsteady aerodynamics design parameters

The main contribution to generalized forces is the contribution of the wing. It is parameterized as a linear function of complex design parameters vector θ :

$$F_a(q, V, k, \theta) = \bar{q}\Gamma\Theta G^T(k)q$$

where $\Gamma, G(k)$ are known matrices and $\Theta = \text{diag}(\theta)$. For the nominal case (basic prediction model),

$$\theta = \bar{\theta}, \bar{F}_a = F_a(q, V, k, \bar{\theta})$$

For the actual aircraft,

$$F_a = F_a(q, V, k, \theta)$$

where θ will be identified.

Other contributions to generalized forces are assumed to be known and constant.

The generalized forces are then linearized and developed at first order in the frequency domain [6]:

$$F_a(q, V, p, \theta) = \bar{q}(A_0(\theta) + \frac{p}{V}A_1(\theta))q \quad (2)$$

where A_0 et A_1 are computed for convenient fitting of F_a at given reduced frequencies k_1, k_2 in the bandwidth concerned by flutter. In the nominal case :

$$\begin{aligned} \bar{A}_0 &= \Gamma\Re(\bar{\Theta}G_0^T) \\ \bar{A}_1 &= \Gamma\Im(\bar{\Theta}G_*^T) \end{aligned} \quad (3)$$

and for the actual aircraft:

$$\begin{aligned} A_0(\theta) &= \Gamma\Re(\Theta G_0^T) \\ A_1(\theta) &= \Gamma\Im(\Theta G_*^T) \end{aligned}$$

with

$$\begin{aligned} G_0 &= \frac{G(k_1) + G(k_2)}{2} \\ G_* &= \frac{k_1 G(k_1) + k_2 G(k_2)}{k_1^2 + k_2^2} \end{aligned}$$

Full state space representation

With the previously described parameterization, flutter prediction equation (1) yields:

$$\begin{bmatrix} \dot{q} \\ \mu\ddot{q} \end{bmatrix} = \begin{bmatrix} 0 & I \\ \bar{q}A_0 - \gamma & \frac{\bar{q}}{V}A_1 - \beta \end{bmatrix} \begin{bmatrix} q \\ \dot{q} \end{bmatrix} + \dots + \begin{bmatrix} 0 & 0 \\ \bar{q}A_{0\delta} & \bar{q}A_{0w} \end{bmatrix} \begin{bmatrix} \delta \\ w \end{bmatrix}$$

$$y = \Phi_s \ddot{q}$$

Including the actuators dynamics $A_a, B_a, C_a, D_a = 0$ leads to the following state space representation:

$$\begin{bmatrix} \dot{x}_a \\ q \\ \mu\ddot{q} \end{bmatrix} = \begin{bmatrix} A_a & 0 & 0 \\ 0 & 0 & I \\ \bar{q}A_{0\delta}C_a & \bar{q}A_0 - \gamma & \frac{\bar{q}}{V}A_1 - \beta \end{bmatrix} \begin{bmatrix} x_a \\ q \\ \dot{q} \end{bmatrix} + \dots + \begin{bmatrix} B_a & 0 \\ 0 & 0 \\ 0 & \bar{q}A_{0w} \end{bmatrix} \begin{bmatrix} \delta_c \\ w \end{bmatrix}$$

$$y = \Phi_s \ddot{q}$$

Preliminary flutter prediction

The nominal model is computed with nominal parameters $\theta = \bar{\theta}$. This leads to the nominal unsteady aerodynamics on the wing illustrated figure 1 by lift amplitude distribution at $f = 3f_0$ where f_0 is a normalized reference frequency.

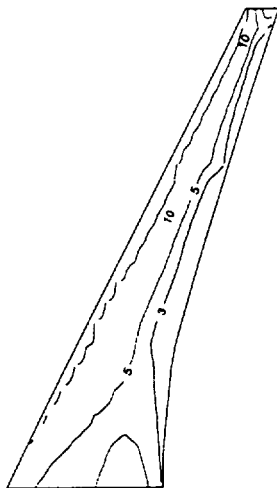


Figure 1: Nominal wing lift distribution (amplitude at $3f_0$)

A preliminary flutter prediction is then performed. As illustrated on figure 2 for a specific configuration, no flutter can be clearly predicted. However, coupling effects between modes can be observed when velocity reaches 200 to 250 kts. As some parameters of the prediction model are uncertain, there is a potential risk for a worse flutter behaviour.

3 Identifiability

Before designing algorithm for identification of unsteady aerodynamics parameters, it is necessary to check they can be identified. This is done using formal analysis of the prediction model, showing that, under some simple assumptions, there is existence and uniqueness of an optimal set of parameters θ that lead to a given state space representation.

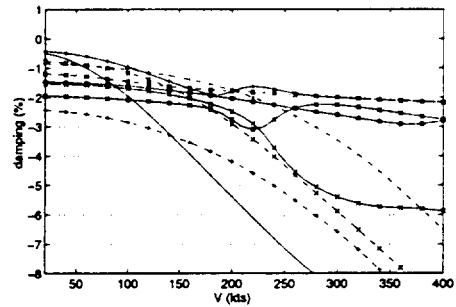
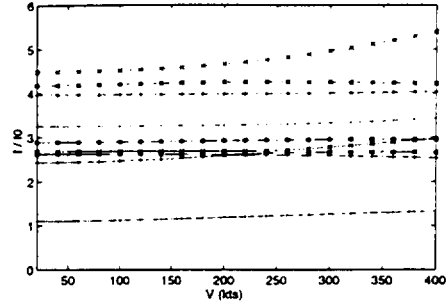


Figure 2: Preliminary flutter prediction, using nominal model

Modal sensitivity to parameter variations

A first order formal analysis of the eigenstructure variations versus parameters variations $\delta\theta$ leads to:

$$\begin{aligned} \delta\lambda_i &= \frac{1}{2} \frac{1}{V} \bar{q} U_i^T \mu^{-1} \Gamma \mathcal{I}m (\delta\theta G_*^T) V_i + \dots \quad (4) \\ &\dots \frac{1}{2} \frac{1}{\lambda_i} \bar{q} U_i^T \mu^{-1} \Gamma \mathcal{R}e (\delta\theta G_0^T) V_i \end{aligned}$$

where $\lambda_i = \pm j\omega_i$, U_i , V_i respectively are the purely imaginary eigenvalues, left and right real eigenvectors of the conservative structure

$$\mu \ddot{q} + \gamma q = 0$$

The first term is real and gives the effect of parameter variations on the damping ratio of the modes. The second one is imaginary and gives the effect on the frequencies. Figure 3 illustrates the sensitivity of mode #4 to all parameter variations at 300 kts. It appears that some parameters have a higher influence on both frequency and damping than others. They will obviously be easier to identify and a good accuracy on this parameters will be necessary for flutter prediction enhancement. Figure 4

shows how a specific parameter alters characteristics of all modes.

This kind of analysis indicates that some modes are insensitive to any parameter variations (such as modes #2 and 9). The dynamics of the structure (which includes 10 modes, i.e. 20 states), could then be split into its sensitive part (8 modes, 16 states) and its insensitive one (2 modes, 4 states). Moreover, some parameters have no significant effect on any mode: they should either be removed from the parameterization of the model, or not be included in the identification procedure.

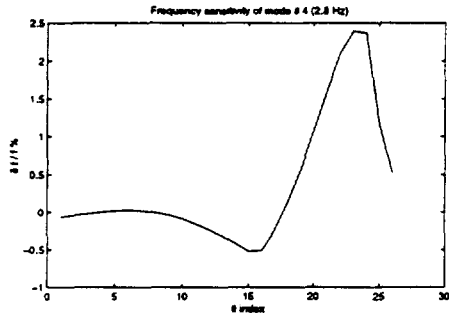


Figure 3: Sensitivity of mode #4 (VEM) for arbitrary 10% variation on each parameter

Formal inversion

It is shown here how unsteady aerodynamics parameters could be mathematically computed from a known state space representation, proving that a perfect identification of the global dynamics of the structure leads to a unique set of parameters.

Equations (3) write :

$$\begin{bmatrix} A_0 - \bar{A}_0 & A_1 - \bar{A}_1 \end{bmatrix} = \Gamma \dots$$

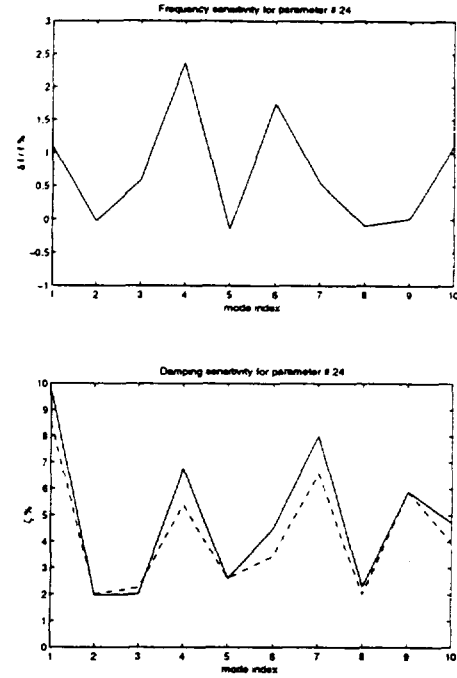


Figure 4: Sensitivity of all modes for arbitrary 10% variation on parameter θ_{24}

$$\dots \begin{bmatrix} \Re(\Theta - \bar{\Theta}) \\ \Im(\Theta - \bar{\Theta}) \end{bmatrix}^T \begin{bmatrix} \Re(G_0) & \Im(G_*) \\ -\Im(G_0) & \Re(G_*) \end{bmatrix}$$

with $\Theta, \bar{\Theta}$ both diagonal. Under rank assumptions, this equation is invertible for θ , with uniqueness. The assumptions are satisfied if there are enough modes in the structural dynamics, which are sensitive to variations of parameters θ (see previous section).

This mathematical inversion is not part of the identification procedure, but a preliminary test for existence and uniqueness of solution for θ . In practice, the assumptions are not satisfied. Noise and turbulence may corrupt the measurements and prevent exact identification. Moreover, there is no way to identify structured matrices A_0, A_1 , and there are some uncertainties on the structural dynamics. However, from the mathematical point of view, this formal analysis can be extended to models with uncertainties on the structural dynamics. Models at different velocities must be considered simultaneously, and equation (5) is non linearly dependent on the parameters.

4 Identification procedure

Description of the algorithms

Two different algorithms have been implemented for the search of an *optimal* set of parameters θ to fit flight (or simulated) data: Output Error (OE) and Spectral Estimation (SE), the principle of which are presented on figure 5 et 6.

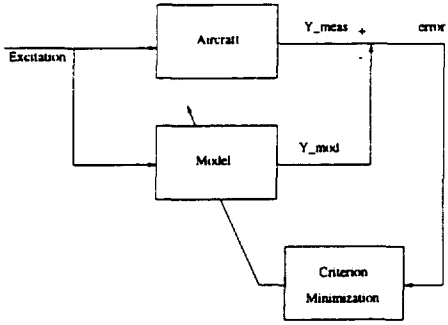


Figure 5: Output Error identification scheme

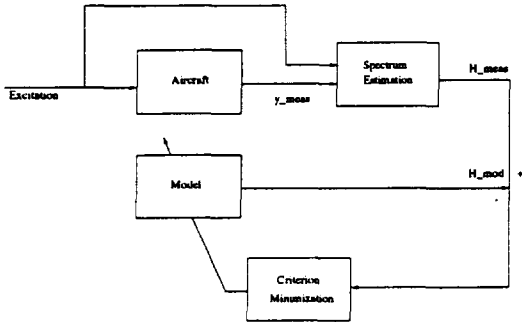


Figure 6: Spectral Estimation identification scheme

For OE, the objective is to minimize a criterion:

$$J = \frac{1}{2} \int_{-\infty}^{\infty} (Y(\theta) - Y_{meas})^* Q(\omega) (Y(\theta) - Y_{meas}) d\omega$$

with Y_{meas} , Y the Fourier transform of the actual measurements and the prediction model outputs, and Q a weighting matrix for emphasizing some specific frequency range, for instance having sufficient coherence. Parameters θ are updated with a Gauss-Newton like algorithm:

$$\theta^{n+1} = \theta^n - \left[\frac{\partial^2 J}{\partial \theta \partial \theta^T} \right]_{|\theta^n}^{-1} \frac{\partial J}{\partial \theta}_{|\theta^n}$$

Under linear assumptions of equation (2) and using results of the sensitivity analysis from section 3, there is an analytical formulation for the gradient

$$\frac{\partial J}{\partial \theta} = \mathcal{R}e \left(\int_{-\infty}^{\infty} \frac{\partial Y^*}{\partial \theta} Q(\omega) (Y - Y_{meas}) d\omega \right)$$

and the Hessian

$$\frac{\partial^2 J}{\partial \theta \partial \theta^T} \approx \int_{-\infty}^{\infty} \frac{\partial Y}{\partial \theta} Q(\omega) \frac{\partial Y^*}{\partial \theta} d\omega$$

This approach remains valid for more complex (potentially non linear) modeling of the unsteady aerodynamics $F_a(q, V, k, \theta)$ with explicit dependence on θ .

For SE, the identification is conducted in two steps. The first one is the estimation of the frequency response $H_{meas}(\omega)$ of the actual aircraft, using Welch like spectral computation [1]. This assumes that the dynamics is linear. The second one consists in fitting the estimated and predicted transfer functions [5], minimizing a criterion:

$$J = \frac{1}{2} \int_{-\infty}^{\infty} (H(\theta) - H_{meas})^* Q(\omega) (H(\theta) - H_{meas}) d\omega$$

with $H(\theta)$ the frequency response of the prediction model. Parameters θ are updated using a similar Gauss-Newton algorithm, based on analytical gradient and Hessian.

Validation

The algorithms are first validated with simulated data:

- A perturbed model is designed, using a specific set of parameters θ .
- Excitations are swept sinusoids, the climbing rate and length of which are adjusted for each identification algorithm (typically from f_0 to $7f_0$ in 40s at $50f_0$ sampling rate).
- Measurement locations are chosen on the structure to give good information on modes which are sensitive to parameter variations.
- Time responses are simulated in noise free and turbulence free conditions, at velocity

$V_{id} = 250kts$ where preliminary prediction showed some aeroelastic coupling characterized by a small damping decrease (see figure 2).

Both algorithms showed capability to estimate the true set of parameters θ , confirming practical *identifiability* of the design parameters.

5 Identification in turbulence

Modeling of turbulence

For simulation purpose, the effect of turbulence w is modeled as a non-white noise having Karman Spectra [4], going through a specific input as illustrated figure 7. The intensity of the noise is tuned to fit a given noise to signal ratio on a reference output (max amplitude ratio from 10 to 40% on time response). Figure 8 shows the time responses for simulated 30% turbulence. Figure 9 compares the frequency responses of the outputs without turbulence and the contribution of such turbulence to the outputs. Figure 10 illustrates the coherence of the data. A lack of coherence can be observed around $3f_0$, where coupling effects have already been detected.

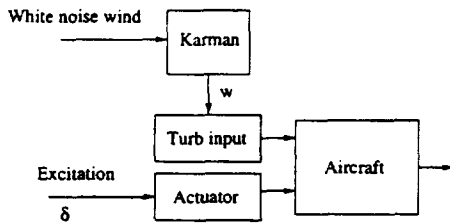


Figure 7: Simulation of turbulence

Application

Maximum Likelihood Parameter Estimation Technique [7] are difficult to apply to systems with high order dynamics. In order to keep good convergence properties, OE and SE techniques are preferred, though they are significantly perturbated by turbulence. Identification is performed at $V_{id} = 250kts$ for simulated turbulent data at various turbulence rates (from 10 to 40%), with the same

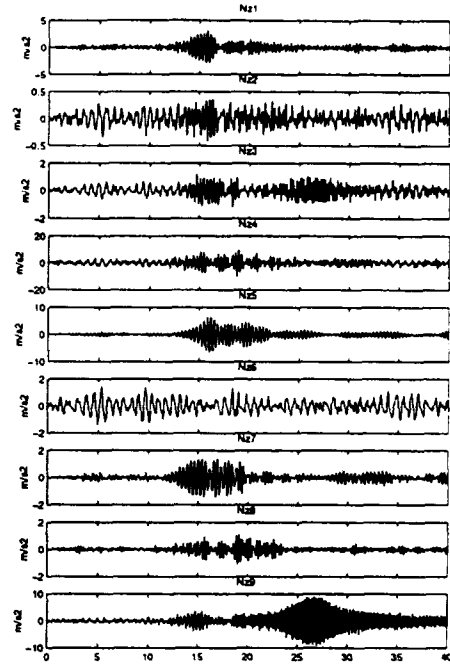


Figure 8: Time responses with swept sinusoids and 30% turbulence

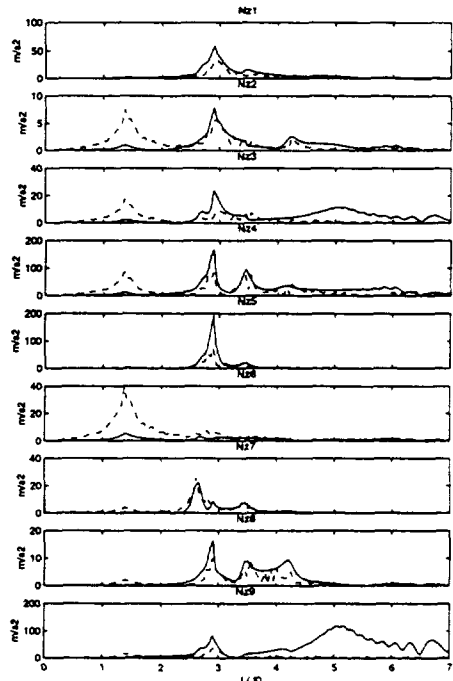


Figure 9: Frequency responses: - turbulence free outputs for swept sinusoids; - - contribution of 30% turbulence to the outputs

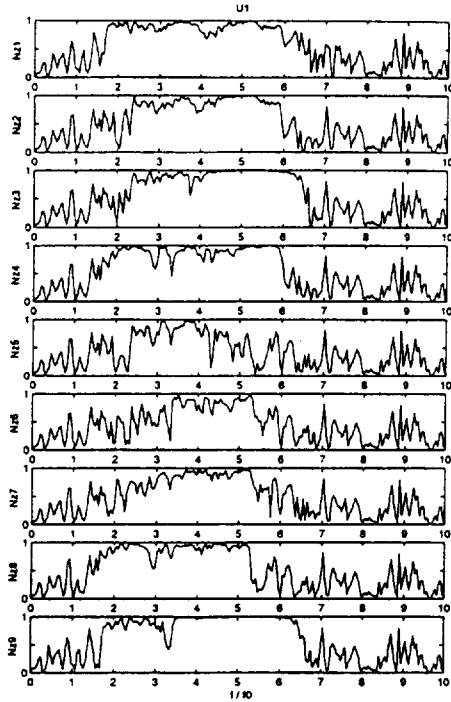


Figure 10: Data coherence with first input for 30% turbulence

excitations as for turbulence free validation. Because of non perfect decorrelation between turbulence and measurements, the algorithms cannot perfectly estimate the true set of parameters θ but still work correctly to provide a reasonably good estimation in terms of unsteady aerodynamics. The identified parameters $\hat{\theta}$ lead to the wing lift distribution of figure 11. Section 6 analyzes the impact of parameters estimation error on the accuracy of flutter prediction.

Statistics on the estimated parameters

Exact determination of the confidence region for parameters $\hat{\theta}$ is impractical [2], especially in presence of turbulence. A simple approximation is

$$var(\hat{\theta}) \approx \beta \left[\frac{\partial^2 J}{\partial \theta \partial \theta^T} \right]_{|\hat{\theta}}^{-1}$$

where β is chosen to fit statistics obtained with random Monte Carlo runs for a specific case. Figure 12 gives an estimation of confidence region for modulus of parameter #24 versus turbulence level,

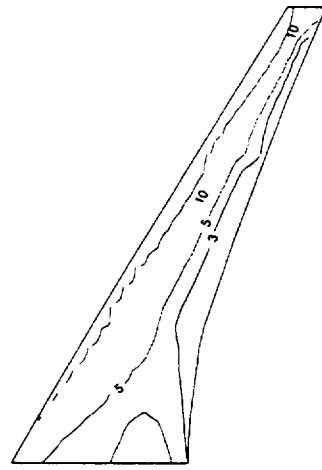


Figure 11: Wing lift distribution with identified parameters (amplitude at $3f_0$)

obtained by identification at $V_{id} = 250 \text{ kts}$. Obviously, the higher turbulence is encountered, the poorer accuracy is obtained for parameter estimation.

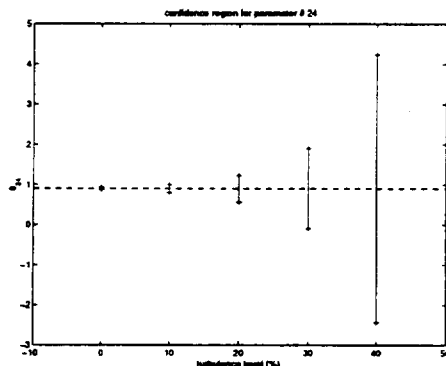


Figure 12: Confidence region for modulus of parameter #24

6 Accuracy of flutter prediction

Predictability of flutter in case of turbulence

The best estimated parameters $\hat{\theta}$ are used to compute $F_a(q, V, k, \hat{\theta})$ and the flutter curve for any

speed V . As illustrated on figure 13, parameters identified with a 30% turbulence level indicate flutter occurrence on mode #4 at $2.8f_0$, the damping ratio of which decreases from 1.8 to 0.7% between 300 and 350 kts. Despite high level of turbulence, the updating algorithms on a unique flight condition allow prediction of initially unexpected damping loss. In the next section, we discuss the accuracy of flutter prediction.

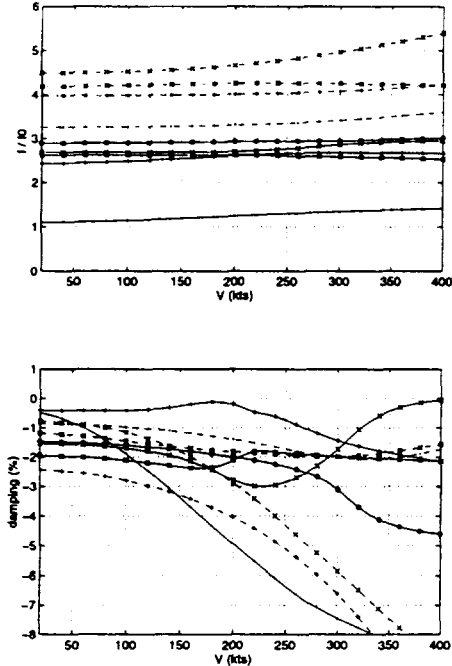


Figure 13: Flutter prediction, using parameters identified at $V_{id} = 250$ kts with 30% turbulence

Accuracy of damping and damping gradient estimate

The accuracy of flutter prediction can first be evaluated via the damping ratio ζ at given velocity. This can be done using sensitivity equation (4) to compute standard deviations on ζ from errors on the estimated parameters:

$$var\zeta_i = \frac{1}{2} \frac{1}{V} \frac{\bar{q}}{\omega_i} U_i^T \mu^{-1} \Gamma \mathcal{I}m (\varTheta G_*^T) V_i$$

Figure 14 gives a confidence region for the damping ratio of the destabilized mode ζ_4 at 300 kts versus

level of turbulence and for identification at various velocities:

- Though some parameters may have a large confidence region, the accuracy on damping ratio ζ_4 remains satisfactory up to high levels of turbulence. In this sense, a maximum acceptable turbulence level could be between 20 and 30%. For higher turbulence levels, identification algorithms still significantly correct the preliminary estimation of damping ratios (preliminary prediction was $\zeta_4 = 5.4\%$ at 300 kts and identification performed at $V_{id} = 250$ kts with 40% turbulence estimates $\zeta_4 = 1.8 \pm 0.6\%$).
- Identification performed at velocities significantly lower than aeroelastic coupling speed gives early accurate information for updating flutter prediction, but with a higher sensitivity to turbulence, as illustrated for identification at $V_{id} = 170$ kts and 250 kts to estimate damping at 300 kts.

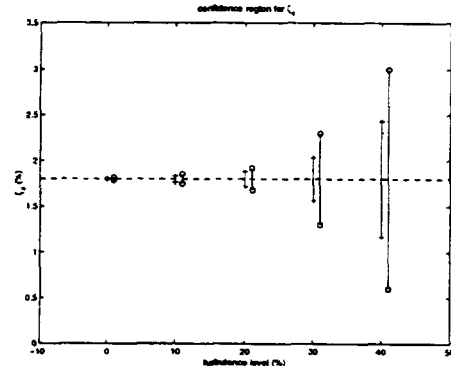


Figure 14: Confidence region for damping ζ_4 at 300 kts, identification performed with data at: o $V_{id} = 170$ kts, + $V_{id} = 250$ kts

The knowledge of the damping ratio is not sufficient for good flutter prediction. The accuracy must also be evaluated via the damping ratio gradient $\partial\zeta/\partial V$ at velocity where coupling between modes occurs, in order to be able to extrapolate to higher velocities. From sensitivity equation (4), one can compute

$$\partial\zeta_i/\partial V = \frac{1}{4} \frac{\bar{q}}{\omega_i} U_i^T \mu^{-1} \Gamma \mathcal{I}m (\Theta G_*^T) V_i$$

and the corresponding variance $\text{var}[\partial\zeta_i/\partial V]$ from variance of parameter estimates, as illustrated figure 15 for mode #4 with identification at $V_{id} = 250 \text{kts}$. Again a reasonable level of turbulence for acceptable confidence region is 20 to 30%. Higher levels give too large uncertainties.

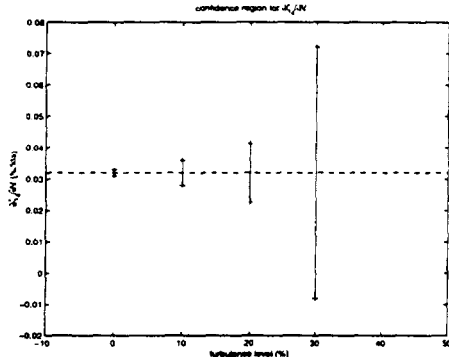


Figure 15: Confidence region for damping gradient $\partial\zeta_4/\partial V$ at 300kts

Perspective

The identification procedure is currently applied to real flight data. Different problems must be controlled:

- As the unsteady aerodynamics parameters have a physical interpretation, all optimal solutions obtained by the algorithms are not valid. Constraints on the parameters must be included in order to make solutions physical.
- The structural dynamics model is not perfect, and modeling errors may remain due to uncertainties on mass distribution. Tricky selection of tests at different velocities may minimize effects on mass distribution uncertainties (however loosing strictly real-time potential).
- In order to determine flutter speed, the accuracy of damping and damping gradient estimate can be improved cumulating estimations obtained by different identification at increasing velocities, as suggested in [3].

7 Conclusion

An identification procedure from flight data is proposed, for quasi real time updating of flutter prediction models. Parameters introduced in the unsteady aerodynamics model are estimated during flight test, while velocity is increased.

Performance of identification is evaluated in terms of accuracy for unsteady aerodynamics estimation, and of flutter prediction capability, with and without turbulence. Though turbulence may significantly alter the accuracy of parameter identification, it is shown that the estimation of modal damping ratios is accurate enough for flutter prediction enhancement. Moreover, identification performed at velocities significantly lower than aeroelastic coupling speed gives early accurate information for updating flutter prediction.

Acknowledgment

This applied research was performed at ONERA, France, under a contract with Service des Programmes Aéronautiques in Paris, and with the technical support of Aerospatiale-Avions in Toulouse.

References

- [1] S. M. Kay. *Modern Spectral Estimation: Theory and Application*. Prentice-Hall, Inc., 1988.
- [2] E. R. Maine and K. W. Iliff. Identification of dynamical systems. RP 1138, NASA, February 1985.
- [3] E. Nissim and G. B. Gilyard. Method for experimental determination of flutter speed by parameter identification. TP 2923, NASA, June 1989.
- [4] Capt W. J. Norton. Random air turbulence as a flutter test excitation source. In *20th SFTE Annual Symposium: Flight Test ... Racing Towards the 90's*, pages 6.4.1–6.4.11, Reno, NV, USA, September 1989.
- [5] R. Pintelon, P. Guillaume, Y. Rolain, J. Schoukens, and H. Van hamme. Parametric

identification of transfer functions in the frequency domain—

A survey. *IEEE Transactions on Automatic Control*, 39(11):2245–2260, November 1994.

- [6] S. H. Tiffany and M. Karpel. Aeroservoelastic modeling and applications using minimum-state approximations of the unsteady aerodynamics. Technical Report TM-101574, NASA, 1989.
- [7] H. Van der Auweraer and P. Guillaume. A maximum likelihood parameter estimation technique to analyse multiple input/multiple output flutter test data. In *AGARD Advanced Aeroservoelastic Testing and Data Analysis CP 566*, pages 12.1–12.7, Rotterdam, The Netherlands, May 1995.

Parameter Estimation in Flutter Analysis by Wavelet and Neural Network*

Y.S. Wong¹, B.H.K. Lee² and T.K.S. Wong³

^{1,3}*Department of Mathematical Sciences, University of Alberta, Edmonton, Canada*

²*Institute for Aerospace Research, National Research Council, Ottawa, Canada*

1. INTRODUCTION

Despite rapid advances in the development of computational aerodynamics and wind tunnel testing techniques, flight tests are still required to determine flutter boundaries of aircraft. Normally, modal frequencies and damping values are measured, but these quantities can be difficult to determine accurately when noise is present or when modal frequencies are close to each other. Various methods have been considered for parameter estimation in flutter tests, and these include curve fitting based on non-linear least squares, maximum likelihood estimation, Kalman filters and filter error method, to name but a few. Extensive discussions on these methods are given in Refs. [1-6]. Some of these techniques require considerable amount of computations, and hence real time evaluation of frequency and damping values may require efficient algorithms.

Wavelet theory for signal processing [Refs. 7-9] has made great progress in recent years. Also, artificial neural networks [Refs. 10-11] capable of modeling complex characteristics in nonlinear systems have contributed to the development of more advanced methods in analyzing aeroelastic response signals. Unlike conventional methods discussed in Refs. [1-6], these approaches do not require explicit mathematical manipulations. Furthermore, the required parameters can be estimated in real time once the neural network has been properly trained. To achieve optimal computational efficiency, the required parameters can be determined by a group of neural networks using a parallel algorithm. This study is an extension of the approach suggested by Lee and Wong [Ref. 12] where only one neural network was used to analyze a one-degree-of-freedom time signal represented by an exponentially decaying sine wave corrupted with noise.

*This work is supported by the National Sciences and Engineering Research Council of Canada.

¹Professor, email: yaushu.wong@ualberta.ca

²Principal Research Officer

³Research Student

2. REPRESENTATION OF FLUTTER SIGNALS

To simulate a flutter time series, we represent it by a linear superposition of a number of exponentially decaying sine waves

$$W(t) = \sum_{i=1}^N A_i e^{-\alpha_i t} \sin(\omega_i t + \phi_i) \quad (1)$$

where N denotes the number of modes, A_i , α_i , ω_i and ϕ_i represent the amplitude, damping ratio, frequency and phase angle associated with the i -th mode. This time signal represents the response of the aircraft structures excited by an impulsive load, or the decaying portion of the response signal from a sine dwell or sine sweep excitation. In practice, all signals are subject to noise corruption. Thus, a realistic flutter signal can be expressed in the form

$$Y(t) = W(t) + n(t) \quad (2)$$

where the noise is defined by

$$n(t) = \varepsilon \times W(t) \times \text{Gaussian random number.} \quad (3)$$

Here, the value ε represents the noise level. For example, when $\varepsilon = 0.2$, the original signal $W(t)$ is contaminated with at most 20% noise.

3. NEURAL NETWORKS

A neural network can be regarded as an information processing system which has the capability to model highly complex nonlinear systems. Simply stated, when a given input information and a desired output are prescribed, a neural network provides a nonlinear mapping to the input-output subspace. A particular attractive feature of a neural network is its ability to learn through examples, and it can be trained to perform a specific task such as parameter estimation.

The network consists of a set of computing unit known as neurons, and they are connected to other units by weights. Each unit computes a weighted sum of the inputs and translates it to outputs by making use of a transfer function. The transfer function may be linear or nonlinear and is chosen in order to satisfy some specifications of a given problem for which the solution is sought. Various transfer functions are available, and they have been discussed by Hagan et al. [10]. Lee and Wong [12] developed a simple two-layer neural network model (Fig. 1) which consists of one hidden layer for parameter estimation. In the figure, p and a are the input and output vectors, f is the transfer function, W and b denote the components of the weighted matrix and the bias vector.

Let W^1, b^1, f^1 denote the components of the weighted matrix, bias vector and transfer function corresponding to the first layer, the resulting output a^1 is expressed by

$$a^1 = f^1(W^1 p + b^1), \quad (4)$$

which is then taken to be the input for the second layer. The output for the second layer a^2 is given by

$$a^2 = f^2(W^2 a^1 + b^2) = f^2(W^2 f^1(W^1 p + b^1) + b^2). \quad (5)$$

For the neural network shown in Fig. 1, information travels only in the forward direction, and it is usually referred as a feed forward neural network.

In the present application to flutter parameter estimation, the input vector p consists of the discrete data values of a given signal $Y(t)$, and the output variables are the required estimated damping ratio α_i and frequency ω_i , for $i = 1, 2, \dots, N$.

Following the output formula given in equations (4) and (5), once the input p is given and the transfer function f has been determined, the remaining task is to compute the weighting matrix W and the bias vector b . This can be achieved by using a learning rule or a training algorithm. Here, we use a supervised learning procedure, in which a set of examples of proper network behavior $\{p_i, t_i\}$, $i = 1, 2, \dots$, known as a training set is provided, where p_i is input to the network and t_i is the corresponding correct output. The input $\{p_i\}$ is applied to the network to obtain the network output $\{a_i\}$, the weights W and biases b are then adjusted after comparing the network output $\{a_i\}$ with the correct output $\{t_i\}$. We introduce an error vector e given by $e = t - a$, and define the performance index F as the mean square error, i.e.,

$$F = e^T e. \quad (6)$$

The performance index provides a measure of the neural network performance, F being small when the network performs well, and large when the network performs poorly. Back-propagation algorithm is applied to the present two-layer network, in which W and b are adjusted so that the performance index is minimized using an optimization procedure based on the conjugate gradient algorithm. The detail implementation of the algorithm is described by Hagan et al [10]. Depending on a particular problem, the learning (training) process may require a considerable amount of computing time in order to reduce the performance index to a sufficiently small level. However, once the training process is completed (i.e. the values of W and b are determined), the outputs for the neural network can be computed almost instantaneously according to Eq. (5). This attractive feature makes it feasible for applications in a real time on-line environment while the training process can be executed off-line.

The complexity of a neural network is determined by the number of hidden layers, and the number of neurons in each layer including the input and output layers. This in turn

defines the size of the weighting matrices W . Most of the computing time used in the training process is to determine the elements of W .

We consider a two-layer neural network shown in Fig. 1. The input vector p consists of R neurons, and the output a has S neurons. For a simple network model, the number of neurons J for the hidden layer is usually chosen so that $J \geq \sqrt{R \times S}$. The weighted matrix for the first layer is given by

$$W^1 = \begin{bmatrix} w_{1,1} & w_{1,2} & \cdots & w_{1,R} \\ w_{2,1} & w_{2,2} & \cdots & w_{2,R} \\ \cdots & \cdots & \cdots & \cdots \\ \cdots & \cdots & \cdots & \cdots \\ w_{J,1} & w_{J,2} & \cdots & w_{J,R} \end{bmatrix}, \quad (7)$$

and consists of $R \times J$ elements. Similarly, the weighted matrix for the second layer W^2 consists of $S \times J$ coefficients. During a training process, the total number of elements needed to be adjusted are $(R + S) \times J$. The determination of the weight coefficients is the most time consuming part in the development of a neural network. Since the weight coefficients are modified using nonlinear optimization routines, solving a nonlinear problem with a smaller number of neurons for input and output will result in a significant reduction in computing time for the training process. In using a two-layer neural network to estimate frequency and damping coefficients for a given flutter signal, the input neurons R consist of 600 discrete values of $Y(t)$ given in (2), and the output neurons S represent α_i and ω_i for $i = 1, 2, 3$. The complexity of the network for this case (i.e. Case 1) is shown in Table 1. In the same table, the complexity for Case 2 is also given in which the input R has 60 neurons and the output S has only one neuron. The complexity of a neural network is greatly reduced when the size of the input and output neurons is small. The total number of elements of W^1 and W^2 for Case 2 is less than 1.5% of that needed for Case 1.

Table 1. Complexity of 2-layer Network

Case	R	S	$J \geq \sqrt{R \times S}$	$W^1 = R \times J$	$W^2 = J \times S$
1	600	6	60	36000	360
2	60	1	8	480	8

4. WAVELET ANALYSIS

In recent years, extensive publications on wavelet analysis and their applications in signal

processing can be found in the open literature [7-9]. Wavelets are particularly useful in data compression, signal decomposition and signal denoising, and these features can be used in conjunction with neural networks for parameter estimation.

Wavelet transforms can be regarded as harmonic analysis tools which provide time and frequency representations in the form of localized waveforms. For a given function $f(t)$, a discrete wavelet expansion can be expressed as

$$F(\psi) = \sum \beta_k^n 2^{n/2} \psi(2^n t - k) \quad (8)$$

where ψ is called the wavelet, β_k^n are the wavelet coefficients which are defined as

$$\beta_k^n = \int_{-\infty}^{\infty} f(t) \psi(2^n t - k) dt. \quad (9)$$

The reconstruction of a function $f(t)$ is achieved by applying an inverse transform to Eq. (8). The commonly used wavelets include the Harr wavelet [9], Daubechies' wavelets [8], Coifman's wavelets [7], localized sine and cosine transforms [9]. When a wavelet transform is applied to a given signal, the transform process convolves to a series of selected local waveforms with data identifying the correlated features associated with the signal. The resulting wavelet coefficients can thus be interpreted as multi-dimensional correlation coefficients.

To illustrate that a wavelet transform can be effectively used to perform signal decomposition, data compression and signal denoising, we consider the following example. We let $W(t)$ be a signal consisting of two modes, where

$$\begin{aligned} W(t) &= W_1(t) + W_2(t) \\ &= e^{-0.7t} \sin(12\pi t) + e^{-0.5t} \sin(8\pi t). \end{aligned} \quad (10)$$

Here, the amplitudes A_i and the phase angles ϕ_i as defined in Eq. (1) are chosen such that $A_i = 1$, $\phi_i = 0$ for $i = 1, 2$. Different values for A_i and ϕ_i can be used, but they will not affect the performance of a wavelet transform. In Fig. 2, we display the signal $W(t)$ using 500 data points where $t = n\Delta t$, $\Delta t = 0.004$, $n = 0, 1, \dots, 500$. Applying a wavelet transform with local cosine as basis to $W(t)$, the resulting 500 wavelet coefficients are plotted in Fig. 3. In Fig. 4, we show the first 100 wavelet coefficients presented in Fig. 3. From the results given in Figs. 3 and 4, we observe the following: First, the amplitudes of most of the wavelet coefficients are very small, except for the first 50 coefficients while the remaining 450 wavelet coefficients can be considered to have approximately zero amplitude. Secondly, the signal contains two components with two distinct frequencies, which correspond to two separated groups of wavelet coefficients shown in Figs. 3 and 4. Another way to identify the signal components is to display the wavelet coefficients in a time-frequency plane, where the

signal is decomposed into rectangular cells of equal area, and each cell is related to the amplitude of the corresponding wavelet coefficient. The total number of cells is equal to the dimension of the data representing the given signal. By applying an inverse wavelet transform to a selected group of wavelet coefficients, the individual signal component which associates with a particular frequency is then reconstructed. In Figs. 5 and 6, we display the reconstructed $W_1^*(t)$ and $W_2^*(t)$ where each component is reconstructed by using only ten wavelet coefficients, namely the coefficients 11 to 20 and 21 to 30 as shown in Fig. 4. The reconstructed components represented by dash lines are compared with the exact components $W_1(t)$ and $W_2(t)$ shown by solid lines in Figs. 5 and 6. Excellent agreement in using wavelet transform for signal decomposition is obtained. Combining $W_1^*(t)$ and $W_2^*(t)$ as $W^*(t) = W_1^*(t) + W_2^*(t)$, $W^*(t)$ now represents the reconstructed signal using 20 wavelet coefficients. In Fig. 7, $W^*(t)$ is compared to the original signal $W(t)$, and again excellent agreement is obtained.

The results applying a wavelet transform for signal decomposition and reconstruction are illustrated in Figs. 2-7 for a clean signal $W(t)$ given in Eq. (10). To investigate the effect of noise, we repeat the numerical simulation by adding a noise level of 20%, i.e. $\epsilon = 0.2$ in Eq. (3), to the signal $W(t)$. In Fig. 8, we show the reconstructed signal $W^*(t)$ by a dash line and the noise-free signal $W(t)$ by a solid line. $W^*(t)$ is reconstructed by using 20 wavelet coefficients which are obtained by applying wavelet transform to the noisy data defined in Eq. (2). Comparing the results presented in Figs. 7 and 8, we conclude that the application of a wavelet transform for signal decomposition is effective even if the signal is corrupted by noise. Since noise is usually represented by wavelet coefficients with small amplitudes, it can be effectively removed by selecting only a number of appropriate wavelet coefficients for signal decomposition.

5. WAVELET-NEURAL NETWORK MODEL

When the number of neurons associated with the input and output layers are small, the neural network can be trained efficiently. We have shown that applying a wavelet transform to a signal of the form given by Eq. (1), the amplitudes of the majority of the wavelet coefficients are practically zero. Since the important features of the original signal can be represented by a small number of non-zero wavelet coefficients, we can use these coefficients as network input instead of the original data set. In addition to its usefulness in data compression, wavelets can also be used for signal decomposition. The wavelet-neural network model for parameter estimation is illustrated in Fig. 9.

We consider a signal $Y(t)$ which consists of N exponentially decaying sine waves is given by

$$Y(t) = Y_1(t) + Y_2(t) + \dots + Y_N(t) + \text{noise} \quad (11)$$

where $Y_i(t) = A_i e^{-\alpha_i t} \sin(\omega_i t + \phi_i)$ and the damping values and frequencies, respectively.

In using a wavelet-neural network model to estimate α_i and ω_i , we apply a wavelet transform to decompose the signal into N components where each $Y_i(t)$ is a single-mode time series defined by a single frequency and a damping value. A wavelet transform is then carried out for the individual single-mode signals, and we select only a small number of the largest wavelet coefficients as input to two neural networks so that the outputs provide an estimated α_i and ω_i , respectively. To compute the damping values and frequencies for an N -mode signal, we need $2N$ neural networks. The attractive feature of the present model is that it logically leads to a parallel algorithm, and is a promising technique for estimating signal parameters in a real-time environment.

6. APPLICATIONS TO SIMULATED DATA

To investigate the performance of the two-layer neural network (Fig. 1) and the wavelet-neural network (Fig. 9), we apply both models to a simulated flutter data set. The test signal is generated from Eq. (11) and it consists of two modes with 512 data points. The noise is defined in Eq. (3) with ϵ varying between 0 to 0.2. The set contains 1000 test signals, and the values of damping ratio and frequency are determined by a random number generator such that $0.3 < \alpha_1, \alpha_2 < 0.8, 3 < \omega_1, \omega_2 < 8$. Initially, the training set starts with 200 random signals which are generated in the same manner as the test data set. The relative error is denoted by the absolute value of the difference between the network output and the correct output normalized by the correct output solution. Upon completion of the initial training, 500 test signals are constructed and the relative error recomputed. The training data set can be increased until the relative error is less than 0.1. A more accurate network can be achieved by decreasing the relative error at the expense of increasing training time.

The two-layer neural network is implemented in a *C⁺⁺* computer code program for a desktop personal computer. The input layer consists of 512 neurons representing the discrete data for a given signal, and the output has four neurons giving the values for $\alpha_1, \omega_1, \alpha_2, \omega_2$. The wavelet-neural network model consists of four neural networks, the input layer for each network contains 60 neurons where the first 30 neurons correspond to the largest 30 wavelet coefficients for a given signal and the remaining 30 neurons provide the locations of the selected wavelet coefficients. The output layer for each network has only one neuron.

The two-layer network is first tested for a single mode signal (i.e. $\alpha_2 = \omega_2 = 0$), using input vector containing the original 512 discrete data of a given signal or the largest 30 wavelet coefficients and the corresponding locations. In both cases, the relative errors from a 1000 testing set are within 5% accuracy. As expected, significant training time is reduced when the wavelet coefficients are taken as network input. Rapid convergence of the estimated damping value is achieved when wavelet coefficients are used as input.

When the testing signal contains two modes, the two-layer network fails to converge even after a long training process. This can be explained from examining the network outputs where $(\alpha_1, \omega_1, \alpha_2, \omega_2)$ and $(\alpha_2, \omega_2, \alpha_1, \omega_1)$ are both acceptable solutions. When the solutions in the nonlinear optimization step during the training process oscillated between these two sets, difficulties in convergence arise. Although it is possible to overcome this difficulty by reordering the network output to $(\alpha_A, \omega_A, \alpha_B, \omega_B)$, where $\omega_A > \omega_B$, α_A and α_B are the damping coefficients corresponding to frequencies ω_A and ω_B , respectively. The convergence rate for the training process becomes extremely slow compared to parameter estimation for one-mode signal, this approach will not be practical for parameter estimation applied to multi-mode signals. However, the wavelet-neural network model presented in this paper does not encounter this problem. The relative errors for the 1000 test data set for the estimating damping and frequency are shown in Figs. 10 and 11, and the results are within 4.5 and 6% for the damping value and frequency, respectively. The model has also been tested for cases in which the time series signals are represented by set of 256 to 1024 data. In all cases, it has been found that it is sufficient to represent the signal using its 30 largest wavelet coefficients.

7. CONCLUSIONS

The novel wavelet-neural network presented in this paper has the capability to estimate parameters for a given signal with good accuracy. The model employs signal decomposition and data compression using wavelet transforms. This leads to an efficient training process and the network outputs can also be determined by a parallel algorithm. The only limitation of the present method is that the frequencies of the signal components can not be too close in order that decomposition can be performed. The method can also be used applied to non-stationary signals by dividing the signal into segments. Each segment is then used as input to the present wavelet-neural network model.

REFERENCES

1. Lee, B.H.K. and Laichai, F (1993), *Development of post-flight and real time flutter analysis methodologies*, Proceedings Forum International Aéroelasticité et Dynamique de Structures, Strasbourg, pp. 7043-719.
2. Klein, V. (1989), *Estimation of aircraft aerodynamic parameters from flight data*, Progress in Aerospace Sciences **26**, 1-77.
3. Shinbrot, M. (1951), *A least-squares curve fitting method with applications to the calculation of stability coefficients from transient response data*, NACA TN-2341.
4. Mehra, R.K. (1971), *Identification of stochastic linear dynamic systems using Kalman filter representation*, AIAA Journal **9**, 28-31.
5. Murphy, P.C. (1984), *An algorithm for maximum likelihood estimation using an efficient method for approximating sensitivities*, NASA TP-2311.

6. Advanced Aeroseervoelastic Testing and Data Analysis, (1995), AGARD-CP-566.
7. Coifman, R. and Wickerhauser, M.V. (1993), Wavelets and adapted waveform analysis, Proceedings of Symposia in Applied Mathematics, Vol. 47, American Mathematical Society, pp. 119-154.
8. Daubechies, I. (1990), The wavelet transform, time-frequency localization and signal analysis, IEEE Trans. Inform. Theory 36, no. 9, 961-1005.
9. Strang, G. and Nguyen, T. (1996), Wavelets and Filter Banks, Wellesley-Cambridge Press.
10. Hagan, M.T., Demuth, H.B. and Beale, M. (1996), Neural Network Design, PWS Publishing Company, Boston, U.S.A.
11. Freeman, J. and Skapura, S. (1991), Neural Networks: Algorithms, Applications, and Programming Techniques, Addison-Wesley, MA, U.S.A.
12. Lee, B.H.K. and Wong, Y.S. (1998), Neural network parameter estimation with application to flutter signals, Journal of Aircraft 35, 165-168.

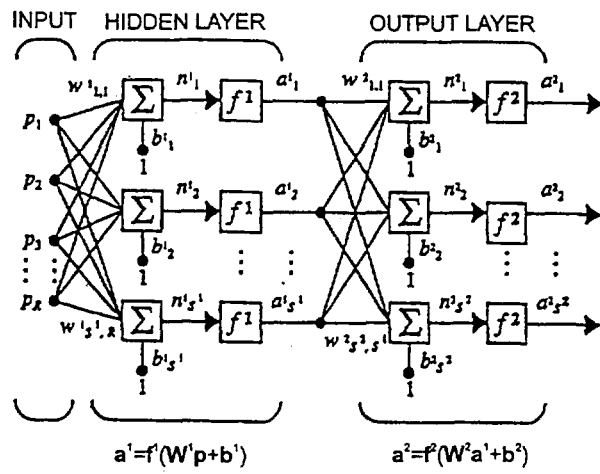


Fig. 1 Two - layer neural network model

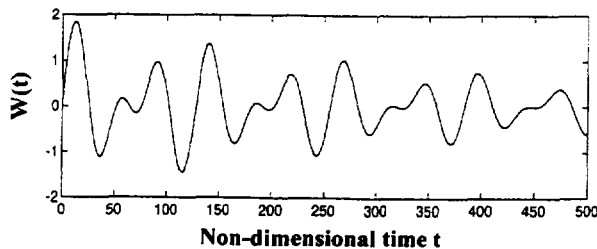


Fig. 2 Time series for signal $W(t)$

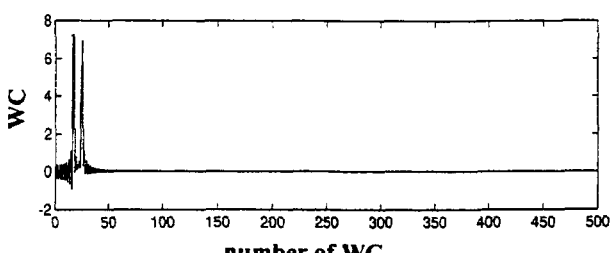


Fig. 3 Wavelet coefficients WC for $W(t)$

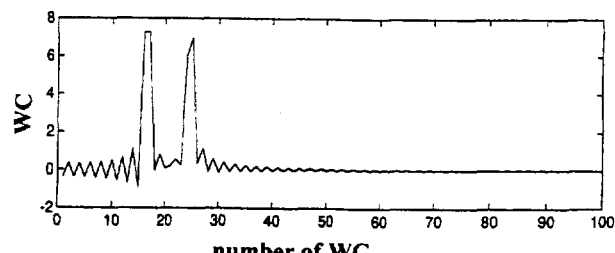
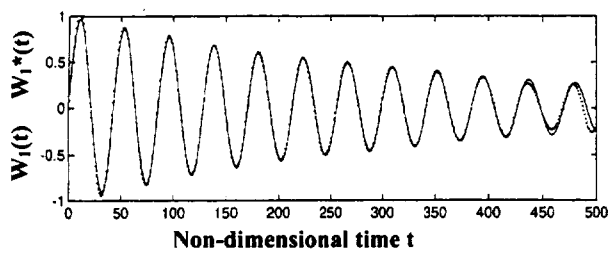
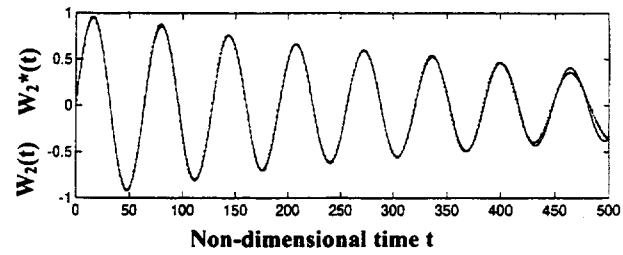


Fig. 4 Wavelet coefficients WC for $W(t)$



**Fig. 5 Original signal $W_1(t)$ ——
reconstructed signal $W_1^*(t)$ ——**



**Fig. 6 Original signal $W_2(t)$ ——
reconstructed signal $W_2^*(t)$ ——**

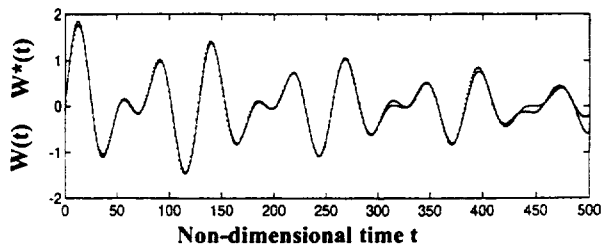


**Fig. 7 Original signal $W(t)$ ——
reconstructed signal $W^*(t)$ ——**

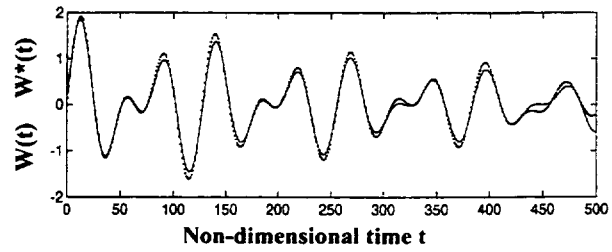


**Fig. 8 Original signal $W(t)$ ——
reconstructed signal $W^*(t)$ ——
with 20% noise added to $W(t)$**

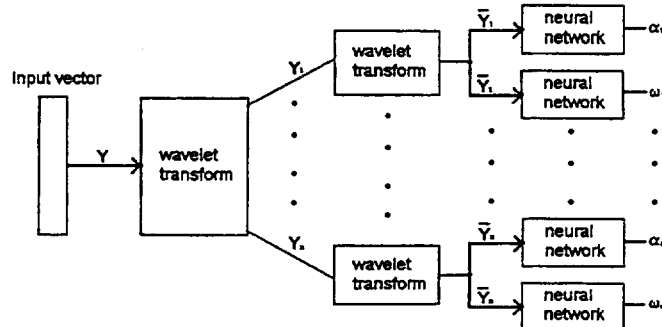


Fig. 9 Wavelet - neural network model

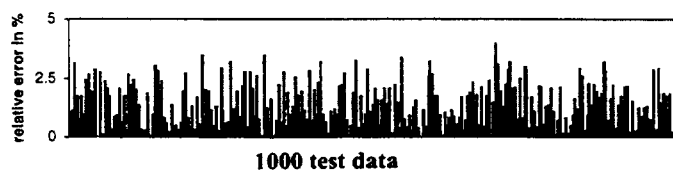


Fig. 10 Relative error in % for estimated damping

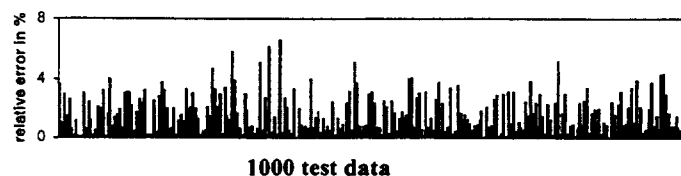


Fig. 11 Relative error in % for estimated frequency

Flutter Speed Prediction During Flight Flutter Testing Using Neural Networks

**J.E. Cooper & W.J. Crowther
Manchester School Of Engineering
University of Manchester
Oxford Road, Manchester, M13 9PL, UK.**

523-08

ABSTRACT

Flight flutter testing is a crucial part in the certification of a prototype aircraft. The flight envelope must be expanded safely, however, there is always the pressure to complete the tests as quickly as possible. Although there will be an aeroelastic model of the system for comparison, the decision to proceed to the next test point is usually based upon the modal parameters estimated from the flutter test data. A number of different methods have been proposed to determine the speed at which flutter occurs, however, the most commonly used approach is simply to extrapolate the estimated damping ratios. In this paper, a method for the prediction of flutter speed from flutter test data is proposed based upon the use of Neural Networks. The method is demonstrated upon a simulated aeroelastic model.

INTRODUCTION

Flutter is a violent unstable oscillation that occurs due to the interaction of inertial, aerodynamic and elastic forces. Flight Flutter Testing [1] is a mandatory part of the certification process that must be undertaken in order to demonstrate that the aircraft is flutter free throughout the desired flight envelope. The flutter testing procedure [2,3] can be difficult due to the conflicting requirements of completing the tests safely in as short a time as possible.

The flutter test procedure consists of three elements aiming to clear the flight envelope shown in figure 1 at a number of constant height and also constant Mach no cases:

1. The aircraft is excited in some manner and the response measured
2. The modal parameters are estimated using system identification methods [4]
3. The decision is made to proceed to the next flight test point

Arguably it is the last element that is the most difficult. In essence, the flutter test engineer needs to ensure that an adequate degree of stability is maintained at the next test point, and this is usually determined by considering the modal parameters estimated from the measured test data. Any deficiencies in the first two elements of the test will be passed through to the prediction stage causing greater uncertainty. It must also be remembered that the stability of the system can change abruptly with only a small increase in flight speed. The computational aeroelastic model is generally only used for guidance regarding the characteristics of the flutter behaviour, and it is rare to update the model as the envelope is expanded.

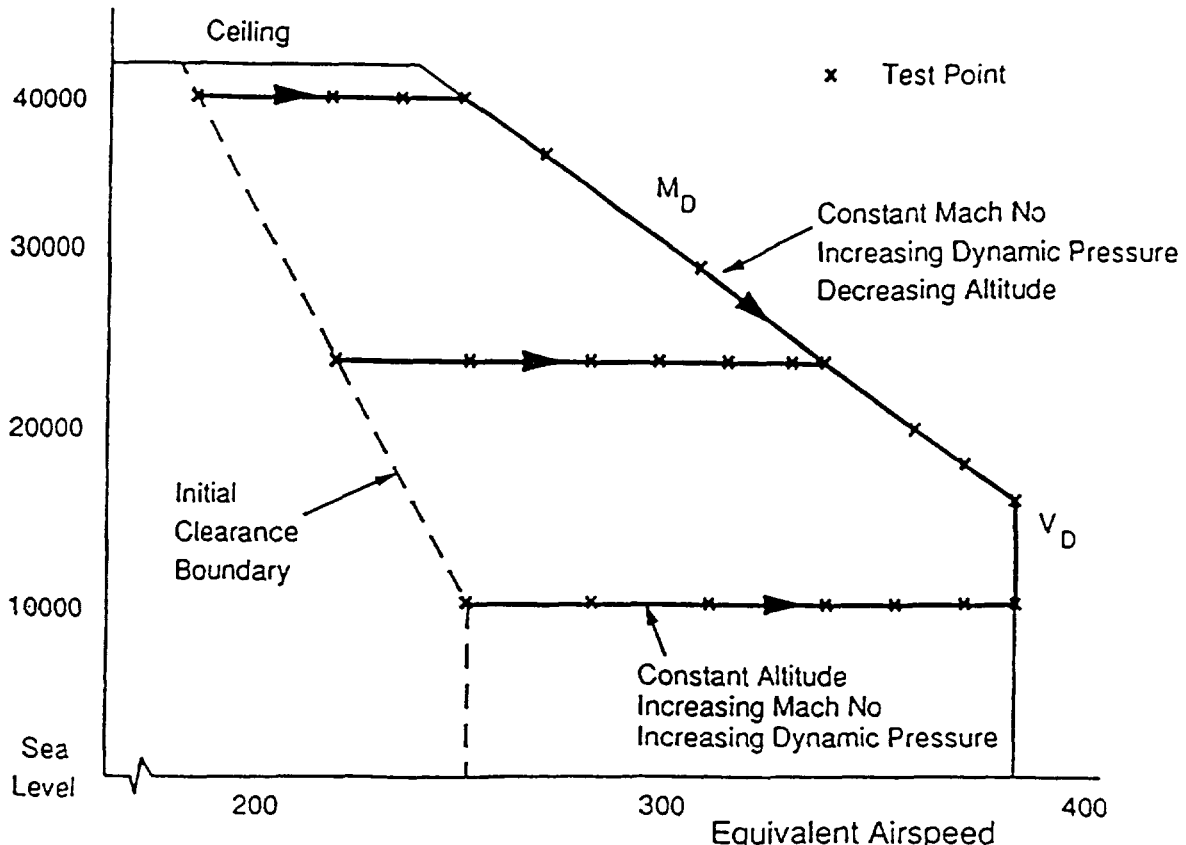


Figure 1. Flight Test Envelope Clearance.

By far the most common approach to extrapolating the test results is simply to consider the damping trends. Often this approach is performed by hand. There is somewhat of an art to this procedure, particularly when there are closely coupled modes. Figure 2 shows typical frequency and damping trends for a civil aircraft, and it can be seen how difficult it can be to follow the damping trends. It is often useful to include information about the mode shapes, see [5] for an automated procedure to do this, in order to reduce problems with the mode tracking.

A number of methods have been proposed that attempt to automate the flutter speed prediction from test data process. The Flutter Margin method [6] is based on the premise that a more fundamental stability criterion (the Routh Stability criterion) should be used rather than simply tracking the damping ratios. Originally, the method was formulated for binary systems and the user has to know a-priori which of the modes are going to form the flutter mechanism. A recent extension [7] has produced a formulation for ternary flutter.

The envelope function [8] was developed based on the assumption that the impulse response function contained information about the overall stability of the system. A shape function based upon the centroid of the impulse response envelope is plotted and then extrapolated to predict the flutter speed. Similarly, a time domain ARMA method [9,10] using the Jury Stability criterion has also been tried that also considers the overall stability of the system. This method was developed for the response to unmeasured turbulent excitation although the method can be extended to the measured input case.

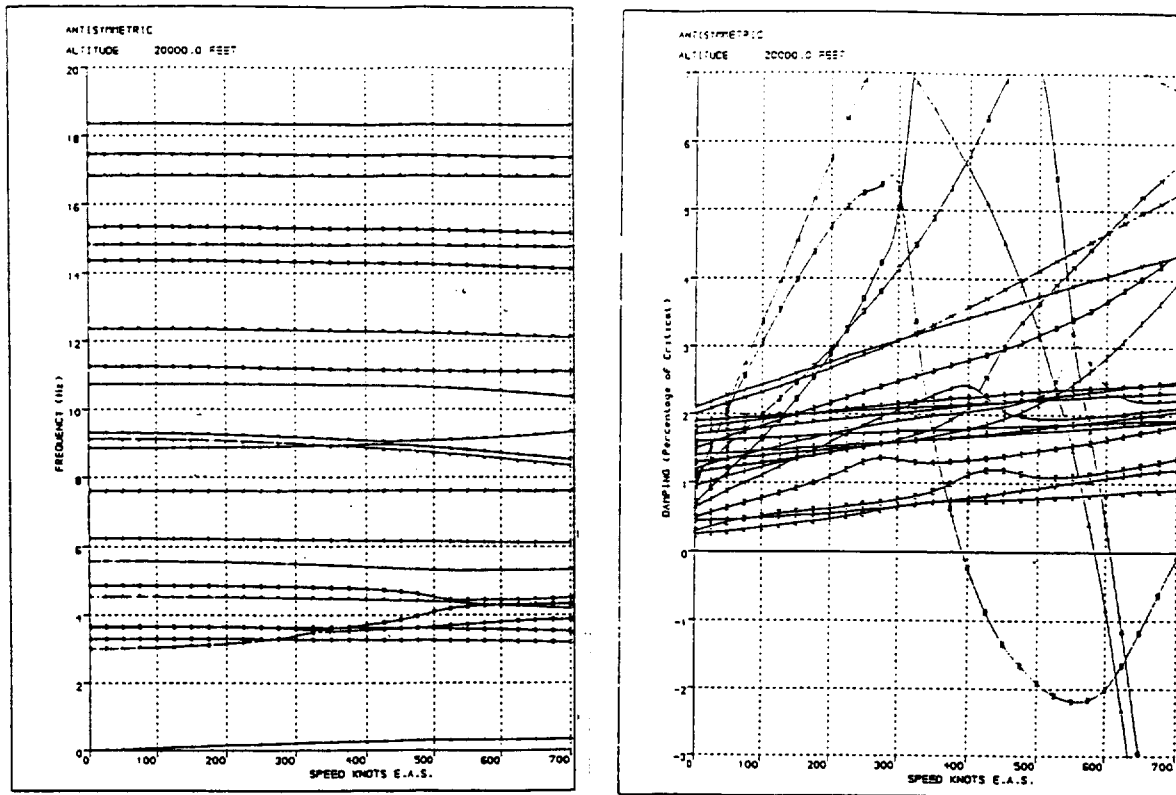


Figure 2. Frequency and Damping Trends for a Civil Aircraft Model [8]

Nissim and Gilyard [11], extended a method introduced by Gaukroger et al. [12], adopted a different approach by attempting to identify the entire aeroelastic system. If data from two different flight test points is measured, then it is possible to identify all of the matrices in the conventional aeroelastic model. Once the model is known, an eigenvalue solution of the system equations can be performed at increasing speeds until the flutter speed is found. Although this approach is the most ideal from a mathematical viewpoint, there are problems in its implementation with large order systems. Finally, recent work [13] has developed an approach for determining the flutter speed based upon worst case robust stability theory.

In this paper, an approach is introduced to determine the stability at the next flight test point using Neural Networks. The network is trained upon sub-critical modal parameter estimates using the computational aeroelastic model. During the flight test, previous frequency and damping values are used to help predict damping values at future test points. The method is intended to be used during flight flutter testing, unlike a previous implementation [14], as an extra tool to aid the safe expansion of the flight envelope. The approach is demonstrated upon a simple simulated aeroelastic system.

NEURAL NETWORK APPROACH

Consider the damping trend versus speed for a single mode shown in figure 3 as an example of the approach that is taken in this paper. A number of numbered test points are shown. Once the expansion of the flight envelope is underway, the flight test engineer has to decide whether it is safe to proceed to, say, point 6 based upon the previous 5 test points. This procedure is then repeated for all the other test points. Obviously, in practice there will be damping and frequency values from other modes.

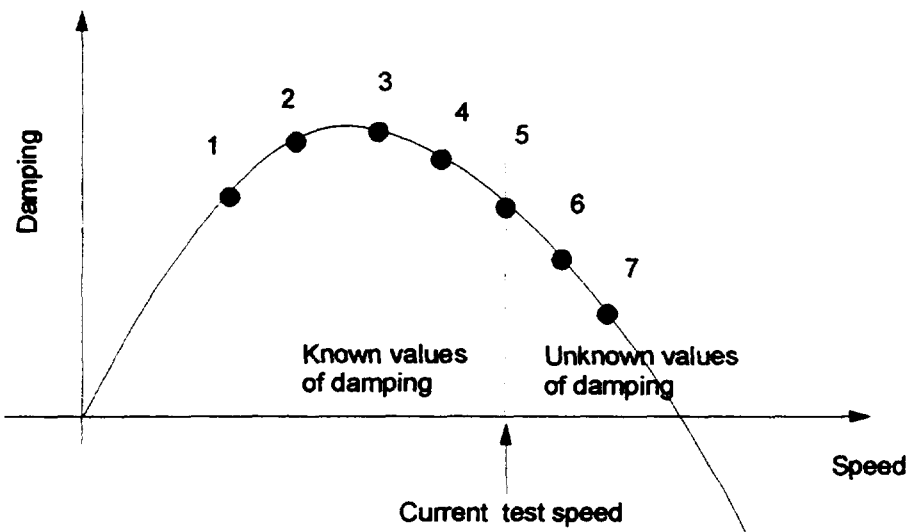


Figure 3. Test Points on a Single Damping Trend.

In this paper, training of the Neural Network was achieved by mimicking the approach used during a conventional flight test, i.e. five consecutive sets damping values were used to predict the damping at the next three test points. The basis of this method is data extrapolation using a nonlinear autoregressive moving average (NARMA) model. In the present case the NARMA model is implemented in the form of a neural network, with the free parameters in the model represented by the connection strengths in the network. The advantage of using a NARMA model as opposed to ordinary algebraic extrapolation is that the former method allows inclusion of problem-specific information. This information is provided through the examples used to train the network.

The network used was a feed-forward multi-layer perceptron trained using error back propagation. Networks were implemented and trained using commercial neural network software (Neuframe) running on a PC.

A simple simulated binary flutter model [15] was used to demonstrate the proposed approach. 5 data sets were produced for different values of the wing root stiffness. Data sets 1,3 and 5 were used to train the network with data set 4 used as a control set during

training to test for over fitting. Finally, data set 2 was used as an independent query set to validate network performance on new data.

One training example consists of a training input vector and a training target vector. The input vector consists of frequency and damping values for modes 1 and 2 for 5 contiguous speed increments. The target vector consists of damping values for modes 1 and 2 for the next three contiguous speed increments. For each data set, 23 training examples were produced to give a training input matrix and a training target matrix (shown below). The purpose of network training is to establish the mapping between the input and target vectors by repeated cycling through the training examples, updating the network weights to minimise the network error after each cycle.

$$\begin{bmatrix} \omega_1^1 \omega_1^2 \omega_1^3 \omega_1^4 \omega_1^5 \xi_1^1 \xi_1^2 \xi_1^3 \xi_1^4 \xi_1^5 \omega_2^1 \omega_2^2 \omega_2^3 \omega_2^4 \omega_2^5 \xi_2^1 \xi_2^2 \xi_2^3 \xi_2^4 \xi_2^5 \\ \omega_1^2 \omega_1^3 \omega_1^4 \omega_1^5 \omega_1^6 \xi_1^2 \xi_1^3 \xi_1^4 \xi_1^5 \xi_1^6 \omega_2^2 \omega_2^3 \omega_2^4 \omega_2^5 \omega_2^6 \xi_2^2 \xi_2^3 \xi_2^4 \xi_2^5 \xi_2^6 \\ \vdots \quad \vdots \quad \vdots \quad \vdots \quad \vdots \quad \vdots \\ \vdots \quad \vdots \quad \vdots \quad \vdots \quad \vdots \quad \vdots \\ \omega_1^{23} \omega_1^{24} \omega_1^{25} \omega_1^{26} \omega_1^{27} \xi_1^{23} \xi_1^{24} \xi_1^{25} \xi_1^{26} \xi_1^{27} \omega_2^{23} \omega_2^{24} \omega_2^{25} \omega_2^{26} \omega_2^{27} \xi_2^{23} \xi_2^{24} \xi_2^{25} \xi_2^{26} \xi_2^{27} \end{bmatrix}$$

Training input matrix

$$\begin{bmatrix} \xi_1^6 \xi_1^7 \xi_1^8 \xi_2^6 \xi_2^7 \xi_2^8 \\ \xi_1^7 \xi_1^8 \xi_1^9 \xi_2^7 \xi_2^8 \xi_2^9 \\ \vdots \quad \vdots \\ \vdots \quad \vdots \\ \xi_1^{28} \xi_1^{29} \xi_1^{30} \xi_2^{28} \xi_2^{29} \xi_2^{30} \end{bmatrix}$$

Training target matrix

(the subscript refers to the mode number and the superscript refers to the speed number)

A three layer network was used. As dictated by the training data, the network has 20 input neurons and 6 output neurons. The number of middle layer neurons was 10 (optimised by trial and error).

RESULTS AND DISCUSSION

The frequency and damping characteristics for the 5 test cases are shown in figure 4. Classic binary flutter behaviour is exhibited. In the present case, the unstable mode (tendency to negative damping) is always mode 2. This is not generally the case and has not been assumed in the present study.

A numerical conditioning problem is clearly anticipated by the large numerical difference between the damping values of the two modes, bearing in mind that the unstable mode can not necessarily be predicted.

Network training proceeded robustly, with no evidence of false minima. Typical training runs took 1000 iterations through the training data (2 minutes on a P166). With 10 hidden neurons and 23 training examples, overfitting was not observed.

Results from querying the trained network with previously unseen data are shown in figure 5. The network predicts mode 1 damping values accurately, apart from at the corner where actual values saturate at 100%. The results for mode 2 (the unstable mode) are less good. The reason for the difference in accuracy between the modes is the lack of resolution at the small damping values presented by mode 2. The network minimises the global error function and thus small values contribute less to the overall weight distribution.

Note that if the network is queried with mode 2 data that was used in the training set, the accuracy of the predicted values is considerably better than that shown in figure 5.

The prediction error increases only slightly with increasing number of steps. This suggests that predictions further forward are viable with this method.

To improve the accuracy of prediction for the modes with lower damping (usually the unstable modes of interest) a modified approach is required that provides better conditioned training data for the network. This might be achieved by selective normalisation of the data as it proceeds.

CONCLUSIONS

An approach using neural networks to predict whether it is safe to move to the next test point in a flight flutter test has been demonstrated. The initial results show that the approach is promising and further work is ongoing to determine the robustness for full scale simulated flutter models and actual flight test data.

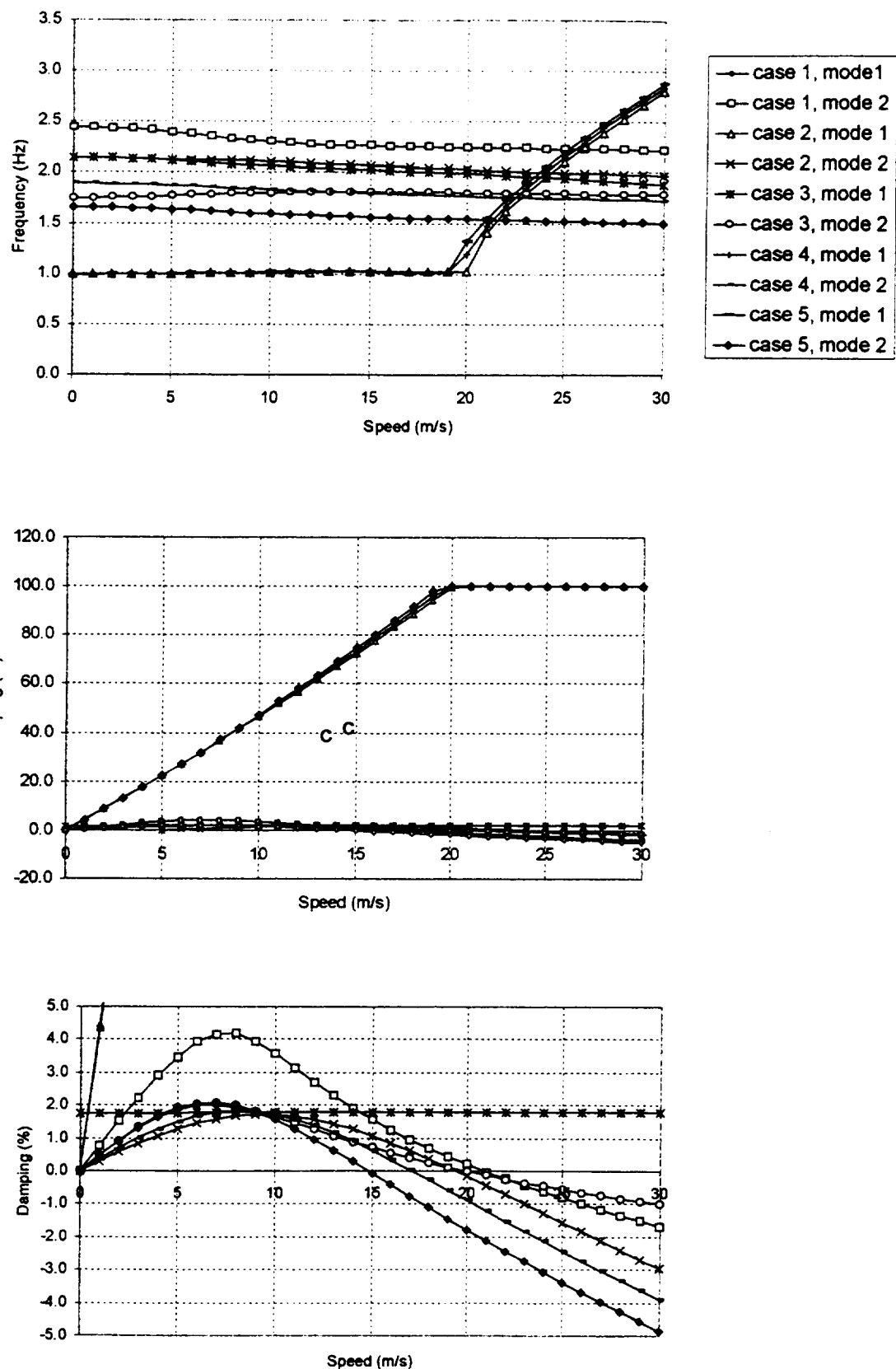


Figure 4 Frequency and damping characteristics for binary flutter

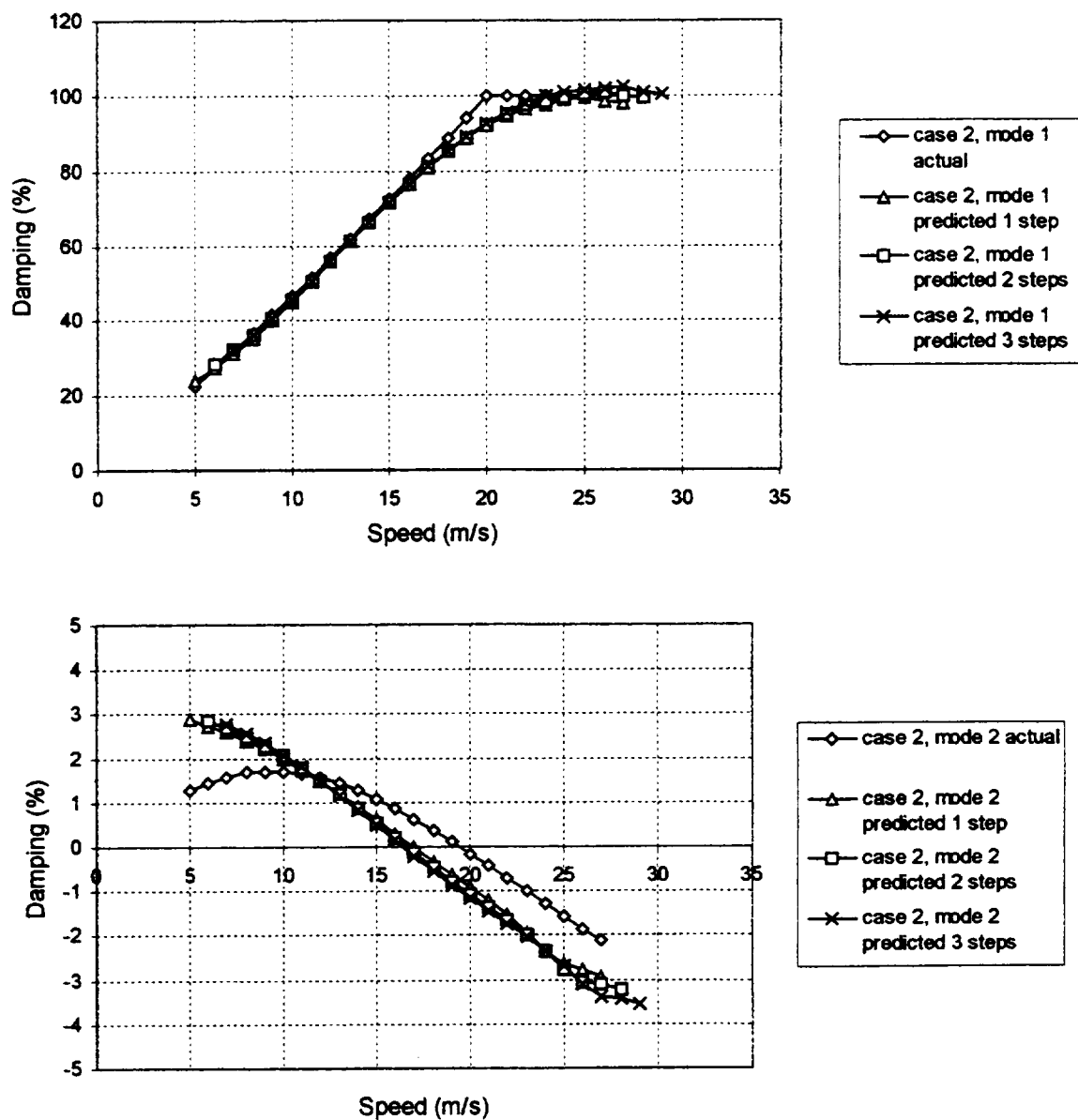


Figure 5 Actual and neural network predicted damping values

REFERENCES

1. M.W. Kehoe, 'A Historical Overview of Flight Flutter Testing' In AGARD CP-566 Advanced Aerostervoelastic Testing and Data Analysis Paper 1. 1995.
2. J.R. Wright, 'Flight Flutter Testing' Lecture Series on Flutter of Winged Aircraft. Von Karman Institute. 1991.
3. J. Johnson, 'Flutter Testing of Modern Aircraft' AIAA Student Journal Spring pp 6-11. 1989.
4. J.E. Cooper, 'Parameter Estimation Methods for Flight Flutter Testing' In AGARD CP-566. Advanced Aerostervoelastic Testing and Data Analysis. Paper 10. 1995.
5. M.J. Desforges, J.E. Cooper & J.R. Wright, 'Mode Tracking During Flutter Testing using the Modal Assurance Criterion' Proc I.Mech.E Part G J.Aerospace Engineering v210 pp 27-37. 1996.
6. N.H. Zimmermann & J.T. Weissenberger, 'Prediction of flutter onset speed based on flight testing at subcritical speeds' J. Aircraft v1 n4 pp 190 – 202 1964.
7. S.J. Price & B.H.K. Lee, 'Evaluation and Extension of the Flutter Margin methods for Flight Flutter Prediction' J. Aircraft v30 n3 pp 395- 402 1993.
8. J.E. Cooper, P.R. Emmett, J.R. Wright & M.J. Schofield, 'Envelope Function – A tool for analyzing Flutter Data' J. Aircraft v30 n5 pp 785 – 790 1993.
9. Y. Matsuzaki & Y. Ando, 'Estimation of Flutter Boundary from Random Responses due to turbulence at subcritical speeds' J.Aircraft v18 n10 pp862-868. 1981.
10. Y. Matsuzaki & H. Torii, 'Response Characteristics of a Two Dimensional Wing Subjected to Turbulence near the Flutter Boundary' J.Sound & Vibration v136 n2 pp 187 – 199 1990.
11. E. Nissim & G.B. Gilyard, ' Method for Experimental Determination of Flutter Speed by Parameter Identification' AIAA-89_1324-CP 1989.
12. D.R. Gaukroger, C.W. Skingle & K.H. Heron, 'An Application of System Identification to Flutter Testing' J. Sound & Vibration v72 n2 pp 141-150. 1980.
13. R.C. Lind & M.J. Brenner, 'A Worst Case Approach for On-Line Flutter Prediction' Int. Forum on Aeroelasticity & Structural Dynamics, Rome 1997 pp 79-86.
14. L. Lecce, M. Pucci & M. Pecora, 'Flutter Speed Prediction using the Artificial Neural Network Approach' Int. Forum on Aeroelasticity & Structural Dynamics, Manchester, Paper 13 1995.
15. G.J. Hancock, J.R. Wright and A. Simpson, 'On the Teaching of the Principles of Wing Flexure – Torsion Flutter' Aeronautical Journal, pp 285 – 305 1985.

Overview of Recent Flutter Boundary Prediction Techniques Based on Testing Data Analysis¹

Pei Chengming², Qiu Zihua, Zhai Kun
Data Processing Center
Northwestern Polytechnical University
Xi'an 710072, P. R. China

524-08

KEY WORDS: Flutter Boundary Prediction, Testing Data Processing

ABSTRACT: FBP (Flutter Boundary Prediction) due to subcritical signal analysis is becoming a significant research subject in the field of flutter testing. In this paper, traditional modal damping and modern system stability analysis are reviewed. The principle and specifics of the methods are also briefly discussed. Especially, a new hybrid prediction method based on NNES (Neural Network Expert System) is proposed integrated current FBP techniques and human experiences from experts.

1. INTRODUCTION

During a flutter testing of a new aircraft, how to decide the critical speed on line is of great important to flutter envelop expansion and testing safety and testing efficiency. Flutter Boundary Prediction (FBP), directly using subcritical response analysis, has been interested in two decades. To meet the requirements with accurate, rapid and reliable, FBP techniques have been quickly developed and applied in actual data processing of wind-tunnel and flight flutter experiments.

To improve the quality and reliability of FBP, there are two paths to consider. First, being difference with theory prediction using aeroelastic calculation, FBP depend mainly on test. And so, test techniques and the quality of measured signal are the foundation. Except for data communication and data record, measurement and excitation are the both key factors in flutter test. For measurement, the kind and position of sensor will be considered and generally not too difficult in test preparing stage. But for excitation, there exist two problems, namely, excitation pattern and excitation signal design. The former includes natural airflow, rocket, operation lift, etc. The latter are separated to sine, sweep, impulse and turbulence. The signal measured has different characteristics under different excitation manner. And obviously, the excitation using the natural airflow or turbulence is relatively economic, safety and easy use in engineering, but the excitation is more difficult than other excitation cases in signal processing. And so, we have to pay more attention on the data with lower quality. As a matter of fact, the excitation force is unmeasured and the affection of airflow or turbulence is also not avoidable in test.

The second way is to find more advanced method to meet the data functions and requirements of FBP analysis. The present FBP methods can be divided into two branches, i.e., modal damping vs speed and system stability parameter vs speed. Damping techniques is a traditional method and has

¹ This paper is supported by Aeronautic Scientific Foundation of China

² Professor, Director of Data Processing Center

been widely used in flutter testing field. NASA and other professional organizations of the world use the way to flutter testing in wind-tunnel and flight. Damping is mainly developed based on Fourier theory and human experiences play an important role in using. System stability analysis (SSA) is quickly developed in recent year, which primarily consisted of data modeling (system identification) and stability criteria. SSA has a different idea with damping and flutter is considered to be an unstable or divergence behavior of testing object. 1964, Zimmerman and Weissenburger gave a stability parameter called Flutter Margin related to Routh-Hurwitz criterion firstly in FBP field. Although the parameter calculation requires measured values of the frequencies and dampings of both modes involved in the flutter condition, it has a more monotonous property than damping. After that, many methods have been developed in time-domain. Yuji Matsuzaki built an ARMA model to random response of aeroelastic model by using RPEM method and Jury criterion was used to determine stability parameter. H. Wendler-Bruce adopted AR model for measured data fitting, and AR coefficients were estimated by Levinson algorithm and also Jury being as the stability criterion. 1986, Dr. Xiao Chuangbai completed the ARMA modeling using Overdetermined Instrumental Variable algorithm and presented a Lyapunov criterion. The authors proposed a fast algorithm integrated data modeling and stability criterion, in which AR and ARMA were considered and the stability parameter were directly obtained from reflection parameter in Lattice algorithm. Several hybrid methods were also developed by authors and used in actual flutter testing. The successful experiences have been accumulated in practice.

Note, although every FBP method has its theoretical principle, the actual prediction results for different methods are usually not consistent, even a big gap among them. It's no doubt that the human experience is a very important factor about how to use FBP techniques and to judge the final flutter speed in engineering application. And so, we need to find a more reasonable FBP technique due to subcritical turbulence response and human experiences. In this paper, traditional damping and SSA methods are reviewed at first. Hybrid FBP problem is discussed and a new method named FBP-NNES is presented. Finally, some suggestions for next research are suggested.

2. DAMPING TECHNIQUES

Basic Description

The basic idea of damping extrapolation is (Fig. 1) : the major flutter modal frequency and damping are firstly obtained, and then the onset speed value is extrapolated by fitting the varied trend of the damping vs speed with zero damping.

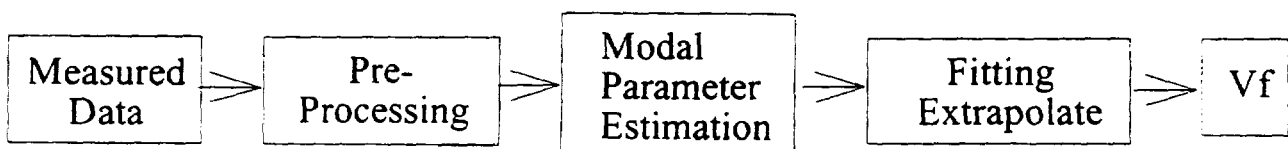


Fig. 1 Damping Prediction Diagram

Pre-processing is a significant but skillful primary work, the purpose of which is improving the quality of measured signal, namely, canceling the unnecessary department or noise and keeping the interested information. Honestly, the foundation of damping prediction is the vibration modal analysis and generally Fourier analysis is used in frequency domain and Random Decrement Technique (RDT) is used in time domain. The important work is how to correctly separate or confirm the structure flutter modes and how to estimate damping parameter. Be careful, the damping value may be not same with the different estimation methods and measured data selected from same testing.

By authors' opinion, the key problem is the variable trend but not the concrete damping value. Because damping is sensitive to noise (from measurement or calculation) and the time-variant in flutter process, the kind of FBP method is not suitable to occasions of closed modal arrangement and sudden flutter.

Frequency Methods

In frequency domain, the data spectrum is first obtained by FFT. Frequency and damping are generally determined from the response peak bandwidth at the half power point. Of course, if the excitation signal is supposed to be available, the approximate transform function method can be used.

In practice, there are many concrete ways to determine modal damping. Sometimes, the equivalent method are also used, such as Peak-Hold, Cross-Spectrum and even to observe the response time history or calculate the points passing zero. Here are several problems should be care when using damping method:

- ▲ The spectrum estimation is the most important step. There are more than ten approaches in modern spectrum analysis, and each of them has its specifics and scope in application. The selection of spectrum estimation method is dependant on data quality, sample internal, data length, modal arranged condition and environment applied. Sometimes several methods may be used at the same time
- ▲ The overlapping rate must be chosen carefully to insure smoothing and an adequate frequency resolution, especially in the case of an aircraft with close modes and low damping.
- ▲ The half power band is derived from system with single degree of freedom. And so, it is careful to face many modes or closed modes.
- ▲ Pre-processing is necessary. Simple technique may be better and more efficiency than a complicated one.
- ▲ Human skills play a very important role in flutter mode confirmation, signal selection, processing strategy and concrete implementation steps.

Time Domain Methods

In time domain, there are also many different ways to get the flutter modal frequency and damping. For examples, Ibrahim Time Domain (ITD) , random process modeling and Random Decrement Technique (RDT). Generally, RDT is widely used in engineering, especially in wind tunnel flutter testing.

What are the problems using RDT? The following viewpoints are suggested:

- ▲ RDT is also derived from system with single degree of freedom and carefully to use under the condition of many modes or closed modes.

- ▲ Human skill is also a very important factor, especially for selecting some related parameter in practice, for example, trigger, the length of the sub-sample and tolerance.
- ▲ The longer data is generally needed to get a smooth Randomdec Signature, from which damping can be obtained by curve fitting or experience formula.
- ▲ Digital FIR bandwidth filter is often used before RDT and right efficiency to those data from high speed wind-tunnel testing because the structural modes of the kind of aeroelastic model can be clearly separated.
- ▲ RDT is a better pre-processing tool to reduce the random noise. And it is possible to partially resolve the closed modes problem by through the integration of RDT and Prony's algorithm.

3. SYSTEM STABILITY ANALYSIS

Basic Description

The basic idea of SSA is shown in Fig. 2. The measured data are used to build a random mathematics model at first. AR parameter is then applied to construct stability criterion, and the relative stability parameter is calculated. The onset speed is finally extrapolated by fitting stability parameter trend vs speed.

The kernel goal of SSA is to generate stability parameter corresponding to damping. In other words, damping is a special stability parameter. According to random process theory, the related pre-processing is also necessary. And fitting extrapolation is same with damping method. We must note the following facts for SSA. A group of model parameter can be used to construct different stability criteria. A criterion may generate many stability parameter with various definition. And the varied trend may be not consistent for different stability parameter, which will directly affect the FBP result. Something for data modeling and stability criterion will be respectively addressed in following sections.



Fig.2 SSA Diagram

Data modeling

About data modeling of SSA, we must decide the kind of model and the order of the model at first. And then, a feasible algorithm will be chosen and used to estimate the model parameter. ARMA (autoregressive moving-average) and AR models are often used in SSA. Because the excitation signal is unmeasured under exact meaning in flutter testing, the parameter estimation of ARMA is a nonlinear problem and little complex in algorithm structure. In fact, system stability or poles distribution is decided by AR part. The characteristic equation and stability criteria are also performed using AR parameter. And thus, AR model is more suitable to application, but the model order may be longer than ARMA.

There exist several criteria to determine model order, such as AIC, BIC and FPE. The principle of these rules requires the fitting error being minimum at a suitable order, and has something to do with algorithm. Except these, the order can be automatically decided for some algorithm. In engineering practice, data spectrum is usually used to judge the order of model.

On algorithm for model parameter estimation, many implementation methods have been developed in the fields of signal processing, system identification and adaptive control. ML (maximum likelihood) and LS (least square) are the general cost criteria on theory. The concrete algorithm must meet the application condition with good numerical specifics. Generally, recursive and adaptive algorithm is considered for real time analysis. From the viewpoint of algorithm structure, free-delay line or transversal filter and lattice are often chosen.

Stability Criteria

Based on the theory of system analysis, the stability criteria of Flutter Margin, Jury and Lyapunov have been developed and used in SSA. The mathematical principles of the criteria are easy to find. A special stability parameter called Reflection Coefficient will be emphasized here. The important contribution of Reflection Coefficient to SSA is making data modeling and stability parameter in one step. The paper's authors completed the related mathematics description and program code[16], and successfully used it to wind-tunnel testing and flight flutter testing supported by Aeronautic Science Foundation of China.

The advantages of Reflection Coefficient are:

- ▲ Reflection Coefficient can be directly obtained before model parameter which needn't to be estimated.
- ▲ AR and ARMA models are covered by lattice algorithm. The model order can be automatically decided by recursive.
- ▲ FBP efficiency is guaranteed and increased by a series lattice algorithm with excellent properties for calculation.
- ▲ Parallel lattice architecture is convenient for Special-purpose hardware implementation.

4. HYBRID FBP

Basic Description

In actual application, the different FBP methods may lead different results. Why? Generally, there are several reasons, including the difference of the theory used, the varied characteristics of the measured data, the restrictions for using and the distinct human experiences or skills.

In many cases, no single technique is sufficient and the use of several techniques is required for reliable flutter onset prediction. To ensure the testing safety and raise the reliability of FBP, scientists and engineer often adopt hybrid method according to their experience in practice. The purpose of damping only synthesis is to get a reasonable damping value. Combination of Damping and SSA is used to choose a suitable FBP value. We will introduce a new hybrid FBP technique integrated much more information in next section.

FBP NNES-based

Aimed to attract the reasonable information from different FBP methods and to bring human experiences into play, a new FBP technique called FBP-NNES based on Neural Network Expert System is proposed by the paper's authors. FBP-NNES is consisted of two kernel parts, namely, Characteristic Information Acquiring (CIA) and NNES, see Fig.3. In CIA, original data will be processed by order and the interested information from time domain and frequency domain will be

carried out. The information is parameterized and optimally synthesized in NNES part, in which the rules from deep knowledge base for theory analysis or shallow knowledge base for human experiences may be adopted. Reasoning Machine is used for rules judgement, trend extrapolation and result confirmation. Finally, FBP value with its occur probability will be presented using statistics analysis and shown on I/O interface to user. The detailed of FBP-NNES on architecture and theory will be found in [35].

The program code of FBP-NNES has been completed. Using computer simulation and a lot of flutter testing data (Low-speed and Transonic Wind-Tunnel, Flight), the related properties on numerical and application are researched, especially, something about prediction accurate, prediction abundance, condition parameter, SNR and data length. The software system also supplies a work station to evaluate various combinations of FBP method and control parameter. For instance, we can change the matter of hybrid or fitting extrapolation by adjusting the corresponding parameter in operation window. The result interface will show us the final prediction speed, probability distribution plot and the distribution map of major modal damping and frequency.

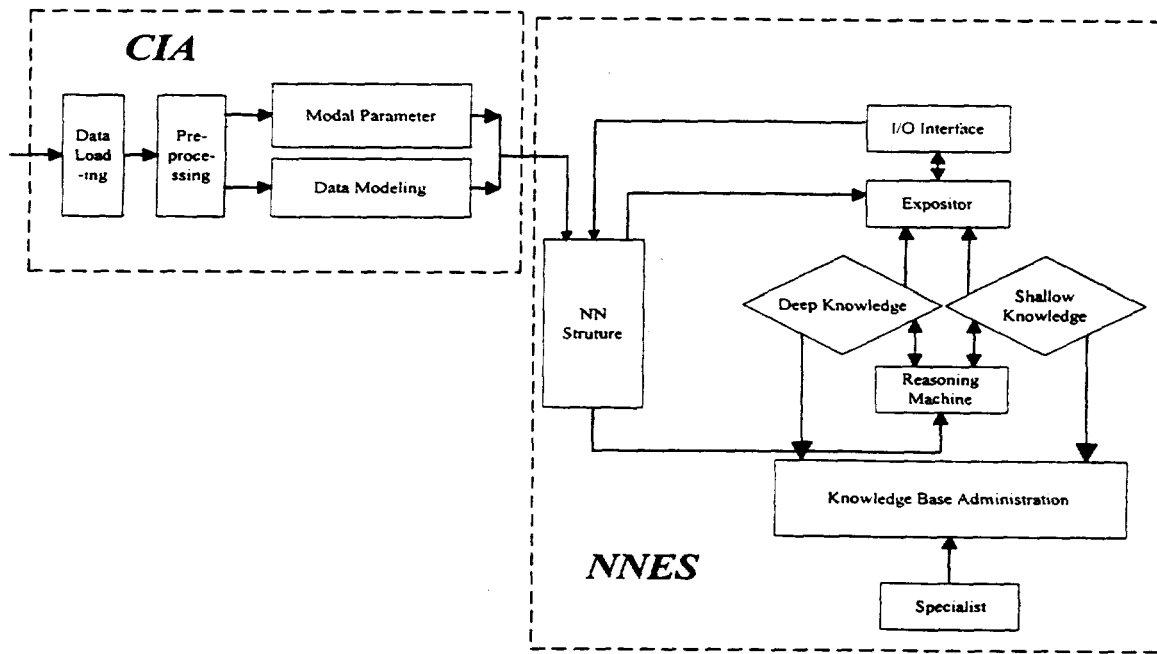


Fig. 3 The basic structure of FBP-NNES

General Discussion

Comparing to other FBP methods, the main advantages of FBP-NNES include:

- ▲ Damping, SSA and human experiences are considered and integrated.
- ▲ AR and ARMA modeling are covered using BP neural network.
- ▲ BP Neural Network is used to complete damping or stability parameter fitting. The accuracy is obviously raised than either linear or quadratic extrapolation.
- ▲ Using Reasoning Machine, the prediction abundance is improved and an early prediction can be obtained.
- ▲ FBP-NNES is developed aimed to the testing excited by airflow turbulence and also suitable to other excitation state.

5. CONCLUTION AND DEVELOPMENT

Flutter testing signal processing has been researched from 1981 in Data Processing Center of Northwestern Polytechnical University of China. A lot of experiences have been accumulated by through various engineering experiments on aeroelastic model and actual aircraft for civil or army aviation. Aimed to the data characteristics and analysis requirements in the fields of classical flutter, ASE and flutter active suppression, a series of techniques have been developed. The theoretical analysis involves modern digital signal processing, adaptive filter, system identification, neural networks, wavelet, chaotic time series analysis, nonlinear realization etc. Four professional software systems are developed. This paper is only a brief summary of our research on FBP. In this paper, the state of the art and the history of FBP techniques are reviewed. Both FBP methods of damping and SSA are generally discussed, and a new FBP method NNES-based is proposed. This paper leaves some questions necessary to be done in the future. Especially, the following subjects will be focused:

- ▲ The operation speed and structure optimization need to be further improved for FBP-NNES.
- ▲ The stability of neural network will be studied and used to predict flutter boundary.
- ▲ Related FBP software and hardware will be developed, which will be directly applied to engineering.

AKNOWLEDGEMENT

The authors gratefully acknowledge the support of K. C. Wong Education Foundation, Hong Kong.

The paper's research has been supported by Aeronautic Science Foundation of China, Chengdu Aircraft Industry Corporation, Shenyang Aircraft Industry Corporation and Xi'an Aircraft Industry Corporation. The authors would like to thank Professor Zhao Lingcheng, Dr. Xiao Chuangbai and other people for very kind of concern and help.

REFERENCE

- [1] Norman H.Zimmerman and Jason T.Weissenbureer, "Prediction of Flutter Onset Speed Based on Flight Testing at Subcritical Speeds", J.Aircraft, Vol.1, No.4, July-Aus.1964. pp.190-202.
- [2] Yuji Matsuzaki , Yasukatsu Ando, "New Estimation Method for Flutter or Divergence Boundary from Random Responses at Subcritical Speed" ,Technical report of national aerospace Laboratory TR-667T,1981.
- [3] Robert M. Bennett, " Application of Zimmenman Flutter-Margin Criterion to a Wind-Tunnel Model ", NASA Technical Memorandum 84545, 1982.
- [4] Charles L.Ruhlin, Judith J.Watsonect, "Evaluation of Four Subcritical Response Methods for On-line Prediction of Flutter Onset in Wind-Tunnel Tests" , AIAA82-0644, 1982.
- [5] H. Wendler-Bruce, " Near-Real-Time Flutter Boundary Prediction from Turbulence Excited Response ", AIAA Paper 83-0814, 1983.
- [6] M. W. Kehoe, "Aircraft Flight Flutter Testing at the NASA Ame-Dryden Flight Research Facility" , AIAA-86-9730.
- [7] Xiao Chuangbai, "Flutter Boundary Prediction for Aeroelastic Mode in Low Speed Wind Tunnel", B. S. Thesis, Northwestern Polytechnical University, 1986.

- [8] Larry Shelly, "Trend in Real-Time Flight Test Systems", American Institute of Aeronautics and Astronautics, 89-3086-cp.
- [9] A. Schenk, Dipl.Ing, "Flutter Analysis from Ambient Random Responses", DGLR-Bericht-89-01, 1989.
- [10] Zeng Qingfu, Pei Chengming and Lu Junming, "Time Domain Method on Flutter or Divergence Boundary Prediction", HJB890690, 1990.
- [11] Pei Chengming and Cheng Bingxun, "A Fast Prediction Method of Flutter Boundary Based on AR Modeling and Lyapunov Stability Criterion", ICAS'92, Beijing, 1992.
- [12] C. G. Pak and P. P. Friedmann, "New Time-Domain Technique for Flutter Boundary Identification", AIAA-92-2102-cp.
- [13] S. J. Price, B. H. K.Lee, "Development and Analysis of Flight Flutter Prediction Methods", AIAA-92-2101-cp.
- [14] C. F. Lo, G. Z. Shi, "Wind-Tunnel Compressor Stall Monitoring Using Neural Networks", Journal of Aircraft, Vol.29, No.4, July-August,1992.
- [15] J. k. Pinkelman, etc., "An Evaluation of Excitation Techniques for Time Based Flutter Data Processing", AIAA-93-1602-cp.
- [16] Pei Chengming and Tan Yunhai, "A New Method Integrated Data Modeling and Stability Criterion for Flutter Boundary Prediction", JSASS 31st Aircraft Symposium, #3A6,Tokyo, Japan, Aug.1993.
- [17] H. Raza, P. Ioannou, etc, "Surface Failure Detection for an F/A-18 Aircraft Using Neural Networks and Fuzzy Logic", IEEE, 0-7803-1901-X/94.
- [18] Pei Chengming, "Fast Time - Series Method of Modal Parameter Estimation", IMAC'93, Florida, USA. Feb. 1993.
- [19] Pei Chengming, He Jun and Ren Hui, "CAT System Design for Flutter Testing in Wind-Tunnel", HJB931186, 1993.
- [20] Pei Chengming, "Flutter Testing Data Processing (FTDP)", Proc. of 8th Aeroelastic Conference of China, Nov. 1993.
- [21] Tan Yunhai and Pei Chengming, "A Method to Determine Flutter Speed Based on Subcritical Sweep Response", Proc. of 8th Aeroelastic Conference of China, Nov. 1993.
- [22] Tan Yunhai and Pei Chengming, "Study of Data Processing Method for Structural Nonlinear Flutter Analysis", JSASS 32nd Aircraft Symposium, Kitakyushu,Japan, Nov.1994.
- [23] He Jun and Pei Chengming, "Applied Investigation of Improving Randomdec Method for Flutter Test in Wind-Tunnel", JSASS 32nd Aircraft Symposium, Kitakyushu, Japan, Nov. 1994.
- [24] Qiu Zhihua and Pei Chengming, "FBP Based on HOPFIELD Neural Networks", Proc. of 9th Aeroelastic Conference, Oct. 1995.
- [25] Tan Yunhai, Pei Chengming and Zzhao Lingcheng, "Study of Dynamic Behavior of a 2d Wing/Store with Freeplay Joint Stiffness", JSASS 33rd Aircraf Symposium, Hiroshima, Japan, Nov. 1995.
- [26] Tang Liyu and Pei Chengming, "Digital Waveletand Application in FTDP", Proc. of 9th Aeroelastic Conference, Oct. 1995.
- [27] Ren Hui and Pei Chengming, "Modal Parameter Estimation for Flutter Test Using Matrix Pencil Approach", IMAC'95, USA. Feb. 1995.
- [28] Dimitris A.Karras, "An Efficient Constrained Training Algorithm for Feedforward Networks",

- IEEE Transactions on Neural Networks. Vol.6, No. 6, November, 1995.
- [29] Hiroshi Torii, Yuji Matsuzaki, "Flutter Boundary Prediction Based on Nonstationary Data Measurement" , AIAA-95-1487-CP, 1995.
- [30] Ren Hui and Pei Chengming, "A Signal Processing Method of Flight Flutter Testing" , JSASS 33rd Aircraft Symposium, Hiroshima, Japan, Nov. 1995.
- [31] Pei Chengming, "Flutter Testing Signal Analysis with Wavelet and Hopfield Neural Network" , JSASS 33rd Aircraft Symposium, Hiroshima, Japan, Nov. 1995.
- [32] Pei Chengming, etc., "An Evaluation of Real Time Flutter Boundary Prediction System" , The Proc. of 10th International Sessions, The 34th Aircraft Symposium, Tottori, Japan, 1996.
- [33] Brenner, Martin J., Lind, Richard C., Voracek, David F., "Overview of Recent Flight Testing Research at NASA Dryden" , Conference Paper NASA-TM-4792, 3, 1997.
- [34] DePold, etc, "Application of Expert Systems and Neural Networks to Gas Turbine Prognostics and Diagnostics" , American Society of Mechanical Engineers (Paper) n GT 1998. ASME, Fairfield, NJ, USA. 98-GT-101.
- [35] Zhai Kun, "FBP-NNES Method due to Turbulence Excitation" , B. S. Thesis, Northwestern Polytechnical University, 1998.

Aeroelasticity Simulations in Turbulent Flows

Jean-Pierre Grisval, Cédric Liauzun

523-34

Office National d'Etudes et de Recherches Aérospatiales
B.P. 72, 92322 Châtillon cedex, France

Zdeněk Johan

Centric Engineering Systems, Inc.
624 East Evelyn Avenue, Sunnyvale, CA 94086, USA

April 7, 1999

Abstract. Unsteady turbulent flow calculations involving moving boundaries and fluid-structure interaction problems are solved using a finite element method and Spalart-Allmaras and $k-\varepsilon$ turbulence models. These models are tested on buffeting problems with 2D airfoils. Wall functions have been implemented for both turbulence models in order to perform 3D simulations with the Dyvas wing.

1. Introduction

The objective of this study is to develop numerical techniques for performing aeroelasticity simulations with turbulent viscous flow models using the multiphysics software SpectrumTM. This software developed and commercialized by Centric Engineering Systems, Inc. is based on the finite element method for both aerodynamic and structural analyses. It is therefore able to handle unstructured meshes. Two turbulence models have been used in this study:

1. the Spalart-Allmaras model, which is a one-equation model solving for the turbulent kinematic viscosity
2. the classical two-equation $k-\varepsilon$ model.

In order to perform three-dimensional simulations with a reasonable number of mesh nodes, wall functions have been implemented for both turbulence models.

An outline of this paper follows: After a brief description of the numerical techniques relevant to fluid-structure interactions problems, we present numerical results for fluid-structure interaction involving the RA16SC1 airfoil and the DYVAS wing.

2. Numerical approach

We present in this section a brief description of the numerical techniques implemented in the Spectrum software and applied to the present project.

2.1. Fluid analysis

The compressible Navier-Stokes equations written in a symmetric form [6] in an arbitrary Lagrangian-Eulerian (ALE) frame of reference are used to model the fluid flow. The ALE formulation is used to take into account the deformation of the structure imbedded in the fluid domain. Moreover, the fluid is modeled as an ideal gas and the stress tensor is that of a Newtonian fluid.

$$\tau_{ij} = \lambda u_{k,k} \delta_{ij} + \mu(u_{i,j} + u_{j,i}) \quad (1)$$

where λ is determined by the Stokes law ($\lambda + 2\mu/3 = 0$) and μ by the Sutherland's law.

Spatial discretization of the Navier-Stokes equations is done using the Galerkin/least-squares (GLS) finite element formulation [5]. Time discretization is done using the Hilbert-Hughes-Taylor (HHT) algorithm [4] based on Newmark's implicit scheme. Both spatial and temporal discretizations of the finite element formulation lead to a nonlinear system of equations to be solved at each time-step. This system is linearized through a Newton-like algorithm, yielding a series of nonsymmetric linear systems of equations. Each system is solved using a matrix-free implicit iterative solver based on the preconditioned GMRES algorithm with a tolerance ranging from 10^{-1} for static problems to 10^{-2} for dynamic problems.

The mesh deformation approach used in this study models the fluid domain as a hyperelastic material (i.e., a rubber-like material) and uses a large-deformation neo-hookean formulation. Displacements of mesh nodes are computed using a preconditioned conjugate gradient algorithm with a tolerance usually of the order of 10^{-3} .

2.2. Turbulence models

Two turbulence models have been used in this study: the classical two-equation $k-\varepsilon$ model and the Spalart-Allmaras model.

The $k-\varepsilon$ model is a "low Reynolds" model based on the Chien's formulation [2,12]. The variables k and ε are computed in down to the wall, thus requiring a very fine mesh near the no-slip wall. The first grid point away from wall should be such that $y^+ < 0.5$. The partial differential equations within $k-\varepsilon$ are coupled. They are solved using a GLS formulation like the one for the Navier-Stokes equations. But the turbulence equations are uncoupled from the Navier-Stokes equations and solved in a staggered fashion. The linearized systems from the turbulence equations are solved using a GMRES algorithm.

The Spalart-Allmaras model [10] was developed by Boeing at the beginning of the 1990's to compute external turbulent flows. It is a one-equation model that governs the kinematic viscosity. We can note that:

1. The model does not require the knowledge of any non local quantity like thickness of the boundary layer. It is then more useful for unstructured meshes than algebraic models like the Baldwin-Lomax model.
2. The kinematic viscosity is linear close to the no-slip wall. The model therefore requires less refined meshes than the $k-\varepsilon$ model to reach the same accuracy. Reasonable solutions can be obtained with the first grid point as far away from the wall as $y^+ = 5$ to 10 and $y^+ = 20$ if only pressure is of interest.
3. The model is based on only one equation to solve. It is considerably less expensive computationally than the $k-\varepsilon$ model. Moreover the use of iterative solvers is easier.

In order to perform three-dimensional simulations with a reasonable number of mesh nodes, wall functions have been implemented for both turbulence models. In the wall function approximation, the fluid is assumed to follow the "law of the wall" in the finite elements adjacent to solid boundaries. In these elements, the flow is determined by Spalding's law [13]:

$$y^+ = u^+ + e^{-\kappa B} \left(e^{\kappa u^+} - 1 - \kappa u^+ - \frac{(\kappa u^+)^2}{2} - \frac{(\kappa u^+)^3}{6} \right) \quad (2)$$

with $y^+ = \rho y u^* / \mu$; $u^+ = \|u\| / u^*$; $\kappa = 0.41$ et $B = 5.0$. The values of y and $\|u\|$ being known, the shear velocity is deduced from (2) with a Newton method. The wall friction is given by

$$\tau_n = -\rho u^{*2} \frac{u}{\|u\|} \quad (3)$$

This approximation leads to having both a slip-velocity Dirichlet boundary condition to satisfy the condition of zero mass flux, and a friction Neuman boundary condition by specifying

$$\int_{\Gamma_{wall}} \mathbf{F}_i^{diff} n_i d\Gamma = \int_{\Gamma_{wall}} \begin{Bmatrix} 0 \\ \tau_n \\ \tau_n \cdot \mathbf{u} - q_n \end{Bmatrix} d\Gamma \quad (4)$$

where q_n is the heat flux at wall.

2.3. Structural analysis

A large-deformation elasticity formulation is used to model the structural part of aeroelastic problems [11]. Structures can be modeled either with three-dimensional continuum elements, or with structural elements such as shells, beams or trusses. Time-marching is performed with an

implicit integrator based on the HHT algorithm. This semi-discrete scheme is identical to the one used for the fluid equations, which simplifies the overall time-marching process when solving coupled aeroelastic problems. Due to ill-conditioning that arises when the solid is discretized with non-continuum elements, a sparse direct solver is used to solve the linear systems of equations resulting from discretization of the variational formulation.

2.4. Fluid-solid interface

The interface region between the fluid domain and the solid domain is defined by:

1. a list of nodes and element faces on the fluid side; and
2. a list of nodes and element faces on the solid side.

Since nodes on both sides of the interface do not need to match, a search algorithm is used to identify the solid face that contains each fluid interface node. Once this mapping is obtained, local fluid pressure forces are computed at each fluid interface node. They are then interpolated at the solid interface nodes. The resulting pressure load is used as a boundary condition to solve the structural analysis problem. One can note that this approach leads to a total fluid pressure force (i.e., the pressure integrated over the fluid side of the interface) being transferred to the solid side of the interface. Since the fluid mesh is usually finer than the solid mesh (which translates into having a finer fluid surface mesh at the fluid-solid interface), this interpolation strategy would appear to be more accurate than interpolating the fluid pressure directly onto the solid interface nodes and then computing the local pressure forces on that surface using the solid discretization.

In addition to pressure loading on the solid, a velocity boundary condition is applied at the fluid interface nodes. This boundary condition is:

1. $\mathbf{u} = \mathbf{w}$ for a no-slip boundary condition; or
2. $(\mathbf{u} - \mathbf{w}) \cdot \mathbf{n} = 0$ for a slip boundary condition.

Finally, the solid displacement is interpolated at the fluid interface nodes and is used as a boundary condition when solving the mesh deformation problem.

3. Numerical examples

3.1. Buffeting of the RA16SC1 Airfoil

Experiments in a wind tunnel at ONERA show oscillations of the shock at a single frequency of about 100 Hz for a Mach of 0.73 and an angle of attack greater than 3 degrees. The amplitude of the oscillations is about 40% of chord. The fluid flow has the following free-stream conditions:

- $M_\infty = 0.73$

- $Re_\infty = 4.6 \times 10^6$

- $T_{i\infty} = 290.0$ K

The airfoil chord is 180 mm.

Two numerical simulations at an angle of attack of 3 degrees are done to test the Spalart-Allmaras and $k-\epsilon$ models. The first simulation uses the Spalart-Allmaras model. The fluid domain is discretized with 17538 nodes and 17180 wedge elements. Even though this is a two-dimensional problem, three-dimensional meshes made of one layer of elements together with appropriate boundary conditions are generated since Spectrum has only three-dimensional capabilities. The following boundary conditions are applied:

- velocity and static temperature at the inflow
- static pressure at the outflow
- no slip velocity at the wall.

A steady flow is first computed using a local time-stepping and a CFL set to 5. The solution of the 200th time-step initializes the unsteady computation using a global time-step. The experimental frequency f_0 being 108 Hz, the numerical time increment is chosen such that

$$\Delta t = \frac{1/f_0}{1000} = 9.2 \times 10^{-6} \text{ s}$$

The computation does not show any buffeting. The steady case converges well, but the shock oscillations in global time-stepping are rapidly damped. The same results are obtained on a finer mesh or at a greater angle of attack. The Spalart-Allmaras model developed for steady computations does not seem to be appropriate for buffeting simulations.

The second computation using the $k-\epsilon$ model follows the same strategy. The mesh is refined close to wall and contains 25396 nodes and 25014 elements (see figure 1). The local time-step is determined by a CFL equal to 3. The steady computation does not converge (oscillations of residuals of pressure velocity and temperature). The computation is restarted with a global time increment chosen to have 4000 time-steps per period id est $\Delta t = 2.3 \times 10^{-6}$ s. The results illustrated by figures 2 and 4 show that the shock oscillates between 35% and 60% of chord with a frequency of 95 Hz.

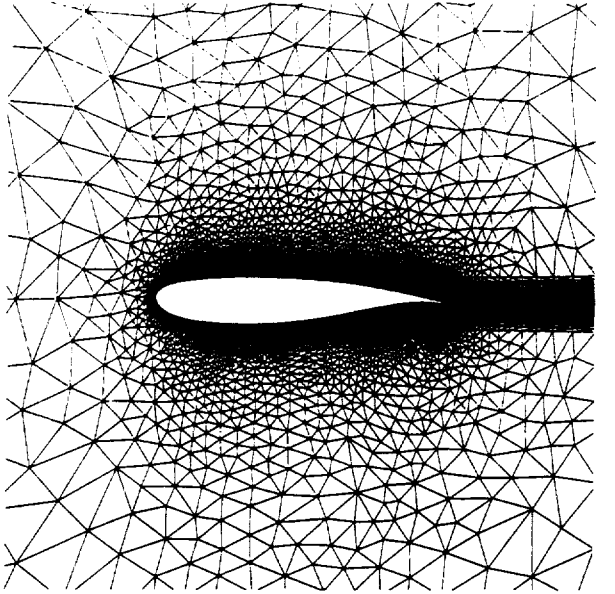


Figure 1. Fluid mesh around RA16SC1 airfoil

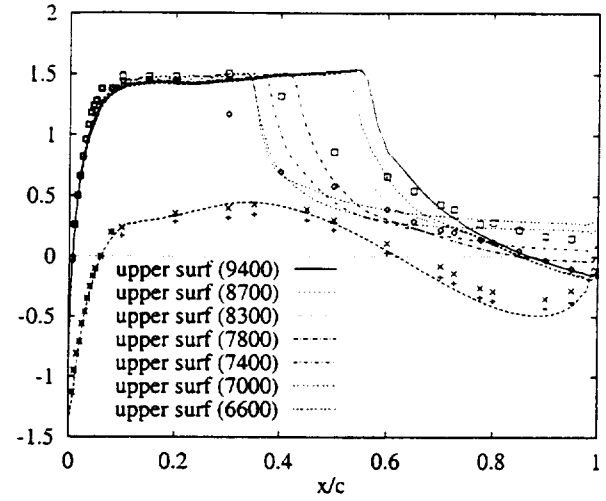


Figure 2. Chord-wise C_p distribution

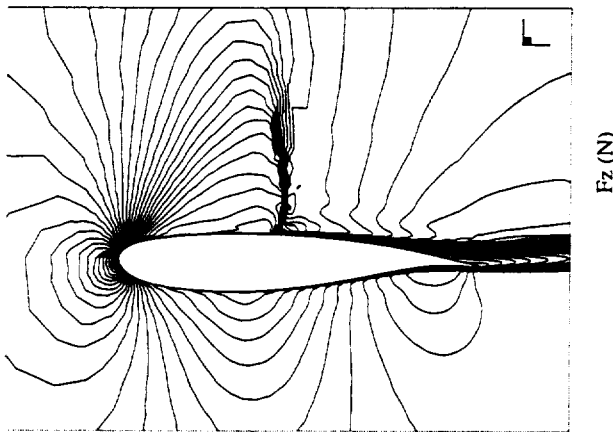


Figure 3. turbulent ($k-\epsilon$) mach contours

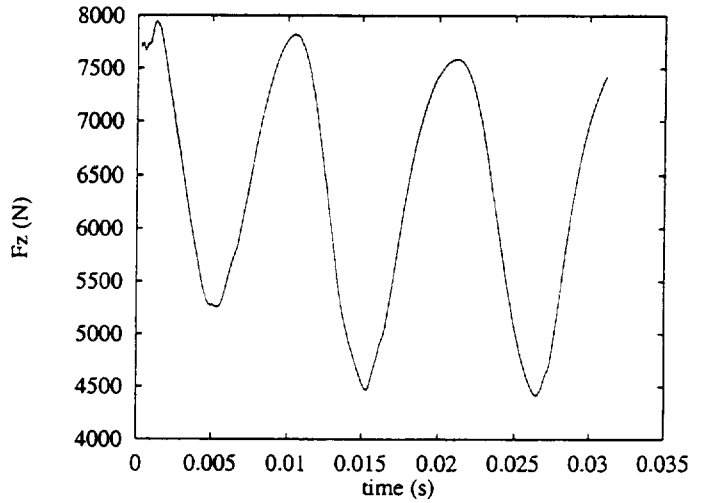


Figure 4. Lift ($k-\epsilon$ model)

3.2. Buffeting of the DYVAS Airfoil

The same computation is done with a 2D airfoil that is deduced from the 3D wing using similarity relations and corresponds to the section at 66% of wing. The similarity relations give the flow conditions:

$$\begin{cases} M_{3D\infty} = 0.82 \\ Re_{3D} = 2 \times 10^6 \\ \alpha_{local3D} = 2.72^\circ \end{cases} \rightarrow \begin{cases} M_{2D\infty} = 0.737 \\ Re_{2D} = 1.165 \times 10^6 \\ \alpha_{local2D} = 3.02^\circ \end{cases}$$

The $k-\varepsilon$ model with wall functions is used with a mesh of 14884 nodes and 14546 elements. The first layer is 5×10^{-4} chord thick (figure 5). The first 1500 time-steps are computed with local time-stepping and CFL set to 3. The following time-steps are computed with a global time increment such that

$$\Delta t = \frac{1/f_0}{2000} = 1.0 \times 10^{-5} \text{ s}$$

where the experimental shock oscillation frequency is $f_0 = 50 \text{ Hz}$.

The computed frequency of the oscillations of lift is 45 Hz, close to the experimental results (see figures 6 and 7).

For the next simulation with the same model, a pitching motion is imposed on the airfoil following the law:

$$\begin{cases} \alpha(t) = \alpha_{2D\infty} + \alpha_{amp} \sin^2(2\pi ft) & \text{for } t < 1/(4f) \\ \alpha(t) = \alpha_{2D\infty} + \alpha_{amp} \sin(2\pi ft) & \text{for } t \geq 1/(4f) \end{cases}$$

where $\alpha_{amp} = 0.2^\circ$. The law in \sin^2 allows a zero initial velocity. The simulation is initialized with a steady case for an angle of attack of $\alpha_{2D\infty}$. This case is computed for the frequencies $f = 40 \text{ Hz}$ and $f = 60 \text{ Hz}$. The computed lift frequencies for the cases at 40 Hz and 60 Hz are respectively 42 Hz and 47 Hz (figure 8).

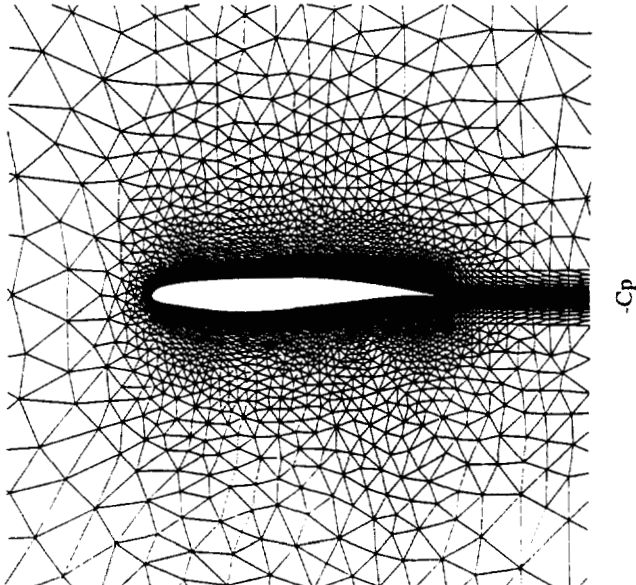


Figure 5. Fluid mesh around Dyvas airfoil

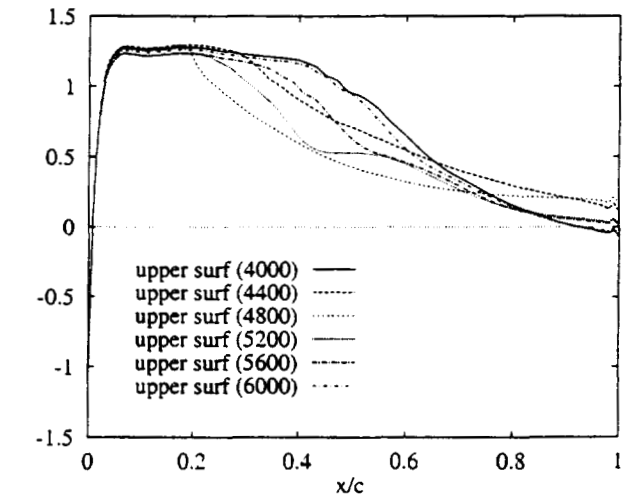


Figure 6. Chord-wise C_p distribution

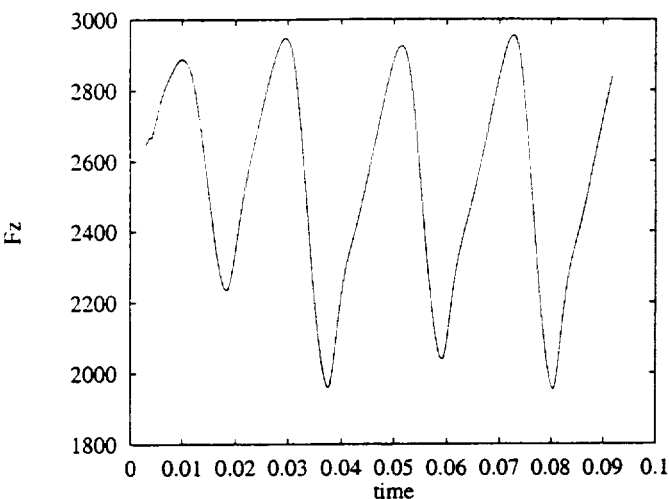


Figure 7. Lift ($k-\varepsilon$ model)

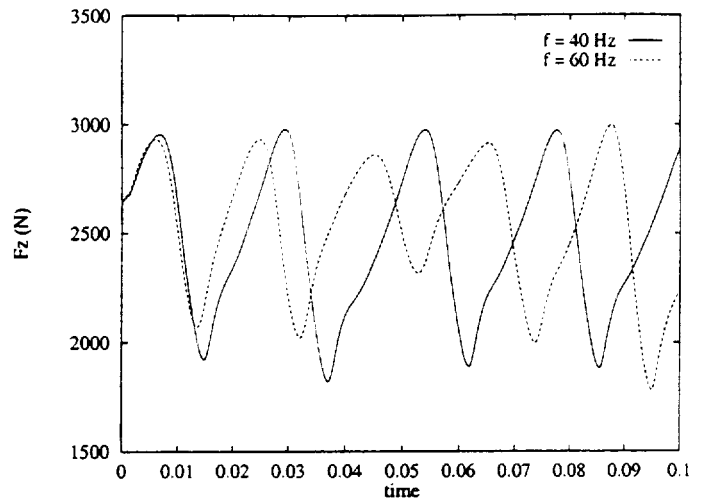


Figure 8. Unsteady lift

3.3. 3D viscous flow around the DYVAS wing

The objective of this numerical example is to perform the coupled fluid-structure interaction analysis with a viscous flow model. Fluid flow accuracy near walls is achieved by generating layers of 6-noded wedge elements. An unstructured fluid mesh made of 229,000 nodes, 344,000 tetrahedra and 321,000 wedges was generated around the DYVAS wing model [14] (see Figure 9). The structural mesh has about 2,500 shell elements and 22 beams (see Figure 10). The characteristics of the structural wing are defined such that the numerical first two modes are identical to the experimental ones. The frequency of the first bending mode is 23.4 Hz, and the one of the first pitching mode is 31.8 Hz. The turbulent viscous flow around the undeformed wing using the $k-\varepsilon$ model with wall functions is initially computed. The pressure distribution along the wing chord at a given section is shown in figure 11. An unsteady fluid-structure computation with an initial velocity applied at the wing requires a time increment of 2×10^{-6} s, which leads to 10000 time-steps per period. It would require too much CPU-time for the currently available computers.

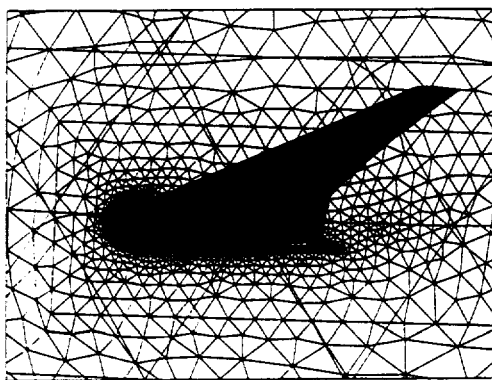


Figure 9. Fluid mesh around the Dyvas wing

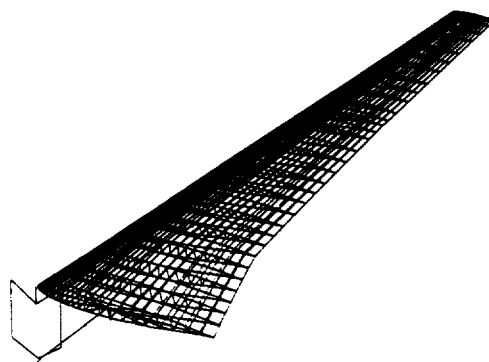


Figure 10. Dyvas wing structural model

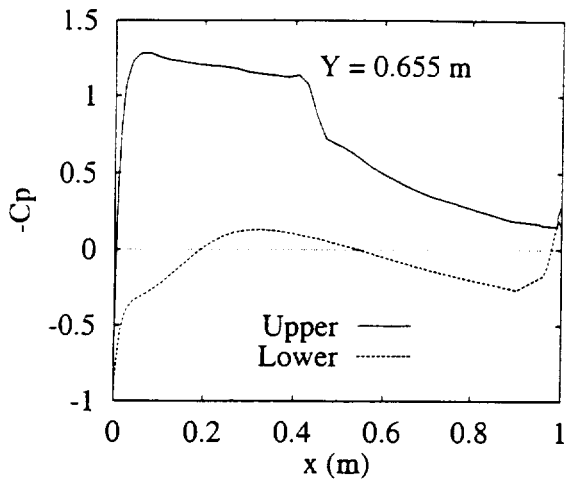


Figure 11. Chord-wise C_p distribution

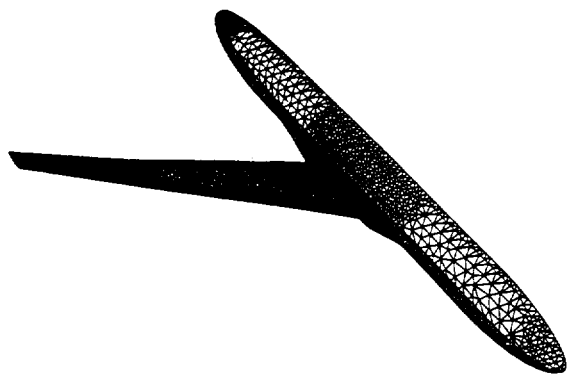


Figure 12. Dyvas wing-fuselage configuration

A steady fluid-structure computation is performed for a wing-fuselage configuration using the Spalart-Allmaras model with wall functions at Mach = 0.78. The structural model is the same as the one of the previous simulation. The fluid domain is discretized with about 88,600 nodes, 42,300 wedges (it corresponds to 3 layers around the wing) and 364,000 tetrahedra (see figure 12). The pressure distribution along the wing chord at a given section is shown in figure 13, and the deformed wing is shown in figure 15. An unsteady computation leads to a time increment too small to perform the simulation.

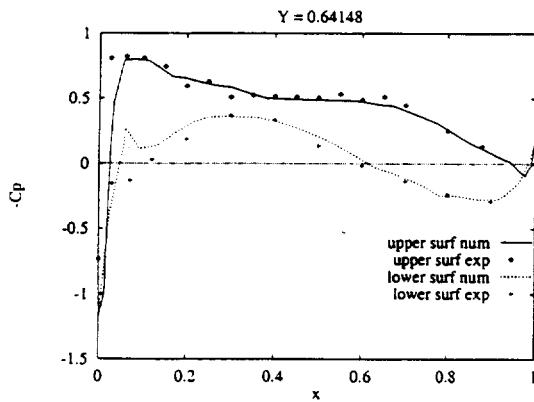


Figure 13. Chord-wise C_p distribution

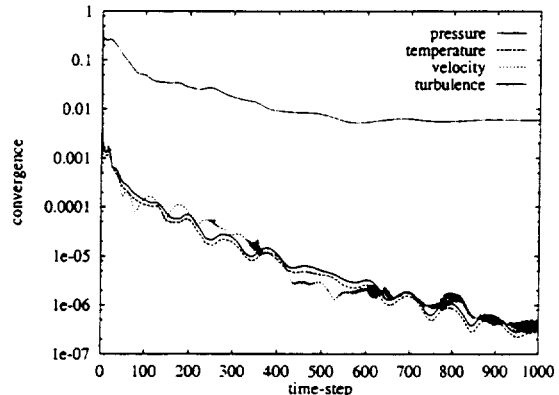


Figure 14. Convergence of steady case

4. Conclusions

Numerical simulations have allowed us to test the Spalart-Allmaras and $k-\epsilon$ turbulence models on buffeting and fluid-structure interaction problems. The numerical solutions obtained with $k-\epsilon$ model for buffeting are close to the experimental data, whereas the shock oscillations on upper

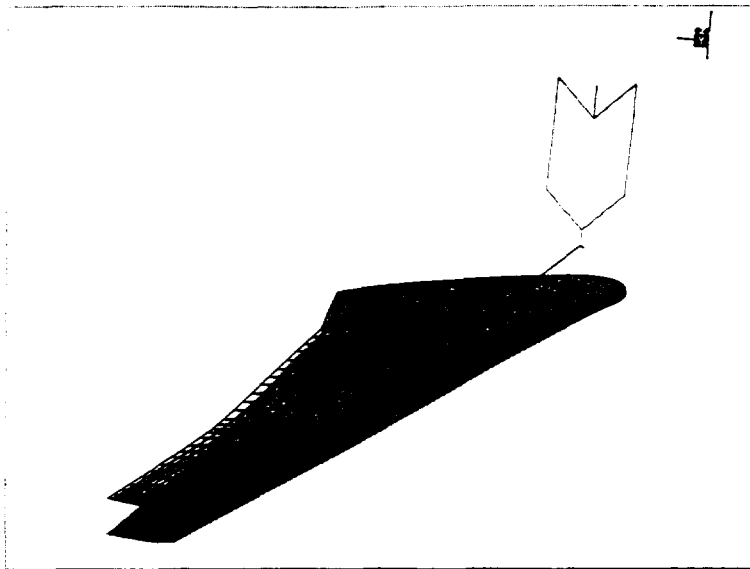


Figure 15. Deformed wing (wing-fuselage configuration)

surface are damped by Spalart-Allmaras model. Wall functions have been developed to make 3D fluid-structure computations possible. Both Spalart-Allmaras and $k-\varepsilon$ models give good steady solutions. But unsteady computations still require too many time-steps to obtain results in a reasonable time.

References

- [1] R.L. Bisplinghoff and H. Ashley, *Principles of Aeroelasticity*, John Wiley and Sons, 1962.
- [2] K.Y. Chien, "Predictions of channel and boundary layer flows with a low-Reynolds-number turbulence model," *AIAA journal*, 20 (1982), 33-38.
- [3] C. Farhat, M. Lesoinne and N. Maman, "Mixed explicit/implicit time integration of coupled aeroelastic problems: three-field formulation, geometric conservation and distributed solution," *International Journal for Numerical Methods in Fluids*, 21 (1995) 807-835.
- [4] T.J.R. Hughes, *The Finite Element Method: Linear Static and Dynamic Finite Element Analysis*, Prentice-Hall, 1987.
- [5] T.J.R. Hughes, L.P. Franca and G.M. Hulbert, "A new finite element formulation for computational fluid dynamics: VIII. The Galerkin/least-squares method for advective-diffusive equations," *Computer Methods in Applied Mechanics and Engineering*, 73 (1989) 173-189.
- [6] T.J.R. Hughes, L.P. Franca and M. Mallet, "A new finite element formulation for computational fluid dynamics: I. Symmetric forms of the compressible Euler and Navier-Stokes equations and

- the second law of thermodynamics," *Computer Methods in Applied Mechanics and Engineering*, **54** (1986) 223–234.
- [7] T.J.R. Hughes, L.P. Franca and M. Mallet, "A new finite element formulation for computational fluid dynamics: VI. Convergence analysis of the generalized SUPG formulation for linear time-dependent multidimensional advective-diffusive systems," *Computer Methods in Applied Mechanics and Engineering*, **63** (1987) 97–112.
 - [8] T.J.R. Hughes and M. Mallet, "A new finite element formulation for computational fluid dynamics: III. The generalized streamline operator for multidimensional advection-diffusion systems," *Computer Methods in Applied Mechanics and Engineering*, **58** (1986) 305–328.
 - [9] G.D. Mortchelewicz, "Résolution des équations d'Euler tridimensionnelles instationnaires en maillage non structuré," *La Recherche Aérospatiale*, **6** (1991) 17–25.
 - [10] P.R. Spalart and S.R. Allmaras, "A one-equation turbulence model for aerodynamic flows," AIAA paper 92-0439, 1992.
 - [11] *Spectrum Solver Theory Manual*, Centric Engineering Systems, 1993.
 - [12] B.E. Launder and D.B. Spalding, "The numerical computation of turbulent flows," *Computer Methods in Applied Mechanics and Engineering*, **3** (1974) 269–289.
 - [13] F.M. White, *Viscous fluid flow*, McGraw-Hill, 1991.
 - [14] H. Zingel et al., "Measurement of steady and unsteady airloads on a stiffness scaled model of a modern transport aircraft wing," *International Forum on Aeroelasticity and Structural Dynamics*, DGLR-Bericht 91-06, 120-131, 1991.

Active Control of Flutter in Compressible Flow and Its Aeroelastic Scaling

E. Presente* and P. P. Friedmann†
 Mechanical and Aerospace Engineering Dept.
 University of California
 Los Angeles, California 90095 – 1597

ABSTRACT

Active flutter suppression of a two dimensional wing section in subsonic flow is studied. Pitch and plunge dynamics, combined with a trailing-edge control surface is considered. Aerodynamic loads are expressed in time-domain using Roger's approximation. Augmented aerodynamic states are reconstructed using a Kalman filter, and linear optimal control is used to design a full-state feedback regulator for flutter suppression. Constraints on actuator deflection and rate limit the flutter envelope expansion. A new two-pronged approach to developing aeroelastic and aeroservoelastic scaling laws is presented and applied to a typical example.

Flutter suppression for a typical cross-section with a conventional trailing edge control surface is compared with that obtained with piezoelectric actuation utilizing bend/twist coupling on a finite span composite wing. Power consumption and its scaling for these two cases is compared.

NOMENCLATURE

a	Nondimensional offset between elastic axis (EA) and midchord
[A]	System matrix
[A_H]	Hamiltonian system matrix
b	Airfoil semi chord
[B]	Open-loop control matrix in state space
C_h, C_l, C_m	Hinge moment, lift and pitch moment coefficients per unit span

*Research Associate

†Currently François-Xavier Bagnoud Professor,
 Dept. of Aerospace Engineering,
 University of Michigan,
 Ann Arbor, MI 48109-2140

C_P, \bar{C}_P	Power coefficient and its average value
c_β	Nondimensional flap hinge location
$C(k)$	Theodorsen's lift deficiency function
$[C_0], [C_1], [C_2]$	
$[\bar{D}], [\bar{E}], [\bar{R}]$	Constant aerodynamic matrices in state-space formulation
$[C]$	Observation matrix ($y(t) = [C]\{x(t)\}$)
$[F]$	Control law gain matrix
G_{LT}	Shear modulus of composite material
G_H	Shear modulus of honey comb
G	Shear modulus of plate wing section
h, h_0	Plunge displacement at the EA, and its initial condition
H, \bar{H}	Hinge moment per unit span and its nondimensional value
I_{EA}	Wing section mass moment of inertia about its EA, per unit span
I_β	Control surface mass moment of inertia about its hinge, per unit span
J	Cost function
J_p	Cross section polar moment of inertia
k	Reduced frequency ($= \frac{\omega b}{V}$)
K_h	Spring stiffness in plunge
K_α	Spring stiffness in torsion
K_β	Control surface torsional stiffness
$[\bar{K}]$	Typical wing section nondimensional stiffness matrix
$[K]$	Modified wing section nondimensional stiffness matrix
L	Lift force per unit span
m	Wing section mass per unit span
M	Mach number
M_{EA}	Pitch moment per unit span acting at the EA
$[\bar{M}]$	Nondimensional mass matrix
$[M]$	Modified nondimensional mass matrix
p, \bar{p}	Pressure and its nondimensional value ($= \frac{p}{\frac{1}{2}\rho V^2}$)
P, \bar{P}, \bar{P}_{av}	Power, its nondimensional and average nondimensional value
$[P]$	Riccati matrix
$[Q]$	Observer Riccati matrix
$\{q\}$	Displacements vector
r_α	Wing section radius of gyration about its EA
r_β	Flap radius of gyration about its hinge
s, \bar{s}	Laplace variable and its modified value ($\bar{s} = \frac{b}{V}s$)
t, \bar{t}	Time and its nondimensional value
$\bar{t}_i, \bar{t}_f, \bar{t}_1, \bar{t}_2$	Various nondimensional time points

t_C	Composite material ply thickness
t_H	Honey comb thickness
t_t	Total airfoil thickness
$T_1 \dots T_{19}$	Coefficiens for Theodorsen's theory
V, \bar{V}	Free stream velocity and its nondimensional value ($= \frac{V}{\omega_a b}$)
V_D, \bar{V}_D	Divergence velocity, and its nondimensional value
V_F, \bar{V}_F	Flutter velocity, and its nondimensional value
$[V_1], [V_2]$	State excitation noise intensity, and measurement noise intensity
$\{x\}$	State vector
x_α	Nondimensional static moment of the airfoil about its EA, for undeflected flap
x_β	Nondimensional static moment of the flap about its hinge axis
y	Output measurement
α	Airfoil angle of attack
β	Flap deflection angle
ζ	Damping coefficient
η_a	Augmented aerodynamic state vector
θ_f	Flap hinge location
μ	Mass ratio ($= \frac{m}{\pi \rho b^2}$)
ξ	Nondimensional plunge displacement ($= \frac{h}{b}$)
ρ	Air density
ϕ_1, ϕ_2	Phase lag angles
ω_h	Natural frequency in plunge ($= \sqrt{\frac{K_h}{m}}$)
ω_α	Natural frequency in pitch ($= \sqrt{\frac{K_\alpha}{I_{EA}}}$)
ω_β	Natural frequency of flap ($= \sqrt{\frac{K_\beta}{I_\beta}}$)
()	Nondimensional time derivative $\frac{d(\cdot)}{dt}$

INTRODUCTION

The field of aeroservoelasticity has been one of the central subjects in aeroelasticity during the last thirty years; excellent surveys on aeroservoelasticity can be found in Refs. 1, 2 and 3. Early theoretical and experimental studies in aeroservoelasticity were performed in frequency domain. This approach was dictated by the frequency domain unsteady aerodynamic theories, limited to simple harmonic motions, that were in widespread use until the mid 70's^{4, 5}. Aeroservoelastic studies performed in frequency domain are inconvenient since they provide limited information on system behavior before and after flutter. Edwards⁶ was among the first to recognize the need for time domain aerodynamics in aeroservoelasticity and by developing the time domain approximation to earlier frequency domain theories, he initiated the use of multi-input multi-output control laws for flutter suppression. Roger⁷

extended Edwards approach and used it to demonstrate active flutter suppression in a flight test. Since then numerous studies have been conducted to demonstrate active flutter suppression in flight, or in wind tunnel tests.

Recent advances in the area of smart structures, have led to the use of such materials, as actuators for aeroservoelastic applications. The attractiveness of such materials is their potential for introducing continuous structural deformations of the lifting surface that can be exploited to manipulate the unsteady aerodynamic loads and prevent undesirable aeroelastic effects such as flutter. Some of the more notable studies in this area include the work of Ehlers and Weisshaar⁸ that has analyzed the application of piezoelectric materials to the control of static aeroelastic problems in a composite wing. Heeg et al^{9,10} have conducted several studies demonstrating flutter suppression using piezoelectric actuation on small scale wind tunnel models, in incompressible flow. Other studies¹¹ have also looked into static aeroelastic control using piezoelectric actuation. Later this research has been extended to flutter suppression using piezoelectric actuation¹²⁻¹⁴, culminating in a wind tunnel test of a swept wing, controlled by piezoelectric patches. An increase in flutter dynamic pressure of approximately 12% was demonstrated in these tests¹⁵. While the potential of piezoelectric actuators in aeroservoelasticity is substantial, currently such materials have major limitations on their stroke and force producing capabilities. Therefore most of the successful demonstration tests were conducted on small models, in incompressible flow. Aeroelastic scaling has been disregarded and the question of how one would scale such actuators for different sized models, or an actual full scale vehicle has not been carefully addressed.

During the last forty years aeroelastically scaled wind tunnel models have been widely used in testing, and aeroelastic scaling laws that enable one to relate wind tunnel test results to the behavior of the full scale system have played an important role in aeroelasticity. Such scaling laws have relied on dimensional analysis to establish a set of scaling parameters used for aeroelastically scaled models, suitable for wind tunnel testing¹⁶⁻¹⁸. More refined laws can be obtained using similarity solutions, which represent closed form solutions to the equations of motion. However, for complex aeroelastic problems such solutions are impractical¹⁹. It is important to emphasize that since the 60's practically no research has been done on aeroelastic or aeroservoelastic scaling.

The general thrust of this paper is the development of innovative scaling laws for aeroelastic problems in compressible flow, where control is implemented either by conventional trailing edge surfaces (i.e. flaps) or by piezoelectric induced actuation, so as to expand the flutter margin. A two-pronged approach is used, in which basic similarity laws are obtained using typical cross sectional information and dimensional analysis, resembling the conventional, or classical, approach. In parallel simulations, playing the role of "similarity solutions", are obtained for each of the aeroservoelastic problems for which innovative scaling laws are desired.

To achieve this general objective several specific goals are pursued, namely: (1) development of a time domain based aeroservoelastic simulation capability for a typical cross-section in compressible flow, using optimal control theory and a conventional trailing edge flap/control device; (2) present a new, two pronged, approach for the development of modern aeroelastic scaling laws and implement it for the aeroservoelastic problem being considered; (3) development of scaling laws for aeroservoelastic problems, emphasizing scaling requirements for actuator forces, hinge moments and power, using the simulation capability

developed; and (4) application of the tools developed to several sample problems.

This research shows how results obtained from aeroservoelastic testing, conducted on small aeroelastically scaled wind tunnel models, can be related to much larger models or the full scale vehicle. Thus, the paper constitutes an important contribution to the state of the art.

AEROSERVOELASTIC MODEL

Aeroelastic Model

The aeroelastic model consists of a typical cross-section of a wing with plunge and pitch degrees of freedom, combined with a trailing edge control surface representing an actively controlled flap, as shown in Fig. 1. The equations of motion of the system are obtained from Lagrange's equations. The equations, in nondimensional matrix form, with viscous damping terms are:

$$[\bar{M}] \ddot{\{q\}} + [\bar{C}] \dot{\{q\}} + [\bar{K}] \{q\} = \frac{\bar{V}^2}{\pi\mu} \begin{Bmatrix} -C_l \\ 2C_m \\ 2C_h \end{Bmatrix} \quad (1)$$

where the nondimensional time $\bar{t} = \omega_a t$ is used. The damping matrix $[\bar{C}]$ is given by:

$$[\bar{C}] = 2 \begin{bmatrix} \frac{\omega_h}{\omega_a} \zeta & 0 & 0 \\ 0 & \zeta & 0 \\ 0 & 0 & \frac{\omega_p}{\omega_a} \zeta \end{bmatrix} \quad (2)$$

The unsteady aerodynamic loads in Eq. (1), can be obtained by various methods. For incompressible flow Theodorsen's theory²⁰ is used, while for the compressible case the doublet-lattice method (DLM)²¹ is a convenient tool for generating frequency domain oscillatory loads. The general form of the compressible aerodynamic loads acting on a typical section is given in Ref. 16. The pressure distribution over the airfoil is related to the downwash velocity through a kernel function, given by:

$$\bar{w}(x) = \frac{1}{8\pi} \int_{-b}^b K(x, \eta, k, M) \bar{p}(\eta) d\eta \quad (3)$$

In the DLM, the airfoil is divided into segments, and downwash boundary conditions, at each segment are imposed. The solution obtained from Eq. (3) yields the distribution of pressure over the airfoil for a given Mach number, reduced frequency and location of flap hinge combination, for a kernel function, $K(x, \eta, k, M)$, given in Ref. 16 (pg. 235). Once the pressure distribution over the airfoil is found, aerodynamic loads - lift, pitching moment and hinge moment are found from an appropriate integration process.

The frequency domain aerodynamic loads are transformed into the time domain using Roger's approximation⁷. The approximation requires first a transformation of the frequency domain loads into the Laplace domain. Subsequently, these loads are expressed as a linear

combination of the system states.

$$\begin{Bmatrix} -C_l(\bar{s}) \\ 2C_m(\bar{s}) \\ 2C_h(\bar{s}) \end{Bmatrix} = \left([C_0] + [C_1]\bar{s} + [C_2]\bar{s}^2 + [\bar{D}](I\bar{s} - [R])^{-1}[E]\bar{s} \right) \{q(\bar{s})\} \quad (4)$$

A vector of aerodynamic lag states is introduced by

$$\{\eta_a(\bar{s})\} = (I\bar{s} - [R])^{-1}[E]\{q(\bar{s})\}\bar{s} \quad (5)$$

Combining Eqs. (4) and (5) and transforming them to the time domain yields

$$([\bar{M}] - \frac{1}{\pi\mu}[C_2])\{\ddot{q}\} + ([\bar{C}] - \frac{\bar{V}}{\pi\mu}[C_1])\{\dot{q}\} + ([\bar{K}] - \frac{\bar{V}^2}{\pi\mu}[C_0])\{q\} - \frac{\bar{V}^2}{\pi\mu}[\bar{D}]\{\eta_a(\bar{t})\} = 0 \quad (6)$$

Equation (6) is rewritten in first order state variable form and combining it with Eq. (5) yields the open-loop equation of motion in state space

$$\dot{\{x\}} = [A]\{x(\bar{t})\} \quad (7)$$

where

$$[A] = \begin{bmatrix} 0 & [I] & 0 \\ -[M]^{-1}[K] & -[M]^{-1}[C] & [M]^{-1}[D] \\ 0 & [E] & \bar{V}[R] \end{bmatrix} ; \quad \{x\} = \begin{Bmatrix} \{q\} \\ \{\dot{q}\} \\ \{\eta_a\} \end{Bmatrix}$$

and the matrices used in $[A]$ are

$$[M] = [\bar{M}] - \frac{1}{\pi\mu}[C_2] ; \quad [C] = [\bar{C}] - \frac{\bar{V}}{\pi\mu}[C_1]$$

$$[K] = [\bar{K}] - \frac{\bar{V}^2}{\pi\mu}[C_0] ; \quad [D] = \frac{\bar{V}^2}{\pi\mu}[\bar{D}]$$

Stability of the open loop system is governed by the eigenvalues of Eq. (7), which are usually represented by root locus plots.

The trailing edge control surface is used for flutter suppression. The control scheme applies an external hinge moment, to the control surface, that modifies the aerodynamic loads acting on the typical cross section. The aeroservoelastic equation of motion is similar to Eq. (6):

$$[M]\{\ddot{q}\} + [C]\{\dot{q}\} + [K]\{q(\bar{t})\} - [D]\{\eta_a(\bar{t})\} = H_e \begin{Bmatrix} 0 \\ 0 \\ 1 \end{Bmatrix} \quad (8)$$

which in first order form is written as:

$$\dot{\{x\}} = [A]\{x(\bar{t})\} + [B]\{u(\bar{t})\} \quad (9)$$

where $[A]$ and $\{x\}$ were defined previously, and:

$$[B] = \begin{bmatrix} \{0\} \\ [M]^{-1} \begin{Bmatrix} 0 \\ 0 \\ 1 \end{Bmatrix} \\ \{0\} \end{bmatrix} ; \quad \{u(\bar{t})\} = H_e$$

Control Approach

A somewhat idealized approach to flutter suppression is the use of optimal control theory with full state feedback. In this case the objective function for flutter suppression is represented by^{6, 12, 22}

$$J = \int_{\bar{t}_i}^{\bar{t}_f} \left(\{x(\bar{t})\}^T [\bar{Q}] \{x\} + \lambda \{u(\bar{t})\}^T [\bar{R}] \{u\} \right) d\bar{t} \quad (10)$$

where $[\bar{Q}]$ is a non-negative cost weighting matrix of the states, and $[\bar{R}]$ is a positive definite weighting matrix involving the control; these are often chosen to be diagonal²². The positive weighting constant λ determines the ratio between state and control cost. The solution to the linear optimal control problem is provided by the solution to the Riccati differential equation²³, which is obtained numerically. The solution to the Riccati differential equation approaches that of the algebraic equation, when $\bar{t}_f \rightarrow \infty$. It is easier to obtain and frequently used^{22, 24}. This solution can be obtained from the Hamiltonian matrix of the system, given by²³

$$[A_H] = \begin{bmatrix} [A] & \frac{1}{\lambda} [B][\bar{R}]^{-1}[B]^T \\ -[\bar{Q}] & -[A]^T \end{bmatrix} \quad (11)$$

The eigenvalues of $[A_H]$ are symmetric with respect to both real and imaginary axes. Each eigenvalue with a positive real part has an image eigenvalue with a negative real part. Only the stable eigenvalues are considered. It can be shown that the number of eigenvalues with negative real parts is equal to the number of eigenvalues of the original open-loop system, and that the closed loop system is always stable. The solution to the Riccati algebraic equation is based on Potter's method²⁵, and the optimal control law is given by

$$\{u(\bar{t})\}_{opt} = -\frac{1}{\lambda} [\bar{R}]^{-1} [B]^T [P] \{x(\bar{t})\} \quad (12)$$

The closed loop dynamic equation of motion is²³

$$\dot{\{x\}} = \left([A] - \frac{1}{\lambda} [B][\bar{R}]^{-1}[B]^T[P] \right) \{x(\bar{t})\} \quad (13)$$

The control design described above does not account for any constraints such as deflection or rate limits on the trailing edge control surface. Addition of these constraints to the cost function in Eq. (10) does not affect the result of the linear optimal control theory²⁶. A potentially rewarding alternative is to recognize that control activity constraints, lead to a nonlinear problem, and use adaptive control for flutter suppression. The studies described in Refs. 27, 28 and 29 indicate that adaptive control may be a suitable tool for flutter suppression in the presence of nonlinearities.

The control approach based on full state feedback requires knowledge of the augmented aerodynamic states. The augmented aerodynamic states cannot be measured and have to be reconstructed from the time response. This is accomplished using a Kalman filter. The steady state observer Riccati matrix $[Q]$, and the steady state observer gain matrix $[K]$ are found in a similar manner to the calculation of the algebraic Riccati matrix $[P]$, and the closed loop control law gain matrix $[F]$ ²³. A new Hamiltonian matrix is formed for the algebraic Riccati observer equation:

$$[A_H] = \begin{bmatrix} [A]^T & -[C]^T[V_2]^{-1}[C] \\ -[V_1] & -[A] \end{bmatrix} \quad (14)$$

and a solution to the matrix $[Q]$, similar to that explained previously for the Riccati matrix $[P]$ leads to the steady state observer gain matrix²³:

$$[K] = [Q][C]^T[V_2]^{-1} \quad (15)$$

It is important to determine the hinge moment requirements needed for control surface actuation and the power required for flutter suppression. These quantities are required for practical implementations of flutter suppression systems

$$\bar{H} = \frac{H}{mb^2\omega_a^2} = 2\frac{\bar{V}^2}{\pi\mu}C_h \quad (16)$$

The instantaneous power is given by

$$P(\bar{t}) = H(\bar{t})\dot{\beta}(\bar{t}) = 2mb^2\omega_a^3\frac{\bar{V}^2}{\pi\mu}C_P$$

and in nondimensional form its average value becomes

$$\bar{P}_{av} = 2\frac{\bar{V}^2}{\pi\mu}\frac{1}{\bar{t}_2 - \bar{t}_1} \int_{\bar{t}_1}^{\bar{t}_2} C_P(\bar{t})d\bar{t} \quad (17)$$

For the cases considered in this study the average power in Eq. (17), represents the power consumed during a period when the response of the wing section, due to control activity, reduces by a predetermined amount.

Piezoelectrically Twisted Wing/Airfoil

As indicated earlier, one of the goals of this paper is to obtain equivalence relations between a conventional airfoil/trailing edge flap combination and a continuously deforming wing section which is piezoelectrically actuated. To achieve this objective consider an

idealized section of the wing structural element used for piezoelectric actuation based on bend/twist coupling, shown in Fig. 2. The typical cross section consists of a layer of honeycomb core between two composite face sheets. Two PZT layers are attached to the top and bottom of the composite cover sheets, and resemble the actuation patches used in Ref. 12. The change in the pitch moment coefficient, as a result of flap deflections, based on static thin airfoil theory³⁰ is given by:

$$\Delta C_m(t) = \frac{1}{2} \sin \theta_f (\cos \theta_f - 1) \beta(t) \quad (18)$$

The static change in pitch moment, due to change in pitch angle, can also be written as

$$\Delta C_m(\bar{t}) = \frac{1}{2} (a + \frac{1}{2}) \Delta C_l(\bar{t}) = \pi (a + \frac{1}{2}) \Delta \alpha(\bar{t}) \quad (19)$$

It is assumed that due to the bend/twist coupling, bending moments acting on the section cause only twist along its spanwise axis, and that no external twisting moments act on it. Furthermore, it is assumed that the structural element, shown in Fig. 2, represents the cross section of a flat plate type airfoil that is being twisted so as to produce the same pitching moment that is induced by an actively controlled trailing edge flap. The power, per unit span, required to twist a flat plate is given by

$$P(\bar{t}) = \omega_\alpha M_y(\bar{t}) \frac{\partial^2 \alpha}{\partial \bar{t} \partial y} \quad (20)$$

where the moment required to twist the plate can be determined, following the analysis described in Ref. 31, for a beam-like wing, from $M_y(\bar{t}) = G J_p \partial \alpha(\bar{t}) / \partial y$. For a constant twist angle along the span, $\partial \alpha / \partial y$ is found directly from the local, instantaneous, angle of attack at the typical section. The shear modulus of the typical section; averaged between the various layers, but excluding actuation layers, and the polar moment of inertia for a rectangular cross section (Ref. 32, ch. 5) are given by:

$$G = \frac{2G_{LT}t_C + G_H t_H}{2t_C + t_H} \quad ; \quad J_p = \frac{20}{9} \frac{(t_t/2)^3 b^3}{(t_t/2)^2 + b^2}$$

The equivalent power required to deform the plate section, expressed in terms of an equivalent control flap deflection acting on a typical cross section located at 0.75 semi-span, is determined from Eqs. (18), (19) and (20):

$$P(\bar{t}) = \frac{16}{9} \frac{G J_p \omega_\alpha}{l^2} \left[\frac{\sin \theta_f (\cos \theta_f - 1)}{2\pi(a + \frac{1}{2})} \right]^2 \beta(\bar{t}) \dot{\beta}(\bar{t}) \quad (21)$$

When Eq. (21) is divided by $m_s b^2 \omega_\alpha^3$ and averaged over time, the resulting expression is comparable with Eq. (17). Additional details can be found in Ref. 33.

AEROELASTIC AND AEROSERVOELASTIC SCALING LAWS

The classical approach to aeroelastic scaling is presented in detail in Ref. 16, Ch. 11. The procedure is best illustrated by considering first the scaling relations in incompressible

flow, for a two dimensional airfoil - control surface combination, under the assumption of simple harmonic motion. The extension of these relations to the compressible case is straightforward. For this case one has

$$\begin{Bmatrix} \xi(t) \\ \alpha(t) \\ \beta(t) \end{Bmatrix} = \begin{Bmatrix} \xi_0 e^{i\omega t} \\ \alpha_0 e^{i(\omega/\omega_\alpha)t + \phi_1} \\ \beta_0 e^{i(\omega/\omega_\alpha)t + \phi_2} \end{Bmatrix} = \begin{Bmatrix} \xi_0 e^{i(\omega/\omega_\alpha)t} \\ \alpha_0 e^{i(\omega/\omega_\alpha)t + \phi_1} \\ \beta_0 e^{i(\omega/\omega_\alpha)t + \phi_2} \end{Bmatrix} \quad (22)$$

The loads corresponding to Theodorsen's theory²⁰ are

$$\begin{Bmatrix} -C_l \\ 2C_m \\ 2C_h \end{Bmatrix} = \frac{1}{V^2} \left[\begin{array}{ccc} -\pi & \pi a & T_1 \\ \pi a & -\pi(\frac{1}{8} + a^2) & -2T_{13} \\ T_1 & -2T_{13} & \frac{1}{\pi} T_3 \end{array} \right] \{q\} + \frac{1}{V} \left[\begin{array}{ccc} 0 & -\pi & -T_4 \\ 0 & \pi(a - \frac{1}{2}) & -T_{16} \\ 0 & -T_{17} & -\frac{1}{\pi} T_{19} \end{array} \right] \{\dot{q}\} + \left[\begin{array}{ccc} 0 & 0 & 0 \\ 0 & 0 & -T_{15} \\ 0 & 0 & -\frac{1}{\pi} T_{18} \end{array} \right] \{q\} + C(k) \left(\begin{array}{ccc} 0 & -2\pi & -2T_{10} \\ 0 & 2\pi(\frac{1}{2} + a) & 2(\frac{1}{2} + a)T_{10} \\ 0 & -T_{12} & -\frac{T_{10}T_{12}}{\pi} \end{array} \right) \{q\} + \frac{1}{V} \left(\begin{array}{ccc} -2\pi & -2\pi(\frac{1}{2} - a) & -T_{11} \\ 2\pi(\frac{1}{2} + a) & 2\pi(\frac{1}{4} - a^2) & T_{11}(\frac{1}{2} + a) \\ -T_{12} & -T_{12}(\frac{1}{2} - a) & -\frac{T_{11}T_{12}}{2\pi} \end{array} \right) \{\dot{q}\} \quad (23)$$

Values of T_1 through T_{14} are defined in Ref. 20, and T_{15} through T_{19} are convenient combinations of the first fourteen T_i 's, as indicated in Ref. 34. The quantities T_i depend only on the nondimensional hinge location c_β and the nondimensional offset a . Substituting Eqs. (22) and (23) into Eq. (1), neglecting damping effects and dividing by $(\omega/\omega_\alpha)^2$ yields:

$$\begin{aligned} -\xi_0 - x_\alpha \alpha_0 e^{i\phi_1} - x_\beta \beta_0 e^{i\phi_2} + \left(\frac{\omega_\alpha}{\omega}\right)^2 \left(\frac{\omega_h}{\omega_\alpha}\right)^2 \xi_0 \\ = F_1(c_\beta, a, k, \mu, \xi_0, \alpha_0, \phi_1, \beta_0, \phi_2) \\ -x_\alpha \xi_0 - r_\alpha^2 \alpha_0 e^{i\phi_1} - (r_\beta^2 + (c_\beta - a)x_\beta) \beta_0 e^{i\phi_2} + r_\alpha^2 \left(\frac{\omega_\alpha}{\omega}\right)^2 \alpha_0 e^{i\phi_1} \\ = F_2(c_\beta, a, k, \mu, \xi_0, \alpha_0, \phi_1, \beta_0, \phi_2) \\ -x_\beta \xi_0 - (r_\beta^2 + (c_\beta - a)x_\beta) \alpha_0 e^{i\phi_1} - r_\beta^2 \beta_0 e^{i\phi_2} + r_\beta^2 \left(\frac{\omega_\alpha}{\omega}\right)^2 \left(\frac{\omega_\beta}{\omega_\alpha}\right)^2 \beta_0 e^{i\phi_2} \\ = F_3(c_\beta, a, k, \mu, \xi_0, \alpha_0, \phi_1, \beta_0, \phi_2) \end{aligned} \quad (24)$$

A convenient rule of thumb derived by Buckingham states that the nondimensional solution can then be written in terms of a reduced set of nondimensional combinations that consist of $n - k$ parameters, where n are the original parameters, and $k = 3$ are the primary parameters - M (mass), L (length) and T (time). The nondimensional parameters that can be extracted from Eqs. (24), using Buckingham's π theorem are listed below:

$$\begin{aligned} \xi_0 = \left(\frac{h_0}{b}\right); k = \left(\frac{\omega b}{V}\right); \mu = \left(\frac{m}{\pi \rho b^2}\right); \left(\frac{\omega_h}{\omega_\alpha}\right) = \sqrt{\frac{K_h/m}{K_\alpha/I_{EA}}} \\ \frac{\omega_\beta}{\omega_\alpha}; \frac{\omega_\alpha}{\omega}; r_\alpha^2; r_\beta^2; c_\beta; a; x_\alpha = \left(\frac{S_\alpha}{mb}\right); x_\beta = \left(\frac{S_\beta}{mb}\right); \alpha_0; \beta_0; \phi_1; \phi_2 \end{aligned}$$

The first twelve parameters can be expressed as combinations of the three primary variables, while the last four are nondimensional quantities. For aeroelastic stability the quantities of interest are: $\frac{\omega_F b}{V_F}$, $\frac{\omega_F}{\omega_\alpha}$ and $\frac{h_0}{b \omega_0}$; where the subscript F refers to the flutter condition. For aeroelastic similarity all other nondimensional parameters such as μ , (ω_h/ω_α) , $(\omega_\beta/\omega_\alpha)$... etc. for the model, must have the appropriate values. The external shape (i.e. airfoil type) and Reynolds number also have to be retained. When compressible flow is considered the list of sixteen parameters, given above, has to be augmented by an additional parameter, the Mach number M . Increasing the Mach number modifies the density of the fluid, and with it the mass ratio. Density is related to the Mach number through its value at stagnation:

$$\frac{\rho_0}{\rho} = \left(1 + \frac{\gamma - 1}{2} M^2\right)^{\frac{1}{\gamma-1}} \quad (25)$$

For the full scale configuration, stagnation density increases with an increase in flight Mach number. The value of the static density remains unchanged and corresponds to the value at the local altitude analyzed. When wind tunnel tests are conducted the value of the stagnation density, related to the value of stagnation temperature and pressure, remains usually unchanged and the value of the static density decreases with an increase in Mach number. When scaling a full size system for wind tunnel tests, the compressibility effect in the tunnel needs to be reflected in the design of a model.

Flutter conditions of similar structural configurations imply that their nondimensional flutter velocity is kept constant, as well as the Mach number. The pitch frequency of a scaled model relates to that of the full scale configuration according to the geometrical scaling ratio:

$$\frac{(\omega_\alpha)_m}{(\omega_\alpha)_w} = \frac{b_w}{b_m} \quad (26)$$

where subscript m stands for model while subscript w for the prototype.

The scaling of damping properties needs to be also addressed. Eqs. (1) and (2) imply that the damping of each mode is related to the natural frequency associated with that mode. Once the natural frequencies change, the damping coefficient of a corresponding mode needs to be modified to match the appropriate damping loads:

$$\frac{\zeta_m}{\zeta_w} = \frac{(\omega_\alpha)_w}{(\omega_\alpha)_m} = \frac{b_m}{b_w} \quad (27)$$

The aeroelastic scaling considerations discussed above are based on classical solutions that are obtained from Eqs. (1) and (22) - (24). Modern aeroelastic studies are based on refined computer simulations, similar to those used in this or other studies²⁸. Figure 3 depicts the new two pronged approach developed for generating refined aeroelastic scaling laws. In this approach basic scaling requirements are established using typical cross sectional information and dimensional analysis, in a manner that resembles the conventional, or classical, procedure. This process is represented by the left hand branch in Fig. 3. In parallel, solutions based on computer simulations are obtained for each of the aeroelastic problems, for which innovative refined scaling laws are desired. These solutions are assumed to represent "similarity solutions"¹⁹, except that they are obtained numerically. These computer simulations enable one to account for additional effects such as: presence of control surfaces

and stores, shock wave motion in transonic flow, and any effect captured by the simulation. This portion is represented by the right hand branch of Fig. 3. By combining the classical aeroelastic scaling requirements with the additional ones obtained from the simulation, a set of expanded or refined aeroelastic scaling requirements is obtained.

In the case of aeroservoelasticity a more general treatment of aeroelastic scaling is required, since scaling requirements for control surface hinge moments and the power needed for flutter suppression play an important role, when considering the practical implementation of the control system on the full-scale vehicle. The nondimensional frequency variable $\frac{\omega_a}{\omega}$ is replaced by the nondimensional time unit $\omega_a t = \bar{t}$, and the reduced frequency is replaced by the nondimensional velocity $\frac{V}{\omega_{a,b}} = \bar{V}$. In this case simulation is used again to obtain numerical "similarity solutions" for the aeroservoelastic system, operating in the closed loop mode. These computer simulations enable one to examine the intricate scaling relations governing control power, control forces and hinge moments. Again, the combination of the classical scaling parameters with the additional information obtained from the simulation, produces the refined aeroservoelastic scaling requirements.

RESULTS AND DISCUSSION

Open and Closed Loop Results for Baseline Configuration

Results presented were calculated for a typical cross section in subsonic flow using a computer code implementing the time domain aeroservoelastic analysis described earlier in this paper. Airfoil parameters used to generate the results were selected to resemble values for an executive jet type of aircraft with a wing span of 52.6 ft, semichord length of $b = 35.0$ inch and a pitch frequency of $\omega_a = 110.0 \frac{\text{Rad}}{\text{sec}}$: $a = -0.2$; $c_\beta = 0.8$; $x_\alpha = 0.2$; $x_\beta = -0.008$; $r_\alpha^2 = 0.25$; $r_\beta^2 = 0.036$; $\omega_h/\omega_a = 0.25$; $\omega_\beta/\omega_a = 2.0$, and a structural damping coefficient of $\zeta = 0.002$. Estimations for a wing weight, from which the mass ratio was deduced were found in Refs. 35 and 36. A value of $\mu = 25.6$ was chosen to represent the typical cross section at sea level conditions.

Aerodynamic loads were calculated from a DLM code, for a specific Mach number, and approximated in the time domain using Roger's approximation. A reduced frequency range of $0.000 \leq k \leq 1.300$ was used for the analyses. Results shown were calculated with four aerodynamic lag roots located at $\gamma_1 = 0.0250$, $\gamma_2 = 0.1500$, $\gamma_3 = 0.6000$ and $\gamma_4 = 1.2000$.

Stability analysis for a typical cross-section representative of this full scale configuration yields a matched point flutter Mach number of $M = 0.702$. Figure 4 depicts the open loop root locus plots for this configuration. The nondimensional open loop flutter velocity found was $\bar{V}_F = 2.441$, which at standard sea level conditions corresponds to a true velocity of $V = 783.2 \frac{\text{ft}}{\text{sec}}$ or a flight Mach number of $M = 0.702$.

The closed loop results were generated for a diagonal state cost matrix in which all the states had a unit cost, i.e. $\bar{Q}_{ii} = 1.00$. The \bar{R} matrix was reduced to a single scalar component given by $\bar{R} = 1.00$, and the cost function parameter was set to $\lambda = 100.00$. The root locus plots in Fig. 5 illustrate the behavior of the closed loop configuration. Three modes are shown. The unstable part of the open loop root locus, shown in Fig. 4 is reflected to the stable half of the s plane, in Fig. 5. A precise reflection occurs only when the control

cost parameter is very high^{6,23}.

When examining the time domain system behavior two initial conditions were used. A ramp input of $10^\circ/\text{sec}$ angle of attack rate, was applied to the system as an initial disturbance. This is denoted as Case I in the discussion that follows. Control surface saturation limits were selected with typical values of $|\beta_{\max}| \leq 4^\circ$, $|\dot{\beta}_{\max}| \leq 90^\circ/\text{sec}$, and a maximum hinge moment of $(H_e)_{\max} = 50000 \text{ lb-in}$ was used for a flap span of 68.5 inch . These values yield a typical cross section hinge moment saturation value of 729.3 Lb-in/in . A second case with initial conditions consisting of a 0.9° step function in angle of attack, denoted Case II, was also considered. It corresponds, at $M = 0.702$, to a gust of approximately 12.5 ft/sec . Flap control saturation levels similar to Case I were used in this case.

Figure 6 depicts a plunge displacement time history plot, for Case I, of the full scale configuration in closed loop at three velocities: \bar{V}_F , $1.025\bar{V}_F$ and $1.05\bar{V}_F$. As velocity increases, peak response in plunge also increases, however values are below 0.05 of a semi-chord length.

To construct a control law it was assumed that all the augmented aerodynamic states, as well as the structural states, were known. In Figs. 5 and 6 it is shown that the closed loop system is stable, that after a few oscillations the initial disturbance is dissipated, and that the system returns to its initial undisturbed state under the action of a control law. To estimate the augmented aerodynamic states, state excitation noise and measurement excitation noise intensities were selected. The dynamic system is assumed to be perfectly modeled, and therefore state excitation noise intensity was selected as $[V_1] = 0$, while a unit matrix was used for the measurement excitation noise intensity. Figure 7 depicts the plunge motion results for Case I, in which four aerodynamic lag roots were used to approximate the aerodynamic states. It appears that at $\bar{V} = \bar{V}_F + 5\%$ results diverge, while for cases with slower speeds above flutter the system oscillates without converging. Clearly, reconstruction of the augmented states causes problems. To avoid these problems it was assumed, for the rest of the results generated here, that the augmented aerodynamic states are known exactly and do not need to be reconstructed.

Aeroelastic Scaling Example

To illustrate the importance of aeroelastic scaling, two approaches to scaling the baseline configuration are explored. For the first case, only geometrical scaling of wing dimensions was used (GSM). In the second case aeroelastic scaling, which requires a change of wing stiffness, was implemented (ASM). Both cases were assumed to represent $1 : 6$ scaled versions of the full scale configuration. The ratio between a model's torsional frequency and that of the full scale configuration, as indicated by Eq. (26), is related to the geometrical scaling between both systems. The ASM pitch frequency was increased by a factor of six. The mass ratio of the ASM also changes. The full scale configuration flutters at a Mach number of $M = 0.702$, at which Eq. (25) results in a density ratio of $\rho_0/\rho = 1.2649$. The mass ratio of the ASM was decreased by the same factor to compensate for the drop in fluid density. This ratio, for the ASM was $\mu = 20.241$, while for the GSM the mass ratio of the baseline configuration was retained. The damping of ASM was also modified according to the relation given in Eq. (27). Table 1 summarizes the parameters describing the two models.

	full scale	GSM	ASM
b	35 inch	5.8333 inch	5.8333 inch
ω_a	110.0 $\frac{\text{Rad}}{\text{sec}}$	110.0 $\frac{\text{Rad}}{\text{sec}}$	660.0 $\frac{\text{Rad}}{\text{sec}}$
μ	25.6	25.6	20.241
ζ	0.002000	0.002000	0.000333

Table 1: Comparison of scaling parameters between three typical cross section models

Open loop results for the baseline and the two scaled configurations are shown in Table 2, depicting flutter velocity - dimensional and nondimensional, Mach number at flutter, flutter frequency, and nondimensional divergence velocity.

	full scale	GSM	ASM
\bar{V}_F	2.441	2.579	2.441
$V_F \frac{\text{ft}}{\text{sec}}$	783.2	137.9	783.2
$\omega_F \text{ Hz}$	46.89	55.84	46.89
M_F	0.702	0.123	0.702
\bar{V}_D	2.636	3.244	2.636

Table 2: Comparison of stability results between three typical cross section models

It is evident that only the ASM has an open loop behavior similar to the full scale configuration. The geometrically scaled model becomes unstable at conditions different from those of the full scale configuration.

Figures 8 and 9 exhibit the closed loop root loci of the geometrically and aeroelastically scaled models respectively. It is evident that the GSM does not display a behavior resembling the full scale configuration, while the ASM does.

A corresponding time history plot for the GSM is shown in Fig. 10, which depicts plunge displacement. Plunge response of the GSM, to the same initial conditions which were applied to the full scale configuration, is very similar to that of the full scale configuration, and oscillation amplitudes are of the same order of magnitude. Note that close to flutter boundary the systems exhibit similar behavior in the time domain, although they are not similar, and will generally behave differently at velocities that exceed the flutter boundary by a considerable amount.

The initial disturbance was nondimensionalized and found to be $\dot{\alpha}(0) = \frac{\dot{\alpha}(0)}{\omega_a} = 0.00158666$. For the ASM case this initial disturbance was applied to the model, and a dimensional value of the similar case was determined as $\dot{\alpha}(0) = \omega_a \dot{\alpha}(0) = 60^\circ/\text{sec}$. The appropriate flap rate limit was also determined from scaling considerations and found to be $|\beta_{max}| \leq 360^\circ/\text{sec}$. In addition a scaled hinge moment limit was determined, based on the relations in Eq. (16). Hinge moment limit of the ASM was reduced by a scaling factor of $1 : l^2$ and found to be 20.26 [lb-in/in]. Figure 11 depicts corresponding plunge results for the ASM. Plunge displacement is similar to the corresponding result of the full scale configuration, shown in Fig. 6.

Influence of Control Saturation

System behavior for Case II type of initial conditions was also considered to illustrate saturation and stabilization loss due to nonlinearities associated with stabilization. Time histories for plunge motion, with a control cost parameter of $\lambda = 10^2$, are shown in Fig. 12, for the full scale configuration, or baseline configuration. Deflection limits were modified to $|\beta_{max}| \leq 1.5^\circ$ and their effect on flutter suppression of the baseline configuration studied. Figure 13 exhibits the plunge displacement of the typical section, similar to that depicted in Fig. 12, for the baseline configuration. A plunge of about 15% of the semichord is evident, at flutter conditions, while in Fig. 12, a plunge of only 10% is observed. Due to tighter control flap deflection limits, the typical cross section reaches nonlinear regions earlier, and flutter boundaries can be expanded by smaller amounts. For higher velocities above the flutter boundary the control system fails to stabilize the system³³.

Comparison of Piezoelectric Actuation to a Conventional TE Device

Hinge moments needed for actuation and power required for flutter suppression are important aspects of aeroservoelastic behavior. Two separate cases are examined. The first case considers the hinge moments and power requirements for the baseline, or full scale, configuration. The second case compares the relative merits of piezoelectric actuation with that of a conventional, equivalent, trailing edge control surface. Two models were studied. The first was an articulated wing section/trailing edge control flap combination, with the same properties as the full scale configuration studied earlier.

Figure 14 depicts time history of the power coefficient required for the full scale configuration, for Case I. Negative values of power imply that the system produces power and such contributions were neglected. Since power decreases rapidly, only the first 50 seconds of nondimensional time history is shown. The maximum power necessary to overcome the initial pulse is needed for only a short duration. This phenomena implies that another measure of power required to suppress flutter should be used such as the average power needed to reduce wing oscillations to a certain level. The average power required to reduce the wing section pitch oscillations by 90% from its maximum value together with the time frame required for this reduction are shown in Table 3.

V	$\Delta V \%$	\bar{t}_1	\bar{t}_2	C_P	P_{av} hp/sec
2.441	0.00	1.700	26.65	$4.254 E^{-9}$	$2.1102 E^{-5}$
2.502	2.50	1.650	27.150	$5.050 10^{-9}$	$2.6319 10^{-5}$
2.563	5.00	1.600	27.550	$5.189 10^{-9}$	$2.8378 10^{-5}$

Table 3: Average power required to suppress flutter of a baseline wing-section, at several nondimensional velocities

It is evident from Table 3 that only small amounts of power are required for flutter suppression, when flying at modest speeds above the open-loop flutter velocity.

The second model, of a flat plate employing a continuous twist of the wing section for flutter suppression, had similar properties to those of the plate used in Ref. 12, and shown in Fig. 2. A half wing span configuration with a semispan of 26.33 feet and a semi chord of 35 inch was used. The plate configuration modeled included an aluminum based honeycomb and a layer of six Glass/Epoxy laminates having a $[30^\circ, 30^\circ, 0^\circ]$, construction. Other parameters required for modeling this configuration were: $(E_L)_a = 8.70$ [Mpsi]; $t_P = 0.11667$ inches; $Z_{ma} = 0.70117$ inches; $G_{LT} = 0.87$ [Mpsi]; $t_C = 6 \times 0.030$ inches; $\nu_C = 0.28$; $G_H = 0.11$ [Mpsi]; $t_H = 1.0325$ inches; $\nu_H = 0.3$; $d_{31} = 7.09 \times 10^{-9}$ [In/Volt];

Next, comparison of the power requirements for flutter suppression for a piezoelectrically twisted wing section and a conventional wing section/flap combination were addressed. Power required obtained from the relations described earlier, Eq. (21), are presented in Table 4. These results are similar to those presented in Table 3 for the baseline configuration.

V	\bar{t}_1	\bar{t}_2	\bar{C}_P	P_{av} hp/sec
2.441	1.700	26.65	2.255×10^{-8}	1.1186×10^{-4}
2.502	1.650	27.150	1.655×10^{-8}	8.6253×10^{-5}
2.563	1.600	27.550	1.436×10^{-8}	7.6222×10^{-5}

Table 4: Average power required to suppress flutter of a piezoelectrically actuated wing-section, at several nondimensional velocities

Actuation strains are shown in Fig. 15, and the corresponding voltages are depicted in Fig. 16. Limits reported in Ref. 37 are $200 \mu\epsilon$ for actuation strains and 200 volts for voltage source. From these results it appears that PZT materials are suitable candidate materials for flutter suppression, particularly in view of the fact that the initial impulse required to overcome the first response of the controller is artificial in nature. It is interesting to note that the power requirements of the actively controlled flap are an order of magnitude lower than those required for the piezoelectrically twisted wing section. The main reason for this is that piezoelectric actuation requires actual structural deformations of the wing. This additional energy is not needed for the case of the conventional airfoil/flap combination. Additional results can be found in Ref. 33.

CONCLUDING REMARKS

This study re-examines the issue of aeroelastic and aeroservoelastic scaling within the framework of modern aeroelasticity. This is a very important and somewhat neglected aspect of aeroelasticity. The principal findings of this study are summarized below.

1. A new, two pronged approach to aeroelastic and aeroservoelastic scaling was developed. It combines the classical approach with computer simulation of the specific problem. It is capable of providing useful scaling information on hinge moments and power requirements for flutter suppression.
2. Solutions to the nondimensional aeroelastic or aeroservoelastic problems provide similarity solutions. Only such solutions predict correctly the behavior of a full scale con-

figuration, as well as that of aeroelastically scaled models. A partially scaled model, such as the GSM, does not provide accurate predictions of the behavior of a full scale configuration.

3. Saturation of flap deflection and rate may limit in some cases the extent of flutter margin expansion. This introduces a nonlinearity that can not be treated conveniently by currently available methods in the control field.
4. Power requirements for flutter suppression were calculated for two models of a typical cross section: one with an actively controlled flap, and the other with a piezoelectrically actuated continuously distributed twist. The average power required for piezoelectric actuation is approximately an order of magnitude larger than that required by a typical wing section employing an actively controlled flap.
5. Using time domain unsteady aerodynamics with full state feedback requires reconstruction of the unsteady aerodynamic states that can not be measured. This introduces considerable additional complexity in the aeroservoelastic problem. This issue has been overlooked in previous studies.

ACKNOWLEDGMENT

This research grant was supported by the Air Force Office of Scientific Research under grant number F49620 – 94 – 1 – 0400, with Major Brian Sanders, Ph.D. as grant monitor.

References

- [1] Noll, T. E., "Aeroservoelasticity," *Flight-Vehicle Materials, Structures, and Dynamics-Assessment and Future Direction*, A. K. Noor and S. L. Venneri, Eds., Vol. 5, ASME, 1993, Ch. 3, pp. 179 – 212.
- [2] Livne, E., "Integrated Aeroservoelastic Optimization: Status and Direction," *Journal of Aircraft*, Vol. 36, No. 1, January - February 1999, pp. 122 – 145.
- [3] Friedmann, P. P., "Renaissance of Aeroelasticity and its Future," *Journal of Aircraft*, Vol. 36, No. 1, January - February 1999, pp. 105 – 121.
- [4] Newsom, J. R., Pototzky, A. S., and Abel, I., "Design of a Flutter Suppression System for an Experimental Drone Aircraft," *Journal of Aircraft*, Vol. 22, No. 5, May 1985, pp. 380 – 386.
- [5] Roger, K. L., Hodges, G. E., and Felt, L., "Active Flutter Suppression — A Flight Test Demonstration," *Journal of Aircraft*, Vol. 6, No. 12, June 1975, pp. 551 – 556.
- [6] Edwards, J. W., "Unsteady Aerodynamic Modeling and Active Aeroelastic Control," Ph.D. Dissertation, Dept. of Aeronautics and Astronautics, Stanford Univ., 1977.

- [7] Roger, K. L., "Airplane Math Modeling Methods for Active Control Design," CP-228, *Structural Aspects of Active Controls*, AGARD, August 1977, pp. 4-1 – 4-11.
- [8] Ehlers, S. M., and Weisshaar, T. A., "Static Aeroelastic Behavior of an Adaptive Laminated Piezoelectric Composite Wing," AIAA Paper 90-1078, *Proceedings of the 31st AIAA/ASME/ASCE/AHS/ASC Structures, Structural Dynamics, and Materials Conference*, Long Beach, CA, May 1990, pp. 1611 – 1623.
- [9] Heeg, J., Scott, R. C., and McGowan, Anna-Maria R., "Aeroelastic Research Using Smart Structures Concepts," *Aeroelasticity and Fluid Structure Interaction Problems*, P. P. Friedmann and J. C. I. Chang, Eds., AD-Vol. 44, Chicago, ASME, November 1994, pp. 161 – 173.
- [10] Heeg, J., McGowan, A., Crawley, E., and Lin, C., "The Piezoelectric Aeroelastic Response Tailoring Investigation," *International Forum on Aeroelasticity and Structural Dynamics 1995*, Manchester, UK, The Royal Aeronautical Society, June 1995, pp. 8.1 – 8.11.
- [11] Lazarus, K. B., Crawley, E. F., and Bohlmann, J. D., "Static Aeroelastic Control Using Strain Actuated Adaptive Structures," *Journal of Intelligent Material Systems and Structures*, Vol. 2, No. 3, July 1991, pp. 386 – 410.
- [12] Lin, C. Y., "Towards Optimal Strain Actuated Aeroelastic Control," Ph.D. Dissertation, Dept. of Aeronautics and Astronautics, Massachusetts Institute of Technology, January 1996. SERC #3-96.
- [13] Lin, C. Y., Crawley, E. F., and Heeg, J., "Open- and Closed-Loop Results of a Strain-Actuated Active Aeroelastic Wing," *Journal of Aircraft*, Vol. 33, No. 5, Sep.-Oct. 1996, pp. 987 – 994.
- [14] Lazarus, K. B., Crawley, E. F., and Lin, C. Y., "Multivariable Active Lifting Surface Control Using Strain Actuation: Analytical and Experimental Results," *Journal of Aircraft*, Vol. 34, No. 3, May - June 1997, pp. 313 – 321.
- [15] McGowan, A., Heeg, J., and Lake, R. C., "Results of Wind-Tunnel Testing from the Piezoelectric Aeroelastic Response Tailoring Investigation," AIAA Paper 96-1511, *Proceedings of the 37th AIAA/ASME/ASCE/AHS/ASC Structures, Structural Dynamics and Materials Conference*, Salt Lake City, UT, April 15-17 1996, pp. 1722 – 1732.
- [16] Bisplinghoff, R. L., Ashley, H., and Halfman, R. L., *Aeroelasticity*, Cambridge Massachusetts, Addison-Wesley Publishing Co., 1955.
- [17] Hunt, G. K., "Similarity Requirements for Aeroelastic Models of Helicopter Rotors," Aeronautical Research Council, CP 1245, January 1973.
- [18] Regier, A. A., "The Use of Scaled Dynamic Models in Several Aerospace Vehicle Studies," in *Proceedings of ASME Colloquium on the Use of Models and Scaling in Simulation of Shock and Vibration*, Philadelphia, PA, ASME, New York, November 19 1963, pp. 34 – 50.

- [19] Baker, W. E., Westine, P. S., and Dodge, F. T., *Similarity Methods in Engineering Dynamics: Theory and Practice of Scale Modeling*, Elsevier, Revised Edition, 1991.
- [20] Theodorsen, T., "General Theory of Aerodynamic Instability and the Mechanism of Flutter," NACA, TR 496, 1935.
- [21] Albano, E., and Rodden, W. P., "A Doublet-Lattice Method for Calculating Lift Distribution on Oscillating Surfaces in Subsonic Flows," *AIAA Journal*, Vol. 7, No. 2, February 1969, pp. 279 – 282.
- [22] Mukhopadhyay, V., "Flutter Suppression Control Law Design and Testing for the Active Flexible Wing," *Journal of Aircraft*, Vol. 32, No. 1, January - February 1995, pp. 45 – 51.
- [23] Kwakernaak, H., and Sivan, R., *Linear Optimal Control Systems*, John Wiley & Sons, 1972.
- [24] Dowell, E. H., *et al.*, *Aeroelastic Control in A Modern Course in Aeroelasticity*, 3rd ed., Kluwer Academic Publishers, 1995, Ch. 12.
- [25] Potter, J. E., "Matrix Quadratic Solutions," *SIAM J. on Applied Mathematics*, Vol. 14, No. 3, May 1966, pp. 496 – 501.
- [26] Bryson, A. E. Jr., and Ho, Y. C., *Applied Optimal Control*, Washington, D. C., Hemisphere Publishing Co., 1975.
- [27] Roy, I. D., and Eversman, W., "Adaptive Flutter Suppression of an Unswept Wing," *Journal of Aircraft*, Vol. 33, No. 4, July - August 1996, pp. 775 – 783.
- [28] Friedmann, P. P., Guillot, D., and Presente, E. H., "Adaptive Control of Aeroelastic Instabilities in Transonic Flow and its Scaling," *Journal of Guidance, Control, and Dynamics*, Vol. 20, No. 6, Nov. - Dec. 1997, pp. 1190 – 1199.
- [29] Eversman, W., and Roy, I. D., "Active Flutter Suppression Using Multi-Input/Multi-Output Adaptive Least Mean Square Control," *Journal of Aircraft*, Vol. 34, No. 2, March - April 1997, pp. 244 – 250.
- [30] Kuethe, A. M., and Chow, C., *Foundations of Aerodynamics*, 4th ed., John Wiley & Sons, 1986.
- [31] Lazarus, K. B., "Multivariable High-Authority Control of Plate-Like Active Lifting Surfaces," Ph.D. Dissertation, Dept. of Aeronautics and Astronautics, Massachusetts Institute of Technology, June 1992.
- [32] Shames, I. H., and Dym, C. L., *Energy and Finite Element Methods in Structural Mechanics*, Taylor & Francis, 1985.
- [33] Presente, E., "Innovative Scaling Laws for Aeroelastic and Aeroservoelastic Problems in Compressible Flow," Ph.D. Dissertation, University of California, Los Angeles, 1999.

- [34] Theodorsen, T., and Garrick, I. E., "Nonstationary Flow About a Wing-Aileron-Tab Combination Including Aerodynamic Balance," NACA, TR 736, May 1942.
- [35] Raymer, D. P., *Aircraft Design: A Conceptual Approach*, 2nd ed., AIAA Education Series, 1992.
- [36] Nicolai, L. M., *Fundamentals of Aircraft Design*, San Jose, CA, METS Inc., 1984.
- [37] Reich, G. W., van Schoor, M. C., Lin, C. Y., and Crawley, E. F., "An Active Aeroelastic Wing Model for Vibration and Flutter Suppression," AIAA Paper 95-1193-CP, *Proceedings of the 36th AIAA/ASME/AHS/ASC Structures, Structural Dynamics, and Materials Conference*, New Orleans, LA, April 10 - 13 1995, pp. 314 - 324.

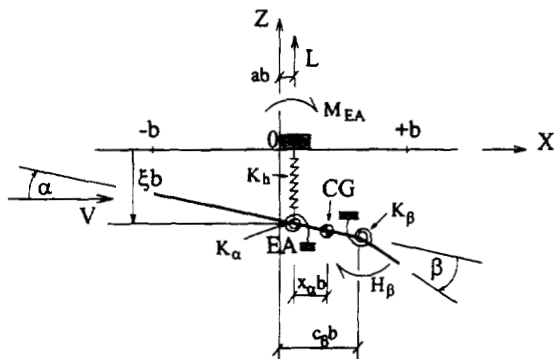


Figure 1: Definition of parameters for three degree of freedom aeroservoelastic model

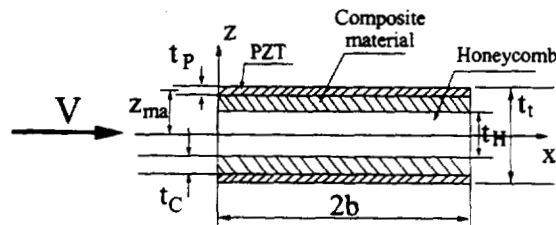


Figure 2: Idealized wing section using piezoelectric actuation

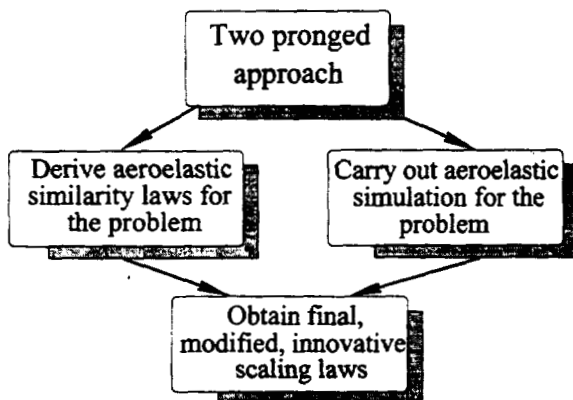


Figure 3: Two pronged approach for generating refined aeroelastic scaling laws

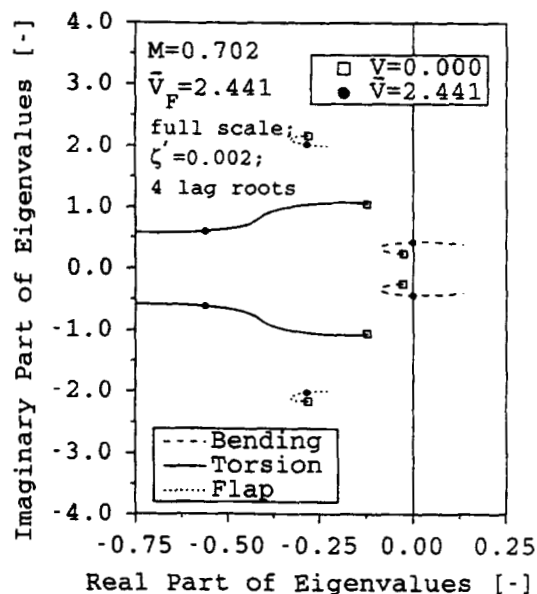


Figure 4: Open loop root locus of full scale configuration, at a Mach number of $M = 0.702$

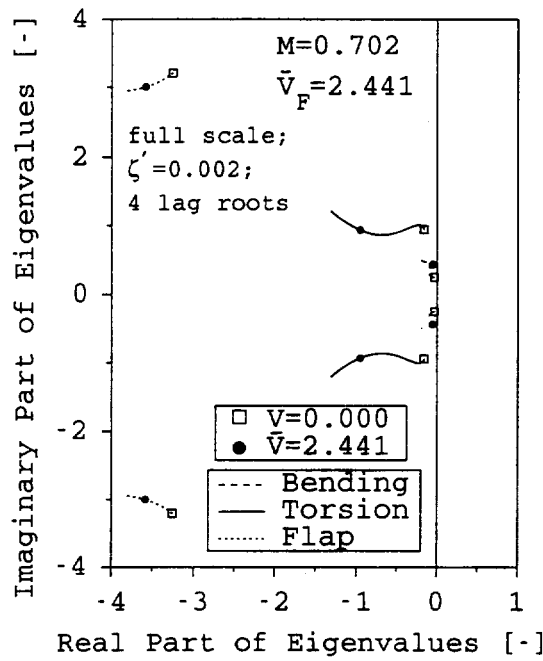


Figure 5: Closed loop root locus of full scale configuration, at a Mach number of $M = 0.702$

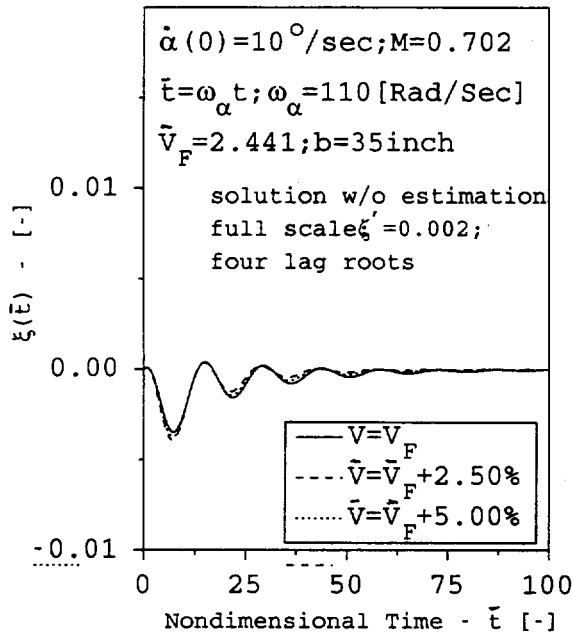


Figure 6: Closed loop time history of plunge displacement for the full scale configuration, at a Mach number of $M = 0.702$

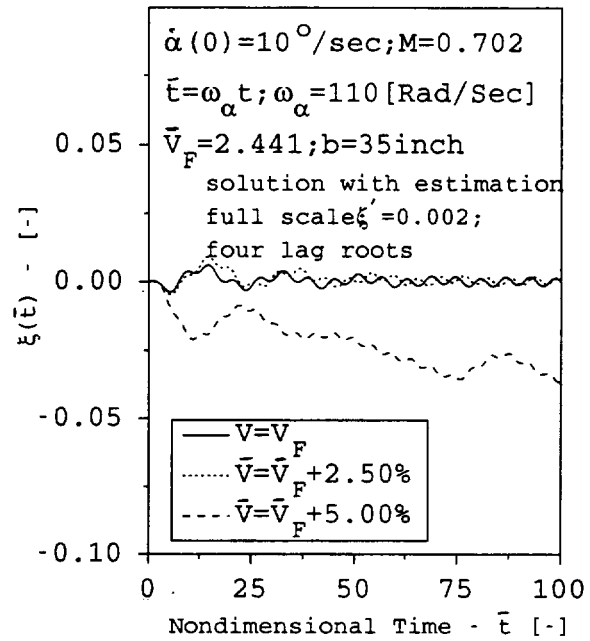


Figure 7: Closed loop time history of full scale configuration in plunge $\xi(\bar{t})$, Case-I

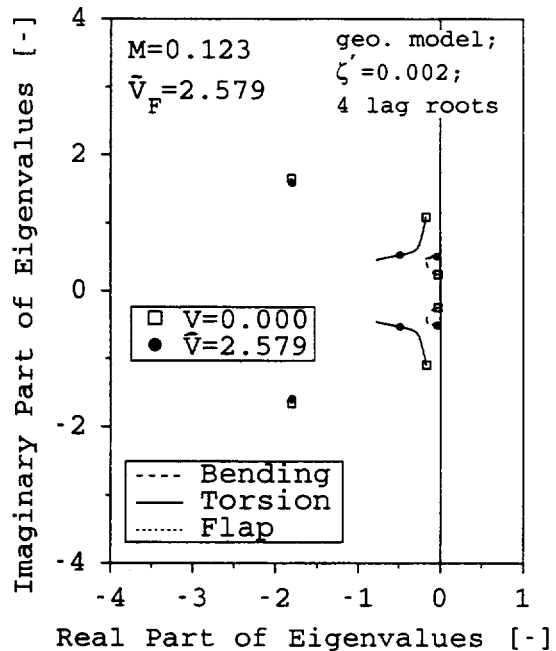


Figure 8: Closed loop root locus of geometrically scaled model, at a Mach number of $M = 0.123$

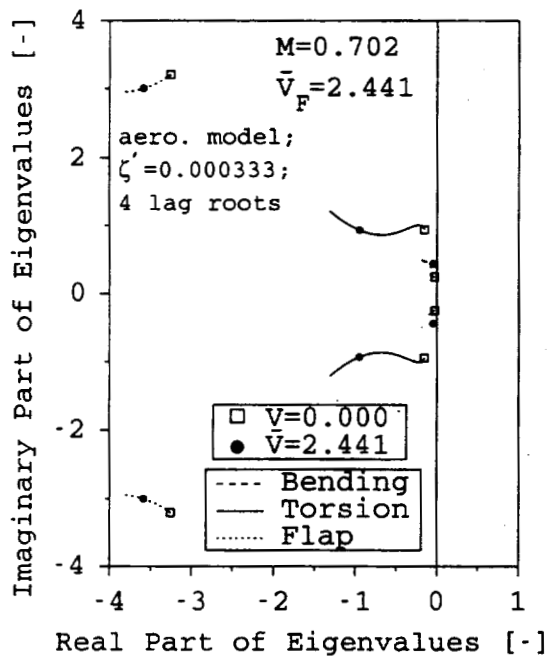


Figure 9: Closed loop root locus of aeroelastically scaled model, at a Mach number of $M = 0.702$

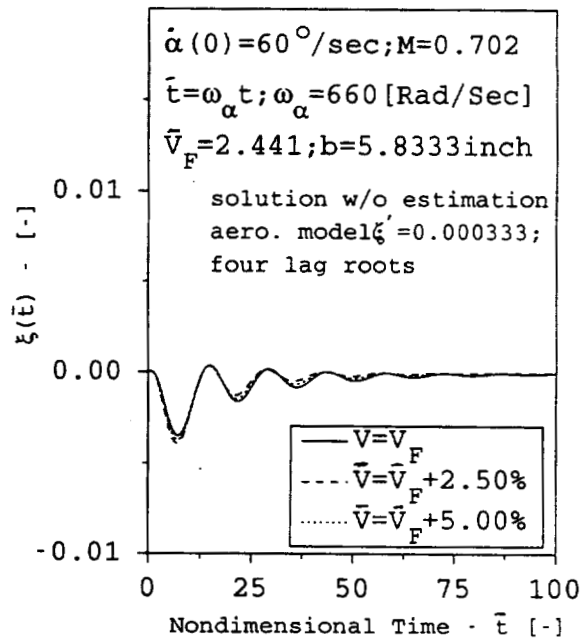


Figure 11: Closed loop time history of plunge displacement for the aeroelastically scaled model, at a Mach number of $M = 0.702$

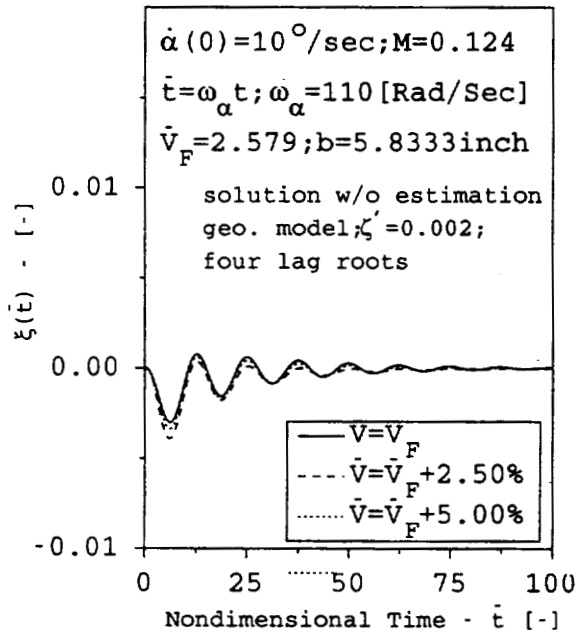


Figure 10: Closed loop time history of plunge displacement for the geometrically scaled model, at a Mach number of $M = 0.123$

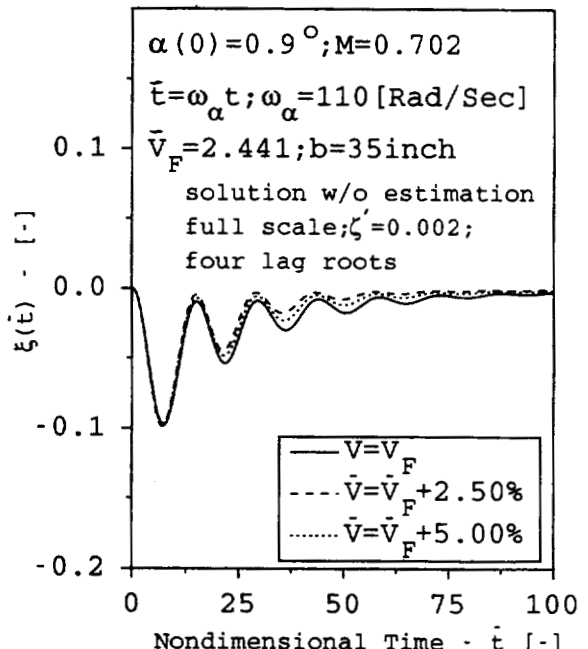


Figure 12: Closed loop time history of full scale configuration plunge displacement $\xi(\bar{t})$, Case-II

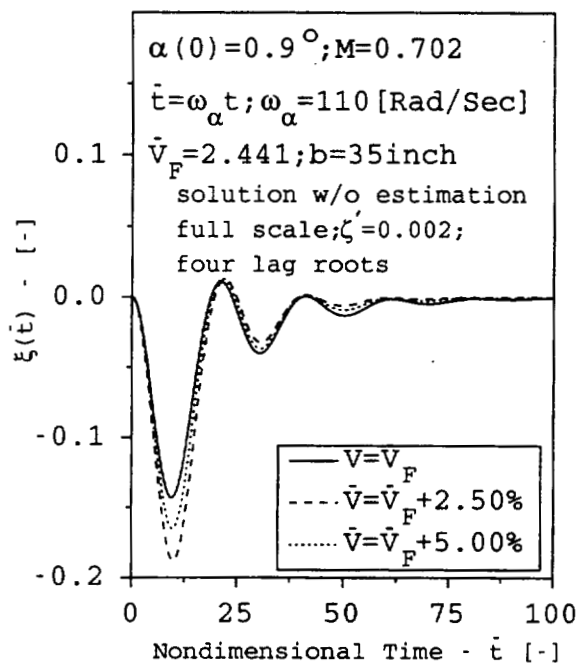


Figure 13: Closed loop time history of full scale configuration in plunge $\xi(\bar{t})$, Case-I, with a different control saturation level

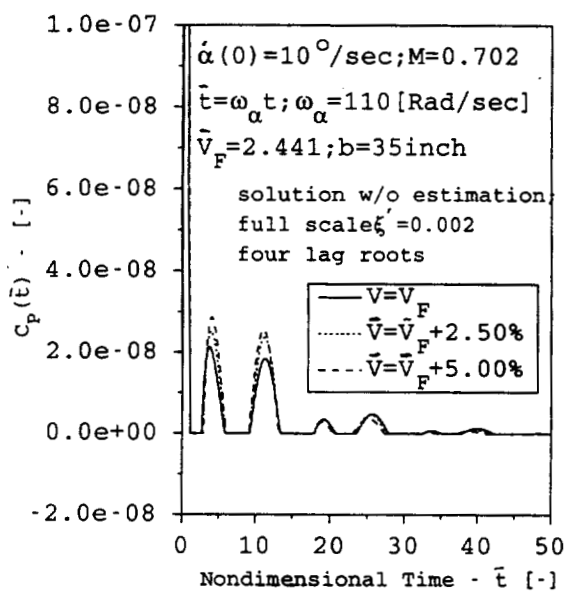


Figure 14: Closed loop time history of power coefficient for the full scale configuration, at a Mach number of $M = 0.702$

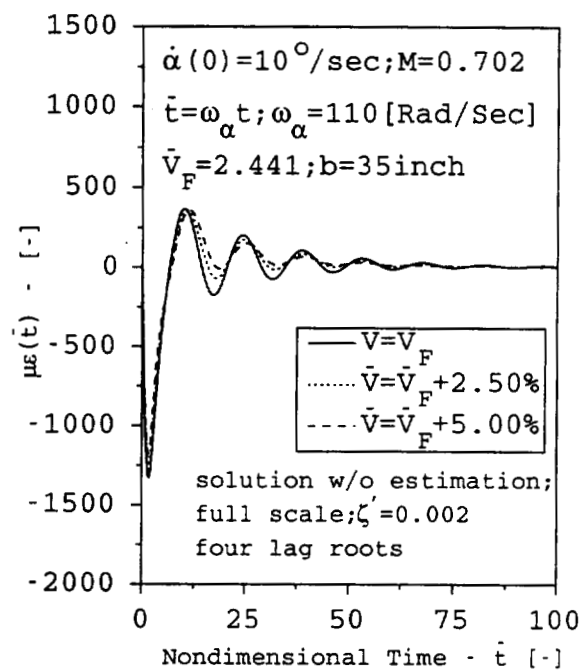


Figure 15: Closed loop time-history of actuation strain $\Lambda_y(\bar{t})$, case-I

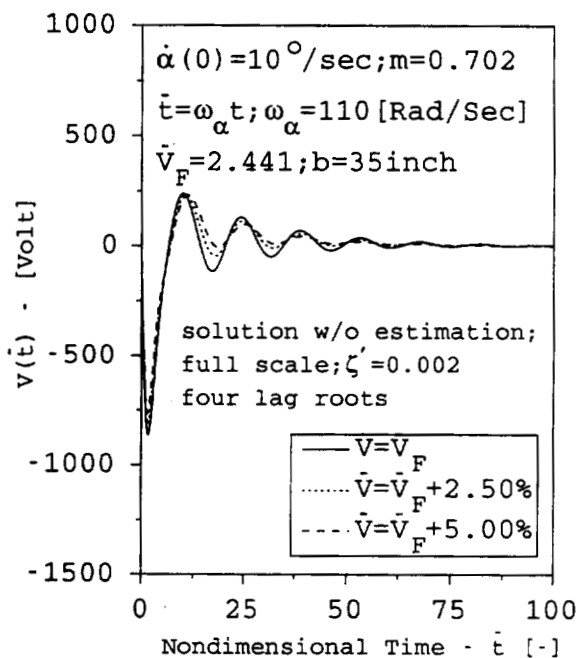


Figure 16: Closed loop time-history of voltage $V(\bar{t})$, case-I

NEW EXPERIMENTAL STALL FLUTTER ACTIVE CONTROL OF A BRIDGE SECTION

527-08

L. LECCE, E. SELVAGGI, F. NICOLOSI, M. BARUFFO, A. ABATE

Department of Aeronautical Engineering

University of Naples "FEDERICO II"

Via Claudio 21 - 80125 - NAPLES - ITALY

email address: leonardo@unina.it

Abstract

In this paper experimental activities on stall flutter phenomenon will be presented. Tests have been performed in the low speed wind tunnel at the Department of Aeronautical Engineering (DPA) of the University of Naples on a model using a typical single deck box girder bridge section. In the first part of the work, the stall flutter has been controlled using a leading edge (i.e.) movable surface (tab) deflecting downward. Application of a new active control system has been performed using the previous movable surface. The stall flutter in dynamic conditions has been controlled using an active system which automatically changes the tab position (from 0 to 10°) and is able to suppress the stall phenomenon. The control system consists of a mixed digital-analogue feedback circuit with an accelerometer as error sensor and two electromagnetic actuators to control the tab rotation.

In the second part a new approach has been tested. The new methodology consists of a rotating cylinder placed at the section leading edge. Through the cylinder rotation it is possible to change the section aerodynamic behaviour and then to increase stall flutter critical speed up to 60% at certain angles of attack.

Introduction

During the last decades the span length of suspension bridges has grown rapidly. During 1998 two very long suspension bridges were opened for traffic: the Akashi Kaikyo Bridge in Japan (the longest suspended bridge in the world) with span length of 1991 m and the Great Belt Bridge in Denmark with span length of 1624 m. Future ultra-long span suspension bridges that may be constructed are the Messina Crossing with the span length 3300 m and the crossing of the Gibraltar Straits, 3500 m.

The increase of span length leads to some aeroelastic problems that must be solved, ensuring the bridge stability up to a design wind speed ranging from 60 to 80 m/s.

Traditionally the increase of the structural stiffness of the bridge girders have been used for flutter suppression. For example a deep truss section with high torsional stiffness was selected for the Akashi suspension bridge. Improvement in aerodynamic stability can also be obtained by streamlining the bridge deck. Other possibilities are the use of passive or active control tools to limit bridge vibrations.

Passive control systems, e.g. viscoelastic damping elements, tuned mass dampers and eccentric masses can be useful to this aim. Also active control systems as a gyroscope [1] whose motion is coupled with torsional motion of the deck can be used for the prevention of onset of flutter.

Active and passive flutter suppression methods, discussed above, aim to modify the dynamic properties of the bridge structure itself.

Modification of the flow around the bridge deck or generation of stabilising aerodynamic forces from the flow is another approach to the flutter problem. Passive aerodynamic dampers have been proposed, most of them consisting in wing profiles fixed at the section leading or trailing edge zone [2, 3].

Passive aerodynamic control can be obtained also through additional surfaces moved by a pendulum which "feels" deck rotations and accelerations [4]. Control surfaces rotation is then used to generate stabilising aerodynamic forces. Advanced active flutter control can be accomplished by using aerodynamic control surfaces or tools controlled by signals through an appropriate feedback control law.

This methodology comes from the aeronautical field where advanced aircraft actively controlled surfaces are moved relative to the main surfaces (wings, flaps or ailerons) they control [5]. An example of flutter control obtained with a trailing edge tab on an airfoil was previously noted by the authors through a wind tunnel experimental activities presented in [6] and [7].

The same principle can be used to control vibration and flutter of bridges as originally proposed by Ostenfeld & Larsen [8] and as also shown by the authors [7] through wind tunnel tests on a bridge section with leading edge movable surface.

In this work experimental activities on stall flutter control of a bridge section will be presented. The stall flutter control experiment has been performed in the small low speed wind tunnel of D.P.A. (Department of Aeronautical Engineering) usually used for aeroelastic applications. In the first part of the paper the control has been obtained using a movable surface at the bridge leading edge, using a very innovative and general active system developed in collaboration with Glasgow University and also applied on wing flutter control [7]. In the second part the section flutter control has been accomplished by using an innovative solution with a rotating cylinder mounted in the section frontal part. This new approach is still a work in progress but seems to be an attractive solution to increase bridge flutter wind critical speed.

Test Facilities and Model

Wind Tunnel

The experimental activity has been carried out at DPA, in the low speed wind tunnel shown in fig. 1. The main characteristics of the tunnel are shown below :

- Close circuit – Open test section
- Test section dimensions : 1.0 m x 0.9 m (width x height)
- Maximum speed : 45 m/s
- Low turbulence level

Model characteristics

The model used in the tests is an aluminium model with leading and trailing edge wood fairings. The model properties are reported in table 1. The section shape is shown in fig. 2.

The model is connected to the wind tunnel support system by means of torsional springs which allow only the rotational d.o.f.. The model is provided with two Plexiglas end-plates to achieve two-dimensional flow conditions. A picture, showing the model mounted in the test section, is shown in fig. 3. The model and the stiffness of the elastic support were designed in order to have a flutter speed as low as possible and with a sufficient speed margin with respect to the wind tunnel maximum speed.

The aerodynamic instability is due to the stall flutter phenomenon, because the classical flutter is characterised by two d.o.f. systems.

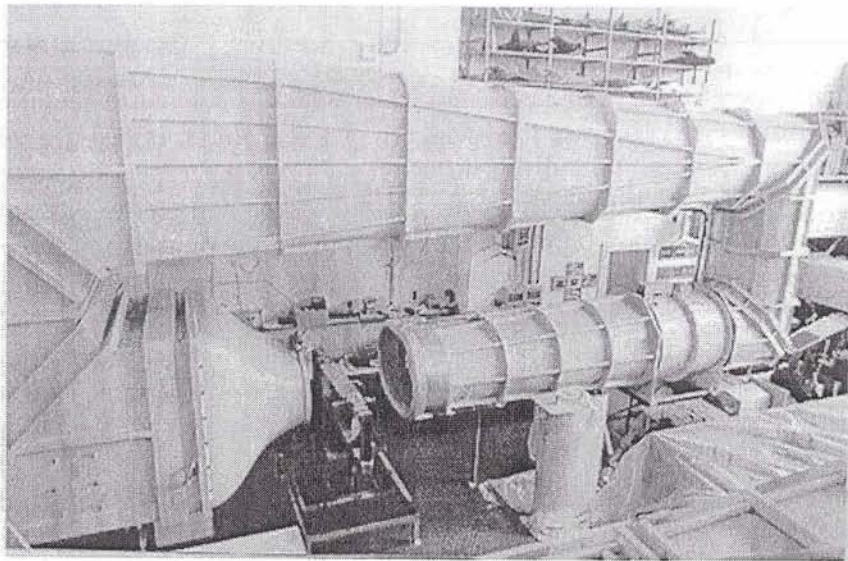


Fig. 1 : DPA Low Speed Wind Tunnel

Span	l	0.770 m
Chord	c	0.202 m
Model mass	M	7.50 Kg
Moment of Inertia referred to the elastic axis	I_α	0.042 Kg m ²
Torsional Stiffness	K_α	193 Nm /rad
1 st Torsional Frequency	F_α	7.1 Hz

Tab. 2 : Model Properties



Fig. 2 : Model section

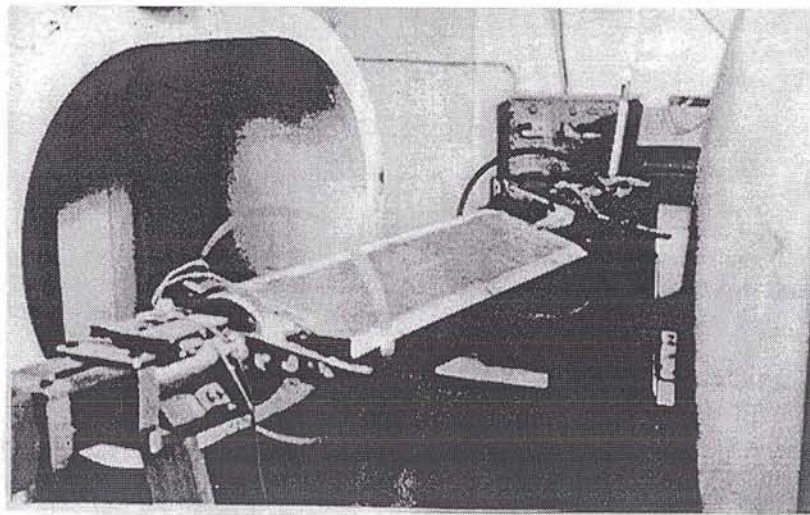


Fig. 3 : Model mounted in the test section

Stall flutter

The stall flutter phenomenon is an aeroelastic instability which is related to sections operating at high angles of attack. The difference respect to the two d.o.f. classical flutter is that the role of flow viscosity (Reynolds number) is not negligible and the influence of flow separation on stall flutter is revealed through the hysteresis effect. As explained in more detail in [9] stall flutter is a self-excited torsional oscillation induced by flow separation which occurs when the angle of attack is close to the section stall angle. This behaviour is related to the aerodynamic hysteresis loop represented in fig. 4.

The section post-stall aerodynamic behaviour (represented with a dotted line in fig. 4) plays a crucial role in the stall flutter section instability in relation to the amount of energy which can be extracted from the flow in the hysteresis loop. A section characterised by an abrupt stall with massive flow separation and big lift loss will have an explosive stall flutter behaviour with high-degree of instability and thus a relatively low flutter critical wind speed.

An device which can modify the section aerodynamic behaviour at high angles of attack, trying to keep the flow attached, delaying the stall or reducing the negative lift-curve slope in post-stall condition will be a way to increase section stall flutter speed.

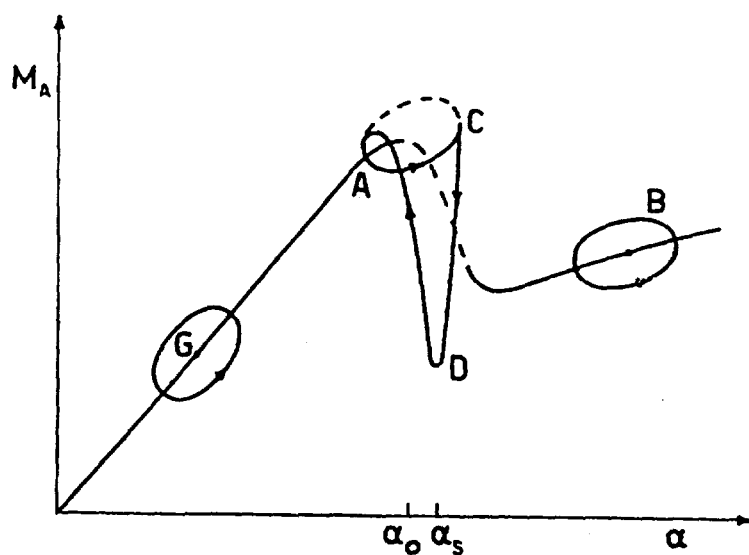


Fig. 4 : Stall flutter phenomenon

Leading edge tab stall flutter control

The model exhibited signs of stall flutter instability conditions for an angle of attack α of 9° and a wind speed of 20 m/s. The model front wood fairing was then connected to the aluminium model through a hinge which allows the leading edge surface (called tab) to be deflected downward (see fig. 5) up to an angle β of 20° . The section static aerodynamic behaviour has been obtained at different tab deflection angles β . The model moment coefficient curves (obtained by measuring the section moment through strain gauges mounted on the torsional springs) measured for different tab positions are shown in fig. 6. The tab deflection changes the section aerodynamic behaviour and it is possible to see that a deflection β of 10° allows an higher stall angle and an improved post-stall behaviour.

It is evident that the original section with $\beta=0^\circ$ at an angle of attack of 9° is close to its stall angle and then presents stall flutter instability even at relatively low speeds.

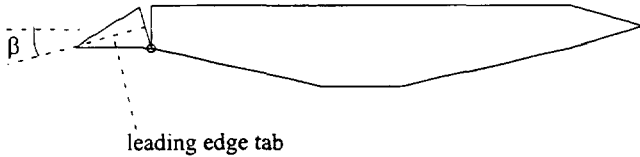


Fig. 5 : Leading Edge Tab

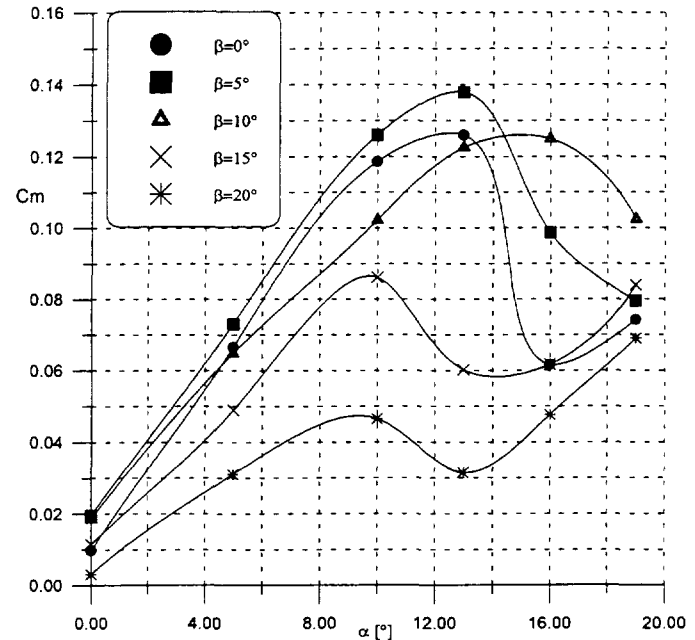


Fig. 6 : Section moment coefficient versus alpha at different tab deflection

A numerical investigation on optimal design of leading edge fairing shape has been done and presented in [7]. A deep wind tunnel test campaign on model dynamic behaviour at different angles of attack alpha, angles of tab deflection β and wind speed has been performed [7].

At $V=20$ m/s and $\beta=0^\circ$ at $\alpha=9^\circ$ (close to the stall angle for the basic configuration) the model shows unstable dynamic behaviour and a strong stall flutter instability is present, see fig. 7.

With a tab deflection $\beta=10^\circ$, which delays section stall and improves post-stall conditions (see fig. 6), the model is stable up to a wind speed of 40 m/s (close to the wind tunnel maximum speed). In fig. 8 it is clearly shown that at $V=40$ m/s and $\alpha=9^\circ$, changing tab deflection from $\beta=15^\circ$ (flutter, like $\beta=0^\circ$) to $\beta=10^\circ$, the flutter has been suppressed.

Then it is evident that, changing the configuration at section leading edge, it is possible to suppress stall flutter instability.

An active control system has been implemented, using an accelerometer as error sensor and two electromagnetic actuators to control the tab rotation. The control algorithm consists of a synchronising circuit that links the accelerometer signal to the actuator action and is explained in more details in [7].

The active control was performed changing the deflection from 15° to 10° with $V=25$ m/s and $\alpha=9^\circ$.

A continuous control was applied. The model dynamic response together with the tab deflection ($\beta=15^\circ$ corresponds to the OFF position, 0 Volt and $\beta=10^\circ$ corresponds to the ON condition, 0.4 Volt) is shown in fig. 9. Through the tab deflection it is possible to keep the system in stable conditions.

The active system is also able to automatically recover the system from incipient stall flutter instability conditions. The model has been brought to deep stall flutter instability with the active system put in the OFF position such that activating the active control, the stall flutter has been suppressed, see fig. 10.

The measured flutter frequency is about 7 Hz and is almost equal to the model first torsional frequency, as well known from the theory.

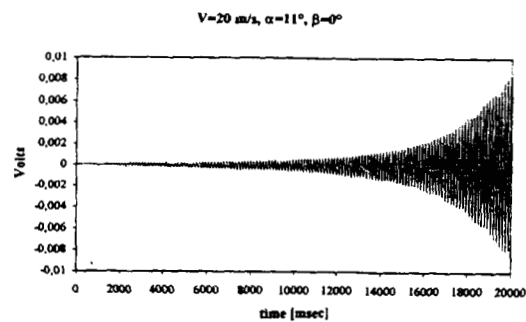


Fig. 7 : Stall flutter - $V=20$ m/s, $\alpha=11^\circ$, $\beta=0^\circ$

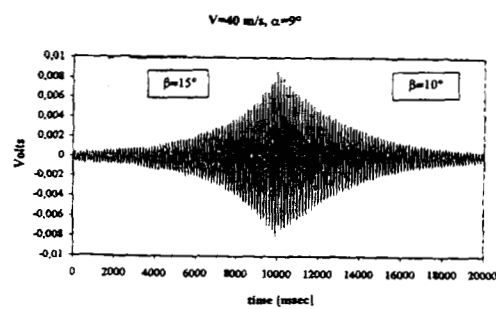


Fig. 8 : Stall flutter suppression
 $V=40$ m/s , $\alpha=9^\circ$

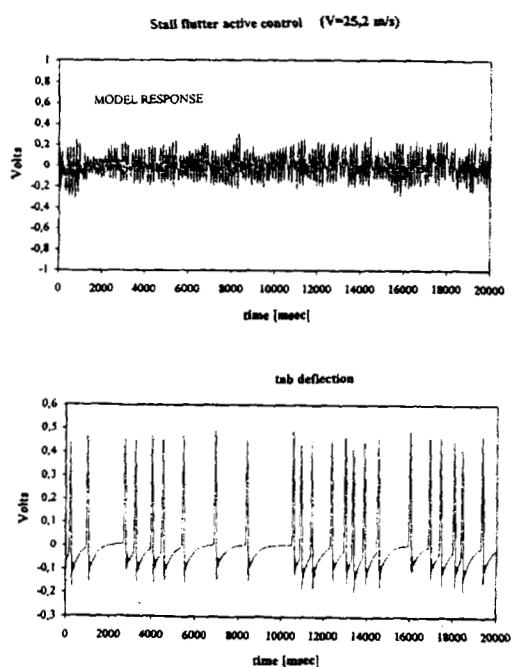


Fig. 9 : Continuous control $V=25$ m/s

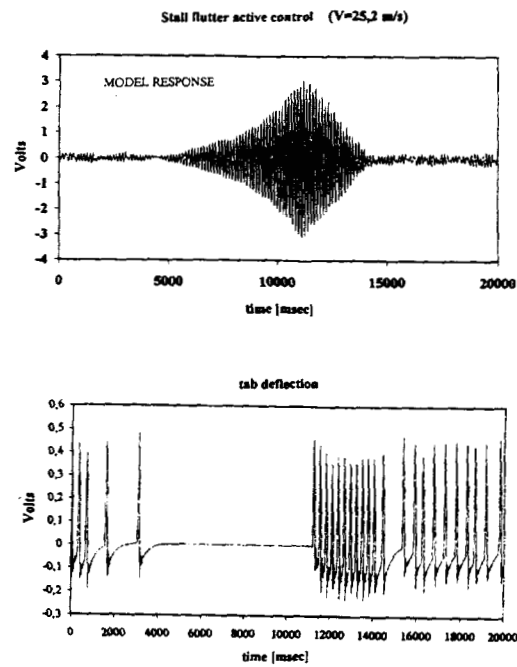


Fig. 10 : Stall flutter suppression

Rotating Cylinder

The model shown in fig. 2 has been modified at the leading edge substituting the wood fairing with a new geometry composed by an aluminium cylinder with a diameter of 14 mm and its billet fixed to the model, see fig. 11. The cylinder is free to rotate and is connected to an electromagnetic small engine. The engine allows the cylinder to rotate up to a speed of about 9000 rpm. The cylinder rotation speed in rpm will be indicated with "n".

The rotating cylinder should change the section stall and post-stall behaviour. The idea is based on coanda effect. In our case not a very strong effect is expected due to the very small ratio between the tangential speed at the cylinder surface and the freestream velocity (about 0.20 with $n=8500$ rpm and $V=30$ m/s). The maximum effect should be present with a ratio of 4 [10].

The cylinder rotation should not change the model dynamic properties. A modal analysis has been performed on the torsionally oscillating model with the cylinder locked and with the cylinder rotating at its maximum rotation speed. The analysis does not show a change in the first torsional frequency which is still about 7.1 Hz, see fig. 12.

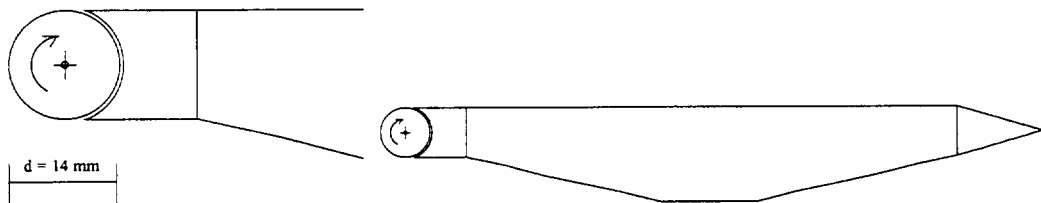


Fig. 11 : Model modified with rotating cylinder

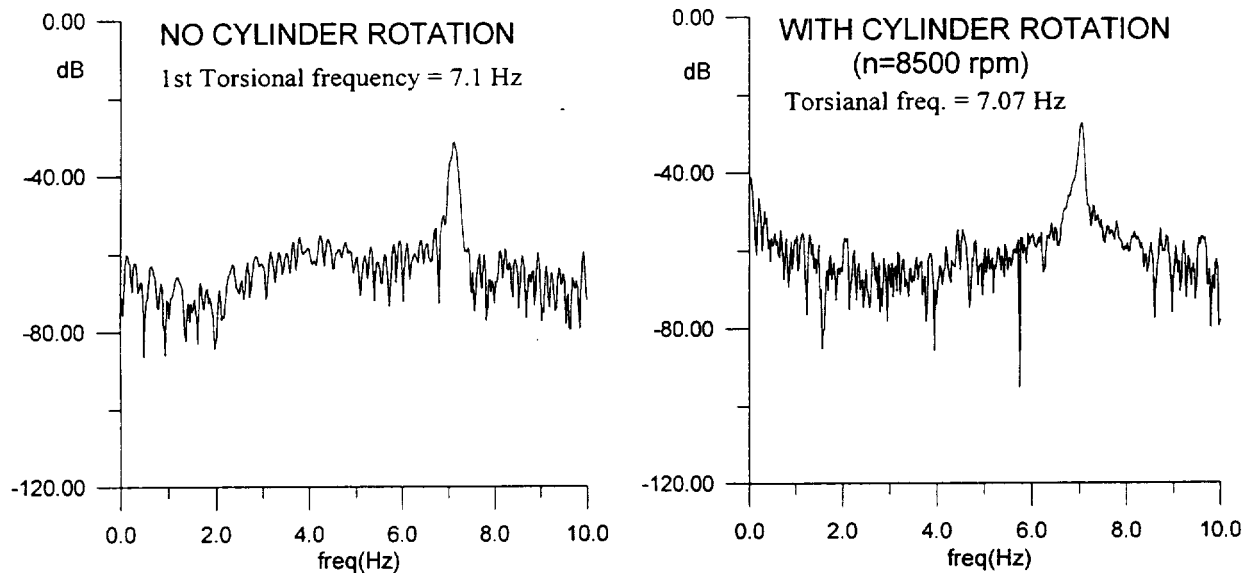


Fig. 12 : Influence of cylinder rotation on model torsional frequency

Steady aerodynamic analysis

A steady aerodynamic analysis has been performed to check the effect of cylinder rotation on section aerodynamic behaviour. The section moment coefficient (respect to the model elastic axis) versus alpha obtained with a wind speed $V=14$ m/s at different cylinder rotation speeds is shown in fig. 13.

It is clearly shown that the cylinder rotation changes the section aerodynamic behaviour at high angles of attack. The stall still occurs at an incidence of about 7° but the cylinder rotation changes the post-

stall conditions. The rotation (through the coanda effect) reduces flow separation on section upper surface at high alpha and the moment curve slope is not negative anymore in post-stall conditions (see fig. 13). Thus different model dynamic behaviour is expected with the rotating cylinder.

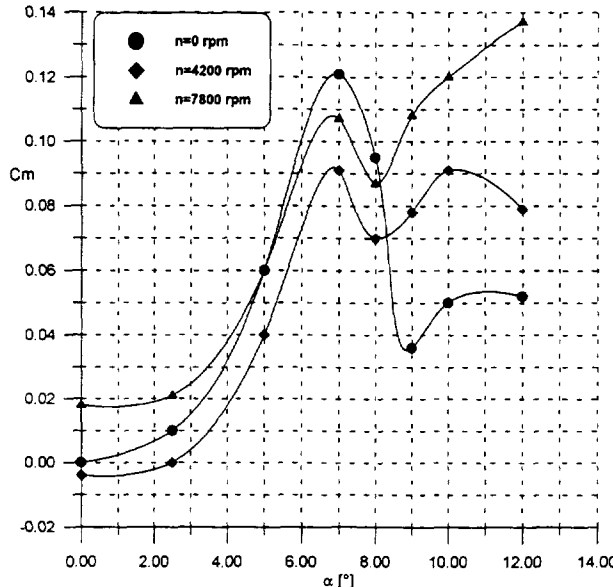


Fig. 13 : Section moment coefficient versus angle of attack at different cylinder rotation speeds

Flutter analysis without cylinder rotation

Different tests have been performed to check model stall flutter instability at different angles of attack and by varying the wind speed.

With the cylinder locked (no rotation) at each angle of attack the model vibration has been measured through an accelerometer varying the wind speed. An example is shown in fig. 14 (on the vertical axis accelerometer output, in Volt). At $\alpha=5.75^\circ$ is possible to see that at $V=12.6 \text{ m/s}$ the model is stable (dumped response due to an external excitation), while at $V=22 \text{ m/s}$ the model has about a zero degree of stability and at $V=31 \text{ m/s}$ the model is unstable. At higher angles of attack, always with the locked cylinder, the flutter unstable condition takes place at lower wind speed. In fig. 15 the dynamic behaviour at $\alpha=7.75^\circ$ is shown. At this angle of attack, at $V=12 \text{ m/s}$ the model already presents stall flutter conditions.

Then it is possible to evaluate from the model dynamic response the logarithmic decrement which is a measure of damping and also of model stable/unstable conditions. A plot of logarithmic decrement versus wind speed at different angles of attack is shown in fig. 16.

It is possible to notice that at high wind speed, although the model is always unstable for α greater than 5.75° , the degree of instability (which indicates if the flutter takes place in a more or less strong and explosive manner) is stronger at $\alpha=7.75^\circ$ than at $\alpha=9.75^\circ$. This is mainly due to the fact that the incidence $\alpha=7.75^\circ$ is really close to the stall condition and the energy extraction due to the hysteresis loop is stronger. It can be seen from fig. 13 that at $\alpha=9.75$ and $n=0$ the section is in post-stall condition and the moment coefficient curve slope is slightly positive. In this condition the flow is strongly separated on section upper surface and model oscillations cannot lead to flow attached condition. As we know when stall flutter conditions are present (due to the hysteresis loop) the section is oscillating between two extreme positions, one characterised by attached flow (and high moment forces) and the

other by strongly separated flow (low mom. forces). From this graph it is then possible to evaluate stall flutter critical speed at each angles of attack (the wind speed for which the damping is zero).

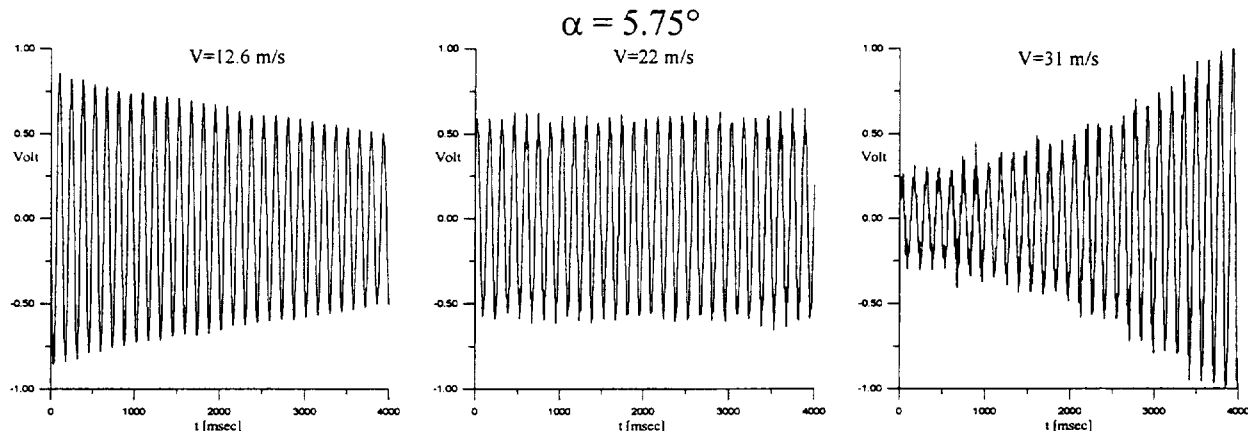


Fig. 14 : Model forced vibrations at $\alpha=5.75^\circ$ and different wind speeds

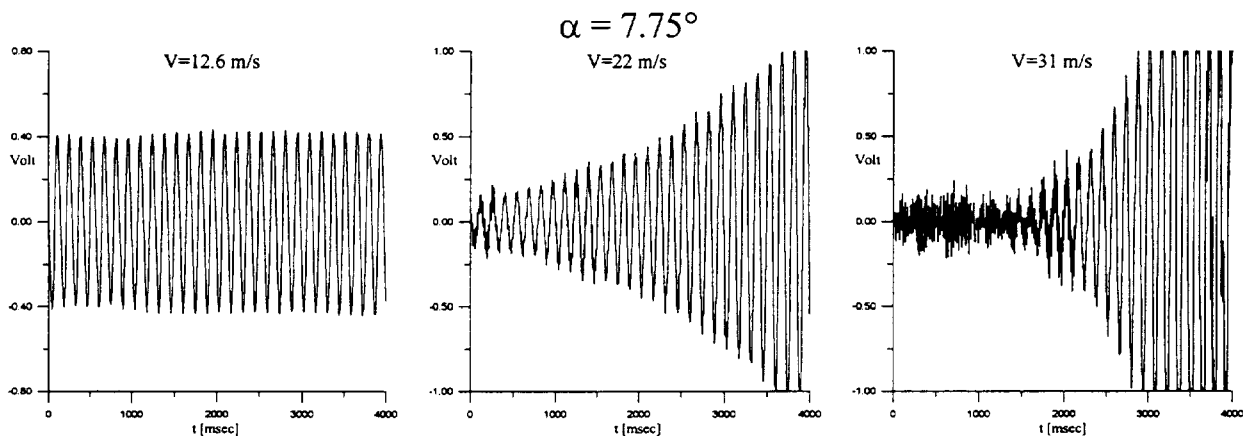


Fig. 15 : Model forced vibrations at $\alpha=7.75^\circ$ and different wind speeds

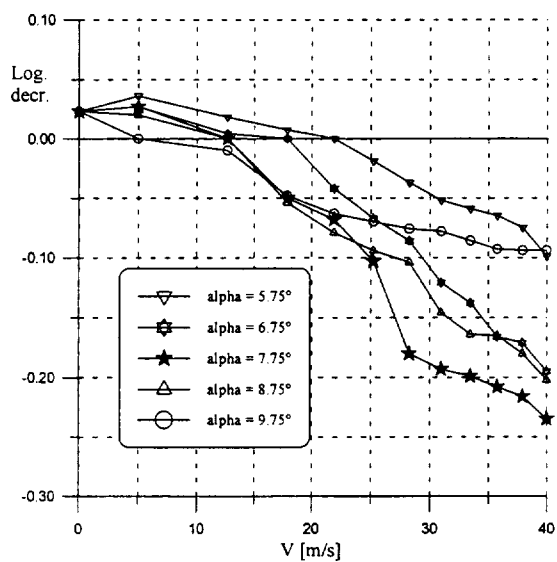


Fig. 16 : Logarithmic decrement versus wind speed

Effect of cylinder rotation on stall flutter speed

Tests at different angles of attack and at different wind speed have been repeated with the cylinder rotating clockwise at different speed.

Fig. 17, 18 and 19 show test results at an angle of attack of 6.75° . In fig. 17 the model unstable behaviour without the cylinder rotation is evident at a wind speed of 22 m/s. The stall flutter starts due to natural freestream excitation and is quite strong. In fig. 18 the rotating cylinder control action is shown. At a certain moment, when flutter brought the model to high amplitude vibrations, the electric engine controlling cylinder rotation was put in the ON position. With the cylinder rotating at a speed of 8500 rpm the model vibrations are damped and stall flutter has been suppressed. In fig. 19 the same has been repeated, but at a wind speed of 25 m/s. The cylinder rotation is able to damp vibrations and suppress the stall flutter, but the action is less powerful and effective. It is evident that increasing wind speed, even with the rotating cylinder the model is unstable and stall flutter conditions are present. In fact, at this incidence, the measured critical speed with $n=8500$ rpm is about 29 m/s (see fig. 22).

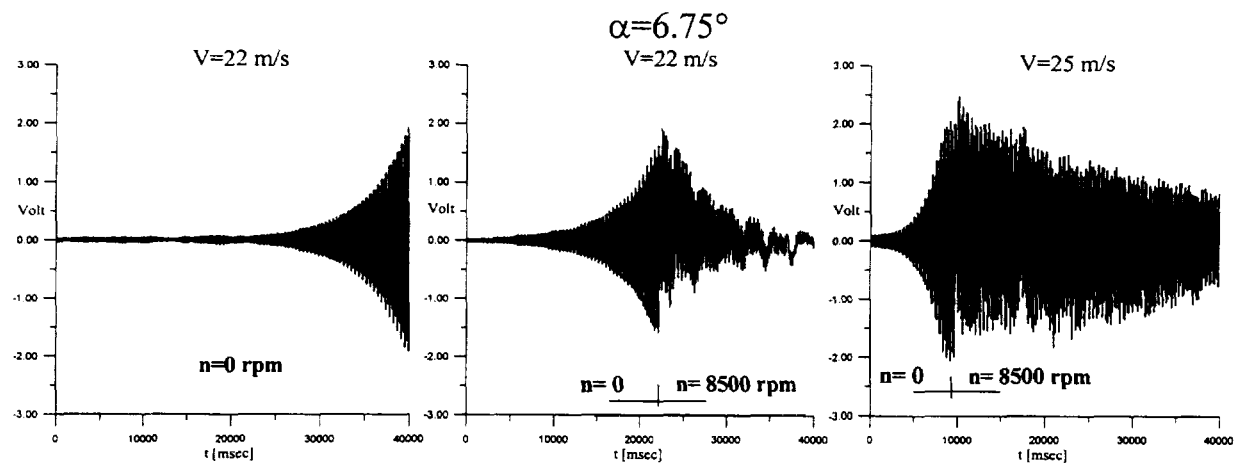


Fig. 17

Fig. 18

Fig. 19

The same tests have been performed at different angles of attack. Obviously at higher angles the critical wind speed is higher compared to that one obtained at small angles. The effect of cylinder rotation on suppressing flutter and increasing critical flutter speed is still present.

The effect of cylinder rotation speed is shown in fig. 20-21. At an angle $\alpha=9.75^\circ$ and $V=14$ m/s the stall flutter has been controlled with $n=7000$ rpm (fig. 20) and with $n=8200$ rpm. With a higher rotation speed the flutter has been suppressed in a more efficient way. It is clear that the increase in cylinder rotation speed results in an increase in flutter critical speed, at a fixed angle of attack.

Tests have been performed fixing the angle of attack and cylinder rotation speeds and increasing wind speed up to unstable conditions (stall flutter critical speed). In fig. 22 the stall flutter speed versus angle of attack at different rotation speeds is plotted. The flutter speed decreases increasing angle of attack. At low angles of attack a flutter critical speed increase up to 60% (at maximum rotation speed, $n=8500$ rpm) has been obtained with the cylinder rotation. An increase of about 50% has been obtained at high angles of attack (see always fig. 22). At the stall angle $\alpha=7.75$ the control is very difficult, due to the large amount of energy which is extracted from the flow with the hysteresis loop and then the strong intensity of stall flutter. At this angle, an increment of about 40% of stall flutter speed has been measured, but there seems to be no effect of rotation speed.

$$\alpha=8.75^\circ \quad V=21 \text{ m/s}$$

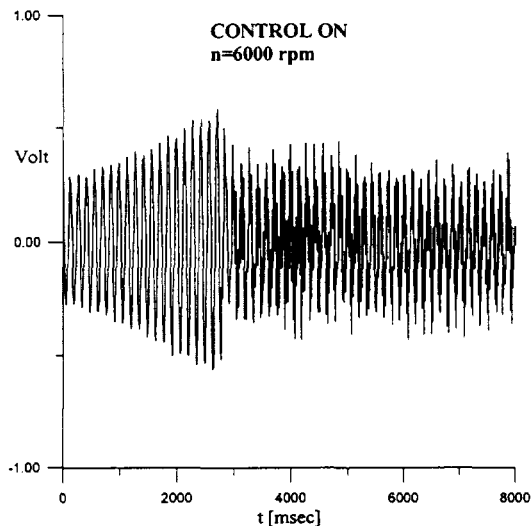


Fig. 20 : $\alpha=8.75^\circ$, $V=21$ m/s, $n=6000$ rpm

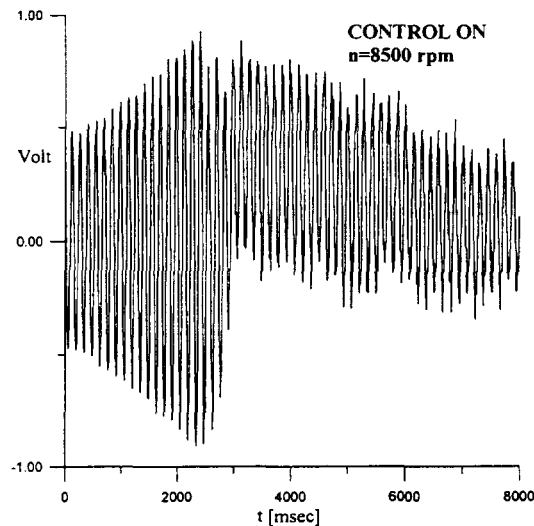


Fig. 21 : $\alpha=8.75^\circ$, $V=21$ m/s, $n=8500$ rpm

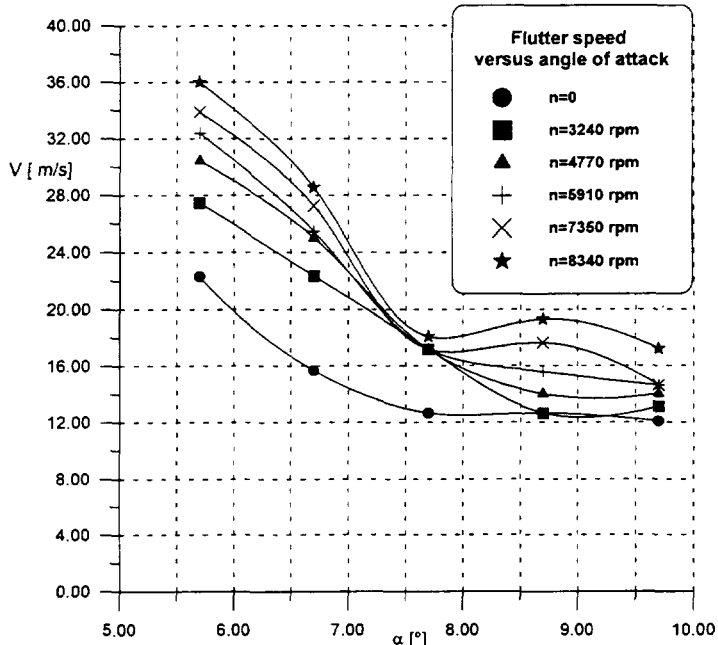


Fig. 22 : Flutter speed versus angle of attack at different cylinder rotation speeds

Conclusions

Experimental activities on a typical bridge section stall flutter has been carried out at D.P.A. low speed wind tunnel and have been presented in this paper. Two different flutter control systems have been proposed and tested. A leading edge tab deflection improves section aerodynamic behaviour at stall conditions and is a good way to increase flutter critical speed. This method has been tested with an active control system which automatically controls and suppresses stall flutter phenomenon.

In the second part a new approach has been tested. A rotating cylinder on section leading edge is another approach to change the section aerodynamic behaviour reducing separations at high angles of

attack and leads to an increase of model flutter critical speed up to 50÷60%. A study of the possible application of such a system on real streamlined deck bridges is in course. Concerning application of this system to real bridges, although for safety reasons it is not possible to believe that the aeroelastic stability of the structure could depend only on the active control system, the control can be used for incrementing the overall performances in term of global safety and further margin of maximum sustainable wind speed, but also in terms of comfort, rail and road runnability, fatigue life-expectance.

References

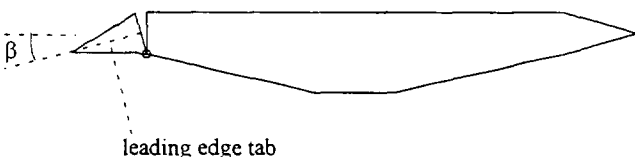
- [1] Murata M., Ito M., 1971,"Suppression of Wind Induced Vibration of a Suspension Bridge by Means of a Gyroscope", *Wind Effects on Buildings and Structures*, Vol. 4, 40, pp. 1-10.
- [2] Cobo del Arco D., Aparicio Bengoechea A.C., "Some proposal to improve the wind stability performance of long span bridges", *2nd EACWE International Conference, Genova, ITALY, 1997*
- [3] Zasso A., Cigada A., Curami A., Paini A., "Ponte sospeso per l'attraversamento dello Stretto di Messina: Ottimizzazione aerodinamica e aeroelastica dell'impalcato su modello sezonale in scala 1:30", *Rapporto Interno del Dipartimento di Meccanica del Politecnico di Milano, 1993*
- [4] Fujino Y., Wilde K., Kawakami T., "New Control Method for Flutter Suppression of Long-Span Bridges", 1998.
- [5] Danda Roy, I., and Eversman, W., "Active Flutter Suppression of an airfoil using an Adaptative LMS Controller," *Active 95, Newport Beach, CA, USA, July 1995*.
- [6] Lecce L., Selvaggi E., De Luca S., Iorio C., Anderson J., Pecora M., "Numerical And Experimental Results on a 2-D Wing Model with a New General Purpose Active Flutter Suppression System," *International Forum on Aeroelasticity and Structural Dynamics, 17-20 June 1997, Rome (Italy)*
- [7] Lecce L., Selvaggi E., Nicolosi F., Anderson J., "A new General Purpose Active System for Controlling Aeroelastic Behaviour of Long-Span Bridges", *INVENTO 98, 5° Convegno Nazionale di Ingegneria del Vent, Perugia 1998*
- [8] Ostenfeld K. And Larsen A., "Bridge Engineering and Aerodynamics", *Aerodynamics of Large Bridges, Copenhagen,A.A. Balkema, Rotterdam, pp.3-22*
- [9] Fung Y.C., *An Introduction to the Theory of Aeroelasticity*, John Wiley & Sons, 1955
- [10] Bergeson L., Greenwald C.K., "Magnus rotor test and evaluation"

The section dynamic behaviour has been tested with the rotating cylinder. In fig. 4 the section flutter speed (freestream speed at which the section become unstable and stall flutter appears) versus angle of attack for different cylinder angular speeds is represented. The cylinder rotation is able to increase section flutter speed up to 55% at low angles of attack and about 40% at high incidences.

The i.e. tab deflection changes the static aerodynamic behaviour of the section and leads to different stall flutter instability conditions. It is then evident that a different tab position can increase the model aeroelastic stability and delay the stall flutter to higher angles of attack. For instance a downward deflection of about 10° allow an higher stall angle and a less critical post-stall behaviour. Numerical aerodynamic analysis has been also performed to improve section aerodynamic behaviour through an appropriate shape of the section leading edge. Numerical prediction are in good agreement with experimental results.

Application of a new active control system has been performed using the previous movable surface. The stall flutter in dynamic conditions has been controlled using an active system which automatically changes the tab position (from 0 to 10°) and is able to suppress the stall phenomenon. The control system consists of a mixed digital-analogue feedback circuit with an accelerometer as error sensor and two electromagnetic actuators to control the tab rotation.

In the second part a new approach has been tested. The new methodology consists of a rotating cylinder placed at the section leading edge (see fig. 2). Through the cylinder rotation is possible to change the section aerodynamic behaviour as well. In fig. 3 the section moment coefficient versus angle of attack for three different cylinder angular speed are shown. The section stall angle is always about 7° and does not change with the cylinder angular motion. The post-stall section behaviour is on the contrary strongly influenced by the cylinder angular speed. Cylinder angular motion can be a successful way to control and suppress stall flutter phenomenon. The section dynamic behaviour has been tested with the rotating cylinder. In fig. 4 the section flutter speed (freestream speed at which the section become unstable and stall flutter appears) versus angle of attack for different cylinder angular speeds is represented. The cylinder rotation is able to increase section flutter speed up to 55% at low angles of attack and about 40% at high incidences.



15°	<i>flutter</i>			
------------	----------------	--	--	--

Table 1 : Section behaviour at different angle of attack and tab deflections

####/###	0°	10°	13°	16°	19°
0°		<i>flutter</i>	<i>flutter</i>		
5°		<i>flutter</i>	<i>flutter</i>		
10°					<i>flutter</i>

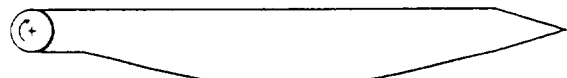


Fig. 2 : Rotating cylinder at section leading edge

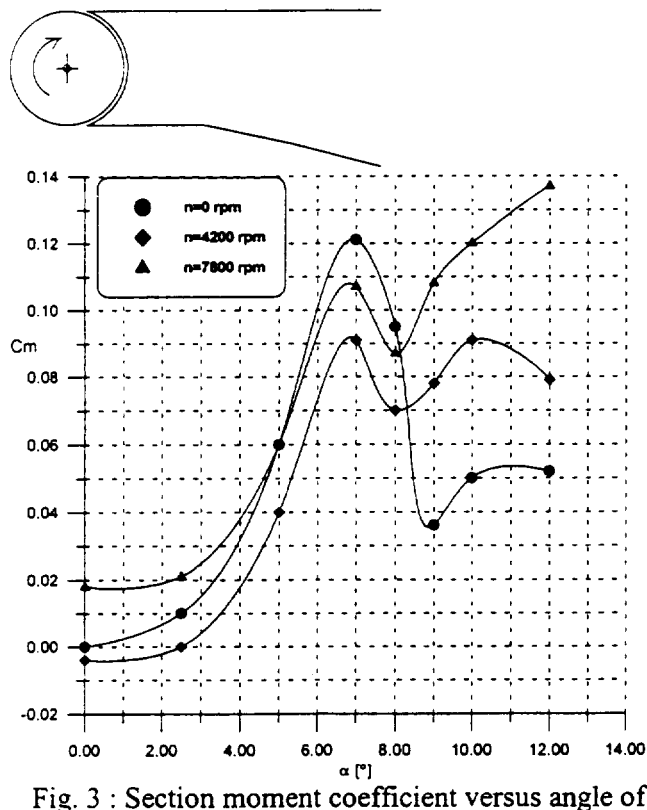


Fig. 3 : Section moment coefficient versus angle of attack at different cylinder rotation speeds

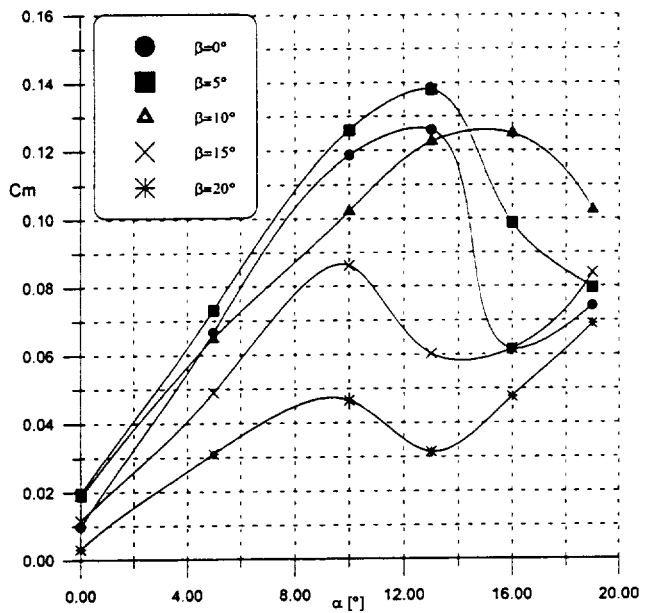


Fig. 1 : Effect of leading edge tab deflection on section aerodynamic characteristics

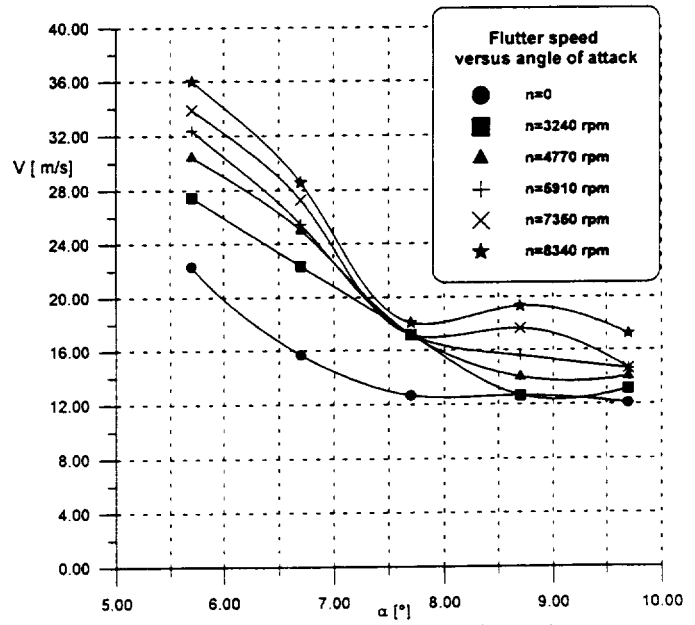


Fig. 4 : Flutter speed versus angle of attack at different cylinder rotation speeds

A REDUCED BASIS MODEL FOR AEROELASTIC OPTIMIZATION

S.Grihon, J.P Esquerre
Aerospatiale Airbus Division
Design Office
Toulouse, France

523 -02

ABSTRACT

A method is proposed by which the computational efficiency of the aeroelastic sizing optimization process is improved. It uses a reduced basis model approach.

This reduced basis model is first validated through flutter simulations under large structural modifications. The test case is a simplified model of a four engine aircraft wing.

It is then applied to a flutter optimization study. The case studied is a full model of a large four engine aircraft. The flutter behavior of this model is controlled through an optimization of engine pylons.

For a comparison purpose, two optimization methods are applied to this second case. The first one is the classical approach using exact modal and flutter reanalysis at each iteration, the second one uses the reduced basis model. Results are very close, but the optimization with the reduced basis model is considerably faster. It facilitates mode tracking during the optimization process as well as rapid evaluations of alternative optimization problem formulations.

NOTATIONS

K	finite element stiffness matrix
M	finite element mass matrix
ΔK	stiffness matrix modification
ΔM	mass matrix modification
x	current modal shape for the perturbed structure
λ	associated squared angular frequency
α	mean value for perturbed squared angular frequencies
m	rank of the truncated modal basis
$(\varphi_j)_{j=1..m}$	j th modal shape (increasing frequency order)
$(\lambda_j)_{j=1..m}$	associated squared angular frequency
Φ	modal matrix for the initial structure
q_i	component of x relative to φ_i
q	associated vector
np	number of design variables

$(p_i)_{i=1..np}$	i th design variable defined as a global scaling factor applied to the i th group of elements
p	associated vector
K_i	assembled stiffness matrix of the i th group of elements
M_i	assembled mass matrix of the i th group of elements
Ψ	extended modal basis matrix
r_j	j th modal shape vector of components in Ψ
s	complex frequency
\bar{q}	dynamic pressure
$(\delta_i)_{i=1..nl}$	lag terms
nl	number of lag terms
F_i	aerodynamic matrices
d	damping coefficient = Re(s)/Im(s)

INTRODUCTION

Statement of the Problem

Flutter Analysis requires full aircraft modeling and expensive modal analysis, which generally lead to heavy optimization tasks.

It is not compatible with the several studies often necessary to tune an optimization problem. Moreover a mode tracking procedure is often required to optimize the flutter behavior of a large aircraft whose normal mode frequencies are very close. It supposes a continuation approach with additional modal and flutter reanalysis which is difficult to perform in a reasonable time with a large size dynamic model.

This paper presents a method to overcome these difficulties by accelerating the structural optimization process. This method uses a model reduction.

Review of model reduction methods

In Ref. 2.,3. Giles proposes to build a reduced model for a wing by using an equivalent plate formulation. But it appears difficult to get significant results with such an approach. The flutter behavior is indeed very sensitive to modeling hypothesis and

quality. One serious difficulty is the complexity of the engine pylon-to-wing attachment idealization which can be obtained through a quite detailed finite element model only.

A classical approach, described in Ref. 7., consists in using a truncated modal basis to represent displacement vectors. A reduced model is built through the Lagrange equations using, as generalized coordinates, the components of the displacement vector in this basis. This is the Rayleigh-Ritz approach. This approach is used in flutter simulation where the truncated modal basis is restrained to the sixty lowest frequency modes. It is natural to extend it to flutter optimization which means that the modal basis is kept constant along the optimization process, thus avoiding the modal reanalysis. This method was tested but with no satisfactory result even if the truncation frequency is much higher than in flutter simulations.

In Ref. 8.,9. Karpel proposes a method to control the modal truncation error. It consists in using additional masses, called "fictitious masses" located in the area of structural changes so as to lower the frequencies of relevant modes. But the difficulty encountered when using this method is the choice of well-suited values for fictitious masses.

In Ref. 10.,11. Kirsch presents an approximation method used for static responses of trusses or grillage-type structures. He derives an analytical expression of static displacements for trusses and shows it is exact.¹⁰ This method uses a first order reduced basis method. It is extended to grillage-type structures with satisfactory results.¹¹

The approach proposed in this paper can be seen as an extension to modal analysis of the method proposed by Kirsch and comparisons will be pursued in the next section.

PROPOSED APPROACH

Introduction

The proposed method is a Ritz-type method based on an extended modal basis. As mentioned before a truncated modal basis gives no accurate results even if the truncation is made at a high frequency. Thus a new basis of displacements is developed.

This basis is an extension of the modal basis with complementary vectors capturing the effect of structural modifications on the modal shapes.

As explained in the next section, structural modifications are linear with respect to design variables in most of our sizing optimization tasks. This important property is exploited further.

Design variables and structural modifications

Structural modifications are parameterized by the design variables used in optimization. These design variables are associated with predefined structural regions. The i^{th} design variable is a scaling factor p_i applied to all element properties of the corresponding region. These properties are generally skin thicknesses or stiffener cross sectional areas. Moreover airframes have thin-walled structures whose elements essentially work as membranes.

Regarding the choice of design variables and the mechanical behavior of the structure, stiffness matrix modifications are linear and can be written as :

$$\Delta K = \sum_{i=1}^m (p_i - 1) K_i \quad (1)$$

Mass matrix modifications are obviously linear and can be expressed as :

$$\Delta M = \sum_{i=1}^m (p_i - 1) M_i \quad (2)$$

Extended Modal Basis Derivation

The modal equations of a structure involving stiffness and mass changes ΔK and ΔM is given by:

$$(K + \Delta K)x = \lambda(M + \Delta M)x \quad (3)$$

The effect of pure structural mass changes on frequencies being negligible, ΔM is not taken into account further.

Let introduce a parameter α , which represents a mean value for the squared angular frequency λ in the frequency domain of interest. Then equation (3) can be written as a fixed-point equation :

$$x = (\lambda - \alpha)(K - \alpha M)^{-1}Mx - (K - \alpha M)^{-1}\Delta Kx \quad (4)$$

If x is written as a combination of the initial eigenvectors:

$$x = \sum_{j=1}^n q_j \varphi_j \quad (5)$$

then x can be expressed as $x_1 - x_2$ with :

$$x_1 = (\lambda - \alpha) \sum_{j=1}^n \frac{q_j}{\lambda_j - \alpha} \varphi_j \quad (6)$$

$$x_2 = \sum_{i=1}^{n_p} \sum_{j=1}^n (p_i - 1) \lambda_j (K - \alpha M)^{-1} K_i \varphi_j \quad (7)$$

x_1 can be represented by a truncated modal basis because $\frac{\lambda - \alpha}{\lambda_j - \alpha}$ is negligible in the high frequency domain (large values of λ_j).

x_2 leads to a completion of the initial modal basis with displacement vectors of the kind

$$(K - \alpha M)^{-1} K_i \varphi_j \quad (8)$$

These considerations give the following displacement basis :

$$\Psi = (\Phi, (K - \alpha M)^{-1} K_i \Phi, i = 1, \dots, n_p) \quad (9)$$

where Φ is a truncated modal matrix which is usually selected as a satisfactory modal basis for a flutter analysis of the initial structure.

Remarks

As explained below, this method is close to the method developed by Kirsch for grillage-type structures. Kirsch uses a second order Taylor expansion of the static response to build the basis. It can be considered as a second iteration of the fixed-point equation (4) following the method used by High to compute the modal shape derivatives.

But applications with the proposed method show that the first order is enough even with large magnitude structural changes.

This is because an appropriate selection of modal shapes enables to cover the rank of the matrices K_i with the vectors $K_i \varphi_j$.

In this sense, the extended modal basis method joins the exact reanalysis method proposed by Kirsch for trusses¹⁰. Its success leans on the fact that the elementary stiffness matrix of a free-free compression bar has rank one.

Reduced structural model

Stiffness and mass matrices are then written in the "extended modal basis" Ψ . As Ψ is constant, their updating consists in simple linear combinations of small order matrices:

$$\Psi^T K(p) \Psi = \Psi^T K \Psi + \sum (p_i - 1) \Psi^T K_i \Psi \quad (10)$$

$$\Psi^T M(p) \Psi = \Psi^T M \Psi + \sum (p_i - 1) \Psi^T M_i \Psi \quad (11)$$

The vectors $(r_j)_{j=1..m}$ which approximately represent modal shapes of the modified structure are calculated with a Ritz method using the basis Ψ . The squared angular frequencies λ_j and the new modal shapes $x_j = \Psi r_j$ are thus given by the resolution of the generalized eigenvalue problem:

$$\Psi^T K(p) \Psi r = \lambda_j \Psi^T M(p) \Psi r \quad (12)$$

Reduced aerodynamic model

Aerodynamic influence coefficients are issued from a Doublet Lattice Method. They are converted to generalized aerodynamic forces by a projection on the extended modal basis.

The approximation derived by Roger in Ref. 12. is then used. It takes the form of a rational function:

$$F(s) = \bar{q} (F_0 + \frac{s}{V} F_1 + \left(\frac{s}{V}\right)^2 F_2 + \sum_{i=3}^{n+2} \frac{s F_i}{s + V \delta_{i-2}})$$

The advantage of such an approach is to reduce the flutter equation at a given speed to an eigenvalue problem for a real matrix. It simplifies flutter simulations and damping coefficient sensitivity computations. More details can be found in Ref. 2. Hence aerodynamic data consist of $3+nl$ matrices $(F_i)_{i=0..nl+2}$ constant along the optimization process. nl is the number of lag terms δ_i . A current value for nl is 3.

RESULTS

Validation on a simplified wing model

After some convincing validations on modal reanalysis of a bending-torsion beam, the method is applied to flutter reanalysis.

A simplified wing model of a four engine aircraft is used. This model is clamped at the root rib and has about 5000 degrees of freedom. It is divided into 20 optimization regions. In each region, one design variable is defined as explained before. Two additional design variables are added to control the stiffness of engine pylon-to-wing attachment elements. For a total of 22 design variables and with a rank 15 modal basis, the extended modal basis consists of 160 displacement vectors (the model dimension is thus reduced by a factor 30).

Very large modifications are made to validate the robustness of such a basis. One example is presented for which the mid-wing shows an 80% under-sizing and the inner wing a 50 % over-sizing.

The quasi-perfect similarity of the damping plots obtained with the proposed approach versus those

obtained with the exact reanalysis approach can be seen in figure 1. It shows the performance of the reduced basis model (especially for whom knows the sensitivity of flutter results to wing modal shapes).

Application to engine pylon aeroelastic optimization

Statement of the problem

The extended modal basis method is then applied to flutter optimization.

The application case is a full four engine large aircraft dynamic model based on a finite element model with 20000 degrees of freedom. Figure 2 shows the powerplant area for this finite element model and illustrates the role of pylons.

Preliminary sensitivity computations on the four pylons show that the outer pylon stiffness is an essential driving parameter to improve the flutter behavior. Indeed the studied case mainly presents a smooth coupling involving engine modes and yielding a critical flutter speed. Thus it has been decided to perform sizing optimization of outer pylons with flutter requirements.

The flutter optimization problem is stated as a minimization of the structural mass $m(p)$ with a constraint on the damping coefficient $d_i(V_c)$ of the unstable mode at the critical speed. Side constraints on design variables are also included so as to take into account stress and design requirements.

Thus the problem solved is given by

$$\begin{aligned} & \text{Min } m(p) \\ & \text{w.r.t.} \\ & d_i(V_c) > d_{\min} \\ & \text{s.t.} \\ & (p_i)_{\min} < p_i < (p_i)_{\max} \end{aligned}$$

29 optimization regions are defined for each outer pylon. A modal basis with 60 vectors is selected.

The extended modal basis retains about 120 vectors (the model dimension is thus reduced by a factor 200).

Comparison of two methods

The problem is treated following two algorithmic approaches.

The first one is the classical approach using exact modal and flutter reanalysis at each iteration. It is associated with the sequential approximation used by most structural optimization codes. The optimization algorithm used is CONLIN, recognized as one of the most well-suited to structural optimization problems.

The second one uses the reduced basis model presented above. All small order computations are

made in a same FORTRAN program and the damping coefficients and their analytical sensitivities are provided to a library algorithm as subroutines. This library algorithm is the NAG implementation of the Sequential Quadratic Programming Algorithm (E04UCF subroutine).

As shown in figure 3, for the approach using the reduced basis model, large order computations are concentrated in the reduction stage, while modal and flutter reanalysis are then made at a small order.

A first comparison between both method results is made with realistic side constraints for design variables. Results are similar but the comparison is biased because most of the side constraints are active at the optimum. It has thus been decided to relax these side constraints for a comparison purpose.

It involves for the exact reanalysis method to run again the optimization process at a large order. For the extended basis method, as the definition of design variables is not modified, it is not necessary to compute again the basis. Hence large order computations are avoided. This is a major advantage of the proposed method: as long as the design variables are not redefined, several formulations of the problem can be run at a low computational cost, which is very useful for industrial applications in aircraft design.

With relaxed design variable bounds, much design variables are free at the optimum and both methods show very close values, as shown in figure 4.

The conclusion is that the reduced basis model gives satisfactory optimization results but is much less computationally expensive : 1 hour against 50 hours due to a reduction of the full aircraft model from 20000 degrees of freedom to 120 generalized degrees of freedom. This comparison completes the validation of the extended modal basis approach in the scope of an optimization process.

Analysis of results

Results show that, the flutter behavior can be improved by outer engine pylon optimization, with reasonable weight penalties. The structural improvement leads to a shift at a higher speed of the aeroelastic coupling with a significant increase of the damping giving no flutter, as shown on figure 5.

In preliminary applications, an asymmetrical pylon is studied. The over-sizing exhibits a "bevel shape" whose objective is to increase the combined lateral and yaw stiffness of the pylon. But these structural modifications are not easy to use in an industrial process. So further optimization cases are then treated with symmetrical constraints, without computing again the extended modal basis, showing

once again the interest of the approach. Symmetrical results have a slightly higher mass for the same flutter improvement. Main modifications are on the side panels and on the upper spar, as shown on figure 6.

New parameters are then included (internal ribs, forward engine-to-pylon attachment), and lead to better weight performances. The process is then completed by a multi-disciplinary work between aeroelastic, design and stress specialists.

CONCLUDING REMARKS

A new method has been developed to facilitate flutter optimization. This method uses a basis reduction process, allowing a control of the truncation error with respect to a modal approach. This basis is dedicated to sizing design variable modifications. A part of its success is due to the linearity of finite element models for thin-walled structures with respect to this kind of variables. The performance of this method has been demonstrated on a simplified wing model. Then an industrial application was performed showing very reliable results, when compared to classical approaches, while great computational time reductions.

The method presented here enables to include mode tracking in flutter optimization with a reasonable computational time and to solve rapidly variants of the optimization problem. More generally, it authorizes intensive modal or flutter reanalysis, and can help to better understand flutter mechanisms.

Hence it is really well-suited to flutter parametric studies during the concept phasis of new aircraft. Applications to global analysis (uncertainties modeling) or global optimization are made possible with this approach. It could also be used to accelerate model updating based on modal tests.

REFERENCES

- ¹Fleury, C., Braibant, V., "Structural optimization: a new dual method using mixed variables" Int. J. Numer. Meth. in Eng., vol.23, 1986.
- ²Giles, G.L., "Equivalent Plate Analysis of Aircraft Wing Box Structures with General Planform Geometry" J.of Aircraft, vol.23 n°11 (1986)
- ³Giles, G.L., "Further Generalization of an Equivalent Plate Representation for Aircraft Structural Analysis" J.of Aircraft, vol.26 n°1 (1989)
- ⁴Grihon, S., Seigneuret, F., "Model Reduction for modal reanalysis and flutter optimisation" submitted to Int. J. Numer. Meth. in Eng.
- ⁵Haftka, R.T., Gürdal Z., "Elements of Structural Optimization" Kluwier Academic Publishers (1992).
- ⁶High, G.D., "An iterative method for eigenvector derivatives" Proceedings of 1990 MSC World Users Conference, vol.1, MacNeal Scwendler Corp., Paper 17, Los Angeles, March 1990
- ⁷Imbert, J.F., "Analyse des structures par éléments finis" Cépaduès, 1984
- ⁸Karpel, M., "Modal Coordinates for Aeroelastic Analysis with Large Local Structural Variations" J.of Aircraft, vol.29 n°2 (1992)
- ⁹Karpel, M., "Multidisciplinary Optimization of Aeroviscoelastic Systems Using Reduced-Size Models" J.of Aircraft, vol.31 n°2 (1994)
- ¹⁰Kirsch, U., Liu, F., "Exact structural reanalysis by a first-order reduced basis approach" Struct. Opt. 10, 153-158, Springer Verlag, 1995
- ¹¹Kirsch, U. and Moses, F., "An improved reanalysis method for grillage-type structures" Comput. and Struct. 68 (1998) 79-88, Pergamon Press
- ¹²Roger, K., "Airplane Math Modelling Method for Active Control Design" AGARD, CP-228 (1977)

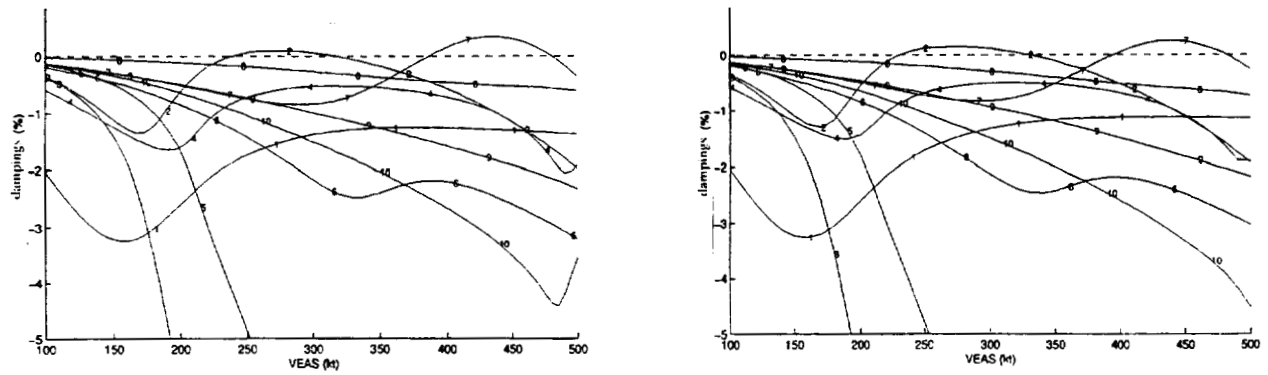


Fig 1. Comparison of flutter plots - extended modal basis vs exact reanalysis.
Damping coefficient (%) vs. air speed (EAS, kts) variations for each mode as computed with the exact reanalysis (left) and the extended basis model (right).

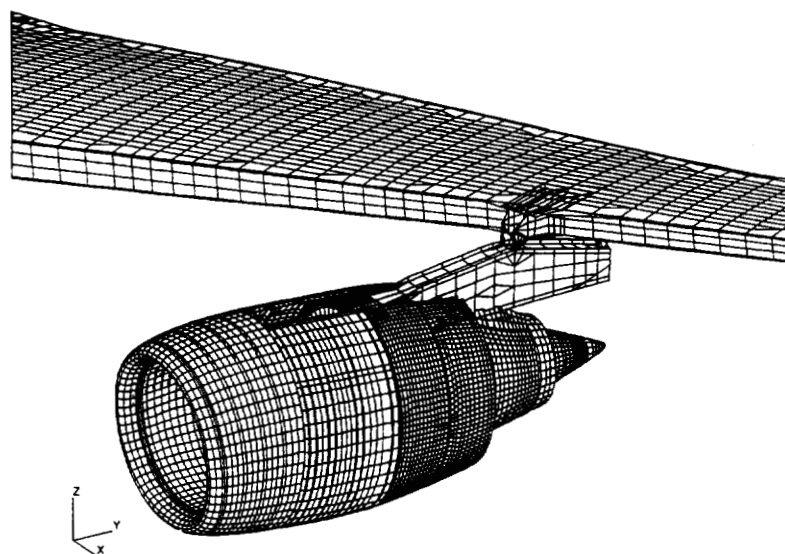


Fig 2. Powerplant sketch. The engine pylon is a torsion box used to attach the engine to the wing lower part.

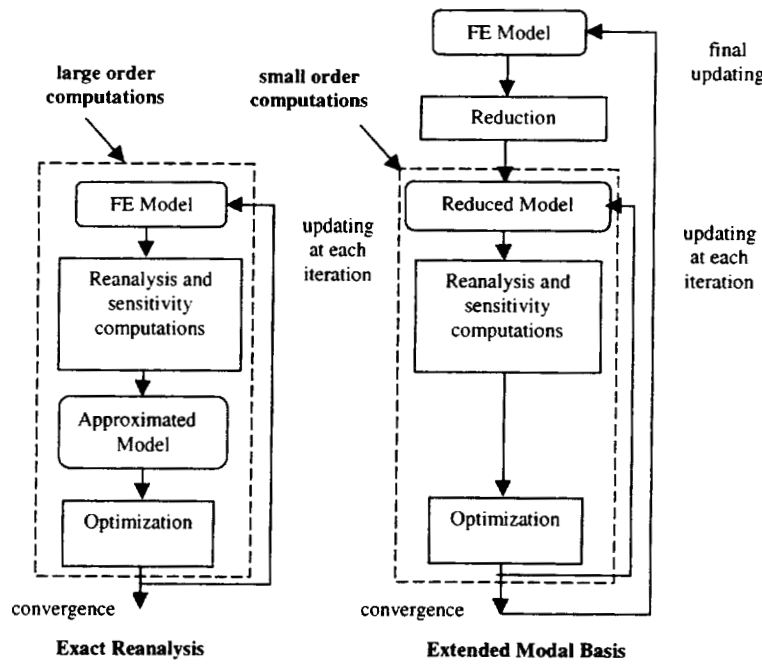


Fig 3. Comparison of both optimization approaches. In the extended modal basis approach large order computations are in the reduction process, optimization iterations only involved small order computations.

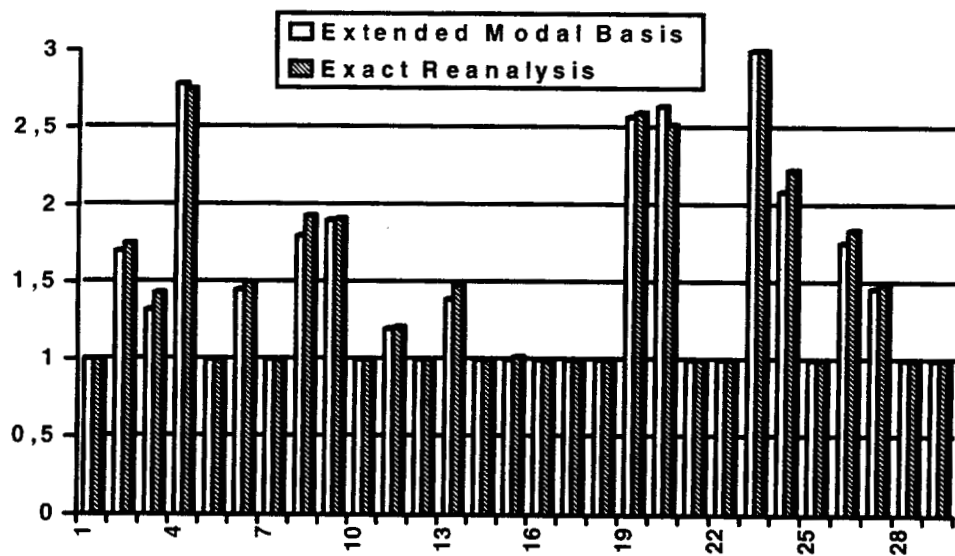


Fig 4. Comparison of optimization results – extended modal basis vs exact reanalysis - case with relaxed side constraints. White bars represent design variables (scaling factors) obtained with the extended modal basis approach, hatched bars those obtained with the exact reanalysis.

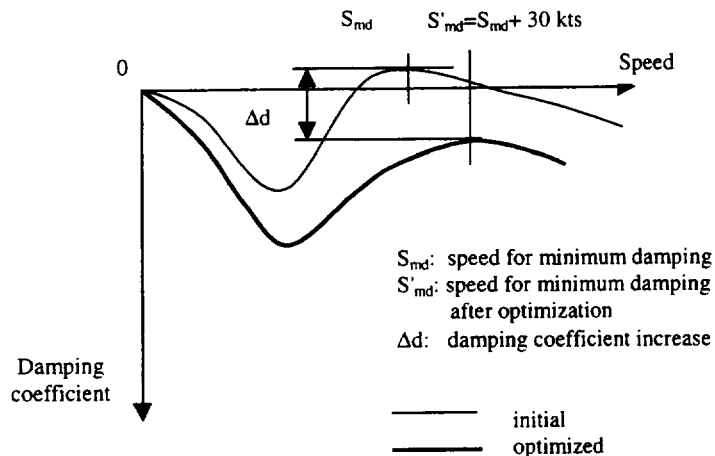


Fig 5. Comparison of flutter plots – initial vs optimized.
Results show that there is no more instability. The critical mode has got an increased damping.

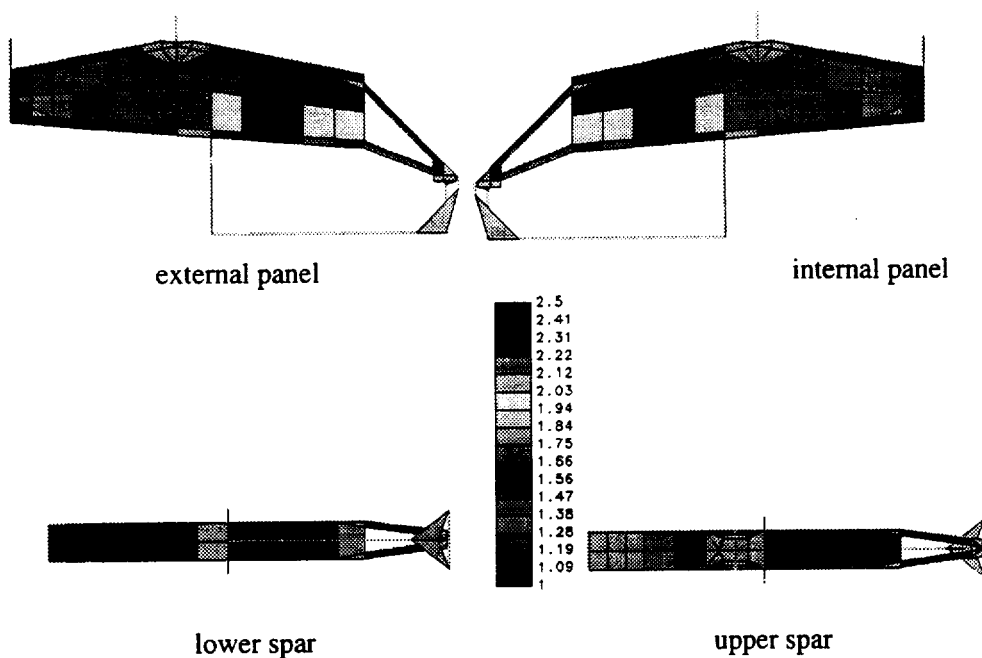


Fig 6. Pylon over-sizing after flutter optimization. The most stiffened area are the rear part of the upper spar and the front lower part of the panels.

A SURVEY OF SHAPE PARAMETERIZATION TECHNIQUES

Jamshid A. Samareh *
NASA Langley Research Center, Hampton, VA 23681

This paper provides a survey of shape parameterization techniques for multidisciplinary optimization and highlights some emerging ideas. The survey focuses on the suitability of available techniques for complex configurations, with suitability criteria based on the efficiency, effectiveness, ease of implementation, and availability of analytical sensitivities for geometry and grids. The paper also contains a section on field grid regeneration, grid deformation, and sensitivity analysis techniques.

Nomenclature

B	Bernstein polynomial
\bar{c}	polynomial coefficients
f	response
J	cell Jacobian
k	spring stiffness
N	B-spline basis function
\bar{P}	coordinates of NURBS control point
\bar{R}	coordinates of deformed model
\bar{r}	coordinates of baseline model
\bar{U}	deformation vector
u	independent parameter coordinate
V	baseline cell volume
\bar{v}	design variable vector
W	NURBS weights

Subscripts

f	field (volume) grid
g	geometry
i	control point index
j	grid point index
k	grid point index
m	element index
p	degree of Bernstein polynomial and B-spline basis function
s	surface grid
ϵ	small positive number

Superscripts

i	polynomial power
n	number of design variables

*Research Scientist, Multidisciplinary Optimization Branch,
AIAA Senior Member.

This paper is a work of the U.S. Government and is not subject to copyright protection in the United States.

Introduction

IMAGINE that you have been asked to perform multidisciplinary shape optimization (MSO) for a complete aircraft model during the preliminary design phase. During this phase, the focus is on the mathematical modeling, with sufficient accuracy, of the outside skin of an aircraft. After this phase, the geometry is frozen, and any change could be costly.

Generally, multidisciplinary design optimization (MDO) should exploit the synergism of the primary, mutually interacting phenomena to improve the design. The MDO applications commonly involve sizing, topology, and shape optimization. Sizing optimization is used to find the optimum cross-sectional area for bars and trusses and thickness for plate and shell elements. Sizing optimization is a matured technology and is available in most commercial computational structural mechanics (CSM) tools. Topology optimization is a technique for determining the optimal material distribution, which could suggest the optimum layout of the structure. Shape optimization finds the optimum shape for a given structural layout. Obviously, the selection of shape parameterization technique has enormous impact on the formulation and implementation of the optimization problem. This paper reviews and evaluates the available shape parameterization techniques.

Over the past several decades, single discipline shape optimization has been successfully applied to two-dimensional and simple three-dimensional configurations.^{1,2} In recent years, there has been a growing interest in the application of MSO to complex three-dimensional configurations.³ The MSO for a complete airplane configuration is a challenging task, especially if the MSO application is based on high-fidelity analysis tools. The analysis models, also referred to as grids or meshes, are based on some or all of the airplane components.

The aerodynamic analysis uses the detailed definition of the skin shape, also referred to as the outer mold

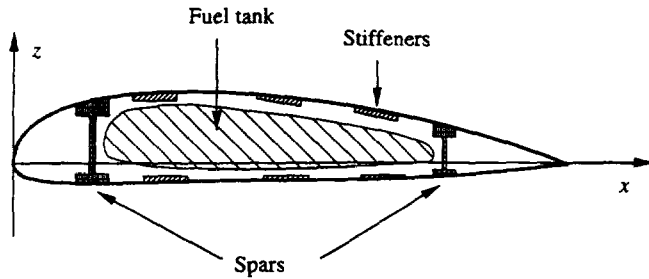


Fig. 1 Internal components of a wing.

line, whereas the CSM tools use all components. Generally, the structural model only requires a relatively coarse grid, but it must handle very complex internal and external geometries. In contrast, the computational fluid dynamics (CFD) field grid is very fine, but it only needs to model the external geometry. The MSO of an airplane must treat not only the external geometry (i.e., wing skin, fuselage, flaps, nacelles, and pylons), but also the internal structural elements such as spars, ribs, and fuel tanks (see Fig. 1). The treatment of internal structural elements is especially important for detailed finite element (FE) analysis.

For a high-fidelity MSO application to be successful, the parameterization model must yield a compact and effective set of design variables so the solution time would be feasible. For more details, readers are referred to an overview paper by this author⁴ on geometry modeling and grid generation for design and optimization.

Multidisciplinary Shape Parameterization

The complexity of geometry models is increasing for today's preliminary design applications. It is not unusual for a computer-aided design (CAD) model to use over twenty thousand curves and surfaces to represent an aircraft. This level of complexity underscores the importance of automation. With any multidisciplinary application come the problems of consistent and accurate shape parameterization.

The shape parameterization must be compatible with and adaptable to various analysis tools ranging from low-fidelity tools, such as linear aerodynamics and equivalent laminated plate structures, to high-fidelity tools, such as nonlinear CFD and detailed CSM. For a multidisciplinary problem, the application must also use a consistent parameterization across all disciplines. An MDO application requires a common geometry data set that can be manipulated and shared among various disciplines.

In addition, an accurate sensitivity derivative analysis is required for gradient-based optimization. The sensitivity derivatives are defined as the partial derivatives of the geometry model or grid-point coordinates with respect to a design variable. The sensitivity derivatives of a response, f , with respect to the design variable vector, \bar{v} , can be written as

$$\frac{\partial f}{\partial \bar{v}} = \left[\frac{\partial f}{\partial \bar{R}_f} \right] \left[\frac{\partial \bar{R}_f}{\partial \bar{R}_s} \right] \left[\frac{\partial \bar{R}_s}{\partial \bar{R}_g} \right] \left[\frac{\partial \bar{R}_g}{\partial \bar{v}} \right] \quad (1)$$

where \bar{R}_f is the field (volume) grid, \bar{R}_s is the surface grid, and \bar{R}_g is the geometry. In some of the CSM literature, the sensitivity derivatives are referred to as the design velocity field.

The first term on the right-hand side of Eq.(1) represents the sensitivity derivatives of the response with respect to the field grid point coordinates. For a detailed discussion, readers are referred to Refs. 1, 2, 5 for CSM and to Refs. 6–8 for CFD disciplines. Newman et al.⁶ have provided an overview of the recent advances in steady aerodynamic shape-design sensitivity derivative analysis and optimization based on advanced CFD. The second term on the right-hand side of Eq.(1) is vector of the field grid-point sensitivity derivatives with respect to the surface grid points. The sensitivity derivative vector must be provided by the field grid generator, but few grid generation tools have the capability to provide the analytical grid-point sensitivity derivatives.⁹ The third term on the right-hand side of Eq.(1) denotes the surface grid sensitivity derivatives with respect to the shape design variables, which must be provided by the surface grid generation tools. The fourth term on the right-hand side of Eq.(1) signifies the geometry sensitivity derivatives with respect to the design variable vectors; this must be provided by the geometry construction tools.

Figure 2 shows a high-speed civil transport with seven planform design variables. Figure 3 shows errors involved in using a central-difference approximation for shape sensitivity derivative calculations for the high-speed civil transport shown in Fig. 2. This error behavior is typical of finite-difference approximations to sensitivities. For larger step sizes, the truncation error is predominant, and for smaller step sizes, the round-off error is predominant. There is an optimal step size where the error is minimum. This optimal step size is different for each design variable, and it would also vary for each optimization cycle. As a result, it is difficult to estimate the error involved in finite-difference approximation of sensitivity derivatives. If the source codes are written in FORTRAN or C, and are available, they can be differentiated with automatic tools* such ADIFOR¹⁰ or ADIC.¹¹

An important ingredient of shape optimization is the availability of a model parameterized with respect to

*Argonne National Laboratory maintains a www site with information on automatic differentiation tools <<http://www-unix.mcs.anl.gov/autodiff>>

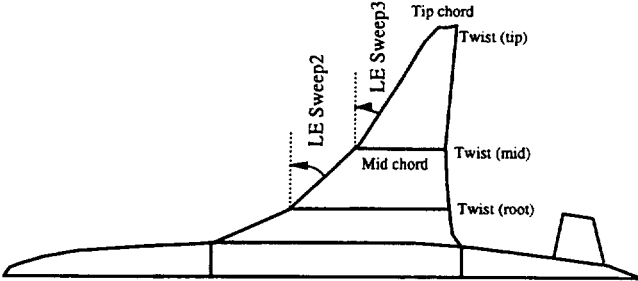


Fig. 2 Design variables for a high-speed civil transport.

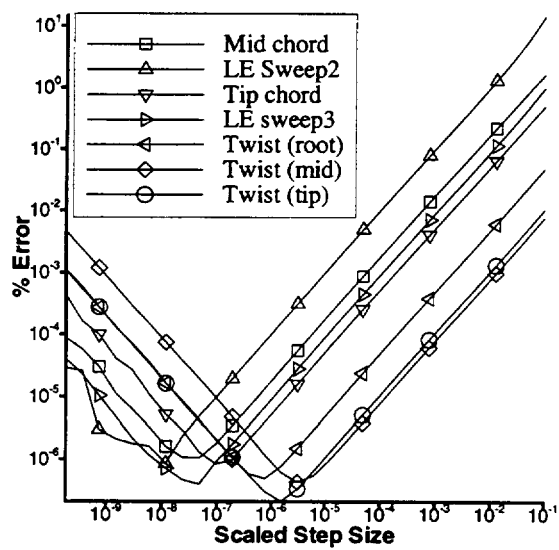


Fig. 3 Error in using central-difference approximation for shape sensitivity derivatives calculations.

the airplane shape parameters such as planform, twist, shear, camber, and thickness. The parameterization techniques are divided into the following categories: basis vector, domain element, partial differential equation, discrete, polynomial and spline, CAD-based, analytical, free form deformation (FFD), and modified FFD. Readers are referred to reports by Haftka and Grandhi¹ and Ding² for surveys of shape optimization and parameterization up to 1981. The present focus is on some recent developments in the area of shape parameterization for complex models and their suitability for MSO applications. The suitability criteria are based on the efficiency, effectiveness, ease of implementation, and availability of analytical sensitivities for geometry and grid models.

Basis Vector Approach

Pickett et al.¹² proposed a technique that combines the second through fourth terms of Eq.(1) into a set of basis vectors. The shape changes can be expressed as

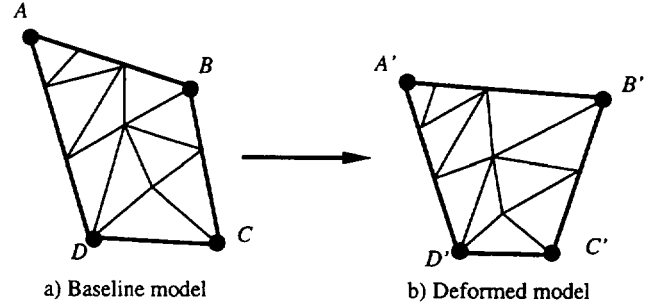


Fig. 4 Domain element.

$$\bar{R} = \bar{r} + \sum_i \bar{v}_i \bar{U}_i \quad (2)$$

where \bar{R} is the design shape, \bar{r} is the baseline shape, \bar{v}_i is the design variable vector, and \bar{U}_i is design perturbation based on several proposed shapes. Assuming that the reduced basis is constant throughout the optimization cycle, this technique is a good approach and is available in most commercial CSM codes.¹³⁻¹⁶ However, it is difficult to generate a set of consistent basis vectors for multiple disciplines. As a result, this method can be applied only to problems involving a single discipline with relatively simple geometry changes.

Domain Element Approach

The domain element approach is based on linking a set of grid points to a macro element, domain element, that controls the shape of the model. Figure 4a shows a domain element with four nodes ($A-D$) for the baseline model. As the nodes of the domain element move ($A'-D'$), the grid points belonging to the domain will move as well (see Fig. 4b). The movement is based on an inverse mapping between the grid points and the domain element, and the parametric coordinates of the grid points with respect to the domain element are kept fixed through the optimization cycles.¹⁴ The domain element technique is available for shape optimization in some commercial software.¹⁶ This method is useful only for problems with relatively simple geometry changes.

Partial Differential Equation Approach

Bloor and Wilson¹⁷ presented an efficient and compact method for parameterizing the surface geometry of an aircraft. The method views the surface generation as a boundary-value problem and produces surfaces as the solutions to elliptic partial differential equations (PDE). Bloor and Wilson showed that it was possible to represent an aircraft geometry in terms of a small set of design variables. Smith et al.¹⁸ extended the PDE approach to a class of airplane configurations. Included in this definition were surface grids, volume grids, and grid sensitivity derivatives for CFD. The general airplane

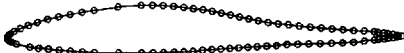


Fig. 5 Airfoil designed by a set of points.

configuration had wing, fuselage, vertical tail, horizontal tails, and canard components. Grid sensitivity was obtained by applying the automatic differentiation tool ADIFOR.¹⁰

Using the PDE approach to parameterize an existing complex model is time-consuming and costly. Also, because this method can only parameterize the surface geometry, it is not suitable for the MSO applications that must model the internal structural elements such as spars, ribs, and fuel tanks. As a result, this method is suitable for problems involving a single discipline with relatively simple external geometry changes.

Discrete Approach

The discrete approach is based on using the coordinates of the boundary points (see Fig. 5) as design variables (e.g., Refs. 19,20). This approach is easy to implement, and the geometry changes are limited only by the number of design variables. However, it is difficult to maintain a smooth geometry, and the optimization solution may be impractical to manufacture, as pointed out by Braibant and Fleury.²¹ To control smoothness, one could use multipoint constraints and dynamic adjustment of lower and upper bounds on the design variables. For a model with a large number of grid points, the number of design variables often becomes very large, which leads to high cost and a difficult optimization problem to solve.

The natural design approach is a variation of the discrete approach that uses a set of fictitious loads as design variables (e.g., Ref. 22). These fictitious loads are applied to the boundary points, and the resulting displacements, or natural shape functions, are added to the baseline grid to obtain a new shape. Consequently, the relationship between changes in design variables and grid-point locations is established through a finite element analysis. Zhang and Belegundu²³ provided a systematic approach for generating the sensitivity derivatives and several criteria to determine their effectiveness. The typical drawback of the natural design variable method is the indirect relationship between design variables and grid-point locations.

For an MDO application, grid requirements are different for each discipline. So, each discipline has a different grid and a different parameterized model. Consequently, using the discrete parameterization approach for an MDO application will result in an inconsistent parameterization.

The most attractive feature of the discrete approach

is the ability to use an existing grid for optimization. The model complexity has little or no bearing on the parameterization process. It is possible to have a strong local control on shape changes by restricting the changes to a small area. When the shape design variables are the grid-point coordinates, the grid sensitivity derivative analysis is trivial to calculate; the third and fourth terms in Eq.(1) can be combined to form an identity matrix.

Polynomial and Spline Approaches

Use of polynomial and spline representations for shape parameterization can obviously reduce the total number of design variables. For example, Fig. 6 shows an airfoil definition with only nine control points. Braibant and Fleury²¹ showed that Bezier and B-spline curves are well suited for shape optimization. A polynomial can describe a curve in a very compact form with a small set of design variables. Automatically taken into account are the additional optimization constraints most often needed to avoid unrealistic design when the shape variables are the grid-point coordinates. The analytical sensitivity derivatives with respect to the design variable vector can be computed efficiently and accurately.

For example, a curve can be described as the polynomial

$$\bar{R}_g(u) = \sum_{i=0}^{n-1} \bar{c}_i u^i \quad (3)$$

where n is the number of design variables, and u is the parameter coordinate along the curve. The \bar{c}_i is a set of coefficient vectors corresponding to three-dimensional coordinates, and the components of these vectors can be used as design variables. The sensitivity derivatives of geometry, \bar{R}_g , with respect to \bar{c}_i is u^i . The polynomial representation in Eq.(3) is in the power basis form, and the \bar{c}_i coefficient vectors convey very little geometric insight about the shape. Also, the power basis form is prone to round-off error if there is a large variation in the magnitude of the coefficients. Nevertheless, the polynomial form is a powerful and compact representation for shape optimization of simple curves (e.g., Refs. 24, 25).

The Bezier representation is another mathematical form for representing curves and surfaces. For example, a Bezier curve can be described by

$$\bar{R}_g(u) = \sum_{i=1}^n \bar{P}_i B_{i,p}(u) \quad (4)$$

where n is the number of control points (design variables), and the $B_{i,p}(u)$ are degree p Bernstein polynomials. The \bar{P}_i are the control points (forming a control polygon), and they are typically used as design variables.

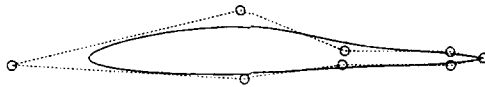


Fig. 6 Airfoil designed by a set of control points.

Readers are referred to Farin²⁶ for further discussions on the properties of Bezier form. The Bezier form is a far better representation than the power basis, even though mathematically equivalent. The control points are more closely related to the curve position. In fact, the control points approximate the curve. Also, the computation of Bernstein polynomials is a recursive algorithm, *de Casteljau* algorithm,²⁶ which minimizes the round-off error. The convex hull of the Bezier control polygon contains the curve. This property is very useful, especially in defining the geometric constraints. The first and the last control points are located exactly at the beginning and the end of the curve, respectively. The sensitivity derivative of geometry, \bar{R}_g , with respect to \bar{P}_i is $B_{i,p}(u)$, the Bernstein polynomial functions. These functions are independent of the Bezier control points (i.e., design variables); therefore, the sensitivity derivatives stay fixed during the optimization cycles.

The Bezier form is an effective and accurate representation for shape optimization of simple curves (e.g., Ref. 27). However, complex curves require a high-degree Bezier form. As the degree of a Bezier curve increases, so does the round-off error. Also, it is very inefficient to compute a high-degree Bezier curve. To use Bezier representation for a complex curve, one can use several low-degree Bezier segments to cover the entire curve. The resulting composite curve is referred to as a spline or, more accurately, a B-spline. A multisegmented B-spline curve can be described by

$$\bar{R}_g(u) = \sum_{i=1}^n \bar{P}_i N_{i,p}(u) \quad (5)$$

where \bar{P}_i are the B-spline control points, p is the degree, and $N_{i,p}(u)$ is the i -th B-spline basis function of degree p . In addition to the desirable properties of the Bezier representation, the low-degree B-spline form can represent complex curves efficiently and accurately. The sensitivity derivatives of geometry, \bar{R}_g , with respect to \bar{P}_i is $N_{i,p}(u)$, the B-spline basis function. Similar to a Bezier form, the sensitivity derivatives of a B-spline curve stay fixed during the optimization cycles.

There are some limited applications in the literature that are based on polynomial and spline representations. Cosentino and Holt²⁸ optimized a transonic wing configuration by using a cubic spline representation for two-dimensional airfoils that define a wing geometry. Then, they used the position of the spline control points—in

particular those points that affect the wing region wetted by supersonic flow—as design variables to be optimized. In a design case study on the Lockheed C-141B aircraft, they reduced the number of design variables from 120 to 12 by using the cubic spline technique. In recent years, Schramm and Pilkey²⁹ used a B-spline representation to perform structural shape optimization for the torsion problem with direct integration and B-splines. Similarly, Anderson and Venkatakrishnan³⁰ used B-splines for aerodynamics design optimization with an unstructured grid CFD code.

The only drawback of the regular B-spline representation is its inability to represent implicit conic sections accurately. However, a special form of B-spline, nonuniform rational B-spline (NURBS), can represent most parametric and implicit curves and surfaces without loss of accuracy.²⁶ NURBS can represent quadric primitives (e.g., cylinders, cones) as well as free-form geometry.²⁶ There are some implicit surfaces (e.g., helix and helicoidal)³¹ that cannot be directly converted to NURBS, but these surfaces are not common in most aerospace applications. A NURBS curve is defined as

$$\bar{R}(u) = \frac{\sum_{i=1}^n N_{i,p}(u) W_i \bar{P}_i}{\sum_{i=1}^n N_{i,p}(u) W_i} \quad (6)$$

where the \bar{P}_i are the control points, W_i are the weights, and the $N_{i,p}$ are degree p B-spline basis functions. Similar to the Bezier form, the sensitivity derivatives of a NURBS with respect to the control points are fixed during the optimization cycles. However, if the weights are selected as design variables, the sensitivity derivatives will be a function of the weight design variables. Schramm et al.³² have successfully used the two-dimensional NURBS representations for shape optimization.

Despite recent progress, it is still difficult to parameterize and construct complex, three-dimensional models based solely on polynomial and spline representations. Complex shapes require a large number of control points, and optimization is prone to creating irregular²¹ or wavy³³ geometry. Nevertheless, these techniques are well suited for two-dimensional or simple three-dimensional models.

CAD-Based Approach

Use of CAD systems for geometry modeling could potentially save development time for an MDO application. For a more detailed account of the role of CAD in MDO, readers are referred to Ref. 4. Most solid modeling CAD systems use either a boundary representation (B-Rep) or a constructive solid geometry method to represent a

physical, solid object.³⁴ Based on a complete mathematical definition of a solid, it is possible to create a complete geometry that is suitable for detailed CFD and CSM codes.

Feature-based solid modeling (FBSM) CAD systems³⁵ are capable of creating dimension-driven objects. These systems use Boolean operations such as intersection and union of simple features. Examples of simple features include holes, slots (or cuts), bosses (or protrusions), fillets, chamfers, sweep, and shell. Today's CAD systems allow designers to work in a three-dimensional space while using topologically complete geometry (solid models) that can be modified by altering the dimensions of the features from which it was created. The most important capability of FBSM is the ability to capture the design intent. The FBSM tools have made design modification much easier and faster. The developers of FBSM CAD systems have put the "design" back in CAD. Because FBSM CAD tools enable today's design engineers to create a new, complete, and parametric model for a configuration, these tools are being incorporated into the design environment.

Even though use of parametric modeling in design would make the FBSM tools ideal for optimization, existing FBSM tools are not capable of calculating sensitivity derivatives analytically. Townsend et al.³⁶ discussed issues involved in using a CAD system for an MDO application. They identified the analytical sensitivity derivative calculations as one of the important integration issues. Blair and Reich³⁷ presented a vision to integrate an FBSM CAD system with full associativity into a virtual design environment. Within such an environment, however, calculations of the analytical sensitivity derivatives of geometry with respect to the design variables could prove to be difficult.

It is possible to relate some design variables to the NURBS control points.³⁸ Then the analytical sensitivity derivatives can be calculated outside the CAD system. For some limited cases, the analytical shape sensitivity derivatives can be calculated based on a CAD model;³⁸ however, this method will not work under all circumstances. One difficulty is that, for some perturbation of some dimensions, the topology of the CAD part may be changed.

Another way to calculate the sensitivity derivatives is to use finite differences, as long as the perturbed geometry has the same topology as the unperturbed geometry. Both methods—the analytical and finite-difference approximations—have their difficulties and limitations. He et al.³⁹ presented a procedure for integrating CAD and CAE systems to support geometry- and detailed-analysis-based optimization. The sensitivity derivatives were calculated by a finite-difference approximation.

So, it is not a trivial matter to incorporate FBSM CAD

systems into a design optimization, and it is even more difficult to use them for an MDO application. Also, it is still a challenging task to parameterize an existing model that is not parametric.

Analytical Approach

Hicks and Henne⁴⁰ introduced a compact formulation for parameterization of airfoil sections. The formulation was based on adding shape functions (analytical functions) linearly to the baseline shape. The contribution of each parameter is determined by the value of the participating coefficients (design variables) associated with that function. All participating coefficients are initially set to zero, so the first computation gives the baseline geometry. The shape functions are smooth functions based on a set of previous airfoil designs. Elliott and Peraire²⁵ and Hager et al.⁴¹ used a formulation similar to that of Hicks and Henne, but a different set of shape functions. This method is very effective for wing parameterization, but it is difficult to generalize it for a complex geometry.

Free Form Deformation Approach

The field of soft object animation (SOA) in computer graphics⁴² provides algorithms for morphing images⁴³ and deforming models.^{44,45} These algorithms are powerful tools for modifying shapes: they use a high-level shape deformation, as opposed to manipulation of lower level geometric entities. The deformation algorithms are suitable for deforming models represented by either a set of polygons or a set of parametric curves and surfaces. The SOA algorithms treat the model as rubber that can be twisted, bent, tapered, compressed, or expanded, while retaining its topology. This is ideal for parameterizing airplane models that have external skin as well as internal components (e.g., see Fig. 1). The SOA algorithms relate the grid-point coordinates of an analysis model to a number of design variables. Consequently, the SOA algorithms can serve as the basis for an efficient shape parameterization technique.

Barr⁴⁴ presented a deformation approach in the context of physically based modeling. This approach uses physical simulation to obtain realistic shape and motions and is based on operations such as translation, rotation, and scaling. With this algorithm, the deformation is achieved by moving the grid points of a polygon model or the control points of a parametric curve and surface. Sederberg and Parry⁴⁵ presented another approach for deformation, based on the FFD algorithm, that operates on the whole space regardless of the representation of the deformed objects embedded in the space. The algorithm allows a user to manipulate the control points of trivariate Bezier volumes. Coquillart⁴⁶ extended a Bezier parallelepiped to a nonparallelepiped cubic Bezier volume.

Lamousin and Waggenspack⁴⁷ modified FFD to in-

clude NURBS definition and multiple blocks to model complex shapes. The modified technique has been used for design and optimization by Yeh and Vance⁴⁸ and Perry and Balling.⁴⁹ Yeh and Vance⁴⁸ developed an application based on NURBS where the user can change the shape of a virtual object and examine the effect the shape change has on the displacement of the structural deformation and stress distribution throughout the object. Perry et al.⁵⁰ successfully used FFD algorithm for the optimization of an automobile air conditioning duct system.

Hsu et al.⁵¹ presented a method to directly manipulate the object, which creates a more intuitive and transparent environment for FFD. Borrel and Rappoport⁵² presented a simple, constrained deformation that allows the user to define a set of constraint points, giving a desired displacement and radius of influence for each. Each constraint point determines a local B-spline basis function centered at the constraint point, falling to zero for points beyond the radius. This technique directly influences the final shape of the deformed object.

Multidisciplinary Aero/Struc Shape Optimization Using Deformation (MASSOUD) Approach

Creation of CFD and CSM grids is time-consuming and costly for a full airplane model: it takes several months to develop detailed CSM and CFD grids based on a CAD model. To fit into the product development cycle times, the MSO must rely on the parameterization of the analysis grids, for which the FFD algorithm is ideal. The disadvantage of FFD is that the design variables may have no physical significance for the design engineers. This drawback makes it difficult to select an effective and compact set of design variables. This author developed a set of modifications to the original SOA algorithms to alleviate this and other drawbacks; the modified algorithm set is referred to as MASSOUD.⁵³

MASSOUD is a novel parameterization approach for complex shapes suitable for a multidisciplinary design optimization application. The approach consists of three basic concepts: 1) parameterizing the shape perturbations rather than the geometry itself, 2) utilizing SOA algorithms used in computer graphics, and 3) relating the deformation to aerodynamics shape design variables such as thickness, camber, twist, shear, and planform.

The MASSOUD formulation is independent of grid topology, and that makes it suitable for a variety of analysis codes such as CFD and CSM. The analytical sensitivity derivatives are available for use in a gradient-based optimization. This algorithm is suitable for low-fidelity (e.g., linear aerodynamics and equivalent laminated plate structures) and high-fidelity analysis tools (e.g., nonlinear CFD and detailed FE modeling). The report by this author⁵³ contains the implementation

details of parameterizing for planform, twist, dihedral, thickness, and camber. The results presented were for a multidisciplinary optimization application consisting of nonlinear CFD, detailed CSM, performance, and a simple propulsion module.

Typically, the optimization starts with an existing wing design, and the goal is to improve the wing performance by using numerical optimization. The geometry changes (perturbations) between the initial and optimized wings are very small,^{28,40} but the difference in wing performance can be substantial. By parameterizing the shape perturbations instead of the shape itself, MASSOUD reduces the number of shape design variables. Throughout the optimization cycles, the surface grid can be updated as

$$\bar{R}(\bar{v}) = \bar{r} + \bar{U}(\bar{v}) \quad (7)$$

where \bar{r} is the baseline grid, \bar{R} is the deformed (perturbed) grid, \bar{U} is the change (perturbation), and \bar{v} is the design variable vector. It takes far fewer design variables to parameterize the shape perturbation \bar{U} than to parameterize \bar{r} itself.

The MASSOUD algorithm has been used for parameterizing a simple wing, a blended wing body, and several high-speed civil transport configurations. The algorithm has been successfully implemented for aerodynamic shape optimization with analytical sensitivity derivatives with structured grid⁵⁴ and unstructured grid CFD⁵⁵ codes. In addition to ease of use and implementation, MASSOUD has the following benefits: 1) parameterization is consistent, 2) the analytical sensitivity derivatives are available, 3) complex existing grids can be parameterized, 4) there is a strong local control, 5) smoothness can be controlled, and 6) few design variables are required.

Summary of Multidisciplinary Shape Parameterization

Figure 7 presents a summary and rating of the nine approaches surveyed in this paper. There are three ratings: 1) good (thumb-up), 2) fair (neutral), and 3) poor (thumb-down). The summary uses ten criteria that are important for multidisciplinary applications of complex, three-dimensional configurations.

- Consistent: Is the parameterization consistent across multiple disciplines?
- Airplane shape design variables: Are the design variables directly related to the airplane shape design variables such as camber, thickness, twist, shear, and planform?
- Compact: Does the parameterization provide a compact set of design variables?

Approaches \ Criteria	Basis vector	Domain element	PDE	Discrete	Polynomial and spline	CAD	Analytical	FFD	MASSOUD
Consistent parameterization	👎	👎	👎	👎	👎	👍	👎	👍	👍
Airplane shape design variables	👎	👎	👎	👎	👎	👎	👍	👎	👍
Compact set of design variables	👍	👍	👍	👎	👎	👍	👍	👎	👍
Smooth geometry	👎	👍	👍	👍	👍	👍	👍	👍	👍
Local control	👍	👍	👎	👍	👎	👎	👎	👍	👍
Analytical sensitivity	👍	👍	👍	👍	👍	👎	👍	👍	👍
Grid deformation	👍	👍	👎	👍	👎	👎	👍	👍	👍
Setup time	👎	👍	👎	👍	👎	👎	👎	👍	👍
Existing grids	👍	👍	👎	👍	👎	👎	👍	👍	👍
CAD connection	👎	👎	👎	👎	👎	👎	👎	👎	👎

Fig. 7 Comparisons of parameterization approaches.

- Smooth: Does the shape perturbation maintain a smooth geometry?
- Local control: Is there any local control on shape changes?
- Analytical sensitivity: Is it feasible to calculate the sensitivity analytically?
- Grid deformation: Does the parameterization allow the grid to be deformed?
- Setup time: Can a shape optimization application be set up quickly?
- Existing grid: Does the parameterization allow the existing grid to be reused?
- CAD: Is there a direct connection to the CAD system?

Field Grid Movement and Sensitivity Derivatives

The parameterization techniques are used to move the grid points and geometry of the design surfaces. The next step is to propagate the changes and sensitivity into the field. The field sensitivity derivatives can either be calculated analytically or approximated with finite

differences. As discussed before, there is some error involved in the finite-difference approximation that could slow the optimization.

For a CFD calculation, the field (volume) grid may contain several million grid points. There are two basic techniques to propagate the surface grid-point movements into the field: 1) grid regeneration and 2) grid deformation.

Structured Field Grid Movement

Most structured grid regeneration and deformation techniques are based on transfinite interpolation (TFI). Gaitonde and Fiddes⁵⁶ used a regenerating grid technique based on using TFI with exponential blending functions. The choice of blending functions has a considerable influence on the quality and robustness of the field grid. Soni⁵⁷ proposed a set of blending functions based on arc length that is extremely effective and robust for grid regeneration and deformation. His algorithm has been incorporated in most commercial structured grid generation packages.

Jones and Samareh⁹ presented an algorithm for grid regeneration and deformation based on Soni's blending functions, and they also provided analytical sensitivity derivatives by using an automatic differentiation tool, "ADIC".¹¹ The method is suitable for a general, multiblock, three-dimensional volume grid deformation. The idea of volume grid deformation was also used by Hartwich and Agrawal.⁵⁸ They introduced two new techniques: 1) the use of the "slave/master" concept to semiautomate the process and 2) the use of a Gaussian distribution function to preserve the integrity of grids in the presence of multiple body surfaces. Reuther et al.⁸ used a modified TFI approach with blending functions based on arc length, and they used finite-difference approximation to compute the sensitivity derivatives for the field grid.

Leatham and Chappell⁵⁹ used the Laplacian technique, commonly used for unstructured grid deformation, for moving structured grids. They have been successful in deforming structured grids with this technique.

Unstructured Field Grid Movement

For unstructured grids with large geometrical changes, Botkin⁶⁰ proposed to regenerate a completely new grid at the beginning of each optimization cycle. However, for gradient calculations many small changes must be made, and it would be too costly to regenerate the grid for each design variable perturbation. Botkin has introduced a local regridding procedure that operates only on the specific edges and faces associated with the design variables being perturbed. Similarly, Kodiyalam et al.⁶¹ used a grid regeneration technique based on the assumption that the solid model topology stays fixed for small perturbations. The solid model topology contains

the number of grid points, edges, and faces. Any change in the topology will cause the model regeneration to fail. To avoid such a failure, a set of constraints must be satisfied among design variables, in addition to constraints on their bounds.

For a dynamic aeroelastic case with unstructured grids, Batina⁶² presented a grid deformation algorithm that models grid edges with springs. The spring stiffness for a given edge $j-k$ is taken to be inversely proportional to the element edge length as

$$k_m = \frac{1}{|\bar{r}_j - \bar{r}_k|}. \quad (8)$$

The grid movement is computed through predictor and corrector steps. The predictor step is based on an existing solution from the previous cycle, and the corrector step uses several Jacobi iterations of the static equilibrium equations by using

$$\bar{U}^{n+1} = \frac{\sum k_m \bar{U}^n}{\sum k_m} \quad (9)$$

where the sum is over all edges of the elements. This is similar to a Laplace operator, which has a diffusive behavior. In contrast to its use for dynamic aeroelasticity, the previous optimization cycle may not provide a good initial guess to be used by the corrector step.

Zhang and Belegundu²³ proposed a similar algorithm to handle large grid movement. The equation for grid update is similar to Batina's⁶² approach,

$$\bar{R}^{\text{new}} = \frac{\sum k_m \bar{R}^{\text{old}}}{\sum k_m}, \quad \text{where } k_m = \frac{8|J|}{V}, \quad (10)$$

J is the cell Jacobian defined within cell parametric coordinates, and V is the cell volume.

Crumpton and Giles⁶³ found the spring analogy to be inadequate and ineffective for large grid perturbations. They proposed a technique based on using the heat transfer equation

$$\nabla \cdot \{k_m \nabla (\bar{U})\} = 0 \quad \text{where } k_m = \frac{1}{\max(V, \epsilon)}, \quad (11)$$

V is the cell volume, and ϵ is a small positive number needed to avoid a division by zero. This technique is similar to the spring analogy,⁶² except that it uses the cell volume for k_m . The coefficient k_m is relatively large for small cells. Therefore these small cells, which are usually near the surface of the body, tend to undergo rigid body motion. This rigid body movement avoids rapid variations in \bar{U} , thus eliminating the possibility of small cells

having very large changes in volume, which could lead to negative cell volumes. Crumpton and Giles⁶³ used an underrelaxed Jacobi iteration, with the nonlinear k_m evaluated at the previous iteration.

Summary

The results of this study are summarized in Fig. 7. Traditional shape parameterization techniques are not suitable for application to multidisciplinary shape optimization for complex, three-dimensional configurations. At first look the CAD approach appears to be ideal, but there are some unresolved issues, such as analytical sensitivity, that require more research. In the interim, the MASSOUD approach will be useful. Ideally, the CAD and MASSOUD approaches can be combined to form a powerful parameterization tool for multidisciplinary shape optimization application. This combined approach will 1) be automated, 2) provide consistent geometry across all disciplines, 3) provide analytical sensitivity derivatives, 4) fit into the product development cycle times, and 5) have a direct connection to the CAD systems used for design.

Acknowledgments

The author would like to thank James Townsend and Tom Zang of Multidisciplinary Optimization Branch of NASA Langley Research Center for reviewing this paper.

References

- ¹Haftka, R. T. and Grandhi, R. V., "Structural Shape Optimization—A Survey," *Computer Methods in Applied Mechanics and Engineering*, Vol. 57, 1986, pp. 91–106.
- ²Ding, Y., "Shape Optimization of Structures: A Literature Survey," *Computers & Structures*, Vol. 24, No. 6, 1986, pp. 985–1004.
- ³"Special Issue: Multidisciplinary Design Optimization," *Journal of Aircraft*, edited by E. Livne, Vol. 36, Jan. 1999.
- ⁴Samareh, J. A., "Status and Future of Geometry Modeling and Grid Generation for Design and Optimization," *Journal of Aircraft*, Vol. 36, No. 1, 1999, pp. 97–104.
- ⁵Yang, R. J. and Botkin, M. E., "Accuracy of the Domain Method for the Material Derivative Approach to Shape Design Sensitivities," *AIAA Journal*, Vol. 25, No. 12, 1987, pp. 1606–1610.
- ⁶Newman, J. C., Taylor, A. C., Barnwell, R. W., Newman, P. A., and Hou, G. J., "Overview of Sensitivity Analysis and Shape Optimization for Complex Aerodynamic Configurations," *Journal of Aircraft*, Vol. 36, No. 1, 1999, pp. 87–96.
- ⁷Jameson, A., "Essential Elements of Computational Algorithms for Aerodynamic Analysis and Design," NASA CR-97-206268, Dec. 1997.
- ⁸Reuther, J. J., Jameson, A., Alonso, J. J., Rimlinger, M. J., and Saunders, D., "Constrained Multipoint Aerodynamic Shape Optimization Using an Adjoint Formulation and Parallel Computers, Part 1," *Journal of Aircraft*, Vol. 36, No. 1, 1999, pp. 51–60.
- ⁹Jones, W. T. and Samareh, J. A., "A Grid Generation System for Multidisciplinary Design Optimization," Paper 95-1689, AIAA, Jun. 1995.

- ¹⁰Bischof, C., Carle, A., Khademi, P., and Mauer, A., "ADIFOR 2.0: Automatic Differentiation of Fortran 77 Program," *IEEE Computational Science & Engineering*, Vol. 3, No. 3, 1996, pp. 18-32.
- ¹¹Bischof, C., Roh, L., and Mauer-Oats, A., "ADIC: An Extensible Automatic Differentiation Tool for ANSI-C," *Software: Practice and Experience*, Vol. 27, Dec. 1997, pp. 1427-1456.
- ¹²Pickett, R. M., Rubinstein, M. F., and Nelson, R. B., "Automated Structural Synthesis Using a Reduced Number of Design Coordinates," *AIAA Journal*, Vol. 11, No. 4, 1973, pp. 498-494.
- ¹³Kodiyalam, S., Vanderplaats, G. N., and Miura, H., "Structural Shape Optimization With MSC/NASTRAN," *Computers & Structures*, Vol. 40, No. 4, 1991, pp. 821-829.
- ¹⁴Leiva, J. P. and Watson, B. C., "Automatic Generation of Basis Vectors for Shape Optimization in the GENESIS Program," *7th AIAA/USAF/NASA/ISSMO Symposium on Multidisciplinary Analysis and Optimization Conference Proceedings*, AIAA, Sep. 1998, pp. 1115-1122, also AIAA-98-4852-CP.
- ¹⁵Kiltroy, K., editor, *NASTRAN Software User's Manual*, MSC, CA, 1998.
- ¹⁶Anonymous, editor, *GENESIS Structural Optimization Software*, VMA, CO, 1997.
- ¹⁷Bloor, M. I. G. and Wilson, M. J., "Efficient Parameterization of Generic Aircraft Geometry," *Journal of Aircraft*, Vol. 32, No. 6, 1995, pp. 1269-1275.
- ¹⁸Smith, R. E., Bloor, M. I. G., Wilson, M. J., and Thomas, A. T., "Rapid Airplane Parametric Input Design (RAPID)," *AIAA 12th Computational Fluid Dynamics Conference*, AIAA, Jun. 1995, pp. 452-462, also AIAA-95-1687-CP.
- ¹⁹Campbell, R. L., "An Approach to Constrained Aerodynamic Design With Application to Airfoils," Report NASA-TP-3260, Nov. 1992.
- ²⁰Jameson, A., Pierce, N. A., and Martinelli, L., "Optimum Aerodynamics Design Using the Navier-Stokes Equations," Paper 97-0101, AIAA, 1997.
- ²¹Braibant, V. and Fleury, C., "Shape Optimal Design Using B-Splines," *Computer Methods in Applied Mechanics and Engineering*, Vol. 44, Aug. 1984, pp. 247-267.
- ²²Belegundu, A. D. and Rajan, S. D., "A Shape Optimization Approach Based on Natural Design Variables and Shape Functions," *Computer Methods in Applied Mechanics and Engineering*, Vol. 66, Jan. 1988, pp. 87-106.
- ²³Zhang, S. and Belegundu, A. D., "A Systematic Approach for Generating Velocity Fields in Shape Optimization," *Structural Optimization*, Vol. 5, No. 1-2, 1993, pp. 84-94.
- ²⁴Taylor, C. A., Hou, G. J., and Korivi, V. M., "Sensitivity Analysis, Approximate Analysis, and Design Optimization for Internal and External Flows," Paper 91-3083, AIAA, Sep. 1991.
- ²⁵Elliott, J. and Peraire, J., "Practical Three-Dimensional Aerodynamic Design and Optimization Using Unstructured Meshes," *AIAA Journal*, Vol. 35, No. 9, 1997, pp. 1479-1486.
- ²⁶Farin, G., *Curves and Surfaces for Computer Aided Geometric Design*, Academic Press, New York, 1990.
- ²⁷Baysal, O. and Ghayour, K., "Continuous Adjoint Sensitivities for General Cost Functions on Unstructured Meshes in Aerodynamic Shape Optimization," *7th AIAA/USAF/NASA/ISSMO Symposium on Multidisciplinary Analysis and Optimization Conference Proceedings*, Sep. 1998, pp. 1483-1491, also AIAA-98-4904-CP.
- ²⁸Cosentino, G. B. and Holst, T. L., "Numerical Optimization Design of Advanced Transonic Wing Configurations," *Journal of Aircraft*, Vol. 23, No. 3, 1986, pp. 193-199.
- ²⁹Schramm, U. and Pilkey, W. D., "Structural Shape Optimization for the Torsion Problem Using Direct Integration and B-Splines," *Computer Methods in Applied Mechanics and Engineering*, Vol. 107, Aug. 1993, pp. 251-268.
- ³⁰Anderson, W. K. and Venkatakrishnan, V., "Aerodynamics Design Optimization on Unstructured Grids With a Continuous Adjoint Formulation," *AIAA Paper 97-0643*, Jan. 1997.
- ³¹Letcher, J. S. and Shook, M., "NURBS Considered Harmful for Gridding (Alternative Offered)," *4th International Meshing Roundtable*, Sandia National Laboratories, Oct. 1995, pp. 253-264.
- ³²Schramm, U., Pilkey, W. D., DeVries, R. I., and Zebrowski, M. P., "Shape Design for Thin-Walled Beam Cross Sections Using Rational B-Splines," *AIAA Journal*, Vol. 33, No. 11, 1995, pp. 2205-2211.
- ³³Jameson, A. and Reuther, J., "A Comparison of Design Variables for Control Theory Based Airfoil Optimization," *6th International Symposium on Computational Fluid Dynamics*, Vol. 4, Sep. 1995, pp. 101-107.
- ³⁴LaCourse, D. E., *Handbook of Solid Modeling*, McGraw-Hill, New York, 1995.
- ³⁵Shah, J. J. and Mantyla, M., *Parametric and Feature-Based CAD/CAM*, John Wiley & Sons, New York, 1995.
- ³⁶Townsend, J. C., Samareh, J. A., Weston, R. P., and Zorumski, W. E., "Integration of a CAD System Into an MDO Framework," Tech. Rep. NASA-TM-207672, May 1998.
- ³⁷Blair, M. and Reich, G., "A Demonstration of CAD/CAM/CAE in a Fully Associative Aerospace Design Environment," Paper 96-1630, AIAA, Apr. 1996.
- ³⁸Hardee, E., Chang, K.-H., Choi, K. K., Yu, X., and Grindeanu, I., "A CAD-Based Design Sensitivity Analysis and Optimization for Structural Shape Optimization Design Applications," *8th AIAA/USAF/NASA/ISSMO Symposium on Multidisciplinary Analysis and Optimization Conference Proceedings*, Sep. 1996, pp. 77-87, also AIAA-96-3990-CP.
- ³⁹He, B., Rohl, P. J., Irani, R. K., Thamboo, S. V., and Srivatsa, S. K., "CAD and CAE Integration With Application to the Forging Shape Optimization of Turbine Disks," Paper 98-2032, AIAA, Apr. 1998.
- ⁴⁰Hicks, R. M. and Henne, P. A., "Wing Design by Numerical Optimization," *Journal of Aircraft*, Vol. 15, No. 7, 1978, pp. 407-412.
- ⁴¹Hager, J. O., Eyi, S., and Lee, K. D., "A Multi-Point Optimization for Transonic Airfoil Design," Paper 92-4681-CP, AIAA, Sep. 1992.
- ⁴²Watt, A. and Watt, M., *Advanced Animation and Rendering Techniques*, Addison-Wesley Publishing Company, New York, 1992.
- ⁴³Hall, V., "Morphing in 2-D and 3-D," *Dr. Dobb's Journal*, Vol. 18, No. 7, 1993, pp. 18-26.
- ⁴⁴Barr, A. H., "Global and Local Deformation of Solid Primitives," *Computer Graphics*, Vol. 18, No. 3, 1984, pp. 21-30.
- ⁴⁵Sederberg, T. W. and Parry, S. R., "Free-Form Deformation of Solid Geometric Models," *Computer Graphics*, Vol. 20, No. 4, 1986, pp. 151-160.
- ⁴⁶Coquillart, S., "Extended Free-Form Deformation: A Sculpturing Tool for 3D Geometric Modeling," *SIGGRAPH*, Vol. 24, No. 4, 1990, pp. 187-196.
- ⁴⁷Lamousin, H. J. and Waggoner, W. N., "NURBS-Based Free-Form Deformation," *IEEE Computer Graphics and Applications*, Vol. 14, No. 6, 1994, pp. 95-108.
- ⁴⁸Yeh, T.-P. and Vance, J. M., "Applying Virtual Reality Techniques to Sensitivity-Based Structural Shape Design," *Proceedings of 1997 ASME Design Engineering Technical Conferences*, No. DAC-3765 in DETC97, Sep. 1997, pp. 1-9.
- ⁴⁹Perry, E. and Balling, R., "A New Morphing Method for Shape Optimization," Paper 98-2896, AIAA, Jun. 1998.
- ⁵⁰Perry, E., Balling, R., and Landon, M., "A New Morphing Method for Shape Optimization," Paper 98-4907, AIAA, Sep. 1998.

⁵¹Hsu, W. M., Hughes, J. F., and Kaufman, H., "Direct Manipulation of Free-Form Deformation," *Computer Graphics*, Vol. 26, No. 2, 1992, pp. 177-184.

⁵²Borrel, P. and Rappoport, A., "Simple Constrained Deformations for Geometric Modeling and Interactive Design," *ACM Transactions on Graphics*, Vol. 13, No. 2, 1994, pp. 137-155.

⁵³Samareh, J. A., "A Novel Shape Parameterization Approach," Tech. Rep. NASA-TM-1999-209116, Mar. 1999.

⁵⁴Biedron, R. T., Samareh, J. A., and Green, L. L., "Parallel Computation of Sensitivity Derivatives With Application to Aerodynamic Optimization of a Wing," *1998 Computer Aerosciences Workshop*, NASA CP-20857, Jan. 1999, pp. 219-224.

⁵⁵Nielsen, E. J. and Anderson, W. K., "Aerodynamic Design Optimization on Unstructured Meshes Using the Navier-Stokes Equations," *7th AIAA/USAF/NASA/ISSMO Symposium on Multidisciplinary Analysis and Optimization Conference Proceedings*, Sep. 1998, pp. 825-837, also AIAA-98-4809-CP.

⁵⁶Gaitonde, A. L. and Fiddes, S. P., "A Three-Dimensional Moving Mesh Method for the Calculation of Unsteady Transonic Flows," *Aeronautical Journal*, Vol. 99, No. 984, 1995, pp. 150-160.

⁵⁷Soni, B. K., "Two- and Three-Dimensional Grid Generation for Internal Flow Applications," Paper 85-1526, AIAA, 1985.

⁵⁸Hartwich, P. M. and Agrawal, S., "Method for Perturbing Multiblock Patched Grids in Aeroelastic and Design Optimization Applications," Paper 97-2038, AIAA, 1997.

⁵⁹Leatham, M. and Chappell, J. A., "On the Rapid Regeneration of Hybrid Grids Due to Design Driven Geometry Perturbation," *The Sixth International Conference on Numerical Grid Generation in Computational Field Simulation*, Mississippi State, MS, 1998, pp. 533-542.

⁶⁰Botkin, M. E., "Three-Dimensional Shape Optimization Using Fully Automatic Mesh Generation," *AIAA Journal*, Vol. 30, No. 5, 1992, pp. 1932-1934.

⁶¹Kodiyalam, S., Kumar, V., and Finnigan, P., "Constructive Solid Geometry Approach to Three-Dimensional Structural Shape Optimization," *AIAA Journal*, Vol. 30, No. 5, 1992, pp. 1408-1415.

⁶²Batina, J. T., "Unsteady Euler Airfoil Solutions Using Unstructured Dynamic Meshes," Paper 89-0115-CP, AIAA, Jan. 1989.

⁶³Crumpton, P. I. and Giles, M. B., "Implicit Time-Accurate Solutions on Unstructured Dynamic Grids," *International Journal for Numerical Methods in Fluids*, Vol. 25, No. 11, 1997, pp. 1285-1300.

530-39

REDUCED ORDER DESIGN-ORIENTED STRESS ANALYSIS USING COMBINED DIRECT AND ADJOINT SOLUTIONS

by

Eli Livne* and Guillermo D. Blando**
University of Washington, Seattle, Washington

Abstract

A new method for extracting accurate stress information from reduced order structural and aeroelastic models is presented. The method has second order accuracy when approximate reduced order direct and adjoint solutions (based on different reduced order bases) are used simultaneously to obtain approximate stresses. The method is applicable to both static and dynamic linear analysis. A review of four common methods for structural model order reduction (two variants of the mode displacement (MD) method, the Mode Acceleration (MA) method, and the Ritz Vector (RV) method) identifies sources of difficulty and causes of errors in stress behavior sensitivity calculations. The new method is then presented and its relations with the other methods examined. Considerations used for selection of the reduced order direct and adjoint bases are discussed. A series of static and dynamic test cases is used to assess accuracy of the new method in an analysis mode. Accuracy studies of sensitivity calculations follow. The present work hopes to contribute to the field of design-oriented structural dynamics in terms of both insight and practice.

Introduction

Methods for order reduction of mathematical models have always been an important part of structural dynamics (Refs. 1-5). In early years the need for order reduction was motivated by limited numerical and computational capabilities for solving large, coupled, dynamic equations of motion. Today powerful computers and sophisticated computer codes are available for modeling and simulation of dynamic behavior of systems with hundreds of thousands of degrees of freedom. Still, when design optimization, rather than just a single analysis, is involved, even these powerful tools lead to considerable computational costs and times. The need to solve, as the design evolves, tens of thousands of equations repetitively, over time, including their sensitivities with respect to design variables, is still a formidable task.

Even in the linear static structural analysis case, when design optimization is involved, it is still demanding computationally to carry out large numbers of detailed analyses with static models tens or hundreds of thousands of degrees of freedom large. In the case of linear static aeroelastic analysis (Refs. 6-7) a structural stiffness matrix (which, in the case of finite element methods, is banded and sparse) is modified by an aerodynamic stiffness matrix, which is usually fully populated. The resulting combined structures-aerodynamic matrix does not have the sparseness and small bandwidth of the purely structural stiffness matrix. As a result, even with smaller numbers of equations (hundreds to few thousands) the computational cost of solving static aeroelastic problems and obtaining sensitivities of static aeroelastic behavior can be considerable.

An examination of order reduction methods in structural analysis reveals a wide selection of methods for a variety of applications. Order reduction methods include, among others, the well known Guyan reduction (Ref. 8), Ritz functions (Ref. 9), substructure synthesis (Refs. 10-12), Lanczos coordinates (Refs. 13,14), and Ritz vectors (Refs. 15-18), to name a few. The importance of order reduction has been well recognized for nonlinear structural analysis (Refs. 19,20). Modal order reduction methods, the cornerstone of structural and aeroelastic dynamic analysis, have also been used for static aeroelasticity (Ref. 21) and buckling prediction (Ref. 22).

Common to all these methods is the search for a group of reduced basis vectors (reduced order set of deformation shape functions) superposition of which will lead to accurate enough results, while reducing the order of the resulting model as much as possible. The difficulty with all displacement based finite element or Rayleigh-Ritz formulations is that it is much harder to obtain accurate stress results from a reduced order model than just deformations or deformation related entities such as natural frequencies and mode shapes. With a set of modes which can capture the deformation with satisfactory accuracy, differentiation of approximated deformations to obtain strains and stresses can lead to large stress

* Associate Professor, Department of Aeronautics and Astronautics, Associate Fellow AIAA.

** Graduate Student, Department of Aeronautics and Astronautics .

errors. Additional difficulties with order reduction methods arise in cases with concentrated loads, and cases in which sensitivity of structural behavior with respect to design variables of local nature is sought (Refs. 23, 24).

It is the purpose of this work to present a new method for extracting accurate stress information from reduced order structural and aeroelastic models. The method is applicable to both static and dynamic linear analysis. In the following four common methods for structural model order reduction are reviewed: two variants of the mode displacement (MD) method, the Mode Acceleration (MA) method, and the Ritz Vector (RV) method. The new method is then presented and its relations with the other methods examined. A series of static test cases and dynamic test cases is used to assess accuracy of the new method in an analysis mode. Accuracy studies of sensitivity calculations follow. It is hoped that the present work will contribute to the field of design-oriented structural dynamics in terms of both insight and practice.

Order Reduction Methods in Structural Dynamics

Mode Displacement method

In the Mode Displacement (MD) method (Refs. 1-5 and Ref. 25, pp. 298-301) the original structural dynamic equations of motion

$$[M]\{\ddot{u}(t)\} + [C]\{\dot{u}(t)\} + [K]\{u(t)\} = \{F(t)\} \quad (1)$$

with n degrees of freedom, are reduced in order by using a subset of modes (deformation shape vectors)

$$\{u_{MD}(t)\} = [\{\phi_1\}, \{\phi_2\}, \dots, \{\phi_N\}]\{q(t)\} = [\Phi]\{q(t)\} \quad (2)$$

The number of mode shape vectors used is N, and the dimension of the $[\Phi]$ matrix is, thus, $n \times N$. The stress in a particular point on the structure is obtained from the displacement vector by

$$\sigma = \{c\}^T \{u\} \quad (3)$$

The $\{c\}$ vector contains only a few non-zero entries if the finite element method is used. These non-zero entries are associated with the degrees of freedom of the nodes connected by the element in which the stress is evaluated.

In the mode displacement method, then, the order of the problem is reduced by introducing Eq. 2 into Eq. 1, and pre-multiplying Eq. 1 by $[\Phi]^T$. The result is a set of N differential equations

$$[\Phi]^T [M] [\Phi] \{\ddot{q}(t)\} + [\Phi]^T [C] [\Phi] \{\dot{q}(t)\} + [\Phi]^T [K] [\Phi] \{q(t)\} = [\Phi]^T \{F(t)\} \quad (4)$$

which are solved (with given initial conditions and excitation force) for the generalized displacements $\{q(t)\}$. Approximate ("reduced order") stresses are calculated by using Eq. 2 in Eq. 3 leading to

$$\sigma_{MD} = \{c\}^T [\Phi] \{q\} \quad (5)$$

In the most common application of the MD method, the deformation shape vectors used are the natural modes of vibration of the structure - the eigenvectors of the problem

$$[K] - \omega^2 [M] \{\phi\} = \{0\} \quad (6)$$

corresponding to the lowest N natural frequencies. With this choice of reduced basis vectors the Mode Displacement method is known to lead to inaccurate stress results, especially when concentrated forces are involved. When sensitivity of stresses with respect to sizing type design variables is required, accuracy of the MD method is even poorer, and the rate of convergence of results (as the number of modes is increased) is slow (Ref. 25).

It has long been recognized that a major reason for the loss of stress accuracy in the MD method is due to the reduction in order of the stiffness matrix from $[K]$ into $[\Phi]^T [K] [\Phi]$. A similar loss of accuracy of stresses is encountered in the static problem if the full order static problem

$$[K]\{u\} = \{F\} \quad (n \times 1) \quad (7)$$

where $\{F\}$ is a static force vector, is reduced in order, using natural modes (Eq. 2), to yield

$$[\Phi]^T [K] \Phi \{q\} = [\Phi]^T \{F\} \quad (N \times 1) \quad (8)$$

and (where r.o. denotes reduced order solution)

$$\{u\}_{r.o.} = [\Phi] \{q\} \quad (9)$$

$$\sigma_{MD.r.o.} = \{c\}^T [\Phi] \{q\} \quad (10)$$

By examining the static case it becomes clear that another reason for the loss of accuracy in the reduced order model is the projection of the load vector $\{P\}$ onto $[\Phi]^T \{P\}$. If the load vector represents concentrated forces and excitation action of localized nature, then, the pre-multiplication by the transpose of the modal matrix leads to errors due to “smearing” of this localized action over the structure.

Mode Acceleration Method

The Mode Acceleration method (MA) (Refs. 1-4,26,27) is based on the observations outlined above. It relies on the modally reduced order dynamic equations (Eq. 4) for displacement approximation, but for stress recovery the full order stiffness matrix is used. Eq. 1 is rewritten in the form

$$[K]\{u(t)\} = \{F(t)\} - [M]\{\ddot{u}(t)\} - [C]\{\dot{u}(t)\} \quad (11)$$

and then the velocities and accelerations on the right hand side are replaced by their reduced order approximations from the MD solution of Eq. 4:

$$[K]\{u_{MA}(t)\} = \{F(t)\} - [M][\Phi]\{\ddot{q}(t)\} - [C][\Phi]\{\dot{q}(t)\} \quad (12)$$

The effect is to create a time dependent right hand side load vector based on the reduced order model of Eq. 4, but solve for new displacements based on the static full order model, from which stresses will be later extracted:

$$\sigma_{MA} = \{c\}^T \{u_{MA}\} \quad (13)$$

Eq. 11 captures the external load vector $\{F(t)\}$ fully. The dynamic loads on the right hand side of Eq. 11 due to inertia and damping, being distributed in nature in most structures (rather than concentrated), can be captured well using reduced order results, provided enough modes are used in the reduced order model to cover the frequency content of the excitation and response vectors $\{F(t)\}$ and $\{u\}$.

Ritz vectors and “fictitious mass” modes

Because low frequency natural vibration modes of common aerospace structures involve motion of the whole structure in some form (while patterns of inherently local motion are more typical of high frequency modes), it is no wonder that the MD method cannot capture local behavior accurately when low-frequency modes are used for order reduction. Based on this observation the Ritz vector (Refs. 15-19) method for order reduction was developed to generate deformation shape vectors capable of capturing structural response to loading of local nature. This is done by loading the structure with static loads reflecting the spatial distribution of the actual loading, and, then, augmenting with static deformation shapes due to loads reflecting the inertia distribution in the structure. Based on the same observations, the method of “fictitious masses” (FM) had been developed (Refs. 28-31), in which not the natural modes of the structure are used for order reduction, but, rather, the modes of a related “fictitious” structure. In this fictitious structure, the original structure under consideration is loaded with a set of very large concentrated masses at key degrees of freedom. The resulting mode shapes now contain information reflecting higher weighting on local inputs and outputs in the areas where these large masses are added. Actually, when fictitious large masses are added to a small number of degrees of freedom in a structure, the corresponding set of lowest-frequency mode shapes tends to span the same subspace spanned by static deformation shapes due to concentrated forces at these degrees of freedom (Ref. 23). The masses are fictitious, because they are only used to create shape vectors for the order

reduction process. Order reduction itself, with the fictitious mass modes, is carried out with the original structure (Eq. 4). Generalized mass and stiffness matrices in this case are not diagonal any more, but with the resulting low order model, integration of Eq. 4 can still be done orders of magnitude faster than the full order analysis. In aeroelastic analysis, when aerodynamic generalized force matrices are not diagonalized anyway with any structural mode shapes, the replacement of the actual mode shapes of the structure by FM mode shapes or any other mode shapes makes little difference in terms of computing time.

Results of solving the dynamic reduced order equations (whether natural modes of vibration, Ritz vectors, a mix of Ritz vectors and modes of vibration (Ref. 19), or fictitious mass modes are used) can, of course, all be used in a subsequent mode acceleration (MA) step to obtain accurate stress information. The thrust behind the Ritz vector and FM methods is to get good stress information directly from the reduced order deformation approximation (Eq. 5) without the need to use the MA step. Thus, in most applications of the MA method, it is used to improve stress accuracy when the dynamic equations of motion are reduced by using natural modes of vibration.

Structural order reduction and behavior sensitivity analysis

The full order structural behavior sensitivity equation in the static case is (Ref. 25)

$$[K] \left\{ \frac{\partial u}{\partial x} \right\} = \left\{ \frac{\partial F}{\partial x} \right\} - \frac{\partial [K]}{\partial x} \{u\} \quad (14)$$

If the load vector does not depend on the structural design variables ($\left\{ \frac{\partial F}{\partial x} \right\} = 0$), and if sizing-type design variables, x , (Ref. 25, p. 239) are considered, this equation contains a right-hand-side which has the nature of a vector of forces applied to the structure locally. Because individual sizing type design variables in typical finite element models affect only the element they belong to, the vector $\left\{ \frac{\partial [K]}{\partial x} \right\} \{u\}$ contains non-zero entries only in degrees of freedom associated with a single element. The

sensitivity vectors $\left\{ \frac{\partial u}{\partial x} \right\}$ can, thus, be viewed as displacements due to concentrated local loads, and the set of mode shapes used in order reduction (Eqs. 8-10) for sensitivity analysis has to be created accordingly to capture these local effects (Ref. 23, 24 and 25).

Using Ritz vectors or fictitious mass modes to obtain a reduced order model capable of capturing both analysis and sensitivity responses accurately is problematic. To load the structure (in order to generate the deformation response vectors) with concentrated forces or fictitious masses at the degrees of freedom loaded by the actual input forces might be practical if these local inputs are small in number. If sensitivities are involved, we now need to load the structure with concentrated forces or fictitious masses at all degrees of freedom affected by each design variable. This will lead to a large number of deformation shape vectors for the reduced basis, resulting in a large reduced order model. Indeed, the realization that "fictitious mass" modes lead to inaccurate reduced order sensitivity results motivated the improvement of fictitious mass reduced order bases by the addition of vectors representing changes in deformation response due to changes in design variables (Ref. 31).

The Adjoint Method for Static Stress Analysis and its order reduction

Equation 3 for obtaining stresses from displacements can be, in the static case (Eq. 7) for a restrained structure, written in the form

$$\sigma = \{c\}^T \cdot (K^{-1} \cdot \{F\}) = \{\eta^T\} \{F\} \quad (15)$$

where $\{u\} = [K]^{-1} \cdot \{F\}$, and the static adjoint vector is defined by

$$\{\eta\}^T = \{c\}^T \cdot [K]^{-1} \quad (16)$$

leading (due to the symmetry of $[K]$) to

$$[K]\{\eta\} = \{c\} \quad (17)$$

The adjoint method is widely used in optimization when the number of constraints is small (Refs. 25, 32,33). In the case of Eq. 17 here an adjoint vector is associated with each evaluated stress. Because the vector $\{c\}$ in a typical finite element application contains non-zero terms only at a small number of degrees of freedom (associated with the element involved) Equation 17 represent a case of "adjoint" static loading involving "local action" in the form of equivalent concentrated forces and moments at these nodes.

Can a mode displacement (MD) type method be used to reduce the order of the adjoint static problem, in a manner similar to MD order reduction of the static direct problem? The challenge here is to find a reduced basis

$$\{\eta\} = [\{\psi_1\}, \{\psi_2\}, \dots, \{\psi_M\}] \{p\} = [\Psi] \{p\} \quad (18)$$

so that the reduced order static adjoint problem

$$[\Psi]^T [K] [\Psi] \{p\} = [\Psi]^T \{c\} \quad (19)$$

$$\sigma_{A.r.o.} = \{\eta_{r.o.}\}^T \{F\} = \{p\}^T [\Psi]^T \{F\} \quad (20)$$

will lead to accurate approximate stresses (the index A denotes stress from adjoint formulation, and r.o denotes reduced order solution).

Because of the local nature of the loading represented by the $\{c\}$ vector, it is quite clear that to use the natural modes of the structure (portraying global behavior in the lower frequency modes) will lead to large errors. Two options suggest capability to capture the local behavior at the stress evaluation points with a reduced basis: Ritz vectors (solutions of the static adjoint equation (Eq. 17) with the $\{c\}$ right hand sides associated with the required stresses), or fictitious mass modes (where the structure is loaded with fictitious masses at the degrees of freedom corresponding to the non-zero entries in the $\{c\}$ vectors). Recall that in most applications of the fictitious mass method to the direct problem, fictitious masses were added to the points where concentrated forces acted and not to points where stresses were evaluated. In Ref. 29 fictitious masses were added at stress points, but only in a way to generate rigid body motions of sections of the structure for loads calculation purposes, not for the order reduction of the structural model itself.

In the case of reduced order adjoint method based on static Ritz vectors, Eqs. 19, and 20 can lead to exact results if the $[\Psi]$ matrix is used for the same structure on which it was created. The reduced order results are approximate if a reference structure is used to create the reduced basis, and then this reduced order basis is used to reduce the order of different structures (evolving from the reference structure in the course of optimization).

The second order approximation

Examine the full order direct problem, Eq. 7, and associated reduced order direct problem, Eqs. 8,9. The full order adjoint problem, Eq. 16, has a reduced order associated adjoint problem, Eqs. 18,19. Now, the full order stress at some point is given by

$$\sigma = \{c\}^T \{u\} = \{\eta\}^T \{F\} \quad (21)$$

and the error associated with the direct reduced order problem based on mode displacement is

$$\delta\sigma_D = \sigma_{MD.r.o.} - \sigma = \{c\}^T \{\delta u\} \quad (22)$$

where

$$\{\delta u\} = \{u_{r.o.}\} - \{u\} \quad (23)$$

Similarly, the stress error associated with the reduced order adjoint method is

$$\delta\sigma_A = \sigma_{A.r.o.} - \sigma = \{\delta\eta\}\{F\} \quad (24)$$

where

$$\{\delta\eta\} = \{\eta_{r.o.}\} - \{\eta\} \quad (25)$$

We can substitute Eq. 7 into Eq. 24 to yield

$$\delta\sigma_A = \sigma_{A.r.o.} - \sigma = \{\delta\eta\}\{F\} = \{\delta\eta\}^T[K]\{u\} \quad (26)$$

similarly, Eq. 22 combined with Eq. 17 lead to (K is symmetric)

$$\delta\sigma_D = \sigma_{D.r.o.} - \sigma = \{c\}^T\{\delta u\} = \{\eta\}^T[K]\{\delta u\} \quad (27)$$

Examination of Eqs. 26 and 27 suggests the following way for obtaining an equation for the stress which will have second order accuracy. Consider the expression $\{\eta\}^T[K]\{u\}$. If instead of full order $\{u\}$ and $\{\eta\}$ we use approximate vectors based on reduced order direct and adjoint solutions, then, the approximate expression can be written in terms of the full order expression and error terms as follows:

(28)

$$\{\eta_{r.o.}\}[K]\{u_{r.o.}\} = \{\eta + \delta\eta\}[K]\{u + \delta u\} = \{\eta\}^T[K]\{u\} + \{\delta\eta\}^T[K]\{u\} + \{\eta\}^T[K]\{\delta u\} + \{\delta\eta\}[K]\{\delta u\}$$

The first order error terms of Eqs. 26 and 27 can be easily recognized. If Eq. 28 can be subtracted from the sum of Eqs. 26 and 27, a second order error term will result. A new expression for stress in terms of direct and adjoint solutions can now be constructed (Refs. 34,35).

$$\sigma = \{\eta\}^T\{F\} + \{c\}^T\{u\} - \{\eta\}^T[K]\{u\} \quad (29)$$

If the static full order direct $\{u\}$ and adjoint $\{\eta\}$ solutions are replaced by approximate solutions (with errors, $\{\delta u\}$ and $\{\delta\eta\}$),

$$\sigma_{2.o.} = \{\eta_{r.o.}\}^T\{F\} + \{c\}^T\{u_{r.o.}\} - \{\eta_{r.o.}\}^T[K]\{u_{r.o.}\} \quad (30)$$

then, the error in stress obtained by Eq. 30 is of second order.

Similarly, the following expression for stress, based on direct and adjoint solutions, also has second order accuracy:

$$\sigma = \frac{(\{c\}^T\{u\})(\{\eta\}^T\{F\})}{\{\eta\}^T[K]\{F\}} \quad (31)$$

This can be shown by taking the first order variation of the following equivalent of Eq. 31:

$$\sigma[\eta]^T[K]\{u\} = (\{c\}^T\{u\})(\{\eta\}^T\{F\}) \quad (32)$$

$$\begin{aligned} \delta\sigma[\eta]^T[K]\{u\} + \sigma \cdot \{\delta\eta\}^T[K]\{u\} + \sigma \cdot \{\eta\}^T[K]\{\delta u\} = \\ = (\{c\}^T\{\delta u\})(\{\eta\}^T\{F\}) + (\{c\}^T\{u\})(\{\delta\eta\}\{F\}) \end{aligned} \quad (33)$$

Substituting Eq. 31 into Eq. 33 and multiplying by $\{\eta\}^T[K]\{u\}$, and then, using Eqs. 3,7,15,17 and 21 leads to

$$\delta\sigma = 0 \quad (34)$$

The first variation of the stress, obtained using Eq. 31, is zero. It is straight forward to show, then, that Eq. 31 is 2nd order accurate.

Implementation of Reduced Order Second Order Stress Evaluation for Static Structural Analysis

Approximation-Concepts based Structural Synthesis (Ref. 25, pp. 209-254) follows a strategy in which a small number of detailed analyses of a system to be optimized are used to construct robust,

computationally fast approximate analyses. These numerically inexpensive approximations are, then, used to communicate with the optimization algorithm used to search for an optimal design satisfying all constraints.

Consider a baseline linear elastic structure, represented by a stiffness matrix $[K_0]$ and a mass matrix $[M_0]$, with a full order model of n degrees of freedom. Let it be loaded by N_L load cases, represented by the right hand side vectors $\{F_1\}, \{F_2\}, \dots, \{F_l\}, \dots, \{F_{N_L}\}$. The number of stresses to be evaluated is N_σ . Stress number s is obtained from the deformation vector $\{u\}$ (Eqs. 7, 21) using the vector $\{c_s\}$. There are, thus, N_σ vectors $\{c_1\}, \{c_2\}, \dots, \{c_s\}, \dots, \{c_{N_\sigma}\}$.

In the course of sizing type design optimization the topology, geometry, boundary conditions, and many times, the load cases remain unchanged. What does change are the thickness and cross sectional areas of structural elements, such as skin or web elements, and rib and spar cap elements in typical aerospace thin walled structures. Based on the baseline structural model, we want to create reduced basis matrices $[\Phi]$ and $[\Psi]$ for reducing the order of the analysis problems when the structure is modified by changing sizing-type design variables.

The following procedure is examined for design-oriented reduced order stress analysis of static linear structures. First, a baseline (reference) structure is used to obtain reduced basis matrices for the direct and adjoint problems. For the direct problem, a reduced order basis can be formed using (A) the lowest frequency natural vibration modes of that structure

$$[[K_0] - \omega^2 [M_0]]\{\phi_i\} = \{0\} \quad (35)$$

or, alternatively, (B) the natural vibration modes of a modified reference structure, where large "fictitious" masses (Ref. 28) are added at the degrees of freedom loaded by the largest concentrated forces in the load vectors

$$[[K_0] - \omega_{FMi}^2 [M_0 + M_{FM}]]\{\phi_{FMi}\} = \{0\} \quad (36)$$

Two other alternatives include (C) Ritz vectors (Ref. 15), and (D) a combination of Ritz vectors (based on the loading vectors) and natural mode shapes (Ref. 19). The result is a matrix $[\Phi]$ for order reduction of the direct static problem.

For the stresses required prepare a set of reduced basis vectors for the matrix $[\Psi]$. Each stress is usually associated with a small number of degrees of freedom - those connected by the element in which the stress is calculated. Alternative sets of $\{\psi\}$ vectors include (a) the same vectors as in the $[\Phi]$ matrix used for the direct problem. Also there are two sets of vectors more capable of capturing local behavior in the area where stress is calculated: (b) for each stress required, a set of "adjoint" Ritz vectors corresponding to reference static solutions with unit loads applied one at a time to the degrees of freedom corresponding to the non-zero entries in the $\{c\}$ vector used for this stress; (c) a set of vibration modes of the reference structure loaded with fictitious masses at the degrees of freedom associated with the required stresses. It becomes clear, then, that when many stresses are required, there is a need to solve static problems with many right-hand sides (corresponding to all the $\{c\}$ vectors involved, or find modes of the structure with fictitious masses at many degrees of freedom. The second order approximation, then, is most effective when a relatively small number of stresses are calculated. However, in the context of optimization, even if a large number of stresses is required, the $\{\psi\}$ vectors are generated only once, at the beginning of the optimization, and they are then used to reduce the order of the structure for all structures evolving throughout an optimization step.

For structures obtained from the reference structure by changing any sizing type design variables, let the stiffness matrix be $[K]$, and mass matrix $[M]$. A reduced order direct problem is now generated using (Eq. 8)

$$[\Phi]^T [K] [\Phi] \{q\} = [\Phi]^T \{F\} \quad (37)$$

with reduced order approximation of $\{u\}$ ($\{u_{r.o.}\} = [\Phi]\{q\}$). The number of right hand sides is equal to the number of load cases.

A reduced order adjoint equation is now created (Eq. 19) for the reduced order approximation of the adjoint vector ($\{\eta_{r.o.}\} = [\Psi]\{p\}$)

$$[\Psi]^T [K] [\Psi] \{p\} = [\Psi]^T \{c\} \quad (38)$$

If the same $[\Psi]$ matrix is used for all stresses, then, Eq. 38 is solved for N_o right hand sides, each corresponding to one of the calculated stresses. More right-hand sides per stress point can be used in the form of unit loads on all degrees of freedom of the element containing the stress point. Alternatively, a different $[\Psi]$ matrix can be used for each of the required stresses. In that case, Eq. 38 leads to N_o equations, each with its own single right hand side.

The second order stress expression (Eq. 30) can now be used for the evaluation of each stress in each load case

$$\sigma_{S.O.A} = \{\eta_{r.o.}\}^T \{F\} + \{c\}^T \{u_{r.o.}\} - \{\eta_{r.o.}\}^T [K] \{u_{r.o.}\} \quad (39)$$

Note that if we choose $[\Psi] = [\Phi]$, Eq. 39 loses its second order nature. This can be shown by substituting $\{u_{r.o.}\} = [\Phi]\{q\}$ and $\{\eta_{r.o.}\} = [\Psi]\{p\}$ into Eq. 39 and using either Eq. 37 or Eq. 38.

Static sensitivities using reduced order models

In the case of reduced order direct problem, using fixed modes (Refs. 25,36) and assuming fixed external loads, differentiation of Eq. 8 with respect to a design variable x , leads to

$$[\Phi]^T [K] [\Phi] \left\{ \frac{\partial q}{\partial x} \right\} = -[\Phi]^T \left\{ \frac{\partial K}{\partial x} \right\} [\Phi] \{q\} = -[\Phi]^T \left\{ \frac{\partial K}{\partial x} \right\} \{u_{r.o.}\} \quad (40)$$

Then

$$\left\{ \frac{\partial u_{r.o.}}{\partial x} \right\} = [\Phi] \left\{ \frac{\partial q}{\partial x} \right\} \quad (41)$$

and the derivative of a first order mode displacement (MD) stress is

$$\frac{\partial \sigma_{MD}}{\partial x} = \{c\}^T \left\{ \frac{\partial u_{r.o.}}{\partial x} \right\} + \left\{ \frac{\partial c}{\partial x} \right\}^T \{u_{r.o.}\} = \{c\}^T [\Phi] \left\{ \frac{\partial q}{\partial x} \right\} + \left\{ \frac{\partial c}{\partial x} \right\}^T [\Phi] \{q\} \quad (42)$$

In the case of the adjoint problem, using a fixed reduced basis for order reduction, differentiation of Eq. 19 with respect to a design variable x leads to

$$[\Psi]^T [K] [\Psi] \left\{ \frac{\partial p}{\partial x} \right\} = [\Psi]^T \left\{ \frac{\partial c}{\partial x} \right\} - [\Psi]^T \left\{ \frac{\partial K}{\partial x} \right\} [\Psi] \{p\} \quad (43)$$

The approximate adjoint sensitivity solution associated with a particular stress is now

$$\left\{ \frac{\partial \eta_{r.o.}}{\partial x} \right\} = [\Psi] \left\{ \frac{\partial p}{\partial x} \right\} \quad (44)$$

The derivative of the approximate stress obtained by the adjoint method is (assuming fixed external loads)

$$\frac{\partial \sigma_{AD.r.o.}}{\partial x} = \{F\}^T \left\{ \frac{\partial \eta_{r.o.}}{\partial x} \right\} = \{F\}^T [\Psi] \left\{ \frac{\partial p}{\partial x} \right\} \quad (45)$$

In the case of the second order approximation, the sensitivity of a stress with respect to design variable x is (Eq. 39)

$$\frac{\partial \sigma_{S.O.A}}{\partial x} = \left\{ \frac{\partial \eta_{r.o.}}{\partial x} \right\}^T \{F\} + \{c\}^T \left\{ \frac{\partial u_{r.o.}}{\partial x} \right\} + \left\{ \frac{\partial c}{\partial x} \right\}^T \{u_{r.o.}\} - \left\{ \frac{\partial \eta_{r.o.}}{\partial x} \right\} [K] \{u_{r.o.}\} \\ - \{\eta_{r.o.}\}^T [K] \left[\frac{\partial u_{r.o.}}{\partial x} \right] - \{\eta_{r.o.}\}^T \left[\frac{\partial K}{\partial x} \right] \{u_{r.o.}\} \quad (46)$$

$$\frac{\partial \sigma_{S.O.A}}{\partial x} = \left\{ \frac{\partial \eta_{r.o.}}{\partial x} \right\}^T (\{F\} - [K]\{u_{r.o.}\}) + (\{c\}^T - \{\eta_{r.o.}\}^T [K]) \cdot \left\{ \frac{\partial u_{r.o.}}{\partial x} \right\} \\ + \left\{ \frac{\partial c}{\partial x} \right\}^T \{u_{r.o.}\} - \{\eta_{r.o.}\}^T \left[\frac{\partial K}{\partial x} \right] \{u_{r.o.}\} \quad (47)$$

using Eqs. 41 and 44 in Eq. 47, we get

$$\frac{\partial \sigma_{S.O.A.}}{\partial x} = \left\{ \frac{\partial p}{\partial x} \right\}^T ([\Phi]^T \{F\} - [\Phi]^T [K][\Phi]\{q\}) \\ + (\{c\}^T [\Phi] - \{p\}^T [\Psi]^T [K][\Phi]) \left\{ \frac{\partial q}{\partial x} \right\} + \left\{ \frac{\partial c}{\partial x} \right\}^T [\Phi]\{q\} - \{p\}^T [\Psi]^T \left[\frac{\partial K}{\partial x} \right] [\Phi]\{q\} \quad (48)$$

Note that if the $\{c\}$ vector is independent of sizing type design variables, and if we use the same reduced basis vectors for the direct and adjoint methods ($[\Psi] = [\Phi]$), then, based on Eqs. 37 and 38, Eq. 48 yields

$$\frac{\partial \sigma_{S.O.A.}}{\partial x} = -\{p\}^T [\Phi]^T \left[\frac{\partial K}{\partial x} \right] [\Phi]\{q\} \quad (49)$$

We can also use the following sensitivity equation

$$\left(\frac{\partial \sigma_{S.O.A.}}{\partial x} \right)_{Apprx} \approx -\{p\}^T [\Psi]^T \left[\frac{\partial K}{\partial x} \right] [\Phi]\{q\} \quad (50)$$

This is obtained from Eq. 48 when the reduced order equations in the terms multiplying the derivatives $\left\{ \frac{\partial p}{\partial x} \right\}, \left\{ \frac{\partial q}{\partial x} \right\}$ are assumed to vanish in some approximate way.

A full order stress sensitivity equation based on combined, direct and adjoint solutions

Equation 49 is similar to the stress sensitivity equation, when both direct and adjoint solutions of the full order problem are used. We start with the direct stress sensitivity (assuming $\{F\}$ and $\{c\}$ independent of design variables) and use Eq. 16 and the full order sensitivity of the direct problem

$$[K] \left\{ \frac{\partial u}{\partial x} \right\} = - \left[\frac{\partial K}{\partial x} \right] \{u\} \quad (51)$$

to obtain (Ref. 37)

$$\frac{\partial \sigma}{\partial x} = \{c\}^T \left\{ \frac{\partial u}{\partial x} \right\} = -\{c\}^T [K]^{-1} \left\{ \frac{\partial K}{\partial x} \right\} \{u\} = -\{\eta\}^T \left\{ \frac{\partial K}{\partial x} \right\} \{u\} \quad (52)$$

Consider a case involving N_L load cases, N_σ required stresses, and N_{DV} design variables. If the direct method is used, Eq. 7 has to be solved for N_L right hand sides corresponding to all load vectors, and, then, Eq. 51 has to be solved for N_{DV} right hand sides for each load case. That is a total of $(N_{DV} + 1) \times N_L$ right hand sides for the full order direct method. In the case of the full order adjoint method (Eq. 17) there are N_σ right hand sides for the analysis problem. The sensitivity equation requires solution of

$$[K] \left\{ \frac{\partial \eta}{\partial x} \right\} = - \left[\frac{\partial K}{\partial x} \right] \{\eta\} \quad (53)$$

for each stress required and each design variable. Sensitivity analysis of the full order adjoint equation requires $N_\sigma \times N_{DV}$ right hand sides, adding up to a total of $(N_{DV} + 1) \times N_\sigma$ for the adjoint method.

In the combined direct - adjoint method (Ref. 37), as seen in Eq. 52, only N_L right hand sides for the direct analysis equation plus N_σ right hand sides for the adjoint full order solutions are required adding up to a total of $(N_\sigma + N_L)$ right hand sides.

If a few displacements constraints on the structure are also required, then, similar to stresses, their sensitivities can be evaluated by Eq. 52, using adjoint solutions with proper $\{c\}$ vectors. Each of these additional $\{c\}$ vectors will contain zero entries except for a unit entry in the degree of freedom where displacement is required.

Dynamic Response

The mode displacement (MD) method in the case of dynamic response has already been discussed above (Eqs. 4 and 5)

$$[\Phi]^T [M][\Phi]\{\ddot{q}(t)\} + [\Phi]^T [C][\Phi]\{\dot{q}(t)\} + [\Phi]^T [K][\Phi]\{q(t)\} = [\Phi]^T \{F(t)\} \quad (54)$$

which are solved (with given initial conditions and excitation force) for $\{q(t)\}$. Approximate ("reduced order") stresses are calculated using

$$\sigma_{MD}(t) = \{c\}^T [\Phi]\{q\} \quad (55)$$

Note that the choice of mode shapes can, again, be the natural modes of the original structure, or fictitious mass (FM) modes, with large concentrated masses placed at the degrees of freedom where "local action" takes place.

Dynamic adjoint equations can be formulated (Ref. 25 pp. 299-301) then reduced in order, integrated in time, and the dynamic reduced order adjoint solution used (together with the direct reduced order dynamic solution) to construct a second order dynamic stress approximation. The computational cost of time integration, even in the case of reduced order models, makes it undesirable to solve a large number of dynamic adjoint cases for the many $\{c\}$ vectors associated with all required stresses. Instead, the insight gained to this point regarding stress-oriented order reduction of the static problem can be used to obtain reduced order dynamic stresses based on the Mode Acceleration (MA) method as follows:

Stress recovery in the MA method is based on the solution of a full order quasi-static problem with a dynamic right hand side (Eqs. 3., 4, 12, 13). The static adjoint (Eqs. 19, 20) can, then, be used together with the dynamic Mode Displacement direct solution $\{q(t)\}$ to obtain either a quasi-static adjoint or a second order approximation.

In the quasi-static adjoint method, the Mode Displacement deformations (Eq. 4) are used to create a dynamic pseudo load (right hand side) for Eq. 20. Static reduced order adjoint solutions of Eq. 19, can now be used to calculate approximate stresses by

$$\sigma_{MA(r.o.)} = \{\eta_{r.o.}\}^T \{F(t) - [C][\Phi]\{\dot{q}\} - [M][\Phi]\{\ddot{q}\}\} = \{p\}^T [\Psi]^T \{F(t) - [C][\Phi]\{\dot{q}\} - [M][\Phi]\{\ddot{q}\}\} \quad (56)$$

A second order approximation for the dynamic cases can also be constructed, based on Eq. 30)

$$\begin{aligned} \sigma_{SOA} &= \{\eta_{r.o.}\}^T \{F(t) - [C][\Phi]\{\dot{q}\} - [M][\Phi]\{\ddot{q}\}\} + \{c\}^T \{u_{r.o.}(t)\} - \{\eta_{r.o.}\}^T [K]\{u_{r.o.}(t)\} = \\ &\{p\}^T [\Psi]^T \{F(t) - [C][\Phi]\{\dot{q}\} - [M][\Phi]\{\ddot{q}\}\} + \{c\}^T [\Phi]\{q(t)\} - \{p\}^T [\Psi]^T [K][\Phi]\{q(t)\} \end{aligned} \quad (57)$$

In Eq. 57 the dynamic Mode Displacement reduced order solutions (corresponding to different load cases) $\{q(t)\}$ are used together with the static adjoint solutions $\{p\}$ (corresponding to different stresses). Since in the MA method the quasi-static problem (Eq. 12) is solved with the full order stiffness matrix

for all time steps (right hand sides), and since in the approximate reduced order methods presented here, this problem is solved in reduced order, considerable computational savings can be materialized.

Stress Sensitivity in the Dynamic Cases

For Mode Displacement dynamic deformations, differentiation of Eq. 4, with respect to a sizing type design variable x , using fixed modes and assuming an excitation force which does not depend on the design variables, leads to

$$\begin{aligned} [\Phi]^T [M] [\Phi] \left\{ \frac{\partial \ddot{q}(t)}{\partial x} \right\} + [\Phi]^T [C] [\Phi] \left\{ \frac{\partial \dot{q}(t)}{\partial x} \right\} + [\Phi]^T [K] [\Phi] \left\{ \frac{\partial q(t)}{\partial x} \right\} = \\ -[\Phi]^T \left[\frac{\partial M}{\partial x} \right] [\Phi] \{ \ddot{q}(t) \} - [\Phi]^T \left[\frac{\partial C}{\partial x} \right] [\Phi] \{ \dot{q}(t) \} - [\Phi]^T \left[\frac{\partial K}{\partial x} \right] [\Phi] \{ q(t) \} \end{aligned} \quad (58)$$

with zero initial conditions on $\left\{ \frac{\partial q}{\partial x} \right\}, \left\{ \frac{\partial \dot{q}}{\partial x} \right\}$.

Design sensitivity of MD dynamic stresses is obtained from:

$$\frac{\partial \sigma_{MD}}{\partial x} = \{c\}^T [\Phi] \left\{ \frac{\partial q(t)}{\partial x} \right\} + \left\{ \frac{\partial c}{\partial x} \right\}^T [\Phi] \{ q(t) \} \quad (59)$$

For Mode Acceleration dynamic stresses, assuming invariable external force vectors $\{F(t)\}$, and fixed modes, solutions of Eqs. 12, 58 are used to yield the sensitivity of dynamic displacements and stresses:

$$\begin{aligned} [K] \left\{ \frac{\partial u_{MA}(t)}{\partial x} \right\} = - \left[\frac{\partial M}{\partial x} \right] [\Phi] \{ \ddot{q}(t) \} - \left[\frac{\partial C}{\partial x} \right] [\Phi] \{ \dot{q}(t) \} - [M] [\Phi] \left\{ \frac{\partial \ddot{q}(t)}{\partial x} \right\} - [C] [\Phi] \left\{ \frac{\partial \dot{q}(t)}{\partial x} \right\} - \left[\frac{\partial K}{\partial x} \right] \{ u_{MA}(t) \} \end{aligned} \quad (60)$$

$$\frac{\partial \sigma_{MA}}{\partial x} = \{c\}^T \left\{ \frac{\partial u_{MA}(t)}{\partial x} \right\} + \left\{ \frac{\partial c}{\partial x} \right\}^T \{ u_{MA}(t) \} \quad (61)$$

For quasi-static reduced order adjoint dynamic deformations we use the solutions of the reduced order static adjoint problem (Eq. 19) together with the dynamic pseudo load of Eq. 12, the static sensitivities in Eqs. 43, 44, and the dynamic sensitivities of Eq. 58:

$$\begin{aligned} \frac{\partial \sigma_{AD}}{\partial x} = \left\{ \frac{\partial \eta_{r,o}}{\partial x} \right\}^T \{ F(t) - [M] [\Phi] \{ \ddot{q}(t) \} - [C] [\Phi] \{ \dot{q}(t) \} - \right. \\ \left. - \{ \eta_{r,o} \}^T \left(\left[\frac{\partial M}{\partial x} \right] [\Phi] \{ \ddot{q}(t) \} + \left[\frac{\partial C}{\partial x} \right] [\Phi] \{ \dot{q}(t) \} + [M] [\Phi] \left\{ \frac{\partial \ddot{q}(t)}{\partial x} \right\} + [C] [\Phi] \left\{ \frac{\partial \dot{q}(t)}{\partial x} \right\} \right) \right\} \end{aligned} \quad (62)$$

using $\{u_{r,o}\} = [\Phi] \{ q(t) \}$ Eq. 62 can also be written as

$$\begin{aligned} \frac{\partial \sigma_{AD}}{\partial x} = \left\{ \frac{\partial \eta_{r,o}}{\partial x} \right\}^T \langle \{ F(t) - [M] \{ \ddot{u}_{r,o}(t) \} - [C] \{ \dot{u}_{r,o}(t) \} - \right. \\ \left. - \{ \eta_{r,o} \}^T \left(\left[\frac{\partial M}{\partial x} \right] \{ \ddot{u}_{r,o}(t) \} + \left[\frac{\partial C}{\partial x} \right] \{ \dot{u}_{r,o}(t) \} + [M] \left\{ \frac{\partial \ddot{u}_{r,o}}{\partial x} \right\} + [C] \left\{ \frac{\partial \dot{u}_{r,o}}{\partial x} \right\} \right) \rangle \right\rangle \end{aligned} \quad (63)$$

Finally, with the reduced order static adjoint solutions (Eqs. 19, 43) and the dynamic reduced order direct solutions in Eqs. 4 and 58, an analytic sensitivity equation for the second order approximate stresses can be obtained, by differentiating Eq. 30:

$$\begin{aligned}
\frac{\partial \sigma_{S.O.A}}{\partial x} = & \left\{ \frac{\partial p}{\partial x} \right\}^T [\Psi]^T \langle \{F\} - [M]\Phi\{\ddot{q}(t)\} - [C]\Phi\{\dot{q}(t)\} \rangle + \\
& + \{p\}^T [\Psi]^T \left\langle -[M]\Phi\left\{ \frac{\partial \ddot{q}(t)}{\partial x} \right\} - [C]\Phi\left\{ \frac{\partial \dot{q}(t)}{\partial x} \right\} - \left[\frac{\partial M}{\partial x} \right] \Phi\{\dot{q}(t)\} - \left[\frac{\partial C}{\partial x} \right] \Phi\{\dot{q}(t)\} \right\rangle \\
& + \left\{ \frac{\partial c}{\partial x} \right\}^T [\Phi]\{q(t)\} + \{c\}^T [\Phi] \left\{ \frac{\partial q(t)}{\partial x} \right\} - \\
& - \left\{ \frac{\partial p}{\partial x} \right\}^T [\Psi]^T [K]\Phi\{q(t)\} - \{p\}^T [\Psi]^T \left[\frac{\partial K}{\partial x} \right] \Phi\{q(t)\} - \{p\}^T [\Psi]^T [K]\Phi \left\{ \frac{\partial q(t)}{\partial x} \right\}
\end{aligned} \tag{64}$$

Using the static reduced order adjoint and the dynamic MD direct solutions, analytic sensitivity of the second order stress approximation can be written in the form:

$$\begin{aligned}
\frac{\partial \sigma_{S.O.A}}{\partial x} = & \{c\}^T \left\{ \frac{\partial u_{r.o}(t)}{\partial x} \right\} + \left\{ \frac{\partial c}{\partial x} \right\}^T \{u_{r.o}(t)\} + \\
& - \{\eta_{r.o}\}^T \left\langle \{[M]\left\{ \frac{\partial \ddot{u}_{r.o}(t)}{\partial x} \right\} + [C]\left\{ \frac{\partial \dot{u}_{r.o}(t)}{\partial x} \right\} + \left[\frac{\partial M}{\partial x} \right] \{u_{r.o}(t)\} + \left[\frac{\partial C}{\partial x} \right] \{\dot{u}_{r.o}(t)\} \right\rangle \\
& + \left\{ \frac{\partial \eta_{r.o}}{\partial x} \right\}^T \langle F(t) - [M]\{\ddot{u}_{r.o}(t)\} - [C]\{\dot{u}_{r.o}(t)\} \rangle - \\
& - \left\{ \frac{\partial \eta_{r.o}}{\partial x} \right\}^T [K]\{u_{r.o}(t)\} - \{\eta_{r.o}\}^T \left[\frac{\partial K}{\partial x} \right] \{u_{r.o}(t)\}
\end{aligned} \tag{65}$$

While the reduced order adjoint solutions, $\{p\}$, $\left\{ \frac{\partial p}{\partial x} \right\}$ are static, the reduced order direct solution

$\{q\}$, $\left\{ \frac{\partial q}{\partial x} \right\}$ are time dependent and are obtained from a mode displacement simulation. Both approximate direct and adjoint solutions are obtained using reduced order models, with much less degrees of freedom than the full order model, or the MA method using the full order quasi-static solution. Computer implementation of the sensitivity equations presented above will take advantage of the sparsity of $[M]$, and $[K]$ and the small number of non-zero elements in $\left[\frac{\partial M}{\partial x} \right]$, $\left[\frac{\partial K}{\partial x} \right]$ and $\left[\frac{\partial c}{\partial x} \right]$. Many

of the vector and matrix products in the reduced order equations can be prepared once for a reference structure, and then used in the course of optimization for generations of structures obtained by large variations of sizing type design variables. While some of the reduced order sensitivity equations might look long and time consuming, they actually involve vector and matrix products of low dimensions. Given the localized nature of stiffness and mass matrix sensitivities and the low order of the reduced order vectors, it is believed that significant computational savings can be realized. To precisely assess these savings depends on the actual implementation of the methods, the type of design variables and structures involved, and is beyond the scope of this paper. For the assumptions and approach used to study computational performance of sensitivity analyses in the case of structural dynamic response the reader is referred to Refs. 38-40. In the work reported in these references a number of methods were considered including mode displacement and full order mode acceleration (where "full order" relates to the static solution). To make the study general, so that it would apply to general finite element code implementation, the work in Refs. 38-40 is based on finite difference techniques to obtain derivatives of

system matrices with respect to design variables. In the work reported here, all sensitivities were obtained analytically.

Test Case

While the methods presented here apply to both purely structural and aeroelastic problems, the focus of this study is on the structural aspect. The structural model chosen is that of a model wing structure, for which analytic as well as experimental results for stresses under loading are available. Of major concern is, of course, the accuracy of predicted stresses and stress sensitivities with the different reduced order alternatives. This accuracy is evaluated using a fixed-modes approach in all cases, where the mode shapes and adjoint vectors are evaluated on some reference "base" structure. The same basis vectors, then, are used to reduce order of structural models which are modified to various degrees compared to the base structure.

This is aimed at evaluating the adequacy of a base structure, and approximations based on its properties, for constructing reduced order approximations of related different structures, representative of the changes the structure undergoes in the course of design optimization.

Only sizing type design variable changes are considered here. In addition, accuracy of reduced order stress approximations is evaluated for analytic stress sensitivities with respect to sizing type design variables. The stress sensitivities serve, in the context of gradient-based structural and aeroelastic optimization, to construct first order approximation of stress constraints, to be used by the optimization algorithm for fast evaluation of the constraints (Ref. 25, pp. 209-254). Both static and dynamic response cases are considered.

This wing, known as "the Denke wing" (Ref. 41), is an all aluminum 45 degrees swept wing, with an aspect ratio of 5 and a depth to chord ratio of 0.35 (Fig. 1). The chord length is $12\sqrt{2}$. The half span (from root to tip) is $30\sqrt{2}$. There are four internal ribs and a tip rib present along with the front and rear spars. The ribs are parallel to the root and are evenly spaced spanwise. The material properties are taken to be: $E = 10 \times 10^6$ psi, $\nu = 0.3$, and $\rho = 0.000259$ lbm/in³. Thickness for all wing skin panels is 0.032". Thickness for spar and rib web elements is 0.051". Front and rear spar cap areas are 0.371 square inches, and all remaining stringers have an area of 0.061 square inches.

In the finite element model skin panels, spar webs and rib webs have all been modeled using plane-stress 4-noded isoparametric elements. Truss elements were used for spar caps and stringers. The wing mesh is refined by using one "dummy" rib (Ref. 42) between each pair of real ribs. This mesh leads to good correlation of calculated stresses with respect to experimental stresses measured on this wing. Figure 1 shows coarse and refined numerical meshes for the wing. The wing is cantilevered at the root, and the total number of degrees of freedom in the full order finite element model is 300.

Two static and one dynamic load cases were studied. The first load case (Load Case #1) is designed to simulate a wing loaded by a distributed aerodynamic load plus concentrated loads due to engine attachment. Forces of 100 lbs each are applied to all nodes on the upper skin of the wing pointing up. Three 60 lbs concentrated forces are applied along the second real rib, pointing down.

Load Case #2 includes a concentrated force of 100 lbs at node #33 (Fig. 1). Load Case #3 is a 100 lbs concentrated step load applied at t=0 at node #33, for dynamic response simulations.

The following stresses were used for accuracy studies:

1. The normal force at spar cap number 5 (Fig. 2).
2. Normal stress (in the local xx direction) at skin membrane number 7 (Fig. 2).

Normal stress (in the local xx direction) at spar web number 1 (Fig. 2).

Modified stiffness matrices, reflecting changes in the structure from its base design, were calculated for the following cases (Fig. 2):

1. Variation of spar cap areas by factors of 0.2, 0.5, 0.8, 1.3, 2.0 and 5.0. The elements were modified by groups of 10, along the span direction. This way, we can examine the effect of structural

modification on a given stress point, where the modification is at different distances from the stress point.

2. Variation of skin membrane thickness by factors of 0.2, 0.5, 0.8, 1.3, 2.0 and 5.0. Again, the modification is done one group at a time for groups of 8 membrane elements at different locations along the span.

Static Results

In Figures 3-4, (Load Case #1) the relative stress error for different reduced order approximations is shown for selected structures which are modified variants of the base structure as a function of the location of the group of elements modified. The following procedure was followed in creating the data: The full order problem for the nominal (base) structure was solved. Mode shapes, natural frequencies, and Ritz vectors were obtained. The Ritz vectors in this work are the static full order solutions (Eq. 7) corresponding to point loads at degrees of freedom affected by the $\{c\}$ vector corresponding to each stress

The structure was, then, modified to reflect changes in area or thickness of a group of design variables. A new stiffness matrix was created, followed by full order static solution, as well as reduced order Mode Displacement (MD) approximation, and reduced order adjoint approximation. The mode shapes and adjoint Ritz vectors used for order reduction were those of the original unmodified structure.

Next, stresses were calculated using the exact static solution as well as the MD method, adjoint method, and new second order approximation method. In the second order approximation, approximate reduced order MD and adjoint deformation vectors were used, together with "exact" unmodified $\{c\}$, $\{F\}$ vectors and a full order $[K]$ matrix. The stress approximation errors were then calculated for the reduced order approximate methods relative to the full order "exact" results.

This procedure was repeated for design variations in different groups of elements, and for different stresses.

For Load Case #2, additional reduced order stress results were obtained using a variant of the MD method, with "fictitious mass" modes instead of natural modes of the original base structure. The large concentrated mass in this case was added to the degree of freedom where the concentrated force is applied. A concentrated mass four orders of magnitude bigger than the average physical element size was used. Another order reduction method tested in Load Case #2 was the combined Ritz vectors – mode shapes reduced base method of Ref. 19.

For Load Case #1, Figures 3–4 show stress errors with reduced order approximations for two levels of structural change from the original structure (factors of 0.5 and 2.0).

Accuracy of the stress at spar cap number 5 (Fig. 3) is shown versus the group identity defining the group of spar cap and stiffener elements being changed (Fig. 4). Three mode shapes and 6 adjoint Ritz vectors were used. The 6 adjoint Ritz vector are due to unit loading of each of the 6 degrees of freedom of the two nodes defining the truss element representing spar cap number 5.

In Figure 4 (Load Case #1), stress errors are shown for skin membrane number 7 (Fig. 2), and the structural elements modified in groups are skin membranes at different locations along the span. In this case, three mode shapes and twelve Ritz vectors were used. The 12 adjoint Ritz vector are due to unit loading of each of the 12 degrees of freedom of the four nodes defining the quadrilateral element representing skin membrane number 7. The large errors in the MD method, especially when the elements changed are in the region close to the stress point, are evident. The adjoint reduced order method performs much better. Yet, when changes in the structure are in the area of the stress point, this performance deteriorates. The second order approximations shows excellent accuracy independent of where structural changes are introduced. Given the very small number of mode shapes and adjoint Ritz vectors used and the relatively large structural changes, this accuracy is quite remarkable.

Typical stress errors in Load Case #2 are shown in Figure 5, presenting stress errors at skin membrane 7, with skin membrane element groups modified by a factor of 2.0. Three modes were used in the MD and MD/FM methods and 12 adjoint Ritz vectors in the adjoint and second order approximations. The Ritz

vector / Modes method used one Ritz vector (at the location of the actual concentrated force plus 3 modes. The superior performance of the second order method is again clearly evident. It is interesting to note disappointing performance of the fictitious mass method in many cases where the stress point is not too far away from the load point. This is not surprising. While the fictitious mass method leads to excellent stress results when fictitious mass modes are used with the original base structure, it performs poorly in the case of sensitivity calculation for modified structures, as discussed in the preceding sections. The Ritz / Mode method produces similar results to those of the MD/FM method. This is not surprising, since by adding a large fictitious mass to a degree of freedom, a mode shape of the "fictitious" structure will be created that will be similar to the static deformation of the structure under a concentrated force at that degree of freedom.

One might argue that it is unfair to compare accuracy of MD or MD/FM reduced order models based on 3 modes with the second order method with 3 modes and 6 (or 12) adjoint Ritz vectors. Perhaps the accuracy of the second order method (with Nm modes and NR adjoint Ritz vectors) should be compared to MD or MD/FM methods with Nm+NR modes. In order to study the effect of the number of MD mode shapes used on the accuracy of the approximation, we turn next to a typical case. For stress at skin membrane number 7, Load Case #2, and skin membrane elements in group 3 (Fig. 2) modified by a factor of 2.0, the accuracy of stress as a function of the number of modes used (3,6,9,12,15) is shown in Fig. 6. The adjoint method results shown are only with 12 adjoint vectors. The accuracy of the second order method (with 3 modes and 12 adjoint Ritz vectors) is clearly superior to that of either the MD reduction or the MD/FM reduction with 15 modes, or the Ritz / Modes method with 1 Ritz vector and 14 modes. That with only 3 natural mode shapes and 6 to 12 (depending on the element in which the stress is calculated) adjoint Ritz vectors such good stress accuracy is obtained is quite remarkable.

Accuracy of reduced order stresses was studied for the cases described above when the structural stiffness variations were much larger, up to 0.2 and 5 times that of the base structure. While errors in the reduced order stress predictions with MD, adjoint, MD/FM and Ritz/Modes methods were considerable, the second order approximation with only 3 modes and 6 or 12 adjoint Ritz vectors led to stress errors of less than 25% in the worst case studied.

Dynamic Results

Fig. 7 shows time histories of stress at spar cap number 5 due to a concentrated step load as defined for Load Case #3. The structure's stiffness is modified compared to the base structure by changing group number 4 of spar caps and stiffeners by a factor of 1.3. Damping ratios of 2% in all modes is assumed for the base structure. Then, using the procedure described in Ref. 29 (Eqs. 8-12), a full order damping matrix for the reference structure is created and assumed fixed as the structural stiffness is being changed. Mode Displacement (MD) and Mode Displacement with Fictitious Masses approximation results are compared to the full order "exact" results, as well as statically Full Order Mode Acceleration (FO-MA) with 3 MD modes, reduced order mode acceleration (RO-MA) based on reduced order adjoint, and, finally, reduced order second order approximation of the MA method (Eqs. 64, 65).

Three mode shapes are used in Fig. 7 (with six adjoint Ritz vectors). Nine modes are used in Fig. 8. It is not surprising that with only 3 modes (Fig. 7) the second order method cannot capture all the sub-harmonics in the transient response. Yet, the accuracy of maximum stresses is very good.

Figure 9 shows relative error in the maximum peak stress as a function of the number of modes used. Large errors are the result of using the MD method, the MD method with fictitious mass modes, or the Ritz / Modes method of Ref. 19. Errors in the full order MA method, or reduced order MA method based on adjoint Ritz vectors and second order approximations are comparable.

Stress Sensitivity in Reduced Order Static Cases

Convergence study results for stress sensitivity in the static case using increasing numbers of modes are shown in Fig. 10. Compared are the MD, MD with fictitious mass modes, and second order

approximations, shown together with results obtained with the reduced order adjoint method with a fixed number of adjoint Ritz vectors. Results for the Ritz / Modes method are similar to those of the MD/FM method, and will not be discussed further.

Figure 10 shows accuracy of the sensitivity of stress in spar cap number 5 (Fig. 2) with respect to a design variable linking the spar cap areas at caps 4, 14, 24, and 34 (Fig. 2). The sensitivity is evaluated at the base (reference) design.

Large errors are evident in the results with the two variants of the Mode Displacement approximations (based on natural modes of the base structure, and on fictitious mass modes). The reduced order adjoint method (with a fixed number of 6 adjoint Ritz vectors) leads to moderate errors in Fig. 10. In other cases (Ref. 43) the adjoint method lead to very large stress sensitivity errors. The second order stress sensitivity, obtained with the second order approximation, was found to be very accurate in all cases studied. For the case of Fig. 10 comparison of sensitivity errors when Eq. 48 and Eq. 50 were used, showed that Eq. 50 led to almost identical accuracy as Eq. 48 when more than 40 modes were used. When less than 40 modes were used, Eqs. 50 and 48 had comparable accuracy. It is striking that with the MD or MD w/FM methods it takes almost all modes of the structure (almost full order) to converge.

Stress Sensitivity in Reduced Order Dynamic Cases.

Figures 11-13 show time histories of the sensitivities of dynamic stresses at a spar cap with respect to changes in spar-cap linked design variables as functions of time, when 3, 9 and 30 modes are used.

Compared are the MD method, MD method with FM modes, statically full order Mode Acceleration Method, Adjoint method with a fixed number of adjoint vectors (corresponding to unit loads at the 6 degrees of freedom contributing to the local stress calculation in the spar cap - a truss element), and finally the second order method. The excellent accuracy of the reduced order derivatives over time in the second order method is clearly evident. With MD and MD w/FM order reduction, the errors in dynamic sensitivities are large even with a large number of modes. With only 3 modes the second order method cannot capture all the sub-harmonics in the full order response sensitivity, but it does capture sensitivity trends quite well.

Conclusions

Order reduction methods such as Mode Displacement (MD) or Mode Displacement with Fictitious Mass modes (MD w/FM) are widely used for displacement deformation prediction in structural dynamics and aeroelasticity. Yet, their accuracy when stress information is involved is poor, especially when stress sensitivities with respect to sizing type design variables are calculated. When reduced order structural models are generated for a given structure using its modes or adjoint solutions, and then the same modal and adjoint base vectors are used to reduce the order of a modified structure, accuracy of the reduced order modified structure suffers.

The loss of accuracy with modally reduced order models is, in many cases, associated with static truncation effects, making the reduced order static solution not capable of capturing local effects due to the action of concentrated forces. Stress sensitivity analysis, because of the local nature of changes in the stiffness matrix due to changes in a local design variable ($\{\partial K / \partial x\}$), leads to sensitivity equations which are similar to structural response to locally concentrated loads. When using Ritz vectors or fictitious masses for order reduction, a modally reduced vector base is created to reflect actual concentrated forces acting on the structure, or location and identity of stresses required. For sensitivity analysis, however, this reduced order base of Ritz vectors or FM vectors must also reflect local action at the degrees of freedom affected by each and every design variable change. This makes the generation of reduced order bases for the MD method or its variants very difficult and the resulting models cannot be of very low order.

The second order structural reduction method overcomes these difficulties by combining a modal reduction method for the direct problem with a Ritz vector reduction method for an adjoint static solution. The resulting stress and stress sensitivity approximation, using reduced order models based on modes and adjoint responses of the reference structure, has excellent accuracy with a small number of modes and adjoint Ritz vectors for a large group of modified structures obtained from the reference structure by varying sizing type design variables. In a structural optimization process, a set of mode shapes and adjoint Ritz vectors of the original structure is prepared up-front. Those same base vectors are then used to reduce the order of the structure throughout the optimization process as it gets varied and modified. Both static and dynamic stresses and stress sensitivities are accurately calculated using the resulting reduced order models over large design variable variations. In the dynamic case, the method presented here uses a static order reduction method to reduce the order of the full order static solution part of the Mode Acceleration method.

In the case of static aeroelastic analysis, the $[K]$ matrix is augmented by an aerodynamic matrix to lead to a non-symmetric system matrix in the aeroelastic static equation

$$[K - q_D \cdot A]\{u\} = \{F\}$$

The same second order reduction technique can be used now. The only difference from the equations derived for the purely structural case is that the adjoint problem involves the transpose of the system matrix

$$[K - q_D \cdot A]^T \{\eta\} = \{c\}$$

where $\{c\}$ is the vector used to obtain a stress from the deformation vector $\{u\}$.

Further studies of the potential of the second order method for obtaining accurate information in reduced order models are now underway for cases involving static and dynamic aeroelasticity, dynamic (time dependent) adjoint solutions, and reduced order solutions obtained on coarse meshes and then used to approximate the solutions on fine meshes in cases of multi-grid methods or mesh adaptation in structural analysis. Additional work, which is beyond the scope of this paper: extension of the method to the case of free-free structures, reduced order stress approximation for frequency response and structural response to random excitation, study of alternative approximate adjoint solutions for the second order method. The present paper, it is hoped, contributes to both efficiency of design oriented structural analysis and to the understanding of errors sources and the way to overcome them in structural order reduction.

Acknowledgement

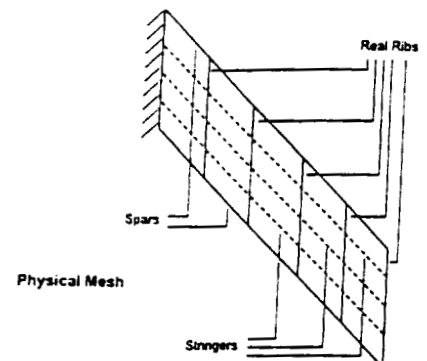
The work reported in this paper was supported by the National Science Foundation through a National Young Investigator award. This support is greatly appreciated.

References

1. Bisplinghoff, R.L., Ashley, H., and Halfman, R.L., *Aeroelasticity*, Addison-Wesley, Reading, Massachusetts, 1955, pp. 641-650 (also available from Dover publications).
2. Hurty, W.C., and Rubinstein, M.F., "Dynamics of Structures", Prentice Hall Inc., Englewood Cliffs, New Jersey, 1964, pp. 299-307.
3. Craig, R.R., *Structural Dynamics*, John Wiley & Sons, New York, 1981.
4. Thomson, W.T., *Theory of Vibration with Applications*, 4th edition, Prentice Hall, Englewood Cliffs, NJ, 1993, Chapter 11.
5. Haftka, R.T., "Optimization of Flexible Wing Structures Subject to Strength and Induced Drag Constraints", AIAA Journal, Vol. 15, pp. 1101-1106, 1977.
6. Rodden, W.P., and Johnson, E.H., *MSC/NASTRAN Aeroelastic Analysis User's Guide*, V68, The MacNeal-Schwendler Corporation, October 1994, Los Angeles, California.

7. Neill, D.J., Herendeen, D.L., and Venkayya, V.B., ASTROS Enhancements, Vol. III – ASTROS Theoretical Manual, WL-TR-96-3006, April 1995.
8. Guyan, R.J., “Reduction of Stiffness and Mass Matrices”, AIAA Journal, Vol. 3, No. 2, p. 380. 1965.
9. Almroth, B.O., Stern, P., and Brogan, F.A., “Automatic Choice of Global Shape Functions in Structural Analysis”, AIAA Journal, Vol. 16, No. 5, pp. 525-528, 1978.
10. Craig, R.R., and Bampton, M., “Coupling Substructures for Dynamic Analysis”, AIAA Journal, Vol. 6, No. 7, pp. 1313-1319, 1968.
11. Meirovitch, L., “Computational Methods in Structural Dynamics”, Sijhoff & Noordhoff, The Netherlands, Chapter 11, 1980.
12. Huttelmaier, H.P., “Instability Analysis using Component Modes”, Computers & Structures, Vol. 43, No. 3, pp. 451-457, 1992.
13. Chowdhury, P.C., “An Alternative to Normal Mode Method”, Computers and Structures, Vol. 5, p. 315, 1975.
14. Nour-Omid, B., and Clough, R.W., “Dynamic Analysis of Structures Using Lanczos Coordinates”, International Journal of Earthquake Engineering and Structural Dynamics, Vol. 12, No. 4., pp. 565-577, 1984.
15. Wilson, E.L., Yuan, M.W., and Dickens, J.M., “Dynamic Analysis by Direct Superposition of Ritz Vectors”, International Journal of Earthquake Engineering and Structural Dynamics, Vol. 10, pp. 813-821, 1982.
16. Wilson, E.L., “A New Method of Dynamic Analysis for Linear and Nonlinear Systems”, Finite Elements in Analysis and Design, Vol. 1, pp. 21-23, 1985.
17. Arnold, R.R., Citerley, R.L., Chargin, M., Galant, D., “Application of Ritz Vectors for Dynamic Analysis of Large Structures”, Computers and Structures, Vol. 21, No. 5, pp. 901-908, 1985. Vol. 21, No. 3, pp. 461-467, 1985.
18. Leger, P., Wilson, E.L., and Clough, R.W., “The Use of Load Dependent Vectors for Dynamic and Earthquake Analysis”, Earthquake Engineering Research Center, College of Engineering, University of California, Berkeley, California, Report No. UCB/EERC-86/04, March 1986.
19. Kline, K.A., “Dynamic Analysis using a Reduced Basis of Exact Modes and Ritz Vectors”, AIAA Journal, Vol. 24, No. 12, December 1986, pp. 2022-2029.
20. Noor, A.K., “Recent Advances in Reduction Methods for Nonlinear Problems”, Computers and Structures, Vol. 13, pp. 31-44, 1981.
21. Sheena, Z., and Karpel, M., “Structural Optimization for Aeroelastic Control Effectiveness”, Journal of Aircraft, Vol. 26, No. 5, 1989, pp. 493-495.
22. Shalev, D., and Unger, A., “Nonlinear Analysis using a Modal Based Reduction Technique”, Journal of Composite Structures, May 1994.
23. Livne, E., “Accurate Calculation of Control-Augmented Structural Eigenvalue Sensitivities Using Reduced-Order Models”, AIAA Journal, Vol. 27, No. 7, July 1989, pp. 947-954.
24. Sandridge, C.A., and Haftka, R.T., “Modal Truncation, Ritz Vectors, and Derivatives of Closed-Loop Damping Ratios”, Journal of Guidance, Control, and Dynamics, Vol. 14, No. 4, July-August 1991, pp. 785-790.
25. Haftka, R.T., and Gurdal, Z., Elements of Structural Optimization, Third revised and expanded addition, Kluwer Academic Publishers, Dordrecht, The Netherlands, 1992.
26. Cornwell, R.E., Craig, R.R., Jr., and Johnson, C.P., “On the Application of the Mode-Acceleration Method to Structural Engineering Problems”, Earthquake Engineering and Structural Dynamics, Vol. 11, No. 5, 1983, pp. 679-688.
27. Blleloch, Paul, “Calculation of Structural Dynamic Forces and Stresses Using Mode Acceleration”, AIAA Journal, Vol. 12, No. 5, 1988, pp. 760-762.
28. Karpel, M., and Raveh, D., “The Fictitious Mass Element in Structural Dynamics”, AIAA Journal, Vol. 34, No. 3, 1996, pp. 607-613.
29. Karpel, M., and Presente, E., “Structural Dynamic Loads in Response to Impulsive Excitation”, Journal of Aircraft, Vol. 32, No. 4, July-August 1995, pp. 853-861.

30. Karpel, M., and Brainin, L., "Stress Considerations in Reduced-Size Aeroelastic Optimization", AIAA Journal, Vol. 33, No. 4, April 1995, pp. 716-722.
31. Karpel, M., Moulin, B., and Love, M.H., "Modal-Based Structural Optimization with Static Aeroelastic and Stress Constraints", Journal of Aircraft, Vol. 34, No. 3, May-June 1997, pp. 433-440.
32. Akgun, M.A., Haftka, R.T., and Garcelon, J., "Sensitivity of Stress Constraints using the Adjoint Method", AIAA Paper No. 98-1752, presented at the 39th Structures, Structural Dynamics and Materials Conference, Long Beach, California, April 1998.
33. Johnson, E.H., "Adjoint Sensitivity Analysis in MSC/NASTRAN", MSC NASTRAN World Users Conference 1997.
34. Van-Niekerk, B., "Computation of Second Order Accurate Unsteady Aerodynamic Generalized Forces", AIAA Journal, Vol. 24, No. 3, 1986, pp. 492-498.
35. Li, W.-L., and Livne, E., "Analytic Sensitivities and Approximations in Supersonic and Subsonic Wing / Control Surface Unsteady Aerodynamics", Journal of Aircraft, Vol. 34, No. 3, May-June 1997, pp. 370-379.
36. Haftka, R.T., and Yates, E.C. Jr., "Repetitive Flutter Calculations in Structural Design", Journal of Aircraft, Vol. 13, July 1976, pp. 454-461.
37. Haftka, R.T., "Second Order Sensitivity Derivatives in Structural Analysis", AIAA Journal, Vol. 20, No. 12, December 1982, pp. 1765-1766 (Eq. 7).
38. Greene, W.H., Computational Aspects of Sensitivity Calculations in Linear Transient Structural Analysis, Ph.D. dissertation, Virginia Polytechnic Institute and State University, August 1989.
39. Greene, W.H., and Haftka, R.T., "Computational Aspects of Sensitivity Calculations in Transient Structural Analysis", Computers and Structures, 32, pp. 433-443, 1989.
40. Green, W.H., and Haftka, R.T., "Computational Aspects of Sensitivity Calculations in Linear Transient Structural Analysis". Structural Optimization, Vol. 3, pp. 176-201, 1991.
41. de Veubeke, F., (editor), "Matrix Methods in Structural Analysis", Pergamon Press, Oxford, 1964.
42. Harvey, M.S., "Automated Finite Element Modeling of Wing Structures for Shape Optimization", MS Thesis, Department of Aeronautics and Astronautics, University of Washington, Seattle, WA, 1993.
43. Blando, G.D., "Accurate Stress Approximation and Design Sensitivities using Combined Direct and Adjoint Reduced Order Solutions", Master of Science thesis, Department of Aeronautics and Astronautics, University of Washington, Seattle, Washington, November 1998.



Physical Mesh

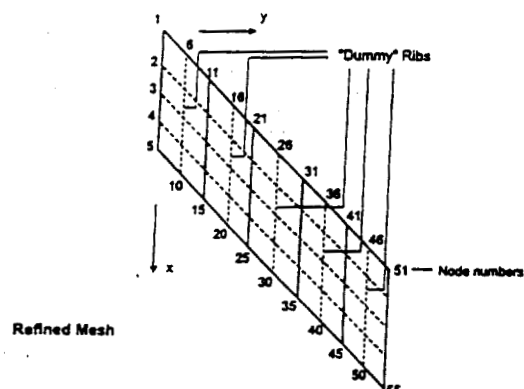
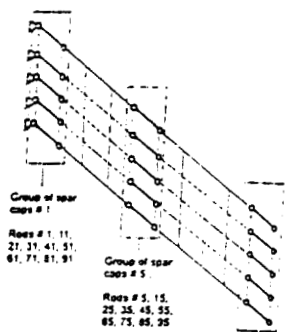
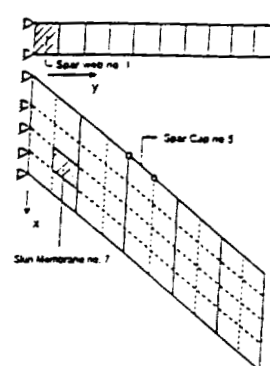


Figure 1. The test wing.

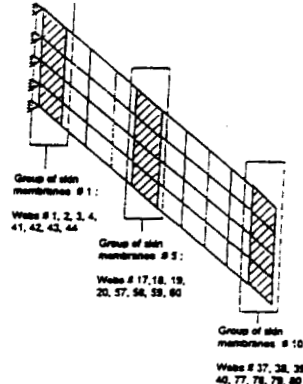


Figure 2. Identification of elements (for stresses) and groups of elements (where structural changes occur).

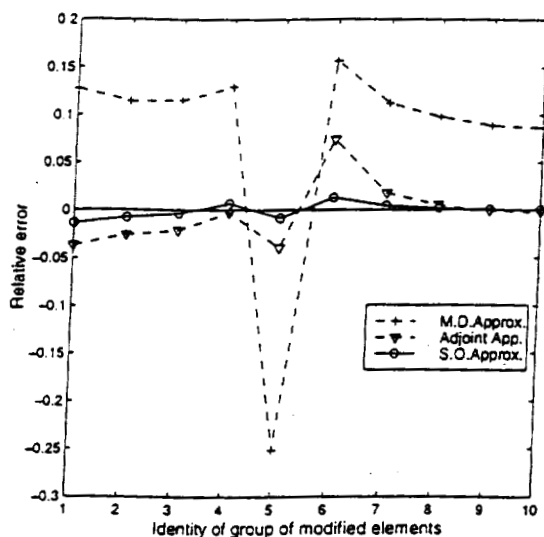


Figure 3. Relative stress error for spar cap #5 in Load Case #1 (Elements modified: area of spar caps and stringers by a factor of 0.5)

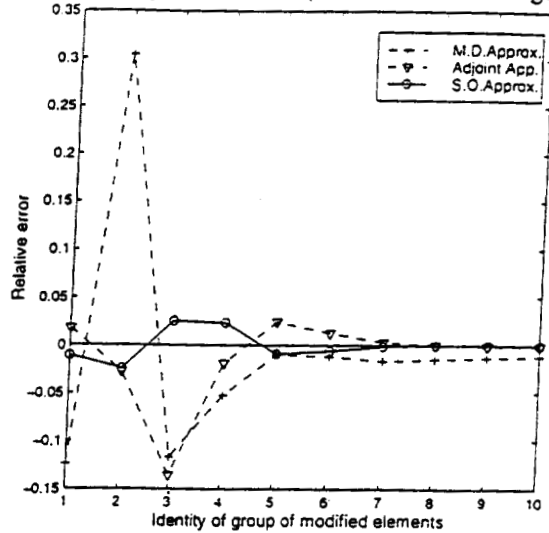


Figure 4. Relative stress error for skin membrane #7 in Load Case #1 (Elements modified: thickness of skin membranes by a factor of 2)

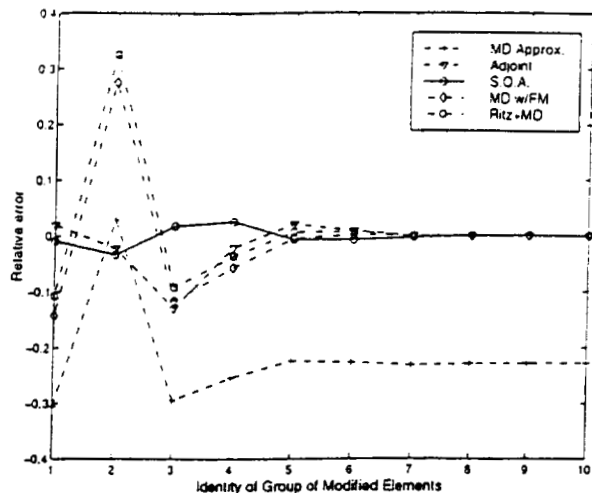


Figure 5. Relative stress error for skin membrane #7 in Load Case #2 (Elements modified: thickness of skin membranes by a factor of 2)

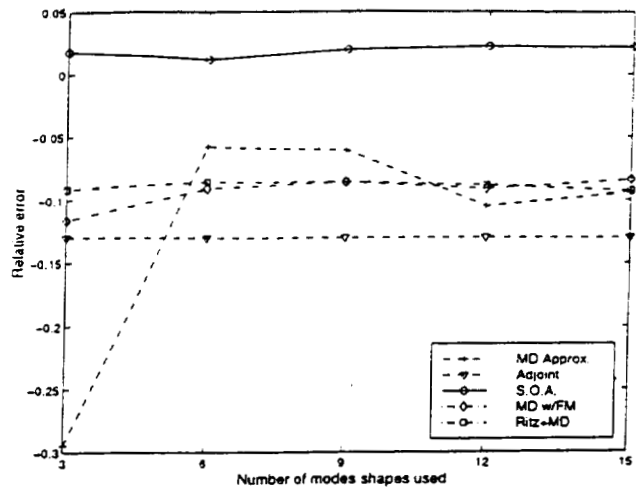


Figure 6. Relative stress error for skin membrane #7 in Load Case #2 as a function of number of mode shape used (Elements modified: thickness of skin membranes in group 3 by a factor of 2)

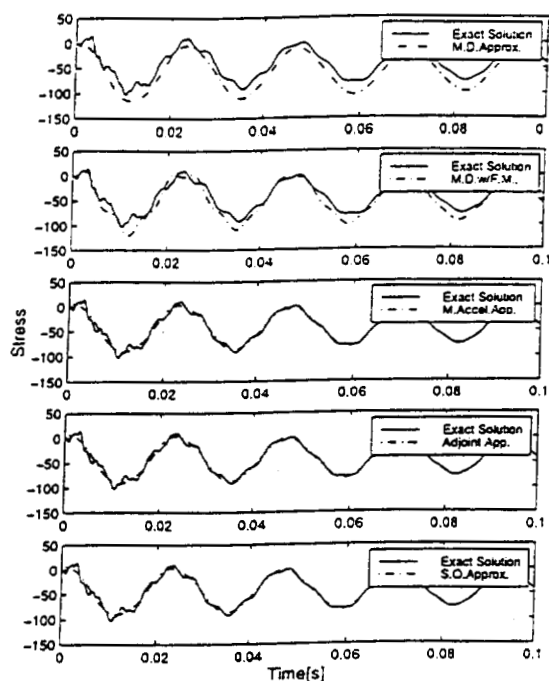


Figure 7. Dynamic stresses in spar cap #5 due to a step load in load case #3 (Elements changed area of spar caps and stringers in group 4 by a factor of 1.3. Number of modes used: 3, Number of adjoint static Ritz vectors: 6)

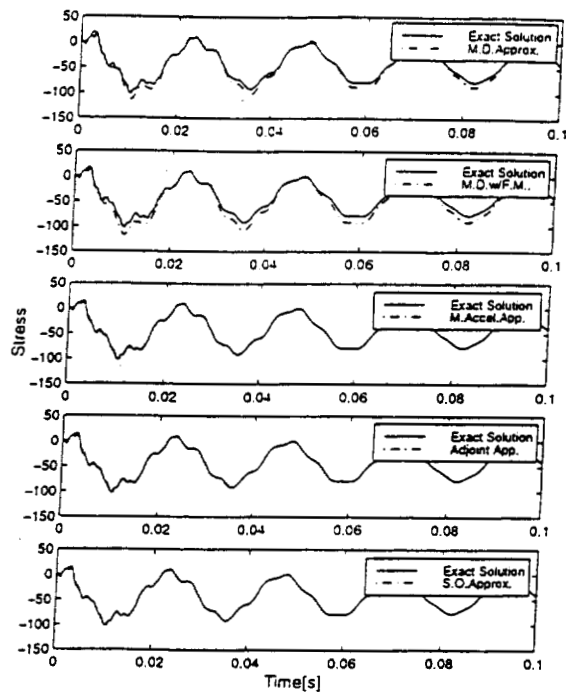


Figure 8. Dynamic stresses in spar cap #5 due to a step load in load case #3 (Elements changed area of spar caps and stringers in group 4 by a factor of 1.3. Number of modes used: 9, Number of adjoint static Ritz vectors: 6)

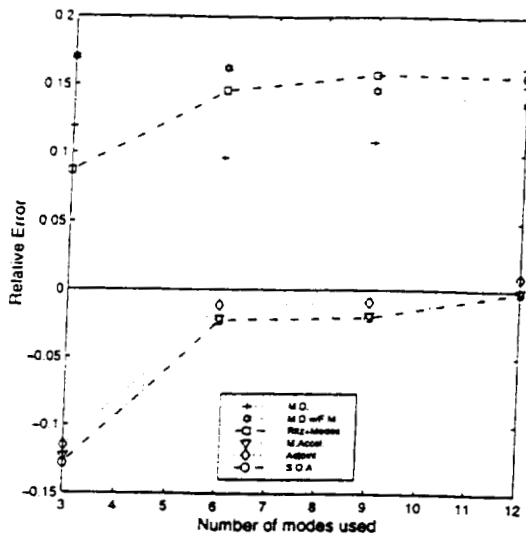


Figure 9. Errors in peak stresses as functions of the number of modes used.

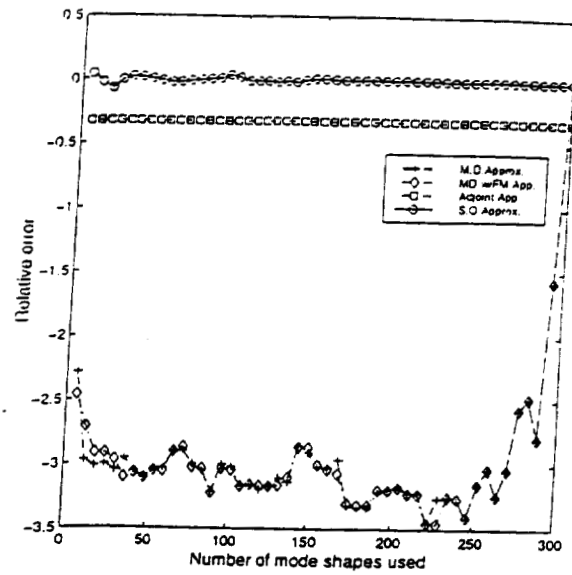


Figure 10. Errors in static stress sensitivity as functions of the number of modes used (stress is at spar cap #5, elements modified are spar caps #4, 14, 24 and 34).

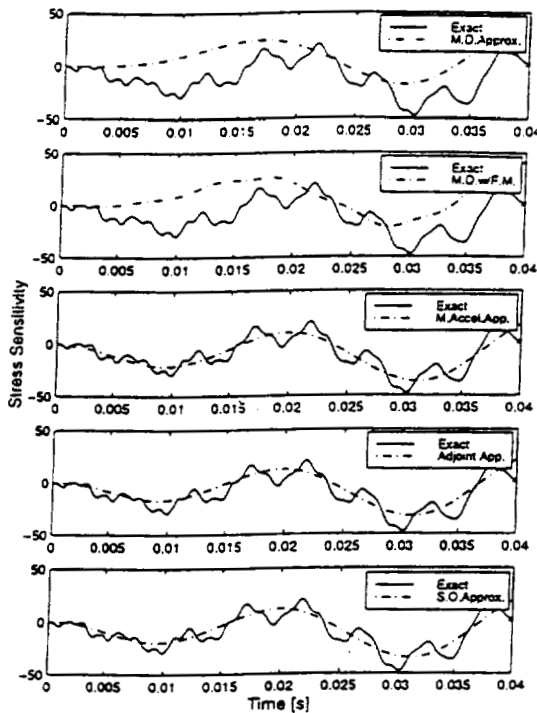


Figure 11. Dynamic stress sensitivity errors for stress sensitivity in spar cap #5 in load case #3. 3 modes used. Elements modified: spar caps #4, 14, 24 and 34.

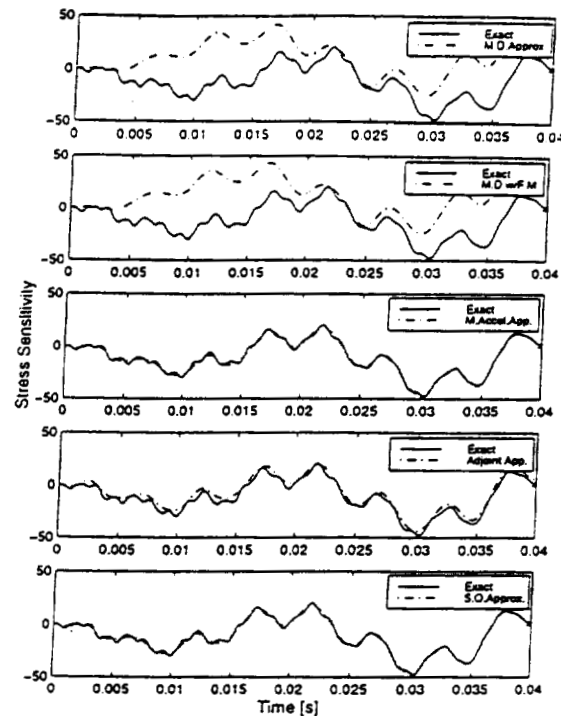


Figure 12. Dynamic stress sensitivity errors for stress sensitivity in spar cap #5 in load case #3. 9 modes used. Elements modified: spar caps #4, 14, 24 and 34.

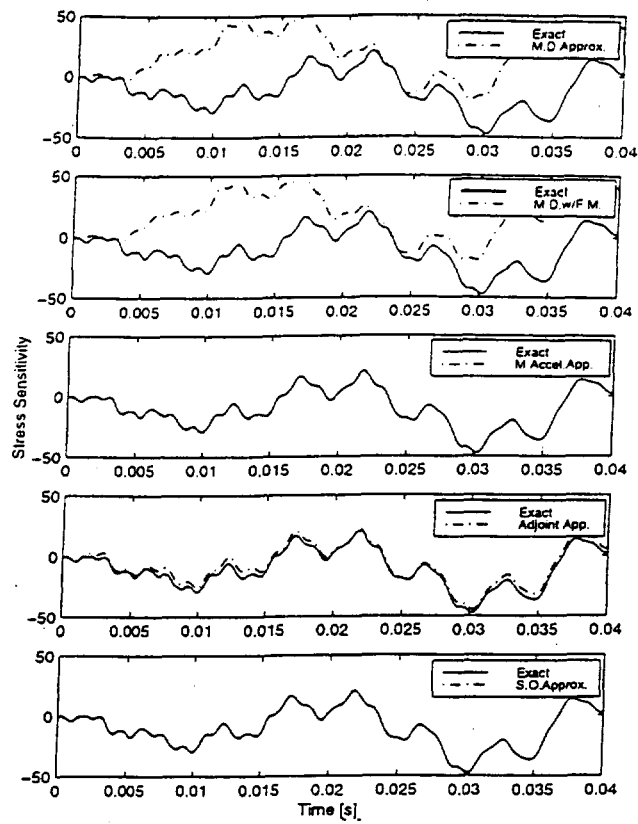


Figure 13. Dynamic stress sensitivity errors for stress sensitivity in spar cap #5 in load case #3. 30 modes used. Elements modified: spar caps #4, 14, 24 and 34.

REDUCED-ORDER MODELS BASED ON LINEAR AND NONLINEAR AERODYNAMIC IMPULSE RESPONSES

531-02

Walter A. Silva*
Aeroelasticity Branch
NASA Langley Research Center

ABSTRACT

This paper discusses a method for the identification and application of reduced-order models based on linear and nonlinear aerodynamic impulse responses. The Volterra theory of nonlinear systems and an appropriate kernel identification technique are described. Insight into the nature of kernels is provided by applying the method to the nonlinear Riccati equation in a non-aerodynamic application. The method is then applied to a nonlinear aerodynamic model of an RAE 2822 supercritical airfoil undergoing plunge motions using the CFL3D Navier-Stokes flow solver with the Spalart-Allmaras turbulence model. Results demonstrate the computational efficiency of the technique.

INTRODUCTION

As the complexity of modern computational fluid dynamics (CFD) codes increases, so does their computational cost and execution time. As a result, these codes are not used routinely in disciplines where the information provided by these codes could be of great benefit. These disciplines include aeroelasticity, aeroservoelasticity, optimization, and preliminary design. In order to improve this situation, the development of reduced-order models has become a major goal of several national and international organizations¹⁻¹².

A reduced-order model is a simplified mathematical model that encapsulates most, if not all, of the fundamental dynamics of a more complex system. Due to its mathematical simplification, the computational cost (CPU

*Research Scientist, Senior Member

Copyright©1999 by the American Institute of Aeronautics and Astronautics, Inc. No copyright is asserted in the United States under Title 17, U.S.Code. The U.S. Government has a royalty-free license to exercise all rights under the copyright claimed herein for Governmental Purposes. All other rights are reserved by the copyright owner.

memory, execution time, and turnaround time) of using a reduced-order model can be orders of magnitude lower than the computational cost of using the original more complex system. In the case of CFD codes, development of aerodynamic reduced-order models provides a cost-effective means for incorporating CFD analyses into several disciplines where, heretofore, it has not been incorporated.

This paper will discuss reduced-order aerodynamic models based on linear and nonlinear aerodynamic impulse responses. Previously⁹⁻¹², the concept of an aerodynamic impulse response was introduced and its relationship to the more traditional aerodynamic functions (Wagner's, Theodorsen's) was defined. Aerodynamic impulse responses are obtained from any CFD model of interest using standard digital signal processing techniques and the Volterra theory of nonlinear systems⁹⁻¹². Computationally-efficient linear and nonlinear digital convolution schemes are then applied for predicting the response of the nonlinear aerodynamic system to arbitrary inputs.

The paper begins with mathematical definitions of time-invariant and time-varying systems. This is followed by a description of the Volterra theory of nonlinear systems, including derivation of the kernel identification equations. These kernel identification equations are then applied to nonlinear systems in order to gain insight into the nature of the kernels. The nonlinear systems investigated include: first, a nonlinear Riccati circuit which will illustrate the nature of kernels and then a plunging airfoil using the CFL3D (Navier-Stokes) flow solver with the Spalart-Allmaras turbulence model.

MATHEMATICAL SYSTEMS

A time-invariant (TI) system, also referred to as a shift-invariant, stationary or autonomous system, is a system whose fundamental properties do not change with time. That is, the equations defining a TI system are not explicit functions of time so

$$f = f(x, \dot{x}, \ddot{x}, \dots)$$

An example of a simple, TI, nonlinear system is a pendulum. Although the full nonlinear equation of a pendulum is certainly a function of time which can exhibit nonlinear, unsteady responses if an unsteady excitation is applied, neither the length of the pendulum nor the mass at the end of the pendulum are functions of time¹³.

Differential equations with constant coefficients are TI because the coefficients are not explicit functions of time. But not all TI systems are defined by equations with constant coefficients. Time-invariance is sometimes mistakenly interpreted as implying functions that are independent of time. Even a classical, fundamental text such as Ref. 14 misinterprets nonlinear, TI systems as systems that do not accept time-dependent forcing functions. This is clearly not correct since the time-invariance of a system refers to the system itself and not to the characterization of the inputs or outputs (i.e., steady or unsteady) of the system.

A time-varying (TV) system, also referred to as a non-stationary or non-autonomous system, is a system whose fundamental properties do change with time. That is

$$f = f(x, \dot{x}, \ddot{x}, \dots, t)$$

An example of a TV system is a rocket during launch. The mass of the rocket, mostly fuel, is spent very quickly. The mass of the rocket, and therefore the rocket's dynamics, are changing with time. The identification of impulse responses for a time-varying system is typically more complicated than for a TI system. Reference 15 addresses the problem of Volterra kernel identification for TV, nonlinear systems.

Fortunately, for many of the problems in aircraft unsteady aerodynamics, aeroelasticity, and aeroservoelasticity, the governing nonlinear equations are time invariant. Although an airplane's fuel quantity, or mass, is certainly not constant, present-day analyses treat an airplane's fuel loading as separate, constant-mass cases (full fuel to near empty, for example) as opposed to a continuously-varying quantity. The linearization of these TI, nonlinear equations about an operating point yields the familiar TI, linear equations that comprise the majority of modern-

day, linear analysis techniques within these disciplines.

The Navier-Stokes equations do not have any coefficients that are explicit functions of time. As a result, the Navier-Stokes equations are, by definition, time invariant^{11,12}. The discretized Navier-Stokes equations, or CFD codes, do exhibit time-varying behavior at certain conditions, especially in the initial time steps when the residual (error) is in the process of converging to an acceptably small number. But the residual term is a byproduct of discretization that is not present in the continuous-time Navier-Stokes equations. A condition of consistency requires that, in the limit, the discretized system approach the original, continuous-time system. Therefore, given appropriate discretization and convergence of the residual, the discretized Navier-Stokes equations should be, and are in fact, TI as well. This is important since it would be unacceptable for a discretization process to transform a TI system into a TV system, as the associated dynamics of a TI system versus those of a TV system are vastly different.

VOLTERRA THEORY

Introduction

The Volterra¹⁶ theory was developed in 1930. The theory is based on functionals, or functions of other functions, and subsequently became a generalization of the linear convolution integral approach that is applied to linear, time-invariant (LTI) systems.

The basic premise of the Volterra theory of nonlinear systems^{17,18} is that any nonlinear system can be modeled as an infinite sum of multidimensional convolution integrals of increasing order. This infinite sum, presented here in continuous-time form, is known as the Volterra series and it has the form

$$\begin{aligned} y(t) = h_0 + & \int_0^{\infty} h_1(t-\tau) u(\tau) d\tau + \\ & \cdots \\ & \int_0^{\infty} \int_0^{\infty} h_2(t-\tau_1, t-\tau_2) u(\tau_1) u(\tau_2) d\tau_1 d\tau_2 + \cdots \\ & \cdots \\ & \int_0^{\infty} \cdots \int_0^{\infty} h_n(t-\tau_1, \dots, t-\tau_n) u(\tau_1) \cdots u(\tau_n) d\tau_1 \cdots d\tau_n + \cdots \end{aligned} \quad (1)$$

where $y(t)$ is the response of the nonlinear system to $u(t)$, an arbitrary input; h_0 is a steady value about which the response is computed; $h_1(t)$ is the first-order kernel or the linear unit impulse response; $h_2(\tau_1, \tau_2)$ is the second-order kernel, and $h_n(\tau_1, \dots, \tau_n)$ is the n^{th} -order kernel. It is assumed that: 1) the kernels, input function, and the output function are real-valued functions; 2) the system is causal ; and 3) the system is time invariant.

Inspection of Equation (1) reveals some very interesting and characteristic features of the Volterra series. The value of h_0 is known based on the steady-state value of the system at a particular condition. It does not require any special identification technique. This will be discussed in more detail when applied to an aerodynamic system. Also, if the kernels of order two and above are zero, then the response of the system is linear and is completely described by the unit impulse response $h_1(t)$, and the first-order convolution integral.

The higher order kernels ($h_2(\tau_1, \tau_2)$, ..., $h_n(\tau_1, \dots, \tau_n)$) are the responses of the nonlinear system to multiple unit impulses, with the number of impulses applied equal to the order of the kernel of interest : e.g., $h_2(\tau_1, \tau_2)$ is the response of the nonlinear system to two unit impulses applied at two points in time, τ_1 and τ_2 . The variation of the time difference between these two times characterizes the second-order (nonlinear) memory of the system. Therefore, the second-order kernel is a two-dimensional function of time: t and the time difference $T = \tau_1 - \tau_2$. This mathematical definition follows directly for the n^{th} -order kernel, although visualization of these functions can become difficult for orders greater than three. As will be shown, these kernels are also a function of the amplitude of the input used for identification.

The impulse response of a linear system is referred to as the memory of the system. Convolution then allows exact prediction of the response of the system to an arbitrary input because all responses of the system are scaled and shifted superpositions of this memory function¹². It is important to understand that the set of arbitrary inputs includes any and all possible inputs, from steady (step) inputs to random inputs, thus the term "arbitrary". For the linear case, the arbitrary input has no amplitude or frequency limitations.

For a nonlinear system approximated by a Volterra series, the higher-order kernels are a measure of the nonlinear memory of the system. Unlike the linear system, however, the arbitrary nature of the input, primarily with respect to amplitude, does have some limitations due to the fact that the Volterra series is truncated for practical applications. As Boyd¹⁹ has shown, the convergence of the Volterra series is limited by the infinity norm of the input (maximum value). If this norm exceeds a particular value, then convergence of the series, and, therefore, the predictive ability of the series, is not guaranteed. The infinity norm of the input is, of course, system dependent and will not usually be known a priori. Similarly, the convergence of the series is a function of the number of components that are identified for a particular kernel. Rugh¹⁷ and Boyd¹⁹ discuss Volterra's (and Frechet's) extension of the Weierstrass theorem to nonlinear systems with finite (or fading) memory, and its relationship to the Volterra series.

Wiener²⁰ contributed significantly to the development of the Volterra theory and, as a result, the theory is sometimes referred to as the Volterra-Wiener theory of nonlinear systems. Reference 21 presents a kernel identification technique based on auto- and cross-correlation functions. References 22-29 are additional, excellent sources of information regarding the Volterra theory of nonlinear systems.

This research focuses on the time-domain Volterra theory because CFD analyses are typically performed in the time domain. There exists, however, a great deal of information on the frequency-domain Volterra theory^{17,18,30}. The frequency-domain Volterra theory deals with the multidimensional Fourier transforms of the time-domain kernels. The resultant functions are referred to as higher-order spectra^{31,32}. A double Fourier transform of a second-order kernel is referred to as a bispectrum. Whereas time-domain Volterra kernels may be better suited for computational methods, the frequency-domain methods appear to be better suited for experimental identification techniques. Boyd et al³³ describe a frequency-domain technique that was successfully applied to the experimental identification of the second-order kernel of a nonlinear electroacoustic transducer (speaker) system. The theory also has some very interesting applications in the fields of general turbulence³⁴ and low-frequency drift oscillations (LFDO) experienced by moored vessels in

turbulent seas¹⁵. A time-domain Volterra kernel identification technique is described in a subsequent section.

Weakly Nonlinear Systems

One approach for obtaining Volterra series representations of physical systems is to assume that the system is a 'weakly' nonlinear system. A weakly nonlinear system is well defined by the first two kernels of the Volterra series so that kernels of third order and above are negligible. Boyd, Tang, and Chua³³ mention some physical systems that are accurately modeled as weakly nonlinear systems including electromechanical and electroacoustic transducers and some biological systems. In this study, it is assumed that the nonlinear aerodynamic system that is identified from the Navier-Stokes equations is a weakly nonlinear, second-order system. It is important to develop expertise with the application of Volterra methods to nonlinear aerodynamic models in a systematic manner and a weakly-nonlinear model provides this type of gradual approach to the problem.

Although this truncation may exacerbate known convergence and amplitude restrictions of the Volterra series, it is of interest to investigate the effectiveness of this truncated model to practical applications. The truncated, second-order Volterra series is

$$y(t) = h_0 + \int_0^\infty h_1(t-\tau) u(\tau) d\tau + \int_0^\infty \int_0^\infty h_2(t-\tau_1, t-\tau_2) u(\tau_1) u(\tau_2) d\tau_1 d\tau_2 \quad (2)$$

For the applications considered in this study, kernel identification will consist of the identification of the first- and second-order kernels with h_i clearly stated as appropriate.

Kernel Identification

The advantage of the Volterra series approach for modeling nonlinear systems is that once the kernels are identified, the response of the nonlinear system to an arbitrary input can be predicted. The problem of kernel identification, therefore, is central to the successful generation of an accurate Volterra series representation of a nonlinear system. The most obvious approach for identifying the kernels is to derive analytical

expressions for the kernels from the governing nonlinear equations of the system of interest^{20,22,23}. Although this approach is theoretically applicable to any set of nonlinear equations, including the nonlinear fluid flow equations such as TSD, Euler, and Navier-Stokes equations, it would require a significant amount of effort to analytically compute the kernels for different configurations and for various inputs. Instead, a kernel identification technique is desired that uses the output of a CFD model directly for quick and efficient kernel identification, regardless of the CFD code being used and the particular model geometry.

In Eq. (2), analytical application of unit impulses (Dirac delta functions) results in equations that define the first- and second-order kernels. The equations are derived in detail in Ref. 12 and are presented here in final form:

$$h_1(\tau_1) = 2y_0(\tau_1) - (1/2)y_2(\tau_1) \quad (3)$$

$$h_2(\tau_1, \tau_2) = (1/2)(y_1(\tau_1, \tau_2) - y_0(\tau_1) - y_0(\tau_2)) \quad (4)$$

where $y_0(\tau_1)$ is the response of the nonlinear system to a single unit impulse applied at time τ_1 ; $y_0(\tau_2)$ is the response of the nonlinear system to a single unit impulse applied at time τ_2 ; $y_1(\tau_1, \tau_2)$ is the response of the nonlinear system to two unit impulses, one at time τ_1 and one at time τ_2 ; and $y_2(\tau_1)$ is the response of the nonlinear system to a single impulse at time τ_1 (same time as $y_0(\tau_1)$) but with double the amplitude. For a TI system, $y_0(\tau_2)$ is just $y_0(\tau_1)$ shifted in time to τ_2 . It should be noted that τ_1 is held constant (usually at $t=0$) while τ_2 is varied for the computation of $y_1(\tau_1, \tau_2)$.

The first-order kernel, $h_1(\tau_1)$, is a one-dimensional function of time. Clearly, for a purely linear system, the first-order kernel is identical to the linear unit impulse response. For a nonlinear system, the first-order kernel captures a first-order, amplitude-dependent deviation from linearity (i.e., nonlinearity) because it is comprised of two impulse responses of different amplitudes.

Once the first-order kernel has been computed, computation of the second-order kernel requires computation of several $y_1(\tau_1, \tau_2)$ responses for varying values of τ_2 . As a result, the second-order kernel is a two-dimensional function of time. It is a function of time t and a

function of the time difference between τ_1 and τ_2 . As the time difference between τ_1 and τ_2 is varied, this leads to several values of $y_1(\tau_1, \tau_2)$ that, in turn, leads to several values of the second-order kernel. These responses are hereby referred to as "components" of the second-order kernel. Subsequent examples will clarify this concept.

EXAMPLE- NONLINEAR CIRCUIT

A simple nonlinear system that can be used to illustrate the kernel identification technique is a series circuit consisting of a linear inductance, a nonlinear resistance, and a voltage source²⁸, shown in Figure 1. The governing equation for this circuit is the Riccati equation

$$\frac{dy}{dt} + \alpha y + \varepsilon y^2 = x(t)$$

with $y(t)$ the current around the circuit, $x(t)$ the input voltage, and α and ε parameters from the nonlinear resistance. After discretization of the Riccati equation, the first-order kernel and several components of the second-order kernel, for this system, are generated using a time step of 0.01. A time lag (difference between τ_1 and τ_2) of $T = 0.01$ (or one time step) is used for computation of the components of the second-order kernel. The first component of the second-order kernel corresponds to $T=0.0$ with both impulses at same point in time; the second component corresponds to $T=0.01$ (one time step apart); the third component corresponds to $T=0.02$ (two time steps apart); and so on.

Two cases will be investigated. In the first, $\alpha = 1.0$ and $\varepsilon = 0.0001$; in the second, $\alpha = 0.1$ and $\varepsilon = 0.001$. The effect of these variations on the nonlinearity of the system and the resultant first- and second-order kernels is investigated. For this system, the constant term in Eq. (2) (h_0) is zero.

Case 1: $\alpha = 1.0, \varepsilon = 0.0001$

The first-order kernel for this case is presented in Figure 2 for 1000 time steps. Selected components for the corresponding second-order kernel are presented in Figure 3. Shown in Figure 3 are the first component, the one-hundred-and-first component, and so on. As can be seen, the largest component of the second-order kernel (the first) is very much (seven orders

of magnitude) smaller than the first-order kernel (Fig. 2) and goes to zero in about half the time. As might be expected with $\varepsilon = 0.0001$, Figure 3 indicates that nonlinear effects for this case are quite small. Verification of this is presented in Figure 4, a comparison of various step responses obtained directly from the numerical solution of the Riccati equation (actual) and those obtained from the convolution of the step inputs with the first-order kernel of Figure 2. These indistinguishable results indicate that the first-order kernel is sufficient to capture the response of this system for the range of amplitudes investigated.

Case 2: $\alpha = 0.1, \varepsilon = 0.001$

The first-order kernel for this case is presented in Figure 5, along with the first-order kernel from Case 1 (Fig. 2) for comparison purposes. The net effect of the change in the two parameters results in an increased effect of the nonlinearity of the Riccati equation. This is evidenced by the increased memory of the first-order kernel (slower approach to zero) as compared with the first-order kernel of Case 1. Selected components from the second-order kernel for this case are presented in Figure 6, revealing a kernel two orders of magnitude larger than the second-order kernel of Case 1 (Fig. 3). Figure 7 is a comparison of step responses obtained directly from numerical solution of the Riccati equation (actual) and those obtained via convolution of the step inputs with the first-order kernel of Figure 5 for this system. A noticeable difference between step responses, as step amplitude is increased, indicates the effect of increased nonlinearity in the system and the need for the second-order kernel.

The sign of the second-order kernel is important since it is an indication of the effect of the second-order nonlinearity on the total response of the system. That is, since the second-order kernel of Figure 6 is negative, then the effect of the second-order convolution, which provides the effect of the second-order kernel, is to decrease the magnitude of the total response of the system from that obtained from the first-order convolution alone. This is clear in Figure 7, which shows that the response due to the first-order term "overshoots" the actual response. Addition of the negative second-order response to the first-order response would cause the sum (both terms in Eq. (2)) to approach the actual response. The second-order kernel can therefore

provide an indication of the additive effect of the second-order nonlinearity with respect to the first-order term. The additional accuracy achieved, due to the inclusion of the second-order convolution, for the viscous Burger's equation has been demonstrated^{11,12} but is not presented here.

This example demonstrates the identification of first- and second-order kernels of a simple nonlinear system. Inspection of the kernels can provide very useful information regarding the level of nonlinearity as well as the net effect of the nonlinearity of a particular system. These techniques will now be applied to a CFL3D model.

RESULTS USING THE CFL3D CODE

The CFL3D code^{36,37} (version 5.0) solves the time-dependent, Reynolds-averaged Navier-Stokes equations in conservation law form. Upwind-biasing is used for the pressure and convective terms, central differencing is used for the shear stress and heat transfer terms, and the spatial discretization is based on a semi-discrete finite-volume concept. Accelerated convergence can be achieved using multigrid and mesh sequencing capabilities and implicit time-stepping is used. The code provides several turbulence models, including the Spalart-Allmaras turbulence model used in the subsequent analyses.

Results for RAE Airfoil

Navier-Stokes results for a dense-grid RAE 2822 airfoil³⁶ with the Spalart-Allmaras turbulence model undergoing plunge at a Mach number of 0.75, Reynold's number of 6.2 million, and a zero degree angle of attack were computed using a time step of 0.001. At this condition, this non-symmetric supercritical airfoil induces a net normal force coefficient of 0.2953. This corresponds to the h_0 term in Eq. (2). When generating the first- and second-order kernels for this system, h_0 has to be subtracted from the kernel computations. The response to a particular input is computed using the convolution procedures and then the h_0 ($= 0.2953$) term is added back to obtain the total response.

The CFL3D code has several computational options, depending on the type of analysis desired. Accelerated convergence can be obtained using the sub-iteration and multigrid capabilities³⁷. In addition, a method is available

that diagonalizes the governing matrices (diagonally dominant) based on the spectral radius. Limited experimentation with these techniques, including the effects of first-order-in-time versus second-order-in-time numerical accuracies are presented and discussed in Ref. 12. An optimal procedure for using multigrid and diagonalization to identify kernels has not yet been developed. As a result, the remainder of the results presented in this section are limited to solutions corresponding to second-order-in-time accuracy with no multigrid and no diagonalization.

These first- and second-order-in-time solutions refer to the numerical algorithm within CFL3D and should not be confused with first- and second-order kernel functions.

Recall that the first-order kernel is identified using a response due to a unit plunge amplitude and a second response due to double that amplitude. An important question is "What is the effect of varying these amplitudes on the identification of the kernels and on their predictive capability?" Figure 8 is a comparison of non-diagonalized, no-multigrid, second-order accurate-in-time first-order kernels for two different identification input plunge amplitudes. The small-amplitude kernel of Figure 8 was identified using the primary amplitude of 0.01 and a secondary (doubled) amplitude of 0.02. The large-amplitude kernel was identified using the primary amplitude of 0.1 and a secondary amplitude of 0.2. The correlation between these two first-order kernels (Fig. 8) is not linear, as expected. That is, one kernel is not exactly ten times the other, indicating a deviation from linearity or some measure of nonlinearity. Therefore, for small amplitudes (linear regime), the first-order kernel is identical to a linearized (small perturbation) impulse response. At larger amplitudes, however, the first-order kernel can capture a certain level of nonlinearity. It is important to note how quickly these first-order kernels reach equilibrium (go back to zero). This quick return to zero provides significant computational efficiency when extracting these functions from a CFD model, as will be seen.

The first five components of the second-order kernel for this airfoil in plunge are presented in Figure 9. The input amplitude used to identify these components of the second-order kernel was 0.10, consistent with the large-amplitude first-order kernel of Figure 8. Even so, the first component of the second-order kernel is an order

of magnitude smaller than the large-amplitude first-order kernel. The remaining components approach zero rather quickly, an indication that, for this condition and for this motion (plunge), the first-order kernel may be sufficient for predicting nonlinear plunge responses.

Figure 10 is a comparison of two nonlinear sinusoidal plunge responses from CFL3D and the convolved responses using the large-amplitude first-order kernel and including the addition of the h_0 term to the total response. The smaller, CFL3D response corresponds to a plunge amplitude of 0.01 (based on chord length). The larger CFL3D response corresponds to a plunge amplitude of 0.05. The reduced frequency of the plunging motions is 0.67. These results indicate that the first-order kernel can be used to accurately predict the nonlinear plunge responses of this CFL3D model over a wide range of amplitudes. Of great importance is the fact that the first-order kernel, which has a temporal duration of less than 20 time steps, can be used to predict the response of an input of arbitrary length (5000 time steps, in this case). This is due to the mathematical efficiency of convolution.

It is important to properly choose the amplitude used for identifying the first- and second-order kernels. One possible approach for determining this identification amplitude is to base it on 1) physical considerations and 2) code execution limitations. If the CFD code executes properly for the largest input amplitude of interest (a sinusoidal input, for example) and the input amplitude is physically realistic, then the accuracy and effectiveness of the first- and second-order kernels, identified within this amplitude range, will be nearly optimal assuming convergence issues are satisfied.

Computational Efficiency

The cost of each sinusoidal plunge response using CFL3D was about 2,000 CPU seconds and a turnaround time of about a day. These responses were for a particular frequency of motion that required a particular length of time for a certain number of cycles. A change in the input (frequency, for example) requires another execution of the CFL3D code. This translates into large (and expensive) turnaround times due to: 1) the time spent waiting for job execution in the queue of a supercomputer, for example, and 2) the time spent in actual execution of the code. The latter becomes even more expensive if

several cycles of a low-frequency response are desired.

On the other hand, the results presented in this paper show that the application of the Volterra theory to CFD codes reduces computational turnaround time significantly. This computational efficiency is achieved by virtue of the following: 1) the short duration of the first- and second-order kernels (see Figs. 8 and 9) and 2) the mathematical efficiency of convolution. The short duration of the kernels leads to very small turnaround times. In fact, the kernels presented here were generated using the debug queue of a Cray supercomputer. The debug queue is limited to no more than 300 time steps for the purpose of code debugging. The average turnaround time for the responses needed for computing the kernels was about five minutes. The computation of the first-order kernel, for the RAE airfoil using the CFL3D code, cost 400 CPU seconds; 200 for each of the two required responses (Eq. (3)). Once the kernels were identified, costly re-execution of the CFD code was side-stepped by applying convolution for every new input of interest. The cost of each convolution, for the plunge motions investigated, was 30 seconds per motion on a workstation.

CONCLUSIONS

Reduced-order aerodynamic models based on linear and nonlinear aerodynamic impulse responses have been discussed. The autonomous (time-invariant) nature of the Navier-Stokes equations was described in detail and the applicability of the Volterra theory of nonlinear systems to the Navier-Stokes equations was formally presented. The nature and computational efficiency of linear and nonlinear discrete-time convolution was described as well.

The method was applied first to a nonlinear circuit described by the Riccati equation and then, to a plunging airfoil using the CFL3D (Navier-Stokes) flow solver with the Spalart-Allmaras turbulence model. Results presented include the linear and nonlinear impulse responses for these systems as a function of several parameters. These parameters range from equation coefficients (Riccati circuit) to varying the amplitude of identification of the first-order kernels (CFL3D model).

The nonlinear impulse responses capture the nonlinear nature of the system under investigation. Computational cost comparisons were presented for the CFL3D/RAE 2822 model. It was shown that Volterra kernels provide significant computational efficiency over the full (and repetitive) solution of the complete system (CFL3D).

REFERENCES

- ¹Leishman, J.; and Crouse, G., "A State-Space Model of Unsteady Aerodynamics in a Compressible Flow for Flutter Analyses," AIAA Paper No. 89-0022, 27th Aerospace Sciences Meeting, January 9-12, 1989, Reno, Nevada.
- ²Nixon, D., "Alternative Methods for Modeling Unsteady Transonic Flows, Unsteady Transonic Aerodynamics, Vol. 120 of Progress in Astronautics and Aeronautics, Ed. by D. Nixon, AIAA, 1989.
- ³Reisenthel, P.H., "Development of a Nonlinear Indicial Model for Maneuvering Fighter Aircraft," AIAA Paper No. 96-0896, 34th Aerospace Sciences Meeting & Exhibit, January 15-18, 1996, Reno, Nevada.
- ⁴Marques, F.; and Anderson, J., "Modelling and Identification of Non-Linear Unsteady Aerodynamic Loads by Neural Networks and Genetic Algorithms," Proceedings of the 20th International Council of the Aeronautical Sciences, Sorrento, Italy, 8-13 September, 1996, Volume 1, ICAS-96-7.1.1, pp 243-251.
- ⁵Dowell, E.H.; Hall, K. C.; and Romanowski, M. C.: "Eigenmode Analysis in Unsteady Aerodynamics: Reduced Order Models," ASME Applied Mechanics Review, Volume 50, Number 6, June 1997, pp371-386.
- ⁶Baker, M.L., "Model Reduction of Large, Sparse, Discrete Time Systems with Application to Unsteady Aerodynamics," PhD Dissertation, University of California at Los Angeles, 1996.
- ⁷Stalford, H.; Baumann, W. T. ; Garrett, F. E. ; and Herdman, T. L. : "Accurate Modeling of Nonlinear Systems Using Volterra Series Submodels," Presented at the 1987 American Control Conference, Minneapolis, MN, June 10-12, 1987.
- ⁸Rodriguez, E.A., "Linear and Nonlinear Discrete-Time State-Space Modeling of Dynamic Systems for Control Applications," PhD Dissertation, Purdue University, December 1993.
- ⁹Silva, W.A., "Application of Nonlinear Systems Theory to Transonic Unsteady Aerodynamic Responses," *Journal of Aircraft*, Volume 30, Number 5, September-October 1993, pp. 660-668.
- ¹⁰Silva, W.A., "Extension of a Nonlinear Systems Theory to General-Frequency Unsteady Transonic Aerodynamic Responses," AIAA Paper No. 93-1590, Presented at the 34th Structures, Structural Dynamics, and Materials Conference, La Jolla, California, April 19-21, 1993.
- ¹¹Silva, W.A., "Identification of Linear and Nonlinear Aerodynamic Impulse Responses Using Digital Filter Techniques," AIAA Paper No. 97-3712, Presented at the AIAA Atmospheric Flight Mechanics Conference, August 11-13, 1997, New Orleans, LA.
- ¹²Silva, W. A., "Discrete-Time Linear and Nonlinear Aerodynamic Impulse Responses for Efficient CFD Analyses," PhD dissertation, College of William & Mary, December 1997.
- ¹³Khalil, H.K., Nonlinear Systems, Macmillan Publishing Company, New York, 1992.
- ¹⁴Bisplinghoff, R. L.; and Ashley, H., Principles of Aeroelasticity, Dover Publications, Inc., New York, 1975.
- ¹⁵Ku, Y. H.; and Su, C. C.: "Volterra Functional Analysis of Nonlinear Time-Varying Systems," *Journal of the Franklin Institute*, Volume 204, Number 6, December 1967.
- ¹⁶Volterra, V.: Theory of Functionals and of Integral and Integro-Differential Equations, Dover Publications, Inc., New York, 1959.
- ¹⁷Rugh, Wilson J. : Nonlinear System Theory, The Volterra-Wiener Approach, The Johns Hopkins University Press, 1981.

¹⁸Schetzen, Martin : The Volterra and Wiener Theories of Nonlinear Systems, John Wiley & Sons, 1980.

¹⁹Boyd, S.P.: "Volterra Series: Engineering Fundamentals," PhD Dissertation, University of California, Berkeley, 1985.

²⁰Wiener, N.: "Response of a Nonlinear Device to Noise," dissertation No. 129, Radiation Laboratory, M.I.T., Cambridge, Massachusetts, April 1942. (Also published as U.S. Department of Commerce Publications PB-58087.)

²¹Lee, Y.W.; and Schetzen, M.: "Measurement of the Wiener Kernels of a Non-linear System by Crosscorrelation," *International Journal of Control*, Volume 2(3), pp. 237-254, September 1965.

²²Flake, R. H., "Volterra Series Representation of Nonlinear Systems," Transactions of the American Institute of Electrical Engineers, Volume 81, 1962, Part II: Applications and Industry.

²³Ibrahim, R. A., "Response Analysis of Nonlinear Systems Using Functional-Perturbational Type Approach," 6th International Modal Analysis Conference, February 1-4, 1988, Kissimmee, FL.

²⁴Boyd, S. ; Chua, L. O. ; and Desoer, C. A. : Analytical Foundations of Volterra Series, *IMA Journal of Mathematical Control & Information*, 1984, Volume 1, pp. 243-282.

²⁵Brilliant, M. B.: "Theory of the Analysis of Nonlinear Systems," Technical dissertation 345, M.I.T. Research Laboratory of Electronics, March 1958.

²⁶Boyd, S. P.; and Chua, L. O.: "Fading Memory and the Problem of Approximating Nonlinear Operators with Volterra Series" *IEEE Transactions on Circuits and Systems*, Volume CAS-32, Number 11, November 1985.

²⁷Ku, Y. H.; and Wolf, A. A.: "Volterra-Wiener Functionals for the Analysis of Nonlinear Systems," *Journal of the Franklin Institute*, Volume 281, Number 1, January 1966.

²⁸Bedrosian, E.; and Rice, S. O.: "The Output Properties of Volterra Systems (Nonlinear Systems with Memory) Driven by Harmonic and Gaussian Inputs," *Proceedings of the IEEE*, Volume 59, Number 12, December 1971.

²⁹Sandberg, I. W.: "Nonlinear Input-Output Maps and Approximate Representations," *AT&T Technical Journal*, Volume 64, Number 8, October 1985, pp. 1967-1983.

³⁰Bendat, J. S., Nonlinear System Analysis & Identification from Random Data, A Wiley-Interscience Publication, 1990.

³¹Tryon, P. V., "The Bispectrum and Higher-Order Spectra: A Bibliography," National Bureau of Standards Technical Note 1036, April 1981.

³²Nikias, C. L.; and Petropulu, A. P., Higher-Order Spectra Analysis: A Nonlinear Signal Processing Framework, Prentice-Hall Signal Processing Series, Alan V. Oppenheim, Series Editor, 1993.

³³Boyd, Stephen ; Tang, Y. S. ; and Chua, Leon A. : "Measuring Volterra Kernels," *IEEE Transactions on Circuits and Systems*, Volume CAS-30, Number 8, August 1983.

³⁴Ritz, C. P.; and Powers, E. J., "Estimation of Nonlinear Transfer Functions for Fully Developed Turbulence," *Physica D 'Nonlinear Phenomena'*, May 1986, pp320-334.

³⁵Roberts, J. B., "Nonlinear Analysis of Slow Drift Oscillations of Moored Vessels in Random Seas," *Journal of Ship Research*, Volume 25, Number 2, June 1981, pp. 130-140.

³⁶Krist, S.L.; Biedron, R.T.; and Rumsey, C.L., "CFL3D User's Manual (Version 5.0)," November 1996, First Edition.

³⁷Rumsey, C. L.; Sanetrik, M. D.; Biedron, R. T.; Melson, N. D.; and Parlette, E. B., "Efficiency and Accuracy of Time-Accurate Turbulent Navier-Stokes Computations," AIAA Paper No. 95-1835, Presented at the 13th AIAA Applied Aerodynamics Conference, June 19-22, 1995, San Diego, CA.

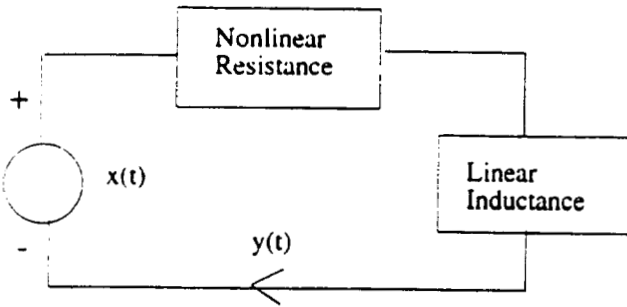


Fig 1 Simple nonlinear circuit defined by the Riccati equation with $x(t)$ (voltage) as input and $y(t)$ (current)

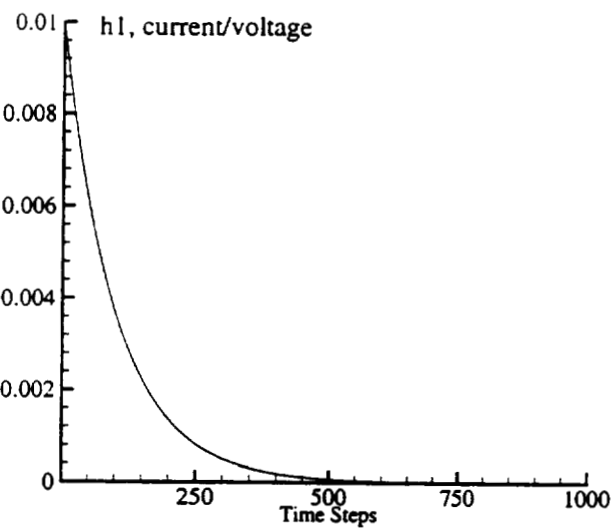


Fig 2 First-order kernel for the Riccati nonlinear circuit, Case 1.

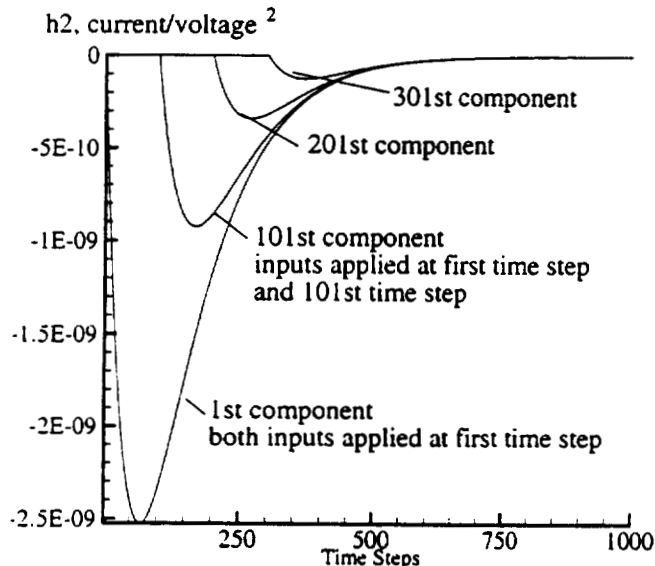


Fig 3 Selected components of the second-order kernel for the Riccati nonlinear circuit, Case 1.

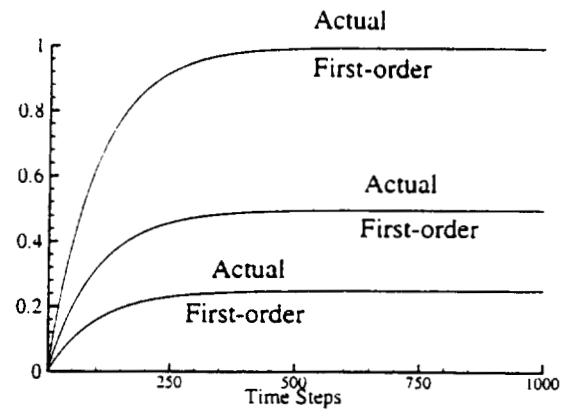


Fig 4 Comparison of actual and first-order step

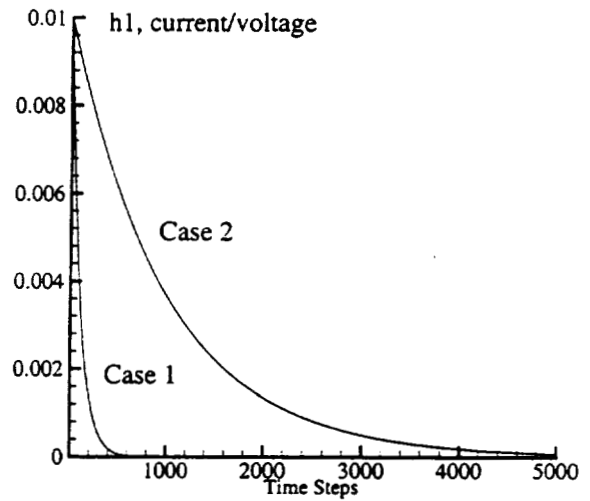


Fig 5 First-order kernels for Riccati nonlinear circuit, Case 1 and Case 2.

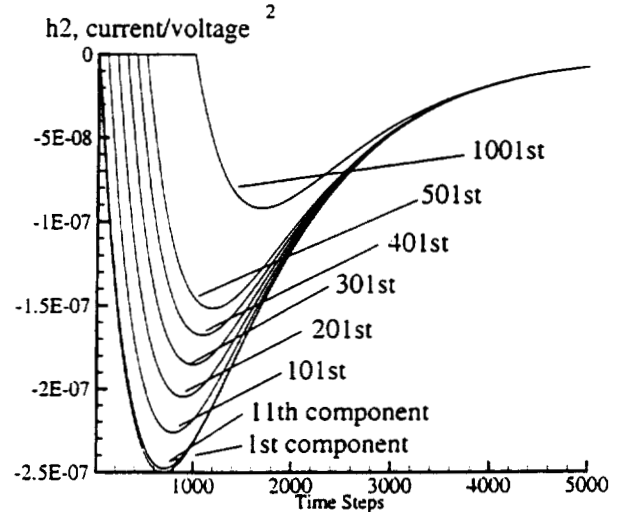


Fig 6 Selected components of the second-order kernel for the Riccati nonlinear circuit, Case 2.

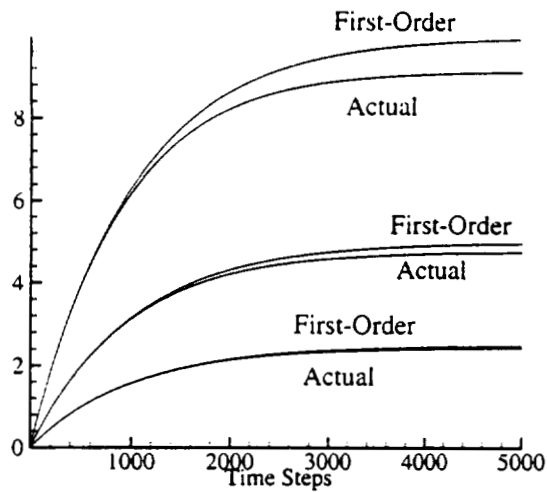


Fig 7 Comparison of actual and first-order step responses for the Riccati nonlinear circuit, Case 2.

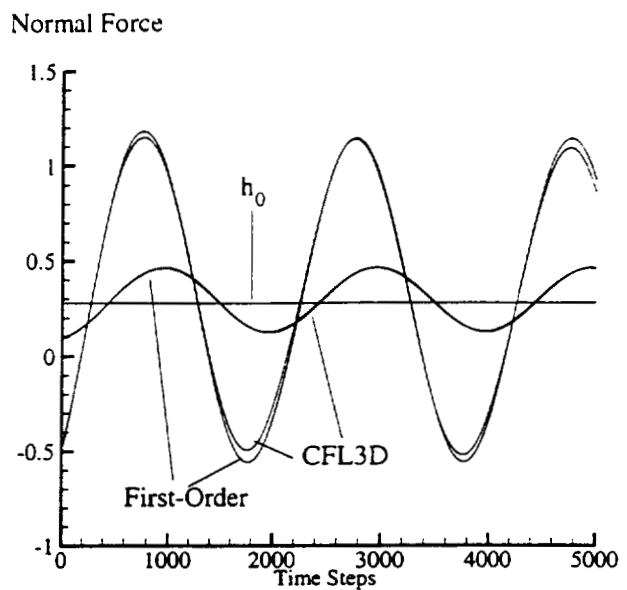


Fig 10 Comparison of CFL3D and first-order responses for two plunge amplitudes (0.01, 0.05).

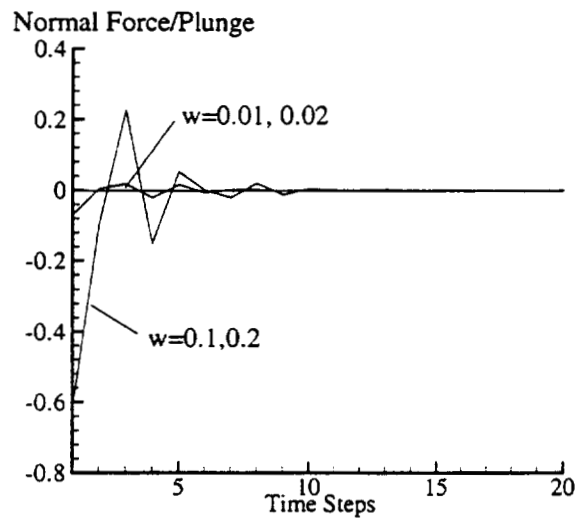


Fig 8 First-order kernels for RAE airfoil in plunge, effect of identification amplitudes.

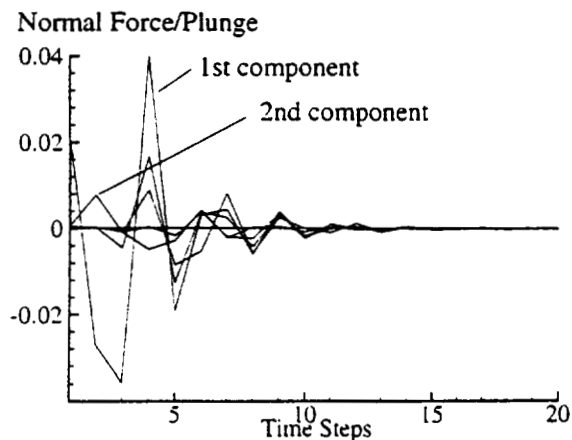


Fig 9 First five components of the second-order kernel for the RAE airfoil in plunge, largest ID amplitude.

1999066507

IFA 1999

TRANSONIC FLUTTER SUPPRESSION CONTROL LAW DESIGN, ANALYSIS AND WIND TUNNEL RESULTS

Vivek Mukhopadhyay
NASA Langley Research Center, Hampton, VA, USA

532-08
381334 P.12

Abstract

The benchmark active controls technology and wind tunnel test program at NASA Langley Research Center was started with the objective to investigate the nonlinear, unsteady aerodynamics and active flutter suppression of wings in transonic flow. The paper will present the flutter suppression control law design process, numerical nonlinear simulation and wind tunnel test results for the NACA 0012 benchmark active control wing model. The flutter suppression control law design processes using (1) classical, (2) linear quadratic Gaussian (LQG), and (3) minimax techniques are described. A unified general formulation and solution for the LQG and minimax approaches, based on the steady state differential game theory is presented. Design considerations for improving the control law robustness and digital implementation are outlined. It was shown that simple control laws when properly designed based on physical principles, can suppress flutter with limited control power even in the presence of transonic shocks and flow separation. In wind tunnel tests in air and heavy gas medium, the closed-loop flutter dynamic pressure was increased to the tunnel upper limit of 200 psf. The control law robustness and performance predictions were verified in highly nonlinear flow conditions, gain and phase perturbations, and spoiler deployment. A non-design plunge instability condition was also successfully suppressed.

Introduction

The benchmark active controls technology (BACT) and wind tunnel test program at NASA Langley Research Center was started with the objective to investigate the nonlinear, unsteady aerodynamics and active flutter suppression of wings in transonic flow. Under the initial wind tunnel test program, a NACA 0012 airfoil rectangular wing, equipped with pressure transducers, active trailing edge control surface, and two spoilers were constructed for active flutter suppression tests. The model was mounted on a pitch and plunge apparatus in the NASA Transonic Dynamics Tunnel in order to test flutter suppression control laws and measure unsteady pressure distributions in nonlinear flows with oscillating shocks and boundary layer separation. It was necessary to develop a flutter suppression system that would be stable under these flow uncertainties.

This paper describes flutter suppression control law design processes using classical and unified linear-quadratic Gaussian minimax techniques. A unified general formulation for the linear quadratic Gaussian and minimax methods based on the steady state differential game theory is presented. Lessons learned in evaluating and improving the singular value based multi-input multi-output system robustness are described. Design considerations for digital implementation are outlined. Numerical simulation of the control law performance, and wind-tunnel test results for flutter suppression, are also presented.

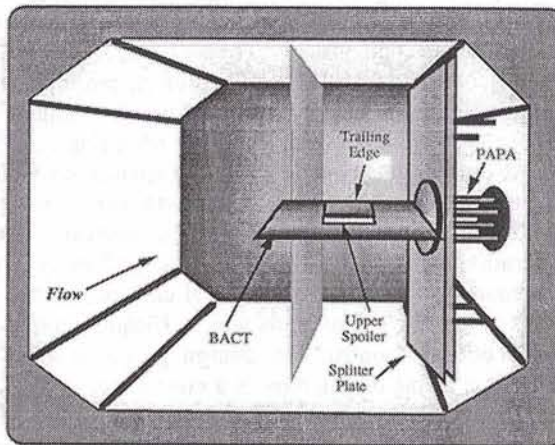


Fig. 1 BACT model test setup in wind tunnel

Wind Tunnel Model Description

A perspective view of the BACT model test set up on the Pitch and Plunge Apparatus (PAPA) in the wind tunnel is shown in Fig. 1. Fig. 2 shows the control surface and sensor locations. The rigid wing section has pitch and plunge degrees of freedom. The accelerometer sensors are located near the section leading edge (z_{le}) and trailing edge (z_{te}) at the section inboard. An identical pair of sensors is located at the section outboard as a spare. The partial span spoilers are located on the upper and lower surfaces, just ahead of the trailing edge control surface. Each of the control surfaces stretched over 30% of the span and 25% of the chord. The bending and torsion frequencies of the PAPA mounted NACA 0012 wing model were 3.3 Hz and 5.2 Hz respectively.

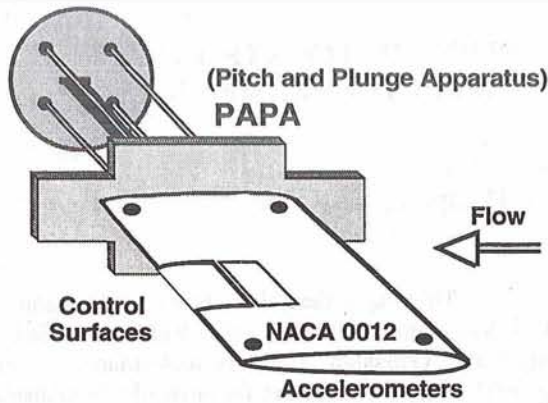


Fig. 2 NACA 0012 BACT wing on PAPA.

Preliminary Analysis

The preliminary analysis, control surface sizing, and flutter suppression control law design were based on the analytical state-space equations of motion of the BACT wing model.¹⁻⁴ These equations were developed analytically, using structural dynamic analysis and unsteady doublet lattice aerodynamics with rational polynomial approximations⁵. These linear state space equations consisted of 14 States (plunge, pitch, plunge rate, pitch rate, 3 aerodynamic states for plunge, 3 aerodynamic states for pitch, 2 trailing edge flap actuator states, 2 Dryden gust states), 2 inputs (actuator command and gust input noise) and 7 outputs (z_{te} and z_{le} acceleration, flap command, flap deflection, rate, acceleration, and gust velocity). This 14th order state space equation was used for classical control law design and for performance simulation and verification purposes. For the optimal control law design purposes and for presentation of the design data in a concise form, the 14th order state-space equations were reduced to 4th state-space equations, using residualization and Schur's balanced reduction method^{6,7}. First, it was reduced to an 8th order system using residualization technique, in which only the static part of all modes above 15 Hz were retained. The resulting 8th order system was then balanced and the four states of the system with largest balanced singular values were retained. A sample of the 4th order model design data is presented in the Appendix.

Open-loop Responses

The analytical open-loop flutter dynamic pressure in air was 128 pounds per square feet (psf) at a flutter frequency of 4.5 Hz. Fig. 3 shows the response of the wing trailing edge and leading edge accelerometers due to a 1 degree step input of the trailing edge control surface in air at 225 psf dynamic pressure. The primary plunge motion mixed with small pitch diverges rapidly. The unsteady lift forces oscillate about 8 lbs mean lift and

diverges at the rate of 6 lbs/sec. The moment diverges at a rate of 1 lb/sec.

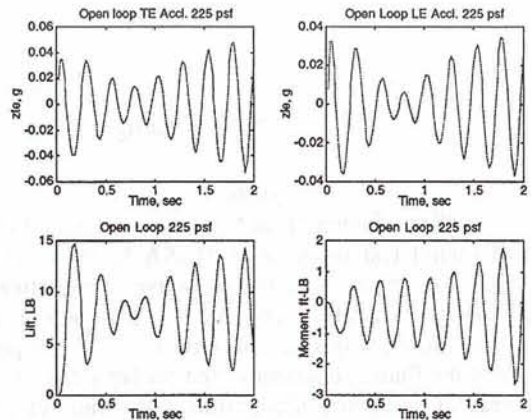


Fig. 3 Open loop transient responses in air at 225 psf.

Frequency Responses

The open loop frequency responses were studied using this 14th order plant model, to select a possible candidate for feedback signal in the flutter suppression control law design. The Bode diagram of the trailing edge and leading edge accelerometers (z_{te}) and (z_{le}) and their difference ($z_{te} - z_{le}$) due to the trailing edge control surface excitation (δ_{te}) in air at 225 psf at Mach 0.5, are shown in Fig. 4. The magnitude plots indicate predominant plunge response at 3.3 Hz excitation frequency. At 4.2 Hz excitation, the motion is a combination of pitch and plunge with pitch motion leading the plunge. The ($z_{te} - z_{le}$) represents a signal proportional to the pitch acceleration and can be integrated to provide a pitch-rate signal. Feedback of this signal with proper gain can provide maximum pitch damping at the flutter frequency.

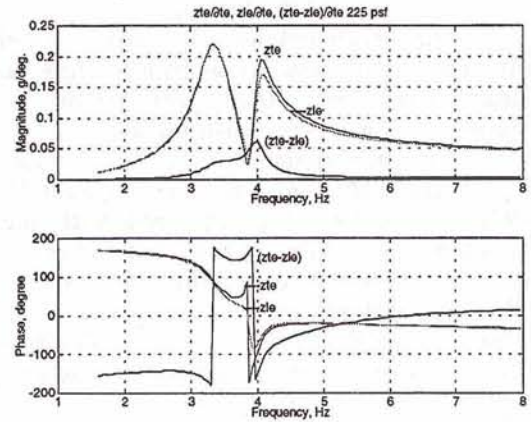


Fig. 4 The Bode diagrams of z_{te} and z_{le} and $(z_{te} - z_{le})$ due to δ_{te} excitation in air at 225 psf, Mach 0.5.

Classical Control Law Design

Based on this Bode plot, a classical flutter suppression scheme using pitch-rate proportional feedback from the zte and zle accelerometers was first devised by studying the Nyquist diagrams. The Nyquist diagram of the difference between trailing edge and leading edge accelerometers ($z_{te} - z_{le}$) due to the trailing edge control surface excitation (δ_{te}) in air at 200 psf, is shown in Fig. 5(a). The arrow indicates increasing frequency of excitation from 2 Hz to 6 Hz, with each * representing frequency increment of 1 radian/second. Since the open-loop plant had a pair of complex unstable poles, and the Nyquist contour did not encircle the -1 point, the unit feedback closed loop system would be unstable. However, if the ($z_{te} - z_{le}$) signal was integrated to provide a 90 degree phase lag and then used for feedback with sufficient gain, the Nyquist contour would rotate 90 degrees clockwise and then expand to encircle the -1 point to achieve stability. A washout filter of type $s/(s + \alpha)$ was also required, to remove any static bias that would otherwise be amplified by the integration. The series connection of integrator $1/s$ and washout filter was equivalent to a first order lag filter $\alpha/(s + \alpha)$, where s is the Laplace operator.

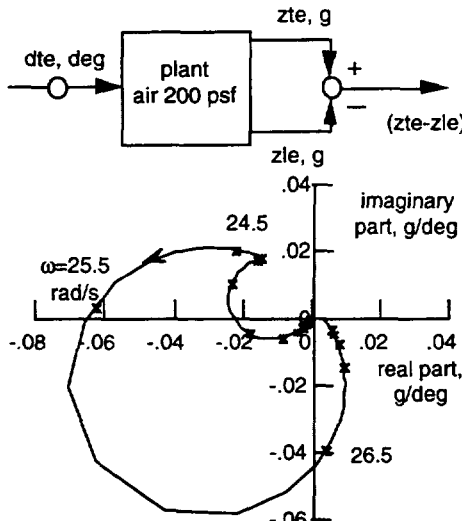


Fig. 5(a) Nyquist diagram of ($z_{te} - z_{le}$) due to δ_{te} excitation in air at 200 psf, Mach 0.5

Gain Selection

Two types of lag filters, namely $5/(s + 5)$ and $10/(s + 10)$ were examined. The latter was selected to achieve a higher phase margin at the plant input above the flutter frequency. Higher phase margin was desirable for two reasons⁷. First, the 25 Hz antialiasing filter and the 1/200 seconds computational delay contribute about 20 degrees of phase lag at the flutter frequency. Secondly, with increasing dynamic pressure, the actuators may have additional unknown phase lag, as the control surface

moves against higher aerodynamic loads. The Nyquist diagram of the difference between trailing edge and leading edge accelerometers ($z_{te} - z_{le}$) with $10/(s + 10)$ lag filter and a gain $KR = 500$ due to the trailing edge control surface excitation (δ_{te}) in air at 200 psf, Mach 0.5, is shown in Fig. 5(b). The unit circle is also shown. Because the Nyquist contour encircled the -1 point, the unit feedback closed loop system would be stable. As desired, the phase margin at the plant input above the flutter frequency was about 60 degrees, but the phase margin below the flutter frequency was only 20 degrees. Preliminary analysis indicated that this basic simple control law 1

$$\delta_{te} = 500 \frac{10}{s+10} (z_{te} - z_{le})$$

can suppress the flutter instability in the dynamic pressure range from 0 to over 225 psf, both in air and in heavy gas medium. However, the closed loop transient responses and stability margins required substantial improvement.

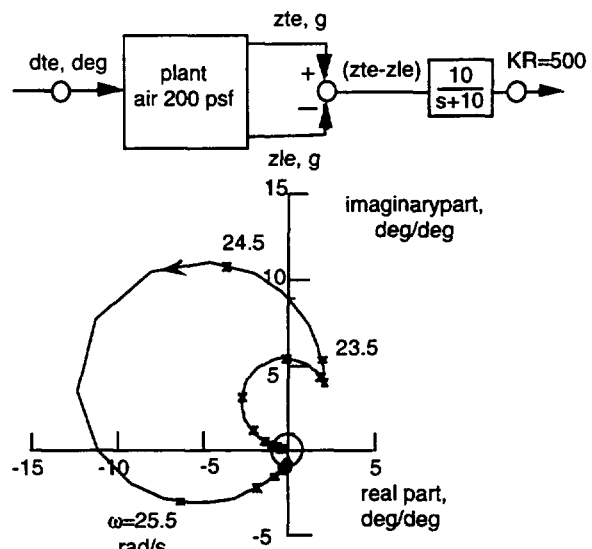


Fig. 5(b) Nyquist diagram of ($z_{te} - z_{le}$) with $10/(s+10)$ lag filter and a gain $KR = 500$, due to δ_{te} excitation in air at 200 psf, Mach 0.5.

Root Locus

Analysis of the root locus with pitch acceleration ($z_{te} - z_{le}$) feedback through a $10/(s + 10)$ lag filter with increasing gain $KR = 0, 500, \dots, 2500$ is shown in Fig. 6(a). The stabilization was achieved by increasing the pitch model damping and lowering the plunge mode frequency. An additional feedback of the pitch rate proportional signal through a $5/(s + 5)$ lag filter with $KR = 500$ and increasing gain $KP = 0, 500, \dots, 2500$ was used to increase the damping and frequency separation further, as indicated by the root-locus diagram shown in Fig. 6(b).

This design strategy was equivalent to pitch-angle and pitch-rate proportional feedback that increased the pitch mode frequency and plunge mode damping.

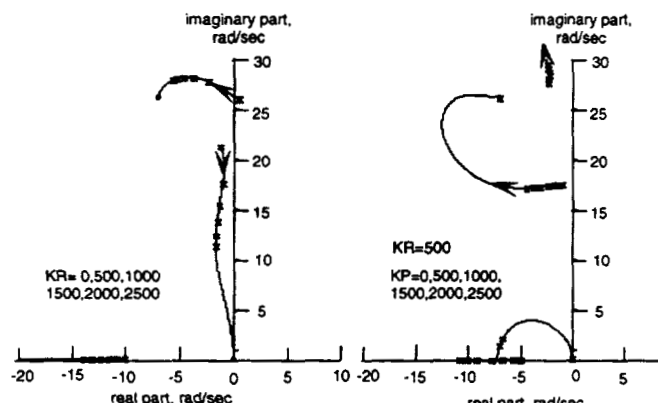


Fig. 6(a) Root-locus with $(zte - zle)$ feedback through a $10/(s + 10)$ lag filter, with increasing gain KR (at left). 6(b) Root-locus with additional pitch-rate feedback through a $5/(s + 5)$ lag filter with $KR = 500$ and increasing gain KP . The arrows indicate increasing gain.

Pitch and Pitch-Rate Feedback Control Law

From the root-locus study, the feedback gains were selected as $KR = 500$ and $KP = 1$. Thus, the second order state space equations of the initial pitch and pitch-rate feedback control law 2 is given by

$$\begin{cases} \dot{x}_1 \\ \dot{x}_2 \end{cases} = \begin{bmatrix} -10 & 0 \\ 5 & -5 \end{bmatrix} \begin{cases} x_1 \\ x_2 \end{cases} + \begin{bmatrix} 10 & -10 \\ 0 & 0 \end{bmatrix} \begin{cases} \ddot{z}_{te} \\ \ddot{z}_{le} \end{cases}$$

$$\delta_{te} = [500 \quad 1] \begin{cases} x_1 \\ x_2 \end{cases}.$$

The control law inputs are z_{te} and z_{le} in g unit and the output δ_{te} is in degrees. The high feedback gain was required because the maximum $(z_{te} - z_{le})$ signal was only of the order 0.1 g/deg. The response exhibited 2% settling time in 1.5 seconds. However, the high gain resulted in a severe sensitivity with respect to plant perturbation and individual sensor uncertainty, as indicated by the corresponding singular value plots in Fig. 7. Here G , K and Δ denote plant, controller and uncertainty block, respectively^{8,9}. This figure indicates that the minimum singular value $\underline{\sigma}(I+KG)$ is 0.3 at plant input and $\underline{\sigma}(I+GK)$ is only 0.01 at plant output. This means that at 225 psf dynamic pressure, the closed-loop system has very little robustness to multiplicative perturbation^{8,9} at the plant output.

These singular value $\underline{\sigma}$ plots can be related to multivariable gain and phase margins using the universal gain and phase margin diagram⁸ shown in Fig. 8. For example, minimum singular value $\underline{\sigma}(I+KG)$ of 0.3 is

equivalent to ± 20 degrees phase and ± 3 dB gain margins at the plant inputs. The singular value $1/\underline{\sigma}(K(I+GK)^{-1})$ is close to 0.005 g/degrees near 2 Hz. This means that the plant has very little tolerance to an additive perturbation Δ to the plant. The complex determinant locus of $(I+KG)$ and its distance from the origin is a measure of its closeness to singularity.

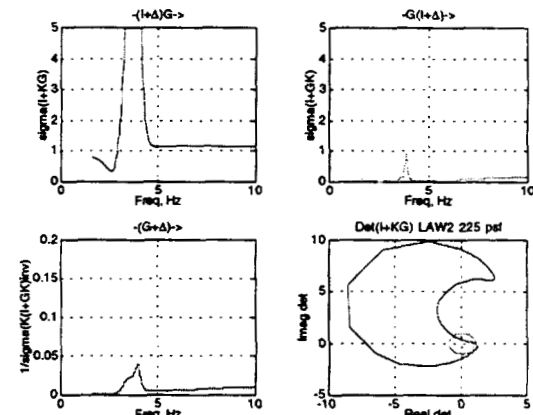


Fig. 7 Singular value plots for analysis of multivariable stability margins to a perturbation Δ , at the plant input or output, with classical control law 2, at 225 psf, in air.

$\underline{\sigma}$ Minimum singular value

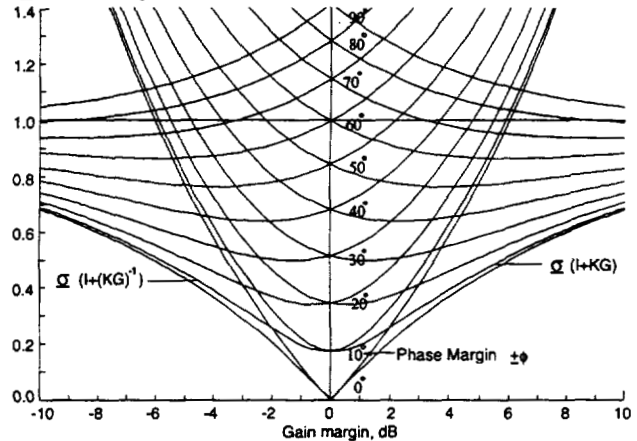


Fig. 8 Universal gain and phase margin analysis diagram.

Final Pitch and Pitch-Rate Feedback Control Law

This lack of robustness associated with this pitch and pitch rate feedback control law was alleviated by choosing a feedback of a proper linear combination of the two sensors with lower gains for KR , instead of using the difference $(z_{te} - z_{le})$. The linear combination of z_{te} and z_{le} , which is equivalent to feeding back both pitch acceleration $(z_{te} - z_{le})$ and plunge acceleration $(z_{te} + z_{le})$ in the ratio $0.7(z_{te} - z_{le}) + 0.3(z_{te} + z_{le})$, appeared to provide a superior control law. The final classical feedback control law, using this combination that is equivalent to $(z_{te} - 0.4 z_{le})$ feedback, along with reduced

gains of $KR = 50$ and $KP = 1$, was analyzed and implemented. The basic control is shown here in state-space form and is denoted by classical control law 3.

$$\begin{cases} \dot{x}_1 \\ \dot{x}_2 \end{cases} = \begin{bmatrix} -10 & 0 \\ 5 & -5 \end{bmatrix} \begin{cases} x_1 \\ x_2 \end{cases} + \begin{bmatrix} 10 & -4 \\ 0 & 0 \end{bmatrix} \begin{cases} \ddot{z}_{te} \\ \ddot{z}_{le} \end{cases}$$

$$\{\delta_{te}\} = [50 \quad 1] \begin{cases} x_1 \\ x_2 \end{cases}$$

Response and Robustness Analysis

The closed-loop transient responses due to 1 degree step deflection of δ_{te} , in air at 225 psf, at Mach 0.5, is shown in Fig. 9. The trailing edge control surface shows only 0.25 degrees overshoot with a maximum rate of 12 degrees/sec. The lift and moment forces indicate about 20% load alleviation compared to the open-loop initial transient values shown in Fig. 3. Figure 10 shows the singular-value plots for analyzing the system stability margins^{8,9} with law 3 at 225 psf dynamic pressure. Here G , K and Δ denote plant, controller and uncertainty block transfer function, respectively. This figure indicates that the minimum singular value $\sigma(I+KG)$ is increased to 0.8 at plant input and at plant output $\sigma(I+GK)$ is increased to 0.3 from the corresponding values with law 2 presented in Fig. 7. The minimum singular value $\sigma(I+KG)$ of 0.8 is equivalent to ± 45 degrees phase and -5 dB to 12 dB gain margins at the plant inputs. These gain and phase margins are determined from Fig. 8 as previously described. The minimum singular value $1/\sigma[K(I+GK)^{-1}]$ is also increased from 0.005 g/degree to 0.04 g/degree near flutter frequency, thus increasing the plant's tolerance to additive plant perturbation. The complex determinant loci of $(I+KG)$ ideally should be outside the unit circle to achieve ± 6 dB gain margins and ± 60 degrees phase margins. The computational delay and antialiasing filters added 20 degrees phase lag. Hence, the system nearly attained these margins. The singular value plots indicate that the system is stable with adequate singular value based multivariable stability margins even at this high design dynamic pressure of 225 psf. This pressure is 97 psf above the open-loop flutter dynamic pressure $q_{\text{flutter}} = 128$ psf, representing a 75% increase.

Unified Optimal Design

Flutter suppression control law design using an unified (1) linear quadratic Gaussian (LQG) and (2) Minimax method^{10,11} is presented next. The Minimax approach is analogous to the time domain H-infinity design¹² and is based on the steady state differential game formulation. The unified formulation of these optimal design techniques provide a basic understanding of the relation between them. The derivation from basic principles using variational principles are provided. The

solution only requires an eigen-solver. The corresponding Matlab script is presented in the Appendix.

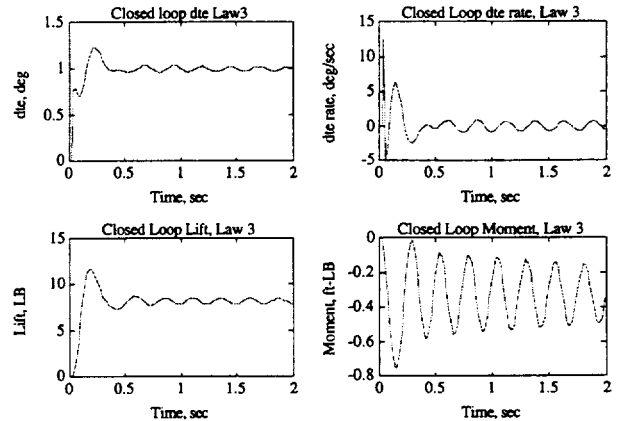


Fig. 9 Closed-loop responses: control surface deflection and rate, lift and pitching moment, due to step input δ_{te} with control law 3, at 225 psf, in air, at Mach 0.5 (open loop $q_{\text{flutter}} = 128$ psf).

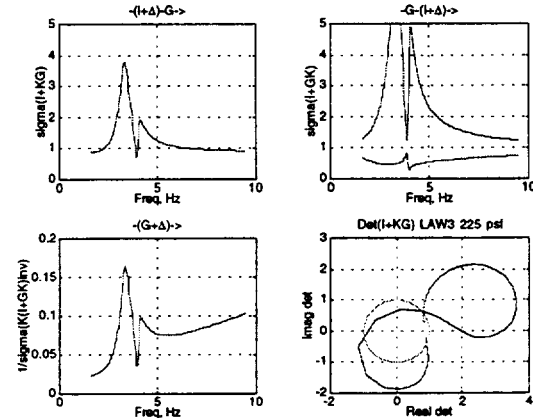


Fig. 10 Singular value plots for analysis of multivariable stability margins to perturbation Δ , with classical control law 3, at 225 psf, in air.

Unified Minimax Formulation

Consider the state space Eqs.(1-3) representing the n th order plant, control input $u(t)$, disturbance $w(t)$, design output y_d and sensor output y_s , where all necessary rank, controllability and observability conditions are assumed to be satisfied.

Plant state-space equations

$$dx(t)/dt = F x(t) + G u(t) + G_w w(t) \quad (1)$$

and $x(0) = x_0$

Design output

$$y_d(t) = H_d x(t) + E_d u(t) \quad (2)$$

Sensor output

$$y_s(t) = H_s x(t) + E_s w(t) \quad (3)$$

State-Feedback Minimax Regulator Problem

The Minimax problem is to determine the plant input $u(t)$ which would minimize the quadratic performance index J , and find the worst plant disturbance $w(t)$ and initial condition x_0 , which would maximize J defined in Eq. (4),

$$J = \frac{1}{2} \int_0^{\infty} (x^T Q_x x + x^T Q_{xu} u + u^T Q_u u) dt \quad (4)$$

subject to the constraint Eq.(1) with $x_0^T x_0 = I$ and specified W defined by,

$$W = \frac{1}{2} \int_0^{\infty} (w^T R_w w) dt \quad (5)$$

Usually, the constant weighting matrices Q_x , Q_u are unity, and $Q_{xu} = [0]$ in a H-infinity exposition. These are included herein to derive a unified general time-domain formulation. The cross weighting matrix Q_{xu} originates if one uses y_d from Eq. (2) in the performance index J to replace x . Then, $Q_x = H_d^T Q_{yd} H_d$, $Q_{xu} = H_d^T Q_{yd} E_{du}$, and Q_u is replaced by $[Q_u + E_{du}^T Q_{yd} E_{du}]$. The significance of the cross weighting matrix Q_{xu} and how it can be selected for pole-placement of the state regulator will be shown later in the state-feedback regulator subsection.

The minimax solution is given by the stationary condition of the augmented performance index J

$$\begin{aligned} J = & \frac{1}{2} \int_0^{\infty} (x^T Q_x x + 2x^T Q_{xu} u + u^T Q_u u - \gamma^2 w^T R_w w) dt \\ & + \lambda^T \int_0^{\infty} (Fx + Gu + G_w w - \frac{dx}{dt}) dt + \gamma^2 W \end{aligned} \quad (6)$$

where, γ is a scalar parameter. Using the calculus of variation with respect to $x(t)$, $u(t)$, $w(t)$ and the vector Lagrange multiplier $\lambda(t)$, the conditions for $\partial J = 0$ are given by Eq.(1) and Eqs. (7) to (9).

$$\frac{d\lambda}{dt} = -Q_x x - F^T \lambda - Q_{xu} u \quad (7)$$

$$Q_u u = -G^T \lambda - Q_{xu}^T x \quad (8)$$

$$\gamma^2 R_w w = G_w^T \lambda \quad (9)$$

Solving for $u(t)$ and $w(t)$ from Eqs. (8-9) and substituting them in Eqs. (1) and (7), the necessary stationary conditions for J are obtained as,

$$u = -Q_u^{-1} (G^T \lambda + Q_{xu}^T x) \quad (10)$$

$$w = \gamma^2 R_w^{-1} G_w^T \lambda \quad (11)$$

$$\begin{cases} \frac{dx}{dt} \\ \frac{d\lambda}{dt} \end{cases} = \begin{bmatrix} (F - GQ_u^{-1}Q_{xu}^T) & (-GQ_u^{-1}G^T + \gamma^{-2}G_wR_w^{-1}G_w^T) \\ -(Q_x + Q_{xu}Q_u^{-1}Q_{xu}^T) & -(F - GQ_u^{-1}Q_{xu}^T)^T \end{bmatrix} \begin{cases} x(t) \\ \lambda(t) \end{cases}$$

with $x(0) = x_0$ and $\lambda(\infty) = 0$ (12)

State-Feedback Regulator

Substituting $\lambda(t) = S(t)x(t)$, in Eqs.(10-12), leads to Eqs.(13-15). The general Riccati Equation (15) is then solved for the unknown n by n matrix S .

$$u(t) = -Q_u^{-1} (G^T S + Q_{xu}^T) x(t) \quad (13)$$

$$w(t) = \gamma^2 R_w^{-1} G_w^T S x(t) \quad (14)$$

$$\begin{aligned} dS/dt + SF + F^T S + Q_x - (SG + Q_{xu})Q_u^{-1}(SG + Q_{xu})^T \\ + S(\gamma^2 G_w R_w^{-1} G_w^T)S = 0 \end{aligned} \quad (15)$$

The positive definite symmetric solution for S is obtained from the $(2n \times n)$ eigenvectors of the n stable eigenvalues of the Hamiltonian matrix inside the square bracket [] in Eq.(12). For the steady state problem (i.e. $dS/dt = 0$), only the steady part of the Riccati Equation (15) is solved in order to obtain the symmetric positive-definite matrix S . If the eigenvectors are partitioned into two $n \times n$ matrices X and $\underline{\Lambda}$ which represent the stable subspace eigenvectors of x and λ , then $S = X^{-1} \underline{\Lambda}$. The constant optimal feedback gains, C_o and C_w , and the closed-loop system matrix are given by,

$$C_o = -Q_u^{-1} (G^T S + Q_{xu}^T) \quad (16)$$

$$C_w = \gamma^2 R_w^{-1} G_w^T S \quad (17)$$

$$dx/dt = [F + G_w C_w + G C_o]x. \quad (18)$$

Using Eqs.(1),(15) and (18), it can be shown¹¹ that optimal J and W defined in Eqs.(4) and (5) are given by,

$$J = 0.5 \text{ Trace } [S] \quad (19)$$

$$W = 0.5 \text{ Trace } [C_w^T R_w C_w X]. \quad (20)$$

where X is the solution of the Lyapunov Equation (21)

$$\begin{aligned} & [F + G_w C_w + G C_o] X + X[F + G_w C_w + G C_o]^T + \\ & x(0)x(0)^T = [0] \end{aligned} \quad (21)$$

The worst $x(0)$ that maximizes J is given by the eigenvector of the maximum eigenvalue of S . The

standard linear quadratic regulator (LQR) solution is obtained when $\gamma = \infty$, (i.e. $C_w = 0$). As γ^2 is decreased, the worst response due to the disturbance $w(t)$, measured by the maximum singular value of $[x^T Q_x^{1/2} \ u^T Q_u^{1/2}]$, is reduced. The minimum value of γ^2 for which a stable solution of Eq. (15) exists provides the minimax state-feedback regulator that minimizes the maximum singular value of $[x^T Q_x^{1/2} \ u^T Q_u^{1/2}]$.

The State-Estimator Equation

The derivation of coupled state-estimator equations using linear quadratic minimax approach is still a subject of research. Here the equivalent state-space solutions¹² of the H-infinity problem are presented. The state estimator gain $B_o D_o$ is obtained by finding the symmetric positive definite solution for P from the state estimator Riccati Eq. (24) which is dual to the state regulator Riccati Eq. (15).

$$B_o = -(P H_s^T + R_{wv}) R_v^{-1} \quad (22)$$

$$D_o = (I - \gamma^2 P S)^{-1}, \quad \rho(PS) < \gamma^2 \quad (23)$$

$$\begin{aligned} dP/dt &= P F^T + F P + G_w R_w G_w^T - (P H_s^T + R_{wv}) R_v^{-1} \\ &\quad (P H_s^T + R_{wv})^T + P(\gamma^2 Q_x) P \end{aligned} \quad (24)$$

where $R_v = E_{sw} R_w E_{sw}^T$ and must be positive definite and $R_{wv} = G_w R_w E_{sw}^T$. In Eq. (23) the spectrum $\rho(PS)$ must be less than γ^2 for D_o to exist. The positive definite symmetric steady-state solution for P in Eq. (24) is obtained from the $(2n \times n)$ eigenvectors of the n stable eigenvalues of the estimator Hamiltonian matrix,

$$\begin{bmatrix} (F - R_{wv} R_v^{-1} H_2)^T & (-H_2^T R_v^{-1} H_2 + \gamma^{-2} H_1^T Q_y^{-1} H_1) \\ -G_w R_w G_w^T - R_{wv} R_v^{-1} R_{wv}^T & -(F - R_{wv} R_v^{-1} H_2) \end{bmatrix} \quad (25)$$

which is dual to the state regulator Hamiltonian matrix inside [] in Eq.(12). If the eigenvectors are partitioned into two $(n \times n)$ matrices X and $\underline{\Lambda}$, then $P = X^{-1} \underline{\Lambda}$. The state estimate vector z is given by the Eq. (26).

$$dz/dt = F z + G_w w + G u + D_o B_o (H_2 z - y_2) \quad (26)$$

The complete duality relations between the state regulator problem and the state estimator problem are presented in Table 1.

<u>state regulator</u>	<u>state estimator</u>
F	F^T
G	H_s^T

G_w	H_d^T
Q_x	$G_w R_w G_w^T$
Q_u	R_v
S	P
Q_{xu}	R_{wv}
$(t_f - t)$	$(t - t_0)$

Table 1. Duality relations between linear quadratic state-regulator and state-estimator equations.

The Controller Equation

Substituting Eqs. (13), (14), (22) and (23) in Eq. (26), the state-estimation feedback controller equations

$$dz/dt = [F + G_w K_w + G C_o + D_o B_o H_s] z - D_o B_o y_s \quad (27)$$

$$u = C_o z \quad (28)$$

are obtained. The standard LQG solution is obtained when $\gamma = \infty$. The minimum value of γ^2 for which a stable solution exists for P in Eqs. (22-24), provides the minimax control law that minimizes the maximum singular value of the matrix $[y_s^T Q_{ys}^{1/2} \ u^T Q_u^{1/2}]$, for the closed loop system.

Unified Design Procedure

In this design, the output y_d was chosen to be the linear combination of the trailing edge and leading edge accelerometer output ($z_{te} - 0.4 z_{le}$), same as that used in the final classical design. One advantage of this choice was that the plant had no transmission zeros in the open right half plane. Usually in a frequency domain H-infinity design, the plant equations are augmented with weighting transfer functions. In this time domain formulation, the weights were chosen as constants. These weighting constants are chosen as inverse of the desired magnitude of the weighted quantities. The initial controller was designed with a large value of γ^2 , using the plant Eqs. (1-3), at 225 psf, in air, at Mach 0.5, assuming $G_w = G$. The block diagram for this unified design procedure is shown in Figure 11. The detailed design steps are described next.

State-feedback Regulator Design

Initially, the maximum output of the accelerometer sensors were of the order $0.1g$, (see figure 3), and control surface maximum root-mean-square deflection was desired to be of the order 1 degrees. Thus, the initial values of the weighting matrices were chosen as follows: $Q_x = [H_s^T Q_{ys} H_s]$, $Q_{ys} = [100]$, and $Q_u = [1]$. It was interesting to note that, instead of setting the cross weighting matrix $Q_{xu} = [0]$ as usual practice, the cross weighting matrix Q_{xu} can be selected to place all state

regulator poles beyond a certain distance α to the left of imaginary axis. This selection is accomplished by using

$$Q_{xu} = -\alpha G_u (G_u^T G_u)^{-1} Q_u \quad (29)$$

so that in Eq. (12), the eigenvalues of the diagonal matrix block F are off-set by

$$G Q_u^{-1} Q_{xu}^T = -\alpha I. \quad (30)$$

The control-weighting matrix Q_u was subsequently reduced to 0.01 after a few design cycles to improve the regulator performance. This process of reducing Q_u is equivalent to the state estimator loop-transfer recovery technique at the plant output.

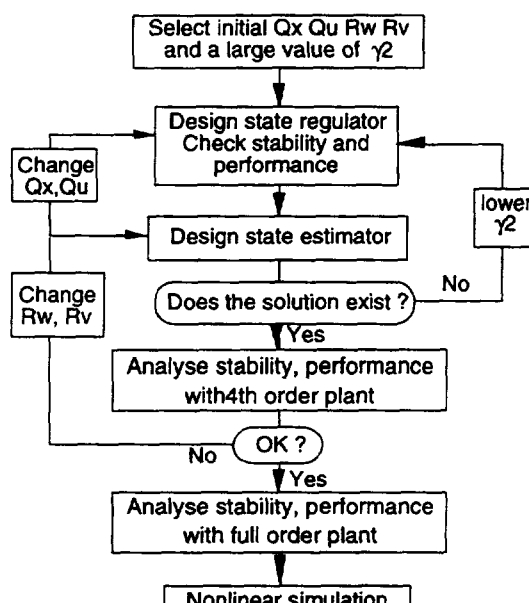


Fig. 11. Unified minimax control law design and evaluation procedure block diagram.

State-estimator Design

The state estimator was designed as a dual to the state-regulator with $R_w = I$, each diagonal elements of $R_v = 0.01$, and $R_{vv} = [0]$. After a few design cycles the performance of the combined full-order controller was examined, and then R_w was increased to 36. Since we also choose $G_w = G$, this was equivalent to asymptotic state-regulator loop-transfer recovery at the plant input.

4th Order Optimal Control law

Subsequent solutions to the state-regulator and state-estimator were obtained with the same choice of weighting matrices but for decreasing value of γ^2 , for which positive definite solutions for S and P could be obtained. Note that feasible solutions can be obtained for

lower values of γ^2 up to $\gamma^2 > p/PS$, below which the disturbance authority exceeded the control authority. The 4th-order optimal control law was designed with $\gamma^2 = 50$ in order to obtain a low bandwidth controller. Fig. 12 shows the key singular value plots for analysis of multivariable stability margins to multiplicative and additive perturbation Δ at the plant input and output, with this minimax optimal control law, denoted as control law 4. The minimum singular value $\sigma(I+KG)$ is increased to 0.9 at plant input and at plant output $\sigma(I+GK)$ is increased to 0.5 from the corresponding values of 0.8 and 0.3 for control law 3, shown in Fig. 10.

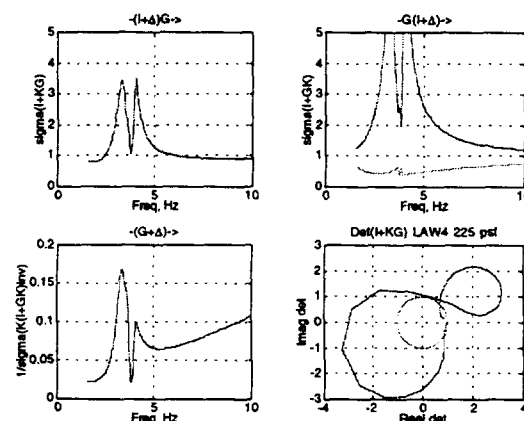


Fig. 12 Singular value plots for analysis of multivariable stability margins with minimax optimal control law 4, at 225 psf, in air.

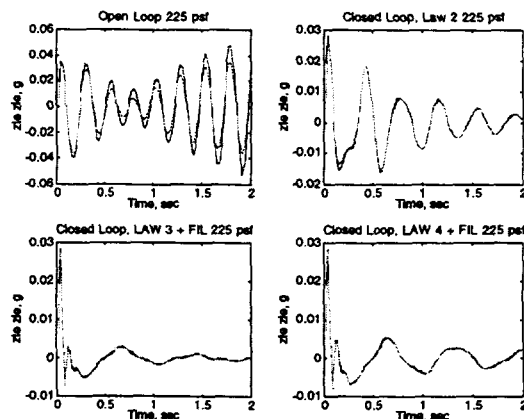


Fig. 13 Open-loop and closed-loop responses due to step input δ_{te} , with classical control laws 2, and 3, and minimax optimal control law 4, at 225 psf, in air.

Fig. 13 shows the open-loop and closed-loop responses due to unit step input δ_{te} of trailing edge control surface, at 225 psf, in air, at Mach 0.5, with initial control law 2, classical control law 3, and minimax optimal control law 4. The transient responses indicate

that the classical control law 3 provided better damping with lower control surface activity although the minimax control law 4 provided better robustness properties. This is the traditional trade-off between performance and robustness. The classical control law 3 was implemented and tested in wind tunnel. These test results along with those using two optimal control laws designed by Waszak¹³ are presented next.

Flutter Suppression Test Results

The performance and robustness of the final design was tested using the original full plant state-space equations and filters required for digital implementation. The 25 Hz antialiasing filters $157/(s+157)$ were added to the plant output. The washout filter $5s/(s+5)$ and computational delay were added to the controller output equations. The 1/200 second computational delay was modeled by a $(400-s)/(400+s)$ filter. Before the wind-tunnel test entry, the digital implementation was also numerically simulated. The numerical simulation block diagram of the control system using the final classical control law 3 is shown in Figure 14. This nonlinear simulation also included the effects of a dead-band present in the electro-hydraulic actuator. Application of the upper and lower spoiler for transonic flutter suppression with the same digital control law was also investigated using this simulation.

The active flutter suppression control-law using classical design was successfully tested in air and in heavy gas medium at transonic speeds up to Mach 0.95. The tests in air indicated an increase in the flutter instability boundary from the open-loop dynamic pressure of 158 psf (Mach 0.38) to the tunnel limit of 200 psf. A summary of flutter suppression test results in heavy gas is shown in Fig. 15. The solid line indicates the experimental flutter boundary, with the transonic dip at Mach 0.8. The tests at Mach 0.8 indicated an increase in the flutter stability boundary from the open-loop dynamic pressure of 142 psf to the tunnel upper limit of 200 psf. A non-design plunge instability condition was also successfully suppressed. Classical control law 3 exhibited superior performance and was demonstrated to be stable with gain variation from 0.25 to 7, and phase variation from -90 to 60 degrees. A non-design plunge instability condition was also successfully suppressed. Comparison of open-loop and closed-loop root mean square (RMS) responses of trailing edge accelerometer and control surfaces using the present classical control law 3 and two other control laws designed by Waszak¹³ are shown in Figs. 16 and 17, respectively. These two control laws used upper and lower spoilers as control surface, for flutter suppression. Fig. 16 indicates that when the system is open loop stable, closing the loop actually reduces the response by 30%. Fig. 17 indicates that the classical control law 3 generally requires less control activity. All three control

laws are comparable in performance, with control law 3 exhibiting higher stability margins.

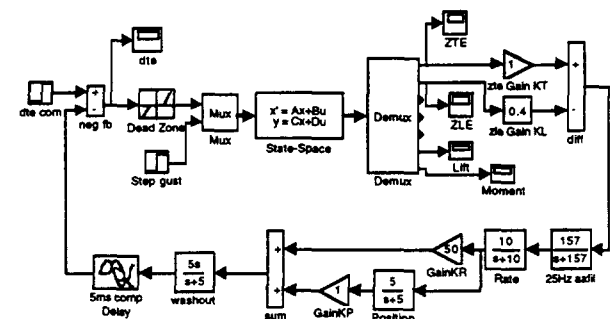


Fig.14 Numerical simulation block diagram of the control system implementation using the final classical control law 3 for flutter suppression.

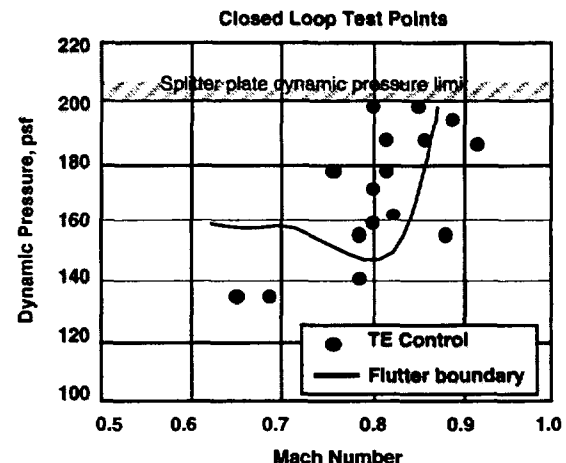


Fig. 15 Open-loop flutter boundary and closed-loop flutter suppression results from wind-tunnel tests in heavy gas.

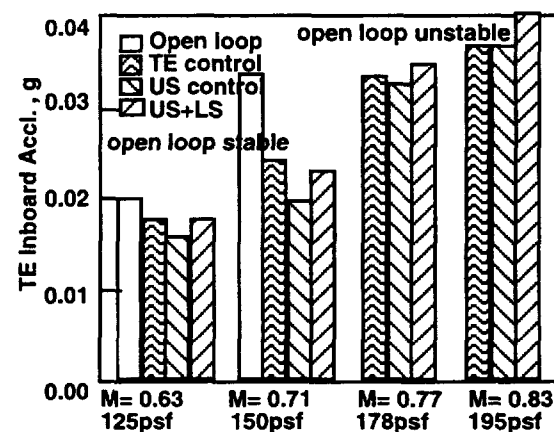


Fig. 16 Open-loop and closed-loop RMS responses with classical control law 3 and two control laws employing spoilers from wind-tunnel tests in heavy gas medium.

Conclusions

Simple classical control laws, when properly designed based on physical principle, can successfully suppress transonic flutter and provide significant stability robustness in presence of shock and flow separation. Comparable robust optimal control laws can also be designed using a new generalized unified minimax formulation. Verification and improvement of the multivariable system stability robustness to unstructured perturbations at the plant, input and output were important steps in such a design process. Wind-tunnel tests in air and heavy gas indicated an increase in the transonic flutter dynamic pressure to the tunnel limit upper limit of 200 psf. The control law robustness and performance predictions were verified in highly nonlinear flow conditions, gain and phase perturbations, and spoiler deployment.

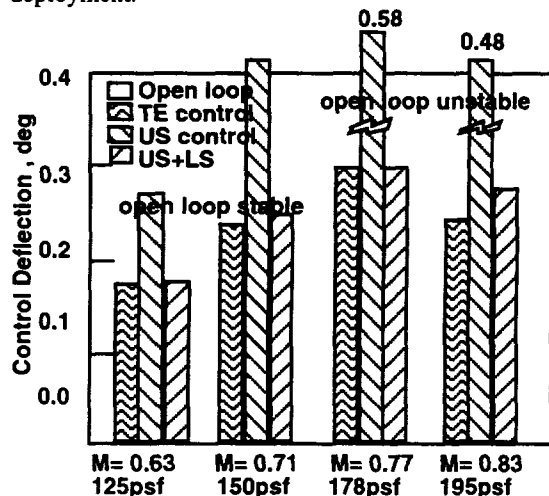


Fig. 17 RMS responses of the control surfaces with the classical control law 3 and two control laws from wind-tunnel tests in heavy gas medium.

References

- ¹Bennett, R. M.; Eckstrom, C.V.; Rivera, J. A. Jr., Dansberry B. E.; Farmer M. G.; and Durham, M.H.: The Benchmark Aeroelastic Models Program - Description and Highlights of Initial Results. NASA TM 104180, 1991.
- ²Rivera, J. A. Jr.; Dansberry B. E.; Farmer M. G.; Eckstrom, C.V.; Seidel, D. A.; and Bennett, R. M.: Experimental Flutter Boundaries with Unsteady Pressure Distribution for the NACA 0012 Benchmark Model. AIAA Paper No. 91-1010, 1991 (NASA TM-104072, 1991)
- ³Rivera, J. A. Jr.; Dansberry B. E.; Bennett, R. M.; Durham, M.H. and Silva, W. A.: NACA 0012 Benchmark Model Experimental Flutter Results with Unsteady Pressure Distribution. AIAA Paper No. 92-2396, April 1992.

⁴Durham, M.H.; Keller, D.F.; Bennett, R. M.; and Wieseman, C. D.: A Status Report on a Model for Benchmark Active Control Testing. AIAA Paper No. 91-1011, 1991.

⁵Hoadley, S. T.; and Adams, W.M. Jr.: ISAC - Interaction Structures, Aerodynamics, and Controls. Version 5.1 Sample Cases with Guides for UNIX Operating Systems, NASA TM-100667, January, 1992.

⁶Mukhopadhyay, V.: Flutter Suppression Control Law Design and Testing for the Active Flexible Wing, *Journal of Aircraft* (Special Adaptive Flexible Wing Issue) Vol. 32, No. 1, Jan-Feb. 1995, pp. 45-51.

⁷Perry, B. III; Cole, S. R.; and Miller, G. D.: A Summary of an Active Flexible Wing Program, " *Journal of Aircraft* , Vol. 32, No. (1995), pp.10-15.

⁸Mukhopadhyay, V.: Stability Robustness Improvement Using Constrained Optimization Techniques. *Journal of Guidance, Control, and Dynamics*, Vol. 10, No. 2, March-April 1987, pp. 172-177.

⁹Pototsky, A. S.; Wieseman, C. D.; Hoadley, S. T.; and Mukhopadhyay, V.: On-line Performance Evaluation of Multiloop Digital Control Systems, *Journal of Guidance, Control, and Dynamics*, Vol. 15, (1992), pp. 878-884.

¹⁰Bryson, A. E. Jr.; and Carrier, A.: A comparison of Control Synthesis Using Differential Games (H-Infinity) and LQR. AIAA Paper 89-3598 CP, August 1989.

¹¹Ghaoui, E. L.; Carrier, A.; and Bryson, A. E. Jr.: Linear Quadratic Minimax Controllers. *Journal of Guidance, Control, and Dynamics*, Vol. 15, No. 4, July-August 1992, pp.953-951.

¹²Doyle, J. C.; Glover K.; Khargonekar, P. P.; and Francis, B. A.: State-Space Solutions to Standard H2 and H-Infinity Control Problems. *IEEE Transactions on Automatic Control*, Vol. 34, No. 8, August 1989, pp.831-847.

¹³Waszak, M. R.: Robust Multivariable Flutter Suppression for the Benchmark Active Control Technology (BACT) Wind-Tunnel Model, *Proc. 11th Symposium on Structural Dynamics and Control*, VPISU, Blacksburg,VA,1997.

Appendix

Reduced 4th order state space equations in air at 225 psf. and Matlab script for unified minimax formulation and solution

$$F = \begin{bmatrix} -1.6073 & 21.0010 & 0. & 0. \\ -21.0010 & -1.6073 & 0. & 0. \\ 0. & 0. & 0.7515 & 25.1670 \\ 0. & 0. & -25.1670 & 0.7515 \end{bmatrix}$$

$$[G \quad G_w] = \begin{bmatrix} -3.8259 & 0.0597 \\ 12.7130 & 0.2720 \\ -2.2202 & -0.1107 \\ 4.1351 & -0.1745 \end{bmatrix}$$

```

H_d = [ -0.0517 -0.0132 -0.0668 0.0063
        -0.0542 -0.0090 -0.0482 -0.0016
        0.         0.         0.         0.
        0.         0.         0.         0.
        0.         0.         0.         0.
10.3780  0.6369  7.9924  0.0671
0.3897  -0.9373 -2.7625  0.9909 ]

[E_du E_dw] = [0.0440  0.0002
                 0.0421  0.0004
                 1.0000  0.
                50.0000  0.
                 0.      0.0968
                0.5758  -0.0004
                0.0358  -0.0003]

% Matlab script for unified formulation and solution
% xdot = F x + G w + G u
% yd = Hd x + Edw w + Edu u Design output
% ys = H x + Esw w + Esu u Sensor output
% 7 design output [zte zle dte ddte gust lift moment]
%
Q11 = h*qh*h+hd*qhd*hd;
Q22 = [q2]+[Edu*qhd*Edu];
% pole placement using cross weight Q12
alpha = 3.0;
Q12=-alpha*g*((g'*g)\Q22)+[hd*qhd*Edu];
WW = [Q11 Q12; Q12' Q22];
% Generalized LQR Weights
Ru = [gw*rw*gw'+nu*g*g'];
Rv = [rv]+[Esw*rw*Esw'];
Rwv = [gw*rw*Esw'];
% generalized EST Weights
VW = [Ru Rwv; Rwv' Rv];
% Generalized DESIGN with Edw=0
[af,bf,cf,df]=lqg(f,g,h,Edu,WW,VW);
%
% STATE REGULATOR
% Check if Q11 is positive semi-definite and symmetric
if any(eig(Q11) < -10*eps) | (norm(Q11'-Q11,1)/norm(Q11,1) > eps)
    error('Q11 must be symmetric positive semi-def'), end
% Check if Q22 is positive definite and symmetric
if any(eig(Q22) <= 0) | (norm(Q22'-Q22,1)/norm(Q22,1) > eps)
    error('Q22 must be sym. positive definite'), end
%
% Construct Hamiltonian
Hm=[(f-g*[Q22\Q12']) -g*[Q22\g']+gw*[rw\gw']/mu
    -Q11-Q12*[Q22\Q12'] -(f-g*[Q22\Q12'])];
[v,d]=eig(Hm);
%
% Sort eigen vector of neg eigenvalues
d = diag(d);
[d,index] = sort(real(d));
if (~(~(d(n)<0) & (d(n+1)>0)))
    error('Can''t order eigenvalues'), end
%
% select vectors with negative eigenvalues
chi = v(1:n,index(1:n));
lambda = v((n+1):(2*n),index(1:n));
S = real(lambda/chi);
%
% Positive feedback gain ku
ku=-Q22\g'*S+Q12';
kw=[rw\gw]*S/mu;
%
% closed loop plant f = fcl
fcl=f+g*ku+gw*kw;
X=lyap(fcl,eye(n)) % assume xo*xo'=I
Xg=lyap(fcl,gw*gw'*36)
W=0.5*trace(kw*rw*kw*Xg)
Jo=0.5*trace(S)
Uu=trace(ku*ku*Xg)
Ycov=Hd*Xg*Xg'*Hd'
%
% H-inf ESTIMATOR DESIGN
% define Hamiltonian Jam
Ru = [gw*rw*gw'+nu*g*g'];
J = [ (f-[Rwv/Rv]*h)' [-h'/Rv]*h+[hd'/qhd]*hd/mu
      -Ru-[Rwv/Rv]*Rwv' -(f-[Rwv/Rv]*h) ];
[v,d]=eig(J);
%
% sort eigenvector of stable eigenvalues
d = diag(d); [d,index] = sort(real(d));
% sort on real part of eigenvalues
if (~(~(d(n)<0) & (d(n+1)>0)))
    error('Can''t order eigenvalues'), end
%
% select vectors with negative eigenvalues
chi = v(1:n,index(1:n));
lambda = v((n+1):(2*n),index(1:n));
P = real(lambda/chi);
ky = -(P*h'+Rwv)/Rv;
% check positive definiteness of kd
% Is this matrix (I - P*S/mu) nonsingular ?
mumin=max(abs(eig(P*S)))
if (mu > mumin),
kd = inv(eye(n)-(P*S)/mu); , else
error('spectrum(P*S) > mu , increase mu'), end
%
eve=eig(f+kd*ky*h);
% controller structure
Ao=f+g*ku+gw*kw+kd*ky*h;
evc=eig(Ao);
% H-infinity controller
% Kop = [Ao -kd*ky -ku zeros(nc,ns)];
[fc, gc ,hc, ec] = feedback(f, g, h, e, Ao, -kd*ky , -ku,
zeros(nc, ns));
%

```


WAVELET APPLICATIONS FOR FLIGHT FLUTTER TESTING

Rick Lind¹, Marty Brenner², and Lawrence C. Freudinger³
 NASA Dryden Flight Research Center

Abstract

Wavelets present a method for signal processing that may be useful for analyzing responses of dynamical systems. This paper describes several wavelet-based tools that have been developed to improve the efficiency of flight flutter testing. One of the tools uses correlation filtering to identify properties of several modes throughout a flight test for envelope expansion. Another tool uses features in time-frequency representations of responses to characterize nonlinearities in the system dynamics. A third tool uses modulus and phase information from a wavelet transform to estimate modal parameters that can be used to update a linear model and reduce conservatism in robust stability margins.

1. Introduction

Flight flutter testing for envelope expansion is a time-consuming and dangerous procedure because of the relative inefficiency of traditional methods. The most common of these methods is to track damping of structural modes throughout the envelope and predict the onset of flutter through decreases noted in the corresponding trends [11]. The danger with this method, and therein the main cause of inefficiency, is the possibility of unexpectedly encountering a flutter instability as a result of sudden changes in damping that are not indicated by trends. Thus, the envelope is expanded using small increments in flight condition that reduce the possibility of such an occurrence.

NASA Dryden Flight Research Center has been developing tools to increase the efficiency of flight flutter testing by reducing the required amount of flight time while simultaneously increasing safety to aircraft and crew [15]. These tools encompass several areas of flight flutter testing ranging from excitation to data transfer to stability prediction. In particular, tools have been formulated that use wavelets to accurately analyze the types of data that are typically measured during flight flutter testing.

¹Aerospace Engineer, Structural Dynamics, Edwards CA 93523,
 rick.lind@dfrc.nasa.gov, 661.258.3075

²Aerospace Engineer, Structural Dynamics, Edwards CA 93523,
 martin.brenner@dfrc.nasa.gov

³Aerospace Engineer, Structural Dynamics, Edwards CA 93523,
 lawrence.freudinger@dfrc.nasa.gov

Wavelets represent a type of processing that relaxes several constraints on the signal that are assumed to be satisfied when using traditional Fourier processing [24]. The wavelet transform has been used for a wide variety of signal and image processing applications; however, its use for dynamical systems, and particularly flight flutter testing, has been somewhat more limited to applications such as denoising in the time-frequency domain [3, 7].

A tool has been developed recently to use wavelets as basis functions for a correlation filter that identifies modal properties [8]. This tool uses inner products between data and a set of wavelets as a measure of correlation. The modal properties of the system are then identified by noting the associated properties of the wavelets that are highly correlated with the data.

Another wavelet-based tool that has been recently developed uses wavelet maps to extract information about nonlinearities in system dynamics [16, 17]. This tool considers features and trends in the time-domain representations of transient responses to indicate the presence of nonlinearities. Furthermore, these features and trends can be exploited to characterize the nature of the nonlinearities.

A third tool uses wavelets for parametric estimation of modal dynamics and state-matrix elements [4]. This tool is developed in conjunction with a flutter analysis tool such that the parameter estimates are incorporated into the analysis to reduce the amount of modeling error considered by robust stability metrics [12]. This tool is especially appropriate for flight flutter testing by considering an on-line formulation of the tool that estimates modal parameters during flight [5].

This paper presents these wavelet-based tools that have recently been developed for use during flight flutter testing. These tools have been previously documented; therefore, the purpose here is to present a summary and compendium of the recent advances.

This paper is divided into 3 main sections such that each section is devoted to a particular tool. The discussion is limited for brevity to the basic theoretical foundation and an example to demonstrate each tool in a flight test context. References are listed that can be consulted to obtain more extensive information.

2. Correlation Filtering

This section presents the wavelet-based tool for correlation filtering. Laplace wavelets are introduced in terms of damping and natural frequency to represent basis functions for the tool. The filtering uses these functions to generate a correlation coefficient and indicate modal parameters of the system. The tool is demonstrated by filtering data from an envelope expansion flight test.

2.1. Laplace Wavelet

The Laplace wavelet, ψ , is a complex, analytic, single-sided damped exponential.

$$\psi_\gamma(t) = \begin{cases} Ae^{-\frac{\zeta}{\sqrt{1-\zeta^2}}\omega(t-\tau)}e^{-j\omega(t-\tau)} & : t \in [\tau, \tau + T] \\ 0 & : \text{else} \end{cases}$$

The parameter vector, $\gamma = \{\omega, \zeta, \tau\}$, determines the wavelet properties. These parameters are related to modal dynamic properties by associating ω with frequency, ζ with viscous damping ratio, and τ as a time index. The coefficient A is an arbitrary factor used to scale each wavelet to unity norm. The range, T , ensures the wavelet is compactly supported.

This function is called a Laplace wavelet to emphasize that its derivation is related to the Laplace transform. In particular, the Laplace wavelet has a strong similarity to the inverse Laplace transform of the transfer function for an underdamped, second-order system. Thus, the Laplace wavelet is generated by considering features anticipated in mechanical system responses.

2.2. Laplace Wavelet Dictionary

The analysis of response data from dynamical systems often uses assumptions of linearity such that the system response should be a linear combination of subsystem responses [10]. These subsystems are second-order single degree of freedom systems in the case of modal analysis. Signal decomposition of the response into the subsystem responses for steady-state data can be accomplished via Fourier transforms which use a basis of infinite length sinusoids of varying frequencies.

Transient response data are difficult to effectively decompose even for linear systems since the system response is composed of subsystem responses with time-varying magnitudes. The basis of infinitely long sinusoids used by the Fourier transform is not ideal for this nonstationary data. Wavelets may be used for signal decomposition of transient response data since they inherently allow time-varying magnitudes of the subsystem responses.

The concept of a dictionary is introduced to describe a set of wavelets used for signal decomposition [24]. This dictionary is distinguished from a basis since the response of any dynamical system may not necessarily be

expressed as a linear combination of the finite number of entries in the dictionary. The dictionary approximates a basis assuming the responses to be analyzed are similar in nature to the Laplace wavelets. The dictionary is basically a database of waveforms.

A finite set of wavelet parameters is used to generate the dictionary. A discrete gridding of the parameter space results in sets Ω, \mathcal{Z} and \mathcal{T} .

$$\begin{aligned}\Omega &= \{\omega_1, \omega_2, \dots, \omega_p\} \subset \mathcal{R}_+ \\ \mathcal{Z} &= \{\zeta_1, \zeta_2, \dots, \zeta_q\} \subset \mathcal{R}_+ \cap [0, 1] \\ \mathcal{T} &= \{\tau_1, \tau_2, \dots, \tau_r\} \subset \mathcal{R}\end{aligned}$$

The dictionary is defined for the set of Laplace wavelets whose parameters are contained in these sets as denoted by $\gamma \in \Omega \times \mathcal{Z} \times \mathcal{T}$.

2.3. Filtering Approach

An inner product operation measures the correlation between signals. Correlating a signal, $f(t)$, with a Laplace wavelet, $\psi_\gamma(t)$, measures similarity between frequency and damping properties of the wavelet and the system that generated the signal.

A correlation coefficient, $\kappa_\gamma \in \mathcal{R}$, is defined to quantify the degree of correlation between the wavelet and a time signal. This correlation coefficient considers the angle between the vectors such that the maximum coefficient results from correlating parallel vectors.

$$\kappa_\gamma = \sqrt{2} \frac{|\langle \psi_\gamma, f(t) \rangle|}{\|\psi_\gamma\|_2 \|f\|_2}$$

κ_γ is a matrix whose dimensions are determined by the parameter vectors of $\{\omega, \zeta, \tau\}$. A useful correlation coefficient $\kappa(\tau)$ is defined for on-line modal analysis to correlate frequency and damping at each time value. Peaks of the surface plot of κ_γ for a given τ relate the wavelets with the strongest correlation to the data. Define $\kappa(\tau)$ as the peak values of κ_γ at each τ and define $\bar{\omega}$ and $\bar{\zeta}$ as the parameters of the Laplace wavelet associated with the peak correlation.

$$\kappa(\tau) = \max_{\substack{\omega \in \Omega \\ \zeta \in \mathcal{Z}}} \kappa_\gamma = \kappa_{\{\bar{\omega}, \bar{\zeta}, \tau\}}$$

A normalizing factor of $\sqrt{2}$ allows $\kappa(\tau) = 1$ when the signal in some time interval T is a linear combination of the real and imaginary components of a particular wavelet. The formulation of $\kappa(\tau)$ searches for a maximum value across values of ω and ζ . This search can use subsets of Ω and \mathcal{Z} to find local maxima and compute a κ vector at each time index. The subset searching is analogous to finding multiple peaks of interest on a frequency spectrum plot, with the added variables of damping and time.

The support range T is not explicitly used to define κ but it can greatly affect the computed value. Small T

may increase κ for signals not strongly correlated while large T may decrease κ to the noise floor even for signals which are strongly correlated. Thus, T can not be chosen arbitrarily. Knowledge of crest factors, signal-to-noise ratios, and effective decay rates observed in the data can all be used in guiding the choice of T .

A correlation filter approach computes the κ vector for a response signal. The dampings $\bar{\zeta}$ and frequencies $\bar{\omega}$ associated with peak κ values indicate the modal properties of the system which generated the data. This filter acts as a transform from the time domain to a modal parameter, or stability, domain. This stability estimate should be representative of the modal properties of the system if the data represent a linear, time-invariant system in free decay.

2.4. Flight Data Analysis

Application to actual aircraft data is required to evaluate Laplace wavelet correlation filtering for use in a flight test environment. Consider the DAST aircraft (Drones for Aerodynamic and Structural Testing), a remotely piloted research drone which encountered explosive flutter in June 1980 [9].

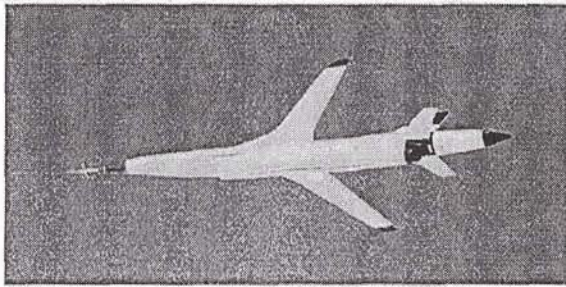


Figure 1: NASA DAST vehicle in flight

The last 40 s of flight data demonstrate the transition from stable flight to the onset of flutter and thus are of interest for evaluating correlation filtering. This data corresponds to flight at 15,000 ft over which the Mach number varies between approximately 0.80 and 0.825. Wingtip accelerations are measured at 500 Hz in response to symmetric aileron pulses and are used to analyze modal properties of the vehicle. A flutter suppression controller was engaged during this flight; however, the vehicle encountered a flutter instability due to an implementation error.

The response data was correlated with a Laplace dictionary based on support $T = 2$ s. The starting time indices for filtering, τ , are data dependent and correspond to local maxima with an emphasis on transient excursions. The remaining elements of the dictionary are members of the sets Ω and Z .

$$\begin{aligned}\Omega &= \{10 : 0.25 : 30\} \\ Z &= \{0 : 0.003 : 0.063\}\end{aligned}$$

The results of correlation filtering are presented in Figure 2. Figure 2a presents the acceleration response of the left wingtip while Figures 2b, 2c, and 2d present the peak correlation, frequency, and damping values as a function of time. A threshold $\kappa(\tau) > 0.8$ is applied to avoid clutter on the plot without discarding interesting information.

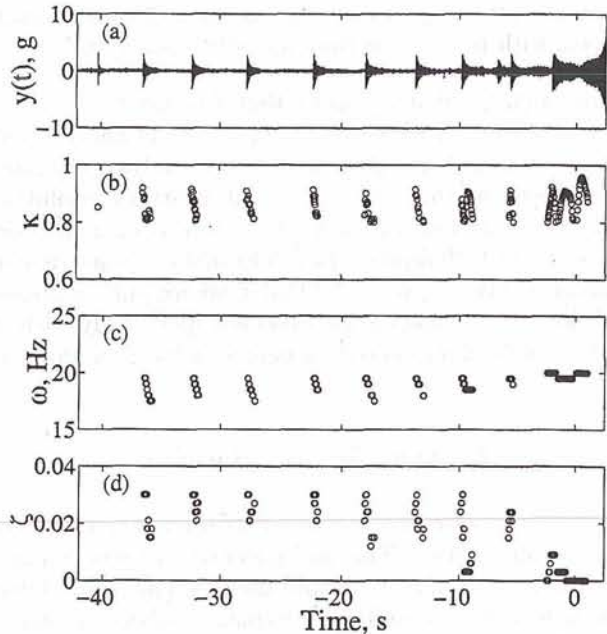


Figure 2: Correlation Filtering of the DAST Data with the Laplace Wavelet Dictionary: Left Wingtip Acceleration (a), Peak Correlation Values $\kappa(\tau) > 0.8$ (b), Wavelet Frequencies Associated with Peak Correlations (c), Corresponding Wavelet Damping Values (d)

Classical flutter testing uses trend analysis based on grouping correlations for a given pulse into an average value. The results from performing this operation on the data in Figure 2 are presented in Table 1.

t, s	ζ	$\bar{\omega}, \text{Hz}$
-36	0.035	18.25
-32	0.030	18.75
-27	0.027	19.0
-22	0.026	19.0
-17	0.025	19.2
-13	0.022	19.0
-9	0.025/0.009	19.5/18.5
-5	0.018/0.0	19.5/18.5
-2	0.005	19.7
-1	0.000	19.7

Table 1: Frequency and Damping Values Estimated by Correlation Filtering

As can be seen in both Figure 2 and Table 1, the average frequency and damping values show a roughly steady trend until the impulse at $t = -13$ s at which time the dominant frequency edges up slightly by 0.5 Hz and the damping tends toward zero. From $t = -9$ s and later, a progressive increase in residual dynamics observed in Figure 2a indicates the arrival of the stability boundary. As the frequency spread converges to a single frequency, the damping values converge to zero. These estimates agree with previous parameter estimation results [1].

This analysis demonstrates that frequency and damping estimates provided by Laplace wavelet analysis are a diagnostic tool useful for free decay analysis because it provides time-varying estimates at arbitrary resolutions, which are not available from Fourier or traditional linear estimation techniques. This information is particularly useful in cases such as the DAST where pulse responses of closed-loop systems are observed specifically with the intent of tracking modal dynamics in the time domain.

3. Analyzing Nonlinearities

This section discusses the tool that uses wavelets to analyze nonlinearities. This tool generates a time-frequency representation of a signal and then uses associated dominant features to indicate information about nonlinearities in the dominant dynamics. Responses from linear and nonlinear pitch-plunge systems are analyzed to demonstrate how nonlinearities are detected and characterized with this tool.

3.1. Extracting Dominant Scales

Wavelet maps can sometimes be difficult to interpret because of the large amount of information contained in this two-dimensional representation. Many applications are only interested in the dominant components of a signal and consequently are only interested in the dominant information from these maps. One method of extracting dominant information is to identify the scales associated with peaks in the wavelet maps, $F(\tau, a)$, that are associated with the Morlet wavelet [24].

Consider a vertical strip $F(t_i, a)$ that represents the magnitude of the correlations between the signal $f(t)$ and wavelets at position $\tau = t_i$ for the vector of scales $a \in A$. Define \bar{F}_i as the maximum peak magnitude correlation for this strip which corresponds to a wavelet with scale defined as $\bar{a}_i \in A$.

$$\bar{F}_i = F(t_i, \bar{a}_i) = \max_{a \in A} F(t_i, a) = \max_{a \in A} F(\tau, a) \Big|_{\tau=t_i}$$

The parameter \bar{a}_i can be utilized to determine sample length period of the dominant wavelet pattern in the data. This periodicity can be interpreted as a measure of the dominant sinusoidal frequency component in the response data under the approximations that the Morlet wavelet is essentially sinusoidal in nature. Thus, the dominant scale is loosely related to the well-known concepts of ridges and instantaneous frequency [23].

Values of \bar{a}_i are computed at each instant of time to produce a time-varying measure of dominant scale and frequency; however, there are instances when no value can be computed. For example, the real Morlet wavelet will be alternating from in-phase to out-of-phase with a sinusoidal signal and so there will be instances when the wavelet does not correlate well with the signal. The possible misinformation that could result from this is eliminated by applying a threshold factor that ignores portions of the wavelet map with no noticeable energy or low correlation factor.

3.2. Nonlinear Testbed

An aeroelastic testbed is used at Texas A&M University for flutter research using a prototypical aeroelastic wing section. This system allows pitch-plunge motion to represent the bending-torsion motion that is often associated with a classical flutter mechanism.

Nonlinearities are introduced to the system dynamics through the stiffness associated with pitch movement. This stiffness is described by a nonlinear polynomial function of the pitch angle. Such structural nonlinearities occur in physical aeroelastic systems and have been investigated to determine their effect on inducing limit cycle oscillations [6].

Models of the Texas A&M aeroelastic system are formulated using three types of stiffness functions to investigate a variety of behaviors related to different nonlinearities. These functions associated with the pitch stiffness are chosen to represent a linear spring, a nonlinear hardening spring, and a nonlinear softening spring.

The linear spring constant is denoted k_{lin} .

$$k_{lin} = 2.82$$

The softening spring function is denoted k_{soft} .

$$k_{soft} = 2.82 - 200\alpha^2 + 10000\alpha^4$$

The hardening spring function is denoted k_{hard} .

$$k_{hard} = 2.82 - 62.3\alpha + 3709.7\alpha^2 - 24196.0\alpha^3 + 48757\alpha^4$$

The models with each of these springs can be linearized around the equilibrium condition at the phase-plane origin by eliminating higher-order terms in α . Each linearized model is identical and has a pitch-mode natural

frequency at 1.29 Hz. Thus, the linear and nonlinear systems at stable flight conditions should behave similarly for responses with small α values.

3.3. Pitch Responses

Simulated free-decay responses are computed for each nonlinear model using a 4th order Runge-Kutta algorithm to integrate the equations of motion with a time step of .001 s. The pitch responses are shown in Figure 3.

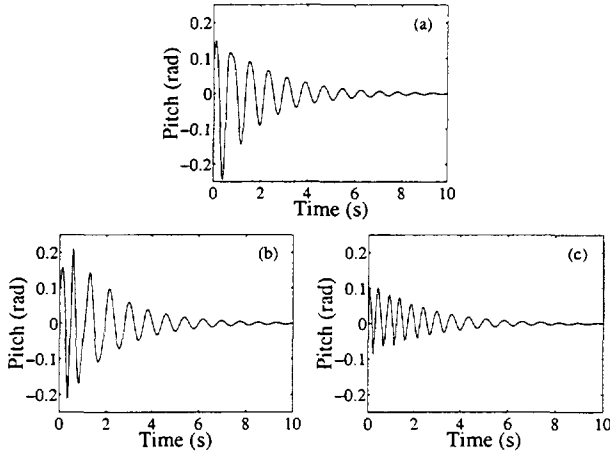


Figure 3: Simulated Time Responses of the Pitch Angle of Each Model at Airspeed $U=8 \text{ m/s}$: Linear k_{lin} (a), Nonlinear Softening k_{soft} (b), Nonlinear Hardening k_{hard} (c)

The plunge responses are not presented here because they are not used for the current analysis. The plunge mode has a higher damping than the pitch mode and consequently the plunge response decays quickly to zero. Conversely, the pitch motion continues with a magnitude that is sufficient to demonstrate properties of the dynamics and so the analysis will focus only on the pitch response.

Time-scale information is obtained by computing the continuous wavelet transform of these time responses. Figure 4 presents the maps $F(\tau, a)$ generated by a wavelet analysis on the pitch data using real Morlet wavelet basis functions.

Figure 4 shows 2-dimensional plots of the 3-dimensional wavelet maps. The correlation magnitude between the wavelet and signal at each position and scale value is represented by a shade of gray with white implying low correlation and black implying high correlation. Such a shading approach is not optimal for representing these wavelet maps since several closely spaced scales will often appear to have a similar correlation magnitude and the resulting signal decomposition appears to be spread over these scales; however the 3-dimensional images are often more difficult to display.

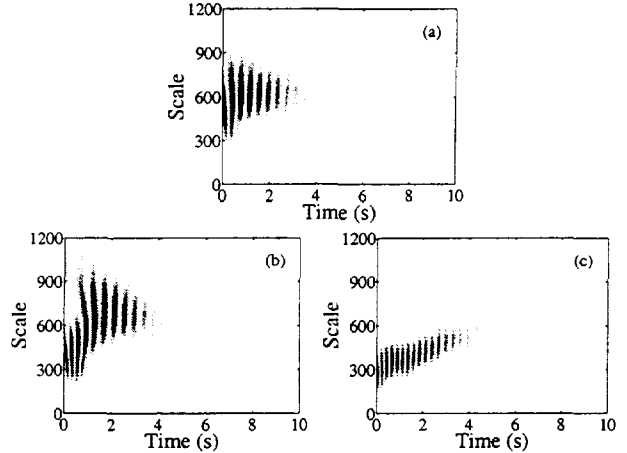


Figure 4: Wavelet Transform Maps of the Pitch Data Obtained from the Models Simulated at Airspeed $U=8 \text{ m/s}$: Linear k_{lin} (a), Nonlinear Softening k_{soft} (b), Nonlinear Hardening k_{hard} (c)

3.4. Detecting Nonlinearities

The detection and characterization of nonlinearities affecting the system dynamics is difficult based on the general time responses of Figure 3 and corresponding time-frequency maps of Figure 4. The concept of dominant scales is therefore introduced as a means to extract the most important information and simplify the analysis of nonlinearities.

Figure 5 presents the plots of \bar{a}_i corresponding to the peak magnitude wavelets from the maps of Figure 4.

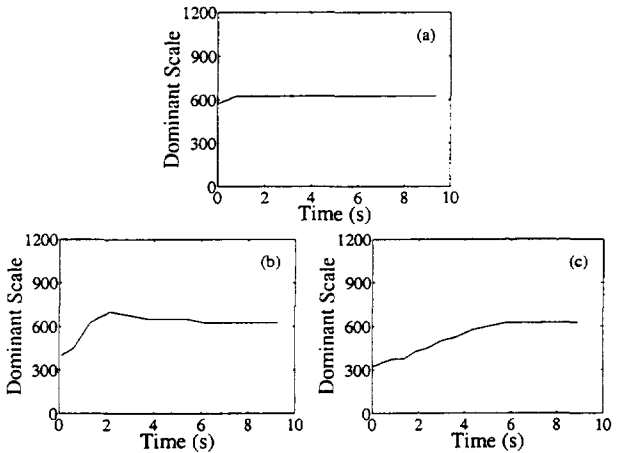


Figure 5: Scale \bar{a}_i Corresponding to Peaks of the Wavelet Transform Maps of the Pitch Data Obtained from the Models Simulated at Airspeed $U=8 \text{ m/s}$: Linear k_{lin} (a), Nonlinear Softening k_{soft} (b), Nonlinear Hardening k_{hard} (c)

The wavelet maps in Figure 4 and the scales \bar{a}_i corresponding to the peaks of those maps in Figure 5 show clear differences in the responses from each spring. These plots may not be immediately obvious to interpret; how-

ever, a careful examination reveals the wavelet analysis presents information which can be directly compared to properties of the dynamical systems. Interpretation is aided by referring to convenient regions of the time response.

Region I	$0 < t < 2 \text{ s}$
Region II	$2 < t < 7 \text{ s}$
Region III	$7 < t < 10 \text{ s}$

Consider the wavelet information from Region I corresponding to the responses for $t < 2 \text{ s}$. This portion of the responses from each system is dominated by the plunge displacement which is evident from further analysis of time-domain plots that are not presented here [16]. The dominant scale associated with each response is initially low and corresponds to the high-frequency dynamics of the plunge mode. The presence of this dynamic is a result of the pitch-plunge coupling through the mass matrix in the equations of motion.

The transition at the end of Region I is caused by the decay of the plunge-mode response and an emerging dominance of the pitch-mode response. This early decay is a result of the larger damping in the plunge mode as compared to the pitch mode. The wavelet map demonstrates an increase in dominant scale to correspond with the decrease in frequency between dominant modes.

The response in Region II is dominated by the dynamics of the pitch motion with only a small contribution from the coupled plunge motion so this data is useful for analyzing the dynamics of a single degree of freedom pitch system. The dominant scale, \bar{a}_i , demonstrates significantly different behavior for the wavelet analysis of the three systems as evident from Figure 5.

The constant scale \bar{a}_i for the linear system response in Region II is directly indicative of linear system dynamics. The response in this Region results from a linear and time-invariant system with a single mode so the dominant frequency in the response should be constant and thus the dominant wavelet scale should be constant. The dominant scale has a value of $\bar{a}_i = 625$ and a corresponding frequency is computed as the sampling rate of 1000 Hz divided by this scale. The true frequency is then computed by normalizing the ratio by 1.2 which is the dominant wavelength of the Morlet wavelet. Thus the linearized responses shows a dominant frequency of 1.333 Hz which is similar to the predicted natural frequency of the pitch mode for the linear system.

The time-varying values of \bar{a}_i associated with the responses in Region II from the system with a nonlinear hardening spring are considerably different than the scale for the linear system. Consider that the response from the system with a hardening spring initially shows

a small dominant scale and increases with time. The effect of a hardening spring is to incur a larger restoring force at large amplitudes as compared to a linear spring. This force returns the system to the origin faster and consequently the response has a higher frequency for the nonlinear system. The difference between nonlinear and linear decreases as the response decays to a smaller amplitude and so the frequency in the responses becomes nearly identical. Thus, the wavelet maps reveal this behavior because an increasing scale is indicative of a decrease in frequency.

A similar analysis on the dominant scales associated with the response of the nonlinear system with the softening spring demonstrates the wavelet maps can detect and characterize this nonlinearity also. In this case, the softening spring results in a lower frequency in the response as compared to the linear system but the difference is small when the response amplitude is small. The dominant scale is initially larger for the response of the nonlinear system as compared to the linear system and decreases as time increases. Thus, the wavelet map reveals the initial frequency is lower in the response of the nonlinear system but it increases as the response decays to small amplitude.

The Region III analysis from Figure 5 notes the dominant scales, and consequently the frequency components, are similar for the responses from each system. This result is expected because the response magnitude has decayed as a result of damping and so each system can be approximated by the same linearized dynamics. The period of the dominant wavelet is $\bar{a}_i = 625$ which corresponds to a frequency of $\omega = 1.33 \text{ Hz}$ and matches the natural frequency of the linearized system.

The wavelet maps of the time responses are clearly indicative of nonlinearities under the assumptions of free-decay responses from single-mode, time-invariant systems. In particular, the responses in Region II reveal distinct differences between the responses of linear and nonlinear systems. Furthermore, these differences can be used to characterize the nature of the nonlinearities in the system dynamics.

4. Model Updating

This section presents the tool for parametric estimation of modal dynamics. A theoretical overview of the wavelet-based estimation is derived in terms of magnitude and phase characteristics. The μ method for flutter analysis is then discussed with respect to extending the baseline method to include the estimation tool. Robust flutter margins are generated for an F/A-18 using a nominal model and a model updated by the wavelet tool.

4.1. Parametric Modal Estimation

Consider $f(t) = k(t)\cos(\phi(t)t)$ as a general harmonic signal that may represent a typical sensor measurement. The corresponding wavelet transform, $F(a, \tau)$, can be analytically derived for a set of Morlet wavelets.

$$F(a, \tau) = \sqrt{a}k(t)e^{-(a\phi(t)-\omega_0)^2}e^{i\phi(t)\tau}$$

The modulus and phase of this wavelet transform are of interest because they indicate modal properties of the system. In particular, these quantities can be evaluated for a given scale, a_i , that corresponds to a natural frequency of the system.

$$\begin{aligned}|F(a_i, \tau)| &= \sqrt{a_i}k(t)e^{-(a_i\phi(t)-\omega_0)^2} \\ \angle[F(a_i, \tau)] &= \phi(t)\tau\end{aligned}$$

A concept of instantaneous frequency can be easily derived using the expression of phase of the wavelet transform [22]. This concept shows that a general time-varying envelope, $k(t)$, or time-varying phase, $\phi(t)$, of the signal can be determined from the modulus and phase of the wavelet transform for specific frequencies.

Flight data measured during flutter testing will often display features associated with viscously-damped, single degree of freedom systems. The corresponding envelope and phase functions can be explicitly written by noting that $f(t) = Ae^{-\zeta\omega_n t}\cos(\omega_d t + \phi_0)$ describes the measured signal. The corresponding wavelet expression for the envelope and instantaneous frequency for these systems can be formulated based on the general expression.

$$\begin{aligned}k(t) &= \frac{|F(a_i, \tau)|}{\sqrt{a_i}e^{-(a_i\phi(t)-\omega_0)^2}} = Ae^{-\zeta\omega_n t} \\ \phi(t)\tau &= \angle[F(a_i, \tau)] = \omega_d t + \phi_0\end{aligned}$$

The expression using phase of the wavelet transform indicates that the relationship between instantaneous frequency and damped natural frequency can be expressed as $\phi \approx \omega_d$. Similarly, the envelope decay rate can be expressed as $\zeta\omega_n$. Thus, modal parameters of the system can be estimated by analyzing modulus and phase of the wavelet transform.

4.2. μ Method with Wavelet Processing

A method to compute stability margins of aeroservoelastic systems has been formulated based on robust stability theory[12]. This method uses a set of structured operators Δ , referred to as uncertainty, to describe errors and unmodeled dynamics in an analytical model. The structured singular value, μ , is used to compute a stability margin for this model that is robust, or worst-case, to the uncertainty operators[20].

The μ framework represents systems as operators with interconnections known as linear fractional transformations. This paper will use the notation $F(P, \Delta)$ to represent a feedback interconnection of the plant, P , and an associated uncertainty, Δ .

Flight data is incorporated into the μ method by formulating an uncertainty description that accounts for observed variations and errors[13]. A model validation analysis is performed on the plant model to ensure the range of dynamics admitted by the uncertainty is sufficient to cover the range observed with the flight data.

An ASE stability margin, Γ , is determined by computing μ with respect to an uncertainty description, $\delta_{\bar{q}}$, that admits variations in dynamic pressure and an uncertainty description, Δ , that describes modeling errors[14]. This margin relates the largest change in dynamic pressure that may be considered while guaranteeing the plant model is robustly stable to all errors described by Δ .

An implementation of the μ method with modal parameter estimation has been formulated that analyzes the wavelet maps of flight data to extract frequencies and dampings. A plant model, P_1 , is computed by updating elements of the nominal plant model, P_0 , with the modal parameter estimates. Only a limited subset of dynamics will be observed in the data so only a correspondingly limited subset of the plant modes will be updated. The parameters describing dynamics that are not observed by the data can not be estimated so the updated plant will directly use the nominal plant elements to describe these dynamics.

An uncertainty description, Δ_1 , is generated for the plant with updated modal parameters, P_1 , using a model validation procedure. This description will generally be smaller than the description associated with the nominal plant because the updated model should be more representative of the flight data. Essentially, the updated model is centered within the range of dynamics observed by the flight data.

The conservatism in robust margins computed by the μ method arises from excessive uncertainty descriptions needed to account for errors in a model. The decrease in uncertainty resulting from updating the model by the parameter estimation process may correspondingly decrease the conservatism in the robust stability margin.

4.3. F/A-18 HARV

Robust stability margins for the aeroservoelastic dynamics of the F/A-18 HARV are computed using the μ method with wavelet filtering. This aircraft, shown in Figure 6, is a twin-seat fighter that was modified to include thrust vectoring paddles on the engines and a research flight control system [21]. The flight system also included a method to generate excitation signals for measuring aeroservoelastic responses by summing programmed digital signals to the controller commands to the actuators [2]. Inputs from 5 to 25 Hz were added to the control surface commands at angles of attack from 5 to 70 deg of α at 1g.

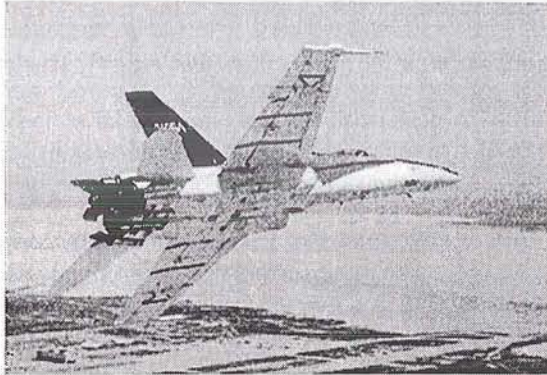


Figure 6: F/A-18 HARV

The μ method was used to analyze the stability margins at several points in the envelope; however, this paper will only consider the worst-case condition [18]. This worst-case margin is associated with the antisymmetric modes of the lateral-directional dynamics for the aircraft at Mach 0.3 and an altitude of 30000 ft with the dynamic pressure at $\bar{q} = 41 \text{ lb}/\text{ft}^2$. The baseline μ method indicates an instability may lie close to the flight envelope so any reduction in conservatism could be significant.

A set of operators are used to indicate uncertainties in an analytical model. A complex operator, Δ_{in} , is a multiplicative uncertainty in the control inputs to the plant and accounts for actuator errors and unmodeled dynamics. Another complex operator, Δ_{add} , relates the control inputs to the feedback measurements to account for uncertainty in the magnitude and phase of the computed plant responses. The remaining operator, Δ_A , is a real parametric uncertainty affecting the modal parameters of the open-loop state matrix to describe errors in natural frequency and damping parameters.

The block diagram for robust stability analysis of the F/A-18 HARV aeroservoelastic dynamics is shown in Figure 7. This figure includes an operator, $\delta_{\bar{q}}$, that affects the nominal dynamics to describe changes in flight condition and is used to interpret μ as a stability margin [14]. Additional operators, W_{add} and W_{in} , are shown as weightings to normalize the frequency-varying uncertainty operators, Δ_{add} and Δ_{in} .

4.4. Models and Uncertainty

An initial model of the aircraft, P_0 , is computed using 6 rigid-body modes and 10 antisymmetric structural modes along with 20 states associated with the unsteady aerodynamics. The control system adds 90 states to account for actuator dynamics and 29 states for the feedback controller.

An updated model, P_1 , is computed by using modal parameter estimates to replace elements of the structural modes of P_0 . These parameters are generated by analyz-

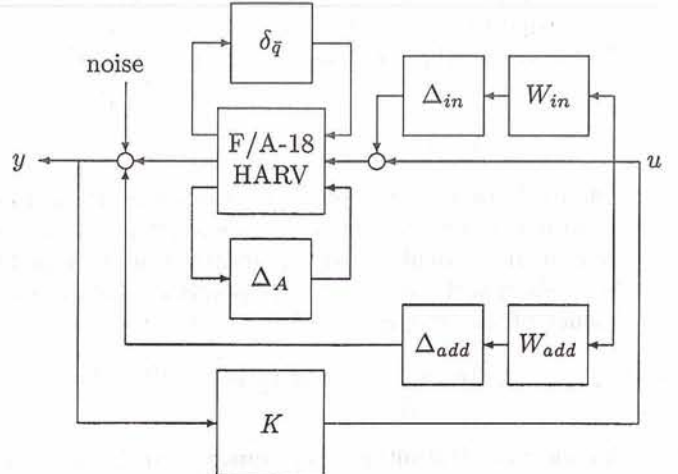


Figure 7: F/A-18 HARV Uncertainty Block Diagram for Robust Stability Margin Analysis

ing the modulus and phase of the wavelet transform of accelerations measured in response to sine sweeps through the control surfaces. An uncertainty description, Δ_1 , is derived to account for features in the data that can not be exactly reproduced by the updated model.

Table 2 presents an example of the modal properties for the original and updated models. The parameters are larger for the updated model than for the original model because the flight data indicates the theoretical values are too low. Consequently, the amount of variation in the parameters that results from uncertainty is considerably less for the updated model than for the original model. Note the absolute amount of variation in damping is actually greater for the updated model; however, the percentage of variation is less and this is the important consideration for this analysis.

model	ω (Hz)	ζ
$F(P_0, \Delta_0)$	$15.69 \pm .63$	$.010 \pm .007$
$F(P_1, \Delta_1)$	$16.51 \pm .35$	$.045 \pm .023$

Table 2: Modal Parameters and Uncertainty Variations for the Wing Fore-Aft Mode for Each Model

4.5. ASE Stability Margins

Nominal stability margins are computed for the plant model using the original theoretical modal parameters and the updated models using parameters estimated from wavelet filtering. These margins are computed from a μ analysis with respect to the variation in flight condition, \bar{q} , but ignoring the modal and complex uncertainty operators. The nominal stability margins, Γ , are given in Table 3 and demonstrate the largest decrease from the nominal dynamic pressure of $\bar{q} = 41 \text{ lb}/\text{ft}^2$ that may be considered before the models incur an ASE instability.

model	Γ	ω
$F(P_0, 0)$	-268 lb/ft ²	14.8 Hz
$F(P_1, 0)$	-368 lb/ft ²	14.8 Hz

Table 3: Nominal Stability Margins for Each Model

The original theoretical model has a nominal stability margin of $\Gamma = -268 \text{ lb/ft}^2$ resulting from a critical instability of the wing fore-aft mode at 14.8 Hz. The margin is increased by updating the model with modal parameter estimates; however, the wing fore-aft mode remains the critical mode. This increase in stability margin associated with wavelet filtering is not guaranteed to occur for all applications; rather, the filtering is designed to make the nominal model more accurate. The nominal model for the F/A-18 HARV had low dampings so the wavelet filtering increased the modal damping levels and, in a sense, made the plant effectively more stable and increased the stability margins.

These nominal margins are all greater than the dynamic pressure at this flight condition so they demonstrate the nearest instability to the flight envelope occurs at a negative dynamic pressure, which is physically unrealizable. Thus, the nominal dynamics are free of ASE instabilities within the research flight envelope.

Robust stability margins are computed with respect to the uncertainty description of Figure 7 and given in Table 4. The original model and uncertainty description is represented by $F(P_0, \Delta_0)$ while the updated model with reduced uncertainty description is given by $F(P_1, \Delta_1)$.

model	Γ	ω
$F(P_0, \Delta_0)$	-4 lb/ft ²	15.4 Hz
$F(P_1, \Delta_1)$	-222 lb/ft ²	7.0 Hz

Table 4: Robust Stability Margins for Each Model

The stability margin of the original model is strongly affected by considering uncertainty. This margin is reduced from $\Gamma = -268 \text{ lb/ft}^2$ for the nominal dynamics to $\Gamma = -4 \text{ lb/ft}^2$ for the dynamics with respect to uncertainty. The critical mode remains the wing fore-aft mode despite the uncertainty; however, the dynamic pressure at which this mode becomes unstable is quite different. This robust stability margin demonstrates the nominal model may be misleading and the nearest unstable flight condition may actually lie close to the flight envelope.

The robust stability margin for the model $F(P_1, \Delta_1)$, which uses modal parameter estimates, is significantly larger than the margin of the original system. The wavelet processing is able to identify a more accurate model with less associated uncertainty so the conservatism in the margin is reduced. The robust stability margin for this model is $\Gamma = -222 \text{ lb/ft}^2$ and indicates

the nearest instability for the updated model, despite the range of dynamics incurred by uncertainty, is at a negative dynamic pressure and so the flight envelope is robustly free of ASE instabilities.

The critical mode associated with the robust stability margin for the updated model is the first fuselage bending mode, which is different than the critical mode associated with the nominal margin. This shift in critical modes results from the inclusion of uncertainty that allows a variation to the fuselage dynamics that becomes unstable before the wing fore-aft mode. Similarly, the critical mode for the robust stability margin of the original model $F(P_0, \Delta_0)$ is the wing fore-aft mode, but the reduced uncertainty associated with $F(P_1, \Delta_1)$ shifts the critical mode so the variation in fuselage dynamics for the updated model encompasses the critical instability.

Comparison between the nominal results in Table 3 and the robust results of Table 4, both in Γ and modal frequency, clearly show the change in stability characteristics resulting from model updating and the corresponding uncertainty updating. The original model showed a substantial decrease in margin for the instability associated with the wing-fore-aft mode when uncertainty was included. The updated model showed a much smaller decrease in margin despite the shift in modal instability. For this model, wing fore-aft modal frequency increased about 1 Hz from its theoretical value to the updated value and thereby became a less significant factor in the stability margin calculation compared with the fuselage mode. This result confirms that the effect of parameter estimation in model validation can be a critical factor for predicting robust stability margins.

5. Concluding Remarks

Wavelet analysis produces a time-frequency representation of data from which informative features may be extracted. This paper has shown several applications of wavelets that are valuable for flight flutter testing. A correlation filter is developed that can identify modal properties and indicate coupling and perhaps the onset of flutter during envelope expansion. Another application can be used to characterize nonlinearities in the system that may indicate behaviors such as limit cycle oscillations. Also, a method of modal parameter estimation is developed that can be used to update models and reduce conservatism in robust stability margins and allow envelope expansion to proceed to points that may be initially considered as dangerous because of excessive conservatism in original models.

References

- [1] R. Bennett and I. Abel, "Application of a Flight Test and Data Analysis Technique to Flutter of a Drone Aircraft," *AIAA Structures, Structural Dynamics and Materials Conference*, Atlanta GA, AIAA-81-0652, April 1981.
- [2] M.J. Brenner, *Aeroservoelastic Modeling and Validation of a Thrust-Vectoring F/A-18 Aircraft*, NASA TP-3647, September 1996.
- [3] M.J. Brenner and E. Feron, "Wavelet Analysis of F/A-18 Aeroelastic and Aeroservoelastic Flight Test Data," *AIAA Structures, Structural Dynamics, and Materials Conference*, AIAA 97-1216 and NASA TM-4793, April 1997.
- [4] M. Brenner and R. Lind, "Wavelet-Processed Flight Data for Robust Aeroservoelastic Stability Margins," *Journal of Guidance, Control, and Dynamics*, Vol. 21, No. 6, November-December 1998, pp. 823-829.
- [5] M. Brenner and R. Lind, "On-Line Aeroelastic Robust Stability Prediction using Wavelet Filtering," *21st Congress of the International Council of Aeronautical Sciences*, Melbourne, Australia, ICAS-98-4.9.1, September 1998.
- [6] E. Dowell, "Nonlinear Aeroelasticity," *AIAA Structures, Structural Dynamics, and Materials Conference*, Long Beach CA, April 1990, AIAA-90-1031, pp. 1497-1509.
- [7] E. Feron, M. Brenner, J. Paduano and A. Turevskiy, "Time-Frequency Analysis for Transfer Function Estimation and Application to Flutter Clearance," *Journal of Guidance, Control, and Dynamics*, Vol. 21, No. 3, May-June 1998, pp. 375-382.
- [8] L. Freudinger, R. Lind and M. Brenner, "Correlation Filtering of Modal Dynamics using the Laplace Wavelet," *International Modal Analysis Conference*, Santa Barbara, CA, February 1998, pp. 868-877.
- [9] G. Gilyard and J. Edwards, *Real-time Flutter Analysis of an Active Flutter Suppression System on a Remotely Piloted Research Aircraft*, NASA-TM-84901, January 1983.
- [10] T. Kailath, *Linear Systems*, Prentice-Hall, Englewood Cliffs, NJ, 1980.
- [11] M.W. Kehoe, "A Historical Overview of Flight Flutter Testing," *Proceedings of the 80th AGARD Structures and Materials Panel*, AGARD-CP-566, Rotterdam, The Netherlands, May 8-10 1995, pp. 1-15.
- [12] R. Lind and M. Brenner, *Robust Aeroservoelastic Stability Analysis*, Springer-Verlag, London, March 1999.
- [13] R. Lind and M. Brenner, "Incorporating Flight Data into a Robust Aeroelastic Model," *Journal of Aircraft*, Vol. 35, No. 3, May-June 1998, pp. 470-477.
- [14] R. Lind and M. Brenner, "Robust Flutter Margins of an F/A-18 Aircraft from Aeroelastic Flight Data," *Journal of Guidance, Control, and Dynamics*, Vol. 20, No. 3, May-June 1997, pp. 597-604.
- [15] R. Lind, M. Brenner and L. Freudinger, "Improved Flight Test Procedures for Flutter Clearance," *International Forum on Aeroelasticity and Structural Dynamics*, Rome, Italy, June 1997, Volume 3, pp. 291-298.
- [16] R. Lind, K. Snyder and M. Brenner, "Investigating Transient and Limit Cycle Behaviors of a Nonlinear Structure by Wavelet Transforms," *AIAA Structures, Structural Dynamics, and Materials Conference* Long Beach, CA, AIAA-98-1808, April 1998.
- [17] R. Lind, K. Snyder and M. Brenner, "Wavelet Analysis to Characterize Nonlinearities and Predict Limit Cycles of an Aeroelastic System," *Mechanical Systems and Signal Processing*, accepted for publication.
- [18] R. Lind and M. Brenner, "Analyzing Aeroservoelastic Stability Margins Using the μ Method," *AIAA Structures, Structural Dynamics, and Materials Conference*, Long Beach, CA, AIAA-98-1895, April 1998.
- [19] T. O'Neil and T. Strganac, "Investigations of Aeroelastic Response for a System with Continuous Structural Nonlinearities," *AIAA Structures, Structural Dynamics, and Materials Conference*, Salt Lake City UH, April 1996, AIAA-96-1390.
- [20] A.K. Packard and J.C. Doyle, "The Complex Structured Singular Value," *Automatica*, Vol. 29, No. 1, 1993, pp. 71-109.
- [21] J.W. Pahle, B. Powers, V. Regenie, V. Chacon, S. Degroote and S. Murnyack, *Research Flight Control Development for the F-18 High-Alpha Research Vehicle*, NASA TM-104232, 1991.
- [22] M. Ruzzene, A. Fasana, L. Garibaldi, and B. Piombo, "Natural Frequencies and Dampings Identification using Wavelet Transform: Application to Real Data," *Mechanical Systems and Signal Processing*, Vol. 11, No. 2, 1997, pp. 207-218.
- [23] W.J. Staszewski, "Identification of Nonlinear Systems using Multi-Scale Ridges and Skeletons of the Wavelet Transform," *Journal of Sound and Vibration*, Vol. 214, No. 4, 1998, pp. 639-658.
- [24] G. Strang and T. Nguyen, *Wavelets and Filter Banks*, Wellesley-Cambridge Press, 1996.
- [25] J. Thompson and H. Stewart, *Nonlinear Dynamics and Chaos*, John Wiley and Sons, Chichester England, 1986.
- [26] S. Wiggins, *Introduction to Applied Nonlinear Dynamical Systems and Chaos*, Springer-Verlag, New York NY, 1990.

AERODYNAMIC AND AEROELASTIC INSIGHTS USING EIGENANALYSIS

Jennifer Heeg *

NASA Langley Research Center
Hampton, Virginia

534-64

Earl H. Dowell §

Duke University
Durham, North Carolina

ABSTRACT

This paper presents novel analytical results for eigenvalues and eigenvectors produced using discrete time aerodynamic and aeroelastic models. An unsteady, incompressible vortex lattice aerodynamic model is formulated in discrete time; the importance of several modeling parameters is examined. A detailed study is made of the behavior of the aerodynamic eigenvalues both in discrete and continuous time. The aerodynamic model is then incorporated into aeroelastic equations of motion. Eigenanalyses of the coupled equations produce stability results and modal characteristics which are valid for critical and non-critical velocities. Insight into the modeling and physics associated with aeroelastic system behavior is gained by examining both the eigenvalues and the eigenvectors. Potential pitfalls in discrete time model construction and analysis are examined.

INTRODUCTION

A standard procedure for solving a structural dynamic problem is to employ eigenanalysis to calculate the structural dynamic eigenvalues and eigenmodes. Recently, this procedure has been extended to unsteady aerodynamics, and to coupled aeroelastic equations^{1,2}.

Because applying eigenmode analysis to aerodynamic and aeroelastic systems is fairly new, there are many modeling issues that may not be familiar to the analyst. The intent of this paper is to discuss several of the many issues which are

associated with these new aeroelastic techniques. To accomplish this, we analyze relatively simple fluid dynamics and aeroelastic models using discrete time techniques and eigenmode analysis.

In computational fluid dynamics, CFD, there are two approximations that are typically employed. One is the construction of a computational grid, which determines the limits of spatial resolution of the computational model. The second is the approximation of an infinite fluid domain by a finite domain. It is a principal purpose of the present discussion to demonstrate that the computational grid not only determines the spatial resolution obtainable by the CFD model, but also the frequency or temporal resolution that can be obtained. Also, as will be shown, the finiteness of the computational domain determines the resolution of the eigenvalue distribution for a CFD model. Both of these observations have important ramifications for assessing the CFD model and its ability to provide an adequate approximation to the original fluid model on which it is founded. To these ends, a finite-wake, time-domain, discretized vortex lattice aerodynamic model has been utilized.

This paper presents results of aerodynamic parametric variations. A detailed discussion of the trends produced by these systematic variations will be presented. The discussion includes the effects on both the discrete- and continuous-time eigenvalues. These studies give new insights into aerodynamic modeling in the discrete time domain including how one may construct reduced order aerodynamic models.

The aerodynamic model was also combined with time-domain discretized structural dynamic equations to examine the aeroelastic behavior of a typical section. Aeroelastic analyses are also discussed in terms of eigenanalysis results. Aeroelastic stability analyses generally focus on the migration of the eigenvalues as a function of the velocity or other flow parameter. Indeed, much flutter analysis in practice today uses at best only an approximation to the true aeroelastic eigenvalues³⁻⁷. Here, the true eigenvalues are found for all aeroelastic

*Aerospace Eng., Aeroelasticity Branch

§Professor, Dept of Mechanical Engr and Matl Sci; Dean, School

of Engineering; Fellow AIAA

Copyright © 1999 by the American Institute of Aeronautics and Astronautics, Inc. No copyright is asserted in the United States under Title 17, U.S. Code. The U.S. Government has a royalty-free license to exercise all rights under the copyright claimed herein for Governmental Purposes. All other rights are reserved by the copyright owner.

modes without iteration. Also in this study, the characteristics of the eigenvectors are examined as the aeroelastic system becomes unstable.

AERODYNAMIC STUDIES

Aerodynamic Modeling

A Vortex Lattice solution to Laplace's equation for incompressible two-dimensional flow is utilized in this study. We consider the flow over an airfoil with a certain number of vortex elements on the airfoil and in the wake. The airfoil is modeled as a 2-dimensional flat plate. The airfoil and the wake are divided into segments, referred to as aerodynamic elements. Vortex lattice aerodynamics are generated by placing vortices of strengths to be determined at points on the airfoil and in the wake. Collocation or control points, usually located aft of the vortex locations, are points where the boundary conditions must be satisfied. Typical placement is for the vortices to be located at the $\frac{1}{4}$ -chord points of the aerodynamic elements. The collocation points are typically placed at the $\frac{3}{4}$ -chord locations of the elements.

The governing equations are presented by Hall in reference 1; they are briefly summarized here. There are 3 basic relationships, detailed in the following paragraph, which are combined to form the matrix equation

$$[A]\{\Gamma\}^{n+1} + [B]\{\Gamma\}^n = \{w\}^{n+1} \quad (\text{Eqn.1})$$

where n and $n+1$ denote the current and the next discrete time sample. Γ is a vector of vorticities and w is a vector of downwashes at each of the collocation points. The number of elements on the wing is denoted M , while the total number of elements is denoted N .

Three basic relationships determine the contents of the A and B matrices seen in Equation 1. These represent N equations with N variables. The first of the three basic relationships equates the velocity induced by the discrete vortices at the collocation points to the downwash caused by the airfoil's motion. This relationship accounts for M rows within equation 1. Applying Kelvin's theorem generates a second basic relationship utilized in deriving equation 1. Quoting Hall, "unsteady vorticity is shed into the wake; its strength is proportional to the time rate of change of circulation about the airfoil. ... The time step is taken to be equal to the time it takes the vorticity to convect from one vortex station to the next." This relationship accounts for the $(M+1)$ row of equation 1. Once the vorticity has been shed into the wake, it is convected in the wake at the freestream velocity. This is the

third basic relationship and appears in equation 1 in rows $(M+2)$ through $(N-1)$. Vorticity convection also provides the final, N th, row of equation 1. Because the wake is modeled with a finite length, the last vortex element must be treated specially. "Otherwise, the starting vortex would disappear abruptly when it reached the end of the computational wake, producing a discontinuous change in the induced wash at the airfoil. To alleviate this difficulty, ... the vorticity is allowed to dissipate smoothly by using a relaxation factor," wrote Hall¹.

The formulation and analysis of the aerodynamic model progresses in the following manner. Discrete, time-marching equations are written, equation 1. Once these equations are written, they inherently contain the approximations of the finite wake and the discretization. A discrete Fourier transformation is performed on the unforced equations, producing the z -plane representation, eqn 2.

$$z\Gamma_0 = (-A^{-1}B)\Gamma_0 \quad (\text{Eqn.2})$$

The discrete time eigenvalues, z , and the eigenvectors, Γ_0 , are extracted from these equations to determine system stability. These eigenvalues are then converted to the continuous time domain, λ -plane, through a zero order hold transformation, equation 3.

$$\lambda = \frac{\log(z)}{\Delta t} \quad (\text{Eqn.3})$$

Baseline Configuration

As the first of several numerical examples, we consider the flow over an airfoil with 20 vortex elements on the airfoil and 180 elements in the wake, equally spaced. This will be referred to as the baseline case. The (finite) length of the wake thus extends 9 chord lengths. The eigenvalues and eigenmodes of the flow can be computed by established methods¹. Because there are 200 elements in the model, 200 eigenvalues result.

The discrete time (z -plane) eigenvalues, extracted from equation 2, approximately form a circle centered at the origin, as shown in figure 1. In addition to these eigenvalues, there are a finite number of eigenvalues at the origin. The number of eigenvalues at the origin is equal to the number of segments or grid points on the airfoil. This conclusion follows from examining the rank of the system matrices in equation 1, from the numerical results obtained here, and appears to be supported by the results presented in reference 1, though it was not noted in this previous work. Eigenvalues at the origin in the discrete time domain transform to negative infinity in the continuous time domain.

The continuous time eigenvalue distribution for the baseline case is shown in figure 2. The real part of the eigenvalue is indicative of the damping and the imaginary part is the damped frequency of each fluid eigenmode. Examining the eigenvalues of the aerodynamic matrix in the continuous domain produces several observations. The continuous domain eigenvalues are discretely spaced and are arranged in "arms" that emanate from the origin and reach up and down in the left half plane. Additionally, the real parts of the arms asymptotically approach a limiting value.

The presence of aerodynamic damping is evidenced by the arms lying in the left half plane. The primary contribution to the damping appears to lie with the overall flow field, however, there is additional damping due to the presence of a vorticity relaxation factor at the last wake element. The relaxation factor used in the vortex lattice model provides energy dissipation in the wake; as the relaxation factor is decreased, more energy is dissipated and the aerodynamic damping increases. If the number of aerodynamic boxes within the wake is increased, the last box will be a smaller percentage of the total wake length and thus, the influence of the relaxation factor will be diminished.

Parametric Variations

Three aspects of the aerodynamic modeling significantly impact the eigenvalue distribution: the size of the aerodynamic elements, the number of these elements that lie in the wake, and the length of the wake. The three aerodynamic configurations, detailed in table 1, compared against each other two at a time, produce the three comparison cases, which are organized in table 2 and discussed next. The three comparison cases are discussed in terms of their discrete time eigenvalue distributions (z -values), their discrete-to-continuous time domain transformations (z -transformations) and their continuous time eigenvalue distributions (λ -values).

Comparison case I compares aerodynamic configurations 2 and 3, examining the effects of varying the size of the aerodynamic elements while maintaining the number of elements which lie in the wake. Because the number of wake elements remains fixed, configuration #2 has a wake that is twice the length of the wake in configuration #3 and elements which are twice as large. Although not shown, the discrete time eigenvalue patterns for configurations 2 and 3 are identical because the number of elements in each wake is identical. However, changing the size of the aerodynamic elements changes the

transformation, which must be applied to convert the discrete time system to continuous time. This difference in transformation produces the change in continuous domain eigenvalues, as illustrated in figure 3.

It is easily shown that the frequency of each eigenvalue scales linearly with the aerodynamic element size. The maximum frequency of the arms can be determined a priori by utilizing Shannon's sampling theorem⁸. The aerodynamic eigenfrequencies are bounded from discrete time considerations similar to those that predetermine the discrete Fourier transform frequencies^{8,9}. The maximum frequency, ω , that can be resolved would have 1 cycle spanning two adjacent aerodynamic panels. Using the velocity, U , to relate the spatial, Δx , and temporal, Δt , sample sizes leads to

$$\max(\omega) = \frac{\pi U}{\Delta x} \quad (\text{Eqn.4})$$

Thus, changing the aerodynamic element size changes the frequencies of the aerodynamic eigenvalues. As the size of the elements becomes infinitesimal, we speculate that the eigenvalue arms will cover the frequency range from +/- infinity.

It should be noted in studying Case I that the number of eigenvalues has remained constant in going from configuration 2 to configuration 3, while the frequency range has doubled. Thus, the density of the eigenvalues has halved. The implications of this will be further discussed in studying Case III.

Comparison case II compares aerodynamic configurations 1 and 2 and examines the effect of varying the number of aerodynamic elements in the wake while holding their size constant. The number of aerodynamic elements in the wake determines the number of discrete time eigenvalues comprising the pseudo-circular pattern. As more elements are placed in the wake, the more crowded pattern expands outward towards the unit circle. As the element size decreases, the radius of the pseudo-circular pattern asymptotically approaches 1. In discrete time eigenvalue analysis, an eigenvalue lying on the unit circle represents a neutrally stable system. In the continuous time domain, the imaginary axis is the line of demarcation for stability. It is thus anticipated that the additional boxes in the wake force the "arms" of the continuous time eigenvalues closer to the imaginary axis. Figure 4 bears this out. As more elements are added to the wake, the closer the aerodynamic roots get to those associated with simple harmonic motion. Thus, changing the number of aerodynamic elements in the wake changes the damping of the aerodynamic eigenvalues. As the number of elements goes to infinity, we speculate that the arms will move to the imaginary axis.

It should be noted in studying Case II, as the wake length is increased, leaving the size of the aerodynamic elements constant, the frequency range of the continuous time eigenvalues remains constant. Doubling the number of elements in the doubles the number of eigenvalues on the "arms." Twice as many eigenvalues reside in arms of the same length. Hence, the continuous time eigenvalue distribution has become denser.

Comparison case III compares aerodynamic configurations 1 and 3 and examines the effects of varying simultaneously and in inverse proportion, the number and length of aerodynamic elements in the wake, such that the wake length remains constant. The expected trends for the behavior of the arms of the continuous time eigenvalues are difficult to predict because, in going from configuration 1 to configuration 3 there are multiple tendencies: increasing the number of elements tends to move the arms closer to the imaginary axis; decreasing element size tends to extend the frequency range of the arms. The combined result on the continuous time eigenvalues, shown in Figure 5, is that the arms of the eigenvalues lie approximately the same distance from the imaginary axis, while the frequency range of configuration 3 is twice that of configuration 1. This corresponds to the effects of smaller element size of configuration 3. Thus, the spacing of the eigenvalues is approximately constant between the two analysis runs.

An approximate formula for eigenvalue spacing is derived using the frequency range and the number of eigenvalues. The maximum frequency was found using equation 4. Accounting for positive and negative values, the frequency range is twice this. Dividing this range by the number of elements or eigenvalues in the wake, and recognizing that the element size times the number of elements in the wake is the wake length, L_{wake} , produces the relationship

$$\Delta\omega = \frac{2\pi U}{L_{wake}} \quad (Eqn.5)$$

The reader may recognize that this is similar to determination of the discrete Fourier transformation frequencies, as determined by the length of the time record. The eigenvalue spacing is approximate due to the eigenvalues not lying on the imaginary axis, that is, due to the discretization-induced damping. For the case of the element size becoming infinitesimally small, the formula is exact.

Thus, the effect of the finite wake is to produce discretely spaced eigenvalues, instead of a continuous line. As the wake length becomes infinite, we speculate that the arms of discretely spaced eigenvalues form continuous lines emanating from the origin.

Discussion

The study of aerodynamic eigenvalues using the vortex lattice code has led to some basic ideas. The eigenvalues have been shown to be artifacts of the discretization and the finite length wake.

The effects of discretization are controlled by two independent factors. The size of the elements determines the range of frequencies covered by the eigenvalues, while the number of elements in the wake drives the damping. Their effects are shown to be independent, as one controls the transformation from discrete to continuous time, and the other controls the discrete time eigenvalue pattern. The effect of the finite wake is to produce discretely spaced eigenvalues, instead of a continuous line.

We offer the following speculations regarding the limiting cases. As the size of the elements becomes infinitesimal, the eigenvalue arms will cover the frequency range from +/- infinity. As the number of elements goes to infinity, the arms will move to the imaginary axis. As the wake length becomes infinite, the arms of discretely spaced eigenvalues form continuous lines emanating from the origin.

AEROELASTIC STUDIES

With the ability to model aerodynamic eigenmodes as well as structural modes, we now have the capability to investigate the coupled fluid/structural modes or aeroelastic modes. We study these in this section of the paper and thereby gain additional insight into the behavior of such system. One intriguing finding, previously foreshadowed in the literature, is that the critical mode may originate in an aerodynamic mode rather than a structural mode.

Aeroelastic Modeling

The discrete time aerodynamic model can be coupled with a discretized structural dynamic model to produce the following time-marching aeroelastic equations of motion ¹ which can then be analyzed to determine the behavior of the system

$$D_2 q^{n+1} + D_1 q^n - f^{n+1} = 0 \quad (Eqn.6)$$

where the vector q contains the structural dynamic degrees of freedom, the vector f represents the

aerodynamic loads and the matrices D_1 and D_2 describe the structural dynamic behavior of the typical section.

The coupling between the aerodynamic and the structural dynamic quantities is present in an aeroelastic system because the vorticity distribution results in the aerodynamic loads, f , which can be expressed in terms of the vorticities, Γ .

$$f^{n+1} = C_2 \Gamma^{n+1} + C_1 \Gamma^n \quad (\text{Eqn.7})$$

For an unforced response, the downwash on the airfoil, w , is produced by the motion of the airfoil.

$$w^n = Eq^n \quad (\text{Eqn.8})$$

Combining equations 1, 6, 7, and 8 produces the unforced aeroelastic system equations.

$$\begin{bmatrix} D_2 & C_2 \\ -E & A \end{bmatrix} \begin{Bmatrix} q \\ \Gamma \end{Bmatrix}^{n+1} + \begin{bmatrix} D_1 & C_1 \\ 0 & B \end{bmatrix} \begin{Bmatrix} q \\ \Gamma \end{Bmatrix}^n = \begin{Bmatrix} 0 \\ 0 \end{Bmatrix} \quad (\text{Eqn.9})$$

Aeroelastic Configuration

A typical section with only a single pitch degree of freedom, figure 6, is analyzed in this paper. For these analyses, 10 aerodynamic elements were placed on the wing; 90 aerodynamic elements were placed in the wake. The structural parameters are given in Table 3.

The stability of this system was analyzed by calculating the equations of motion for a series of reduced velocities. Reduced velocity, V , is defined as the velocity, U , normalized by the pitch frequency and semi-chord. Eigenanalyses of the discrete time systems were performed on each set of equations and the system eigenvalues tracked. The eigenvalues were transformed into the continuous time domain using a zero order hold transformation. Stability can be inferred from either the discrete or the continuous time root locus- both are examined here.

Discrete Time Eigenvalues - The discrete time root locus is presented in figure 7; only the portion of the complex plane near the unit circle's intersection with the real axis is shown. The coupled pitch mode-originating eigenvalue and the aerodynamic-originating eigenvalues, referred to as the aeroelastic eigenvalues, migrate as the reduced velocity is increased. The single structural dynamic eigenvalue can be seen near the unit circle, indicating that it is more lightly damped than the aerodynamic eigenvalues.

An instability occurs when an eigenvalue lies outside the unit circle. For this system, the instability is observed by examining the real aerodynamic-originating eigenvalues on the positive real axis. Figure 7 shows the migration of the structural-dynamic-originating eigenvalue, and also the interplay with several aerodynamic eigenvalues. The lowest complex aerodynamic eigenvalue is clearly influenced, as well as the real aerodynamic eigenvalues, one of which destabilizes. It is difficult to further study system behavior from these graphs because each velocity produces eigenvalues that essentially belong in different z-planes. This will be discussed in detail in a subsequent section of this paper. For a more intuitive interpretation, we turn now to the continuous domain eigenvalues for this aerodynamic model.

Continuous Time Eigenvalues - The systems are converted to the continuous domain by zero order hold transformations. The behavior of the continuous time domain eigenvalues is shown in figure 8. For clarity, only the region near the origin is presented. The influence of velocity on the aerodynamic eigenvalues is now evident. As velocity increases, the eigenvalues' frequencies increase at constant damping. This particular configuration destabilizes at zero frequency, termed divergence. In figure 8, the eigenvalues at the divergence velocity, $V=2.3$, are indicated by square symbols.

It is interesting to note that the eigenvalue of the pitch mode does not go to zero as divergence occurs. The pitch mode eigenvalue maintains a non-zero frequency as the system destabilizes, as one of the real aerodynamic roots migrates into the right half plane. This is contrary to conventional wisdom regarding divergence, although several similar phenomena have been reported by Dashcund¹⁰, Edwards¹¹, Rodden and Stahl¹², and Rodden and Bellinger¹³. The mechanism responsible for the divergence of this configuration appears to have its origin in the aerodynamic terms. Further work is planned to determine the physical and mathematical significance of this discovery.

Modal Participation - Often neglected when interpreting the results of an eigenanalysis, the eigenvectors provide much interesting information. Afolabi, Pidaparti and Yang¹⁴ studied aeroelastic stability from the standpoint of system eigenvectors. In their work, they discuss the orthogonality between eigenvectors associated with the different modes of the system. The approach taken in the current work is to examine the eigenvectors associated with individual modes. The eigenvector associated with a particular eigenvalue can be viewed as the set of modal participation factors for each degree of freedom. Note

that the eigenvectors are invariant under the transformation from discrete to continuous time domain.

In a numerically stiff set of ordinary differential equations¹⁵, the system behavior is seen to be dominated by the lightly damped and unstable modes. The disparity in the time scales of components of the system allows the overall behavior to be studied by observing only a few eigenmodes of the system. Thus, in studying the system behavior, only the modal participation factors associated with the least stable dynamic mode and with the least stable static mode were examined. Here, the complex mode corresponds to the one that originated as the structural pitch mode, and the real mode corresponds to an eigenvalue that originated in the aerodynamics.

Vorticity Associated with the Pitch Mode-

The modal participation at a low reduced velocity, $V=0.2$, is presented for the mode which is primarily the pitch degree of freedom, figure 9. The corresponding eigenvalue is identified in figure 8 by the diamond symbol. For clarity, only the real part of the modal participation is plotted as a function of chord-wise or downstream position. At this low velocity, the aerodynamics are being driven at the frequency of the structural mode. The portion of the eigenvector associated with the vorticity at each aerodynamic control point, referred to as the vorticity participation, shows that most of the aerodynamic energy associated with this mode is in the wake. The first ten participation factors correspond to elements on the airfoil. Only these vorticities can produce forces on the airfoil. At this velocity, there is very little aerodynamic energy being imparted to the airfoil.

The wake portion of the vorticity participation appears as a negatively damped sinusoid when viewed spatially, as in figure 9. The eigenvector provides a snapshot of the vorticity distribution. Initial examination of the data in figure 9 may lead one to conclude that the system is unstable. In fact, the opposite is indicated. For a stable system, the vorticity being shed from the wing into the wake will decrease as time advances. The vorticity on the last wake element at time n is the same as the vorticity on the first wake element at time $n-N_{\text{wake}}$. Thus, the spatial vorticity distribution could also be thought of as a time history, where time originates at the wake trailing edge and proceeds towards the airfoil.

Near the divergence reduced velocity, the eigenvector associated with the structural-dynamic-originating

mode contains significant participation from both the structural dynamic and the aerodynamic states. Figure 10 shows the vorticity participation spatially for a velocity just below divergence, $V=2.3$. The number of oscillations to be expected in the wake, N_{cycles} , can be estimated using the frequency of the associated eigenvalue, ω_{mode} , the reduced velocity, V , and the discretization, N_{wake} and M :

$$N_{\text{cycles}} = \frac{\omega_{\text{mode}} N_{\text{wake}}}{\omega_a M \pi V} \quad (\text{Eqn.10})$$

Using the values for the divergence condition results in a prediction of 0.8 oscillations; the vorticity participation in figure 10 therefore looks reasonable.

Vorticity Associated with the Real Aerodynamic Mode-

The aeroelastic system studied destabilizes as a real eigenvalue moves into the right half plane. It is interesting to examine the progression of the characteristics of this mode as the reduced velocity increases. Regardless of reduced velocity, the associated vorticity participation factor resembles a pressure coefficient distribution on the airfoil elements, while the wake contains almost no participation except for the last element. The vorticity participation factor at an example reduced velocity, $V=2.3$, is presented in figure 11. As the reduced velocity changes, it is the participation of the last wake element which is interesting. The magnitude of this term is plotted versus reduced velocity in figure 12. As this plot is examined, note that these eigenvectors have an overall magnitude of 1. Initially, nearly all of the vorticity participation resides in the last element of the wake. Just prior to divergence, the participation drops sharply. At the divergence velocity, all of the vorticity participation is on the airfoil; the wake factors are zero. As the system moves beyond the divergence velocity, the behavior of all of the vorticity participation factors change. The last wake element quickly becomes influential again, but now with vorticity that is negative, or out of phase, with the airfoil vorticity. As velocity is further increased, the participation of the last wake element smoothly, asymptotically, approaches zero. Also beyond divergence the overall wake vorticity participates.

Transition from stability to instability produces dramatic changes in the associated eigenvector. While the eigenvalue smoothly traverses across the imaginary axis, the character of the vorticity participation changes sharply. Future work will focus on understanding the nature of this instability through examination of the eigenvectors.

Computational Issues for Simultaneous Solution of Aerodynamic and Structural Equations

Transformation Compatibility - To incorporate the discrete time aerodynamic model into aeroelastic equations, the structural dynamic model must be cast in discrete time also. The structural dynamic equations contain first and second derivatives that could be approximated using a central difference technique. While this is convenient and easy, this method results in a mismatch of discrete time transformations. Central differencing produces discrete time equations to which a first order Tustin transformation⁹

$$\lambda = \frac{2(z-1)}{\Delta t(z+1)} \quad (\text{Eqn.11})$$

must be applied to obtain the proper continuous time results. The Tustin transformation is equivalent to the first term in a series expansion of the zero order hold transformation presented in equation 3. In these transformations, the sample interval, Δt , establishes the relationship between the discrete time eigenvalues, z , and the continuous time eigenvalues, λ . The aerodynamic equations which were generated with a zero order hold discretization, are solved simultaneously with the discretized structural dynamic equations. Thus, it is desirable to have structural dynamic equations that would also be correct when a zero order hold transformation is applied. This is easily accomplished through standard discretization techniques⁹. Accepting the mismatch in the transformations results in a phenomenon that resembles aliasing. However, as the time step becomes small, the zero order hold transform and the Tustin transform become approximately equivalent.

Aliasing - The equations have been constructed in the discrete time domain. Given data at discrete times, we can utilize a transformation to approximate the response in continuous time. There are limitations to discrete time transformation methods; aliasing is the primary concern^{8, 9}. To avoid aliasing, a continuous time signal must have 2 samples per period of period of the highest frequency to be resolved. The aerodynamic equations arose from the fundamental concept of vorticity being convected downstream at a velocity, U . The equations are valid only if the relationship $U=\Delta x/\Delta t$ is maintained. It is thus observed that the minimum velocity, at which the system may be accurately analyzed, is set by the spatial discretization and the maximum frequency that is important to the problem. Another interpretation is that for frequency and

velocity ranges of interest, the minimum number of aerodynamic elements required to avoid aliasing can be approximated. This can serve as a guideline in selecting the spatial discretization required for a given problem. There are additional implications of the discrete time effects when the aerodynamic equations are combined with the structural dynamic equations or control laws.

Methods of Stability Analysis - The aeroelastic stability analyses, which require variation of the velocity, were performed using a single spatial aerodynamic discretization. This was accomplished by adjusting the temporal discretization to produce the proper velocities. There are several complications in performing the analyses in this manner: (1) a separate transformation rule must be applied for each velocity; and (2) interpreting the discrete time eigenvalues is not intuitive. The aerodynamic matrices were unchanging for different velocities, but the matrices which couple them to the structural dynamics were not. The resulting aeroelastic eigenvalues change with each velocity. The migration of the eigenvalues in the discrete time domain is not due solely to the velocity change, but to a combination of velocity and sample rate change.

A brief study was conducted to look at the results when a consistent sample rate was utilized, meaning that as the velocity changed, the spatial discretization changed. This required constructing a new aerodynamic model at each velocity. There was negligible effect on the continuous time eigenvalues. The discrete time eigenvalue pattern associated with the structural dynamic mode changed significantly. It was observed, however, that the discrete time eigenvalue pattern in this case is nearly identical to the pattern produced when the eigenvalues from the nominal analysis method are rediscretized using the consistent sample rate.

CONCLUDING REMARKS

Aerodynamic and aeroelastic eigenanalyses were performed utilizing a time-domain vortex lattice aerodynamic code, coupled with discretized structural dynamic equations. The study of aerodynamic eigenvalues using the vortex lattice code has led to some basic ideas. The eigenvalues have been shown to be artifacts of the discretization and the finite length wake. The effects of discretization are controlled by two independent factors. The number of elements in the wake drives the damping, while the size of the elements determines the range of frequencies covered by the eigenvalues. The effect of the finite wake is to produce discretely spaced eigenvalues, instead of a continuous line.

Aeroelastic analyses were performed to examine the stability and modal character as a function of reduced velocity. Insight into the modeling and physics associated with system behavior can be gained by examining the eigenvectors. A novel determination is that under some circumstances an eigenmode of aerodynamic origin can be the critical mode for aeroelastic instability.

REFERENCES

- 1 Hall, K.C, *Eigenanalysis of unsteady flows about airfoils, cascades and wings*, AIAA Journal Vol. 32, No. 12, December 1994
- 2 Dowell, E.H., Hall, K.C, and Romanowski, M.C., *Eigenmode analysis in unsteady aerodynamics: reduced order models*, Applied Mechanics Review Vol. 50, #6, p371-385, June 1997.
- 3 Hassig, H.J., *An approximate true damping solution of the flutter equation by determinant iteration*, Journal of Aircraft Vol. 8, No. 11, November 1971.
- 4 Rodden, W.P., and Bellinger, E.D, *Aerodynamic Lag Functions, Divergence, and the British Flutter Method*, Journal of Aircraft, Volume 19, Number 7, July 1982.
- 5 Rodden, W.P., Harder, R.L., and Bellinger, E.D, *Aeroelastic Addition to NASTRAN*, NASA Contractor Report 3094, 1979.
- 6 Bisplinghoff, R.E., Ashley, H., and Halfman, R.L., *Aeroelasticity*, Dover Publications, Mineola, New York, 1996 (copyright Addison-Wesley Publishing Company, 1955).
- 7 Dowell, E.H., Crawley, E.F., Curtis, H.C., Jr., Peters, D.A., Scanlan, R.H., and Sisto, F., *A modern course in aeroelasticity*, Kluwar Academic Publishers, Dordrecht, The Netherlands, 1995, 3rd edition.
- 8 Hardin, J.C., Introduction to Time Series Analysis, NASA Reference Publication 1145, p83-88, Nov 1990.
- 9 Oppenheim, A.V., and Shafer, R.W., *Discrete time signal processing*, Prentice Hall, Englewood Cliffs, New Jersey, 1989.
- 10 Dashcund, D.E., *The development of a theoretical and experimental model for the study of active suppression of wing flutter*, MAE Technical Report 1496T, Princeton University, December 1980.
- 11 Edwards, J.W., *Unsteady aerodynamic modeling and active aeroelastic control*, SUDAAR 504, Department of Aeronautics and Astronautics, Stanford University, February 1977.
- 12 Rodden, W.P., and Stahl, B., *A Strip Method for Prediction of Damping in Subsonic Wind Tunnel and Flight Flutter Tests*, Journal of Aircraft, Vol 6, No. 1 (Jan-Feb 1969).
- 13 Rodden, W.P., and Bellinger, E.D, *Unrestrained Aeroelastic divergence in a Dynamic Stability Analysis*, Journal of Aircraft, Volume 19, Number 9, September 1982
- 14 Afolabi, D, Pidaparti, R.M.V., and Yank, H.T.Y, *Flutter Prediction Using an Eigenvector Orientation Approach*, AIAA Journal Vol 36, No 1, January 1998.
- 15 Kincaid, D.R. and Cheney, E.W., *Numerical analysis: Mathematics of scientific computing*, p 556 Brooks/Cole Publishing Company, Pacific Grove, California, 1991.

Aero Config No.	Airfoil			Wake		
	No. of elements	Normalized element size	Normalized airfoil length	No. of elements	Normalized element size	Normalized wake length
1 (Baseline)	20	1	1	180	1	1
2	20	1	1	360	1	2
3	40	$\frac{1}{2}$	1	360	$\frac{1}{2}$	1

Table 1. Aerodynamic Configurations

Comparison Case No.	Aerodynamic Configurations Compared			Parametric Variation	Quantity Held Constant
	1	2	3		
I		✓	✓	Size of aerodynamic elements in wake	Number of aerodynamic elements in wake
II	✓	✓		Number of aerodynamic elements in wake	Size of aerodynamic elements in wake
III	✓		✓	Size and number of elements in wake	Length of wake

Table 2. Comparison Cases for Parametric Variations

Semi-chord, (b)	2.875 inches
Distance from midchord to elastic axis, Non-dimensionalized by semi-chord, (a)	-0.1304
Span, (S)	4 inches
Radius of Gyration,(r_α)	0.41
Mass ratio, (μ)	23.1
Pitch frequency, (ω_α)	50.2 radians/second
Distance from aerodynamic center to elastic axis, non-dimensionalized, (e/b)	0.37

Table 3. Structural Parameters of Typical Section

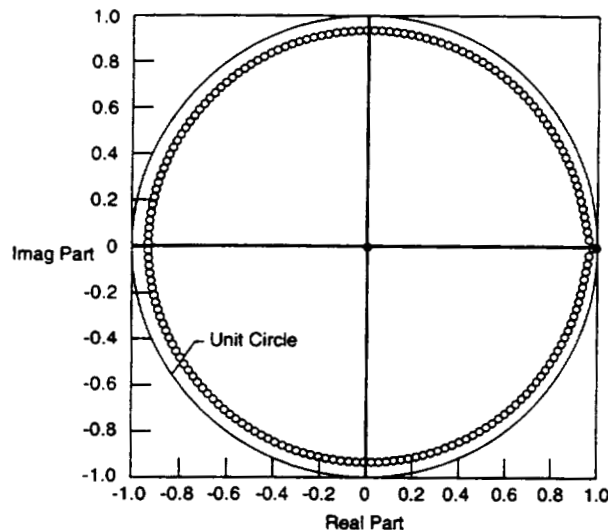


Figure 1 Eigenvalues for baseline case
Discrete time eigenvalues, z

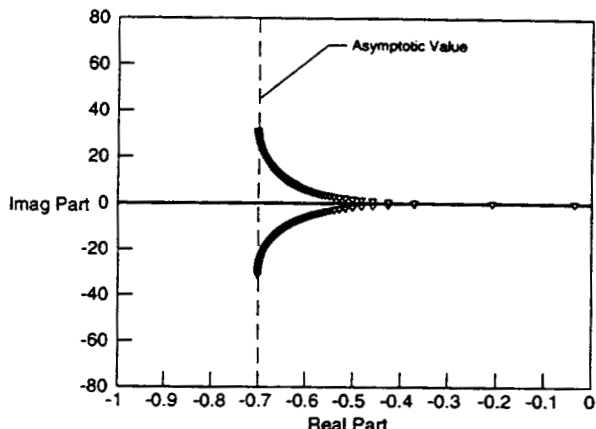


Figure 2 Eigenvalues for baseline case
Continuous time eigenvalues, l

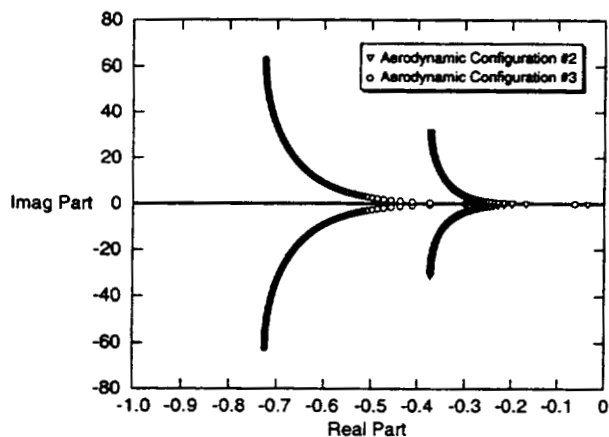


Figure 3 Case I: Influence of varying the size of the aerodynamic elements. Continuous time eigenvalues, l

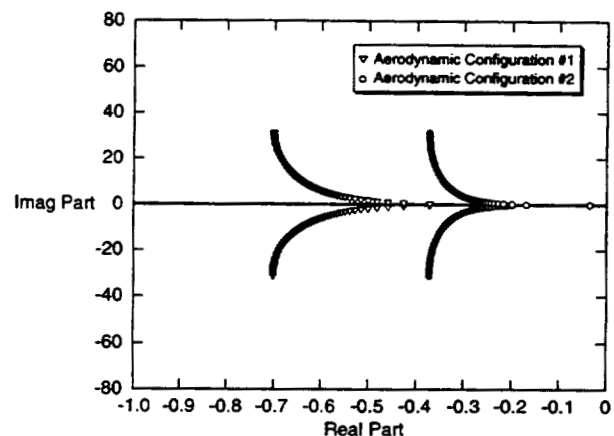


Figure 4 Case II: Influence of varying the number of aerodynamic elements in the wake.
Continuous time eigenvalues, l

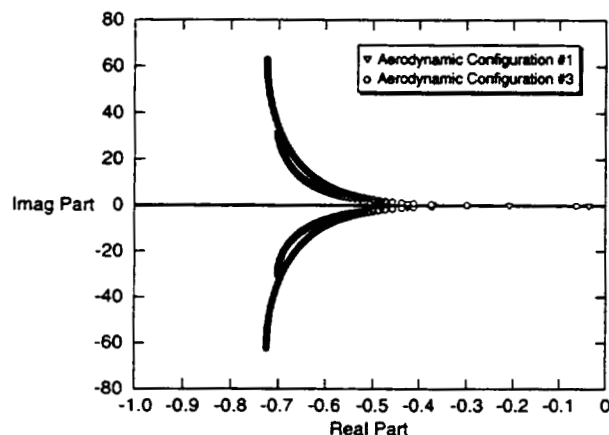


Figure 5 Case III: Influence of simultaneously varying the size and number of aerodynamic elements in the wake, maintaining a constant wake length.
Continuous time eigenvalues, l

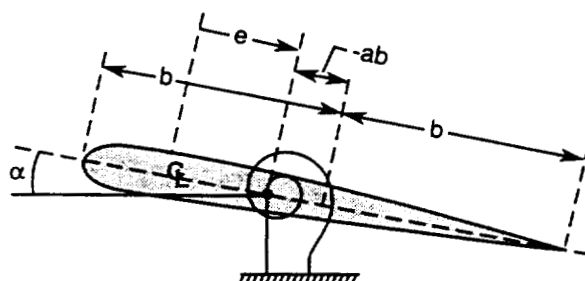


Figure 6 Typical section with pitch freedom.

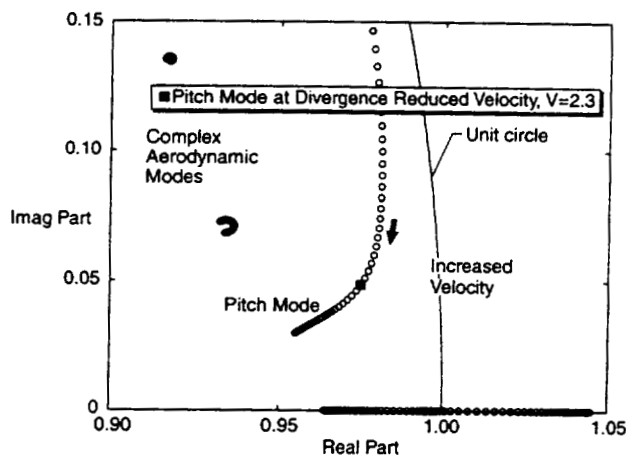


Figure 7 Discrete Time Aeroelastic Eigenvalues as Reduced Velocity is Varied

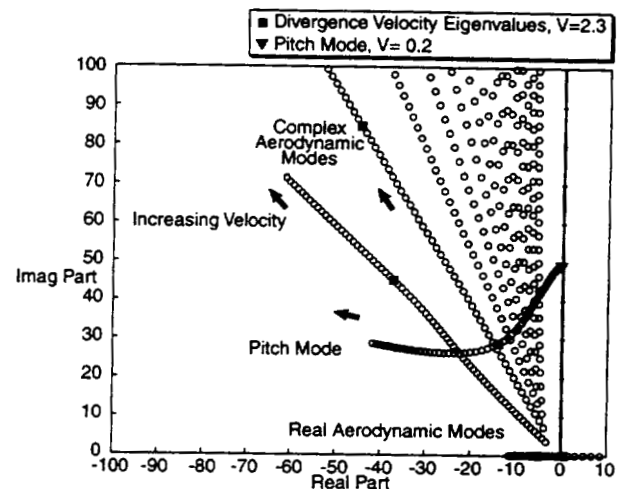


Figure 8 Continuous Time Aeroelastic Eigenvalues as Reduced Velocity is Varied

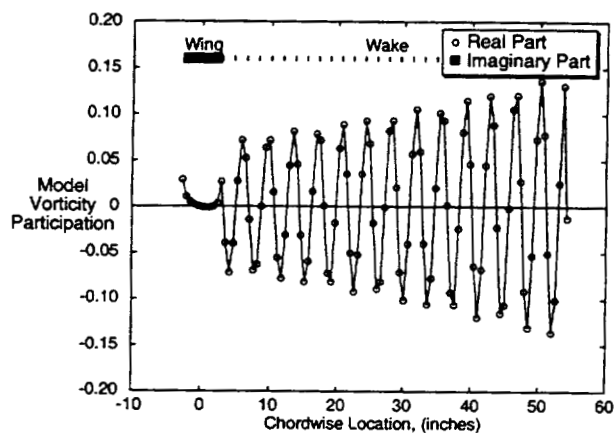


Figure 9 $V = 0.2$, Eigenvector associated with pitch originated mode, $\lambda = 0.40354 + j49.274$

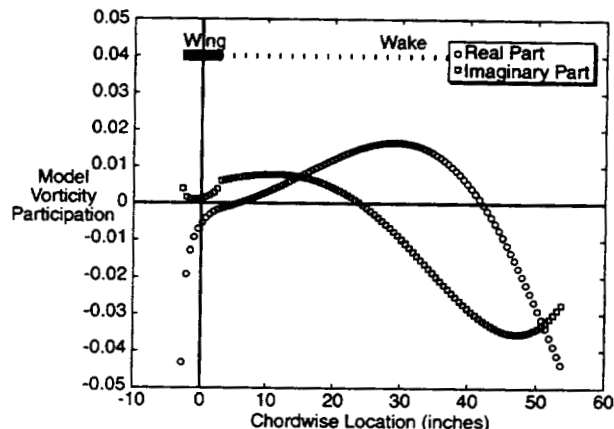


Figure 10 $V = 2.3$, Eigenvector associated with pitch originated mode, $\lambda = 13.9111 + j28.7958$

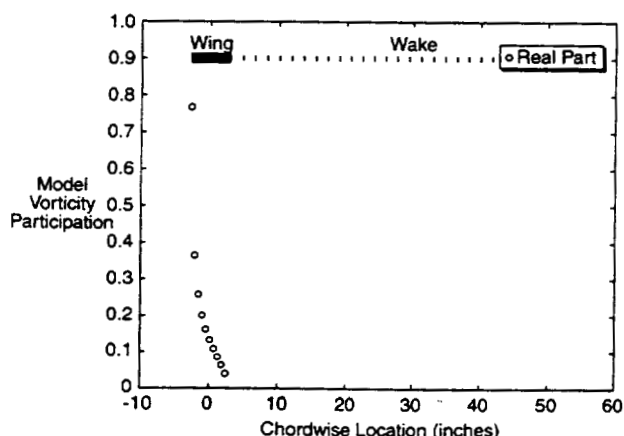


Figure 11 $V = 2.3$, Eigenvector associated with real aerodynamic modes, $\lambda = 0.43435 + jC$

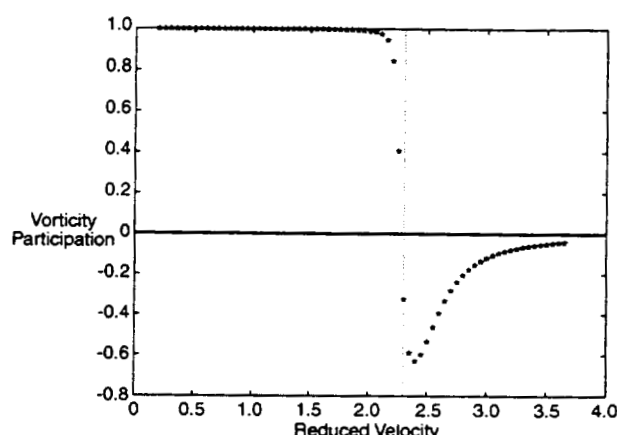


Figure 12 Vorticity participation of last wake element for real eigenvalue

INFLUENCE OF NONPLANAR SUPERSONIC INTERFERENCE ON AEROELASTIC CHARACTERISTICS

V. Kouzmin, S. Kouzmina, V. Mosounov, F. Ishmuratov

Central Aerohydrodynamic Institute (TsAGI),
Zhukovsky, Moscow Reg., Russia, 140160

Abstract. A new version of supersonic panel method for computing the generalized aerodynamic forces on nonplanar lifting surfaces is described. Integral equation relating the velocity potential and a unit value of pressure distribution has been used. A flexible improved numerical procedure has been developed for the achievement the high accuracy at different Mach numbers, reduced frequencies and panels dimensions. In practice proposed computer code has not restrictions for mentioned above parameters.

Applied for the computational flutter investigations a software package KC-2 includes unified computer code for analysis in subsonic and supersonic flow because of the basic data organization is the same in both cases.

Proposed method is illustrated by the flutter and static aeroelastic characteristics calculations for modern aircraft. The influence of nonplanar supersonic interference on obtained results is analyzed.

Nomenclature

x, y, z - orthogonal coordinates on the lifting surface, nondimensionalized with reference length l ,

x_0, y_0, z_0 - orthogonal nondimensional coordinates of a control point ,

$\xi = x_0 - x$
 $\eta = y_0 - y$
 $\zeta = z_0 - z$

$n = \{n_y, n_z\}$ - the direction cosines of the normal to the panel,

$n_0 = \{n_{y0}, n_{z0}\}$ - the direction cosines of the normal at the control point,

$$\begin{aligned} r^2 &= \eta^2 + \zeta^2, \\ \beta^2 &= M^2 - 1. \end{aligned}$$

$$R = \sqrt{\xi^2 - \beta^2 r^2}$$

M - Mach number,

$$k = \frac{\omega l}{V_\infty}$$

ω - circular frequency of harmonic motion,

V_∞ - freestream velocity,

l - reference length,

$$k' = \frac{kM}{\beta^2},$$

ΔC_p - nondimensional pressure coefficient.

1. Introduction

An accurate prediction of unsteady aerodynamic loads is very important problem for the flutter and aeroservoelasticity. Modern vehicle, as a rule, consists of few nonplanar lifting and control surfaces. It is necessary to take into account the interference between all such surfaces in solving the equation of the elastic aircraft vibration in flow. In TsAGI an original version of doublet-lattice method and based on it program module are used with success in static and dynamic aeroelasticity problems during more than 20 years [1]. The problem of creation a similar universal robust linear method for supersonic flow encountered with mathematical difficulties, though many different interesting important publications, concerning calculation of loads on nonplanar oscillating surfaces have arisen in last decade [2-7].

The purpose of this paper is to describe new version of panel method and to evaluate the capability of it to predict unsteady aerodynamic loads on interfering surfaces.

2. The main relations

The integral equation for the velocity potential at the arbitrary point due to a unit nondimensional pressure difference is used for the calculation of the downwash matrix coefficient [2,3]

$$\Phi(x_0, y_0, z_0) = -\frac{1}{2} \int_{\eta_L}^{\eta_U} \int_{\xi_L(\eta)}^{\xi_U(\eta)} \frac{\partial \Phi}{\partial n} d\xi d\eta, \quad (1)$$

where

$$P = \exp(-ik\xi) \int_{\beta}^{\xi} \exp\left(\frac{ik\xi'}{\beta^2}\right) \left[\frac{\cos(k'R')}{R'} \right] d\xi'. \quad (2)$$

The downwash at the control point is determined by the derivative [2,3]

$$w = \frac{\partial \Phi(x_0, y_0, z_0)}{\partial n_0} \quad (3)$$

$$w = \frac{1}{2} \left[(n \cdot n_0) \int_{\eta_L}^{\eta_U} \frac{F(\eta)}{r^2} d\eta + \int_{\eta_L}^{\eta_U} (n_y \eta + n_z \zeta)(n_{y0} \eta + n_{z0} \zeta) \frac{\frac{\partial F(\eta)}{\partial r} r - 2F(\eta)}{r^4} d\eta \right] \quad (4)$$

where

$$F(\eta) = \left[\frac{\exp(-ik'M\xi) \sin(k'R)}{k'} \right]_{\xi_L}^{\xi_U} + iM \int_{\xi_L}^{\xi_U} \exp(-ik'M\xi) \sin(k'R) d\xi + \\ + \frac{1}{2} \int_{\xi_L}^{\xi_U} \exp(-ik\xi) \left(\delta \left\{ \exp\left[-\frac{ik(\xi - MR)}{\beta^2}\right] - 1 \right\} + \left\{ 1 - \exp\left[-\frac{ik(\xi + MR)}{\beta^2}\right] \right\} + ik r S \right) d\xi, \quad (5)$$

$$S = \sum_{m=1}^8 a_m \left(\frac{\exp\left[\frac{-2^m b(\xi + MR)}{\beta^2 r} - \frac{ik(\xi + MR)}{\beta^2}\right] - 1}{D_1} + \delta \frac{1 - \exp\left[\frac{-2^m b|\xi - MR|}{\beta^2 r} - \frac{ik(\xi - MR)}{\beta^2}\right]}{D_2} \right),$$

$$\delta = \text{sign}(\xi - MR), D_1 = 2^m b + ik r, D_2 = \delta 2^m b + ik r.$$

3. Computational procedures

The most essential part of the described method is a computation of the normal velocity, which accuracy determines the precision of the determination of aerodynamic loads.

Numerical integration is performed by using Gaussian quadrature. Two types of Gaussian quadratures are applied in present method:

1) standard formula giving the exact integral values for functions $1, v, v^2, v^3, \dots$ on the interval $[0, 1]$,

2) formula, which can be received from standard formula by replacing the variables $v = \sin \tilde{v}$. In this case new knots and weights quantities are connected with the standard by the obvious relationships

$$\tilde{v}_n = \sin(\pi v_n / 2), \quad \tilde{a}_n = a_n \frac{\pi}{2} \cos(\pi v_n / 2).$$

Using the quadratures the integral can be substituted by the finite sum

$$\int_{\xi_L}^{\xi_U} f(\xi) d\xi \approx (\xi_U - \xi_L) \sum_{n=1}^N a_n f(\xi_n), \text{ where } \xi_n = \xi_L + (\xi_U - \xi_L) v_n.$$

The knots and weights both quadratures are represented in table 1 for seven knots.

Utilization of the two types of quadratures is connected by the variety of the functions in integrals (4) and (5). If the integration limits are determined by the panel limits, then the first (standard) quadrature is applied. In the case of one of integration limits is on the Mach cone, the second quadrature is used.

Table 1. Knots and weights of Gaussian quadratures

n	v_n	a_n	\tilde{v}_n	\tilde{a}_n
1	0.974554	0.06474241	0.999201	0.00406381
2	0.870766	0.139853	0.979466	0.0442896
3	0.702923	0.190915	0.893081	0.134918
4	0.500000	0.208980	0.707107	0.232118
5	0.297077	0.190915	0.449895	0.267825
6	0.129234	0.139853	0.201610	0.215169
7	0.0254460	0.06474241	0.0399599	0.101616

For approaching a high precision of the determination $F(\epsilon)$ (5) and w (4) the integration intervals are divided into some additional parts. In cordwise integration the number of divisions is evaluated by the empirical formula $N_\xi = \text{int} \left[0.6 \frac{kM^2}{M^2 - 1} (R(\xi_U) - R(\xi_L)) + 1 \right]$, where $\text{int}(\cdot)$ is the whole part of number.

The number of divided regions in spanwise integration is obviously depended on the number of crossing points on the leading and trailing edges and can range from 1 to 4. On fig. 1 the example with maximum number of divisions is presented. Each integration region is characterized by the

limit value of the variable $\epsilon = \frac{\eta - \eta_L}{\eta_U - \eta_L}$.

In all regions except central one the integration is executed numerically by the quadratures one of two types mentioned above. The selection of the quadrature type is defined by the behavior of the function $F(\varepsilon)$ in the vicinity of the points in which Mach cone crosses the panel. On figure 2 typical dependence of the function $F(\varepsilon)$ on variable ε is represented for a case of crossing the panel and Mach cone. Figure 2 shows the dependence of real (the solid line) and imaginary (the dotted line) parts of the function F versus ε . On the right side of the figure the disposition of the panel with respect to control point is shown, here the dotted line is the line of crossing panel and cone; Mach number, reduced frequency and altitude of the control point about the panel are represented too. On the presented figure breakages of the function $F(\varepsilon)$ in the crossing points have been well seen. It is obvious that in these points the derivative $\frac{\partial F(\varepsilon)}{\partial r}$ has a singularities.

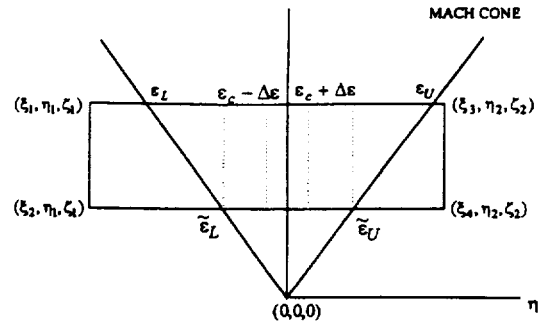


Fig. 1. Domain of influence and subdivision of integration region.

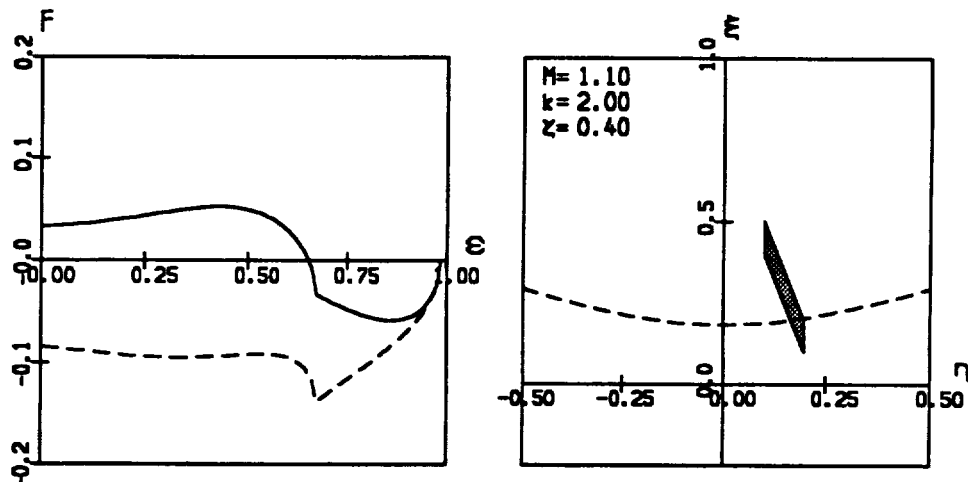


Fig. 2. Real and imaginary parts of function $F(\varepsilon)$ at nonplanar disposition of the control point with respect to panel.

One of the most important moment is the numerical evaluation of the derivative $\frac{\partial F(\varepsilon)}{\partial r}$. The derivative $\frac{\partial F(\varepsilon)}{\partial r}$ can be computed numerically using the central difference (since the function $F(\varepsilon)$ is analytic). Standard value of the increment with respect to r is defined by the formula

$$\Delta r = \Delta \bar{r} \frac{\sqrt{\xi_U^2 - \beta^2 r^2}}{\beta},$$

where $\Delta \bar{r} = 10^{-5}$.

The lower limit of integration in (5) can lie on the trailing panel edge or on Mach cone and derivative $\frac{\partial F(\varepsilon)}{\partial r}$ has singularity in the transition point. Therefore, for the final selection of the increment Δr two conditions are controlled at the leading and trailing edges:

- 1) $R^2(r + \Delta r) > 0$, $R^2(r - \Delta r) > 0$ and
 2) type of lower limit must not be changed with the change of the value r . If at least one of these conditions is not satisfied at the standard increment, then it is decreased up to acceptable value. Described conditions are implemented if magnitudes $r + \Delta r$ and $r - \Delta r$ range in the interval from r_{\max} to r_{\min} , which are determined by the formulas

$$r_{\min} = \begin{cases} 0 & \text{при } \tilde{\xi}_L \geq \beta r, \\ \tilde{\xi}_L / \beta & \text{при } \tilde{\xi}_L < \beta r. \end{cases} \quad r_{\max} = \begin{cases} \tilde{\xi}_L / \beta & \text{при } \tilde{\xi}_L \geq \beta r, \\ \tilde{\xi}_L / \beta & \text{при } \tilde{\xi}_L < \beta r. \end{cases}$$

On figure 3 dependencies of downwash value versus altitude of the control point with respect to the panel plate are represented for different angles between panel normal and control normal ($\phi = \arccos(\eta_1 \cdot \eta_0)$). The solid lines in figure 3 correspond to real downwash part, the dotted lines correspond to imaginary downwash part.

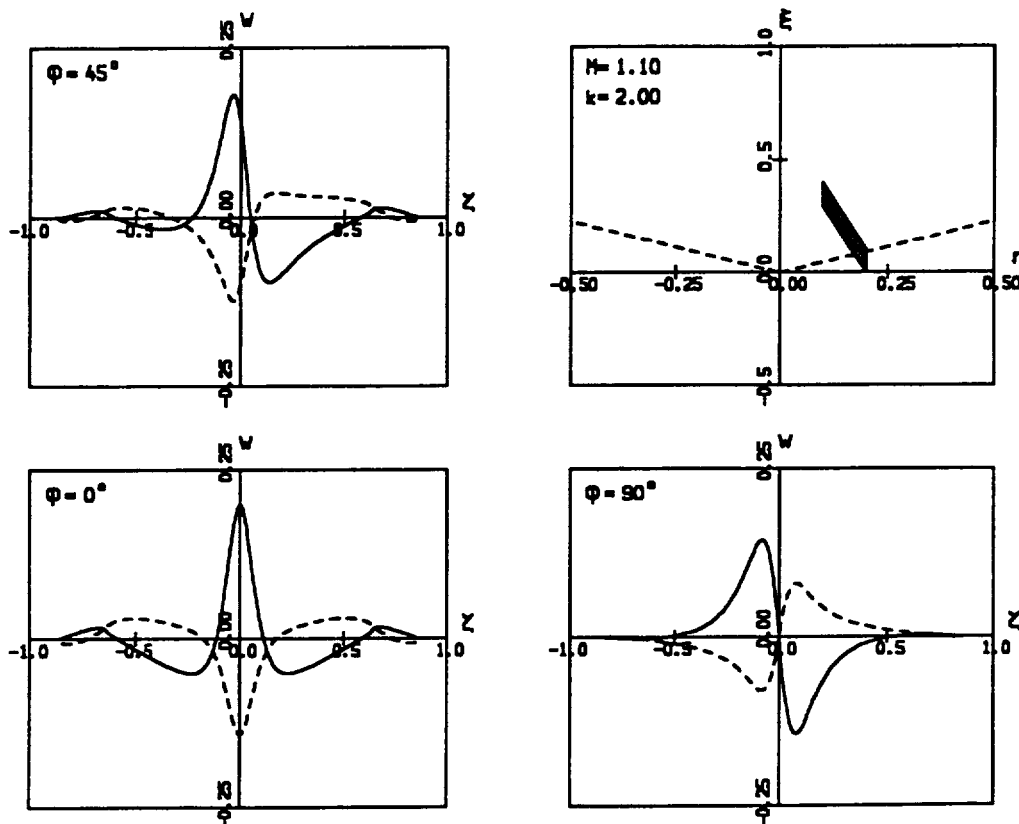


Fig. 3. Downwash complex value W at nonplanar disposition of the control point with respect to panel for three normal directions.

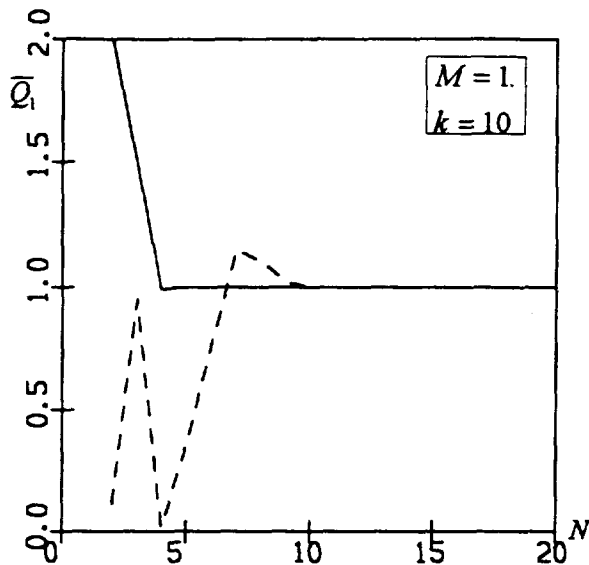


Fig. 4. Coefficient of generalized force versus number of subpanelling for two schemes of integration.

Fig. 4 shows the influence of the downwash calculation accuracy on accuracy of the generalized aerodynamic force computation of the delta wing. The relative variation of the generalized force in heave motion with respect to chordwise and spanwise panel numbers is presented in this figure. The solid line corresponds to exact downwash calculation, which is achieved using appropriate number of additional divisions on integration range. The dotted line corresponds to fixed scheme of the integration with 7 points for all regions. Presented result shows that flexible integration scheme used in this method allows to compute aerodynamic coefficients in wide range of the reduced frequency for rather big panels.

4. Flutter investigation

To demonstrate the capability of the proposed code and the influence of the aerodynamic interference on aeroelastic characteristics theoretical flutter investigations of modern fighter aircraft were conducted.

Aeroelastic equation of motion are derived on the base of methods which are developed in KC-2 computer code. The Ritz method is used in KC-2 when the deformations are represented as polynomial functions of the spatial coordinates.

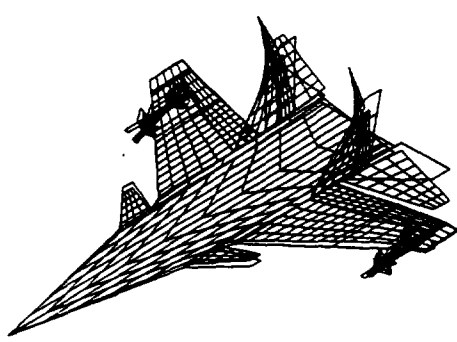


Fig. 5. Aerodynamic model and antisymmetrical flutter mode $f=7$ Hz, $M=1.2$, $\bar{y} = 0.85$.

stabilizer, canard, pylon, missile fuselage and 8 missile wings. The pylon and the missile are supposed to be the rigid surfaces, which have elastic connections with the wing. These connections are modeled by a set of the springs. Figure 6 shows some computed results of antisymmetrical flutter modes of the investigated aircraft with stores under wing. In our flutter analysis the masses of the pylon and the missile and stiffness of the connections were not varied. The critical dynamic pressure was obtained for three different locations of the missile along the

span: $\bar{y}=0.78$, 0.85 and 1.0 of semi-span. The coefficients of the aerodynamic matrices were computed versus Mach number for such three variants:

1. no aerodynamic loads on missile and pylon;
2. complete calculation using mentioned above linear unsteady subsonic/supersonic codes;
3. no aerodynamic interference between lifting surfaces.

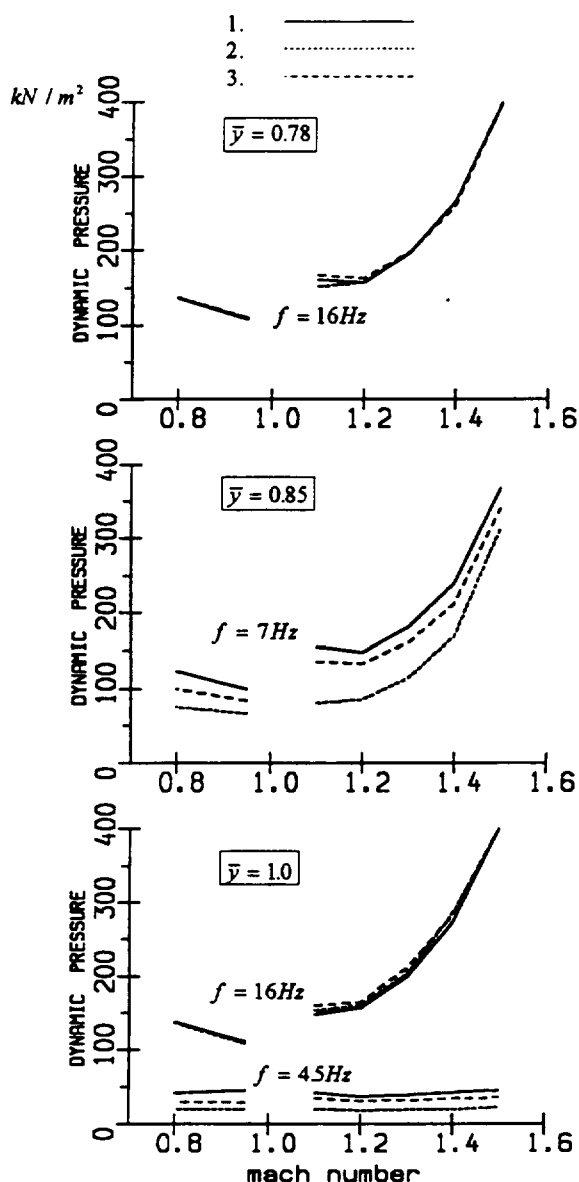


Fig. 6. Flutter dynamic pressure of the fighter aircraft versus Mach number at three missile locations.

by taking into account full aerodynamic interaction between all lifting surfaces it is possible to obtain minimum critical dynamic pressure.

Only the single flutter mode ($f=16 \text{ Hz}$) proved to be when $\bar{y}=0.78$ (fig.6). This is bending-torsion fin flutter coupled with the vibration of the stabilizer. Practically there is no displacement of the wing with store under wing in this flutter mode. Therefore the distinctions of the critical dynamic pressure for three variants of the aerodynamic matrices are small. Since the considerable loads changes are in the root sections of the fin and the stabilizer, where the vibration amplitudes are small, taking into account the interference between vertical and horizontal surfaces gives a small influence on this flutter mode.

If the missile location is near the wing tip the another flutter mode ($f=7 \text{ Hz}$) arises (fig.6). This is bending-torsion wing flutter coupled with the missile yaw vibration. Aerodynamic contribution of the missile and the pylon on summed generalized loads is rather great: the critical flutter pressure increases almost twice at low supersonic Mach number when this aerodynamic contribution is not taking into account (fig.7). The influence of the aerodynamic interference, as it can be seen on figure 6, decreases by increasing Mach number.

In the case of the missile location on the tip of the wing the flutter mode depends on the store mass greater than on its aerodynamic contribution, since the missile mass is 20% from the wing mass and the wing surface is more greater than stores surfaces. Figure 6 shows that the flutter mode at frequency 4.5 Hz almost does not depend on Mach numbers. The critical flutter pressure in this case is the lowest. It is important to note that

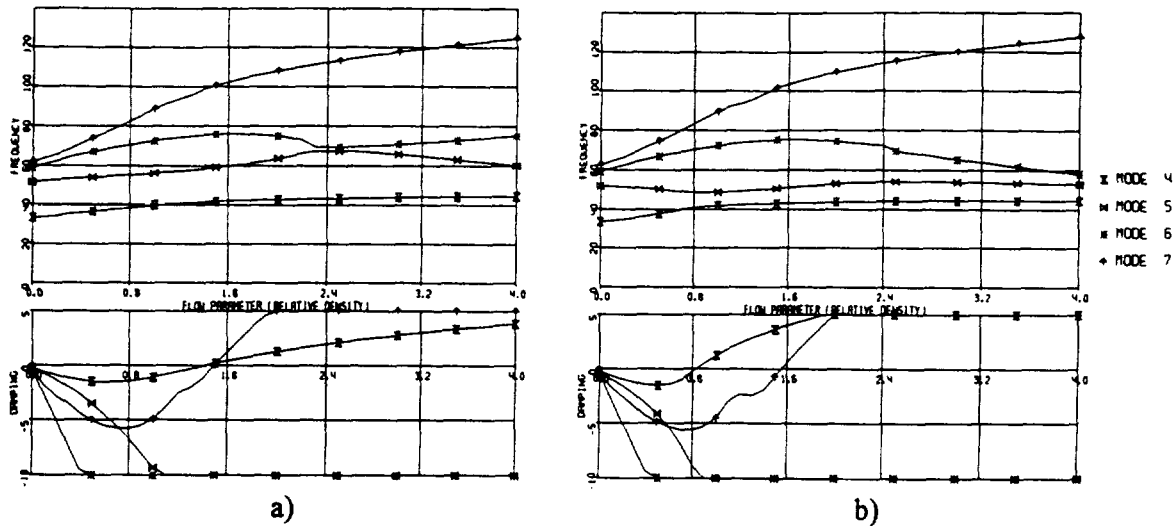


Fig. 7. Flutter analysis, $M=1.2$

a) no aerodynamic loads on missile and pylon;
b) full interaction between all lifting surfaces.

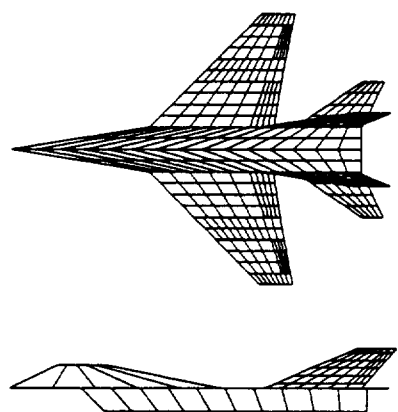
5. Static aeroelasticity

Characteristics of static aeroelasticity can be computed on the base of various aerodynamic theories, including nonlinear methods. But in practice to analyze realistic aircraft often the linear panel methods are employed because the analysis of the characteristics of static aeroelasticity needs variety parametric computations. Therefore it can be treated the application of the present method (and computer code) of computation of aerodynamic forces in supersonic flow to analyze static aeroelasticity.

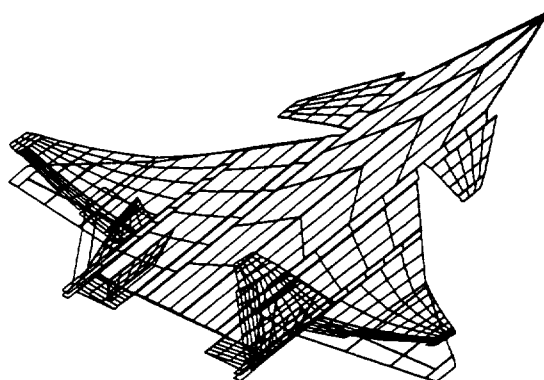
On the base of polynomial Ritz method and KC-2 computer code the original approach is developed to compute static aeroelasticity characteristics. The approach is based on the solving of equilibrium of the elastic aircraft equation in polynomial general coordinates at specified quasi-steady flight condition. Aerodynamic forces are computed at reduced frequency $k=0$.

Using this approach the static aeroelasticity problems are investigated for realistic aircrafts of various structure with the aim to study the significance of the aerodynamic interference between nonplanar lifting surfaces. The computations show that there are cases in which the interference is important. Some results are discussed below concerning tail loading of double-fin airplanes in lateral motion.

For maneuverable aircraft (fig. 8) at low supersonic Mach numbers the considerable decrease of aileron effectiveness is appeared due to structure flexibility. It can be seen from the dependence on dynamic pressure Q of roll moment coefficient derivative m_x^δ with respect to aileron deflection ($Q=0$, corresponds to the case of rigid structure, fig. 8, a). Therefore differential moveable stabilizer is introduced for rolling control; its roll effectiveness less depends on structure flexibility. Nevertheless relative effectiveness $\zeta = (m_x^\delta)_{el} / (m_x^\delta)_{rig}$, which is considered as flexibility factor, falls up to 40% in the case of computing without interference. If that flexibility factor will be introduced for effectiveness determined from rigid model wind tunnel test the incorrect conclusion may be drawn about insufficient stabilizer effectiveness for roll control. When Mach number increasing the interference influence decreases (fig. 8, b).

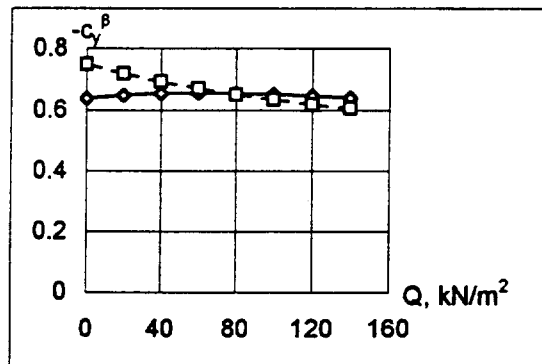
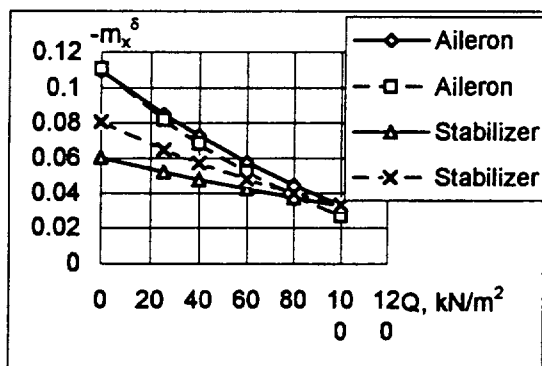


Light maneuverable aircraft



Multifunctional fighter

a) M=1.1



b) M=1.5

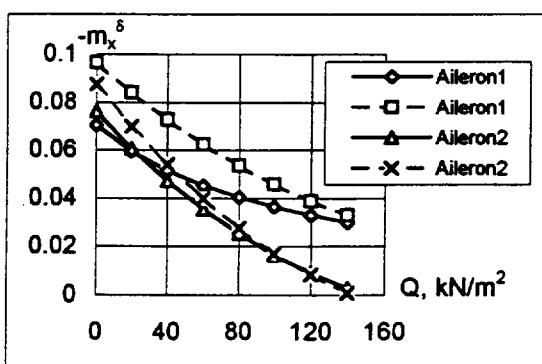
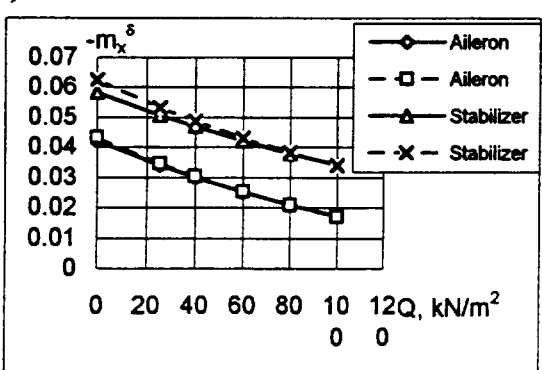


Fig. 8. Roll moment coefficient derivative m_x^δ with respect to control surface deflection versus dynamic pressure.

— with interference
— without interference

Fig. 9. Side force coefficient derivative c_y^B with respect to side-slip angle and rolling moment coefficient derivatives m_x^δ with respect to aileron section deflections versus a dynamic pressure.

— with interference
— without interference

Fig. 9 shows some characteristics of heavy multifunctional fighter: side force coefficient derivative $c_y \beta$ with respect to side-slip angle and rolling moment coefficient derivatives with respect to inboard (Aileron1) and middle (Aileron2) aileron section deflections versus a dynamic pressure at Mach number $M=1.1$ with and without taking into account the interference between horizontal and vertical surfaces. Similar to the case above the interference has a small influence on the characteristics at high dynamic pressure, but the flexibility factors ζ differ significantly.

References

1. Mosounov V. A., Nabiullin E. N. Determination of aerodynamic forces acting in subsonic flow on flexible oscillating surfaces arranged in different planes. // Trudy TsAGI, issue 2118, 1981.
2. Appa K. Constant pressure panel method for supersonic unsteady airloads analysis // Journal of Aircraft. — Oct. 1987, Vol. 24.
3. Appa K., Smith M. J. C. Evaluation of the constant pressure panel method for supersonic unsteady airloads prediction // Journal of Aircraft. — Nov. 1988 . Vol. 26.
4. Lottati I., Nissim E. Nonplanar, supersonic, three-dimensional, oscillatory, piecewise continuous kernel function method // Journal of Aircraft. — Jan. 1987. Vol. 24
6. Liu D. D., Jamest D. K., Chen P. C., Pototzky A.S. Further studies of harmonic gradient method for supersonic aeroelastic applications // Journal of Aircraft. — Sep. 1990. Vol. 28.
6. Kouzmina S. I. Evaluation unsteady aerodynamic loads of the thin wings in supersonic flow. //Trudy TsAGI, issue 2118, 1981
7. Bunkov B. G., Nabiullin E. N. Comparative analysis of the method of calculation of aerodynamic forces on the oscillating wing in supersonic flow. //Trudy TsAGI, issue 2281, 1985

An Application of the P-Transform Method for Transient Maneuvering Analysis

536-05

John R. Dykman
Principal Engineer - Stability, Control & Flying Qualities
The Boeing Company
Long Beach, CA 90807-5309, USA
john.r.dykman@boeing.com

William P. Rodden
Consulting Engineer
William P. Rodden, Ph.D., Inc.
La Cañada Flintridge, CA 91011-2838, USA
billrodden@aol.com

Abstract

The P-Transform method provides an alternative to the Rational Function Approximation (RFA) methods for representing oscillatory aerodynamics in the time domain. It is based on the flutter eigenvalues and eigenvectors obtained for each mode at a given velocity from a PK-flutter analysis. As such it avoids the curve fitting errors of the RFA and assures exact agreement with flutter predictions. Furthermore, it makes no assumptions regarding the transient aerodynamic lagging mechanism and is therefore equally valid at subsonic and supersonic speeds.

An application is presented to a forward-swept wing aircraft configuration that has been the subject of earlier maneuvering studies by quasisteady methods. The differences between the responses using quasisteady aerodynamic loads and general unsteady loads are illustrated in this example.

Keywords. Transient aerodynamics, transient response, P-Transform method, maneuvering loads, dynamic aeroelasticity.

Introduction

The equations of motion for quasistatic maneuvering of a flexible aircraft contain two approximations, e.g., in Ref. 1. The first is that the dynamic behavior of the structure is neglected, i.e., it is assumed that the motions of all structural grid points are in phase with some reference point. The second is that all aerodynamic lags, beyond those accounted for in the first order $\dot{\alpha}$ and $\dot{\beta}$ stability derivatives are also neglected. An extension of Ref. 1 to include dynamic structural effects has been given in Ref. 2 that removes the first approximation but the second approximation is retained. The removal of the second approximation by considering general unsteady aerodynamic loads is the subject of this paper.

The literature on the so-called Rational Function Approximation (RFA) began with exponential curve fitting of the Wagner indicial lift function in two-dimensional incompressible flow by R. T. Jones in 1940 (Ref. 3). The extensive literature on the RFA (e.g., Refs. 4, 5, and 6) is also based on the exponential behavior of subsonic indicial

aerodynamics. The accuracy of the RFA at supersonic speeds would be less than that at subsonic speeds because of the different mechanism of transient supersonic loading. The present formulation does not involve curve fitting and is therefore equally valid at subsonic and supersonic speeds. It is based on the work of Heimbaugh (Ref. 7) as discussed by Winther, Goggin, and Dykman (Ref. 8). It can be regarded as a transient extension of the oscillatory British (PK) flutter method and offers the advantage over the RFA methods of exact agreement with calculated flutter speeds without the need of any additional states to represent aerodynamic lags. All basic data for the analysis may be obtained from the PK-flutter solution sequence in MSC/NASTRAN (Ref. 9) with some minor DMAP modifications.

Aeroelastic Equations of Motion

The fundamental equation of motion of a linear aeroelastic system in generalized (modal) coordinates is given in Eq. (1). The amplitudes of the system free vibration mode shapes are the generalized coordinates \mathbf{q} and the amplitudes of the control surface inputs are generalized coordinates \mathbf{q}_c .

$$\mathbf{M}\ddot{\mathbf{q}} + \mathbf{C}\dot{\mathbf{q}} + \mathbf{K}\mathbf{q} = \bar{q}\mathbf{Q}(M, k)\mathbf{q} + \bar{q}\mathbf{Q}_c(M, k)\mathbf{q}_c + \bar{q}\mathbf{Q}_0(M) + g\mathbf{M} \quad (1)$$

The generalized structural mass, damping, and stiffness matrices are \mathbf{M} , \mathbf{C} , and \mathbf{K} , respectively; g is the acceleration of gravity and $g\mathbf{M}$ is a vector of weight and static unbalance components adjusted for the pitch and bank angles of the body axes. The control surface generalized structural mass matrix is neglected as well as its stiffness and damping. The generalized aerodynamic coefficients $\mathbf{Q}_0(M)$ are intercept values for incidence, twist, and camber and are functions of the Mach number M . The generalized unsteady aerodynamic coefficients for motion $\mathbf{Q}(M, k)$ and for the control surfaces $\mathbf{Q}_c(M, k)$ in the frequency domain are functions of Mach number and reduced frequency k where $k = \omega\bar{c}/2V$ in which ω is the angular frequency, \bar{c} is the reference chord, and V is the flight velocity. The aerodynamic coefficients are based on the modal frequencies. The frequencies may be those of the free vibrations or damped frequencies as determined in a PK-flutter analysis. The aerodynamic coefficients are scaled by the dynamic pressure \bar{q} where $\bar{q} = \rho V^2/2$ in which ρ is the atmospheric density. The generalized unsteady aerodynamic coefficients are complex and can be separated into an aerodynamic stiffness and an aerodynamic damping via

$$\bar{q}\mathbf{Q}(M, k)\mathbf{q} = \bar{q}(\mathbf{Q}^R(M, k))\mathbf{q} + \bar{q}(\bar{c}/2V)(\mathbf{Q}'(M, k)/k)\dot{\mathbf{q}} \quad (2)$$

These coefficients are obtained from an unsteady aerodynamic theory such as the Doublet-Lattice Method (Refs. 10 and 11) where the aerodynamic stiffness $\mathbf{Q}^R(M, k)$ is the real part of \mathbf{Q} and the aerodynamic damping $\mathbf{Q}'(M, k)/k$ is the imaginary part of \mathbf{Q} divided by k . Similarly, for the control surfaces

$$\bar{q}\mathbf{Q}_c(M, k)\mathbf{q}_c = \bar{q}(\mathbf{Q}_c^R(M, k))\mathbf{q}_c + \bar{q}(\bar{c}/2V)(\mathbf{Q}'_c(M, k)/k)\dot{\mathbf{q}}_c \quad (3)$$

Cast into a first order differential equation form after substituting Eqs. (2) and (3), Eq. (1) becomes

$$\begin{aligned} \left\{ \begin{array}{l} \ddot{\mathbf{q}} \\ \dot{\mathbf{q}} \end{array} \right\} &= \left[\begin{array}{c|c} \mathbf{M}^{-1}(\bar{q}(\bar{c}/2V)(\mathbf{Q}^I(M,k)/k) - \mathbf{C}) & \mathbf{M}^{-1}(\bar{q}(\mathbf{Q}^R(M,k)) - \mathbf{K}) \\ \mathbf{I} & \mathbf{0} \end{array} \right] \left\{ \begin{array}{l} \mathbf{q} \\ \mathbf{q} \end{array} \right\} \\ &+ \left[\begin{array}{c|c|c} \mathbf{M}^{-1}\bar{q}(\bar{c}/2V)(\mathbf{Q}_c^I(M,k)/k) & \mathbf{M}^{-1}\bar{q}(\mathbf{Q}_c^R(M,k)) & \mathbf{M}^{-1}(\bar{q}\mathbf{Q}_0(M) + g\mathbf{M}) \\ \mathbf{0} & \mathbf{0} & \mathbf{0} \end{array} \right] \left\{ \begin{array}{l} \dot{\mathbf{q}}_c \\ \mathbf{q}_c \\ 1 \end{array} \right\} \end{aligned} \quad (4)$$

Making the following substitutions into Eq. (4)

$$\mathbf{X} = \left\{ \begin{array}{l} \dot{\mathbf{q}} \\ \mathbf{q} \end{array} \right\}, \quad \mathbf{U} = \left\{ \begin{array}{l} \dot{\mathbf{q}}_c \\ \mathbf{q}_c \\ 1 \end{array} \right\} \quad (5)$$

$$\mathbf{A}(\bar{q}, V, M, k) = \left[\begin{array}{c|c} \mathbf{M}^{-1}(\bar{q}(\bar{c}/2V)(\mathbf{Q}^I(M,k)/k) - \mathbf{C}) & \mathbf{M}^{-1}(\bar{q}(\mathbf{Q}^R(M,k)) - \mathbf{K}) \\ \mathbf{I} & \mathbf{0} \end{array} \right] \quad (6)$$

$$\mathbf{B}(\bar{q}, V, M, k) = \left[\begin{array}{c|c|c} \mathbf{M}^{-1}\bar{q}(\bar{c}/2V)(\mathbf{Q}_c^I(M,k)/k) & \mathbf{M}^{-1}\bar{q}(\mathbf{Q}_c^R(M,k)) & \mathbf{M}^{-1}(\bar{q}\mathbf{Q}_0(M) + g\mathbf{M}) \\ \mathbf{0} & \mathbf{0} & \mathbf{0} \end{array} \right] \quad (7)$$

yields

$$\dot{\mathbf{X}} = \mathbf{A}(\bar{q}, V, M, k)\mathbf{X} + \mathbf{B}(\bar{q}, V, M, k)\mathbf{U} \quad (8)$$

For a fixed flight condition, Eq. (8) becomes

$$\dot{\mathbf{X}} = \mathbf{A}(k)\mathbf{X} + \mathbf{B}(k)\mathbf{U} \quad (9)$$

The P-Transform Method

The P-Transform method eliminates the dependence of \mathbf{A} and \mathbf{B} on the reduced frequency and transforms them into the constant matrices $\tilde{\mathbf{A}}$ and $\tilde{\mathbf{B}}$ for a fixed flight condition, resulting in the following equation of motion.

$$\dot{\mathbf{X}} = \tilde{\mathbf{A}}\mathbf{X} + \tilde{\mathbf{B}}\mathbf{U} \quad (10)$$

Defined in Eq. (5), \mathbf{X} is a vector of generalized coordinates consisting of both modal displacements and velocities for the mean axis and flexible body degrees of freedom and \mathbf{U} is a vector of inputs from control surfaces. The matrices $\tilde{\mathbf{A}}$ and $\tilde{\mathbf{B}}$ are real constant coefficient matrices. In the P-Transform method the matrix $\tilde{\mathbf{A}}$ is approximated using the converged ("lined-up") eigenvalues and eigenvectors from the PK-flutter solution by

$$\tilde{\mathbf{A}} = \hat{\mathbf{T}}\hat{\mathbf{A}}\hat{\mathbf{T}}^{-1} \quad (11)$$

where $\hat{\mathbf{T}}$ and $\hat{\mathbf{A}}$ denote the matrices of the "lined-up" eigenvectors and eigenvalues. The matrix $\tilde{\mathbf{B}}$ then has the frequency response characteristics over a wide frequency range that are necessary to perform transient response analyses *without* any need of curve-fitting the oscillatory aerodynamics as in the RFA methods. The P-Transform method might be called a "zero-state" method in contrast to Karpel's "minimum-state" method (Ref. 6) in that no additional states are required to model the unsteady aerodynamics.

The matrix $\tilde{\mathbf{B}}$ is approximated using the converged eigenvectors from the PK-flutter solution by

$$\tilde{\mathbf{B}} = \hat{\mathbf{T}}\hat{\mathbf{B}} \quad (12)$$

where $\hat{\mathbf{B}}$ denotes the matrix of the assembled converged row pairs from the product $\mathbf{T}(k_i)^{-1}\mathbf{B}(k_i)$. $\mathbf{T}(k_i)$ is the complete eigenvector matrix and $\mathbf{B}(k_i)$ is the input matrix both evaluated at the "lined-up" frequency k_i .

An Example of a Forward-Swept Wing Airplane

The P-Transform method is illustrated by comparison to an example of a forward-swept wing airplane for which the maneuvering solutions are known (Refs. 1 and 2) using other approximations. In Ref. 1 Strip Theory aerodynamics were used and in Ref. 2 the Doublet-Lattice Method was used. The planform with its structural, inertial, and aerodynamic idealizations is shown in Fig. 1. The structural model is shown on the right side with the grid points (GP) numbered. The Doublet-Lattice aerodynamic model is shown on the left side with 8 boxes on the left canard and 32 boxes on the left wing, and body interference is neglected. The airplane has a gross weight of 16,000 lbs. Its wing span is 40 ft, its canard span is 10 ft, and both surfaces have chords of 10 ft. The structural damping is assumed at two percent. The canard mass and aerodynamic damping are neglected, and the intercept coefficients are assumed to be zero. The remaining characteristics are discussed in the references. This simple model has only six vibration modes for out-of-plane motion; their frequencies are 9.89, 18.40, 43.22, 56.77, 71.03, and 138.35 Hz. The example maneuver assumes a dynamic pressure of 1200 psf which corresponds to a speed of 1005 ft/s and a Mach number of 0.90 at sea level.

Numerical integration of Eq. (10) results in the basic modal responses (mean axis and flexible body) of the aeroelastic vehicle. The control surface (canard) input is shown in Fig. 2. The transient maneuvering acceleration responses are shown in Figures 3, 4, and 5 in which the present P-Transform solution is compared to the dynamic solution of Ref. 2. The P-Transform results are shown with solid lines in these figures while the quasistatic aerodynamic results of Ref. 2 are shown with dashed lines. Fig. 3 compares the load factor responses on the mean axis at the reference point of GP 90. Fig. 4 compares the first flexible modal acceleration responses. Finally, Fig. 5 compares the load factors at GP 90. Large differences between the present method and that of Ref. 2 are only found in Fig. 4, the first flexible modal acceleration.

One would not expect significant differences between the mean axis responses or the responses of a particular physical point, in this case GP 90. However, one would expect differences in the fundamental modal responses because the aerodynamic lags are more appropriately considered in this analysis than in Ref. 2. In Fig. 4 the peaks are higher from the P-Transform method which shows a reduction in aerodynamic damping in the first aeroelastic mode.

In the example problem we have neglected the aerodynamic damping on the canard. This was done for consistency in comparing with the results of Ref. 2. Inclusion of the aerodynamic damping (first order in Ref. 2 and general unsteady here) would have been straight-forward but was not done.

Concluding Remarks

The significant feature of the P-Transform method is its adequate accuracy without the use of explicit aerodynamic lag states. Although it is also an approximate method, it does not contain anything comparable to the possible curve fitting errors of the RFA. There may be no advantage in the initial analysis since the requirement for PK-flutter analysis is probably comparable to the computations required by the RFA curve fitting. However, the later computational advantage of the P-Transform method is substantial when the different number of states are recognized: the P-Transform has the same number of states as the vibration problem whereas the RFA requires the additional states for the aerodynamic lag functions, N in each mode where N is the number of terms in the aerodynamic lag approximation.

There are several aspects to the accuracy of the P-Transform method that should be emphasized. Without curve fitting errors, it provides exact agreement with the flutter speeds. Furthermore, the RFA assumes a subsonic character in the aerodynamic lag functions, i.e., exponential decays, whereas transient supersonic behavior is characterized by finite lag times. The P-Transform method is equally accurate for transient motions at both subsonic and supersonic speeds.

The present paper is the third in a series of transient analyses of the maneuvering aeroelastic airplane via approximations with increasing accuracy. An exact solution can be obtained utilizing Fourier transform methods that can be anticipated to be much more computationally intensive. That will be the next phase in this series of investigations.

References

1. Rodden, W. P. and Love, J. R., "Equations of Motion of a Quasisteady Flight Vehicle Utilizing Restrained Static Aeroelastic Characteristics," *Journal of Aircraft*, Vol. 22, No. 9, Sept. 1985, pp. 802-809.
2. Dykman, J. R., and Rodden, W. P., "Structural Dynamics and Quasistatic Aeroelastic Equations of Motion," presented at the Aerospace Flutter and Dynamics Council Meeting, Long Beach, CA, 8-9 May 1997; submitted to the *Journal of Aircraft*.
3. Jones, R. T., "The Unsteady Lift of a Wing of Finite Aspect Ratio," NACA Report 681, 1940.
4. Roger, K. L., "Airplane Math Modeling Methods for Active Control Design; Structural Aspects of Active Controls," AGARD CP-228, Aug. 1977, pp. 4-1 to 4-11.
5. Vepa, R., "Finite State Modeling of Aeroelastic Systems," NASA CR-2779, Feb. 1977.
6. Karpel, M., "Design of Active and Passive Flutter Suppression and Gust Alleviation," NASA CR-3482, Nov. 1981.
7. Heimbaugh, R. M., "Flight Controls Structural Dynamics IRAD," McDonnell-Douglas Report MDC-J2303, March 1983.
8. Winther, B. A., Goggin, P. J., and Dykman, J. R., "Reduced Order Dynamic Aeroelastic Model Development and Integration with Nonlinear Simulation," Paper 98-1897, AIAA/ASME/ASCE/AHS/ASC 39th Structures, Structural Dynamics, and Materials Conference, Long Beach, CA, April 1998.

9. Rodden, W. P., and Johnson, E. H., *MSC/NASTRAN Aeroelastic Analysis User's Guide*, The MacNeal-Schwendler Corporation, 1994.
10. Rodden, W. P., Giesing, J. P., and Kálmán, T. P., "Refinement of the Non-Planar Aspects of the Subsonic Doublet-Lattice Lifting Surface Method," *Journal of Aircraft*, Vol. 9, No. 1, Jan. 1972, pp. 69-73.
11. Rodden, W. P., Taylor, P. F., and McIntosh, Jr., S. C., "Further Refinement of the Nonplanar Aspects of the Subsonic Doublet-Lattice Lifting Surface Method," Paper ICAS-96-2.8.2, 20th Congress of the International Council of the Aeronautical Sciences, Sorrento, Italy, 8-13 Sept. 1996; also, *Journal of Aircraft*, Vol. 35, No. 5, Sept.-Oct. 1998, pp. 720-727.

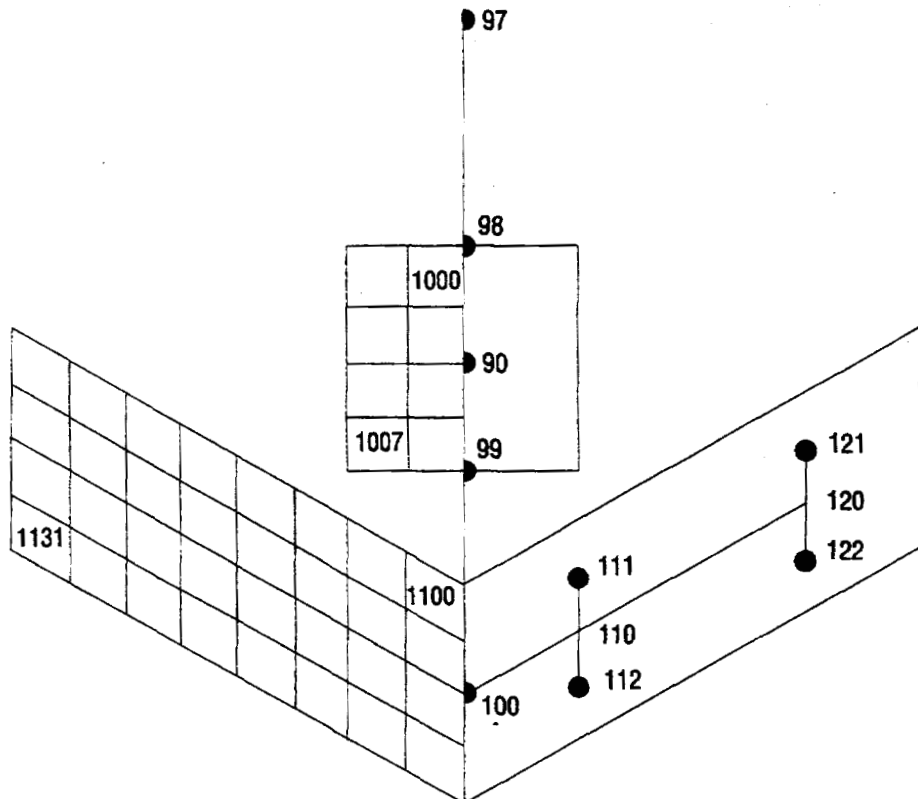


Fig. 1 - Idealization of forward-swept wing airplane

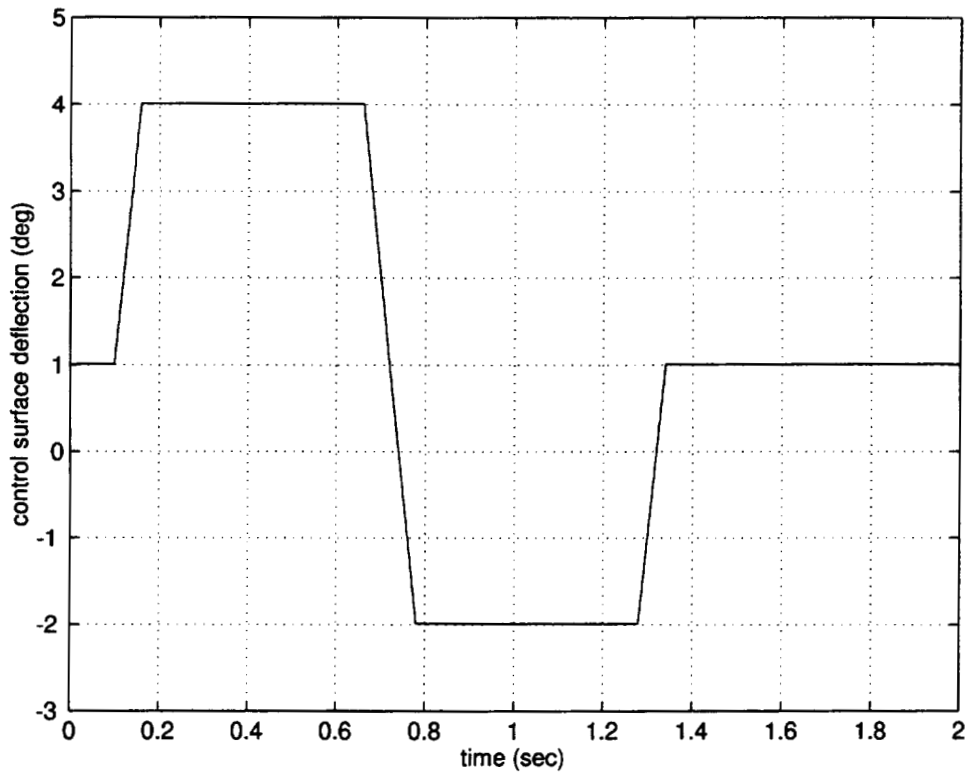


Fig. 2 - Control surface input

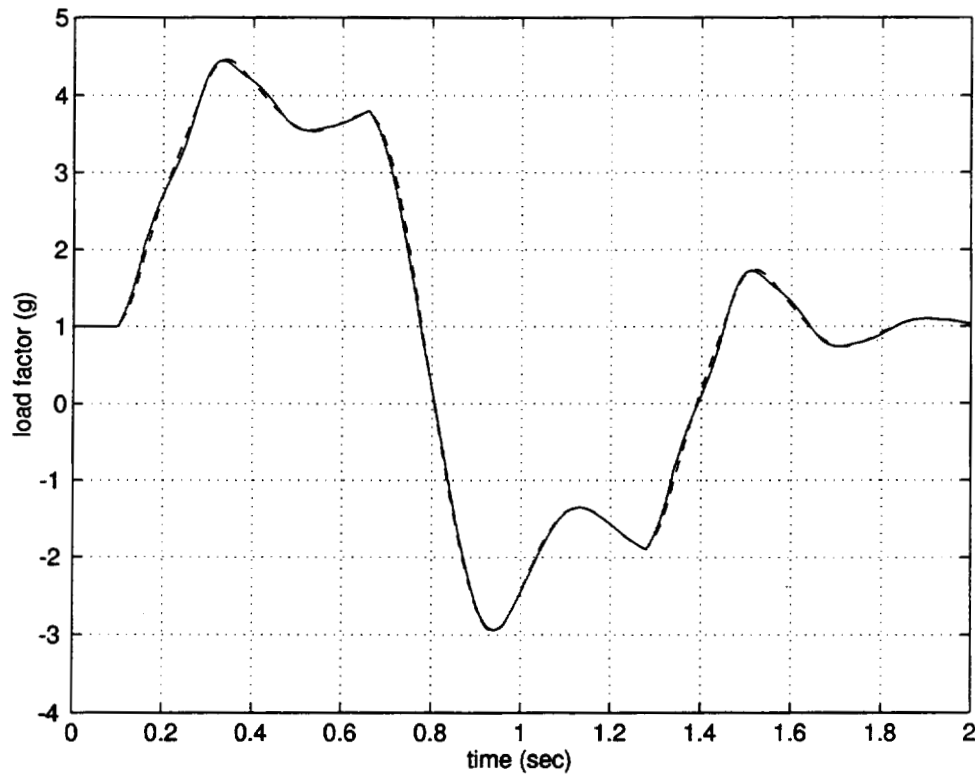


Fig. 3 - Mean axis load factor responses at GP 90

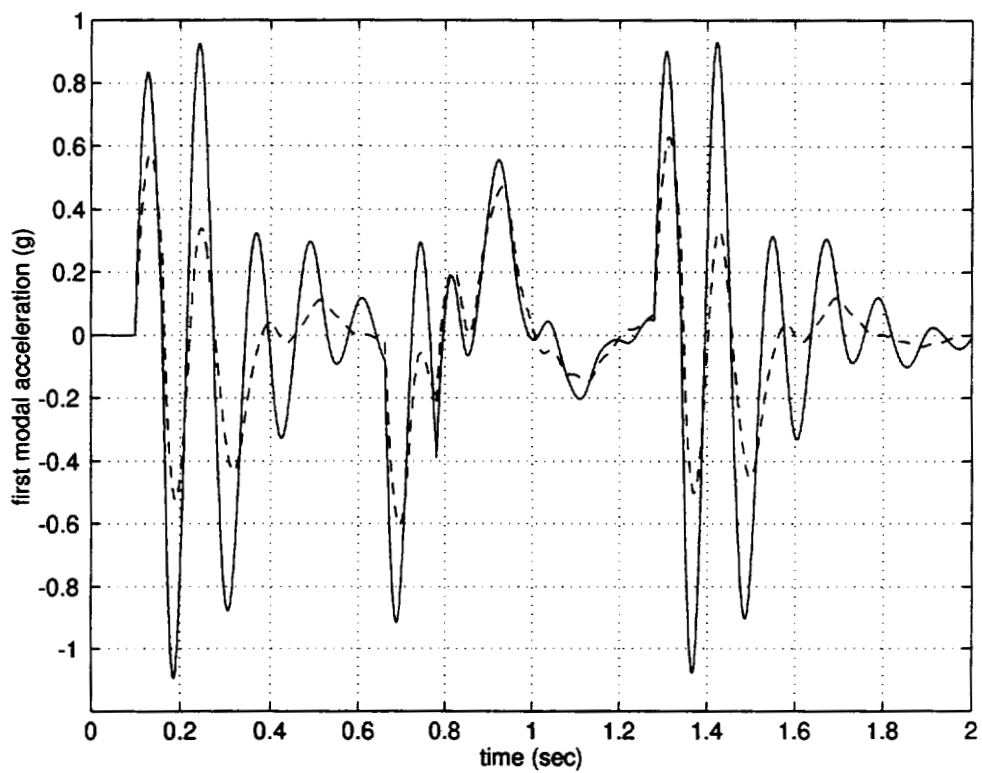


Fig. 4 - First flexible modal acceleration responses

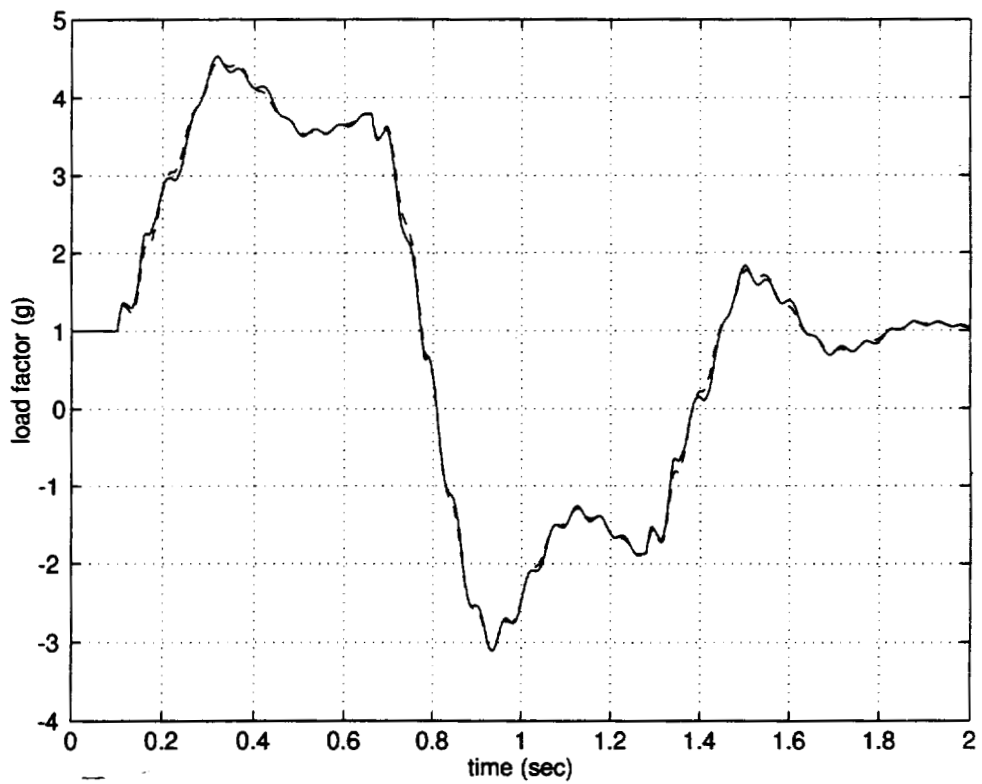


Fig. 5 - GP 90 load factor responses

53 7-08

A Damping Perturbation Method for Flutter Solution: The g-Method

P.C. Chen*
Zona Technology, Inc., Scottsdale, Arizona 85251

Abstract

By utilizing a damping perturbation method, the present g-method includes a first order damping term in the flutter equation that is rigorously derived from the Laplace-domain aerodynamics. The g-method generalizes the K-method and the P-K method for reliable damping prediction. It is valid in the entire reduced frequency domain and up to the first order of damping. The present work also provides a theoretical foundation for the g-method that can be used to estimate the truncation error for large values of damping. The solution algorithm of the g-method is proven to be robust and can obtain an unlimited number of aerodynamic lag roots; as demonstrated by the results of the selected test cases.

1. Introduction

Since its applicability for flutter analysis was first demonstrated by Irwin and Guyett (Ref 1) in 1965, the P-K method has been widely adopted by aeroelasticians as the primary tool for finding flutter solutions. Hassig (Ref 2) has given a detailed description of the superiority of the P-K method over the K-method. In Ref 2, the equation of the P-K method reads:

$$\left[\left(\frac{V^2}{L^2} \right) \mathbf{M} p^2 + \mathbf{K} - \frac{1}{2} \rho V^2 \mathbf{Q}(ik) \right] \{\mathbf{q}\} = 0 \quad (1)$$

where:

V is the true speed

L is the reference length, and usually:

$$L = \frac{c}{2}, \text{ where } c \text{ is the reference chord}$$

and:

ρ is the air density

\mathbf{q} is the generalized coordinates

\mathbf{M} , \mathbf{K} , and $\mathbf{Q}(ik)$ are the generalized mass, stiffness, and aerodynamic forces matrices, respectively.

For simplicity, Eq (1) excludes the structural modal damping matrix, but it can be easily included. p is the non-dimensional Laplace parameter and can be expressed as:

$$p = g + ik \quad (2)$$

where:

k is the reduced frequency:

$$k = \frac{\omega L}{V}$$

ω is the oscillatory frequency, and:

$$g = \gamma k,$$

γ is the transient decay rate coefficient.

The P-K method is an approximation of the P-method that requires the generalized aerodynamic force computed in the Laplace domain, i.e. $\mathbf{Q}(p)$. Since most of the unsteady aerodynamic methods (Ref 3, 4, 5, and 6) used by the aerospace industry are formulated in the frequency domain (i.e. the k -domain), the P-K method can directly adopt $\mathbf{Q}(ik)$ from these unsteady aerodynamic methods for flutter calculation.

Rodden (Ref 7) modified Hassig's P-K method equation by adding an aerodynamic damping matrix into Eq (1). The modified P-K method equation reads:

$$\left[\frac{V^2}{L^2} \mathbf{M} p^2 + \mathbf{K} - \frac{1}{2} \rho V^2 \frac{\mathbf{Q}^I}{k} p - \frac{1}{2} \rho V^2 \mathbf{Q}^R \right] \{\mathbf{q}\} = 0 \quad (3)$$

where:

\mathbf{Q}^R and \mathbf{Q}^I are the real part and imaginary part of $\mathbf{Q}(ik)$, i.e.:

$$\mathbf{Q}(ik) = \mathbf{Q}^R + i\mathbf{Q}^I \quad (4)$$

By substituting $p = g + ik$ into the third term of Eq (3), this equation can be rewritten as:

*Vice President, 7430 E. Stetson Drive, Suite 205. E-mail: pc@zonatech.com

$$\left[\left(\frac{V^2}{L^2} \right) \mathbf{M} p^2 + \mathbf{K} - \frac{1}{2} \rho V^2 \frac{\mathbf{Q}'}{k} g - \frac{1}{2} \rho V^2 \mathbf{Q}(ik) \right] \{q\} = 0 \quad (5)$$

By comparing Eq (5) to Eq (1), it is clearly seen that the extra term:

$$-\frac{1}{2} \rho V^2 \frac{\mathbf{Q}'}{k} g$$

is the added aerodynamic damping matrix. Eq (3) is solved at several given values of V and ρ , for complex roots p associated with modes of interest. This is accomplished by an iterative procedure that matches the reduced frequency k to the imaginary part of p for every structural mode. This iterative procedure is called the *reduced frequency "lining-up" process* (Ref 8).

In the following section, we will show that the added aerodynamic damping matrix in Eq (3), is valid only at small k or for linearly varying $\mathbf{Q}(ik)$. The present g-method provides an aerodynamic damping matrix that is valid in the complete k -domain and includes Eq (3) as a special case.

2. Formulation of the g-Method

The basic assumption of the g-method lies in the existence of an analytic function of $\mathbf{Q}(p) = \mathbf{Q}(g + ik)$ so that $\mathbf{Q}(p)$ can be expanded along the imaginary axis (i.e., $g = 0$) for small g by means of a damping perturbation method:

$$\mathbf{Q}(p) \approx \mathbf{Q}(ik) + g \frac{\partial \mathbf{Q}(p)}{\partial g} \Big|_{g=0}, \text{ for } g \ll 1 \quad (6)$$

The second term on the right hand side of Eq (6) is generally not available from the k -domain unsteady aerodynamic methods. However, due to analytic continuation, it can be replaced by:

$$\frac{\partial \mathbf{Q}(p)}{\partial g} \Big|_{g=0} = \frac{\partial \mathbf{Q}(p)}{\partial (ik)} \Big|_{g=0} = \frac{d \mathbf{Q}(ik)}{d(ik)} = \mathbf{Q}'(ik) \quad (7)$$

Eq (7) is valid in the complete p -domain except along the negative real axis in subsonic flow (Ref 9). This implies that $\mathbf{Q}'(ik)$ can be computed from $\mathbf{Q}(ik)$ by a central differencing scheme, except at $k = 0$. At $k = 0$, a forward differencing scheme is employed to accommodate the discontinuity of $\mathbf{Q}(ik)$ along the negative real axis. Substituting Eq (7) into Eq (6)

yields the approximated p -domain solution of $\mathbf{Q}(p)$ in terms of k and for small g :

$$\mathbf{Q}(p) \approx \mathbf{Q}(ik) + g \mathbf{Q}'(ik) \quad (8)$$

Replacing $\mathbf{Q}(ik)$ in Eq (1) by $\mathbf{Q}(p)$ of Eq (8) yields the g-method equation:

$$\left[\left(\frac{V^2}{L^2} \right) \mathbf{M} p^2 + \mathbf{K} - \frac{1}{2} \rho V^2 \mathbf{Q}'(ik) g - \frac{1}{2} \rho V^2 \mathbf{Q}(ik) \right] \{q\} = 0 \quad (9)$$

At $g = 0$, both the g-method and the P-K method reduce to the same form. This indicates that both methods will provide the same flutter boundary for zero damping. For non-zero g , comparing Eq (9) to Eq (5), it can be seen that the difference between the P-K method equation and the g-method equation lies in the terms \mathbf{Q}'/k in Eq (5) and $\mathbf{Q}'(ik)$ in Eq (9). In fact, \mathbf{Q}'/k is a special case of $\mathbf{Q}'(ik)$. This can be shown as follows:

Expanding $\mathbf{Q}(ik)$ about $ik = 0$ by Taylor's expansion gives:

$$\mathbf{Q}(ik) = \mathbf{Q}(0) + ik \mathbf{Q}'(0) + \frac{1}{2} (ik)^2 \mathbf{Q}''(0) + \dots \quad (10)$$

Since all $\mathbf{Q}''(0)$ are real, $\mathbf{Q}(ik)$ can be split into the real and imaginary parts. It reads:

$$\mathbf{Q}(ik) = \mathbf{Q}^R + i \mathbf{Q}^I \quad (11)$$

where:

$$\mathbf{Q}^R = \mathbf{Q}(0) - \frac{1}{2} k^2 \mathbf{Q}''(0) + \dots \quad (12)$$

and:

$$\mathbf{Q}^I = k \mathbf{Q}'(0) - \frac{1}{6} k^3 \mathbf{Q}'''(0) + \dots \quad (13)$$

Dividing Eq (13) by k gives the term \mathbf{Q}'/k in Eq (5) as:

$$\frac{\mathbf{Q}'}{k} = \mathbf{Q}'(0) - \frac{1}{6} k^2 \mathbf{Q}'''(0) + \dots \quad (14)$$

Differentiating Eq (10) with respect to ik gives the term $\mathbf{Q}'(ik)$ in Eq (9) as:

$$\mathbf{Q}'(ik) = \mathbf{Q}'(0) + ik \mathbf{Q}''(0) + \dots \quad (15)$$

Comparison of Eq (14) with Eq (15) shows that the equality of \mathbf{Q}'/k and $\mathbf{Q}'(ik)$ exists only if $\mathbf{Q}(ik)$ is a linear function of k or at $k=0$. This proves that the

added aerodynamic damping matrix in Eq (5) is valid only if one of the above conditions is satisfied. In fact, if $\mathbf{Q}(ik)$ is highly nonlinear, the P-K method may produce unrealistic roots due to the error from the differences between Eq (14) and Eq (15).

3. Solution Algorithm of the g-Method

Substituting $p = g + ik$ into Eq (9) yields a second-order linear system in terms of g :

$$[g^2 \mathbf{A} + g \mathbf{B} + \mathbf{C}] \{q\} = 0 \quad (16)$$

where:

$$\mathbf{A} = \left(\frac{V}{L} \right)^2 \mathbf{M}$$

$$\mathbf{B} = 2ik \left(\frac{V}{L} \right)^2 \mathbf{M} - \frac{1}{2} \rho V^2 \mathbf{Q}'(ik) + \left(\frac{V}{L} \right) \mathbf{Z}$$

$$\mathbf{C} = -k^2 \left(\frac{V}{L} \right)^2 \mathbf{M} + \mathbf{K} - \frac{1}{2} \rho V^2 \mathbf{Q}(ik) + ik \left(\frac{V}{L} \right) \mathbf{Z}$$

Here, Eq(16) is formally called the g-Method equation. For completeness, in Eq(16), we have included a modal structural damping matrix \mathbf{Z} . The solutions of Eq (16) exist when $\text{Im}(g) = 0$. To search for this condition, we first rewrite Eq (16) in a state space form:

$$[\mathbf{D} - g \mathbf{I}] \{\mathbf{X}\} = 0 \quad (17)$$

where:

$$\mathbf{D} = \begin{bmatrix} 0 & \mathbf{I} \\ -\mathbf{A}^{-1}\mathbf{C} & -\mathbf{A}^{-1}\mathbf{B} \end{bmatrix}$$

Next, a *reduced-frequency-sweep technique* is introduced. This technique searches for the condition $\text{Im}(g) = 0$ and solves for the eigenvalues of \mathbf{D} in term of g ; starting from $k = 0$, incrementally increasing k by Δk , and ending at k_{\max} (k_{\max} is the highest value in the reduced frequency list of the unsteady aerodynamic computations). The reduced frequency-sweep technique searches for the sign change of the imaginary part of the eigenvalues between k and $|k + \Delta k|$. If this occurs, the condition of $\text{Im}(g) = 0$ can be obtained by a linear interpolation in k for the appropriate frequency range. Then the flutter frequency ω_f and damping 2γ are computed by:

$$\omega_f = k \left(\frac{V}{L} \right) \quad (18)$$

$$2\gamma = 2 \frac{\text{Re}(g)}{k} \quad (19)$$

For $k = 0$, an alternative form of Eq (19) is used (Ref 8):

$$2\gamma = \frac{\text{Re}(g) \left(\frac{L}{V} \right)}{\ln(2)} \quad (20)$$

One of the issues in performing the reduced frequency-sweep technique is the eigenvalue tracking from k to $|k + \Delta k|$. In order to monitor the sign change of eigenvalues, it is required that the eigenvalues are lined up at each k and $|k + \Delta k|$. Using the regular sorting scheme by comparing the differences of the eigenvalues at $|k + \Delta k|$ to those at k is certainly not robust and requires small Δk values that may be costly. This eigenvalue tracking issue can be resolved by means of a predictor-corrector scheme.

4. Predictor-Corrector Scheme for Eigenvalue Tracking

The predictor predicts the eigenvalues at $|k + \Delta k|$ by a linear extrapolation from the eigenvalues and their derivatives at k :

$$g_p(k + \Delta k) = g(k) + \Delta k \frac{dg}{dk} \quad (21)$$

where g_p is defined as the predicted eigenvalue. dg/dk can be obtained by using the orthogonality property of the left and right eigenvectors of Eq (17). This leads to:

$$\frac{dg}{dk} = \left(\mathbf{Y}^T \frac{d\mathbf{D}}{dk} \mathbf{X} \right) / \mathbf{Y}^T \mathbf{X} \quad (22)$$

where \mathbf{Y} and \mathbf{X} are the left and right eigenvectors of Eq (17), respectively, and:

$$\frac{d\mathbf{D}}{dk} = \begin{bmatrix} 0 & 0 \\ -\mathbf{A}^{-1} \frac{d\mathbf{C}}{dk} & -\mathbf{A}^{-1} \frac{d\mathbf{B}}{dk} \end{bmatrix} \quad (23)$$

Once g_p is given by the predictor, g_p is used as the baseline eigenvalues for sorting the computed eigenvalues at $|k + \Delta k|$, defined as g_c . The maximum norm of the error between g_p and g_c for all eigenvalues is also computed. If it exceeds a certain level, the predictor could potentially introduce incorrect eigenvalue tracking results due to rapid changes of the eigenvalues. In this case, the corrector is activated.

The corrector reduces the size of Δk by a factor, for instance 100, and recomputes g_p and g_c at $(k + \Delta k/100)$ as well as the maximum norm of the error. This process repeats until the maximum norm of the

error is below a certain level. However, numerical experience shows that when the corrector is activated, this condition can be satisfied by reducing the size of Δk only once. Therefore, the corrector normally would not increase the computational time significantly. It serves only as a fail-safe scheme.

At $k = k_{\max}$, dg/dk is also used to search for the condition $\text{Im}(g) = 0$ at $k > k_{\max}$ by a linear extrapolation. Thus, the reduced-frequency-sweep technique offers a scheme that could find all real roots of Eq (16) in the complete reduced frequency domain.

At this point, the issue of the number of real roots that could exist in Eq (16) is discussed. For n structural modes, the P-K method and K-method normally provide only n roots of the flutter equation. However, as indicated by Ref 10, the number of roots could exceed the number of the structural modes if the aerodynamic lag roots appear. For instance, if the exact Theodorsen function is used, the number of aerodynamic lag roots that would appear is infinite. As one can see, unlike the P-K and K-methods, the reduced frequency-sweep technique employed by the present g-method potentially gives an unlimited number of roots. The inclusion of all activated aerodynamic lag roots could provide important physical interpretations of the flutter solution.

5. Test Cases and Discussed

The test cases for validating the present g-method are selected from those of the User's Guide of MSC/NASTRAN Aeroelastic Analysis (Ref 11). The generalized aerodynamic forces, mass matrices and natural frequencies are obtained from MSC/NASTRAN by the DAMP alter statements. Thus, the difference between the results computed by the P-K method and the g-method is mainly due to the differences in their basic formulation and solution algorithms of these methods.

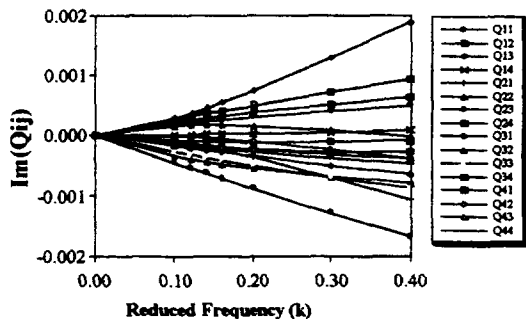


Fig 1 Generalized Aerodynamic Forces vs.
Reduced Frequency of the 15° Sweptback Wing at
 $M = 0.45$, 4 Modes

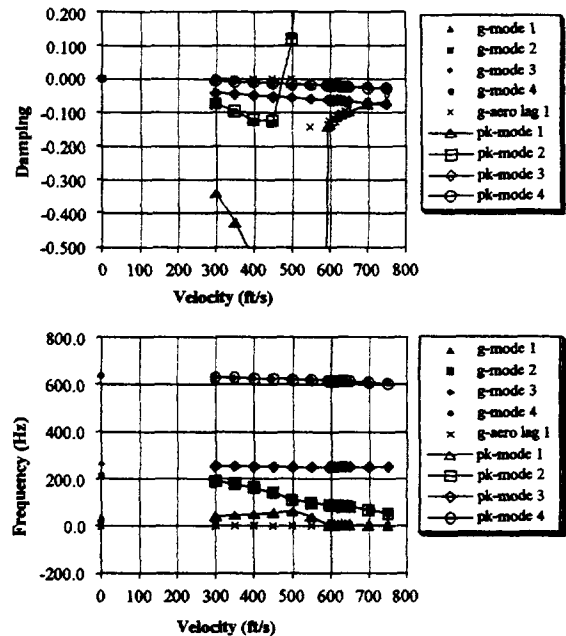


Fig 2 V - g and V - f Diagrams of the 15° Sweptback Wing at $M = 0.45$

The 15-Degree Sweptback Wing at $M=0.45$

This test case is denoted as HA145E in Ref 11. Four structural modes are used for flutter analysis. The imaginary parts of the 4×4 generalized aerodynamic forces matrix (denoted as Q_{ij}) vs. k are presented in Fig 1. Since $\text{Im}(Q_{ij})$ are all nearly linear that gives a close equality of Eq (14) and Eq(15), the agreement between the damping computed by the P-K method and the g-method is expected. Fig 2 shows the damping vs. velocity diagram (v - g diagram) and the flutter frequency vs. velocity diagram (v - f diagram) computed by both methods. Good agreement between these methods is obtained except the g-method predicts one extra aerodynamic lag root (represented by the crosses in Fig 2). This aerodynamic lag root becomes active at $V=550$ ft/sec with stable damping but its frequency remains zero. Since the number of roots computed by the P-K method is restricted to be the same as the number of the structural modes, at $V=600$ ft/sec the P-K method's reduced frequency "lining-up" process skips the bending mode and obtains the aerodynamic lag root; this creates a discontinuity of the damping associated with the bending mode in the v - g diagram (represented by the opened triangles). By contrast, the g-method gives a continuous damping curve of the bending mode (represented by the solid triangles) and a discontinuity in the damping curve of the aerodynamic lag root (the crosses) at $V=550$ ft/sec.

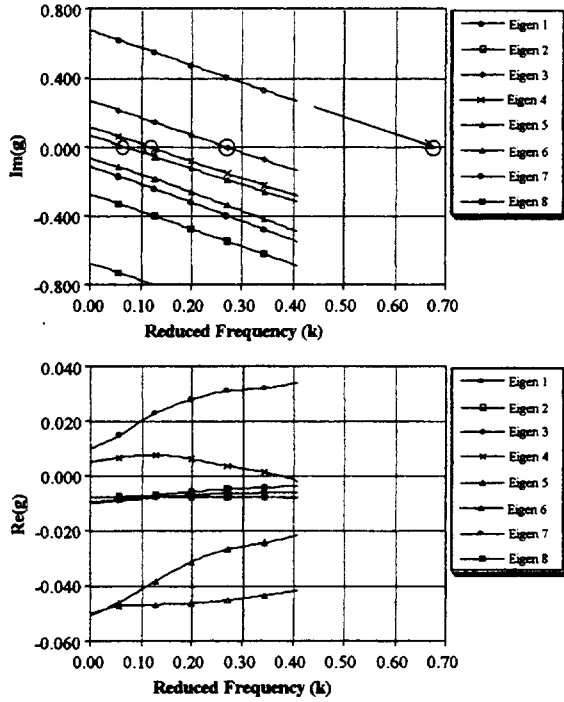


Fig 3 Search History of the Reduced Frequency-Sweep Technique at $V = 500$ ft/sec, (a) Imaginary Damping and (b) Real Damping

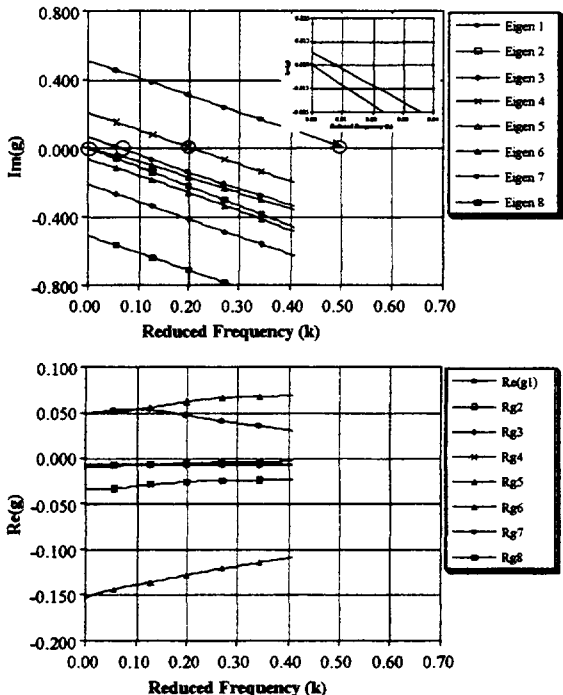


Fig 4 Search History of the Reduced Frequency-Sweep Technique at $V = 600$ ft/sec

In order to investigate how the g-method obtains the aerodynamic lag root, the search history in terms of eigenvalues vs. k for the reduced frequency-sweep technique is presented in Fig 3 for $V=500$ ft/sec and Fig 4 for $V=650$ ft/sec. Since there are 4 structural modes, the state space form of Eq (17) provides 8 eigenvalues. At $V=500$ ft/sec the imaginary parts ($\text{Im}(g)$) of these 8 eigenvalues provide four zero crossings (marked by the opened circles in Fig 3.a). These four zero crossings represent the four roots of the four structural modes. It is noted that the zero crossing of the first eigenvalue is obtained by extrapolation from the eigenvalue and its derivative at $k = k_{\max}$. At $V=650$ ft/sec $\text{Im}(g)$ of the seventh eigenvalue becomes zero at $k=0$ which corresponds to the occurrence of the aerodynamic lag root. This can be seen clearly in the expanded view of $\text{Im}(g)$ at small k (at the upper right corner of Fig 4.a). The real part of this eigenvalue ($\text{Re}(g)$) at $k=0$ has a negative value (Fig 4.b) that indicates this aerodynamic lag root is stable; however, the expanded view shows a potential coupling between the aerodynamic lag root and the sixth eigenvalue since the zero crossing of the sixth eigenvalue already occurs at small k . This indicates an instability may appear at a higher velocity.

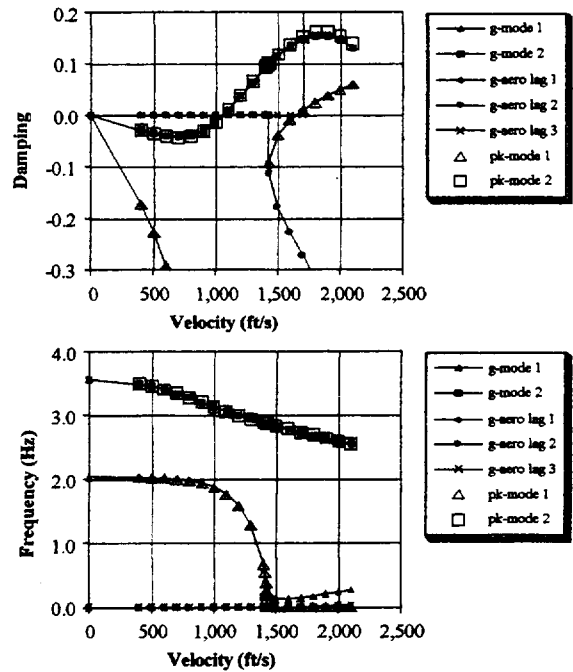


Fig 5 $V-g$ and $V-f$ Diagrams of the BAH Wing, $M = 0.0$, 10 Modes

BAH Wing at $M=0.0$ with 10 Modes

This test case is denoted as HA145b in Ref 11. Ten structural modes are used for flutter analysis but only the results of the first bending and torsion modes are

presented in the v-g and v-f diagrams shown in Fig 5. Two types of instability are predicted by both the P-K method and the g-method: a flutter speed at $V=1056$ ft/sec and a divergence speed at $V=1651$ ft/sec. This agreement is expected since at $g=0$ the flutter equation of both methods reduce to the same form. Three aerodynamic lag roots are obtained by the g-method and their frequencies are all zero throughout the velocity range of interest. Both of the first and second aerodynamic lag roots become active at the same speed ($V=1400$ ft/sec). After this speed, the second aerodynamic lag root forms a super-stable mode but at this speed the damping of the first aerodynamic lag root jumps suddenly from zero to -0.1 then gradually crosses the zero-damping axis, forming a divergence type of instability at $V=1651$ ft/sec. At this divergence speed, the third aerodynamic lag root becomes active and suddenly jumps to a high value of unstable damping (Fig 5.a). This is an interesting phenomenon because it indicates that this divergence speed could be a bifurcation point. Determining the third aerodynamic lag root is bifurcated from the first aerodynamic lag root or originates on its own needs further investigation.

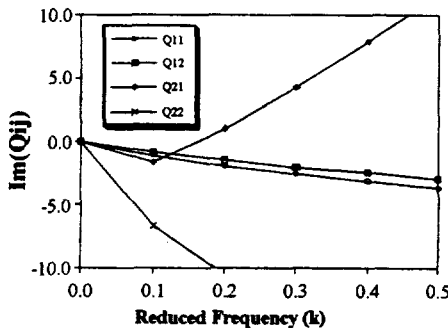


Fig 6 Generalized Forces of 2 D.O.F. Airfoil, C.G. @ 37% Chord (HA145A1), $M = 0.0$, 2 Modes

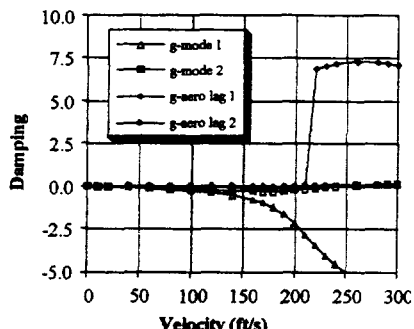


Fig 7 2 D.O.F. Airfoil, C.G. @ 37% Chord (HA145A1), $M = 0.0$, 2 Modes

Similarly to the first test case, the damping curve of the bending mode computed by the P-K method has a discontinuity while that of the g-method remains a smooth curve. The damping curve of the torsion mode computed by both methods are in excellent agreement. The frequency curves of the two structural modes computed by both methods also in good agreement except for the absence of the three aerodynamic lag roots of the P-K method.

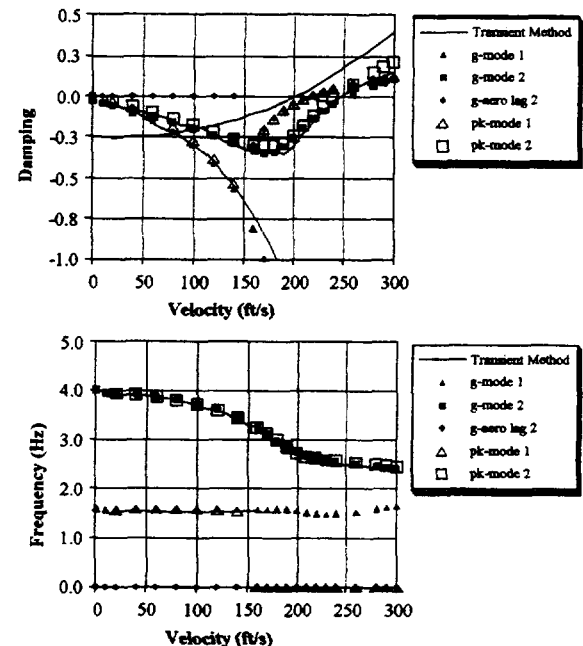


Fig 8 Damping and Frequency vs. Velocity of 2 D.O.F. Airfoil, C.G. @ 37% Chord (HA145A1), $M = 0.0$, 2 Modes

Two Degrees of Freedom Airfoil at $M=0.0$

This test case is adopted from Ref 10 and is derived from the case denoted as HA145A in Ref 11 but with the fuselage grid point being constrained. The center of gravity is located at 37% chord. Fig 6 presents the variations of the 2×2 Q_{ij} vs. k . In this case, Fig 6 shows that the imaginary parts of Q_{ij} is not linear. Therefore, some difference in flutter results between the P-K method and the g-method is expected. First, for clarity, the v-g diagram computed by the g-method alone is presented in Fig 7. Two aerodynamic lag roots are found. Again, it seems that the second aerodynamic lag root is bifurcated from the first one at $V=210$ ft/sec where a divergence instability occurs. The comparison of the damping and flutter frequencies between the P-K method and the g-method is shown in Fig 8; however, for clarity, the second aerodynamic lag root is not repeatedly shown. In Fig 8 the results computed by the transient method (Ref 12) are also presented. The transient method is

based on a time-domain unsteady aerodynamic method, therefore it can be considered as a p-method. All of the three methods predict the same instabilities: a divergence instability at $V=210$ ft/sec and a flutter instability at $V=250$ ft/sec. The damping curves of the first and second modes computed by the g-method correlate well with those of the transient method. But, again, the P-K method gives a discontinuous damping curve of the first mode.

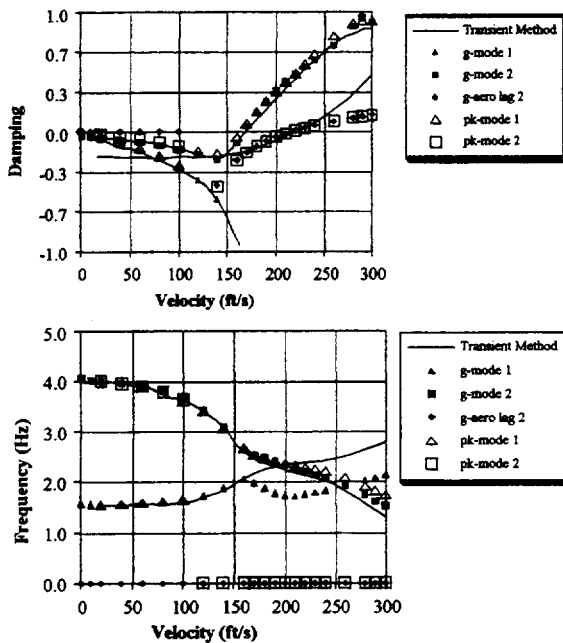


Fig 9 Damping and Frequency vs. Velocity of 2 D.O.F. Airfoil, C.G. @ 45% Chord (HA145A2), $M = 0.0$, 2 Modes

For the case of the center of gravity moved to 45% chord, the v-g diagram shown in Fig 9.a indicates that the flutter instability (at $V=170$ ft/sec) occurs before the divergence instability (at $V=225$ ft/sec). Again, this is well predicted by all three methods. The frequency curves in the v-f diagram (Fig 9.b) computed by the g-method show a similar trend as those of the transient method. But the curves of the P-K method are discontinuous at $V=100$ ft/sec where an aerodynamic lag root appears (not obtained by the transient method but well captured by the g-method). This results a poor correlation of the v-f curves obtained by the P-K method with the other two methods.

Three Degrees of Freedom Airfoil at $M=0.0$

This test case is denoted as HA145A in Ref 11. A fuselage free-free plunge mode is added in the above two degrees of freedom case. The v-g and v-f diagrams for the case of the center of gravity located

at 37% chord are shown in Fig 10 and those for 45% chord are in Fig 11. For both cases, the so-called "dynamic divergence" (Ref 13) occurs and its speeds and frequencies are well predicted by all three methods: the P-K method, the g-method, and the transient method. Both the g-method and the transient method capture one aerodynamic lag root (in the 45% chord case, the g-method obtains a second lag root but it becomes active at the dynamic divergence speed and is not discussed here). Unlike the restrained structures of all previous test cases where the frequency of the lag roots remains zero, the aerodynamic lag root of the present unrestrained structure 'takes off' from the zero-frequency axis then couples with the bending mode. This coupling of the lag root and bending mode forms a "dynamic divergence" instability. As indicated by Ref 13, this dynamic divergence has a non-zero frequency and could be defined as a low-frequency flutter instability. On the other hand, the P-K method generated lag root somehow refuses to 'take off' from the zero-frequency axis. This problem of the P-K method is probably due to the fact that since Q_{ij} of the present test case is nonlinear, the P-K method is valid only at $k=0$ for non-zero damping. This $k=0$ condition restricts the frequency of the lag root from being a non-zero value and results in a poor correlation in the v-f diagram with the other two methods.

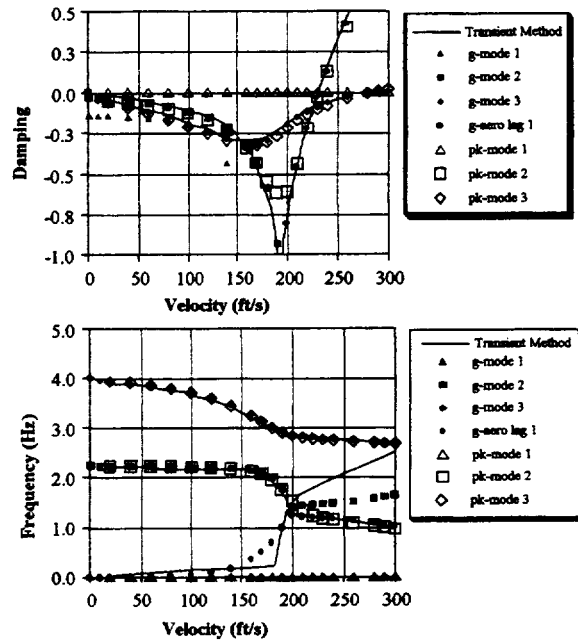


Fig 10 Damping and Frequency vs. Velocity of 3 D.O.F. Airfoil, C.G. @ 37% Chord (HA145A2), $M = 0.0$, 3 Modes

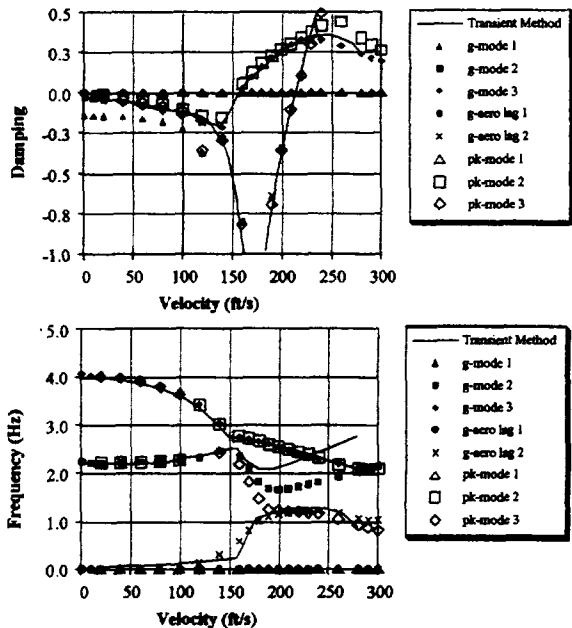


Fig 11 Damping and Frequency vs. Velocity of 3 D.O.F. Airfoil, C.G. @ 45% Chord (HA145A2), $M = 0.0, 3$ Modes

The Johnson Configuration at $M=0.84$ with 17 Modes
 This test case is adopted from Ref 14 and has been discussed in Ref 15. The Johnson configuration has three rigid body modes and 14 elastic modes. The imaginary parts of Q_{ij} vs. k for i and $j = 4, 5$, and 6 presented in Fig 12 show that spikes occur at small k . The cause of the spikes is probably due to poor aerodynamic modeling; but this is not an issue to be discussed here. Since Q_{ij} are highly nonlinear, a large difference between the results obtained from the P-K method and the g-method is anticipated. In fact, in this case the P-K method breaks down (ref 15) and its results are totally unreliable. It is believed that the break-down of the P-K method is caused by the unrealistic roots produced by the nonlinear Q_{ij} . In order to validate the g-method result, the K-method is used for comparison.

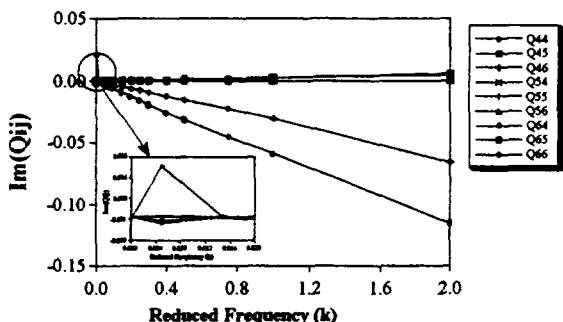


Fig 12 Johnson Configuration Generalized Aerodynamic Forces, $M=0.84, 17$ Modes

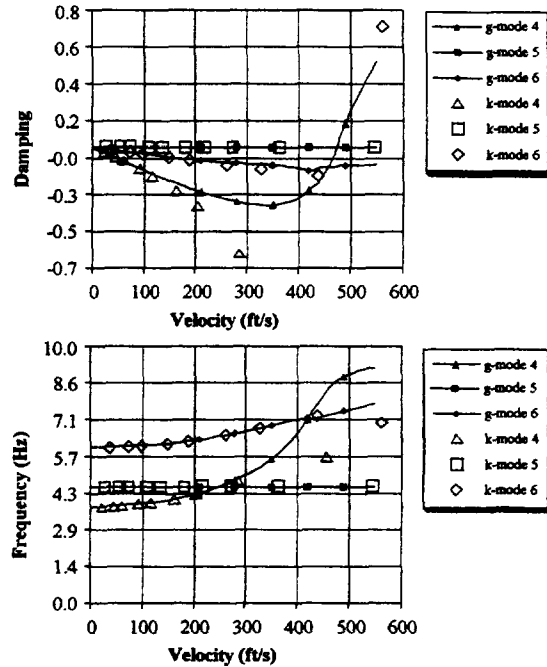


Fig 13 Damping and Frequency vs. Velocity of Johnson Configuration, $M = 0.84, 17$ Modes

There are 13 aerodynamic lag roots obtained by the g-method. Due to the spikes at small k , some of them become active even at very low speed. These lag roots are not presented here. Fig 13 shows the v-g and v-f diagrams obtained by the K-method and the g-method for the first three elastic modes; denoted as mode 4, 5, and 6. It can be seen that both methods predict the same flutter boundary around $V=470$ ft/sec. The good agreement between the K-method and the g-method indicates the robustness of the g-method's solution algorithm.

Conclusions

It is generally believed that the K-method is only valid at the $g=0$ condition. The present work also proves that the P-K method is valid at the conditions of $g=0$, $k=0$, or $d^n Q/dk^n=0$, where $n>1$. The g-method generalizes the K-method and the P-K method. It is valid for all k and up to the first order of g . This first order term of g is rigorously derived from $Q(p)$ by a damping perturbation method.

The present work also provides a theoretical foundation for the g-method that can be used to estimate the error of large damping (beyond the first order assumption) due to the truncation of the higher order terms of g . However, based on the formulation of the g-method, adding higher order terms in g seems to be straightforward.

6. References

1. Irwin, C.A. and Guyett, P.R., "The Subcritical Response and Flutter of a Swept Wing Model," Tech. Rept. 65186, Aug. 1965, Royal Aircraft Establishment, Farnborough, U.K.
2. Hassig, H.J., "An Approximate True Damping Solution of the Flutter Equation by Determinant Iteration," Journal of Aircraft, Vol. 8, No. 11, November 1971.
3. Albano, E. and Rodden, W.P., "A Doublet-Lattice Method for Calculating Lift Distributions on Oscillating Surfaces in Subsonic Flows," AIAA Journal, Vol. 7, No. 2, Feb. 1969, pp. 279-285.
4. Chen, P.C. and Liu, D.D., "A Harmonic Gradient Method for Unsteady Supersonic Flow Calculations," Journal of Aircraft, Vol. 22, No. 5, May 1985, pp. 371-379.
5. Chen, P.C., Liu, D.D., "Unsteady Supersonic Computations of Arbitrary Wing-Body Configurations Including External Stores," Journal of Aircraft, Vol. 27, No. 2, Feb. 1990, pp. 108-116.
6. Chen, P.C., Lee, H.W. and Liu, D.D., "Unsteady Subsonic Aerodynamics for Bodies and Wings with External Stores Including Wake Effect," Journal of Aircraft, Vol. 30, No. 5, Sep-Oct. 1993, pp. 618-628.
7. Rodden, W.P., Harder, R.L., and Bellinger, E.D., "Aeroelastic Addition to NASTRAN," NASA CR 3094, 1979.
8. Rodden, W.P., "Handbook for Aeroelastic Analysis," Volume 1, MSC/NASTRAN Version 65.
9. Stark, V.J., "General Equations of Motion for an Elastic Wing and Method of Solution," AIAA Journal, Vol. 22, No. 8, Aug. 1984.
10. Rodden, W.P. and Bellinger, E.D., "Aerodynamic Lag Functions, Divergence and the British Flutter Method," Journal of Aircraft, Vol. 19, No. 7, July 1982.
11. Rodden, W.P. and Johnson, E.H., "User's Guide of MSC/NASTRAN Aeroelastic Analysis," MSC/NASTRAN V68.
12. Rodden, W.P. and Stahl, B., "A Strip Method for Prediction of Damping in Subsonic Wind Tunnel and Flight Flutter Test," Journal of Aircraft, Vol. 6, No. 1, Jan-Feb. 1969, pp. 9-17.
13. Rodden, W.P. and Bellinger, E.D., "Unrestrained Aeroelastic Divergence in a Dynamic Stability Analysis," Journal of Aircraft, Vol. 19, No. 9, Sep. 1982.
14. Johnson, E.H., Private communication.
15. Johnson, E.H., "MSC/NASTRAN User's Guide for Aeroelastic Analysis," Presented at Aerospace Flutter and Dynamics Council. Seattle, Washington. May 19, 1995.

REPORT DOCUMENTATION PAGE			Form Approved OMB No. 07704-0188
<p>Public reporting burden for this collection of information is estimated to average 1 hour per response, including the time for reviewing instructions, searching existing data sources, gathering and maintaining the data needed, and completing and reviewing the collection of information. Send comments regarding this burden estimate or any other aspect of this collection of information, including suggestions for reducing this burden, to Washington Headquarters Services, Directorate for Information Operations and Reports, 1215 Jefferson Davis Highway, Suite 1204, Arlington, VA 22202-4302, and to the Office of Management and Budget, Paperwork Reduction Project (0704-0188), Washington, DC 20503.</p>			
1. AGENCY USE ONLY (Leave blank)	2. REPORT DATE June 1999	3. REPORT TYPE AND DATES COVERED Conference Publication	
4. TITLE AND SUBTITLE CEAS/AIAA/ICASE/NASA Langley International Forum on Aeroelasticity and Structural Dynamics 1999		5. FUNDING NUMBERS 505-90-52-01	
6. AUTHOR(S) Woodrow Whitlow, Jr., and Emily N. Todd			
7. PERFORMING ORGANIZATION NAME(S) AND ADDRESS(ES) NASA Langley Research Center Hampton, VA 23681-2199		8. PERFORMING ORGANIZATION REPORT NUMBER L-17863A	
9. SPONSORING/MONITORING AGENCY NAME(S) AND ADDRESS(ES) National Aeronautics and Space Administration Washington, DC 20546-0001		10. SPONSORING/MONITORING AGENCY REPORT NUMBER NASA/CP-1999-209136/PT 1	
11. SUPPLEMENTARY NOTES Whitlow: NASA John H. Glenn Research Center at Lewis Field, Cleveland, OH Todd: Institute for Computer Applications in Science and Technology (ICASE), Hampton, VA			
12a. DISTRIBUTION/AVAILABILITY STATEMENT Unclassified—Unlimited Subject Category 02 Availability: NASA CASI (301) 621-0390		12b. DISTRIBUTION CODE	
13. ABSTRACT (Maximum 200 words) These proceedings represent a collection of the latest advances in aeroelasticity and structural dynamics from the world community. Research in the areas of unsteady aerodynamics and aeroelasticity, structural modeling and optimization, active control and adaptive structures, landing dynamics, certification and qualification, and validation testing are highlighted in the collection of papers. The wide range of results will lead to advances in the prediction and control of the structural response of aircraft and spacecraft.			
14. SUBJECT TERMS Aeroelasticity; Unsteady aerodynamics; Computational fluid dynamics; Flutter; Multidisciplinary design optimization; Structural optimization; Structural dynamics; Smart materials; Active control		15. NUMBER OF PAGES 437	
		16. PRICE CODE A19	
17. SECURITY CLASSIFICATION OF REPORT Unclassified	18. SECURITY CLASSIFICATION OF THIS PAGE Unclassified	19. SECURITY CLASSIFICATION OF ABSTRACT Unclassified	20. LIMITATION OF ABSTRACT UL